PASSIVE NONDESTRUCTIVE ASSAY OF NUCLEAR MATERIALS

2007 ADDENDUM

DOUGLAS REILLY – Technical Editor

The nondestructive assay reference; ***Passive Nondestructive Assay of Nuclear Material***; Reilly, Ensslin, Smith, and Kreiner, was published in 1991 although the major technical writing was completed by 1987. This book has become widely known by the acronym ***PANDA***. Although much of the material contained therein is still valid, there has been considerable development in the field during the intervening twenty years. The two remaining editors/authors of the original book felt that it would be valuable to produce an Addendum to cover some of the more recent developments and some of the measurement technology omitted from ***PANDA***.

In 2002, Norbert Ensslin proposed a project to the US Department of Energy that would develop an appropriate set of additional chapters to complement the original ***PANDA***. The DOE agreed to fund this effort and work began on the Addendum early in 2003, when Doug Reilly returned to Los Alamos from the IAEA Safeguards Training Section.

As the writing project neared its conclusion, it was decided that the materials would be issued as Los Alamos National Laboratory reports on a compact disk and as .pdf files available on the internet website of the Safeguards Science and Technology Group, N-1, at LANL. The CD is available by contacting N-1.

Chapter 1, "Gamma-Ray Detectors for Nondestructive Analysis," LA-UR-05-3813, was written by Phyllis Russo and Duc Vo. Whereas ***PANDA*** treated only high-purity germanium and NaI(Tl) detectors, this chapter treats other alkali-halide detectors, scintillator-photodiode detectors, lanthanum scintillators, non-cryogenic semiconductor detectors, high-pressure Xe detectors, Pb-loaded scintillators, and micro-calorimeters, in addition to advances in NaI and HpGe.

Chapter 2, "Plutonium Isotopic Analysis Using PC/FRAM," LA-UR-03-4403, was written by Thomas Sampson. It covers the theory and operation of the PC/FRAM code and its performance in interlaboratory comparisons and various actual applications. It also covers the analysis of uranium spectra.

Chapter 3, "Measurement of Plutonium and Uranium Isotopics with MGA/MGAU," is being written by staff at Lawrence Livermore National Laboratory and is not yet available. These codes are extensively used internationally and the chapter covers theory, operation, and applications.

Chapter 4, "Tomographic Gamma-Ray Scanning of Uranium and Plutonium," LA-UR-07-5150, was written by Steven Hansen. This covers first the basic principles of tomography with simple examples of how tomographic images are formed and how voxel (volume element) mass and opacity are calculated. It then describes the design and operation of TGS systems and the performance of a system to characterize waste sent to the Waste Isolation Pilot Project (WIPP) in New Mexico. The chapter ends with a discussion of lump-correction techniques and an innovative technique for U lump correction.

Chapter 5, "Nondestructive Assay of Holdup," LA-UR-07-5149, was written by Douglas Reilly. This is an extension of ***PANDA*** chapter 20 that covers new corrections developed by Phyllis Russo for the Generalized Geometry Holdup (GGH) method and new applications and performance results.

Chapter 6, "Passive Neutron Multiplicity Counting," LA-UR-07-1402, was written by Norbert Ensslin, Merlyn Krick, Mark Pickrell, Doug Reilly, and Jim Stewart. ***PANDA*** covered neutron coincidence counting, but multiplicity counting was under development when it was published. The chapter covers the mathematical theory of triple coincidence counting, detector design, existing detectors and electronics, the multiplicity shift register, and multiplicity applications and performance.

Chapter 7, "Active Neutron Multiplicity Counting," LA-UR-07-1403, was written by Norbert Ensslin, Bill Geist, Merlyn Krick, and Mark Pickrell. Active multiplicity counting was developed to supplement active coincidence counting for ^{235}U materials. It does not have a "closed" solution as does passive multiplicity counting, but it may offer a promising technique for samples that are not amenable to coincidence counting. The chapter covers the theory and application of the technique.

Chapter 8, "Fast and Epithermal Neutron Multiplicity Counter," LA-UR-07-1602, was written by Mark Pickrell, Kevin Veal, and Norbert Ensslin. This chapter discusses the design and application of Epithermal Neutron (ENMC) and Fiber-Based Fast Neutron counters. Both of these counters address the problem of excessive accidentals from some samples by lowering the neutron die-away time of the counter. The ENMC is already in use and the Fiber-Based counter is still an experimental project.

Chapter 9, "Shufflers," LA-UR-03-4404, was written by Phillip Rinard. The Shuffler uses the principle of Delayed-Neutron Activation Analysis that was investigated using pulsed neutron generators in the very early days of the Los Alamos safeguards program. Instead of a neutron generator, the shuffler uses an intense ^{252}Cf neutron source that is moved close to the measured sample to induce fissions and quickly removed to a shield while delayed-neutrons from the fissions are counted. The chapter discusses basic theory, shuffler design, calibration, data analysis, and performance.

Chapter 10, "Principles and Applications of Calorimetric Assay," LA-UR-07-XXXX, was written by David Bracken and Clifford Rudy. This is a more comprehensive exposition of calorimetry than is given in ***PANDA*** chapters 21 and 22. The chapter covers heat-flow calorimeter theory, operation, calibration, and performance. Calorimetry applications to plutonium and tritium are covered, in addition to recent work on calorimetry of HEU.

Chapter 11, "Useful Nuclear Data," was compiled by Doug Reilly. This includes, among other things, a listing of nuclear data tables and figures in PANDA and Ray Gunnink's tabulation of x rays and γ rays from the principal isotopes of uranium and plutonium.

Index: A comprehensive topical index will be added at a later date. The following Table of Contents shows the contents of the Addendum.

Acknowledgements: I would like to acknowledge, especially, Norbert Ensslin for initiating this project and giving it his continued interest and support, even after his retirement from Los Alamos in 2005. Norbert obtained the necessary funding for the project and was a principal author of three of the chapters. This Addendum to PANDA would never exist were it not for Norbert's efforts. Next, I wish to recognize the support and funding of the U. S. Department of Energy, SO-13/20, and the project manager, Lynne Preston. Of course none of the chapters included herein could exist without the efforts of the fifteen principal authors. Lastly, I must recognize the support and encouragement received from the N-1 group management. Thank you everybody.

TABLE OF CONTENTS – PANDA 2007 ADDENDUM

1. GAMMA-RAY DETECTORS FOR NONDESTRUCTIVE ANALYSIS
P. A. Russo and D. T. Vo
I. Introduction and Overview 1-1
II. Sodium Iodide and other Alkali-Halide Scintillators 1-4
III. Scintillator-Photodiode Detectors 1-8
IV. Inorganic Lanthanum and Rare-Earth Scintillators 1-11
V. GE Detectors and Cryogenics 1-16
VI. Non-cryogenic Portable Semi-Conductor Detectors 1-22
CPG CdZnTe 1-22
Electrically Cooled CdTe 1-23
HgI_2 1-25
VII. Gas-Filled Detectors: High-Pressure Xe Ionization Chambers 1-26
VIII. Organic Scintillators: Pb-Loaded Plastic for DNS 1-30
End Notes 1-32
References 1-35

2. PLUTONIUM ISOTOPIC ANALYSIS USING PC/FRAM
Thomas E. Sampson
I. INTRODUCTION 2-1
A. Purpose of This Chapter 2-1
B. Isotopic Analysis Applications in Nondestructive Assay 2-1
1. Calorimetry. 2-1
2. Neutron Coincidence Counting. 2-2
3. Other Bulk Measurement Techniques. 2-3
4. Process Control 2-3
5. Treaty Verification. 2-4
II. BASIC PRINCIPLES OF GAMMA-RAY ISOTOPIC ANALYSIS FOR THE ARBITRARY SAMPLE 2-4
A. Gamma-Ray Measurement of Isotopic Ratios 2-4
B. Ratio Measurements for the Arbitrary Sample—Without Efficiency Corrections 2-4
C. The Intrinsic Self-Calibration Technique 2-5
D. The Relative Efficiency Concept 2-5
E. Relative Efficiency Models 2-6
1. Empirical Model 2-7
2. Physical Model 2-7
3. Isotopic Heterogeneity 2-8
III. PC/FRAM 2-9
A. Development 2-9
B. Single Detector System 2-9
C. Choice of Detector Type 2-10
D. Shielded Samples 2-10
E. Uranium Isotopic Analysis 2-10
F. Version 4 2-11
IV. HOW FRAM WORKS 2-11
A. Obtain Data 2-11
B. Perform Analysis 2-12

1. Internal Calibrations 2-12
a. Energy Calibration 2-12
b. Initial Background 2-12
c. FWHM Calibration 2-12
d. Peak Shape/Tailing Calibration 2-13
2. Analysis of Spectral Data 2-13
a. Calculate Peak Areas Using Response Functions 2-13
b. Calculate Relative Efficiencies 2-14
c. Calculate Relative Activities 2-14
d. Calculate Isotopic Fractions 2-14
e. Calculate Isotopic Correlation for ^{242}Pu and ^{236}U 2-14
V. Parameter files, the key to FRAM's versatility 2-15
VI. FRAM USER INTERFACE 2-15
A. File 2-15
B. Edit 2-16
C. Measure 2-16
D. Options 2-16
VII. FRAM PERFORMANCE 2-18
A. Measurement Precision or Repeatability 2-18
1. Definitions 2-18
2. Influencing Factors 2-19
a. Count Rate and Throughput 2-19
b. Electronic Settings 2-20
c. Count Time 2-20
d. Energy Range 2-21
e. Detector Type 2-22
f. Sample Characteristics 2-23
3. Prediction of Precision in the FRAM Code 2-23
4. Examples of FRAM's Statistical Precision 2-24
B. Measurement Bias 2-27
1. Introduction 2-27
2. Plutonium Measurement Bias 2-27
3. Uranium Measurement Bias 2-29
4. MOX Measurement Bias 2-29
C. Intercomparison Exercises 2-30
1. The PIDIE Exercise 2-30
2. Uranium Enrichment Measurement Exercise, IRMM 1996 2-31
3. The Pu-2000 Exercise 2-31
D. Factors Influencing Measurement Bias 2-32
1. Sample Composition Characteristics 2-32
2. Branching Ratios 2-32
3. Coincidence Summing 2-32
a. Uranium 2-33
b. Plutonium 2-33
4. Peak Area Determination 2-33
a. Background Shape 2-33
b. Interferences 2-34
E. Bias Correction 2-35
1. Adjustment of Branching Ratios 2-35
2. Observation of Peak Area Biases 2-36

3. Least-Squares Adjustment of Branching Ratios 2-36
4. Use of Standards 2-36
VIII. MAKING MEASUREMENTS FOR FRAM ANALYSIS 2-36
A. Choice of Detector 2-37
B. Choice of Energy Range 2-38
C. Collection of Pulse Height Spectra 2-38
1. Electronics 2-38
2. Count Rate Considerations 2-38
3. Pulse Pileup 2-40
a. Coincidence Summing 2-40
b. Random Summing 2-40
4. Filtering 2-40
5. Shielding 2-42
IX. DIFFICULT MEASUREMENT SITUATIONS 2-43
A. Using FRAM With Rate-Loss Correction Sources 2-43
B. Simultaneous FRAM/AWCC Measurements 2-43
C. Measurements Through Thick Shielding 2-43
1. Steel Shielding 2-43
a. Plutonium 2-43
b. Uranium 2-44
2. Lead Shielding 2-46
3. 9975 Shipping Container 2-46
D. Measurements of Am-Be Neutron Sources 2-47
E. Measuring Samples with ^{237}Np 2-47
F. Measuring Samples with Very High ^{241}Am 2-48
G. Measuring Heat-Source Grade ^{238}Pu 2-49
X. FRAM APPLICATION WITH CADMIUM TELLURIDE (CdTe) DETECTORS 2-50
XI. FRAM APPLICATIONS IN AUTOMATED SYSTEMS 2-51
A. ROBOCAL 2-51
1. Intelligent Isotopic Unit Autoanalysis 2-51
2. Intelligent Isotopic Unit Hardware 2-52
B. ARIES NDA System 2-53
REFERENCES 2-54

3. MEASUREMENT OF PLUTONIUM AND URANIUM ISOTOPICS (MGA/MGAU)

4. TOMOGRAPHIC GAMMA-RAY SCANNING OF URANIUM AND PLUTONIUM
J. Steven Hansen
I. INTRODUCTION 4-1
II. MEASUREMENTS PRINCIPLES 4-2
A. General Concepts 4-2
B. Understanding Tomographic Image Reconstruction 4-6
C. Defining the Geometry 4-10
D. Attenuation and Emission Maps 4-12
E. Detector Response Function 4-13
III. TGS Design Considerations 4-14
A. Transmission Source assembly 4-15
B. Detector Assembly 4-15
C. Sample Positioning System 4-16

D. Data Acquisition System 4-16
E. Data Analysis System 4-16
IV. Performance Evaluation in Blind Tests and Actual Facility Measurements 4-17
A. Performance Demonstration Program (PDP) 4-17
B. RFETS Pyrochemical Salts 4-19
C. Uranium Applications 4-21
1. RFETS Experience 4-21
2. Survey of Excess HEU Materials across the DOE Complex (Refs. 25-26) 4-22
3. Relative Comparison of TGS Measurements of HEU and Pu (Ref. 27) 4-22
V. Lump Correction Techniques 4-24
A. Plutonium Lump Detection and Correction Technique 4-24
B. Standard Pu Lump Correction Doesn't Work for Uranium 4-25
C. Proposed Technique for Uranium Lump Correction 4-25
VI. Commercially Available Systems 4-27
References: 4-28

5. NONDESTRUCTIVE ASSAY OF HOLDUP
T. Douglas Reilly
I. INTRODUCTION 5-1
II. GAMMA-RAY SIGNATURES AND EQUIPMENT 5-1
III. GENERALIZED GEOMETRY HOLDUP (GGH) ASSAY METHOD 5-3
A. Assumptions and Constraints 5-3
B. Calibration 5-4
C. Performing the GGH Measurement and Assay 5-5
D. CORRECTION FOR EQUIPMENT ATTENUATION 5-6
E. CORRECTION FOR FINITE SOURCE DIMENSIONS 5-6
1. Finite Sources in Holdup Measurements 5-6
2. Concept of a Finite Source 5-7
3. Correcting a Measured Holdup Deposit for Finite Source Dimensions 5-7
F. CORRECTION FOR SELF-ATTENUATION EFFECTS 5-8
1. Self-Attenuation Effects in Holdup Measurements 5-8
2. Determining the Self-Attenuation Correction from the Measured Areal Density 5-9
3. Correcting a Measured Holdup Deposit for Self-Attenuation 5-9
IV. HOLDUP MEASUREMENT SYSTEM EXAMPLES 5-9
V. NEUTRON HOLDUP MEASUREMENTS 5-11
VI. ACCURACY OF GAMMA-RAY AND NEUTRON HOLDUP MEASUREMENTS 5-14
VII.SUMMARY 5-15
REFERENCES 5-16

6. PASSIVE NEUTRON MULTIPLICITY COUNTING
N. Ensslin, M. S. Krick, D. G. Langner, M. M. Pickrell, T. D. Reilly, and J. E. Stewart
6.1. INTRODUCTION 6-1
6.1.1 Purpose of the Chapter 6-1
6.1.2. Definition of Neutron Multiplicity Counting 6-1
6.1.3. Basic Principle of Neutron Multiplicity Counting 6-2
6.1.4. Historical Reasons for Multiplicity Counting 6-3
6.1.5. Areas of Application for Multiplicity Counting 6-4
6.1.6. Advantages and Disadvantages of Multiplicity Counting 6-4
6.2. MULTIPLICITY COUNTER DESIGN PRINCIPLES 6-4
6.2.1. Multiplicity Counter Design Goals 6-4

6.2.2. Monte Carlo Design Calculations 6-5
6.2.3. Figure of Merit Calculations 6-6
6.3. SOME EXISTING MULTIPLICITY COUNTERS 6-7
6.3.1. Basic Differences between Multiplicity and Conventional Coincidence Counters 6-7
6.3.2. In-Plant (Pyrochemical) Multiplicity Counter 6-7
6.3.3. Plutonium Scrap Multiplicity Counter 6-9
6.3.4. FB-Line Multiplicity Counter 6-9
6.3.5. 30-Gallon Multiplicity Counters 6-9
6.3.6. High-Efficiency Neutron Counter (HENC) 6-10
6.3.7. Epithermal Neutron Multiplicity Counters 6-11
6.3.8. SuperHENC Multiplicity Counter 6-11
6.4. MULTIPLICITY ELECTRONICS 6-11
6.4.1. Thermal Neutron Detection Electronics 6-11
6.4.2. Derandomizer Circuit 6-12
6.4.3. The Neutron Pulse Stream and Coincidence Gates 6-13
6.4.4. Predelay Circuit 6-13
6.4.5. Multiplicity Shift Register Basics 6-14
6.4.6 Deployed Multiplicity Shift Registers 6-16
6.5. MULTIPLICITY MATHEMATICS 6-16
6.5.1. Assumptions in the Equations 6-16
6.5.2. The Spontaneous Fission Process 6-17
6.5.3. Description of (α,n) Reactions 6-17
6.5.4. Definition of Sample Multiplication 6-18
6.5.5. Measured Singles, Doubles, and Triples Count Rates 6-18
6.5.6. Analytical Definition of Singles, Doubles, and Triples Count Rates 6-19
6.5.7. Final Solution for Sample Mass, Multiplication, α 6-20
6.5.8 Weighted Point Model Equations 6-21
6.6. MULTIPLICITY CALIBRATION AND MEASUREMENT CONTROL 6-21
6.6.1. Multiplicity Data Analysis Software 6-21
6.6.2. Detector Characterization Measurements 6-22
6.6.3. Multiplicity Calibration Procedure 6-22
6.6.4. Multiplication Bias Correction 6-23
6.6.5. Ring Ratio Diagnostic 6-24
6.6.6. Measurement Control Procedures 6-24
6.7. PASSIVE MULTIPLICITY APPLICATIONS AND PERFORMANCE 6-25
6.7.1. Expected Assay Precision 6-25
6.7.2. Typical Assay Bias 6-25
6.7.3. Plutonium Metal 6-26
6.7.4. Plutonium Oxide 6-26
6.7.5. Plutonium Scrap 6-28
6.7.6. Plutonium Residues 6-28
6.7.7. Plutonium Waste 6-29
6.7.8. Mixed Uranium/Plutonium Oxide 6-29
6.7.9. Plutonium Inventory Verification 6-29
REFERENCES 6-31

7. ACTIVE NEUTRON MULTIPLICITY COUNTING
N. Ensslin, W. H. Geist, M. S. Krick, and M. M. Pickrell
7.1. INTRODUCTION 7-1
7.1.1. Definition of Active Neutron Multiplicity Counting 7-1
7.1.2. Historical Reasons for Active Multiplicity Counting 7-1
7.1.3. Areas of Application for Active Multiplicity Counting 7-2

7.1.4. Advantages and Disadvantages of Active Multiplicity Counting 7-2
7.2. ACTIVE MULTIPLICITY EQUATIONS 7-3
7.2.1. Overview 7-3
7.2.2. Singles, Doubles, and Triples Count Rates 7-3
7.2.3. Calculation of Sample Self-Multiplication 7-4
7.2.4. Definition of Sample Coupling 7-5
7.2.5. Determination of Uranium Mass 7-8
7.3. ACTIVE MULTIPLICITY MEASUREMENT PROCEDURES 7-8
7.3.1. Measurement Hardware 7-8
7.3.2. Measurement Software 7-9
7.3.3. Detector Characterization 7-9
7.3.4. Measurement Control and Calibration 7-10
7.3.5. Item Measurement Procedure 7-11
7.4. ACTIVE MULTIPLICITY COUNTING PRECISION 7-12
7.4.1. Calculation of Expected Counting Precision 7-12
7.4.2. Results for Thermal Neutron Counting 7-12
7.4.3. Results for Epithermal Neutron Counting 7-13
7.4.4. Results for a Future Fast Neutron Counter 7-14
7.5. ACTIVE MULTIPLICITY MEASUREMENT PERFORMANCE 7-14
7.5.1. Factors that Affect Measurement Performance 7-14
7.5.2. Uranium Metal Field Measurements 7-15
7.5.3. Uranium Oxide Field Measurements 7-16
7.5.4. Laboratory Measurements of Uranium Metal Standards 7-16
7.5.5. Uranium Metal and Oxide Modeling Results 7-18
7.5.6. Modeling of Inhomogeneous Uranium Items 7-19
7.5.7. Expectations for Other HEU Materials 7-20
REFERENCES 7-20

8. FAST AND EPITHERMAL NEUTRON MULTIPLICITY COUNTERS
Mark M. Pickrell, Kevin Veal, and Norbert Ensslin
I. Introduction and Problem Statement 8-1
II. Measurement Problems Addressed by Epithermal Neutron Counting 8-1
A. Impure Plutonium 8-2
B. HEU Materials 8-2
C. Mixed HEU/Pu 8-2
D. Additional Applications for Fast Neutron Counters 8-3
III. The Physics of High Accidentals Multiplicity Counting 8-3
IV. Fast and Epithermal Neutron Multiplicity Counters 8-9
A. Epithermal Neutron Multiplicity Counter 8-10
B. Fast Neutron Counters 8-15
V. References 8-16

9. SHUFFLERS
Phillip M. Rinard
I. INTRODUCTION 9-1
A. Purpose of this Chapter 9-1
B. The Motivation for Shufflers 9-1
1. History of Shufflers 9-1
2. The Shuffler's Role Among Other NDA Instruments 9-1
3. Applications of Los Alamos Shufflers 9-2

a. Savannah River Uranium Scrap Shuffler 9-3
b. Savannah River Billet Shuffler 9-3
c. The “Standard” 200-liter-Drum Shuffler and Its Predecessors 9-3
d. The “Pass-Through” 200-liter-Drum and Boxed-Waste Shufflers 9-5
e. Spent Naval Fuel Shuffler 9-5
f. Dounreay Reprocessing Solid-Waste Shuffler 9-6
4. Applications of Shufflers in Europe 9-7
C. Shuffler Basics 9-7
1. Delayed Neutrons 9-7
2. The Shuffler Principle 9-8
3. Pertinent Properties of ^{252}Cf 9-9
4. Factors That Complicate Assays 9-12
II. SHUFFLER PERFORMANCE 9-12
A. Precision 9-13
B. Accuracy 9-13
C. Sensitivity or Minimum Detectable Mass 9-16
D. Choosing the Assay Time 9-17
III. CREATING A SHUFFLER 9-18
A. Basic components 9-18
1. Hardware 9-18
2. Software 9-19
3. Safety features 9-19
B. Physics Design 9-20
1. User Specifications 9-20
2. Minimum Delayed Neutron Count Rate 9-20
3. The Minimum ^{252}Cf Mass, Detection Efficiency, and Assay Chamber Shape 9-20
4. The Initial ^{252}Cf Mass 9-21
5. ^{252}Cf Shielding 9-21
a. Storage Block 9-22
b. Assay Chamber Walls 9-22
6. Assay Chamber 9-23
7. Detector Tube Arrays 9-23
8. ^{252}Cf Motion Requirements 9-23
IV. CALIBRATION PROCEDURES 9-24
A. Matrix Issues 9-24
B. Calculated Calibrations 9-25
C. Enrichment Issues 9-26
V. DATA ANALYSIS 9-26
A. Raw Count Rates 9-26
1. Background Counts 9-27
2. Flux Monitor Counts 9-27
3. Post-irradiation Counts 9-27
B. Background Subtraction 9-27
C. ^{252}Cf Decay Correction 9-27
D. Flux Monitor Matrix Correction 9-27
E. Calibration Curve 9-27
F. Measurement Control 9-28
REFERENCES 9-28

10. PRINCIPLES AND APPLICATIONS OF CALORIMETRIC ASSAY

D. S. Bracken, and C. R. Rudy

I. Introduction 10-1
- Uniqueness of Calorimetry NDA 10-1
  - Advantages 10-1
  - Limitations 10-2
- Thermal Power Production from Radionuclides 10-2

II. Heat-Flow Calorimeter Operation, Calibration, and Calculations Heat-Flow Calorimeters 10-3
- Heat-Flow Calorimeters 10-4
- Calorimetric Assay Overview 10-5
  - Mass Calculation 10-6
  - Specific Power 10-6
  - Effective Specific Power 10-6
  - Passive Mode 10-7
  - Servo Mode 10-9
- Assay Error Determination 10-10
  - Mixed Radionuclides Example: Plutonium and ^{241}Am Mass 10-10
  - Single Radionuclide Example Tritium Mass 10-11

III. Measurement Performance 10-12
- Calorimetric Assay Precision and Bias Data 10-12
  - Calorimetry Exchange 10-12
  - Heat Standards 10-14
  - Tritium 10-14
  - Automated Plutonium Assay System (APAS) 10-15
- Possible Sources of Bias Due to Calorimeter Design 10-15
  - Weight Effects 10-15
  - Heat Distribution Error (HDE) 10-16
  - Heater-Lead Error 10-16
- Possible Assay Interferences 10-17
- Parameters Affecting Assay Time 10-18

IV. Types of Heat-Flow Calorimeters 10-19
- Water-Bath Calorimeter 10-19
- Solid-State Calorimeter 10-22
- Large Volume Calorimeter (LVC) 10-23
- Isothermal “Air-Bath” Calorimeter 10-24
- Rod Calorimeter 10-24

V. Calorimetric Assay Applications 10-25
- Plutonium 10-25
- ^{238}Pu Heat Standards Calibration and Traceability 10-26
- Tritium 10-27
- Highly Enriched Uranium (HEU) 10-27
- ^{233}U 10-27

VI. Calorimetry Applied in Unconventional Ways 10-30
- Combined Calorimetry/Neutron/Gamma-Ray Assay 10-30
- Uranium Enrichment by Combined Calorimetry/Neutron Counting 10-32
- Calorimetric Specific Activity Determination 10-33

VII. References 10-33

11. Useful Nuclear Data

1. Principal NDA Gamma-Ray Signatures
2. Major Gamma-Rays from Common Calibration Sources
3. Major K x rays of uranium and plutonium
4. Gamma Rays of ^{238}Pu
5. Gamma Rays of ^{239}Pu
6. Gamma Rays of ^{240}Pu
7. Gamma Rays of ^{241}Pu
8. Gamma Rays of ^{237}U
9. Gamma Rays of ^{241}Am
10. Kα x-ray energies, intensities and intrinsic line widths
11. Mass attenuation coefficients for various elements
12. Spontaneous Fission Neutron Yields
13. (α,n) Neutron Yields
14. Thick-Target Yields from (α,n) Reactions
15. Nuclear Data Table and Figures in PANDA

INDEX

1. GAMMA-RAY DETECTORS FOR NONDESTRUCTIVE ANALYSIS

P. A. Russo and D. T. Vo

I. INTRODUCTION AND OVERVIEW

Gamma rays are used for nondestructive quantitative analysis of nuclear material. Knowledge of both the energy of the gamma ray and its rate of emission from the unknown mass of nuclear material is required to interpret most measurements of nuclear material quantities. Therefore, detection of gamma rays for nondestructive analysis of nuclear materials requires both spectroscopy capability and knowledge of absolute specific detector response.

Some techniques nondestructively quantify attributes other than nuclear material mass, but all rely on the ability to distinguish elements or isotopes and measure the relative or absolute yields of their corresponding radiation signatures. All require spectroscopy and most require high resolution. Therefore, detection of gamma rays for quantitative nondestructive analysis (NDA) of the mass or of other attributes of nuclear materials requires spectroscopy.

A previous book on gamma-ray detectors for NDA[1] provided generic descriptions of three detector categories: inorganic scintillation detectors, semiconductor detectors, and gas-filled detectors. This report described relevant detector properties, corresponding spectral characteristics, and guidelines for choosing detectors for NDA. The current report focuses on significant new advances in detector technology in these categories. Emphasis here is given to those detectors that have been developed at least to the stage of commercial prototypes. The type of NDA application – fixed installation in a count room, portable measurements, or fixed installation in a processing line or other active facility (storage, shipping/receiving, *etc.*) – influences the choice of an appropriate detector.

Some prototype gamma-ray detection techniques applied to new NDA approaches may revolutionize how nuclear materials are quantified in the future. An example is gamma-ray NDA applied to quantitative measurements of in-process nuclear materials. Such measurements are routinely performed with rugged, reliable, stable, sensitive portable detectors[2, 3] but could be accomplished with distributed networked sensors (DNS). The approach requires gamma-ray detectors that are lower in cost (because DNS uses a large number of detectors) but have the ruggedness, reliability, stability, and sensitivity of the portable detectors. Modern safeguards concepts for verifying inventory and tracking transfers and movements of nuclear materials invoke DNS approaches.[4] Sophisticated imaging detectors may eventually satisfy some needs for DNS. Prototype commercial alternatives to traditional gamma-ray detectors that apply to portable applications, DNS, and imaging are described in this report.

Low-resolution alkali halides (NaI and CsI) and bismuth germanate ($Bi_4Ge_3O_{12}$, or BGO) were available previously[5] and have been in use with photomultiplier tubes (PMTs) almost exclusively.[6] A tremendous growth in options for PMT design enhances the usefulness of such scintillators in compact scintillator/PMT detectors that give optimum performance. Semiconductor alternatives to PMTs for converting scintillation light to electronic pulses can further reduce the size of a detector package for a given scintillator and improve the overall ruggedness of the assembly. Ruggedized assemblies now allow good scintillator/PMT performance under high mechanical stress. Analog and digital approaches to gain stabilization are available commercially, and the latter is straightforward to implement with user-developed software.[7]

Families of new scintillator materials with improved characteristics are now available in large sizes. Some with higher-Z metallic species actually compete favorably with BGO for high density but also have a natural radioisotope. An example is lutetium oxyorthosilicate, $Lu_2(SiO4)O(Ce)$ or LSO, which, though slightly better in resolution than BGO, is impractical for many if not most applications because of its relatively high intrinsic radiation.[8, 9] The density range of two cerium-doped lanthanum

halides varies from ~1.1 times that of NaI for $LaCl_3$(Ce), to ~1.5 times that of NaI for $LaBr_3$(Ce). The intrinsic radiation for the lanthanum halides for the same crystal size is 200 times less than that of LSO, the energy resolution is at least two times better than NaI, and large crystals are already available commercially. These lanthanum halides are the likely near future in low-resolution scintillation spectroscopy.[10-15] Some results of testing and implementation of these scintillators for NDA measurements of special nuclear materials are presented here.

Improvements over NaI resolution are now available with room-temperature semiconductor detectors, although crystal size and commercial availability limit practical usefulness. The limits are a result of the characteristics of charge collection for these materials but are also influenced by the status of crystal-growth technology and understanding of the properties of these semiconductors. Advances in size and performance of non-cryogenic semiconductor CdTe and CdZnTe reflect improvements in the production of these materials, new technologies for surface contacts, the development of small electrical coolers, and advances in analog microcircuits.

Commercial, portable, electrically cooled CdTe detectors with crystals at least four times larger than those offered in the past are a new and truly portable alternative to Ge.[16] Implementation of portable CdTe for full, wide-range gamma-ray isotopics of plutonium, uranium up to 80% ^{235}U, and mixed (U-Pu) oxide[17-19] is now a commercial option. The thickness of CdTe is limited to a few millimeters by charge transport properties. Therefore, measurements must use the lower-energy portion of gamma-ray spectra. Both cost and delivery time are moderate for CdTe, compared to low for NaI, but the cooled CdTe detector is a high-resolution detector.

The introduction of the coplanar-grid electrode overcomes some deficiencies of charge collection in CdZnTe, enabling the development and optimization of such detectors in numerous adaptations of this approach with sizes much larger than CdTe.[20-22] Testing and implementation for NDA of special nuclear materials has continued, but despite promise the largest CdZnTe crystals available commercially remain high in cost and require very long wait periods. Multi-element CdZnTe and CdTe detectors compensate for the small sizes of compound semiconductor crystals – or for the scarcity and high costs of the largest crystals. This comes at the expense of the simplicity of designs with single crystals. Commercial prototypes have been developed.[23, 24]

Germanium detectors (Ge) still offer the state-of-the-art in energy resolution. Very large crystals are available commercially and have become more affordable with time. Because of energy resolution and availability in all sizes, most fixed gamma-ray NDA instruments use Ge when access to liquid nitrogen is not an issue. Commercial options for electrical cryogenic coolers for Ge detectors have become increasingly reliable, and are compact and packaged for portable use. Advances in signal processing increase both performance and effective lifetime of Ge detectors.[25-28] Portable Ge shielded by dense scintillator material is a dramatic step toward high-resolution spectroscopy for increased sensitivity and versatility in the most challenging environments.[29] Sensing transitions from superconducting states in supercooled materials is a distant-future option for very-high resolution that approaches the radiation line widths.

Imaging systems that utilize apertures with inorganic scintillators or employ crystal arrays, mechanically segmented crystals, segmented PMTs, *etc*. have been developed[30] and implemented in the field.[31-32] Others use Ge that is “position-sensitive”. Advances in technology for surface contacts and analog/digital circuitry add position sensitivity to Ge detectors through essentially continuous but electronically isolated multiple surface contacts that effectively segment the volume of a planar or coaxial Ge detector. Such detectors enable high-resolution imaging in the 4-π environment surrounding the detector via detection of multiple (three) Compton-scattering events.[33, 34] Imaging achieved in this way uses no aperture and interprets the source distribution in three dimensions. The readout of the Compton imager is a unique gamma-ray spectrum for each three-dimensional source voxel in the detector environment. Interpreting the position and energy of an individual Compton event within the Ge crystal requires analysis of relative pulse amplitudes for all surface-contact segments (10-to-100 contact segments for planar-to-coaxial crystals, respectively) as well as the

analysis of the pulse shapes in each segment. Interpretating the conical locus of the incident gamma trajectory from a sequence of three Compton events from the same gamma ray requires a logical reconstruction of the sequence of these Compton events. Interpretating the spectroscopic image for each gamma-ray energy requires analysis of the intersections of loci for the large number of events of a given gamma-ray energy required for such interpretation. Compton imaging has also been achieved at room temperature using a large CdZnTe detector with a pixelated anode for two-dimensional position sensitivity and analysis of pulse shapes for the third dimension.[35]

Advances in Ge materials now support development of prototype multiple-element Ge for the highest position resolution utilizing 4π Compton imaging.[36-38] These mechanically complex detectors consist of a stack of two-layer orthogonally-oriented narrow and thin Ge strips – up to ~100 strips per two-layer element with each strip read out at both ends. Variance on event position determined by strip pitch is small compared with that interpreted from the readout of a segmented Ge detector. However, operation at liquid-nitrogen temperature burdens the requirements for design, maintenance, and field applications of such mechanically and electronically complex detectors.

Currently, the use of arrays of small semiconductor detectors[39] is demonstrated in spectrometric DNS applications. The benefits of inorganic scintillators for DNS include the availability of crystals of almost any size and the existence of commercial support for needs such as stabilization. However, organic (plastic) scintillators may also emerge for DNS, preceding high-resolution gamma imagers, without or with apertures, in the maturity required for these applications. Plastic scintillators are lower in cost. The promise for these detectors is indicated by the demonstration of the enhanced photoelectric yield achieved by loading heavy elements into the plastic.[40] The spectrometer characteristics of these low-cost and rugged materials are presented in Section VIII. Promise for plastics in the designs of nanoparticulate detectors is on the more distant horizon.

Progress in gas-detector spectroscopy focuses on high-pressure xenon (HPXe) ion chambers.[41-46] This chapter illustrates benefits of HPXe such as insensitivity to changes in temperature,[47] and a factor-of-two improvement in resolution relative to NaI. This plus resistance to damaging effects of radiation encouraged the design and fabrication of several commercial prototypes. The benefits, along with convincing results from six years in the radiation fields of space,[48] are the promise for DNS in continuous NDA of nuclear materials if the manufacturing process succeeds in producing HPXe detectors that are sufficiently low in cost.

Table 1 summarizes the characteristics and performance of each of eight gamma-ray spectrometer detectors that are currently viable commercial options for NDA. Data for detectors that are available since the previous book[49] are included in bold along with data for those detectors that were described previously to emphasize advances in the recent fifteen years. The relevance of the information in Table 1 is discussed in the text below under the appropriate headings.

Much larger NaI(Tl) and Ge detectors are available than the corresponding entries in Table 1. Portable applications require shielded and collimated detectors that can be readily manipulated by hand throughout the plant. The weight of shielding is difficult to manage manually for detectors with areas that exceed ~5 cm^2. Including smaller-diameter NaI(Tl) and Ge detectors in Table 1 simplifies comparisons with newer detectors whose maximum dimensions are generally much smaller than the largest crystals of NaI(Tl) and Ge. The need to specify performance for at least two gamma-ray energies (122 and 662 keV) corresponds to common needs to measure ^{235}U, ^{239}Pu, and ^{238}U using gamma rays of 186-, 414- and 1001-keV, respectively.

Figures 1 and 2 are reference spectra of oxides of low- and high-burnup plutonium (93% ^{239}Pu and 64% ^{239}Pu, respectively). These spectra are measured using four of the detectors specified in Table 1: NaI(Tl) (NaI), co-planar-grid CdZnTe (CZT), electrically cooled CdTe (EC CdTe), and Ge.

The remainder of this report focuses on results obtained with the newer detectors with data appearing as bold entries in Table 1. Detailed discussions address the relevant detectors in each category. Results for certain less mature detectors with future potential, as well as others with potential that has been superseded by newer developments, are presented as well and compared with

the reference data in Table 1. The report also includes some discussion of the impacts of new supporting technologies that enhance the properties and performance of gamma-ray detectors.

II. SODIUM IODIDE AND OTHER ALKALI-HALIDE SCINTILLATORS

The most significant advances in *materials* for alkali halide scintillators are that NaI scintillator crystal spectrometers as large as 40 cm in length are now available from commercial manufacturers. Mechanisms for the production and collection of scintillation light using photomultiplier tubes (PMT) are discussed elsewhere.[50] Discussions in the remainder of this section on alkali halide scintillators as well as most of sections III and IV emphasize usefulness for NDA and, therefore, do not include all such scintillators.

The routine use of shielded compact NaI detectors for portable holdup measurements benefits from an ever-increasing variety (size, shape, spectral sensitivity, heat sensitivity…) of PMTs. This enables optimal mechanical matches with the smallest or largest scintillator and optimal spectral matches between the peak in the spectrum of scintillation photons (PHOTON PEAK λ in Table 1) and the peak in the spectrum of photocathode sensitivity. Newer, rugged, commercial NaI/PMT or CsI/PMT assemblies support acquisition of gamma-ray spectra with detectors that experience >200 G of mechanical shock during measurements performed during borehole drilling.

It is uncommon to implement scintillators in stand-alone NDA instruments because the higher resolution, the availability of liquid nitrogen in most NDA count-rooms, and a continuously decreasing cost differential between detectors with moderate-size Ge crystals and scintillation detectors make Ge an obvious choice. It is still not practical to implement Ge detectors in plant-wide portable applications. Therefore, many NDA needs for scintillators (NaI in particular) focus on portable applications. Fixed on-line installations of gamma-ray detectors in the plant (including DNS applications) are more likely to implement scintillators and other room-temperature detectors. Therefore, discussions of NaI in this section emphasize portable and on-line applications.

Fully optimized, NaI(Tl)/PMT detectors routinely give 6% resolution (FWHM at 662 keV). A similar light yield and emission-spectrum peak – 420 ηm compared to 415 for the NaI:Tl – plus a higher Z and 23% higher density of CsI(Na) compared to NaI(Tl)[51] make the CsI option a somewhat better choice for thin-crystal spectroscopic imaging. Nevertheless, newer lanthanum halides now offer even greater improvements over NaI, as described in section IV.

Table 1. Gamma-Ray Detector Properties and Performance[a]

DETECTOR	BGO ($Bi_4Ge_3O_{12}$)	NaI:Tl (compact)	$LaCl_3$:Ce (La:Ce::10:1)	$LaBr_3$:Ce (La:Ce::200:1)	Xe ($Xe:H_2$::200:1)	(CPG) CdZnTe (Cd:Zn:Te::1-x:x<0.1:1)	CdTe (elect. cooled)	Ge (thick planar) (elect. or LN_2 cooled)
TYPE	scintillator	scintillator	**scintillator**	**scintillator**	**gas (ioniz. chamber)**	**solid-state**	**solid-state**	solid-state
DIMENSIONS: area (cm^2) × thick. (cm)	5 cm^2 × 2.5 cm (or larger)	5 cm^2 × 5 cm (or much larger)	**5 cm^2 × 5 cm (currently up to 20 cm^2 × 5 cm)**	**5 cm^2 × 4 cm (currently up to 20 cm^2 × 5 cm)**	**11 cm^2 × 7.5 cm (up to 100 cm^2 × 75 cm)**	**2.3 cm^2 × 1.5 cm (largest*)**	**1.2 cm^2 × 0.3 cm (largest*)**	5 cm^2 × 1.5 cm (or much larger)
VOLUME (cm^3)	13 (or larger)	26 (or much larger)	**26 (currently up to 100)**	**20 (currently up to 100)**	**83 (up to 7500)**	**3.5 (largest*)**	**0.4 (largest*)**	8
AVERAGE Z	28	32	**28**	**41**	**54**	**49**	**49**	32
DENSITY (g/cm^3)	7.1	3.7	**3.9 (van Loef 01)**	**5.3 (van Loef 01)**	**0.4-0.5 (Knoll 00 716)**	**6.0**	**6.1**	5.3
RESOLUTION: % FWHM @ 662 keV [Intrinsic Photoel. Eff., %][b]	12% (Romano 99) [2.80]	7% (Vo 02a) [1.000]	**3.3% (van Loef 01)** *Commercial spec <4%* **[0.81]**	**2.8% (van Loef 01)** *Commercial spec <3%* **[0.40]**	**2% (Bedding 03a)** *Commercial spec <4%* **[0.20]**	**3.2% (Vo 02a)**** **[0.47]**	**0.6 % (Vo 02a)** **[0.10]**	0.2% Vo 02a [0.10]
RESOLUTION: % FWHM @ 122 keV [Intrinsic Photoel. Eff., %][b]	28% (Romano 99) [1.00]	13% (Vo 02a) [1.000]	***Better than NaI*** *Commercial spec ~8%.* **[1.00]**	***Better than NaI*** *Commercial spec ~7%* **[1.00]**	**7% (Bedding 03a)** **[0.95]**	**6.3% (Vo 02a)** **[1.00]**	**1.5 % (Vo 02a)** **[0.78]**	0.4% Vo 02a [0.81]
PHOTON PEAK λ (ηm)[c]	480	415	**330 (van Loef 01)**	**360 (van Loef 01)**	**NA**	**NA**	**NA**	NA
PHOTON DECAY τ (ηs)	300	230	**25 (60%) 210 (30%)**	**35 (90%)**	**NA**	**NA**	**NA**	NA
AVAILABILITY	~ 6 wks after order	~ 2 wks after order	**~ 4 wks after order**	**4-8 wks after order**	**?**	**~ 1 yr after order**	**~ 24 wks after order**	~ 4-8 wks after order

[a] Intrinsic properties of scintillator materials are from Knoll 00 235 unless noted otherwise.

[b] Calculated intrinsic photoelectric efficiency (normalized to NaI:Tl values: 1.000 at 122 keV and 0.150 at 662 keV) for stated thickness of detector whose resolution is quoted.

[c] Glass transmits down to 350 ηm. Quartz transmits down to 180 ηm. Commercial suppliers currently use glass-window PMTs.

* Larger detectors that use multiple crystal elements have been demonstrated. (Prettyman 00, Redus 04)

** Resolution at 662 keV improves to ~2.5% for thinner crystals.

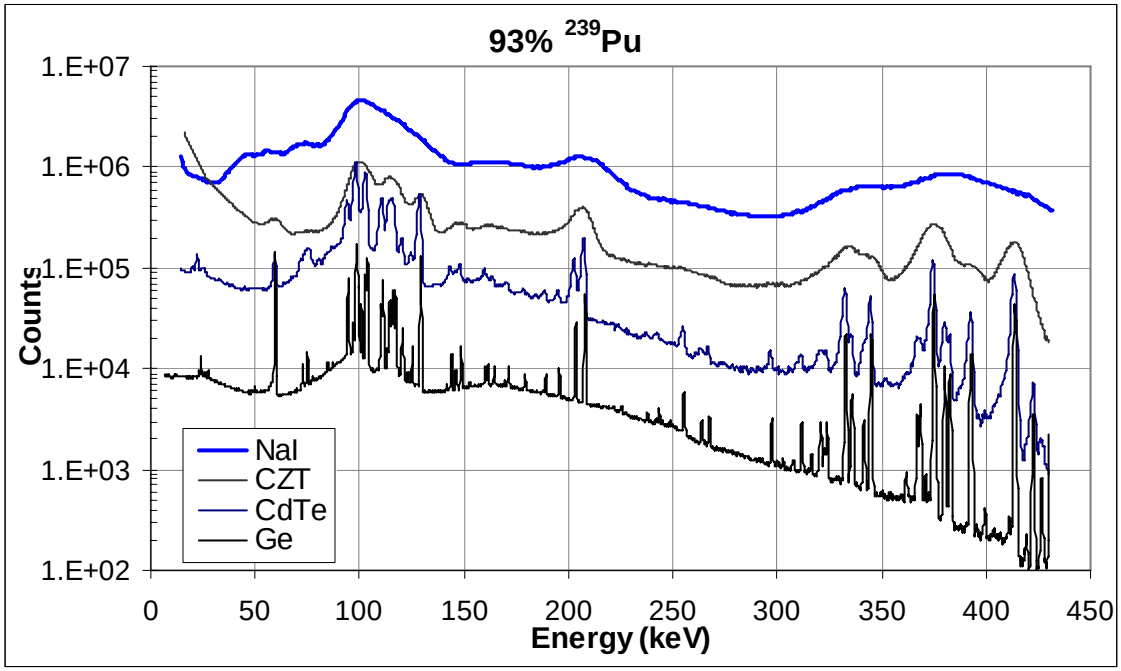

Fig. 1. Gamma-ray spectra of low-burnup (93% ^{239}Pu) plutonium measured with four different gamma-ray detectors: NaI:Tl, CPG CdZnTe, CdTe, and Ge (top to bottom). Refer to Table 1 for specifications on the detectors.

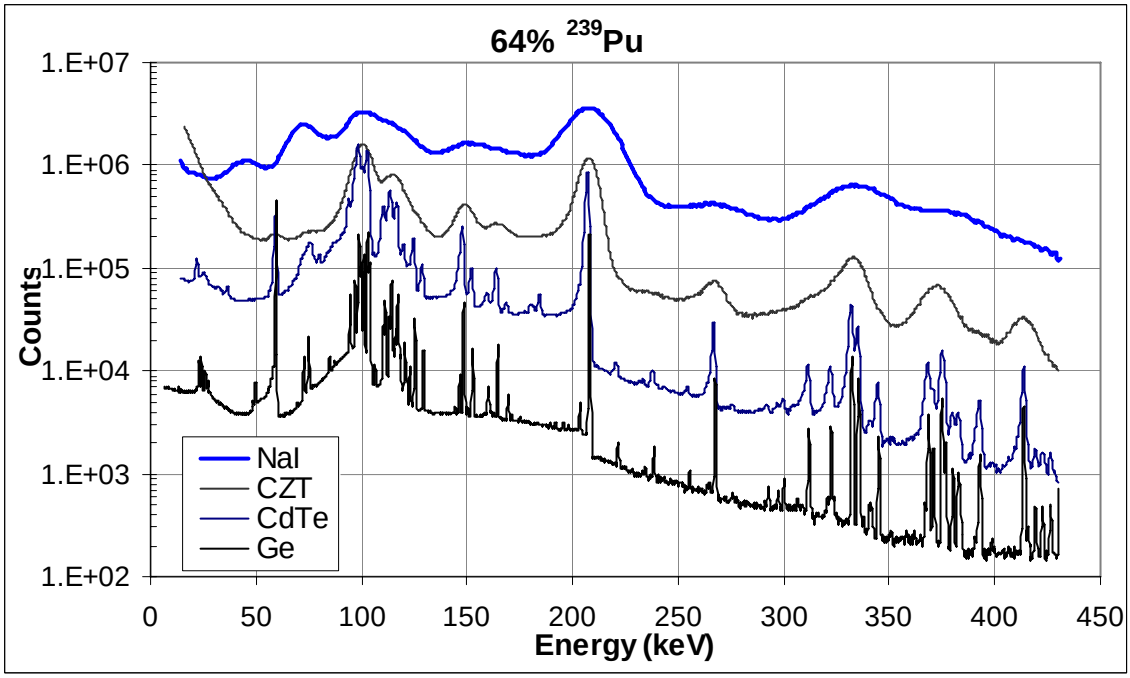

Fig. 2. Gamma-ray spectra of high-burnup (64% ^{239}Pu) plutonium measured with four different gamma-ray detectors: NaI:Tl, CPG CdZnTe, CdTe, and Ge (top to bottom). Refer to Table 1 for specifications on the detectors.

The peak wavelength of the NaI(Tl) scintillation light spectrum is 415 ηm (Tables 1 and 2) which is well-matched to the peak sensitivity of the most common bialkali photocathode material used in PMTs.[52] Table 2 indicates that the blue spectrum of scintillation light from CsI(Na) is much like that of NaI(Tl) with a nearly identical light yield. Table 2 also shows that the light yield of CsI(Tl) exceeds that of CsI(Na) by nearly 70%, but the scintillation light spectrum peaks in the green at 540 ηm. A modified photocathode with enhanced sensitivity at longer wavelengths may be used to optimize the performance of CsI(Tl).[53] Nevertheless, the scintillation spectrum of CsI(Tl) is also suited to use with silicon photodiodes, as discussed in section III.

Table 2. Alakalai Halide Scintillator Properties (Knoll 00 235)

DETECTOR	NaI:Tl	CsI:Na	CsI:Tl
TYPE	scintillator	scintillator	scintillator
Light Yield (photons/MeV)	38,000	39,000	65,000
AVERAGE Z	32	54	54
DENSITY (g/cm^3)	3.7	4.5	4.5
PHOTON PEAK λ (ηm)	415	420	540
PHOTON DECAY τ (ηs)	230	460 4000	680 (64%) 3340 (36%)

A major drawback of spectroscopy with any scintillator, including NaI, is the influence of temperature on the relative light output of (often multiple) scintillation decay modes. The result is a change in gain with temperature. Many commercial spectrometer systems stabilize against gain changes by empirically tracking gain drift and either compensating with analog adjustments of the gain or digital adjustments of the energy regions used to analyze the spectral data. Most scintillator stabilization is applied to NaI spectrometers. Newer intrinsic stabilization of scintillator gain against drift caused by temperature change[54] may widen the range of temperature suitable for use of these scintillators and extend applications to scintillators such as BGO with resolution significantly worse than that of NaI.

Alkali halide scintillators have been demonstrated for spectroscopic imaging with coded apertures.[55] The development of this technology has utilized both arrays of large (10-cm × 10-cm × 10-cm) NaI detectors and large-area (12-cm diameter by 1-cm thick) CsI(Na) scintillators coupled to position-sensitive PMTs.[56] A commercial version of the latter implementation of this imaging approach has been applied to measurements of in process plutonium inventory in a high-throughput, continuous system for aqueous dissolution of low-burnup plutonium.[57] Figure 3 shows the sketch of the dissolver and the two-dimensional spectroscopic image of ^{239}Pu superimposed on a photograph of the process equipment. Applications of this imaging system to in-process measurements of ^{235}U are also reported.[58] Both of these low-resolution applications would benefit from higher energy and position resolution available from a hybrid orthogonal-strip germanium detector[59] but with significant sacrifice in simplicity, as described in section V.

The NaI detector specified in Table 1 has a relatively small crystal, consistent with the other detectors listed. The quoted 7% energy resolution is nominal rather than optimum. Detectors of this size and performance are typical of those used in portable measurements of holdup and in-process nuclear materials.[60]

Figures 1 and 2 show the spectra of low- and high-burnup plutonium measured with this NaI detector and with three of the other detectors described in Table 1. The NaI energy resolution is the lowest of the four detectors. The 414-keV gamma-ray peak of ^{239}Pu appears as an unresolved shoulder on the high-energy side of a group of several peaks in these NaI spectra. The activity in the grouping of peaks is dominated by ^{239}Pu in the low-burnup spectrum but includes significant contributions from ^{241}Am and ^{241}Pu in the high-burnup spectrum. Either low-resolution response-function fitting[61] – which requires very long counts with good statistics – or a conservative setting of energy regions-of-interest[62] is required to use NaI in unbiased measurements of variable-burnup plutonium. Similar interference problems arise with NaI measurements of ^{235}U in most facilities.[63] A long count time is rarely an option in portable applications, and conservative settings give rise to systematic effects in quantitative results. These problems require portable detectors with better resolution than NaI. The important solutions to these problems include lanthanum halide scintillators and CdZnTe. These are discussed in sections IV and VI, respectively.

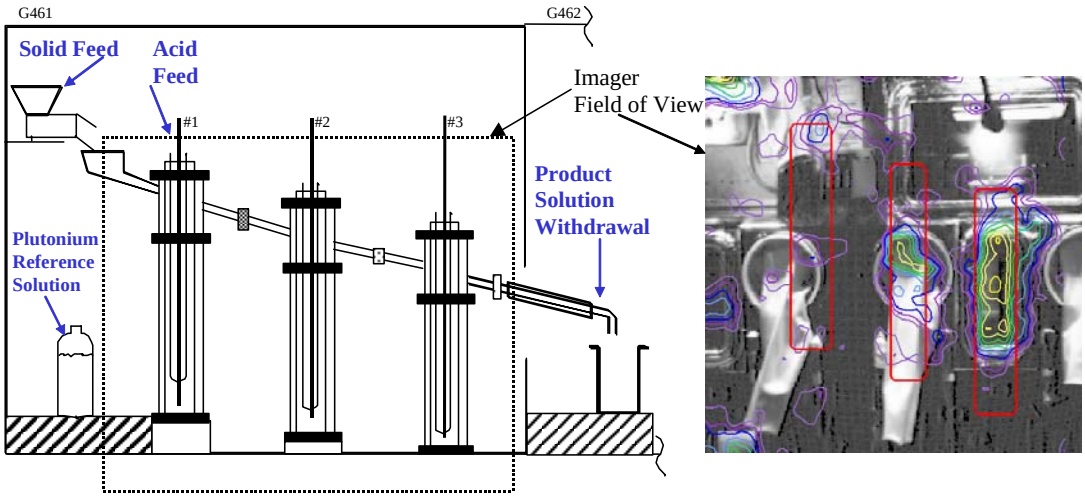

Fig. 3. Three aqueous dissolver columns in the field of view of the spectroscopic imager (sketch at left) are outlined in red in the photograph of the dissolver glove box (right). Colored contours (yellow-to-violet ≡ 900-to-100 counts) show the distribution of ^{239}Pu in the dissolver columns inside the glove box as measured in a 10-min count with the commercial imager. Contour data correspond to a 373-430 keV window in which ^{239}Pu activity dominates in the CsI(Na) spectrum.

III. SCINTILLATOR-PHOTODIODE DETECTORS

Semiconductor photodiodes are alternatives to PMTs for converting scintillation light to charge.[64] The discussion below focuses on efforts to improve the performance in the energy range of 100-1000 keV that is available with NaI(Tl)/PMT detectors with areas of ~5 cm^2.

Photodiodes are more rugged than PMTs, more compact, and unaffected by external electric fields. The thinnest wafer (<0.1 mm thick) of silicon is opaque to visible scintillation light and, under minimal bias, transports all primary electrons rapidly to the collection surface. The quantum efficiency (number of electrons per scintillation photon) of the silicon photodiode exceeds that of the bialkali photocathode by a factor of two to six, typically, for blue to green light (450-550 ηm). The higher yield of primary electrons results in a smaller statistical contribution to the energy resolution.

The high room-temperature thermionic emission caused by silicon's relatively small band gap (see Table 3) introduces a leakage noise that limits resolution, enforces the use of small-area devices, and adds temperature dependence to the resolution in addition to the scintillator's temperature-dependent gain. A lower-noise alternative to Si is a semiconductor material such as mercuric iodide, HgI_2, with a band gap that is twice that of Si. Results with these photodiode options are discussed below.

Table 3. Properties of Solid State Materials Governing Production of Charge

SOLID-STATE DETECTOR	(Average) Z	Density[a] (g / cm^3)	Band Gap[a] (keV)	Ioniz. Energy[a] (eV / e-h pair)
Ge	32	5.3	0.7[b]	2.98[b]
Si	14	2.3	1.1	3.6
CdTe	49	6.1	1.5	4.4
CdZnTe	49	6.0	1.6	4.3
HgI_2	62	6.4	2.1	5.0

[a] Values taken from Knoll 00 483

[b] Results for 77 K. (All others correspond to 300 K.)

Several commercial efforts to take advantage of the 70%-larger light yield of CsI(Tl) used 1-cm^2 Si photodiodes rather than a PMT to benefit from the higher quantum efficiency of the CsI(Tl). Although the resolution at 662 keV improves somewhat with CsI(Tl)/Si compared with NaI/PMT (~6% *vs*. the nominal 7% for NaI/PMTs), the CsI resolution at 122 keV is significantly worse than NaI because of leakage noise. Therefore, larger-area photodiodes required for use with larger (5-cm^2) CsI(Tl) scintillator crystals do not offer improved resolution compared with the NaI/PMT.

As a larger bandgap photodetector, HgI_2 has an advantage over Si of lower leakage noise at room temperature, although the larger ionization energy of HgI_2 reduces this benefit because of the corresponding statistical advantage of Si in primary excitation of electrons. The potential advantage is photodiodes of larger area than would be possible with Si. Commercial efforts implementing thin 1.6-cm^2 photodiodes of HgI_2 with CsI(Tl) scintillator crystals report ~5.6% FWHM at 662 keV.[65] Additional measurements that determined performance at 122 keV are documented in Table 4 for comparison with the performance of the nominal NaI detector. These data indicate a small resolution advantage at 662 keV over NaI/PMT for two CsI(Tl)/HgI_2 detectors. Nevertheless, the resolution at 122 keV is slightly worse than NaI. The reason is, in part, residual leakage noise despite the larger band gap; another contributor is the need for a longer amplifier shaping time for optimum resolution with CsI(Tl) because of its longer decay time. Optimum shaping time for CsI(Tl) is a compromise between the shortest possible to minimize noise and the longest practical to integrate the pulse.

An additional problem with HgI_2 is that even the thinnest photodiode is itself a gamma detector because of its large Z and density. Modeling may be required to determine the contribution of HgI_2 to a given measurement.

Table 4. Compare Prospective Portable Detectors with NaI

Detector		NaI:Tl/PMT *(Table 1)*	CsI/HgI_2 (smaller)	CsI/HgI_2 (larger)	CPG CdZnTe *(Table 1)*
122 keV	%FWHM	13	**15**	**15**	**6.3**
	%FWTM	25	**29**	**29**	**13**
662 keV	%FWHM	7	**5.8**	**6.0**	**3.2**
	%FWTM	13	**11.4**	**12.0**	**8.0**
% Rel. Intr. Photo. Eff.[a]	122 keV	100	**100**	**100**	**100**
$100 \times E / E$(NaI)	662 keV	100	**42**	**60**[aa]	**47**
Crystal shape		Cylindrical	**Rectangular**	**TRCC***	**Rectangular**
Crystal X-sectional area, cm^2		5	**1.6**	**8.6 to 1.3**[o]	**2.3**
Crystal depth, cm		5	**1.3**	**3.8**	**1.5**

[a] Calculated intrinsic photoelectric efficiency (normalized to NaI:Tl values: 1.000 at 122 keV and 0.150 at 662 keV) for stated thickness of detector whose resolution is quoted.

[aa] Used half of the stated thickness of the TRCC to obtain this result.

* Truncated Right Circular Cone (TRCC) with wide end facing the cylindrical collimator

[o] Range (maximum to minimum) of areas of TRCC

Although detector efficiency approaches that of the compact NaI/PMT detector, the data in Table 4 indicate that the CsI(Tl)/HgI_2 detector does not provide improvements over the performance of NaI/PMTs at either gamma-ray energy (122 and 662 keV). Coplanar-grid CdZnTe detectors and the lanthanum halides discussed in sections VI and IV do offer significant improvements.

Avalanche photodiodes amplify primary charge produced when scintillation light reaches the photodiode. These devices, which are documented elsewhere,[66] are also subject to limitations of leakage noise at room temperature. Advances in micro-cooler technology could revive photodiodes with resolution surpassing that available with PMTs.[67] Applications in NDA would include those requiring compact, low-noise, large-area and multi-crystal measurement systems.

Hybrid PMTs[68] utilize a primary photocathode of 5-cm^2-area or more combined with a very small (low-leakage-noise) secondary photodiode biased at a high voltage relative to the photocathode. Although the statistics of the primary production of charge are unchanged from that of the corresponding photocathode of a PMT, the statistics of the secondary production are greatly improved over that of the first dynode of a PMT.

Because the statistics of secondaries define resolution on multiple-photoelectron events, the hybrid PMT resolves single-, double-, and triple- (*etc*.) photoelectron events. This resolution supports diagnostics on statistics of charge production, as illustrated in Figure 4, which shows a few-photoelectron spectrum of the hybrid PMT measured at high gain plotted with a continuum spectrum measured at 50-times lower gain with a scintillator coupled to the hybrid PMT.[69] The data illustrate the advantage of the hybrid PMT as a spectroscopic tool for comparing primary *net* charge produced in the PMT coupled to different scintillators (variable materials, shapes/sizes, surface characteristics, *etc*.). End-use practicality for NDA is limited in that the relative cost of the hybrid PMT is high, and the equivalent in compactness is available with traditional PMTs. Benefits of few-photoelectron resolution rarely exist for end-use spectroscopy applications, which require good primary statistics.

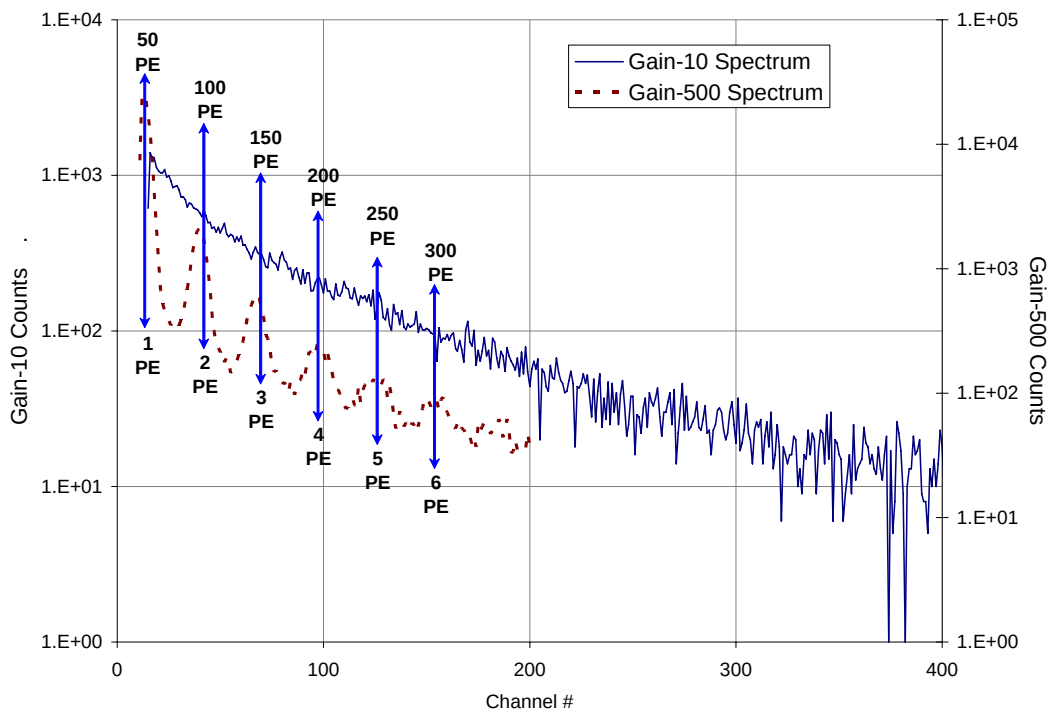

Fig. 4. The few-photoelectron spectrum of the hybrid PMT measured at high gain (dashed line) illustrates the resolution of successive multiple-photoelectron events. It also calibrates the number photoelectrons vs. channel in the spectrum measured at 50-times lower gain with a scintillator coupled to the hybrid PMT (solid line).

IV. INORGANIC LANTHANUM AND RARE-EARTH SCINTILLATORS

The appearance in the last decade of new "bright", relatively high-Z scintillators with densities that equal or exceed that of NaI is a most encouraging phenomenon regarding improvements over NaI/PMT detectors. This section focuses on results for the cerium-doped lanthanum halides compared with NaI/PMT detectors and for cerium-doped lutetium oxyorthosilicate[70, 71] (Lu_2SiO_5(Ce) or LSO) compared with BGO.

Some elemental components of the new materials have naturally occurring beta emitters. The following three are relevant to the discussions in this section:

- ^{176}Lu ($3 \cdot 10^{10}$ y, 2.6% of naturally occurring Lu).
- ^{142}Ce ($5 \cdot 10^{15}$ y, 11.1% of naturally occurring Ce).
- ^{138}La ($1.1 \cdot 10^{11}$ y, 0.1% of naturally occurring La).

Intrinsic background from ^{142}Ce is not significant, however. Relative to La, Ce is a 0.5-10% atomic species,[72, 73] and ^{142}Ce contributes minimally to intrinsic background from ^{138}La. Relative to Lu in LSO, Ce is a 0.055% atomic species,[74] and ^{142}Ce contributes minimally to background from ^{176}Lu. The contribution of intrinsic background from the decay of ^{176}Lu is not negligible.

A large crystal of LSO was tested along with BGO as a reference using a PMT with a bialkali photocathode. Table 5 compares this LSO scintillator with the reference BGO and NaI. (These data also appear in Table 1.) The density and light yield of LSO exceed that of BGO and the resolution is somewhat better. Considering that the spectrum of scintillation light is similar to that of BGO, even better performance than that observed for LSO is expected for a very good crystal of comparable size.[75] However, the need to subtract intrinsic background from LSO spectral data also contributes to the variance in the width of the net peak.

Beta decay of ^{176}Lu limits gamma-ray detection sensitivity in most of the useful energy range, and subtraction of the corresponding background affects the energy resolution. The gamma-ray spectrum of ^{137}Cs measured with BGO detectors and the intrinsic background spectrum for the LSO detector are shown in Figure 5. Also shown there is the net ^{137}Cs spectrum with background subtracted.

Because NDA for nuclear safeguards relies on gamma-ray measurements between 100 and 1000 keV, subtraction of the substantial intrinsic background (~12,000 s^{-1} for a crystal of the size of the LSO test crystal) will often determine the limiting sensitivity for measurements performed with LSO. The measured BGO spectrum includes no intrinsic background. Room background for the spectra plotted in Figure 5 is negligible. Given the substantial intrinsic background and relatively small advantages compared to BGO, LSO is not a compelling alternative to BGO.

Table 5. Compare LSO with BGO and NaI[a]

DETECTOR	**BGO** ($Bi_4Ge_3O_{12}$)	**NaI:Tl**	**LSO (Lu_2SiO_5:Ce)** (Lu:Ce::1800:1)
TYPE	scintillator	scintillator	**scintillator**
DIMENSIONS: area (cm^2) × thick. (cm)	5 cm^2 × 2.5 cm (or larger)	5 cm^2 × 5 cm (or much larger)	**32 cm^2 × 1.3 cm**
VOLUME (cm^3)	13 (or larger)	26 (or much larger)	**41**
AVERAGE Z	28	32	**25**
DENSITY (g/cm^3)	7.1	3.7	**7.4** **(Ludziej 95)**
Light Yield (photons/MeV)	8,200	38,000	**~20,000** **(Ludziej 95)**
RESOLUTION: % FWHM @ 662 keV [Intrinsic Photoel. Eff., %][b]	12% (Romano 99) [2.80]	7% (Vo 02a) [1.000]	**11%** **(Romano 99)** **[1.34]**
RESOLUTION: % FWHM @ 122 keV [Intrinsic Photoel. Eff., %][b]	28% (Romano 99) [1.00]	13% (Vo 02a) [1.000]	**23%** **(Romano 99)** **[1.00]**
PHOTON PEAK λ (ηm)	480	415	**420** **(Knoll 00 244)**
PHOTON DECAY τ (ηs)	300	230	**47** **(Knoll 00 244)**
AVAILABILITY	~ 6 wks after order	~ 2 wks after order	**n.a.**

[a] Intrinsic properties of scintillator materials are from Knoll 00 235 unless noted otherwise.

[b] Calculated intrinsic photoelectric efficiency (normalized to NaI:Tl values: 1.000 at 122 keV and 0.150 at 662 keV) for stated thickness of detector whose resolution is quoted.

Intrinsic background radiation of cerium-doped lanthanum halides is nearly two-orders-of-magnitude less than that of LSO for an equivalent scintillator mass. Coupled with resolution substantially better than that of NaI, material characteristics that equal or exceed those of NaI, and

rapid advances in the manufacture of these materials, lanthanum halides are very promising spectrometer alternatives.

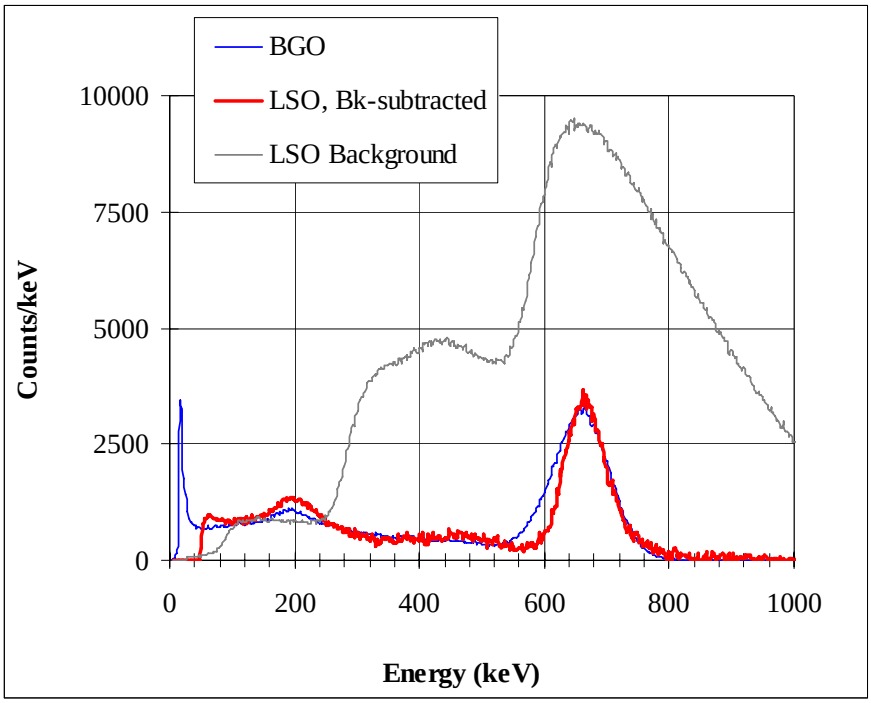

Fig. 5. The spectrum of ^{137}Cs measured with BGO detector and the intrinsic (^{176}Lu beta-decay) background spectrum for LSO are the thin blue and gray lines, respectively. The net gamma-ray energy spectrum of ^{137}Cs (measured spectrum minus intrinsic background) for the LSO detector is the heavy red line.

Table 1 indicates that the resolution of $LaCl_3$(Ce) and that of $LaBr_3$(Ce) at 662 keV are more than two-times better than that of NaI. The Z and density of $LaCl_3$(Ce) are comparable to that of NaI. The Z and density of $LaBr_3$(Ce) are 28% and 43% greater, respectively. Relatively large crystals (~100 cm^3) of both $LaCl_3$(Ce) and $LaBr_3$(Ce) are now available with short delivery times at moderate costs relative to NaI. The sizes of $LaCl_3$(Ce) and $LaBr_3$(Ce) crystals available commercially have increased steadily in the last two years. The performance of both $LaCl_3$(Ce) and $LaBr_3$(Ce) at 122 keV are nearly but not quite two-times better than that of NaI, as indicated in Table 2.

The factor-of-two or more resolution improvement of $LaCl_3$(Ce) and $LaBr_3$(Ce) at high energy is among the best results obtained with room-temperature gamma-ray detectors. The influence of surface nonuniformity has been noted, based on experimental data, as a possible cause of the smaller relative improvement in $LaCl_3$(Ce) and $LaBr_3$(Ce) resolution at lower gamma energy (122 keV) compared to NaI.[76]

Barium x rays following the decay of ^{138}La to ^{138}Ba by electron capture appear in long background spectra measured without a source. The x-ray peak observed at 37.6 keV (FWHM 6.4 keV) corresponds to the 37.4-keV K binding energy of barium. Barium x rays also follow the beta decay of ^{137}Cs to ^{137}Ba, and appear – with over an order-of-magnitude greater intensity than the background contribution – in each spectrum measured with a ^{137}Cs source. The x-ray peak at 32.8 keV (FWHM 8.3 keV) is an empirical average of barium K_α and K_β x rays, and its larger width reflects in part the energies of the barium K x rays. The energy difference of 4.8 keV between the internal and external x-ray peaks corresponds to an empirical average of the mostly undetected barium L_α and L_β x-ray energies. However, the contribution of the K x-ray energy distribution is not sufficient to explain the broadening of the external x-ray peak, relative to that of the x ray from intrinsic ^{138}La decay. The contribution of surface effects to worse resolution for x rays from the external source and for lower-

energy gammas in general is a solvable problem, and the low-energy x rays of barium are an indicator of surface quality for the lanthanum halide crystals.[77]

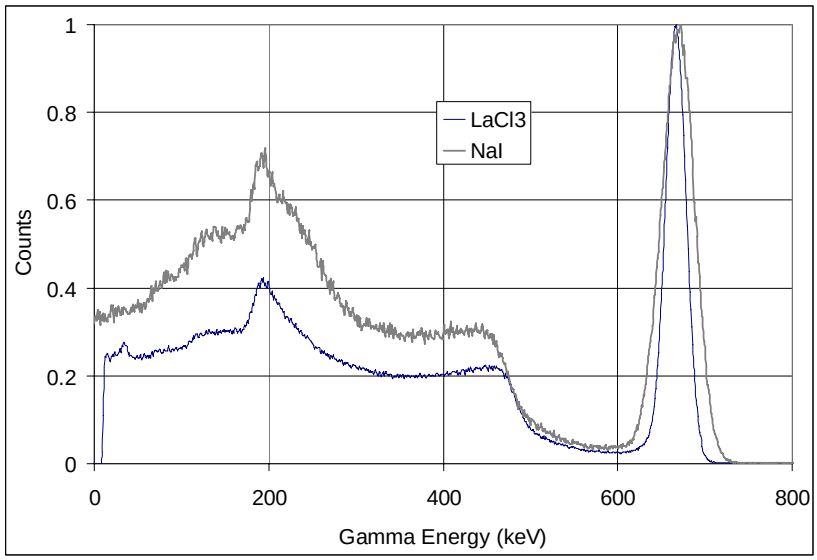

Fig. 6. Gamma-ray spectra of ^{137}Cs measured using a glass-window PMT with a 5-cm^2 by 2.54-cm thick $LaCl_3$(Ce) scintillator and the same-size NaI scintillator. The resolution (FWHM) at 662 keV is 3.9 and 6.9% respectively.

Figure 6 shows gamma-ray spectra of ^{137}Cs measured with a 5-cm^2 by 2.54-cm thick $LaCl_3$:Ce scintillator and with the same-size NaI.[78] Both spectra in Figure 6 were measured with a glass-window PMT. The relative FWHM at 662 keV is 3.9% for the $LaCl_3$ scintillator, not as good as the published results of 3.3% obtained with quartz-window PMTs (Table 1). This is partly a result of the loss of scintillation light from $LaCl_3$(Ce) below 350 ηm caused by absorption in the glass window of the PMT. The emission peak for $LaCl_3$(Ce) with 10% cerium doping is ~340 ηm. The higher wavelength emission peak (~380 ηm) of $LaBr_3$(Ce) with 0.5% cerium doping diminishes the effect of glass on the scintillation light incident on the PMT.

Figure 7 shows the gamma-ray spectra of 5-gram plutonium oxide samples of low-, medium- and high-burnup, measured with $LaCl_3$(Ce) and NaI detectors. Both use 5-cm^2 by 2.54-cm thick crystals and identical electronics.[79] Improved resolution with $LaCl_3$(Ce) at the 414-keV analysis energy for ^{239}Pu will contribute substantially to eliminating bias in measurements of high-americium materials.

Significant additional improvements (better energy resolution, and higher sensitivity because of higher density and Z, as indicated in Table 1) come with $LaBr_3$(Ce) crystals. The higher peak wavelength of the emitted photons compared with $LaCl_3$(Ce) (Table 1) gives $LaBr_3$(Ce) the additional advantage of better light transmission through the glass window of a PMT.

Relative to NaI, the cerium-doped lanthanum halides demonstrate improved performance and intrinsic properties for gamma spectroscopy applied to NDA of nuclear materials at high gamma-ray energies. Prospects for improved resolution at lower energies (below 200 keV) are good. The rapid advances achieved in materials production coupled with moderate costs and off-the-shelf availability of large crystals are strong indicators that cerium-doped lanthanum halides will replace alkali halides in the near future. Because of comparable performance, greater sensitivity, greater availability, and lower cost, the cerium-doped lanthanum halides should also compete favorably with CdZnTe and HPXe for NDA applications, including those described below for CdZnTe and HPXe that do not preclude the use of scintillators.

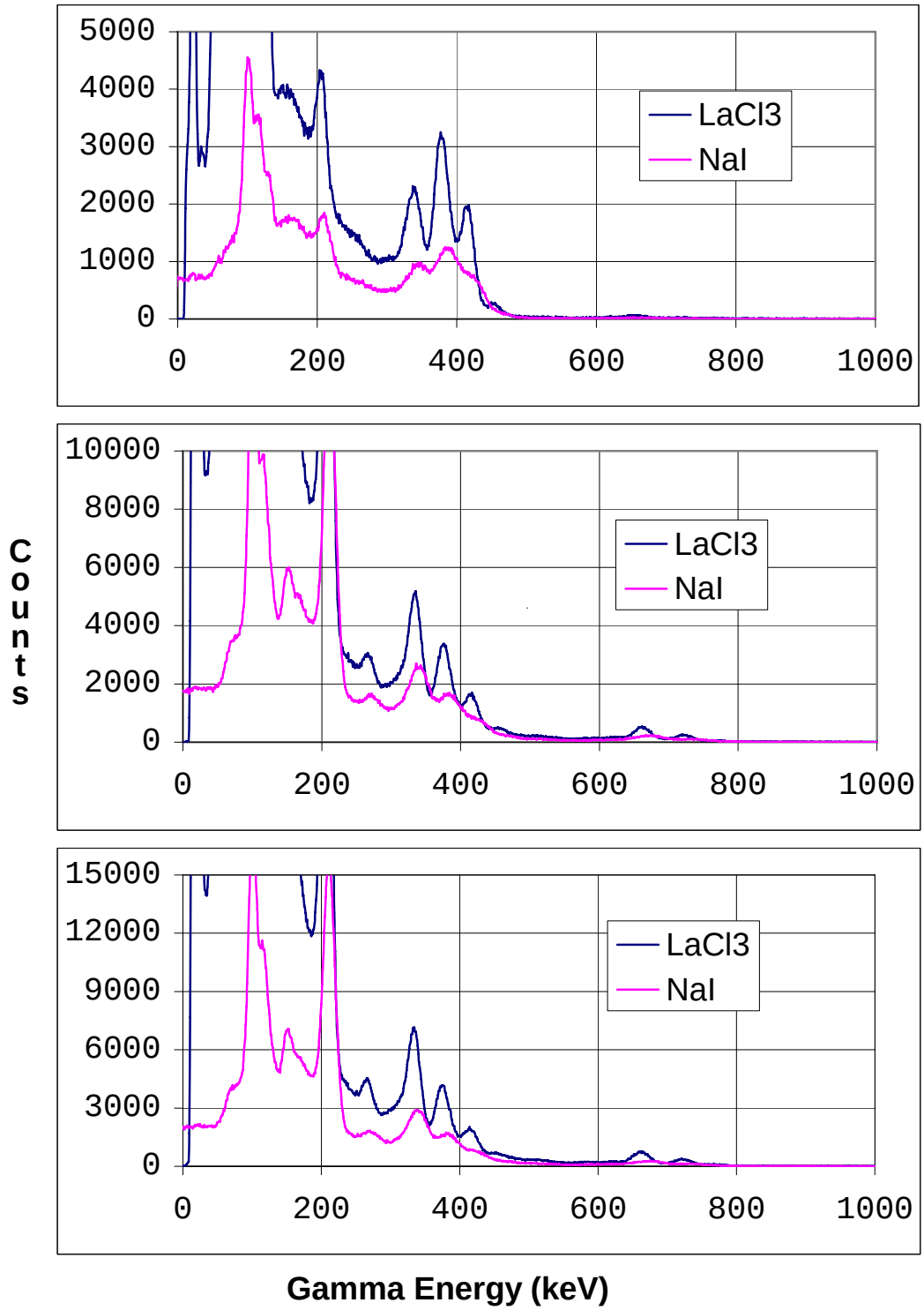

Fig. 7. The gamma-ray spectra, top to bottom, are those of low-, medium- and high-burnup plutonium (6%, 18% and 24% ^{240}Pu, respectively), measured with a 5-cm^2 by 2.54-cm thick ***$LaCl_3$(Ce)*** *scintillator and with the same-size NaI scintillator. The improved energy resolution at 414 keV is illustrated by the distinct peak in the $LaCl_3$ spectrum at this energy in the full range of isotopics.*

V. GE DETECTORS AND CRYOGENICS

Intrinsic germanium cooled to liquid nitrogen temperature continues to be the state-of-the-art in gamma-ray spectroscopy for NDA. Progress since the previous report on gamma-ray detectors for quantitative NDA[80] includes ready availability of very large Ge crystals, electrical cooling technologies, digital signal processing, advances in technology for surface electrical contacts, low-noise analog circuits, breakthroughs on semiconductor surface properties, and the implementation of active shields.

Table 1 includes specifications and performance data for a relatively small (5-cm^2 by 1.5-cm thick) planar Ge detector as a state-of-the-art reference for other spectrometer detectors of lower resolution described in the same table. Figures 1 and 2 show the spectra of low- and high-burnup plutonium measured with this Ge detector. The energy resolution for the Ge detector is the best of the four detectors represented in Figures 1 and 2, illustrating the complexity of these spectra.

A major advance for users who rely on high resolution with sensitivity in the widest energy range is that very large (up to ~300% efficient, relative to the efficiency of a 46-cm^2 by 7.5-cm-thick NaI detector, for detecting 662-keV gamma rays) Ge detectors are available and have become increasingly affordable. Applications to measurements of waste introduce additional criteria beyond those imposed by nuclear materials accountability, criticality safety, and radiation safety. These include requirements imposed by the Department of Transportation and by standards for acceptance of waste. Special nuclear materials represent only a fraction of the many isotopes that must be identified. Waste packages can be large with attenuating container walls. These applications benefit from high resolution and efficiency. Similar benefits accrue in NDA applications such as the security screening of freight.

More reliable, compact and vibration-free thermoelectric cooling extends field applications to measurements that cannot be supported by liquid nitrogen. Energy resolution for fixed electrically-cooled Ge is now comparable to that with liquid nitrogen cooling. The size of commercial electrical coolers has decreased, and the reliability and performance have improved significantly in the last ten years. Commercial portable electrically-cooled Ge detectors are also available now.

The gamma-ray spectra obtained with three high-resolution gamma-ray spectrometer systems are shown for low- and high-burnup plutonium oxide samples in Figures 8 and 9.[81] All three detectors can be used for gamma-ray isotopic measurements of low- to high-burnup plutonium and uranium. The liquid-nitrogen-cooled Ge detector gives the best energy resolution. Second-best is one example of a portable electrically-cooled Ge detector. The CdTe detector is discussed in Section VI.

Figure 10 shows a commercial, electrically-cooled, portable germanium detector. The weight (~10 kg without shielding and collimation) and dimensions are too large to be useful for measurements of deposits in plant equipment. These detectors can operate on a cart equipped with a lift mechanism to address many measurement needs from floor level. Nonetheless, needs for highly portable measurements of gamma-ray isotopics persist. The third set of data plotted in Figures 8 and 9 is that for a highly portable CdTe detector equipped with a small electric cooler. This detector has the resolution capability for the wide-range isotopics measurements.[82-83] However, because of the very small size of the CdTe crystal (the largest crystal size is indicated Table 1), implementation of CdTe isotopics excludes shielded materials. The first three detector columns of Table 6 give crystal dimensions and energy resolution for the three detectors used for Figures 8 and 9.

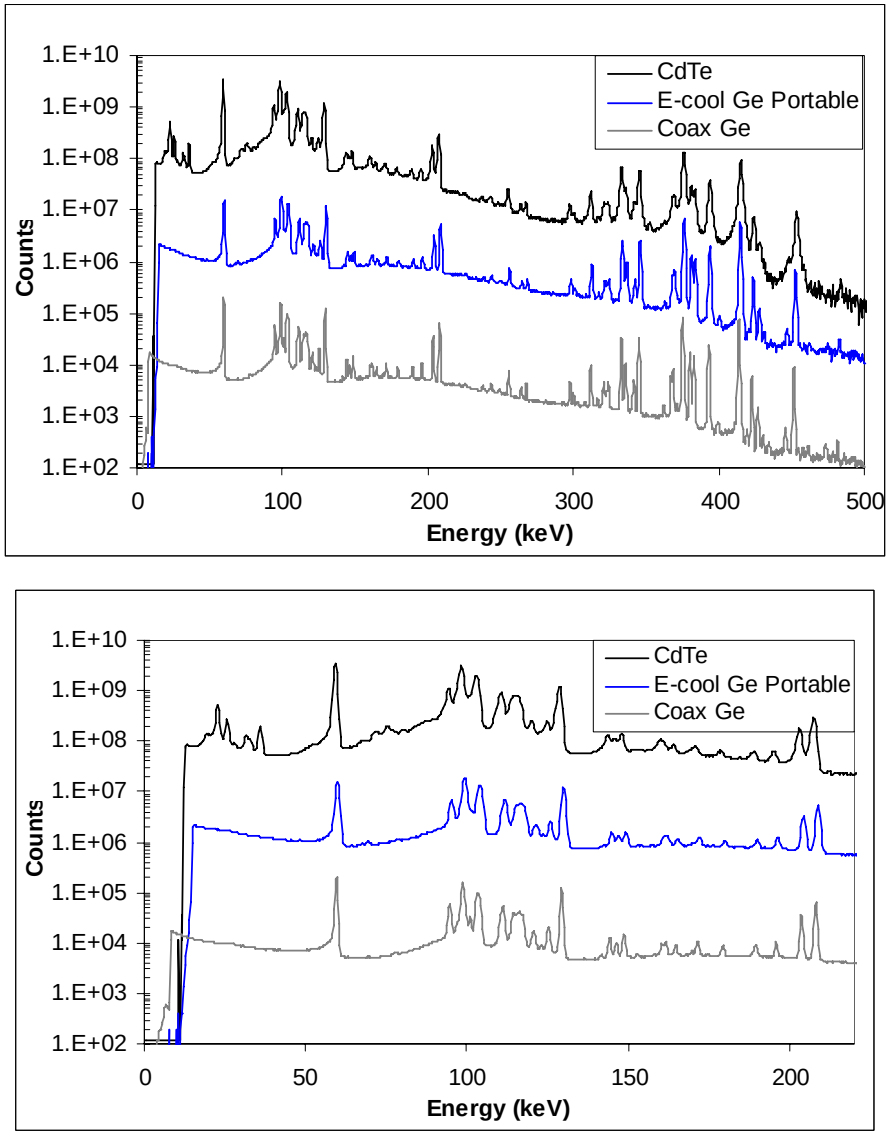

Fig. 8. High-resolution gamma-ray spectra of low-burnup (6% ^{240}Pu) plutonium oxide measured with a liquid-nitrogen-cooled coaxial Ge detector (bottom), portable electrically-cooled coaxial Ge detector (middle), and highly-portable cooled CdTe detector (top). Refer to Table 6 for crystal dimensions and energy resolution. The expanded view (0- 250 keV) shows the small resolution advantage of the portable electrically-cooled Ge over CdTe.

Figure 11 shows an innovative, prototype, portable Ge detector that uses a cylindrical Ge crystal surrounded by an active annular shield of dense BGO scintillator.[84] The packaging for this new electrically cooled detector is extremely compact, and its normal-use battery life exceeds 10 hours. Pulses from the Ge detector processed in anticoincidence with pulses from the 1-cm-thick BGO produce spectra with a suppressed Compton continuum increasing the sensitivity of measurements at low gamma-ray energies.

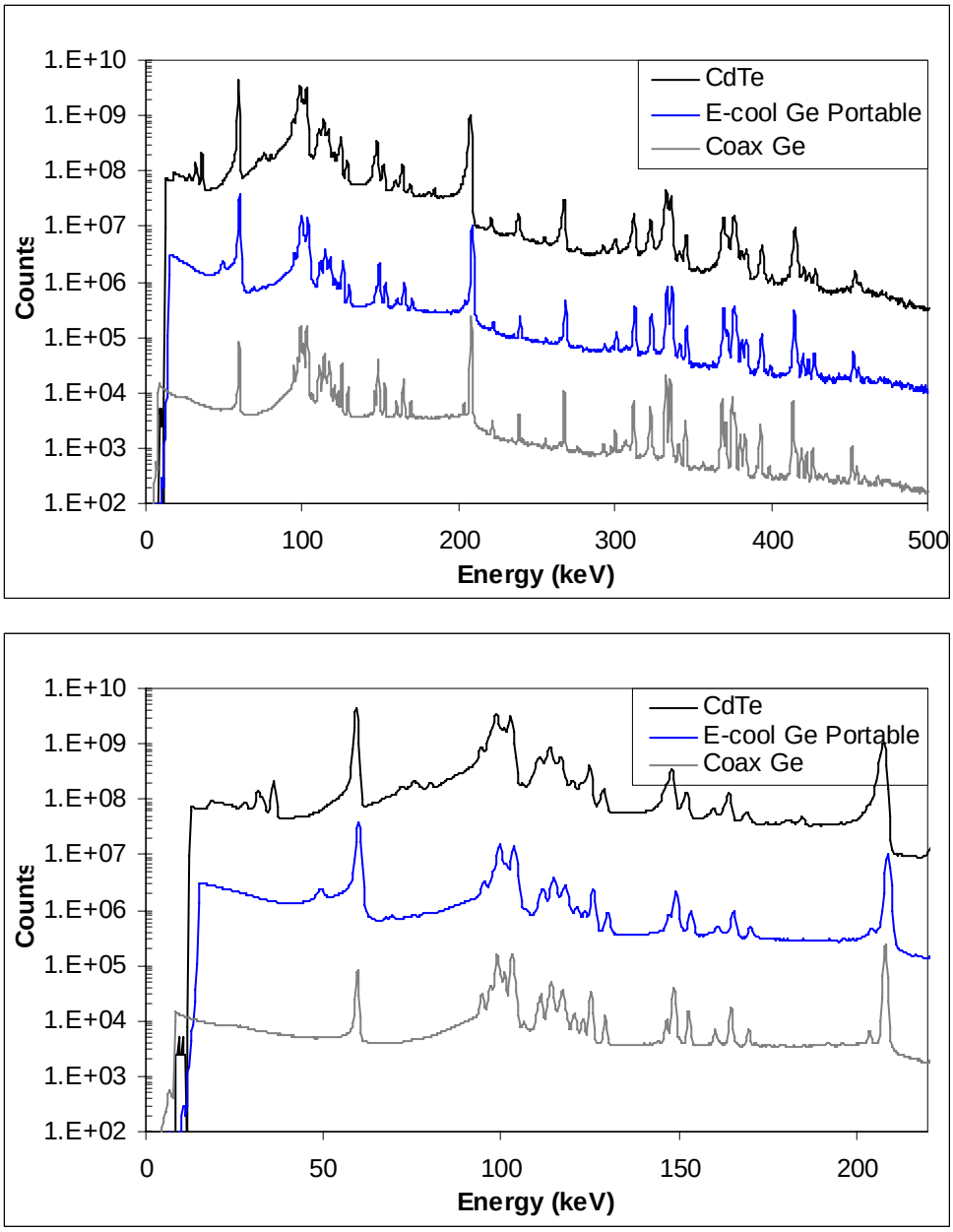

Fig. 9. High-resolution gamma-ray spectra of high-burnup (26% ^{240}Pu) plutonium oxide measured with a liquid-nitrogen-cooled coaxial Ge detector (bottom), portable electrically-cooled coaxial Ge detector (middle), and highly-portable cooled CdTe detector (top). Refer to Table 6 for crystal dimensions and energy resolution. The expanded view (0- 250 keV) shows the small resolution advantage of the portable electrically-cooled Ge over CdTe.

Applications of the prototype portable Ge detector with Compton suppression include measurements over a wide dynamic range. One example is low-enriched uranium, which often requires measurements of gamma rays at both 186- and 1001-keV. Another is uranium in reactor-return (recycled) material with high-energy gamma-ray activity (the 2614-keV gamma ray of ^{208}Tl) from decay of the ^{232}U progeny. The 1-cm-thick BGO annulus is also an effective passive shield, absorbing 100% of gamma rays at 122 keV and 50% at 662-keV.

Table 6. Compare High-Resolution Gamma-Ray Detectors

Detector		Ge, thick planar *(See Table 1)* LN_2 cooled	~14% Ge Portable Elect. cooled	CdTe *(See Table 1)* Highly portable elect-cool	Ge/BGO$_{anti\text{-}Compton}$ Very Portable, Elect. cooled
% FWHM	122 keV	0.4%	**1.3%**	**1.5%**	**TBD**
	662 keV	0.2%	**0.6%**	**0.6%**	**TBD**
% Intrinsic Photo. Eff.[a]	122 keV	81%	**~96%**	**63%**	**100%**
	662 keV	1.4%	**~3%**	**1.0%**	**5%**
Crystal shape		Planar	**Coaxial**	**Rectangular**	**Coaxial**
Crystal X-sectional area, cm^2		5	**~20**	**1.2**	**5.0**
Crystal depth, cm		1.5	**~3**	**0.3**	**5.0**

[a] Calculated intrinsic photoelectric efficiency at the given gamma-ray energy for stated detector thickness

The last detector column of Table 6 compares design parameters of this prototype portable Ge detector with the three commercial high-resolution detectors. The weight of the unshielded commercial portable Ge detector in Figure 10 exceeds that of the new prototype by nearly 40%. Target applications include highly portable, low-background, wide-energy-range, gamma-ray isotopics for low- to high-burnup plutonium and low- to high-enriched uranium. Achieving energy resolution sufficient for gamma-ray isotopics is the design challenge.

Fig. 10. The portable electrically-cooled Ge detector with tungsten collimator is shown mounted on a docking station (rectangular base) used for charging and cool down. The weight without the docking station is 12 kg.

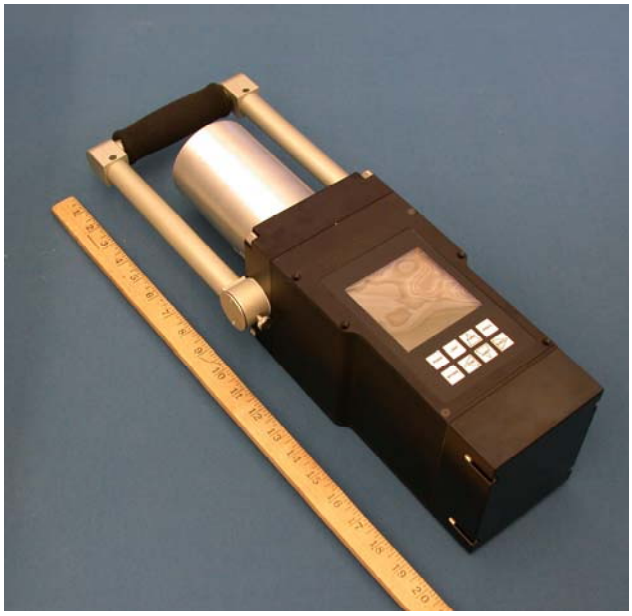

Fig. 11. The GN-5 prototype instrument (Frankle 03) is a self-contained compact high-resolution gamma-ray spectroscopy system. It incorporates an electrically-cooled Ge detector and a BGO anti-Compton annulus for high sensitivity in portable applications.

Micro-calorimetry defines a new field of super-high-resolution gamma-ray spectroscopy. Cryogenic cooling at liquid-nitrogen temperatures, ~77 ^{o}K, permits measuring the energy deposited by individual gamma-ray interactions into multiple discrete electronic transitions of a medium. Statistics of the primary electronic excitation limits energy resolution. When detector materials are cooled by mechanical and magnetic refrigerators to superconducting temperatures, ~0.1 ^{o}K, an individual gamma-ray interaction excites many more transitions (of much lower energy) from states of superconductivity to states of normal conductivity. Measuring the corresponding change in properties related to material conductivity determines the energy deposited by the gamma ray, but energy resolution is now limited by the thermal noise effects, which are very small at the low temperature and by intrinsic line widths.[85-86] Such energy resolution would enable gamma spectroscopy that is effectively independent of the limitations of continuum background and spectral interference. Research underway in micro-calorimeters for gamma-ray spectroscopy gives energy resolution of 42 eV at 103 keV, ten times better than germanium (see Figure 12).[87-88]

Digital signal processing (DSP) is responsible for major improvements in the resolution and throughput of germanium detector systems. The DSP spectrometer digitizes the preamplifier pulse directly, eliminating the linear amplifier. The advantages of this technology, combined with ever-increasing microprocessor memory and speed, include the ability to optimally process a wide dynamic range of pulses. Substantial benefits are realized in the performance of large Ge detectors that are sensitive to high gamma-ray energies and count rates. The spectral quality achieved with commercial DSP multichannel analyzers (MCAs), both benchtop[89] and portable,[90] consistently exceeds that of analog counterparts.

Substantial benefits of DSP are also realized in the performance of noncryogenic solid-state detectors such as CdZnTe and CdTe that are often implemented as portable spectrometers. The performance of these detectors is dependent on the choice of time constants for detector pulse processing. Portable DSP MCAs offer a wide range of time constants, while portable analog MCAs typically offer only a few choices.

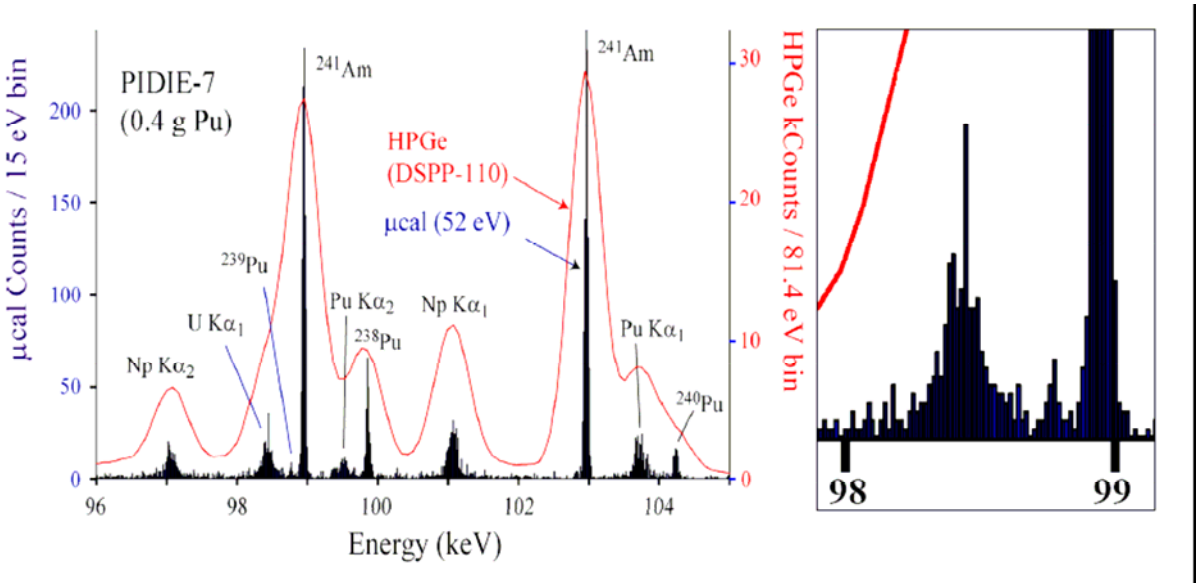

Fig. 12. LANL-NIST X-ray and gamma ray spectrum of Pu in the 100 keV region. Red spectrum taken with HPGe detector with ~500 eV FWHM resolution.. Black spectrum taken with single-pixel microcalorimeter detector with 52 eV FWHM resolution. In the microcalorimeter spectrum, we can identify by eye the U, Pu, and Np X-rays and the isotope-specific gamma rays from 238Pu, 239Pu, 240Pu, and 241Am. On the right, a magnified view of the 98 to 99 keV region, showing the 239Pu in between the U K-alpha X-ray and a very intense 241Am gamma ray. Note that the natural line shape of the Xrays is apparent in the microcalorimeter spectrum.

The impact of DSP on energy resolution is substantial, improving it by up to 50% for large coaxial detectors and high gamma-ray energies when compared analog signal processing with the same energy and detector. The reason is that the analysis of the digitized pulse can compensate to a greater extent for large ballistic deficits in large crystals.[91] Furthermore, data throughput can improve by 300% at high rates that demand shorter analog shaping times.[92] An additional benefit of DSP is that the lifetimes of Ge detectors operating in constant neutron environments can be extended because the analysis of the digitized pulse is less sensitive to changes in pulse shape caused by neutron damage.

Section I gave an overview of germanium detectors used for uncollimated high-resolution 4-π spectroscopic imaging of nuclear materials. Applications of low-energy-resolution aperture imaging to quantitative NDA were discussed in Section III. The benefits of improved energy and position resolution are greater sensitivity and accuracy, but such benefits may not outweigh the cost and maintenance of a cryogenic, hybrid, orthogonal-strip, germanium detector.[93] The implementation of high-resolution, uncollimated, 4-π Compton imaging may be worth the additional investment because of the potential for determining the three-dimensional distribution of isotopics. Most field applications of portable gamma-ray measurements are performed at hundreds or thousands of locations with low resolution, and many are performed in areas with a wide range of isotopic composition. Low-cost spectrometers (Section VIII) may replace many portable measurement needs in DNS implementations. A fixed installation of high-resolution spectroscopic imaging in these areas could greatly reduce the uncertainty caused by assumed stream values for the isotopic distribution at each particular measurement location in both portable and DNS implementations.

Cryogenic cooling is the major contributor to the cost and maintenance of high-resolution gamma-ray spectroscopic imaging. Demands on electronics, algorithms for processing digital pulses, algorithms for interpreting pulse data, logic that defines event sequence, and algorithms for Compton imaging add requirements to the overall investment. Position-sensitive Ge detectors, electronics, and firmware are currently commercial prototypes.

"Segmented" germanium detectors use a single crystal with electronically isolated surface contacts that segment the volume of a detector.[94, 95] Interpreting the position and energy of each of three Compton-scattered events gives a three dimensional spectral image of the gamma-ray sources. Such detectors used in uncollimated applications of gamma-ray Compton spectroscopic imaging rely on new technologies for electrical contacts, low-noise analog preamplifiers, and fast, multichannel, digital pulse processing. Because noise determines the minimum variance in energy and position, cooling of the individual field-effect transistors is a feature that adds complexity to the detector design and increases failure possibilities. Segmentation of this type has also been achieved at room temperature with a cadmium zinc telluride detector to give position in two dimensions using multiple contacts (pixelated anode) on one surface of the rectangular crystal. Compton imaging in three dimensions is achieved by timing of gamma-ray pulses to determine the third coordinate of the interaction position within the crystal.[96]

Orthogonal germanium strip detectors have equivalent complexity of cryogenic cooling but offer improved position resolution in Compton imaging. Although the interpretation of position is simplified in these detectors relative to segmented germanium, they rely on additional material advances such as "amorphous" Ge to eliminate dead layers on the surfaces of narrow germanium strips.[97-99] Sacrificing the higher density of germanium in favor of orthogonal Si strip detectors has several major advantages for Compton imaging. Eliminating cryogenic cooling is among these, as is the maturity of orthogonal silicon strip detectors and the supporting electronics. Although orthogonal silicon strip detectors are most likely for early NDA implementation of high-resolution Compton imaging, another decade may pass before such systems are available for testing.

VI. NONCRYOGENIC PORTABLE SEMI-CONDUCTOR DETECTORS

When large crystals are not required, compound semiconductor materials are potential alternatives to Ge if compromises in resolution are acceptable, and to NaI when better resolution is required. Progress in solid-state gamma-ray detectors that use such materials is significant, and it is far from complete. This section indicates some of the parameters that influence resolution and limit crystal size in compound semiconductors. More detail is published elsewhere.[100]

The production of highly pure elemental semiconductors (Ge and Si) benefits from decades of effort. Development of compound semiconductors is less mature. Compound materials are subject to effects of additional impurities. Furthermore, charge-transport properties of pure compound semiconductors are less ideal than those of Ge or Si, and impurities increase problems from charge trapping. Finally, order-of-magnitude differences between drift velocities of electrons and holes in compounds contrast with very similar drift velocities in Ge and Si.[101] These effects limit the practical crystal size by crystal-growth and charge-transport limitations. Resolution is impacted by all charge-transport issues.

Several material parameters influence energy resolution in solid-state detectors. One is the band gap. Resolution improves as the band gap decreases because more charge is created for a given amount of energy deposited. Table 3 indicates that Ge should give the best resolution based on its smaller band gap. However, resolution also improves with reduction of noise from charge leakage as the band gap decreases. Therefore, high Ge resolution is only possible with cooling to liquid nitrogen temperatures to eliminate thermal noise effects. A qualitative look at the three compound semiconductor materials in Table 3 suggests that CdTe, with the smallest band gap is capable of the best energy resolution of the three and that HgI_2 with the largest band gap, is best-suited for room-temperature operation, both of which are validated empirically. The resolution of these compound semiconductor materials is intermediate between NaI and Ge.

Table 7 describes performance, as well as efficiency and size of the largest available crystals of three noncryogenic, commercial, semiconductor detectors: coplanar-grid cadmium zinc telluride (CPG CdZnTe), electrically cooled cadmium telluride (CdTe), and mercuric iodide (HgI_2). Figure 13

is a plot of the intrinsic photoelectric efficiency as a function of energy. This section discusses these three detector types. Also included as reference data in Table 7 is the corresponding information for a portable electrically cooled Ge detector and a compact NaI.

Table 7. Compare Non-Cryogenic Portable Solid-State Gamma-Ray Detectors

Detector		~14% Ge *(See Table 6)* Portable elect-cool	(CPG) CdZnTe *(See Table 1)*	CdTe *(See Tables 1 & 6)* Highly portable elect-cool	HgI_2[b]	NaI:Tl *(See Table 1)*
% FWHM	122 keV	1.3%	6.3%	1.5%	~5%	13.0%
	662 keV	0.6%	3.2%	0.6%	3-4%	7.0%
% Intrinsic Photo. Eff.[a]	122 keV	~96%	100%	63%	97%	100%
	662 keV	~3%	8%	1.0%	5%	15%
Crystal shape		Coaxial	Rectangular	Rectangular	Rectangular	Cylindrical
Crystal X-sectional area, cm^2		~20	2.3	1.2	6.3	5.0
Crystal depth, cm		~3	1.5	0.3	0.3	5.0

[a] Calculated intrinsic photoelectric efficiency at the given gamma-ray energy for stated detector thickness

[b] http://www.contech.com/Mercuric_Iodide_Detectors.htm

CPG CdZnTe

The development and production of cadmium zinc telluride material[102] and the design and manufacture of detectors that use these crystals[103-107] have taken place since 1985. Stoichiometrically, the material is typically $Cd_{1-x}Zn_xTe_1$, where $0<x<1$.[108] The difference of pulses from coplanar,

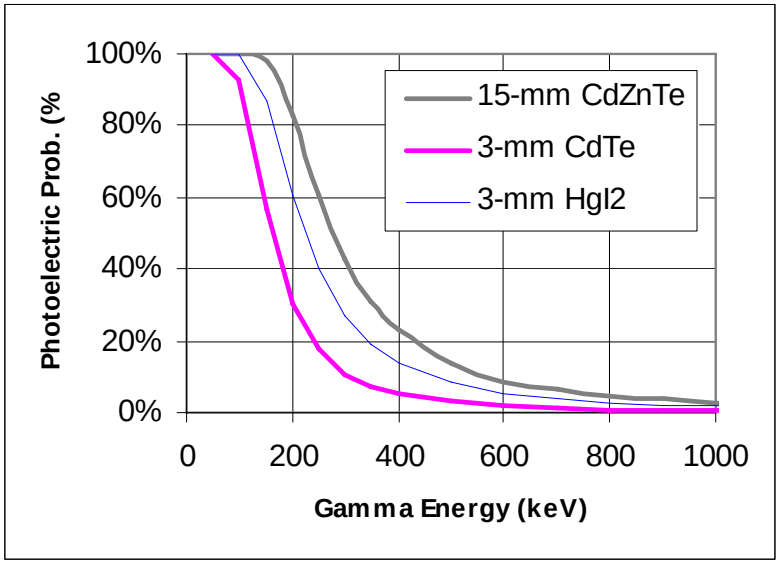

Fig. 13. Intrinsic photoelectric detection efficiency vs. gamma-ray energy for the three compound semiconductor detectors listed in Table 7: the 15-mm-thick CPG CdZnTe (top, gray), 3-mm-thick CdTe (middle, blue), and 3-mm-thick HgI_2 (bottom, pink) detectors.

differentially biased anodes (coplanar-grid or CPG) compensates for the nearly order-of-magnitude difference in transport mobility of electronics and holes in solid-state material.[109, 110] Timing between anode and cathode pulses determines interaction depth, which permits correction for the loss of charge from recombination or trapping effects.[111, 112] A large band gap compared to Ge and Si permits operation of CdZnTe at room temperature. Commercial CdZnTe and CPG CdZnTe detectors are used in portable and DNS applications.[113-117]

The largest CPG CdZnTe detectors are limited in size (cubic crystals 1.5 cm on a side) and have a lower intrinsic efficiency at 662 keV than the compact NaI detector in table 7. However, this detector

is approximately equal in sensitivity to the 2.5-cm-diameter compact NaI detector in many portable measurement applications because the ratio of peak-to-Compton ratio for the CdZnTe exceeds that of NaI. Resolution advantages of CPG CdZnTe over NaI, illustrated in Figures 1 and 2 and Table 7 are also essential in many common interference situations. A CPG CdZnTe detector usually:

- resolves the ^{239}Pu 375-keV complex (which is often dominated by activity from ^{241}Am) from the 414-keV peak of ^{239}Pu.
- permits measurements of ^{235}U at 186 keV in the presence of plutonium.
- resolves the ^{235}U 186-keV peak from the 238-keV peak – from the decay-chain of ^{232}U – that appears in spectra of recycled material.
- resolves 414-keV and other gamma rays (including 345 keV) of ^{239}Pu from lower-energy ^{237}Np gamma rays (especially at 300 keV) to permit evaluation and extraction of less intense but interfering ^{237}Np activity at 416 keV.

The large CPG CdZnTe detector is pictured alongside the compact NaI detector in Figure 14 to illustrate the similar dimensions. The benefits of its superior energy resolution are, unfortunately, outweighed by the high cost of the large CPG CdZnTe detector and by its limited availability.

Electrically Cooled CdTe

Cadmium telluride material properties have improved since 1985. Charge transport problems limit the detector thickness to 3 mm. Although the relatively large band gap (Table 3) permits operation at room temperature, a great advantage in energy resolution is achieved by cooling to just below zero degrees Centigrade because the thin crystals are most useful for spectroscopy at lower gamma-ray energies (< 200 keV) where the noise reduction is very beneficial. Simple circuitry that analyzes pulse shape can be used to assess corrections for charge loss. Both cooling and charge-loss corrections are implemented in commercial CdTe detectors.

Figure 13 and Table 7 show the significant difference in the intrinsic detection efficiency of the largest CdTe and CPG CdZnTe detectors. Because of its small size, the CdTe detector is not practical for measurement of holdup deposits that must use higher-energy gamma rays and many very short counts. However, its good energy resolution –comparable to Ge and five times better than that of CPG CdZnTe – contributes greatly to portable measurements of isotopics.

Fig. 14. The CPG CdZnTe, compact NaI, and CdTe detectors (Table 7) pictured at the left, center, and right, respectively. The rectangular module at the right is the power supply for the Peltier cooler within CdTe detector.

The recent commercial availability of Peltier-cooled CdTe detectors with crystals larger than 1 cm^2 has made gamma-ray isotopic measurement of uranium and plutonium truly portable.[118-120] Figures 1, 2, 8, and 9 illustrate the high resolution of these detectors which operate with automated charge-loss corrections. The energy resolution of the best cryogenically cooled Ge detector is only three times better than that of CdTe. Figures 14 and 15 illustrate the compact dimensions of the CdTe detector and its portable power supply.

The capability of CdTe to analyze the isotopic distribution over a wide range (3%-30% ^{240}Pu and higher), (0.1 to 80% ^{235}U), and mixed oxide. A count time of 15 min. with the CdTe detector measures ^{240}Pu to 2% and ^{235}U to 3%. Figure 15 shows the CdTe detector in use for gamma-ray isotopics measurements of plutonium.

The current large-area, single-crystal CdTe detector is too thin (< 0.3 cm) for practical measurements of holdup. A CdTe thickness of 0.2 cm absorbs 36% of ^{235}U gamma rays at 186 keV but only 12% of ^{239}Pu gamma rays at 414 keV. However, new commercial efforts to develop prototypes composed of stacked CdTe[121] crystals may triple the effective CdTe thickness. Higher noise from the multielement detector will preclude use of the crystal array for gamma isotopics measurements, but the possibility exists for analyzing pulses from the first layer for isotopics while using the full stack to quantify holdup using higher-energy gamma rays.

Fig. 15. A Peltier-cooled CdTe detector and DSP MCA in use for isotopics measurements Pu in a glove box.

Measurements of ^{235}U at 186 keV as well as those of ^{239}Pu, ^{241}Pu, and ^{238}Pu at 129, 149 and 153 keV, respectively, have the advantages that they are intense and easily shielded from room background. Low- or intermediate-resolution measurements of ^{239}Pu using the 414-keV gamma ray require meticulous attention to the determination of room background at each location because no practical shield is thick enough to effectively eliminate gamma rays of this energy. This is not the case for the lower-energy gamma-ray region. Hence, portable gamma-ray measurements of plutonium using the current large-area, single-crystal CdTe detector would be simplified compared to measurements with low- or intermediate-resolution detectors that are unable to resolve gamma rays or sensitively extract peaks from the larger continuum in the lower energy region. Such applications require nuclear materials that are not heavily shielded.

HgI_2

Because of its relatively large band gap (see Table 3), mercuric iodide, HgI_2, is viable at room-temperature as a semiconductor detector. Like other compound semiconductors, charge-transport properties of this material limit the thickness of useful crystals. Mercuric iodide crystals with areas up to 6.3 cm^2 and thickness up to 3 mm are now available with performance indicated in Table 7. A larger area compared to that of the largest CPG CdZnTe detector (2.3 cm^2) is possible without sacrificing energy resolution in part because of the band-gap advantage of HgI_2 discussed in Section III. However, the coplanar grid also contributes additional noise to the CdZnTe pulses. Even 0.1-mm-thick crystals of HgI_2 have reasonable intrinsic absolute photoelectric efficiency at 100 keV (Figure 16) because of their relatively high density and Z (Table 3). The efficiency of the 3-mm-thick HgI_2 detector is better than that of the thickest CdTe detector and approaches that of the thickest CPG CdZnTe detector (Figure 13). Published results (Vaccaro 01) indicate that improved materials give long-term spectral stability not demonstrated previously for HgI_2. Nonetheless, HgI_2 detectors are not included in Table 1, because i) both energy resolution and detection efficiency for large HgI_2 detectors are only comparable to that of the CPG CdZnTe detector (Table 7), ii) the cost of large HgI_2

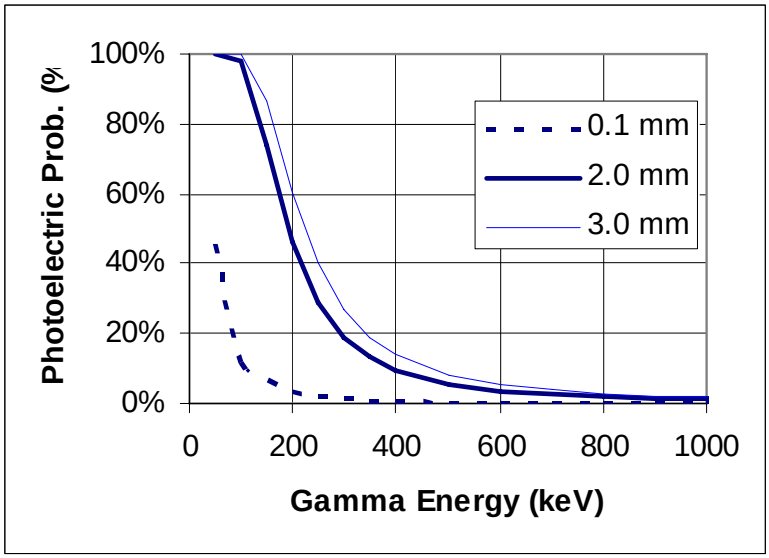

Fig. 16. The intrinsic photoelectric detection efficiency is plotted vs. gamma-ray energy for three thicknesses of mercuric iodide. The thinnest (dashed line) is comparable to a photodiode (Section III).

detectors exceeds that of large CPG CdZnTe detectors, which is already high, iii) there is little field experience with large HgI_2 detectors, and iv) the availability of large HgI_2 detectors is unknown.

VII. GAS-FILLED DETECTORS: HIGH-PRESSURE XE IONIZATION CHAMBERS

The benefits of gas detectors include long-term stability that cannot be equaled by scintillator or solid-state detectors because charge transport properties of gas are not significantly impacted by changes in temperature and the effects of radiation. Stability is a highly desirable characteristic for detectors in unattended monitoring applications, perhaps where climate and radiation vary. High-pressure xenon ionization chambers have emerged recently as gamma-ray spectrometers.[122]

High-pressure xenon ion chambers (HPXe) are cylindrical tubes with a concentric-wire or -rod anode. Most are equipped with a cylindrical Frisch grid[123] that surrounds the anode. The large difference in drift velocity of electrons and positive xenon ions causes the measured pulse amplitude to be sensitive to the interaction position in an ungridded ion chamber. However, the electrostatic

effect caused by vibration and the resulting change in the relative positions of the differentially biased anode and grid is a source of noise. Despite high bias voltages, charge collection time is long in xenon gas, and a long amplifier shaping time is required.

Commercially available HPXe detectors are intermediate-resolution gamma-ray spectrometers. Xenon's high atomic number (Z=54) and resulting high photoelectric cross-section are useful for high gamma-ray energies. Its density is approximately 0.4 g/cm^3. The detectors are available with diameters of 3-11 cm. Figure 17 plots the intrinsic photoelectric efficiency for a 5-cm-thick compact NaI detector, a 1.5-cm-thick (largest) CPG CdZnTe detector, and a 10-cm-diameter HPXe detector with a gas pressure of 0.4 g/cm^3. The similar intrinsic efficiency of the HPXe and CdZnTe detectors is overcome by the larger size of the HPXe, whose overall length can be 10-100 cm compared to 1.5 cm for CdZnTe. Figure 18 shows a small-diameter, commercial prototype HPXe detector.

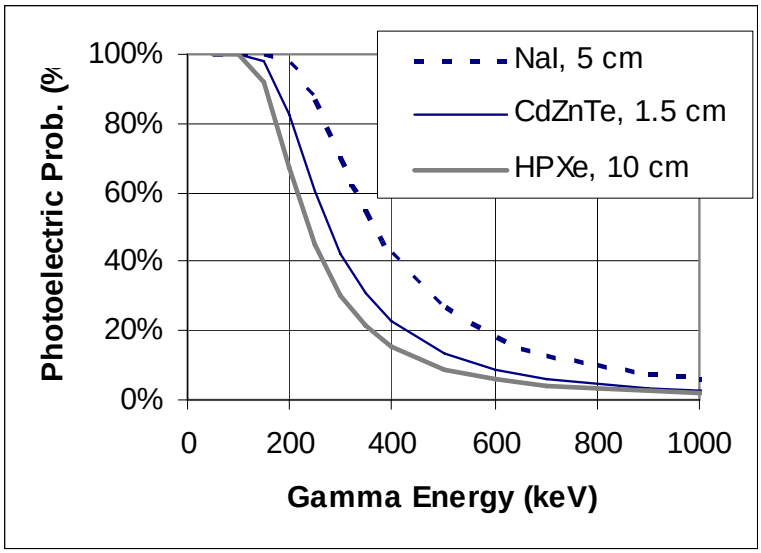

Fig. 17. The intrinsic photoelectric efficiency is plotted vs. gamma-ray energy for a 5-cm-thick compact NaI detector (dashed), the 1.5-cm-thick (largest) CPG CdZnTe detector (light solid line), and 10-cm-diameter HPXe (heavy solid line) detector with gas density of 0.4 g/cm^3.

Fig. 18. Commercial prototype HPXe detector. The diameter and active length are 4.5 and 10 cm.

Figure 19 and Table 1 indicate that the energy resolution of HPXe is similar to that of CdZnTe.[124] However, only HPXe detectors can be scaled up in size for potential applications not available to CdZnTe. All of the benefits of gas detectors apply to the HPXe detectors. Acoustic effects on the grid and electronic effects contribute to limitations in energy resolution. Experimental efforts include investigating alternatives to the grid.[125]

The inherent ruggedness and stability of gas counters is demonstrated by decades of stable operation of He^3 neutron detectors. Equivalent data for HPXe comes from the reliable and stable performance of such a detector monitoring the 511-keV gamma ray during six years of continuous operation on the earth-orbiter MIR.[126] The superior temperature stability of HPXe has been demonstrated with measurements of the 662-keV gamma-ray of ^{137}Cs at different temperatures. Figure 20 is a plot of the energy resolution of the HPXe detector measured at 662 keV as a function of temperature. Also plotted on the graph is the resolution of CdZnTe. The increase in resistivity with increasing temperature of a solid state detector compromises the charge-collection properties, as illustrated in Figure 20. Figure 21 shows the drift in the centroid of the 662-keV peak measured with the HPXe detector as a function of temperature.[127] Comparable data for NaI or other scintillators would show a drift of ~40% in the same temperature range.

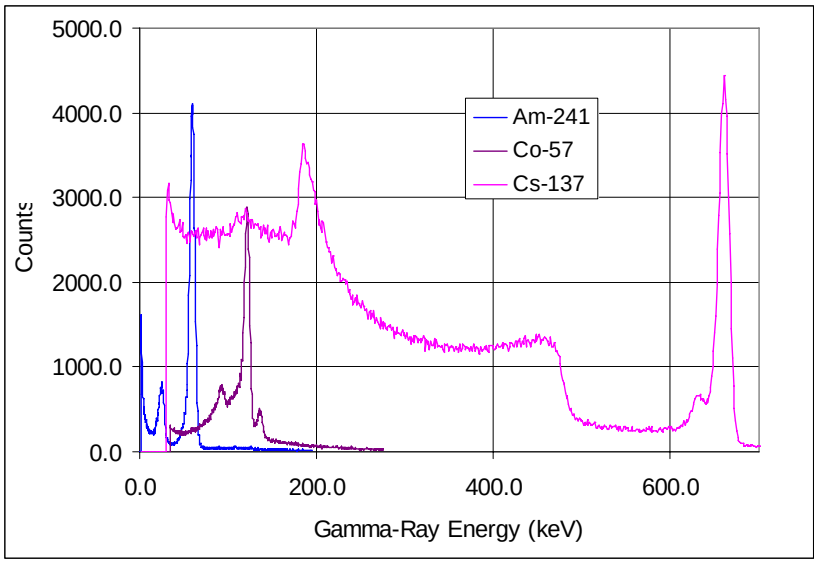

Fig. 19. Gamma-ray spectra of ^{241}Am, ^{57}Co and ^{137}Cs measured with the HPXe detector pictured in Figure 17 indicate energy resolution comparable to that of the CPG CdZnTe detector.

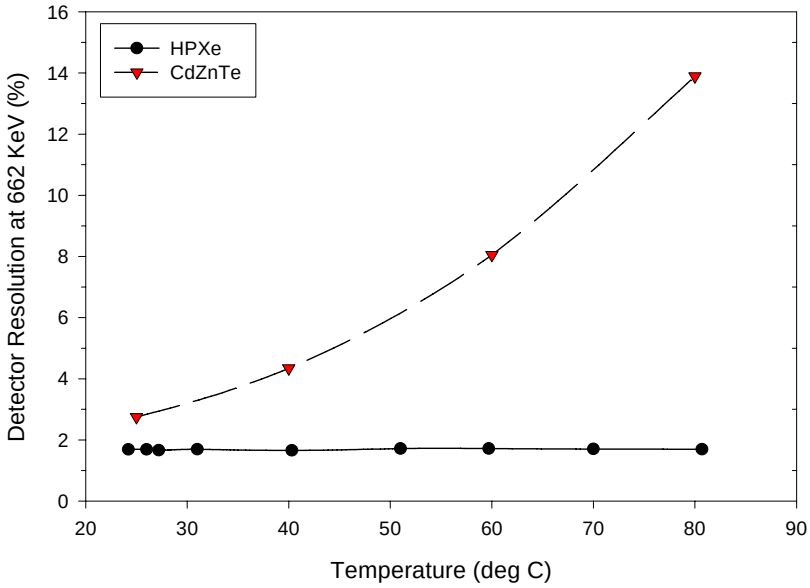

Fig. 20. The resolution (FWHM) at 662 keV of the HPXe detector (circles) and CdZnTe (triangles) is plotted vs. temperature of the detector.

Numerical modeling of the HPXe detector response supports new designs with reduced sensitivity to vibration. Such modeling also supports assessments of novel applications such as the addition of ^{3}He to the high-pressure xenon gas.[128] Figure 22 shows the modeled spectrum for such a detector measuring a ^{137}Cs source and thermal neutrons simultaneously. Other work on electron drift velocities indicates the practical feasibility of spectroscopic measurements of gamma rays and neutron capture using the Xe-^{3}He gas mixture.[129] Such detectors could be most useful for monitoring materials in enrichment facilities, particularly for the processes that operate at high temperature.

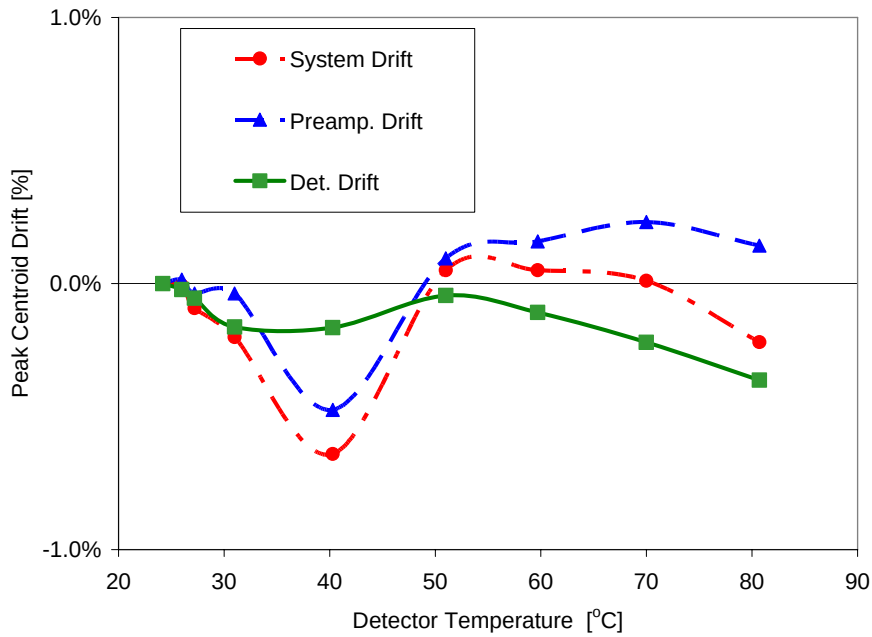

Fig. 21. The percent drift in the 662-keV peak centroid is plotted vs. temperature for the preamplifier (triangles), HPXe detector (squares) and the whole system (circles). Comparable NaI data would show large drifts (40%).

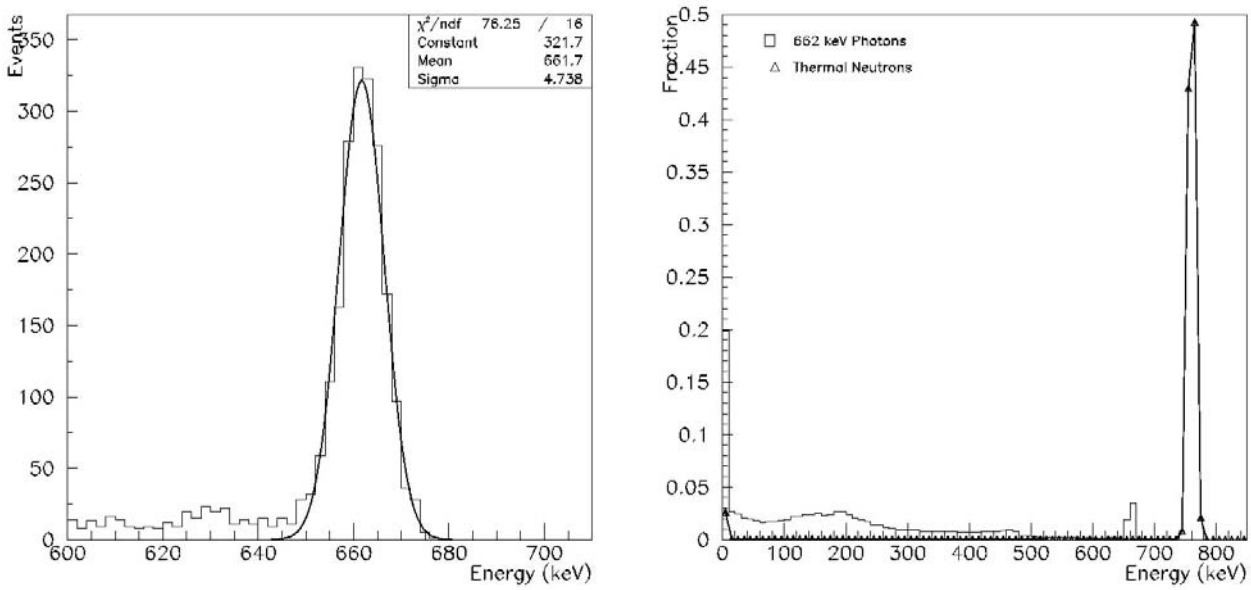

Fig. 22. Simulated pulse-height spectra of ^{137}Cs plus thermal neutrons for the HPXe gas detector with ^{3}He. The 600-700-keV region (left) shows the 662-keV peak with a FWHM of 1.7%, similar to experiment. The full spectrum (right) shows the ^{3}He neutron-capture peak near 750 keV and the ^{137}Cs peak at 662 keV.

The benefits of intermediate energy resolution, ruggedness, resistance to radiation damage, temperature stability far exceeding that of solid-state and scintillator detectors, the ability to scale detectors to large sizes, and the resistance of gas detectors to damaging effects of radiation combine to strongly encourage continued improvement of HPXe detectors for spectroscopy. A practical acoustically desensitized design for the HPXe detector is the promise for continuous unattended monitoring of nuclear materials.

VIII. ORGANIC SCINTILLATORS: PB-LOADED PLASTIC FOR DNS

The ability to create very large scintillators of almost any shape is a characteristic of plastic scintillators, which are used worldwide in portal monitoring of personnel and vehicles. The low cost of plastic scintillators is another benefit. The tendency for personnel and vehicle monitors to alarm from the detection of legitimate radiation (e.g. medical isotopes) far exceeds the alarm rate from detection of illicit radioactive materials, because plastic scintillators have no energy resolution.

The low photoelectric cross-section in low-Z, low-density plastic is the reason that plastic scintillators are not spectrometers. Most gamma rays interact in plastic by Compton scattering and the resulting spectrum is an energy continuum with no peak. However, the loading of plastic scintillators with high-Z materials achieves a dramatic increase in the theoretical photoelectric cross-section. Figure 23 illustrates this increase with theoretical photoelectric and total interaction probabilities of the typical plastic scintillator compared to those with 5% and 10% lead loadings. The results are calculated for three thicknesses of plastic scintillator: 5, 10 and 15 cm. The 5-cm-thick plastic scintillator is used commonly in portal monitors.

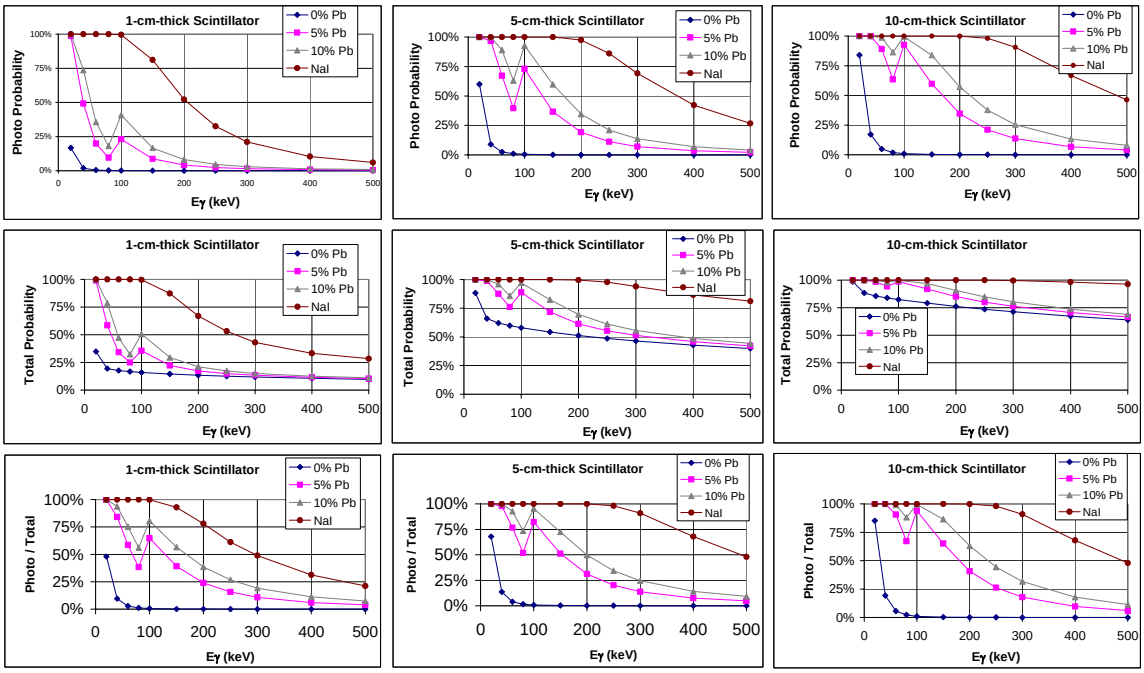

Fig. 23. Theoretical photoelectric and total cross-section (and the ratio of photoelectric to total) of the typical plastic scintillator compared to those with 5% and 10% lead loadings of lead by weight are plotted vs. gamma-ray energy. The results are calculated for three thicknesses of plastic scintillator: 5, 10 and 15 cm. Also plotted for reference are the corresponding data for the NaI scintillator of the same thickness.

Experimental data provide compelling evidence of the spectroscopic capability of lead-loaded plastic scintillators, corroborating the theoretical results in Figure 23. Gamma-ray spectra of ^{109}Cd, ^{57}Co and ^{235}U were measured using a small disk (5-cm-diameter by 1.27-cm-thick) of 5%-lead-

loaded commercial plastic scintillator coupled to a 6.5-cm-diameter photomultiplier tube. The small scintillator piece is clear and colorless and has no apparent flaws to limit light transmission. Figure 24 illustrates the experimental setup with two source positions. Evidence of spectroscopic capability is most apparent with the sources in Position 2, in which some gamma-ray path lengths in the were as long as 5 cm. Figure 25 shows the three gamma-ray spectra measured with the lead-loaded plastic. The energy calibration, gamma-ray-peak energy vs. channel number, in the inset, is linear. The energy resolution at 122 keV (the ^{57}Co is 23%, about twice that of NaI at this energy.[130]

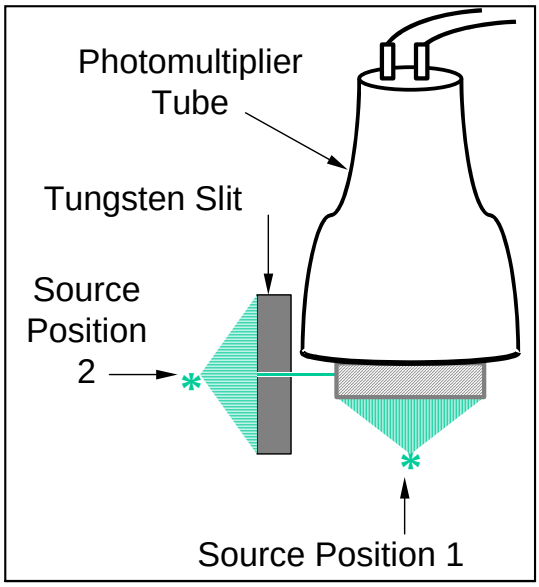

Fig. 24. Hardware setup for measurements of gamma-ray spectra with the 5%-lead-loaded plastic scintillator (diagonally shaded) coupled to a photomultiplier tube. The1.3-cm-thick tungsten collimator is a 5-cm-wide by2-mm-tall horizontal slit.

The 186-keV gamma-ray peak is only partly resolved in the spectrum shown in Figure 25. A higher lead loading should significantly enhance the definition of this peak relative to the continuum, as indicated by the data in Figure 23. Figure 23 also suggests that spectroscopy at higher gamma-ray energies such as 414-keV (^{239}Pu) may not be practical for any of the high-Z-loaded plastics. However, applications to ^{235}U in continuous measurements using distributed networked scintillators should be practical. Unlike portable measurements in which the best possible resolution must combine with a robust analysis algorithm, the algorithms used for each fixed sensor can be tailored to the much smaller range of variations at each fixed location.

The quality of the small commercial 5%-lead-loaded plastic scintillator used to obtain the spectra plotted in Figure 25 is extremely good from the standpoint of clarity and absence of color. Despite momentum provided by the encouraging results obtained with this scintillator, commercial manufacturers have achieved no progress toward production of practical scintillator pieces of larger size or higher lead loadings. Because the potential benefit to portal monitoring and DNS is so great, efforts continue to develop the lead-loaded plastic scintillator materials for these applications.

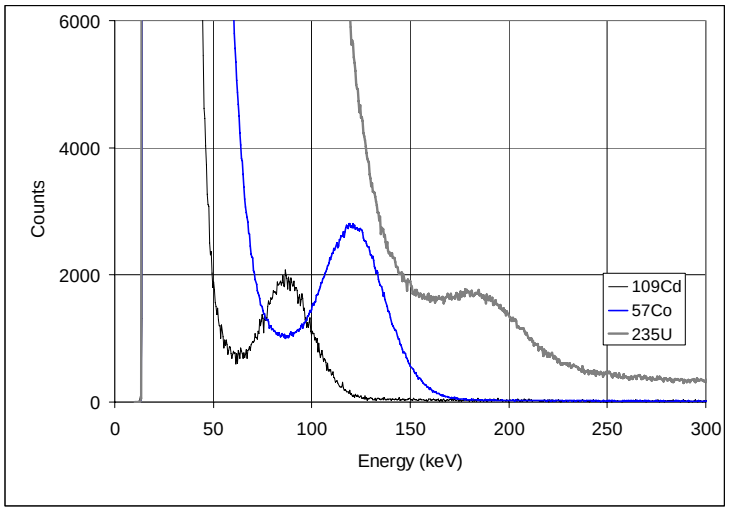

Fig. 25. Pulse-height spectra for three gamma-ray source, ^{109}Cd, ^{57}Co and ^{235}U, in source position 2 (see Figure 22). The energies of the three photopeaks (88, 122 and 186 keV) plotted vs. peak channel in the inset illustrate the linearity of the pulse amplitude with energy.

Another very new approach with plastics serving as host is one which embeds nanoparticles of an active sensor, either semiconductor[131] or inorganic scintillator,[132] in a solid organic – sometimes scintillating – matrix. Growth of large crystals with ideal properties for transporting charge (semiconductor materials) or light (inorganic scintillators) is replaced, in the cases of these new detectors, with production of nanoparticulates[133] of the same material. The organic matrix governs the transport and determines the overall detector geometry while the properties of the nanoparticulates determine performance. The potential includes very large spectrometer detectors, improved resolution, and low cost.

END NOTES

[1] D. Reilly, et. al., *Passive Nondestructive Assay of Nuclear Materials*, 1991, pp. 43-64.
[2] P. A. Russo, 2005.
[3] P. A. Russo, T. R. Wenz, and K. D. Veal, 2000.
[4] V. Longmire, N. Ensslin, C. Files *et al*., 2004.
[5] G. F. Knoll, 2000, pp. 231-242.
[6] G. F. Knoll, 2000, pp. 265-287.
[7] P. A. Russo, T. R. Wenz, and J. A. Painter, 1992.
[8] T. Ludziejewski, K. Moszynska, M. Moszynski, *et al*., 1995.
[9] A. Romano and P. Russo, 1999.
[10] P. Dorenbos, 2002.
[11] P. Dorenbos, J. T. M. de Haas, and C. W. E. van Eijk, 2004.
[12] K. S. Shah, J. Glodo, M. Klugerman, *et al*., 2003.
[13] E. V. D. van Loef, P. Dorenbos, C. W. E. van Eijk, *et al*., 2000.
[14] E. V. D. van Loef, P. Dorenbos, C. W. E. van Eijk, *et al*., 2001.
[15] E. V. D. van Loef, W. Mengesha, J. D. Valentine, *et al*., 2003.
[16] A. Kh. Khusainov, J. S. Iwanczyk, B. E. Patt, *et al*., 2001.
[17] D. T. Vo and P. A. Russo, 2002.
[18] D. T. Vo and P. A. Russo, *Nucl. Instr. Meth.,* 2002.
[19] D. T. Vo and P. A. Russo, 2004.
[20] P. N. Luke and E. E. Eissler, 1996.
[21] Z. He, G. F. Knoll, D. K. Wehe, *et al*., 1996.
[22] T. H. Prettyman, M. K. Smith and S. E. Soldner, 1999.
[23] T. H. Prettyman, M. C. Browne, K. D. Ianakiev, *et al*., 2000.
[24] R. Redus, A. Huber, J. Pantazis, *et al.*, 2004.
[25] D. T. Vo, P. A. Russo, and T. E. Sampson, 1998.
[26] D. T. Vo, August 1999.
[27] D. T. Vo, November 1999.
[28] D. T. Vo and P. A. Russo, February 2002.
[29] C. Frankle, 2003.
[30] K. P. Ziock, W. W. Craig, L. Fabris, *et al*., 2004.
[31] D. Cordle, J. Gross, and B. McGinnis, 2000.
[32] D. H. Beddingfield, A. P. Belian, K. D. Veal, *et al.*, 2003.
[33] G. J. Schmid, D. A. Beckedahl, J. E. Kaameraad, *et al.*, 2001.
[34] K. Vetter, M. Burks, and L. Mihailescu, 2004.
[35] C. E. Lehner, Z. He, and F. Zhang, 2004.
[36] M. Amman and P. N. Luke, 2000.
[37] W. Coburn, S. Amrose, S. E. Boggs, *et al.,* 2002.
[38] K. Vetter, L. Mihailescu, K. Ziock, *et al.,* 2002.
[39] J. Y. Huang and D. T. Vo, 2004.
[40] K. Chung, A. P. Belian, E. A. McKigney, and P. A. Russo, 2004.
[41] A. Bolotnikov and B. Ramsey. *Nucl. Instr. Meth*.,1997.
[42] V. V. Dmitrenko, V. M. Gratchev, S. E. Ulin, *et al.*, 2000.
[43] S. Kobayashi, V. V. Dmitrenko, T. Doke, *et al.*, 2003.
[44] C. Levin, J. Germani, and J. Markey, 1993.
[45] G. J. Mahler, B. Yu, B.; G. C. Smith, *et al.*, 1998.
[46] E. A. McKigney and M. K. Smith, 2004.
[47] D. H. Beddingfield, A. Beyerle, P. A. Russo, *et al*., 2003.

[48] S. E. Ulin, K. F. Vlasik, A. M. Galper, *et al.*, 1997.
[49] D. Reilly, et. al., *Passive Nondestructive Assay of Nuclear Materials*, 1991, pp. 43-64.
[50] G. F. Knoll, 2000, pp. 231-287.
[51] G. F. Knoll, 2000, p. 235.
[52] G. F. Knoll, 2000, pp. 231-260.
[53] G. F. Knoll, 2000, p. 233.
[54] K. D. Ianakiev, M. Abhold, B. Alexandrov, *et al.*, 2005.
[55] F. E. Fenimore and T. M. Cannon, 1978.
[56] K. P. Ziock, W. W. Craig, L. Fabris, *et al*., 2004.
[57] D. H. Beddingfield, A. P. Belian, K. D. Veal, *et al.*, 2003.
[58] D. Cordle, J. Gross, and B. McGinnis, 2003.
[59] K. P. Ziock, M. T. Burks, W. Craig, *et al.*, 2003.
[60] P. A. Russo, 2005.
[61] R. Gunnink, R. Arlt, and R. Berndt, 1997.
[62] P. A. Russo, 2005.
[63] A. P. Belian, T. D. Reilly, P. A. Russo, *et al.*, 2005.
[64] G. F. Knoll, 2000, pp. 287-300.
[65] Y. J. Wang, B. E. Patt, J. S. Iwanczyk, *et al.*, 1996.
[66] K. S. Shah, R. Farrell, R. Grazioso, *et al.*, 2002.
[67] M. Moszynski, W. Czarnacki, W. Klamra, *et al*., 2003.
[68] G. F. Knoll, 2000, pp. 297-300.
[69] A. P. Belian, K. D. Ianakiev, and P. A. Russo, 2001.
[70] G. F. Knoll, 2000, pp. 239-240.
[71] D. W. Cooke, B. L. Bennett, K. J. McClellan, *et al.*, 2002.
[72] P. Dorenbos, J. T. M. de Haas, and C. W. E. van Eijk,, 2004.
[73] E. V. D. van Loef, W. Mengesha, J. D. Valentine, *et al.*, 2003.
[74] D. W. Cooke, B. L. Bennett, K. J. McClellan, *et al.*, 2002.
[75] T. Ludziejewski, K. Moszynska, M. Moszynski, *et al.*, 1995.
[76] K. Chung, A. P. Belian, E. A. McKigney, and P. A. Russo, 2004.
[77] P. Dorenbos, J. T. M. de Haas, and C. W. E. van Eijk,, 2004.
[78] K. Chung, A. P. Belian, E. A. McKigney, and P. A. Russo, 2004.
[79] *Ibid.*
[80] D. Reilly, et. al., *Passive Nondestructive Assay of Nuclear Materials*,1991, pp. 43-64.
[81] D. T. Vo, 2005.
[82] D. T. Vo and P. A. Russo, *Nucl. Instr. Meth*., 2002.
[83] D. T. Vo and P. A. Russo, 2004.
[84] C. Frankle, 2003.
[85] S. Friedrich, S. F. Terracol, T. Miyazaki, *et al.*, 2004.
[86] O. B. Drury, S. F. Terracol, and S. Friedrich, 2005.
[87] M. W. Rabin, C. R. Rudy, M. K. Smith, *et al.*, 2005.
[88] J. N. Ullom, J. A. Beall, W. B. Doriese, *et al.*, 2005.
[89] D. T. Vo, P. A. Russo, and T. E. Sampson, 1998.
[90] D. T. Vo and P. A. Russo, February 2002.
[91] G. F. Knoll, 2000, p. 628.
[92] D. T. Vo, August 1999.
[93] K. P. Ziock, M. T. Burks, W. Craig, *et al.*, 2003.
[94] G. J. Schmid, D. A. Beckedahl, J. E. Kaameraad, *et al.*, 2001.
[95] K. Vetter, M. Burks, and L. Mihailescu, 2004.
[96] C. E. Lehner, Z. He, and F. Zhang, 2004.
[97] M. Amman and P. N. Luke, 2000.

[98] W. Coburn, S. Amrose, S. E. Boggs, *et al.,* 2002.
[99] K. Vetter, L. Mihailescu, K. Ziock, *et al*., 2002.
[100] G. F. Knoll, 2000, pp. 477-488.
[101] G. F. Knoll, 2000, pp. 358-359.
[102] C. Szeles, S. E. Cameron, S. A. Soldner, *et al.*, 2004.
[103] P. N. Luke, 1994 and 1996.
[104] P. N. Luke and E. E. Eissler, 1996.
[105] Z. He, G. F. Knoll, D. K. Wehe, *et al*., 1996.
[106] T. H. Prettyman, M. C. Browne, K. D. Ianakiev, *et al*., 2000.
[107] C. E. Lehner, Z. He, and F. Zhang, 2004.
[108] C. Szeles, S. E. Cameron, S. A. Soldner, *et al.*, 2004.
[109] P. N. Luke, 1994 and 1996.
[110] P. N. Luke and E. E. Eissler, 1996.
[111] Z. He, G. F. Knoll, D. K. Wehe, *et al*., 1996.
[112] C. E. Lehner, Z. He, and F. Zhang, 2004.
[113] M. Rawool-Sullivan, W. Murray, K. Kreuger, and L. Ussery, 1997.
[114] P. A. Russo, A. P. Meier, M. Rawool-Sullivan, *et al.*, 1997.
[115] P. A. Russo, T. H. Prettyman, S. E. Smith, *et al.*, 1999.
[116] D. T. Vo, P. A. Russo, and S. A. Soldner, 1999.
[117] J. Y. Huang, and D. T. Vo, 2004.
[118] A. Kh. Khusainov, J. S. Iwanczyk, B. E. Patt, *et al*., 2001.
[119] D. T. Vo and P. A. Russo, *Nucl. Instr. Meth.,* 2002.
[120] D. T. Vo and P. A. Russo, 2004.
[121] R. Redus, A. Huber, J. Pantazis, *et al.*, 2004.
[122] G. F. Knoll, 2000, pp. 716-717.
[123] G. F. Knoll, 2000, p. 152.
[124] D. H. Beddingfield, A. Beyerle, P. A. Russo, *et al*., 2003.
[125] C. J. Sullivan, Z. He, G. F. Knoll, *et al.*, 2003.
[126] S. E. Ulin, K. F. Vlasik, A. M. Galper, *et al.*, 1997.
[127] D. H. Beddingfield, A. Beyerle, P. A. Russo, *et al*., 2003.
[128] E. A. McKigney and M. K. Smith, 2004.
[129] S. Kobayashi, V. V. Dmitrenko, T. Doke, *et. al.*, 2003.
[130] K. Chung, A. P. Belian, E. A. McKigney, and P. A. Russo, 2004.
[131] I. H. Campbell, and B. K. Krone, 2005.
[132] D. W. Cooke, J.-K. Lee, B. L. Bennett, *et al.*, 2005.
[133] W. Zhang, P. Xie, C. Duan, *et al.*, 1998.

REFERENCES

Amman, M., and P. N. Luke, "Three-Dimensional Position Sensing and Field Shaping in Orthogonal-Strip Germanium Gamma-Ray Detectors," *Nucl. Instr. Meth*. A 452 (2000), pp. 155-166.

Beddingfield, D. H., A. P. Belian, K. D. Veal, P. A. Russo, V. Longmire, V. A. Hatler, C. L. Kowalczyk, and M. K. Romero, “Measuring In-Process Inventory by Spectroscopic Imaging,” Los Alamos National Laboratory report LA-UR-03-4066, 2003. *Proceedings of 44th Annual Meeting of the INMM*, CD ROM, Northbrook IL: INMM (2003).

Beddingfield, D. H., A. Beyerle, P. A. Russo, K. Ianakiev, D. T. Vo, and V. Dmitrenko, “High-Pressure Xenon Ion Chambers for Gamma-Ray Spectroscopy in Nuclear Safeguards,” *Nucl. Instr. Meth.* A 505 (2003), pp. 474-477.

Belian, A. P., K. D. Ianakiev, and P. A. Russo, "Measuring the Number of Photoelectrons from Neutron Capture Events In a LiF/ZnS Scintillator/Fiber Optic Neutron Detector," Los Alamos National Laboratory report LA-UR-01-1818 (2001).

Belian, A. P, T. D. Reilly, P. A. Russo, S. J. Tobin, N. N. Nikolaenko, G. Sokolov, Y. V. Yasko, A. Ustimovich, G. Strygin, Y. Tchyrnuha, A. Chahid, A. LeBrun, and L. Bourva, "Holdup Measurements at the Ulba Metallurgical Plant," Los Alamos National Laboratory report LA-UR-05-2020 (March 2005).

Bolotnikov, A., and B. Ramsey. "The Spectroscopic Properties of High-pressure Xenon," *Nucl. Instr. Meth*. A 396 (1997), pp. 360-370.

Campbell, I. H., and B. K. Krone, "Quantum Dot/Organic Semiconductor Composites for Radiation Detection," Los Alamos National Laboratory report LA-UR-05-2578. (Submitted to *Applied Physics Letters*.)

Chung K., A. P. Belian, E. A. McKigney, and P. A. Russo, "Application of Lanthanum Halide Scintillators and Low-Resolution Dense Plastics for Modern MC&A Needs," Los Alamos National Laboratory report LA-UR-04-4472, 2004. *Proceedings of 45th Annual Meeting of the INMM*, CD ROM, Northbrook IL: INMM (2004).

Coburn, W., S. Amrose, S. E. Boggs, R. P. Lin, M. Amman, M. T. Burks, E. L. Hull, P. N. Luke and N. Madden, "3-D Positioning Germanium Detectors for Gamma-Ray Astronomy," *SPIE* 4784 (2002), pp. 54-63.

Cooke, D. W., B. L. Bennett, K. J. McClellan, R. E. Muenchausen, J. R. Tesmer, and C. J. Wetteland, "Luminescence, Emission Spectra, and Hydrogen Content of Crystalline Lu_2SiO_5:Ce^{3+}," *Philosophical Magazine* B 82, No. 2 (2002), pp. 1659-1670.

Cooke, D. W., J.-K. Lee, B. L. Bennett, J. R. Groves, R. E. Muenchausen, M. Nastasi, K. E. Sickafus, M. Tang, and J. A. Valdez, "Optical Properties of Hydrothermally Prepared Y2SiO5:Ce Nanophosphors," Los Alamos National Laboratory report LA-UR-05-____. (Submitted to *Applied Physics Letters*.)

Cordle, D., J. Gross, and B. McGinnis, "Gamma-Ray Imaging for Qualitative Uranium Material Holdup Position Determination and Improved Quantitative Mass Determination," United States Enrichment Corporation report, 2000. *Proceedings of the 41st Annual Meeting of the INMM*, CD ROM, Northbrook IL: INMM (2000).

Dorenbos, P., "Light Output and Energy Resolution of Ce^{3+}-Doped Scintillators," *Nucl. Instr. Meth*. A 486 (2002), pp. 208-213.

Dorenbos, P., J. T. M. de Haas, and C. W. E. van Eijk, "Gamma Ray Spectroscopy With a ∅ 19 × 19 mm^3 $LaBr_3$: 0.5% Ce^{3+} Scintillator," *IEEE Trans. Nucl. Sci.* 51, (2004), pp. 1289-1296.

Dmitrenko, V. V., V. M. Gratchev, S. E. Ulin, Z. M. Uteshev, K. F. Vlasik, "High Pressure Xenon Detectors for Gamma-ray Spectroscopy." *Appl. Rad. Iso*. 52 (2000), pp. 739-743.

Drury, O. B., S. F. Terracol, and S. Friedrich, "Quantifying the Benefits of Ultrahigh Energy Resolution for Gamma-Ray Spectrometry." *Phys. Stat. Sol.* (C) 2 (2005), pp. 1468-1479.

Fenimore, F. E., and T. M. Cannon, "Coded-Aperture Imaging with Uniformly Redundant Arrays," *Applied Optics* Vol. 17, No. 3 (1978), pp. 337-347.

Frankle, C., Los Alamos National Laboratory, private communication of information contained in patent application S-99,935 ("Handheld Isotope Identification System") 2003.

Friedrich, S., S. F. Terracol, T. Miyazaki, O. B. Drury, Z. A. Ali, M. F. Cunningham, T. R. Niedermayr, T. W. Barbee Jr., J. D. Batteux, and S. E. Labov, "Design of a Multichannel Ultra-High Resolution Superconducting Gamma-Ray Spectrometer," *SPIE* 5540 (2004), pp. 156-164.

Gunnink, R., R. Arlt, and R. Berndt, "New Ge and NaI Analysis Methods for Measuring 235U Enrichments," *Proceedings of the 19th ESARDA Meeting*, Montpellier, France (May, 1997), pp. 431-435.

He, Z., G. F. Knoll, D. K. Wehe, R. Rojeski, C. H. Mastrangelo, M. Hammig, C. Barrett and A. Uritani, "1-D Position Sensitive Single Carrier Semiconductor Detectors," *Nucl. Instr. Meth*. A 380 (1996), pp. 228-231.

Huang, J. Y., and D. T. Vo, "Distributed Miniature Radiation Detectors for Monitoring Plutonium Casting Processes," Los Alamos National Laboratory report LA-UR-04-4449, 2004. (*Proceedings of the Institute of Nuclear Materials Management*, 45th Annual Meeting, Orlando, FL, July 18-22, 2004, CD ROM.)

Ianakiev, K. D., M. Abhold, B. Alexandrov, J. Audia, M. C. Browne and H. Nguyen, "Temperature Behavior of Doped NaI(Tl) Scintillators and Its Impact on Pulse Height Analysis Instrumentation." Los Alamos National Laboratory report LA-UR-05-3409. (Submitted for presentation at the 2005 IEEE NSS/MIC Conference, San Juan USA, October 23-29, 2005.)

Khusainov, A. Kh., J. S. Iwanczyk, B. E. Patt, A. M. Pirogov, D. T. Vo and P. A. Russo, "Approaching Cryogenic Ge Performance with Peltier Cooled CdTe," Los Alamos National Laboratory report LA-UR-01-4123 (2001). *SPIE* 4507 (2001), pp. 50-56.

Knoll, G. F., *Radiation Detection and Measurement*, Third Edition (John Wiley and Sons, Inc., New York, 2000).

Kobayashi, S., V. V. Dmitrenko, T. Doke, V. M. Grachev, N. Hasebe, T. Igarashi, T. Miyachi, H. Okada, E. Shibamura, M. Takenouchi, S. E. Ulin, and K. F. Vlasik, "Measurement of Electron Drift Velocities in the Mixture of Xe and He for a New High-Pressure Xe Gamma-Ray Detector," *Japan. J. App. Phys*. 42:1 (2003), pp. 333-334.

Lehner, C. E., Z. He, and F. Zhang, "4-π Compton Imaging Using a 3-D Position-Sensitive CdZnTe Detector Via Weighted List-Mode Maximum Likelihood," *IEEE Trans. Nucl. Sci*. 51 (2004), pp. 1618-1624.

Levin,C., J. Germani, and J. Markey, "Charge Collection and Energy Resolution Studies in Compressed Xenon Gas near its Critical Point," *Nucl. Instr. Meth*. A 332 (1993), pp. 206-214.

Longmire, V., N. Ensslin, C. Files, J. Joseph, C. Rudy, M. Smith, P. Russo, R. Stevens, R. Strittmatter, D. Wilkey, C. Pickett, W. Brosey, and J. Swanson, "The SO-20.3 MC&A Modernization Plan," Version I, Los Alamos National Laboratory controlled paper LA-CP-04-0235 (April 9, 2004).

Ludziejewski, T., K. Moszynska, M. Moszynski, D. Wolski, W. Klamra, L.O. Norlin, E. Devitsin, and V. Kozlov, "Advantages and Limitations of LSO Scintillator in Nuclear Physics Experiments," *Trans. Nucl. Sci.* 42 (1995), pp. 328-336.

Luke, P. N., "Single-Polarity Charge Sensing in Ionization Detectors Using Coplanar Electrodes," *Appl. Phys. Lett*. 65 (1994), pp. 2884-2886.

Luke, P. N., "Electrode Configuration and Energy Resolution in Gamma-ray Detectors," *Nucl. Instr. Meth*. A 380 (1996), pp. 232-237.

Luke, P. N., and E. E. Eissler, "Performance of CdZnTe Coplanar-Grid Gamma-Ray Detectors," *IEEE Trans. Nucl. Sci*. 43 (1996), pp. 1481-1486.

Mahler, G. J., B. Yu, B.; G. C. Smith, W. Kane, and J. R. Lemley, "A Portable Gamma-ray Spectrometer Using Compressed Xenon," *IEEE Trans. Nucl. Sci*. 45 (1998), pp. 1029-1033.

McKigney, E. A., and M. K. Smith, "Simulation of a High-Pressure Xe-3He Detector" Los Alamos National Laboratory report LA-UR-04-4359, 2004. (*Proceedings of the Institute of Nuclear Materials Management*, 45th Annual Meeting, Orlando, FL, July 18-22, 2004, CD ROM.)

Moszynski, M. W. Czarnacki, W. Klamra, M. Szawlawski, P. Schotanus, and M. Kapusta, "Intrinsic Energy Resolution of Pure NaI Studied with Large Area Avalanche Photodiodes at Liquid Nitrogen Temperatures," *Nucl Instr. Meth*. A 505 (2003), pp. 63-67.

Passive Nondestructive Assay of Nuclear Materials. D. Reilly, N. Ensslin, H. Smith, Jr., eds. (Nuclear Regulatory Commission NUREG/CR-5550, 1991), Los Alamos National Laboratory report LA-UR-90-732 (1990).

Prettyman, T. H., M. K. Smith and S. E. Soldner, "Design and Characterization of Cylindrical CdZnTe Detectors with Coplanar Grids," *SPIE 3768* (1999) 339-345.

Prettyman, T. H., M. C. Browne, K. D. Ianakiev, C. E. Moss, S. E. Soldner, "Characterization of a Large-Volume Multi-Element CdZnTe Detector," *SPIE 4141* (2000), pp. 1-10.

Rabin, M. W., C. R. Rudy, M. K. Smith, D. M. Tournear, and D. T. Vo, J. N. Ullom, and K. D. Irwin, "Nuclear Applications of Large Arrays of High-Resolution Microcalorimeters," Los Alamos National Laboratory report LA-UR-05-3431. (Submitted for presentation at the 2005 IEEE NSS/MIC Conference, San Juan USA, October 23-29, 2005.)

Rawool-Sullivan, M., W. Murray, K. Kreuger, and L. Ussery, "CdZnTe Progress Report for June 1997," Los Alamos National Laboratory report LA-UR-97-2900, 1997.

Redus, R., A. Huber, J. Pantazis, T. Pantazis, T. Takahashi and S. Woolf, “Multielement CdTe Stack Detectors for Gamma-Ray Spectroscopy,” *IEEE Trans. Nucl. Sci*. 51 (2004), pp. 2386-2394.

Reilly, D., Ensslin, N., and Smith, H., Passive Nondestructive Assay of Nuclear Materials, Nuclear Regulatory Commission report NUREG/CR-5550, Los Alamos National Laboratory report LA-UR-90-732 (March 1991).

Romano, A., and P. Russo, “Investigating the Use of Lu(SiO4)O:Ce for Gamma-Ray Spectroscopy,” Los Alamos National Laboratory report LA-UR-99-4332 (1999).

Russo, P. A., T. R. Wenz, and J. A. Painter, “Experimental Evaluation of Software-Driven Digital Gain-Drift Compensation in Scintillator Gamma-Ray Spectroscopy,” Los Alamos National Laboratory report LA-12390-MS (1992).

Russo, P. A., A. P. Meier, M. Rawool-Sullivan, T. H. Prettyman, H. Y. Huang, D. A. Close, M. C. Sumner, R. A. Cole, P. N. Luke and S. A. Soldner, “A New Room-Temperature Gamma-Ray Detector for Improved Assay of Plutonium,” Los Alamos National Laboratory report LA-UR-97-2782, 1997. (*Proceedings of the Institute of Nuclear Materials Management*, 38th Annual Meeting, Phoenix AZ, July 20-24, 1997, CD ROM.)

Russo, P. A., T. H. Prettyman, S. E. Smith, J. F. Harris, J. S. Massengill and E. Stair, Jr., “Comparison of Detectors for Portable Gamma-Ray Spectroscopy at Y-12,” Los Alamos National Laboratory report LA-UR-99-199 (January 1999).

Russo, P. A., T. R. Wenz, and K. D. Veal, “In-Situ Measurement of Process Solution Inventory of ^{235}U,” Los Alamos National Laboratory report LA-UR-00-2470 (June 2000).

Russo, P. A., "Gamma-ray Measurements of Holdup Plant-wide: Application Guide for Portable Generalized Approach", Los Alamos report LA-14206 (March 2005).

Schmid, G. J., D. A. Beckedahl, J. E. Kaameraad, J. J. Blair, K. Vetter, and A. Kuhn, Gamma-Ray Compton Camera Imaging with a Segmented HPGe,” *Nucl. Instr. Meth*. A 459(2001), pp. 565-576.

Shah, K. S., R. Farrell, R. Grazioso, E. S. Harmon, and E. Karplus,” Position-Sensitive Avalanche Photodiodes for Gamma-Ray Imaging,” *IEEE Trans. Nucl. Sci*. 49 (2002), pp. 1687-1692.

Shah, K. S., J. Glodo, M. Klugerman, L. Cirignano, W. W. Moses, S. E. Derenzo, M. J. Weber, “$LaCl_3$:Ce Scintillator for Gamma-ray Detection,” *Nucl. Instr. Meth*. A 505(2003), pp. 76-81.

Sullivan, C. J., Z. He, G. F. Knoll, G. B. Tepper, and D. K. Wehe, “A High Pressure Xenon Gamma-ray Spectrometer Using a Coplanar Anode Configuration,” *Nucl Instr. Meth*. A 505 (2003), pp. 238-241.

Szeles, C., S. E. Cameron, S. A. Soldner, J. O. Ndap, and M. D. Reed, “Development of the High-Pressure Electrodynamic-Gradient Crystal-Growth Technology of Semi-Insulating CdZnTe for Radiation Detector Applications,” *SPIE* 5198 (2004), pp. 191-199. [*Journal of Electronic Materials* 33, No. 6 (2004) 742-751.]

Ulin, S. E., K. F. Vlasik, A. M. Galper, V. M. Grachev, V. V. Dmitrenko, V. I. Liagushin, Z. M. Uteshev, and Yu. T. Yurkin, "Influence of Proton and Neutron Fluxes on Spectrometric Characteristics of a High-pressure Xenon Gamma Spectrometer," *SPIE* 3114 (1997), pp. 499-504.

Ullom, J. N., J. A. Beall, W. B. Doriese, W. D. Duncan, L. Ferreira, G. C. Hilton, K. D. Irwin, C. D. Reintsema, L. R. Vale, B. L. Zink, M. W. Rabin, C. R. Rudy, M. K. Smith, D. M. Tournear, and D. T. Vo, "Development of Large Arrays of Microcalorimeters for Precision Gamma-ray Spectroscopy," NIST Boulder Laboratories report. (Submitted for presentation at the 2005 IEEE NSS/MIC Conference, San Juan USA, October 23-29, 2005.)

van Loef, E. V. D., P. Dorenbos, C. W. E. van Eijk, K. Kramer, and H. U. Gudel, "High-energy-resolution Scintillator: Ce^{3+} Activated $LaCl_3$," *App. Phys. Lett*. 77 (2000), pp. 1467-1468.

van Loef, E. V. D., P. Dorenbos, C. W. E. van Eijk, K. Kramer, and H. U. Gudel, "High-energy-resolution Scintillator: Ce^{3+} Activated $LaBr_3$," *App. Phys. Lett*. 79 (2001), pp. 1573-1575.

van Loef, E. V. D., W. Mengesha, J. D. Valentine, P. Dorenbos, and C. W. E. van Eijk, "Non-proportionality and energy Resolution of a $LaCl_3$:10% Ce^{3+} Scintillation Crystal," *IEEE Trans. Nucl. Sci*. 50 (2003), pp. 155-158.

Vetter, K., L. Mihailescu, K. Ziock, M. Burns, C. Cork, L. Fabris, E. Hull, N. Madden and R. Pehl, "Employing Thin HPGe Detectors for Gamma-Ray Imaging," *Unattended Radiation Sensor Systems for Remote Applications*, AIP 0-7354-0087-3/02 (2002), pp. 129-133.

Vetter, K., M. Burks, and L. Mihailescu, "Gamma-Ray Imaging With Position-Sensitive HPGe Detectors," *Nucl. Instr. Meth*. A 525 (2004), pp. 322-327.

Vo, D. T., P. A. Russo, and T. E. Sampson, "Comparisons Between Digital Gamma-Ray Spectrometer (DSPec) and Standard Nuclear Instrumentation Methods (NIM) Systems," Los Alamos National Laboratory report LA-13393-MS, March 1998.

Vo, D. T., "Evaluations of the Commercial Spectrometer Systems for Safeguards Applications," Los Alamos National Laboratory report LA-13604-MS, August 1999.

Vo, D. T., "Comparisons of the DSPEC and DSPEC Plus Spectrometer Systems," Los Alamos National Laboratory report LA-13671-MS, November 1999.

Vo, D. T., P. A. Russo, and S. A. Soldner, "Experimental Investigation of the Spectroscopic Performance of the Coaxial CdZnTe Detector," Los Alamos National Laboratory report LA-UR-99-580, 1999.

Vo, D. T., and P. A. Russo, "Comparisons of the Portable Digital Spectrometer Systems," Los Alamos National Laboratory report LA-13895-MS, February 2002.

Vo, D. T., and P. A. Russo, "PC/FRAM Plutonium Isotopic Analysis of CdTe Gamma-Ray Spectra," *Nucl. Instr. Meth*. A 486 (2002), pp. 813-824.

Vo, D. T., and P. A. Russo, “Plutonium and Uranium Isotopic Analysis in the X-ray Region with the CdTe Detector,” Los Alamos National Laboratory report LA-UR-03-4730. *SPIE* 5198 (2004), pp. 182-190.

Vo, D. T., “Testing the Detective Systems,” Los Alamos National Laboratory report LA-UR-05-3156, April 2005.

Wang, Y. J., B. E. Patt, J. S. Iwanczyk, S. R. Cherry, and Y. Shao, “Detector Optimization for Handheld CsI:Tl/HgI2 Gamma-ray Scintillation Spectrometer Applications,” ,” *IEEE Trans. Nucl. Sci*. 43 (1996), pp. 1277-1281.

Zhang, W., P. Xie, C. Duan, K. Yan, M. Lin, L. Lou, S. Xia, and J.-C. Krupa, “Preparation and Size Effect On Concentration Quenching Of Nanocrystalline Y_2SiO_5:Eu,” *Chem. Phys. Lett*. 292 (1998), pp. 133-136.

Ziock, K. P., M. T. Burks, W. Craig, L. Fabris, E. L. Hull, and N. W. Madden, “Real-Time Generation of Images With Pixel-by-Pixel Spectra For a Coded Aperture Imager with High Spectral Resolution,” *Nucl. Instr. Meth*. A 505 (2003), pp. 420-424.

Ziock, K. P., W. W. Craig, L. Fabris, R. C. Lanza, S. Gallagher, B. K. P. Horn, and N. W. Madden, “Large Area Imaging Detector for Long-Range, Passive Detection of Fissile Material,” *IEEE Trans. Nucl. Sci*. 51 (2004), pp. 2238-2244.

2. PLUTONIUM ISOTOPIC ANALYSIS USING PC/FRAM

Thomas E. Sampson

I. INTRODUCTION

A. Purpose of This Chapter

It has been 20 years since Chapter 8, "Plutonium Isotopic Composition by Gamma-Ray Spectroscopy" in the *Passive Nondestructive Assay of Nuclear Materials* (Sampson 91) book was first drafted in 1983. This book, commonly referred to as the "PANDA Manual," is one of the principal resources for passive Nondestructive Assay (NDA) measurements throughout the worldwide nuclear community. Since 1986, when the material in Ch 8 was expanded and updated (Sampson 86), there has been an explosion of activity in the field of gamma-ray isotopic analysis. New codes and new analysis methods have been developed and applied worldwide to complement improvements in both detectors and data acquisition devices.

This chapter will describe the developments that have taken place at the Los Alamos National Laboratory concentrating on the PC/FRAM* isotopic analysis software. A review of the principles of gamma ray isotopic analysis will expand on the principles developed in PANDA to include the physics behind the current techniques used in FRAM. This chapter will cover all aspects of the FRAM software, including usage, development principles, algorithms, parameter files, performance, and measurement applications.

B. Isotopic Analysis Applications in Nondestructive Assay

1. Calorimetry.

A calorimeter (Likes 91a) determines the power produced by a sample of special nuclear material (SNM), the power arising primarily from the alpha decay of the isotopes making up the SNM. Elemental plutonium usually contains a mixture of isotopes with ^{238}Pu, ^{239}Pu, ^{240}Pu, ^{241}Pu, ^{242}Pu, and ^{241}Am present in most plutonium-bearing items. Each isotope produces a characteristic amount of heat proportional to its decay energy. This decay heat, when quantified per gram of isotope, is called the specific power, has the customary units of (W or mW)/gram isotope, and is denoted by P_i. The specific powers can be calculated from fundamental principles and can also be directly measured from pure isotopes. The accepted values for the specific powers of the plutonium isotopes and ^{241}Am are given in Table I-1.

---

* FRAM is the name of the gamma-ray isotopic analysis software developed over the years in the Safeguards Science and Technology group, N-1 at the Los Alamos National Laboratory. FRAM is a word of Scandinavian origin meaning "forward" or "onward." In addition, it can be viewed as an acronym, Fixed energy, Response function Analysis with Multiple efficiencies, describing the general features of the code.

Table I-1. Specific Power Values for the Isotopes of Plutonium (ANSI 1987)

Isotope	Half Life (yr)	Specific Power (mW/g isotope)	Standard Deviation (mW/g isotope)
^{238}Pu	87.74	567.57	0.26
^{239}Pu	24119	1.9288	0.0003
^{240}Pu	6564	7.0824	0.002
^{241}Pu	14.348	3.412	0.002
^{242}Pu	376300	0.1159	0.0003
^{241}Am	433.6	114.2	0.42

The sum of the specific powers of the individual heat-producing isotopes, weighted by their relative abundances, yields the effective specific power P_{eff} in units of mW/g Pu (Likes 91a).

P_{eff} is the important factor required to convert the measured Watts from the calorimeter to grams elemental plutonium. The mass of elemental plutonium (all the heat-producing isotopes) is given by

$$M = W / P_{eff} \quad , \tag{I-1}$$

where W is the measured Watts from the calorimeter and P_{eff} in units of Watts/g Pu is the effective specific power.

The measurement of P_{eff} is one of the most important applications of gamma-ray isotopic analysis. Calorimetric Assay, the combination of a calorimetric measurement of Watts and a gamma ray isotopic measurement of P_{eff}, provides the most accurate and precise method available for nondestructively determining the mass of elemental plutonium in bulk samples. As a result, tabulating the accuracy and precision of the measurement of P_{eff} is one of the principal methods for characterizing isotopic analysis software. The characteristics and errors involved in the measurement of P_{eff} by FRAM will be discussed in detail later in this document.

2. Neutron Coincidence Counting.

The even isotopes of plutonium (^{238}Pu, ^{240}Pu, and ^{242}Pu) have large spontaneous fission yields that dominate the fission neutron output from plutonium. The spontaneous fission yields of the plutonium isotopes are shown in Table I-2 (Ensslin 91a). Spontaneous fission neutron emission in conjunction with sensitive neutron coincidence counting systems provides a widely used measurement technique (Ensslin 98, Reilly 91). All three of the even isotopes contribute to the response of a neutron coincidence counter with the contribution from ^{240}Pu dominating for most plutonium-bearing materials. For this reason it is customary to define the effective ^{240}Pu mass by

$$^{240}Pu_{eff} = 2.52 * {}^{238}Pu + {}^{240}Pu + 1.68 * {}^{242}Pu, \tag{I-2}$$

where $^{240}Pu_{eff}$ is the mass of ^{240}Pu that would give the same coincidence response as that observed from the actual measured item.

We define the effective ^{240}Pu fraction in an analogous fashion by

$$fract^{240}Pu_{eff} = 2.52 * fract^{238}Pu + fract^{240}Pu + 1.68 * fract^{242}Pu \tag{I-3}$$

Table I-2. Spontaneous Fission Neutron Yields From the Isotopes of Plutonium

Isotope	Spontaneous Fission Yield (n/s-g)
^{238}Pu	2.59×10^{3}
^{239}Pu	2.18×10^{-2}
^{240}Pu	1.02×10^{3}
^{241}Pu	5×10^{-2}
^{242}Pu	1.72×10^{3}

The isotopic fractions are obtained from either mass spectrometry or from nondestructive gamma-ray isotopic analysis. Combining the measured effective ^{240}Pu mass with the effective ^{240}Pu fraction yields the plutonium mass in a fashion completely analogous to calorimetry as

$$M = \text{grams } ^{240}Pu_{eff} / \text{fract}^{240}Pu_{eff} \qquad \text{(I-4)}$$

where the grams $^{240}Pu_{eff}$ comes from the neutron coincidence counting of the bulk item and fract$^{240}Pu_{eff}$ comes from the isotopic analysis. In addition to the isotopic information required in computing fract$^{240}Pu_{eff}$, coincidence counting requires knowledge of the complete isotopic distribution, including ^{241}Am, for computing (α,n) rates for multiplication corrections.

Characterizing the accuracy and precision of the measurement of fract^{240}Pu is important for characterizing the performance of isotopic analysis software.

3. Other Bulk Measurement Techniques.

The FRAM isotopic analysis software has been applied to essentially every bulk measurement problem that quantifies individual isotopes.

The Active Well Coincidence Counter (AWCC) is an instrument commonly used to assay ^{235}U (Menlove 91). Thus, for application to ^{235}U in the AWCC, we require knowledge of the ^{235}U isotopic fraction. The FRAM software was the first gamma-ray isotopic analysis code to demonstrate measurements on uranium.

The Segmented Gamma Scanner (SGS) uses transmission-corrected passive assay techniques (Parker 91) to quantify individual isotopes (usually ^{239}Pu or ^{235}U) in items of scrap and waste. FRAM is widely used to support this common measurement technique, as well as the Tomographic Gamma Scanner (TGS) especially for application to permanent waste disposal at the Waste Isolation Pilot Plant.

4. Process Control

There are numerous applications of gamma-ray isotopic analysis in providing information necessary for the control of various fabrication processes. Isotopic analysis may be required anytime material from two different batches is mixed to produce a product that must meet designated specifications.

One example might be that of blending materials with different ^{240}Pu fractions to meet a given “weapons grade” specification. Another application is that of blending plutonium from different batches to produce MOX fuel where the fissile isotope concentrations are of interest. The FRAM isotopic analysis software has the capability for verifying isotopic composition with accuracy requisite for performing these blending operations. Another capability of FRAM allows the quantification, relative to plutonium, of the concentration of fission products in the mixture or its components. This capability is also proving to be useful for rapidly and economically characterizing materials that must meet production specifications.

5. Treaty Verification.

Treaty verification is an application that did not exist when the PANDA chapter on isotopic analysis was written. Arms control and plutonium disposition negotiations between the United States (US) and the Russian Federation (RF) consider the disposition of plutonium from dismantled Russian nuclear weapons. The treaties and agreements arising from these negotiations contain requirements to verify the amount and isotopic composition of the plutonium declared as coming from dismantled weapons. A problem arises because in Russia the isotopic composition of the plutonium used in Russian weapons is classified. Nondestructive gamma-ray isotopic analysis techniques are applied behind an information barrier to verify this ratio without revealing the detailed isotopic composition.

The Russian Weapons Plutonium Conversion Line will take plutonium from dismantled weapons, mix it with fuel grade plutonium and produce PuO_2 for MOX fuel. Gamma-ray isotopic analysis provided by the FRAM software will be used to determine the proper mixing ratios and also to verify the isotopic composition of the output PuO_2 (Sampson 98).

II. BASIC PRINCIPLES OF GAMMA-RAY ISOTOPIC ANALYSIS FOR THE ARBITRARY SAMPLE

A. Gamma Ray Measurement of Isotopic Ratios

The development of the fundamental relation governing the measurement of isotopic ratios using gamma-ray spectrometry has been shown in previous publications (Sampson 91, Sampson 03). The well-known result is given in eq. II-1

$$\frac{N^i}{N^k} = \frac{C(E_j^i)}{C(E_l^k)} \times \frac{T_{1/2}^i}{T_{1/2}^k} \times \frac{BR_l^k}{BR_j^i} \times \frac{RE(E_l)}{RE(E_j)} \qquad \text{(II-1)}$$

where

$C(E_j^i)$	=	photopeak area of gamma ray *j* with energy E_j emitted from isotope *i*,
λ^i	=	decay constant of isotope *i*, $\lambda^i = \ln 2 / T_{1/2}^i$ where $T_{1/2}^i$ is the half life of isotope *i*,
N^i	=	number of atoms of isotope *i*,
BR_j^i	=	branching ratio (gamma rays/disintegration) of gamma ray *j* from isotope *i*,
RE_j	=	relative efficiency for photopeak detection of gamma ray with energy E_j. This includes detector efficiency, sample self-absorption, and attenuation in packaging and materials between the sample and the detector.

The relative efficiency *RE* includes the effects of sample self-absorption, attenuation in materials between the sample and the detector, and detector efficiency. The half-lives, $T_{1/2}$ and the branching ratios, *BR* are known nuclear data. The *C(E)* term is determined from the gamma ray spectral data, leaving only the ratio of the relative detection efficiencies to be determined. The need for only an efficiency ratio removes the problems associated with the geometric and sample reproducibility associated with absolute measurements and makes the method applicable to samples of arbitrary size, shape, and composition.

B. Ratio Measurements for the Arbitrary Sample—Without Efficiency Corrections

The earliest application of isotopic ratio measurements on plutonium made the assumption that the two gamma-ray peaks were close enough in energy that the differences in sample self-attenuation, absorption in packaging materials, and the detector efficiency could be neglected. The early applications of this technique at the Mound Laboratory recommended using gamma-ray pairs with energy spacing less than 10 keV.

Efficiency differences even with closely spaced peak pairs can be significant and were the cause of some of the biases observed with this early method.

C. The Intrinsic Self-Calibration Technique

In 1974 Jack Parker and Doug Reilly at Los Alamos proposed the first practical method for accurately measuring the isotopic composition of an arbitrary (size, shape, composition, measurement geometry) plutonium sample via analysis of its gamma-ray spectrum (Parker 74). Key to their method was the incorporation of an internal or intrinsic self-determination of the relative efficiency curve from the gamma-ray spectrum of each unknown sample.

Parker and Reilly noted that you could determine the ratio of the relative efficiency at the selected energies from the measured gamma-ray spectrum of the unknown sample. From eq. II-1, considering a series of gamma rays from a single isotope, we see that the quotient of the photopeak counts at energy E_j^i and the branching ratio BR_j^i is proportional to the efficiency at energy E_j.

$$\frac{C(E_j^i)}{BR_j^i} \propto \left[\frac{N^i \ln 2}{T_{1/2}^i}\right] \quad \varepsilon(E_j) \qquad \text{(II-2)}$$

Thus, this quotient defines the shape of the relative efficiency as a function of energy for the measurement in question. Gamma rays from several isotopes may be used to define the relative efficiency as long as all the isotopes used have the same physical distribution (an important restriction!). The curves from different isotopes with the same physical distribution have the same shape and differ only in their amplitude, the term in brackets in eq. II-2.

The development of Parker and Reilly forms the basis for most isotopic analysis applications that are in use today, including the FRAM code.

D. The Relative Efficiency Concept

The concept of the intrinsically determined self-calibration of the measurement's relative efficiency is the key feature of modern gamma ray isotopic analysis methods. Equation II-2 is used to determine the relative efficiency at the gamma-ray energies used in the peak pair ratio expression of eq. II-1.

The relative efficiency is viewed as a function of energy. Almost any variable that perturbs the absorption or relative intensity of gamma rays emitted from the sample can affect the shape or energy dependence of the relative efficiency curve. Some of these are

- The size, configuration, and efficiency of the HPGe detector.
- The mass of plutonium in the sample.
- The areal density of plutonium in the sample.
- The density and absorption properties of any matrix material.
- Material properties and thickness of the container(s).
- Absorbers between the sample and the detector.

Figure II-1 shows the overall effect seen as the sample gets larger which also usually means thicker (more mass and more areal density). The curves in Fig II-1 are normalized to unity at their maximum value. Because the mean free path increases as energy increases, an isotopic measurement will "see" farther into the item being measured and hence sample more volume and mass at high energy than at low energy. This means that relative to low energies, large samples emit more high-energy gamma rays than low energy gamma rays and the relative efficiency tends to increase with increasing energy more strongly than for small samples. This is illustrated numerically in Table II-1 for plutonium at low density approximating that of PuO_2. The "thickness" or areal density of the plutonium in a sample must be several mean free paths in magnitude to take full advantage of the intensity available at a specific measurement energy.

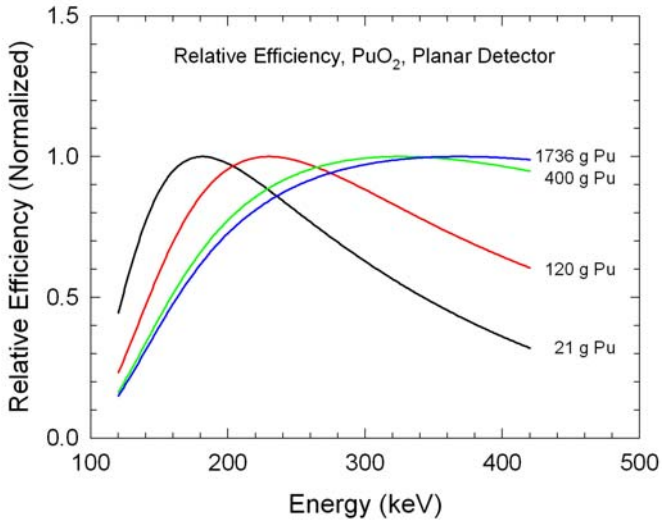

Fig. II-1. The relative efficiency varies for different size samples using the same 16 mm dia x 13 mm deep planar detector. The curves are normalized at their maximum value.

Table II-1. Mean Free Path for Various Gamma Rays in Plutonium of Density 3.0 g/cm^3

Pu-238	λ (cm)	Pu-239	λ (cm)	Pu-240	λ (cm)
152 keV	0.13	129 keV	0.083	104 keV	0.19
766 keV	3.0	414 keV	1.2	160 keV	0.15
				642 keV	2.4

Figure II-1 shows that the user can get qualitative information on the plutonium areal density in the sample just by examination of the shape of the relative efficiency curve.

E. Relative Efficiency Models

After relative efficiency values have been determined for a specific measurement using eq II-2, the user has a series of relative efficiency vs energy points that might appear to look like Fig. II-2. The user then needs to find relative efficiency values for energies not defined by a specific relative efficiency point and sometimes, even outside the range defined by the relative efficiency points. This requirement has led to the development of several models to parameterize the relative efficiency curve.

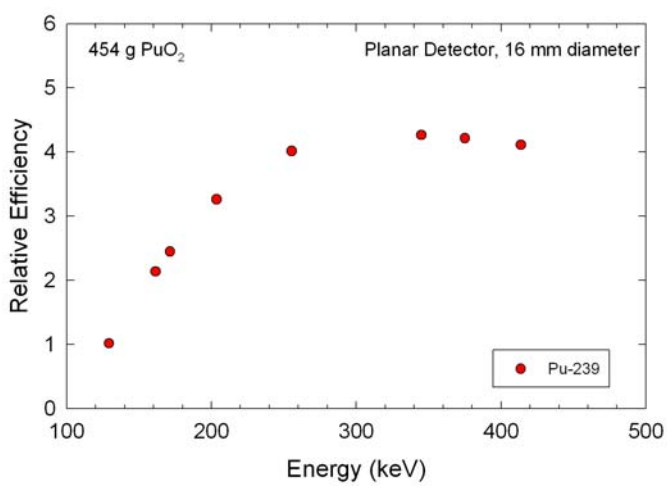

Fig. II-2. "Raw" relative efficiency points from ^{239}Pu for a specific measurement.

Several models are discussed in (Sampson 03) including simple models used in early Los Alamos codes. The models discussed below are more commonly used in modern isotopic analysis applications.

1. Empirical Model

Fleissner and Ruhter used linear least squares fitting of polynomial expressions in lnE in the early 1980s to parameterize the relative efficiency vs energy relationship. This represented the "state-of-the-art" when the PANDA chapter on isotopic analysis was drafted.

Fleissner in his GRPAUT software (Fleissner 81a) used the form

$$\ln \varepsilon_i = a_0 + \sum_{j=1}^{2}\left(a_j E_i^{-j}\right) + \sum_{j=1}^{3}\left(a_{j+2}(\ln E_i)^j\right) + a_6\delta_6 + a_7\delta_7 \qquad \text{(II-3)}$$

in the energy range from 120 keV to above 450 keV with points from ^{239}Pu, ^{241}Pu and ^{241}Am. The delta function terms, a_6 and a_7, normalize the ^{241}Pu and ^{241}Am data points to the ^{239}Pu data points. This form was expanded to include a second relative efficiency curve for cases where ^{241}Am was not isotopically homogeneous with plutonium.

Ruhter's form was similar and was used to fit from 120 keV to 210 keV if the spectrum was limited to that range or 120 keV to 380 keV if the data included the 375-keV region. His expression was simpler because it was used on a system with limited computing resources.

$$\ln \varepsilon_i = a_0 + a_1\delta_1 + \sum_{j=1}^{2or3}\left(a_{j+1}(\ln E_i)^j\right) \qquad \text{(II-4)}$$

The delta function term, a_1 normalizes the ^{241}Pu data points to the ^{239}Pu data points. Ruhter did not use any points from ^{241}Am to determine efficiency.

All versions of FRAM use or have available an empirical relative efficiency curve of essentially the same polynomial form (Sampson 89). FRAM's empirical relative efficiency is

$$\ln \varepsilon_i = C_1 + C_2 E_i^{-2} + \sum_{j=1}^{3}\left(C_{j+2}(\ln E_i)^j\right) + \sum_{k=1}^{m} C_{k+5}\delta_{k+5} + \sum_{l=1}^{n} C_{l+5+m}\delta_{l+5+m}E_i^{-1}, \qquad \text{(II-5)}$$

where the k summation is the normalization for each isotope after the first and the l summation is the normalization for each additional relative efficiency curve. The FRAM empirical relative efficiency curve is not limited with regard to the number of isotopes (We use as many as 6), nor is it limited to the number of different relative efficiency curves applied for isotopic heterogeneity although our principal experience is still with only one additional relative efficiency curve for isotopic heterogeneity.

All applications of this empirical, polynomial-based relative efficiency curve work very well over the range of definition. This form can run into trouble if it extrapolated outside its range of definition or if the relative efficiency data is statistically poor.

2. Physical Model

A physics-based relative efficiency model has been widely used by Gunnink and co-workers at the Lawrence Livermore National Laboratory (Gunnink 90).

$$\varepsilon_j = \exp\left(-\mu_j^{Cd} * x_{Cd}\right) * \frac{1}{\mu_j^{Pu} * x_{Pu}}\left(1 - \exp\left(-\mu_j^{Pu} * x_{Pu}\right)\right) * eff_j * \left(1 + bE_j + cE_j^2\right), \qquad \text{II-6}$$

where

μ_j^{Cd}	=	mass absorption coefficient of cadmium for peak *j*,
μ_j^{Pu}	=	mass absorption coefficient of plutonium for peak *j*,
x_{Cd}	=	thickness (g/cm2) of cadmium absorber,
x_{Pu}	=	thickness (g/cm2 of plutonium in the sample,
eff_j	=	detector efficiency for peak *j* from a "generic" efficiency curve,
b, *c*,	=	coefficients in a quadratic function to account for small deviations in the efficiency from the generic value as well as other slowly varying effects, such as absorption from low Z matrix materials.

This model explicitly accounts for self-absorption in the plutonium in the sample, absorption in a cadmium filter between the sample and detector, and the intrinsic detector efficiency. It has been used very successfully in the region from 59 keV to 300 keV with a planar detector. The variables are determined by iterative non-linear least squares techniques. Because the model is based on physical principles, it can give valid results outside its range of definition in cases where simpler models fail.

Vo at Los Alamos has implemented a very versatile physical model for relative efficiency that allows for multiple absorbers, multiple efficiency curves, and uses a wide-ranging correction factor for slowly varying effects.

$$\begin{aligned}\varepsilon = &\frac{1}{\mu_{Pu} * x_{Pu}}\left(1 - \exp\left(-\mu_{Pu} * x_{Pu}\right)\right) \\ &* \exp\left(-\mu_{Cd} * x_{Cd}\right) * \exp\left(-\mu_{Fe} * x_{Fe}\right) * \exp\left(-\mu_{Pb} * x_{Pb}\right) \\ &* \left(I_i\right) * \exp\left(\frac{c_j}{E}\right) * \left(Det\ Eff\right) * \left(Correction\ Factor\right)\end{aligned} \qquad \text{(II-7)}$$

The first term is self absorption in the plutonium; the second line is the absorption in up to three different materials (out of a choice of seven—Al, Fe, Cd, Er, Pb, H_2O, Concrete); I_i is the activity of isotope *i*; exp[c_j/E] accounts for isotopic heterogeneities (see next section); *Det Eff* is a generic detector efficiency parameterized in the software; and *Correction Factor* corrects for variations of the actual detector efficiency, nuclear material, and matrix from that specified in the model. The *Correction Factor* is a modified Hoerl function.

$$Correction\ Factor = \left(E^b * c^{\frac{1}{E}}\right) \qquad \text{(II-8)}$$

This physical efficiency function is available in FRAM version 4 (Kelley 02) and has been used in various applications in the energy range from below 40 keV to above 1500 keV.

3. Isotopic Heterogeneity

Equation II-1 is very general, but it contains the important assumption that all the measured isotopes in the sample are homogeneous with respect to each other. Another way of saying this is that gamma rays of the same energy from different isotopes must suffer the same attenuation as they escape from the sample. Failure of this assumption is called isotopic heterogeneity.

An example of isotopic heterogeneity occurs in pyrochemical plutonium processing applications. This process produces pure plutonium metal with Am and U removed. The waste Am and U that have been separated reside as a chloride salt along with small amounts of residual plutonium as metal fines in the residue stream. The proper quantification by calorimetric assay of the plutonium in this residue stream is complicated by the isotopic heterogeneity of the plutonium and americium present. The gamma rays from ^{241}Am suffer attenuation predominately in a low-Z chloride salt matrix while the plutonium gamma rays suffer attenuation characteristic of the high-Z plutonium metal fines. The relative-efficiency curve for gamma rays from ^{241}Am is different than that from plutonium. The isotopic ratio expression of eq. II-1 does not work in this instance.

Fleissner first proposed a second relative efficiency curve for ^{241}Am in pyrochemical residues—the ^{241}Am curve being related to the main plutonium relative efficiency by a multiplicative factor of exp[β/E], E being energy and β being a fitted constant . The Empirical (Eq. II-5) and Physical (Eq. II-7) relative efficiency formalisms contained in version 4 of FRAM both include a heterogeneity terms as proposed by Fleissner.

Testing of this heterogeneous model has involved comparison of isotopic measurements on heterogeneous pyrochemical residues with destructive chemical analysis of the entire item (Sampson 89). These destructive chemical analysis studies are very lengthy and extremely expensive so comparison data is limited. The most important parameter determined in the isotopic measurement is P_{eff} in mW/gPu. This is used directly to convert a calorimetry measurement of total sample power to grams elemental plutonium. With the heterogeneous relative-efficiency model of Fleissner, both Fleissner's GRPAUT code and the Los Alamos FRAM code determined P_{eff} with a bias that usually did not exceed 5%. Analysis of the same data without the heterogeneous relative-efficiency correction yielded biases from 10% to 200%.

III. PC/FRAM

A. Development

The first version of FRAM (Sampson 89) was fielded in 1988 at the Los Alamos Plutonium Facility running on Digital Equipment Corporation MicroVAX computers. The FRAM code represented a major advance in measurement flexibility as it was designed to address the shortcomings of the software described in PANDA and also included significant upgrades in the measurement and analysis hardware to the state of the art at that time.

By the early 1990s, computer hardware and software developments made the VAX/VMS-based system obsolete. The program was recoded in C to operate on a PC under Windows 3.1. This advance was necessary to open up the applications for the FRAM code (now called PC/FRAM) at facilities that did not support the previous VAX system. This change has resulted in FRAM becoming commercially available through several vendors and now being used worldwide. Some of the major features of FRAM are described below. [Note: We use the names PC/FRAM and FRAM interchangeably throughout this document.]

B. Single Detector System

Like all previous Los Alamos isotopic analysis systems, PC/FRAM uses only a single detector to acquire its data. We made a conscious choice to keep PC/FRAM a single detector system because single detector systems are inherently

- Easier to use
- More versatile
- More reliable
- Less expensive
- Occupy less facility space

C. Choice of Detector Type

PC/FRAM is the only isotopic analysis software system that can obtain a complete isotopic analysis using either a single planar, a single coaxial HPGe detector, or a CdTe detector.

When using the traditional single planar detector, PC/FRAM has most often been used to collect and analyze data in the 120–420 keV range. PC/FRAM has been used with a single planar detector to measure uranium isotopic composition in the energy range from 120–1024 keV. Recent developments fielded in version 4 of PC/FRAM now allow the analysis of planar detector spectra in the 100-keV region and the 40-keV region (Vo 01a).

The most widely used mode of operation with a single coaxial detector is to acquire a spectrum from 0–1024 keV. Various analysis modes can then be used. If the region between 120 and 200 keV is available, PC/FRAM will work best analyzing from 120–450 keV. When analysis below 200 keV is precluded (sample shielding or thick-walled sample container) PC/FRAM can still obtain a complete isotopic analysis using only gamma rays above 200 keV from a single coaxial detector spectrum. A complete analysis (all measurable isotopes) using only gamma rays above 300 keV is also possible. We have also found that the optimum analysis of coaxial detector data from some samples may come from the 200–800 keV region even when the region between 120 and 200 keV is available.

The optimum choice of planar or coaxial detectors is made only after considering all possible measurement applications. The planar detector is usually chosen if all measured items are unshielded or contained in “thin” containers. If shielded containers, thick-walled containers or a mixture of thin and thick/shielded containers are encountered, then a coaxial detector system is optimum. PC/FRAM is the only available isotopic analysis method using a coaxial detector in the energy range from 120–300 keV.

With a CdTe detector, one collects data in the 125-414 keV range, just like a planar HPGe.

D. Shielded Samples

Most isotopic analysis codes (including the original Vax-based FRAM) <u>require</u> the presence of spectral peaks in the region below 200 keV, regardless of whether they use one or two detectors. When this region is not available, perhaps because the sample is shielded to lower radiation exposure or because it is inside a very heavy-walled container, some isotopic analysis codes may not function. PC/FRAM was the first code to demonstrate the ability to make measurements through thick-walled containers or on shielded samples. Any software that obtains its results from gamma rays and x rays in the region around 100 keV is easily defeated by as little as a few tenths of a mm of lead or about 10 mm of steel. FRAM measurements have been made through as much as 25 mm of lead and very easily through 25 mm of steel.

E. Uranium Isotopic Analysis

Up until 1990 the isotopic analysis techniques originally proposed by Parker and Reilly were applied only to plutonium. There was always the need for uranium isotopic analysis but the features of the uranium gamma-ray spectrum precluded the easy application of the “peak pair” ratio method used in early isotopic analysis applications.

The uranium gamma-ray spectrum is essentially divided into two regions. The low-energy region up to about 200 keV contains only gamma rays from ^{235}U with the major gamma rays at 143.76, 163.33, 185.72, 202.11, and 205.31 keV, all from ^{235}U. The sole gamma ray from ^{234}U above 100 keV is at 120.90 keV and ^{236}U has no measurable gamma rays. The intense ^{238}U gamma rays arise from its ^{234m}Pa daughter with energies of 742.81, 766.36, 786.27, and 1001.03 keV. The wide separation between ^{235}U and ^{238}U gamma rays stymied the application of the early arbitrary-sample isotopic analysis techniques. The weak ^{234m}Pa gamma ray at 258.26 keV plays an important role in current applications of FRAM to uranium.

The formalism of FRAM does not require closely spaced peak pairs. Thus, in the late 1980s, we applied the original VAX version of FRAM to analyze uranium. This required a coaxial detector and data analysis in the 120-1200 keV region. We demonstrated FRAM's ability to measure, *with no code modification*, the $^{238}U/^{235}U$ ratio in samples of arbitrary physical and chemical composition, geometry, and mass, containing only uranium.

In PC/FRAM, uranium analysis was expanded to include ^{234}U and in the latest version we include a correlation to predict ^{236}U and a correction for cases where ^{234m}Pa is not in equilibrium.

F. Version 4

Sampson (Sampson 03) describes the features and improvements in all of the released versions of FRAM. The features and upgrades in the most recent release, version 4, mainly concern enhancements to the physics algorithms, new measurement capabilities, and a new structure to make derivative applications easier to implement.

Version 4.2

- **Relative Efficiency**. This version incorporates a new physical model for calculating the relative efficiency curve.
- **Analysis Engine**. The analysis algorithms have been placed in their own library. This makes it easier for other users to adapt FRAM for their own applications.
- **New Menus for Uranium Analysis**. There are separate dialog boxes for measuring plutonium and uranium and for analyzing Pu and U data files.
- **Intelligence**. There is a selectable capability of automatically switching, in a limited way, from one parameter set to another depending on analysis results.
- **Uranium Analysis Enhancements**. Enhancements for uranium analysis include 1) correction for ^{234}Th nonequilibrium, 2) isotopic correlation to predict ^{236}U, and 3) corrections for coincidence summing effects.
- **CdTe**. FRAM can analyze spectra taken with a CdTe detector in the 120-414 keV energy range (Vo 02).
- **100-keV Region Analysis**. FRAM can analyze plutonium using the 100-keV region (Vo 01a).
- **40-keV Region Analysis.** FRAM can analyze freshly separated plutonium using the 40-keV region (Vo 01a).

IV. HOW FRAM WORKS

A. Obtain Data

There are two basic types of data sources for FRAM.

1) <u>"Live" data from a multichannel analyzer (MCA) acquiring a gamma-ray spectrum from a high-resolution detector (usually HPGe).</u> FRAM can control the data acquisition from several commercial MCA families. The ORTEC line of Multichannel Buffers (MCB) operating with the Maestro MCA emulator can all be controlled via FRAM. Canberra MCAs operating under Genie 2000 can also be controlled from FRAM. Control is limited to the basic functions of count time, start, stop, and readout to a disk file. The user must invoke the appropriate MCA emulator other functions (high voltage, amplifier gain, etc.). The analysis of "live" data acquired under FRAM control proceeds automatically after the acquisition terminates.

2) <u>Data from a disk file.</u> FRAM can read and analyze data from disk files recorded in several data formats. These data formats include, for version 4, the following formats:

- N-1 standard
- Canberra S100
- Ortec ‘spc’
- Ortec ‘chn’
- Canberra CAM
- IAEA MCRS
- IAEA MMCA
- Green Star
- ASCII

If FRAM is purchased from a licensee it will contain only the control and data formats appropriate to the vendor’s own products or that are publicly available. In a version of FRAM from Los Alamos, the user will have access to everything that was current at the version release date. The user will have to purchase and install the appropriate MCA emulator to control the setup of the MCA and make full use of the commercial formats.

B. Perform Analysis

The analysis of a gamma-ray pulse-height spectrum by the PC/FRAM code proceeds in two steps, 1) the internal calibration, and 2) the analysis of the spectral data.

1. Internal Calibrations

The internal calibration uses peaks in the spectrum under analysis to provide a calibration of energy vs. channel, full width at half maximum (FWHM) vs. channel, and peak shape (tailing parameters) vs. channel. These calibrations do not depend on parameters determined from other measurements that may have been taken with different conditions of count rate, resolution, or electronic adjustment. In some cases, there are insufficient peaks to use the unknown spectrum for its own calibrations. In these cases, one can fix the peak calibration parameters to their initial values in the parameter set.

a. Energy Calibration

The first portion of the internal procedure calibrates energy vs. channel number from a list of calibration peaks in the parameter set. A piecewise linear calibration is made between successive pairs of peaks. The algorithm locates the peak at the maximum count found in a region of 10 channels on either side of the default peak position located using the default gain and zero values from the parameter set. FRAM is not constrained to any particular energy calibration. Within the constraints of spectral quality, FRAM can analyze spectra at any gain given that the energy calibration is known well enough to find the calibration peaks within a $\pm$ 10 channel window. The peak centroid is found using a least-squares fit of a quadratic function to the logarithm of the counts. Calibration outside the range of the energy calibration list is linearly extrapolated from the nearest two points.

b. Initial Background

Next, a background is calculated for all peak regions in the parameter set. The calculation uses the background functional shape for each region that is specified in the parameter set.

c. FWHM Calibration

The parameter set contains a user-editable list of peaks for use in the internal calibration of FWHM vs. energy. The FWHM of each peak in the list is calculated after a channel-by-channel subtraction of the initial background. The FWHM is calculated from a least-squares fit of a quadratic to the logarithm of the net counts over a range of channels in which the counts exceed

75% of the peak maximum on the low-energy side and 25% of the peak maximum on the high-energy side (for CdTe, because of the larger tails, the fit starts from 85% on the low-energy side). The FWHM as a function of energy that is used in calculating the response function for an arbitrary fitted peak is found from a least squares fit to the function:

$$FWHM(E) = SQRT\left[A_1 + (A_2 * E) + \left(A_3 / E\right)\right] \qquad \text{(IV-1)}$$

The first two terms are physics-based while the third term accounts for the observation that the FWHM for some detectors tends to "level out" at low energies.

d. Peak Shape/Tailing Calibration

The gamma-ray peak shape is described by a central Gaussian component with a single exponential tail on the low-energy side of the peak.

$$Y(J) = Ht * \exp\left[\alpha * (J - x_0)^2\right] + Tail(J), \qquad \text{(IV-2)}$$

where

Y(J)	=	Net counts in channel J,
Ht	=	Peak height at the peak centroid x_0,
α	=	$2.77259/FWHM^2$ is the peak width parameter,

and the tailing parameter Tail(J) is given by

$$Tail(J) = Ht * \exp\left[(T1 + T2 * E) + (T3 + T4 * E) * (J - x_0)\right] * \left[1 - \exp\left(-0.4 * \alpha * (J - x_0)^2\right)\right]. \qquad \text{(IV-3)}$$

Both the amplitude and slope of the tailing function are permitted to be a function of energy. However, in practice, we set T4 to zero reducing the number of unknowns to three. After subtracting the Gaussian portion of the peak (known because we have calibrations for energy and FWHM), we combine the data from all the FWHM peaks using the net channel contents on the low energy side of the peak from 0.5 to 1.5 FWHM from the peak center to determine the slope and amplitude constants from a least-squares fit.

This completes the internal calibration giving all the parameters necessary to calculate the shape of a gamma-ray peak at any location in the spectrum.

2. Analysis of Spectral Data

After the internal calibration is complete, the analysis proceeds on a region-by-region basis in the order that the regions are entered in the parameter set. The program makes three iterations through all the regions. A very detailed description of the analysis procedure may be found in (Kelley 02, Sampson 03).

The analysis starts by subtracting the initial background to get the net counts in a region. The background for the first iteration was calculated during the internal calibration phase. The analysis is iterative because of the interdependence of the peak areas and relative efficiencies calculated in separate steps.

a. Calculate Peak Areas Using Response Functions

For each of the regions defined in the parameter set, FRAM calculates the peak areas using response functions. The procedure allows peak areas to be fixed to peaks within or outside of the region. The results obtained after the final iteration consist of peak areas and uncertainties for all of the peaks in each region.

b. Calculate Relative Efficiencies

Relative efficiencies are calculated for all of the designated relative efficiency peaks in the parameter set. The individual relative efficiency points are fit via least squares to either the empirical relative efficiency function (Eq. II-5) or the physical relative efficiency function (Eq. II-7). The empirical function is fit by linear least squares methods while the physical relative efficiency function is determined by non-linear least squares using the Levenberg-Marquardt method.

c. Calculate Relative Activities

The relative activities are calculated for each peak by summing over all of the isotopes that contribute to the peak. Some of the peaks from the decay of the ^{237}U daughter of ^{241}Pu also contain an unresolved (exact energy match) gamma ray from ^{241}Am. The model is:

$$Area_i = \sum_j A_j (BR_{ij})(RE_i), \qquad \text{(IV-4)}$$

where,

A_j is the activity ratio for the jth isotope,
BR_{ij} is the branching ratio for the gamma ray emitted by the jth isotope contributing to the area of the ith photopeak
RE_i is the relative efficiency at the energy of the ith peak

The relative activities, the half lives, and atomic masses of the isotopes are then combined to yield the relative masses for each isotope.

d. Calculate Isotopic Fractions

After the third iteration is complete, the final relative masses (relative to the first isotope in the isotope list) are combined to give the absolute isotopic fractions without ^{242}Pu (^{236}U). The fractions are renormalized accounting for ^{242}Pu (^{236}U) computed by correlation or fixed by operator entry. Non-plutonium (uranium) isotopes are quantified relative to total plutonium (uranium). For samples containing no plutonium or uranium, the final results are the relative masses themselves. Auxiliary results such as the effective specific power and effective ^{240}Pu fraction are computed from the plutonium isotopic fractions and the appropriate constants in the parameter set.

e. Calculate Isotopic Correlation for ^{242}Pu and ^{236}U

Plutonium-242 and ^{236}U cannot be measured directly with gamma-ray spectroscopy techniques. It is customary to introduce an empirical isotopic correlation (Gunnink 90, Bignan 95) to predict their concentrations from the measured ratios for the other isotopes.

FRAM predicts ^{242}Pu from:

$$^{242}Pu = A \times \left[\left(^{238}Pu \right)^B \times \left(^{239}Pu \right)^C \times \left(^{240}Pu \right)^D \times \left(^{241}Pu + ^{241}Am \right)^E \right] \qquad \text{(IV-4)}$$

where the five constants, A–E, are user-editable values in the parameter file.

In a similar manner, Vo has developed a correlation to predict ^{236}U in uranium-bearing samples. It is of the form

$$^{236}U = A \times \left[\left(^{235}U \right)^B \times \left(^{238}U \right)^C \right] \qquad \text{(IV-5)}$$

The constants in eq. IV-5 have been determined from mass spectrometry values for US uranium produced by the gaseous diffusion process.

V. PARAMETER FILES, THE KEY TO FRAM'S VERSATILITY

The FRAM code has been structured to give the user as much control as desired over the analysis to increase versatility and applicability. This is accomplished by using Parameter Files (or Parameter Sets). A Parameter File contains the all the parameters required to analyze a gamma-ray spectrum. This includes information on the isotopes to be analyzed, the gamma-ray peaks to use, the nuclear data for the isotopes and gamma-rays, data acquisition conditions such as gain, zero, number of channels, spectral regions to analyze, and diagnostic test parameters.

These parameters reside in a custom-designed database within FRAM. This database can accommodate multiple parameter sets. The Change Parameter Utility, accessed from FRAM, gives the user access to all sets. The utility allows the user to add a new parameter set, delete a set, or modify the values in any set. The utility also allows the user to export the information in a parameter set to a text file on disk and subsequently to import this information back into the database allowing different systems to share parameter sets. Formally, "parameter set" refers to the information residing in the database in computer memory. "Parameter file" refers to the information in a text file residing on a disk.

FRAM is delivered with a variety of parameter files suitable for nearly all routine analyses. These parameter files usually do not need editing or changes to use FRAM for the first time. Routine FRAM analyses can be started with as few as three mouse clicks.

VI. FRAM USER INTERFACE

The FRAM user interface for version 4.2 provides a wide range of options governing data acquisition, data analysis, data display, results output, and parameter set manipulation and editing. We will briefly illustrate the extensive capability available to the user of FRAM.

The main menu of FRAM appears with four major options, File, Edit, Measure, and Options.

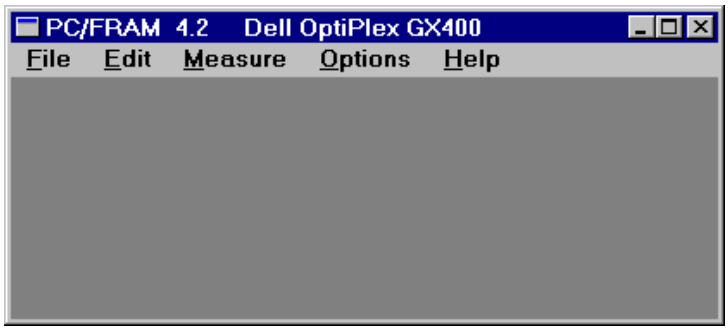

A. File

The File option allows the user to open a spectral data file where it can be viewed under Options. The file can also be saved in any of the supported data formats. Saving the file in the ASCII text format makes it easy to plot the data in most graphical applications.

B. Edit

The Edit menu has three groups of options. The first group allows password-protected access to the Change Parameter Utility. It also contains General Defaults allowing the user to set up

global parameters that govern the data handling in the system such as default paths for accessing FRAM, storing the spectral data and results files, and access to supported MCAs.

The second group of parameters under the Edit menu allows the user to set up default entries in many of the application windows. With the use of these defaults, the user is able to start a measurement with only three clicks of the mouse.

The third group is the password-protected User List. The User List controls access at three levels of password protection to all of the password-protected options.

C. Measure

The Measure menu governs the acquisition and analysis of data from both "live" MCA sources and disk files.

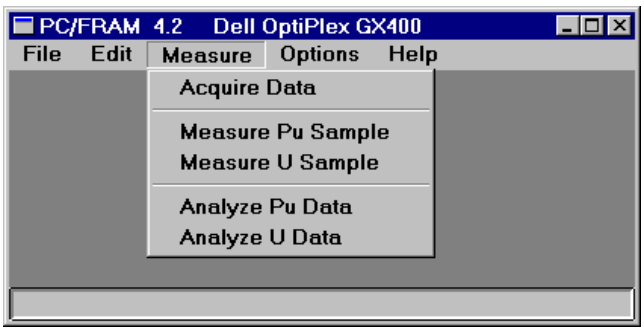

The Acquire Data option controls acquisition of data from a supported MCA and the storage of the data (without analysis) in a disk file. The Measure Pu (U) Sample options follow the data acquisition with an immediate analysis of the acquired spectrum. Analyze Pu (U) Data analyzes the spectral data from an existing disk file. The Measure Pu Sample window appears below as an example.

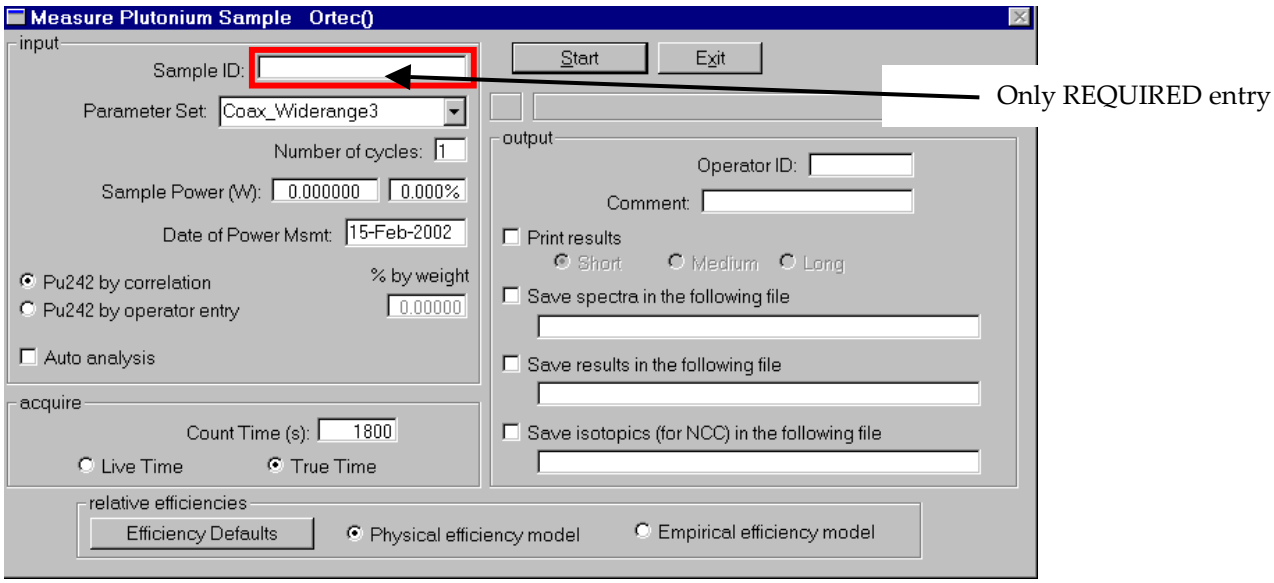

The window above has some of the entries defaulted from the Edit | Measure Pu Sample Defaults option. At this point the only entry *required* to start the measurement and complete the analysis is the Sample ID. With the use of defaults successive measurements may be completed with only identification of the sample and clicking the Start button. In many cases the user will also want to utilize some of the optional output options. To facilitate this, the Sample ID is defaulted as the filename for data storage.

D. Options

The Options menu allows the user several ways to display and view the spectral data and the results of the analysis. The entire spectrum can be displayed and manipulated from the Plot Spectrum option with versatility similar to that of a commercial MCA emulator. The user can also display the peak fits and view the relative efficiency curve (below). These options are invaluable when troubleshooting a suspect analysis. The results of selecting Plot Efficiencies and Display Fits are shown below with fits being displayed showing only the fit envelope (left) or with the individual components (right).

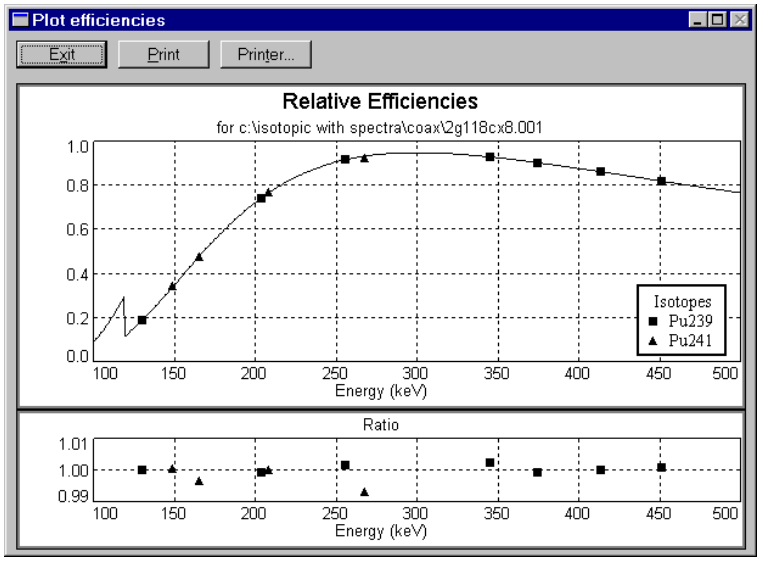

The ISOPOW option gives access to a plutonium and americium decay correction program (Sampson 86a) that can be used on line or off line.

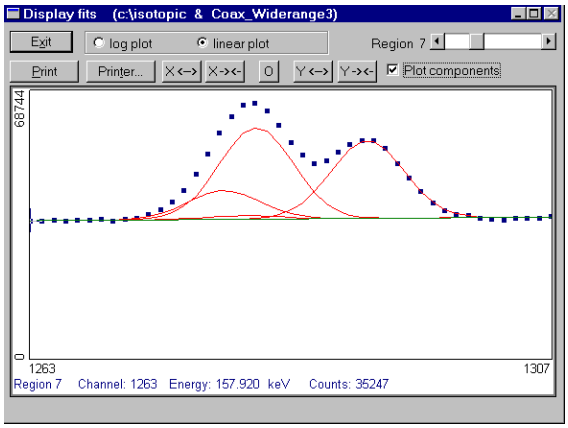

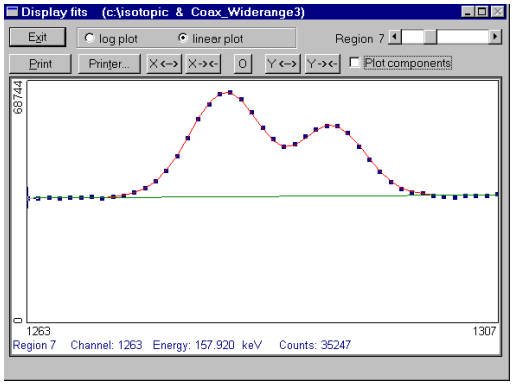

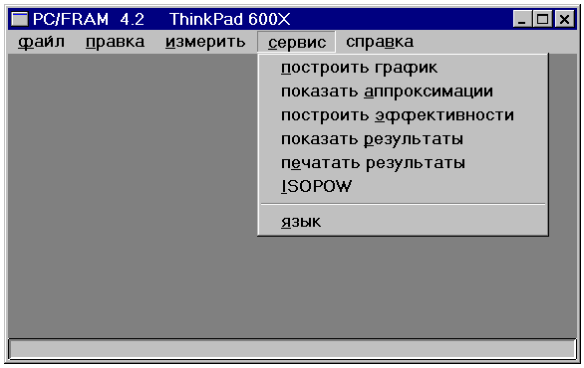

The option Language under the Options menu allows the user to display the operator interface, FRAM program messages, and results in a language other than English. The language strings are kept in a text file allowing any European language to be used as the second language merely by editing the second language text file. The current second language used with

FRAM is Russian. When Russian is selected the Main menu with "Options" pulled down looks like the screen to the left. The user can switch between the two languages with a single mouse click.

VII. FRAM PERFORMANCE

A. Measurement Precision or Repeatability

1. Definitions

In this section, we describe the many interrelated factors that govern the statistical precision of an isotopic measurement. In this context, precision or repeatability refer to the variability arising from counting statistics and are usually denoted by the relative standard deviation (RSD) in per cent.

$$\%RSD = 100 \times \frac{sigma}{measured\ value}\ . \qquad \text{(VII-1)}$$

Here *sigma* is the absolute standard deviation of the *measured value*.

Sigma can be determined in at least two ways. First, the sigma from counting statistics is estimated within FRAM using standard error propagation techniques. This is difficult given mathematical analysis involved, the presence of correlated variables, and the wide range of the magnitude of the measured values. However, this method gives an estimate of sigma for every measurement and is invaluable when one has only a single measurement. The second method uses repeated measurements. From *n* repeated measurements of the variable *x*, we determine *s*, the standard deviation of the sample and use it as an estimate of the standard deviation of the population.

$$\left(s^2\right) = \frac{1}{n-1}\sum_{1}^{n}\left(x_i - \bar{x}\right)^2 \qquad \text{(VII-2)}$$

This expression is useful when comparing the estimated standard deviation with the standard deviation (eq VII-2) observed from repeated measurements. One has to perform many repeated measurements to verify propagated error estimates accurately as Table VI-1 illustrates.

Sigma estimated in this fashion is also a random variable. That is, if the series of n measurements of x is repeated, *s* will be different. The mean value of s will be the population sigma. The relative standard deviation of s values is given by the formula

$$RSD\left(s\right) = \frac{1}{\sqrt{2(n-1)}} \qquad \text{(VII-3)}$$

Table VII-1 The RSD of Sigma (Error of the Error)

No. of Measurements	RSD of Sigma
10	0.235
15	0.189
25	0.144
50	0.101

2. Influencing Factors

In this section we will discuss some of the many, often interrelated factors, which influence the precision or repeatability of the isotopic measurement.

a. Count Rate and Throughput

The net counts in the photopeaks of the analyzed spectrum are the primary factors determining the measurement precision. The count rate directly influences the net photopeak counts. While the count rate in the detector is the parameter that is often observed, it is the actual data storage rate in the MCA that is of direct importance; this depends upon electronics settings including shaping time and the use of pulse-pileup rejection. Measurement systems are usually optimized by simultaneously measuring the throughput and resolution vs. incoming count rate and choosing the compromise settings best for the application at hand. An excellent discussion of these compromises may be found in (Parker 91a).

Throughput curves show a maximum throughput rate beyond which throughput decreases and counting precision worsens. The best compromise for throughput and resolution is usually chosen to be at a counting rate significantly below the throughput maximum. Operating at input counting rates that are 50-60 % of the count rate at the throughput maximum usually yields throughput values that 80-90 % of maximum while simultaneously preserving detector resolution.

Figure VII-1 shows the throughput and resolution measured with a 25% relative efficiency coaxial HPGe detector coupled with first generation digital signal processing electronics operated with a rise time of 4μs (equivalent to a 2μs shaping time in an analog amplifier). Here the throughput maximum occurs at an input rate of 60 kcps but we usually choose to operate at a maximum input rate of around 40 kcps where the resolution is better.

Optimizations performed in this manner affect the primary results of an isotopic analysis measurement. Figure VII-2 shows how the precision of the FRAM result for ^{240}Pu and P_{eff} varies for the same data set presented in Figure VII-1. Collection of spectral data at an input rate of 40 kcps gives essentially the same precision as operating at the 60 kcps peak of the throughput curve. The precision does not change very rapidly in a broad range about the throughput maximum, but it does worsen significantly at low count rates. In the range where the throughput curve is linear at rates below 15 kcps, the precision varies with the square root of the number of counts.

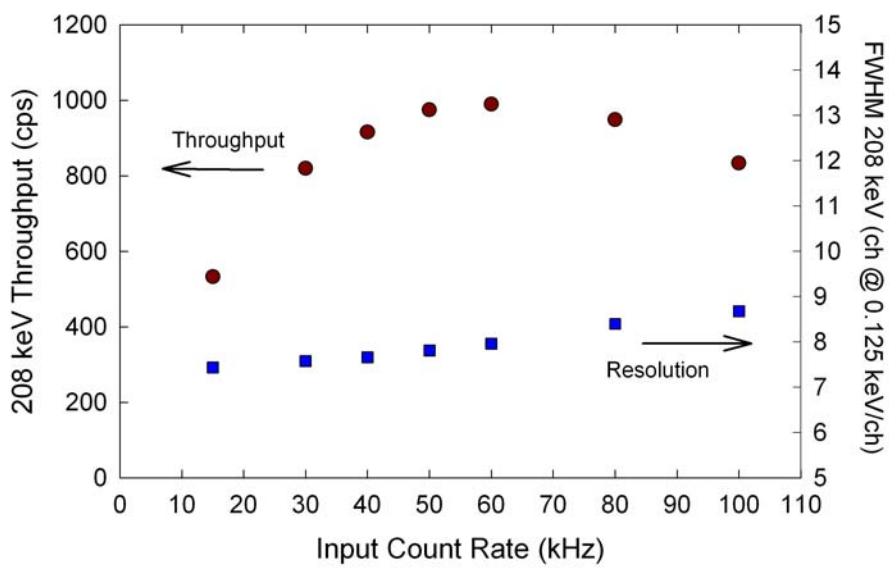

Fig. VII-1. Throughput and resolution for 208 keV peak of ^{241}Pu-^{237}U from 965 g PuO_2 with 16.85 % ^{240}Pu,and a 25%-relative-efficiency HPGe detector.

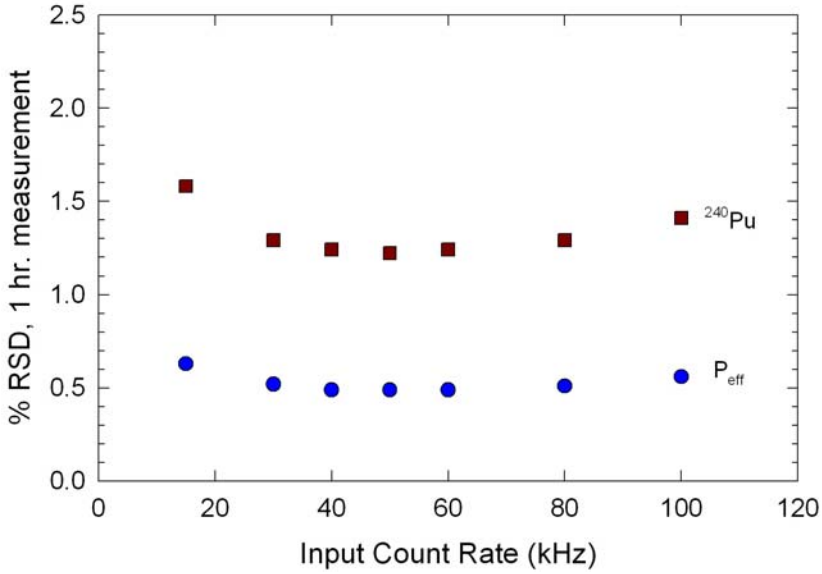

Fig.VII-2. % RSD of FRAM measurement of ^{240}Pu and P_{eff} for 965 g PuO_2 with 16.85 % ^{240}Pu, a 25%-relative-efficiency HPGe detector, an ORTEC DSpec operated at 4-μs rise time with analysis in the 120-450 keV region. Count time was 1 hour.

b. Electronic Settings

The amplifier shaping time is the single most influential electronic setting affecting system performance. The shaping time-resolution tradeoff is well known and is discussed in detail by Parker (Parker 91a). The term "rise time" is usually used in characterizing digital spectroscopy systems with the rise time being about three times the analog shaping time. Throughput generally varies inversely with shaping time. A shorter shaping time improves throughput.

Longer shaping times usually correspond to better resolution and lower throughput, although for any specific system, the user will find that the resolution-shaping time curve goes through a broad minimum that is dependent upon the type of detector being characterized. One always operates on the low or shorter shaping time side of this minimum, giving up a little resolution in order to improve throughput. Fortunately the minimum is broad and resolution does not suffer too much.

For the small coaxial detectors (25-30 % relative efficiency) often used with FRAM, we obtain good results with analog systems using 2-μs Gaussian or triangular shaping. This corresponds to a rise time of 4 μs for digital systems. With these settings, good resolution is obtained at suggested maximum count rates of approximately 30 kcps (analog) and 40 kcps (digital).

For the planar detectors most often used with FRAM (16-25 mm dia. by 13-15 mm deep), we recommend a 1-μs triangular shaping with an analog system or a 2-μs rise time with a digital system.

Since the first Los Alamos isotopic systems in the early 1980s, improvements in amplifiers and pulse processing methods have led to improvements of about a factor of 3 in the precision for ^{240}Pu or P_{eff} for measurements with the same count time.

c. Count Time

Poisson counting statistics are an appropriate model to represent the influence of counting time on the precision of isotopic analysis measurements. That is, the % RSD of a measured isotopic fraction varies inversely with the square root of the counting time, T.

$$\%RSD \approx \frac{1}{\sqrt{T}} \qquad \text{(VII-4)}$$

Increasing the counting time by a factor of 2 improves the % RSD by a factor of 1.4.

d. Energy Range

The energy range used in the analysis is often the single largest factor in determining the precision or repeatability of an isotopic measurement. The foremost factor here is the intrinsic intensity of the gamma rays used in the analysis. Table VII-2 displays the intensities for the principal gamma rays from each of four energy regions that have been used historically. The intensities of the principal gamma rays from the isotopes ^{238}Pu and ^{240}Pu drop by roughly an order of magnitude with each successively higher energy region. This means that the best precision measurements, at least for the important ^{240}Pu and ^{238}Pu isotopes, come from the lowest energy regions.

The 40–60 keV energy region is used only in the special case of freshly reprocessed (^{241}Am and ^{237}U removed) plutonium-bearing solutions, mainly in reprocessing plants. This region is not used widely for isotopic analysis because the Compton continuum from the 59.5-keV ^{241}Am peak swamps the plutonium peaks in the 40-keV region for aged materials and these low energy gamma rays are easily absorbed by many types of containers.

Table VII-2 Intrinsic Gamma-Ray Intensities of Major Gamma Rays in Principal Energy Regions

Region	^{238}Pu		^{239}Pu		^{240}Pu		^{241}Pu-^{237}U(*)		^{241}Am	
(keV)	(keV)	γ/s/g	(keV)	γ/s/g	(keV)	γ/s/g	(keV)	γ/s/g	(keV)	γ/s/g
40–60	43.5	2.5 e8	51.6	6.2 e5	45.2	3.8 e6			59.5	4.5
90–	99.9	4.6 e7	98.8	2.8 e4	104.2	5.9 e5	103.7	3.9 e6	98.9	2.6 e7
									103.0	2.5 e7
120–	152.7	6.1 e6	129.3	1.4 e5	160.3	3.4 e4	148.6	7.2 e6	125.3	5.2 e6
			375.0	3.6 e4			*208.0	2.0 e7	335.4	6.3 e5
			413.7	3.4 e4			*332.4	1.1 e6		
450–	766.4	1.4 e5	646.0	3.4 e2	642.5	1.0 e3			662.4	4.6 e5
									722.0	2.5 e5

The 90–105 keV region has been widely used for isotopic analysis and often offers the best precision for the measurement of ^{240}Pu. Strong attenuation of these low energy gamma rays does preclude their use for samples in thick-walled or shielded containers. An absorber of 10 mm of steel is usually enough to stop measurements using this region.

The 120–450 keV region is the most versatile region for plutonium isotopic analysis and is historically the region used at Los Alamos. Measurement precision for ^{240}Pu in the 120–450 keV region is usually poorer than in the 100-keV region. The advantage of this region is that measurements can easily be performed through as much as 12 mm of steel and even 0.3 mm of lead.

FRAM was the first code to carry out a complete Pu isotopic analysis using the 200–800 keV region. This capability allows measurements on samples in heavy-walled containers or in containers with internal shielding that prevents gamma rays below 200 keV from reaching the detector. Variants of this allow a complete plutonium isotopic analysis through shielding up to 25 mm of lead (Hypes 00).

The ability to analyze the 200-800 keV region for the complete isotopic distribution gives FRAM several more options for the analysis of large samples. The inherent advantage in precision of the 100-keV energy region for ^{240}Pu and ^{238}Pu analysis is reduced for large samples analyzed at high energy because of the increased penetrability of gamma rays in the 600-800

keV range relative to the 100-keV gamma rays. In effect, the high-energy gamma rays sample a larger volume of the sample. This increased penetrability is apparent principally for items with larger areal plutonium densities. Table VII-3 shows the parameters that affect penetrability for the three ^{240}Pu gamma rays at 104, 160, and 642 keV. This is the effect causing the relative efficiency curves for large items to increase in magnitude as one moves to higher energies (see Fig. II-1).

Table VII-3 Absorption Properties for PuO_2 at $\rho = 3 g/cm^3$ for Gamma Rays from ^{240}Pu

Energy (keV)	μ/ρ (cm^2/g)	μ (cm^{-1})	Mean Free Path (cm)
104	1.62	4.9	0.21
160	2.01	6.0	0.17
642	0.131	0.39	2.5

The self-absorption at 160 keV is actually greater than at 104 keV because the plutonium K edge falls at 121.8 keV, between the two energies. The mean free path (mfp) at 642 keV is 15x greater than at 160 keV. Samples with a thickness greater than three mfp at 642 keV will have an emission rate increase at 642 keV over that at 160 keV that nearly compensates for the intrinsic intensity(γ/s/g) difference (Table VII-2) at the two energies. When this is coupled with the lower background continuum present at higher energies, one often obtains better precision for measurement of ^{240}Pu at 642 keV than at 160 keV.

Another consideration for using the 200–800 keV range for larger samples is that one is often able to improve the precision still further by filtering the detector with additional lead. The additional lead removes gamma rays below 200 keV that do not contribute to the 200–800 keV analysis. The sample counts at a constant input counting rate are shifted preferentially to higher energies and a greater fraction of the analyzed gamma rays will fall in the 600-keV region. Measurement precision improves as the analysis moves into the 200–800 keV range and improves further when the spectrum is filtered. Pu-241 does not improve in every case because its analysis is carried out at the lowest energies (200-340 keV) of the analysis range.

e. Detector Type

The influence of the detector type is directly related to the energy range used in the analysis. Two types of HPGe detectors have been most often used for isotopic analysis with FRAM.

Planar Detectors Planar detectors of dimensions 16-mm dia by 13-mm thick and 25-mm dia by 15-mm thick are commonly used for FRAM measurements. These detectors have historically been used in the 120-420 keV energy range and, with version 4, can now be used in the 100-keV region. For most measurements on samples in thin containers analysis in the 100-keV region will provide better precision for all isotopes than the 120–420 keV region. For samples in containers with steel thicknesses in the range 5-10 mm, the optimum analysis region becomes less clear. Above a wall thickness of about 10-mm steel, the 100-keV region analysis fails leaving the 120-420 keV region as the only viable option.

Coaxial Detectors Coaxial detectors of 25-30% relative efficiency (relative to a 7.6-cm-dia x 7.6-cm-thick NaI(Tl) detector for ^{60}Co at a distance of 25 cm) have been often used with FRAM. Coaxial detector measurement precision depends upon the energy range and shielding as discussed previously. It is not always possible to predetermine which detector, planar or coaxial, will have the better precision in the 120-420 keV region. Suffice it to say that the measurement precision in this energy range is often similar for the two detector types and the choice is often made empirically with measurements under realistic conditions. When samples are shielded,

planar detectors will not be viable and the coaxial detector choice often comes down to whether or not to use additional filters.

CdTe Detectors Although version 4 can analyze spectra from CdTe, the precision of CdTe results is not as good as with HPGe detectors. This is because of the small detector size (a few mm^3) giving volumes over a thousand times smaller than a coaxial HPGe detector (Vo 02).

f. Sample Characteristics

Characteristics of the measured item, such as mass, density, and shape, affect measurement precision. Compare a sample with a large area presented to the detector, but with a low areal density (g/cm^2) of plutonium, to a sample of the same mass with less surface area and higher areal density. For the former case, the lower energy gamma rays will be enhanced relative to those at higher energy and the 120–450 keV region may produce the best precision. Conversely, the second sample will have an enhanced high-energy region relative to the low areal density sample. These characteristics can often be observed in the shape of the relative efficiency curve (see Fig. II-1) which tends to fall with energy more rapidly for low areal density samples while samples with a greater areal density tend to have a higher relative efficiency continuing to higher energies.

3. Prediction of Precision in the FRAM Code

Every FRAM measurement includes a predicted value for *sigma*, the absolute error in the measured mass %, from the propagation of counting uncertainties in the photopeak areas. This is also reported as a RSD(%). These fundamental errors are propagated to produce the absolute and relative errors in other parameters. We do not include any systematic error components in *sigma* or RSD(%) so that we may check our purely statistical error prediction with repeated measurements.

We confirm the correctness of the FRAM error propagation by analyzing many sets of repeated measurements on many different types of samples. We compare the sigma predicted by FRAM with that calculated from repeated measurements. The ratio of these two sigmas should be near unity within the uncertainty of the observed sigma (Eq. VII-3). Table VII-4 displays the average ratio, over many data sets, of the predicted sigma to the estimate of sigma observed from repeated measurements on plutonium samples. Table VII-5 displays the same information for repeated measurements on uranium.

We predict the statistical uncertainty very well for ^{238}Pu, ^{239}Pu, and ^{240}Pu. FRAM underestimates the statistical error by about 25% (relative) for ^{241}Pu and ^{241}Am. This likely arises from the difficulty in correctly apportioning the uncertainties for the co-energetic peaks that contain contributions from both ^{241}Pu (and daughter ^{237}U) and ^{241}Am. The error in P_{eff} is overestimated in FRAM likely arising from the correlations resulting from the normalization condition that all isotopic fractions must sum to unity.

Table VII-4 Comparison of Predicted and Observed Uncertainties for Pu Analysis Using FRAM v. 4

Detector	Region (keV)	No. Data Sets	No. Meas.	Average Ratio: Predicted/Observed					
				^{238}Pu	^{239}Pu	^{240}Pu	^{241}Pu	^{241}Am	P_{eff}
Coaxial	120–450	46	751	0.97	0.97	0.98	0.65	0.74	1.28
Coaxial	200–800	53	828	0.73	0.94	0.94	0.59	0.82	1.18

Table VII-5 Comparison of Predicted and Observed Uncertainties for U Analysis Using FRAM

Detector	Region (keV)	No. Data Sets	No. Meas.	Average Ratio: Predicted/Observed		
				^{234}U	^{235}U	^{238}U
Coaxial	120–1001	33	415	1.35	0.84	0.80

The error predictions for uranium are reasonably good. When displayed as a function of ^{235}U enrichment (Fig. VII-3), we do see some ^{235}U dependence. Fig. VII-3 shows the uncertainty from the finite number of measurements (Eq. VII-3) for the observed uncertainty in each data set.

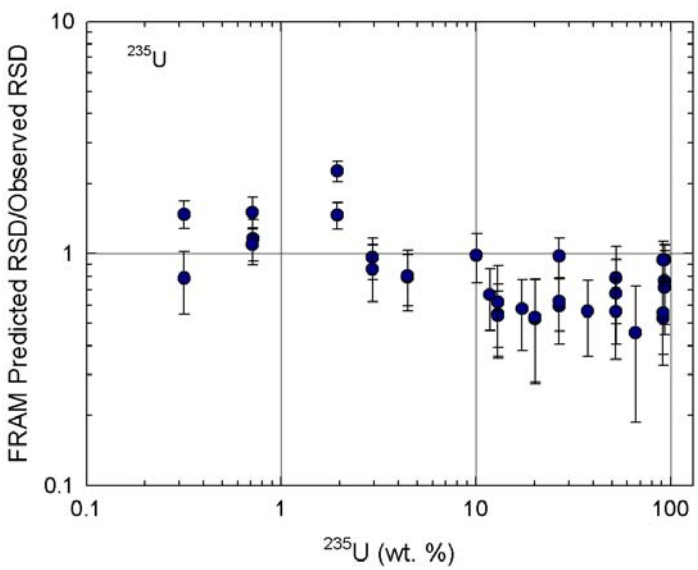

Fig. VII-3. U-235 dependence of FRAM estimate of ^{235}U statistical uncertainty.

4. Examples of FRAM's Statistical Precision

In this section, we present examples of FRAM's statistical precision taken from sets of repeated measurements. In Fig. VII-4 and -5, we display the precision for P_{eff} and ^{240}Pu, plotted vs. sample mass. These data represent not only different samples, masses, and isotopic compositions, but also different detectors, counting times, counting rates, and data acquisition electronics. Counting times for most data sets are 1 h, but some are 30 min or 2 h. The data display the wide range of

precisions that one might expect from the many different measurement conditions applicable to FRAM analysis.

One should also note that these are laboratory measurements, in most cases, where one was able to attain an optimum count rate from the sample. In many field applications, detector-to-sample distance constraints prevent this and lead to poorer measurement precision.

The coax and planar data in the 120–450 (420) keV region show similar results, at least at lower masses. We do see a definite trend (precision becomes poorer as mass decreases) in the precision vs. mass for the 200–800 keV region. This precision is worse than in the 120–450 keV region for small masses but can be, in many cases, the best choice for large mass samples.

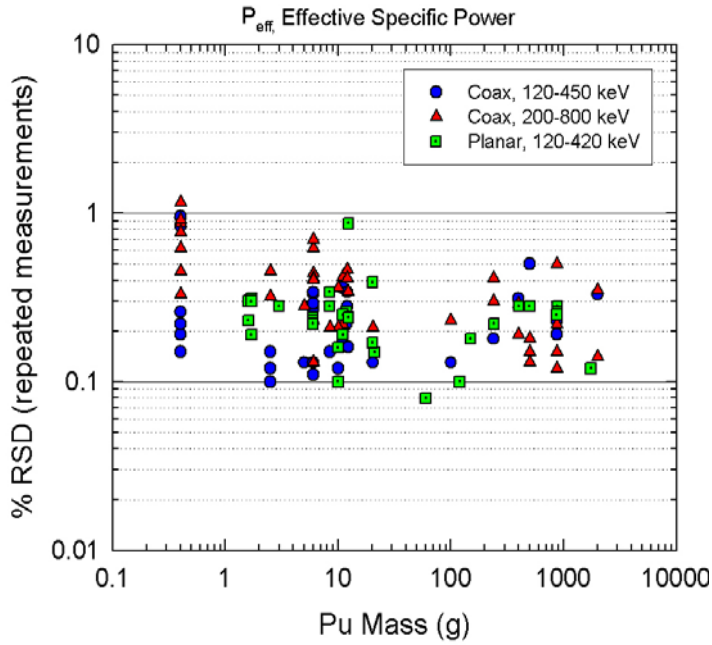

Fig. VII-4. Observed precision for P_{eff} for different detectors, different isotopic compositions, different count times, and different analysis regions as a function of plutonium mass.

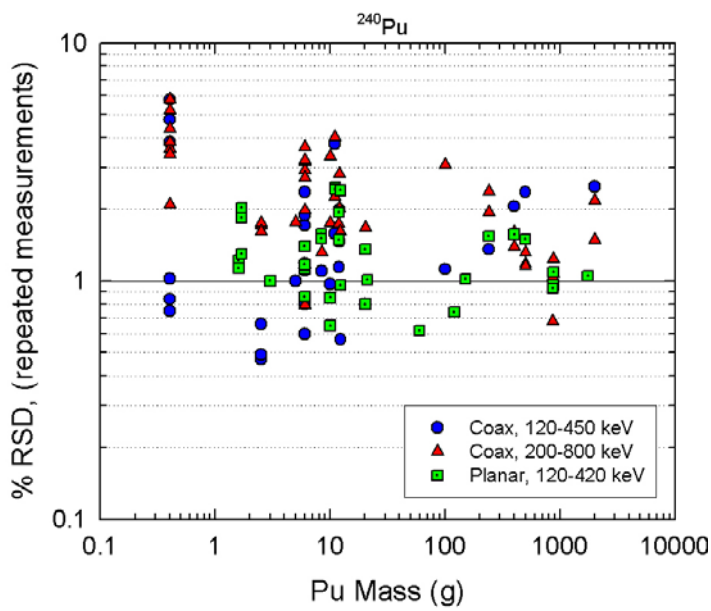

Fig VII-5. Observed precision for ^{240}Pu for different detectors, isotopic compositions, count times, and analysis regions as a function of plutonium mass.

Figure VII-6 extracts data for a single analysis method, coaxial detector in the 120–450 keV region. Each sample's data is analyzed for precision of ^{240}Pu and P_{eff}. The plotted ratio shows that the precision for P_{eff} is better than that for ^{240}Pu for every sample. Figure VII-7 displays the

precision of the measurement of the ^{235}U isotopic fraction in pure uranium samples. The precisions are those from repeated measurements and the data sets represent both 30-min and 1-h data. The detectors used are 25–30 % relative efficiency coaxial detectors. The measurement precision is pretty much constant for ^{235}U enrichments below approximately 10 %. In this case, the measurement precision is driven by the intensity of the 258-keV ^{238}U daughter peak that effectively controls the normalization of the relative efficiency curve. The intensity of this peak does not change very much for enrichments below 10 wt%.

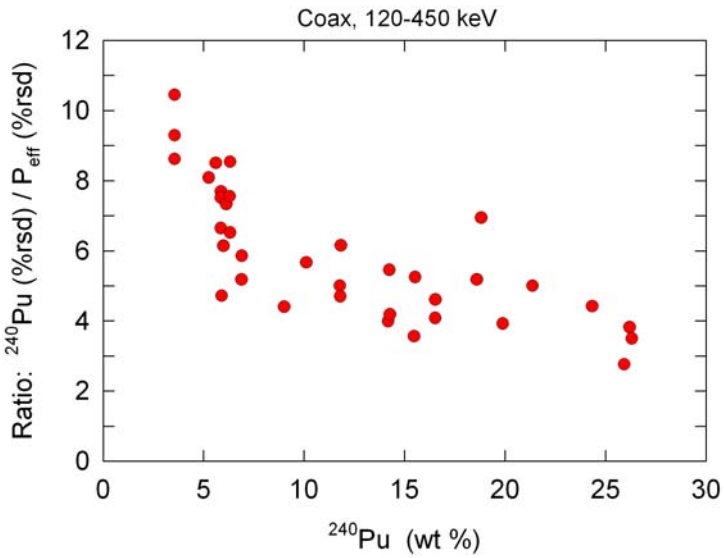

Fig. VII-6. The ratio of the observed precision for ^{240}Pu to that for P_{eff} for a coaxial detector with analysis in the 120-450 keV region is plotted vs % ^{240}Pu in the sample. Every sample shows better precision for P_{eff} than for ^{240}Pu (Ratio > 1) for the same data.

The precision of the measurement of ^{234}U is also of interest for higher enrichment samples as this isotope provides the overwhelming majority of the heat produced for calorimetry measurements. Figure VII-8 displays the ^{234}U precision for all ^{235}U enrichments for which you can measure ^{234}U. Only the enrichments above ~ 90% ^{235}U, coupled with kg-size samples, can currently be measured by calorimetry. For these samples, measurement precision can be in the 1-2 % range for ^{234}U.

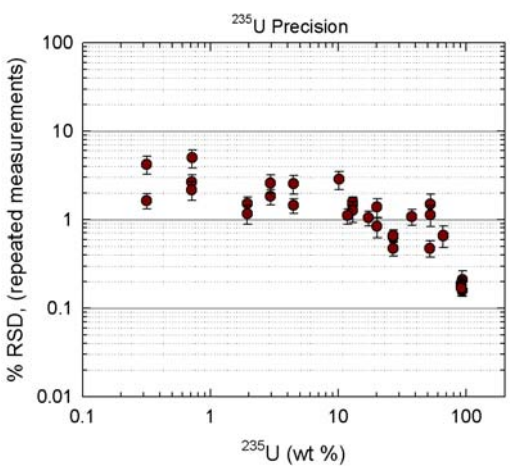

Fig. VII-7. ^{235}U measurement precision

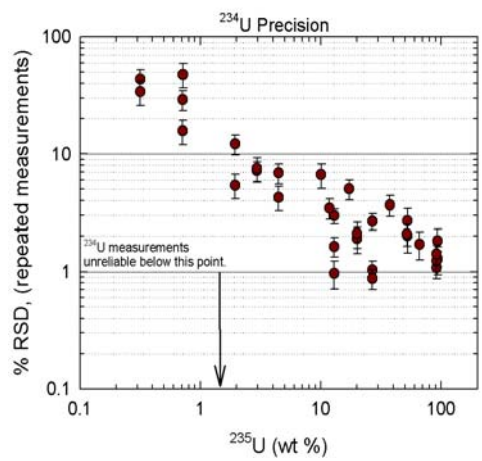

Fig. VII-8. ^{234}U measurement precision

B. Measurement Bias

1. Introduction

Bias is defined as the difference between the measured value and the true value. For all samples, we estimate the true value by using the best available value for the isotopic composition and ^{241}Am content. The best available values almost always are derived from mass-spectrometry measurements, sometimes supplemented with alpha counting for ^{238}Pu and/or ^{241}Am. In this document, bias is expressed as a ratio of the measured value divided by the best available or "accepted value."

Los Alamos has a large number of well-characterized plutonium, uranium, and MOX-bearing items having well-known isotopic distributions and ^{241}Am content. Several items are Certified Reference Materials (CRM) traceable to the national measurement system and are national or international standards. Many items have well documented mass-spectrometry values from routine analytical characterizations. Others have mass-spectrometry values determined by several different laboratories or by extensive measurements at a single laboratory. We find that routine mass-spectrometer measurements on modern instruments are nearly always adequate for characterization of the bias of a gamma-ray isotopic composition measurement. Nevertheless, we always examine the mass-spectrometer and gamma-ray measurements closely. We especially look for problems with ^{238}Pu, ^{241}Pu, and ^{241}Am.

Pu-238 This isotope is one of the most difficult to measure by mass spectrometry. First of all, its low concentration, in the range of 0.01 % for weapons-grade plutonium, approaches the sensitivity limit for mass spectrometry. Second, it has the same mass as ^{238}U. The most careful procedures are necessary to keep the plutonium sample (typically nanograms) from being contaminated with uranium. Any such contamination will result in too large a value for the ^{238}Pu isotopic fraction. We have observed these biases from old (20–30 years) mass-spectrometer measurements of plutonium. Alpha counting can obviate these problems. Under the best circumstances analytical uncertainties for ^{238}Pu fall in the 1-3 % (relative) range and can be the limiting factor in characterizing the ^{238}Pu bias for gamma-ray isotopic composition measurements.

Pu-241 The measurement of ^{241}Pu by mass spectrometry requires a chemical separation of the mass-spectrometry sample to remove isobaric ^{241}Am. If this chemical separation is not complete, the mass-spectrometer measurement of the ^{241}Pu fraction may be biased high.

Am-241 There are no CRMs for characterizing the concentration of ^{241}Am in plutonium. This limits the ability of the analytical chemists to make traceable ^{241}Am measurements. Typical characterizations may be biased by several percent.

We discover these problems by comparing gamma-ray measurements of the sample in question with gamma-ray measurements on another sample of similar isotopic composition that is known to have a bias-free analytical characterization. We have not observed any problems with mass-spectrometry measurements on uranium.

2. Plutonium Measurement Bias

Los Alamos has a large archive of plutonium spectral data going back to 1988. These data encompass many different detectors and varying electronic configurations including NIM, portable MCA, and digital spectroscopy systems. Some of the samples have been measured on different dates, separated in some cases by eight or more years. An archival data set of over 800 coaxial HPGe detector measurements exists for plutonium. The plutonium masses vary from 0.4

to 869 g and the ^{240}Pu fractions vary from 3.56 - 26.4%. Similar, though less extensive, data sets exist for plutonium measurements with planar HPGe detectors as well as coaxial and planar detector measurements on uranium. Analysis consists of averaging results for the multiple runs for each sample and then averaging the averages for all samples to obtain an overall bias for the entire data set. We use the accepted value for ^{242}Pu so the correlation does not affect the results. We have omitted the averages for ^{238}Pu for samples known to have incorrect accepted values or have measurements so statistically poor as to be unreliable. In these cases we also omitted the value for P_{eff} that can depend strongly on ^{238}Pu. Table VII-6 shows the average bias and standard deviation in the bias for the archival coaxial measurements using the 200-800 keV region for analysis. The standard deviation in the bias is a parameter that captures the fluctuations in the measurements caused by different sample (size, isotopic composition) characteristics, container characteristics, detector and data acquisition conditions as well as errors in the accepted values. This becomes the minimum error or uncertainty that could be quoted a priori for an arbitrary measurement on an arbitrary sample and is the limiting uncertainty or minimum bias that should be assigned to an arbitrary measurement. This parameter is similar in interpretation to the between-sample variance from an analysis-of-variance calculation.

Analysis of this type of archival data is available for the 120–450 keV analysis with coaxial detectors and also for planar detector analysis in the 120–420 keV region. The bias analysis for all three data sets is summarized in Table VII-6 for all isotopes. The $^{240}Pu_{eff}$ bias is plotted in Figure VII-9 for coaxial detector data taken in the 120–450 keV region.

Table VII-6. FRAM Version 4, Bias for Plutonium

		^{238}Pu	^{239}Pu	^{240}Pu	^{241}Pu	^{241}Am	P_{eff}
Coax 200–800	Bias	1.0049	1.0003	0.9999	1.0013	0.9982	0.9994
	% RSD	5.83	0.37	1.58	0.76	0.81	0.47
Coax 120–450	Bias	0.9958	1.0001	1.0000	0.9999	0.9955	0.9993
	% RSD	1.81	0.12	0.82	0.59	0.93	0.21
Planar 120–420 keV	Bias	1.0002	1.0002	0.9995	0.9979	0.9965	0.9995
	% RSD	1.91	0.12	0.77	0.61	1.30	0.24

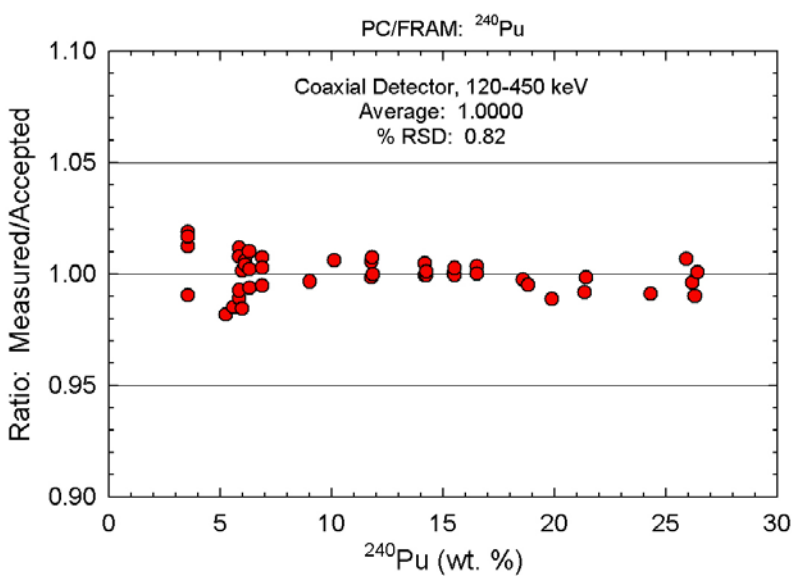

Fig VII-9. Measurement bias for ^{240}Pu, 120-450 keV analysis with coaxial detectors.

3. Uranium Measurement Bias

Just as for plutonium, Los Alamos has a large number of well-characterized, uranium-bearing items used routinely as standards. The extent of these standards and the quality of their characterization is unique in the DOE complex.

For comparison with standards, we use an operator-entered, accepted value for ^{236}U since it does not have detectable gamma rays and is determined by isotopic correlation in FRAM. This is analogous to the method used to analyze plutonium standards for ^{242}Pu.

We also have an extensive archive of uranium measurements from different samples, detectors, acquisition systems, and measurement geometries. The latter is particularly important to note. It demonstrates that version 4 of FRAM does indeed correct properly for the coincidence summing effects that affected earlier uranium measurements. The values for individual items come from the average of repeated measurements of typically 30-min or 1-h duration. For the important ^{235}U isotope, the average bias for all samples, over the enrichment range from 0.3-93 % is 0.25%. The RSD(%), in the same fashion as discussed for plutonium, is just under 1%. Recall that the interpretation of this parameter is the a priori measurement uncertainty for an arbitrary sample attributed to sample and measurement specific conditions. The measurement bias data for ^{235}U are plotted in Fig. VII-10.

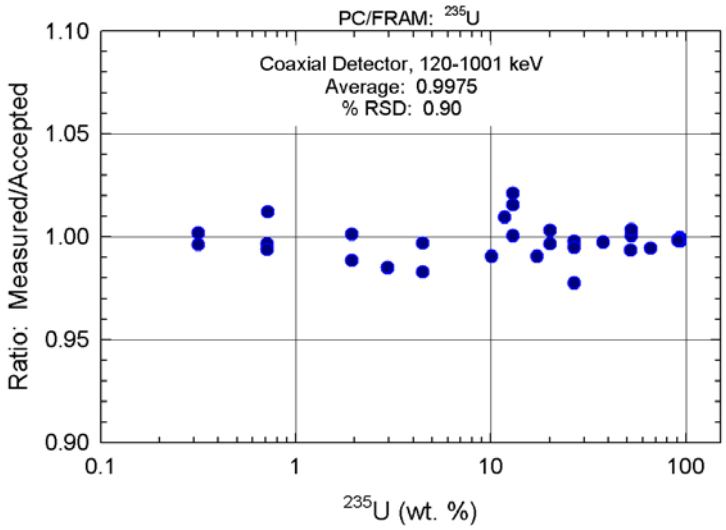

Fig. VII-10. FRAM Version 4 Measurement Bias for ^{235}U.

4. MOX Measurement Bias

Version 4 of FRAM can analyze the gamma-ray spectra from MOX samples giving results, in many cases, for the complete plutonium isotopic distribution, the ^{235}U/Pu ratio and the ^{238}U/Pu ratio.

MOX samples can be measured in several ways by FRAM depending upon the energy region analyzed and the amount of shielding surrounding the sample. U-235 is always analyzed at 185.7 keV. This gamma ray may not be present in a shielded sample and is not visible above the continuum for ^{235}U/Pu ratios below about 0.005. If the sample is lightly shielded, FRAM can obtain both the ^{235}U/Pu ratio at 185.7 keV and the ^{238}U/Pu ratio at 1001 keV. For heavily shielded samples, the ^{238}U/Pu ratio at 1001 keV may be the only uranium measurement available.

Tables VII-7 to 9 display the results of the analysis of five samples in three different ways. Results from unshielded sample measurements analyzed in the 120–450 keV range are given in Table VII-7. In the 120–450 keV analysis range, we only have access to ^{235}U at 185.7 keV. In Table VI-8, we show the results from the analysis of the unshielded samples using data in the 200–800 keV energy range. With this analysis, we are still able to analyze for ^{235}U at 185.7 keV as well as analyzing for ^{238}U at 1001 keV. In Table VII-9, we show results from the third

possible MOX data analysis using data from coaxial detectors. Here the samples are shielded with 3 mm of lead making the 185.7-keV gamma ray undetectable. We can only analyze for ^{238}U/Pu.

All of the MOX measurements tabulated in Tables VII-7 –VII-9 have a one-hour count time at rates between 30 and 40 kcps and were analyzed with FRAM version 4. We typically made 12–15 repeat measurements on each of the five samples. The Average is the average of the five individual sample averages. The % RSD is calculated from the distribution of the five individual averages of the repeated measurements. It can be thought of as the RSD of the bias. The MOX samples contained a few hundred grams of plutonium and had a ^{235}U/Pu ratio that varied from 1.4–6. U-235 enrichment ranged from 0.2–1%.

Table VII-7. Unshielded Measurements, 120–450 keV Analysis

	Ratio: Measured/Accepted							
	^{238}Pu	^{239}Pu	^{240}Pu	^{241}Pu	^{241}Am	Spec.	^{240}Pu$_{eff}$	^{235}U/Pu
Average	0.9765	0.9966	1.0250	1.0022	0.9938	1.0005	1.0238	1.0083
% RSD	0.79	0.15	1.11	0.30	1.67	0.48	1.06	3.96

Table VII-8. Unshielded Measurements, 200–800 keV Analysis

	Ratio: Measured/Accepted								
	^{238}Pu	^{239}Pu	^{240}Pu	^{241}Pu	^{241}Am	Spec.	^{240}Pu$_{eff}$	^{235}U/Pu	^{238}U/Pu
Average	1.0322	0.9986	1.0101	1.0055	0.9938	1.0024	1.0100	1.0136	1.0152
% RSD	5.08	0.04	0.32	0.30	1.66	0.51	0.31	3.67	1.42

Table VII-9. Shielded Measurements, 3-mm Lead, 200–800 keV Analysis

	Ratio: Measured/Accepted								
	^{238}Pu	^{239}Pu	^{240}Pu	^{241}Pu	^{241}Am	Spec.	^{240}Pu$_{eff}$	^{235}U/Pu	^{238}U/Pu
Average	1.00245	1.00077	0.99391	1.00816	0.99373	0.99792	0.99415		1.04488
% RSD	4.29	0.05	0.33	0.21	1.71	0.49	0.34		0.87

C. Intercomparison Exercises

1. The PIDIE Exercise

The Plutonium Isotopic Determination Intercomparison Exercise (PIDIE) was the first exercise designed to characterize gamma-ray isotopic analysis on a worldwide basis. This exercise was organized in Europe and was notable in that the organizers provided identical sets of seven, nominal 0.4 g plutonium as PuO_2, samples to each participant. The international shipment of the sample sets proved to be extraordinarily difficult because of shipping regulations and compliance issues.

These samples came to Los Alamos in 1980 at the time when we were developing our first isotopic analysis software. The Los Alamos measurement results are so obsolete that they will not be discussed, but they were published (Morel 1991). The samples used in PIDIE are a well-documented legacy of the exercise and are still used today at Los Alamos and elsewhere to characterize gamma-ray plutonium isotopic composition measurements.

2. Uranium Enrichment Measurement Exercise, IRMM 1996

The Uranium Enrichment Measurement Exercise, sponsored by the European Safeguards Research and Development Agency (ESARDA) was held at the Institute of Reference Materials and Measurements (IRMM) in Geel, Belgium in 1996. For this exercise, participants brought their own equipment to IRMM and had one week to measure a set of well-characterized standards (Morel 00).

Although the exercise was organized primarily to test "classical" infinite sample ^{235}U enrichment measurements, Los Alamos participated with FRAM giving results for ^{234}U, ^{235}U, and ^{238}U. The organizers only reported certified values for ^{235}U. Table VII-10 displays the average of all FRAM measurements. The biases displayed are very similar to those shown in Fig. VII-10. Samples X and Y are of interest because they are freshly separated and the daughter products ^{234}Pa and ^{234m}Pa used by FRAM to characterize ^{238}U have been removed from the sample. They grow back in with the 24.1-day half-life of ^{234}Th. For samples X and Y in Table VII-10, we made a correction using the known separation time. This correction reduced the error from about 20% to about 4%. The residual error may arise from an incomplete separation. A separation time correction has been incorporated into FRAM v. 4.

Table VII-10 FRAM Results for IRMM Uranium Enrichment Exercise

Sample	Measured wt% ^{235}U mean ± sigma(mean)	Certified wt% ^{235}U	% Difference 100*(M -	Comment
1614	1.521 ± 0.011 (0.71%)	1.4972	1.59 %	
1541	1.984 ± 0.018 (0.91%)	1.9952	-0.56 %	
1542	2.826 ± 0.023 (0.80%)	2.8774	-1.79 %	
1613	3.097 ± 0.061 (2.0%)	3.1094	-0.40 %	
125VA	93.35 ± 0.048 (0.051%)	93.1556	0.21 %	
X	3.316 ± 0.049 (1.48%)	3.4317	-3.37 %	freshly separated
Y	2.547 ± 0.011 (0.43%)	2.6846	-5.13 %	freshly separated
Average difference excluding freshly separated			-0.19 %	

3. The Pu-2000 Exercise

The most recent intercomparison exercise sponsored by the ESARDA NDA Working Group was conducted at IRMM in 2000. This exercise was organized similar to the Uranium Enrichment Measurement Exercise with participants using their own equipment in a one-week measurement window. The purpose of this exercise, known as the Pu-2000 exercise, was to test the performance of recent isotopic analysis methods over a wide range of abundances and investigate possible sources of error. Los Alamos was one of eight participating laboratories. Twenty unknown samples characterized by IRMM were available for measurement. Four certified samples were available as references. Seventeen of the twenty samples contained plutonium or MOX with ^{240}Pu ranging from 1.6 – 26.9 wt %. The remaining three samples were isotopically pure samples of ^{239}Pu, ^{240}Pu, and ^{241}Am.

Table VII-11 displays the average and relative standard deviation (%) for the ratio (%) of the FRAM result to the IRMM certified value. Table VII-12 displays FRAM results for the isotopically pure samples. FRAM was the only code to report results for all three samples. It's versatility allowed us to modify parameter files for these very special samples.

Table VII-11 FRAM/IRMM Results for Pu-2000 Exercise, 17 MOX samples

FRAM/IRMM certified	^{238}Pu	^{239}Pu	^{240}Pu	^{241}Pu	^{241}Am
Average	0.9943	1.022	0.9940	1.0098	1.0194
RSD (%)	4.55	0.41	1.13	1.67	3.05

Table VII-12 FRAM Results for Isotopically Pure Samples (Wt. % Relative to Total Plutonium)

Sample	Type		^{238}Pu	^{239}Pu	^{240}Pu	^{241}Pu	^{241}Am (μg/gPu)
R	Pu-239	FRAM	0.00031	99.964	0.0325	0.0029	75
		Certified	0.0000	99.979	0.0210	0.0001	3
S	Pu-240	FRAM	0.1027	0.0084	99.860	0.0001	13.6
		Certified	0.0119	0.023	99.935	0.00098	20.2
T	Am-	FRAM					100.00
		Certified					100.00

D. Factors Influencing Measurement Bias

Many factors influence the bias of a gamma-ray isotopic measurement.

1. Sample Composition Characteristics

The elemental makeup of the sample influences self-absorption thus influencing the relative efficiency curve. Version 4 accounts for this by allowing up to three different elements or compounds to define the matrix. These elements or compounds may be chosen from Al, Fe, Cd, Er, Pb, H_2O, and Concrete. These materials were chosen not only for their likely presence in the sample, but also to cover the range of atomic number. If the matrix contains elements other than the three designated in the parameter file, FRAM will use a linear combination of these three to approximate the relative efficiency curve. Differences from the true relative efficiency curve are likely to be compensated by the Hoerl function correction factor and the result is almost always a good fit to the relative efficiency points, even if the three chosen components do not match the actual sample matrix.

2. Branching Ratios

The branching ratios used in the analysis directly affect the bias in the measured isotopic ratios (Eq. II-1). Most of the branching ratios have been measured by gamma-ray spectrometry techniques. Absolute measurements of this type are very difficult and the very best results usually have an associated uncertainty of no better than 1% (relative).

3. Coincidence Summing

Coincidence summing occurs when a gamma-ray decay includes cascades of two or more gamma rays that are emitted simultaneously. These two gamma rays may be detected simultaneously and the single pulse will not represent either gamma ray. This takes events away from the full energy peak in a manner that is dependent upon the measurement geometry.

Summing effects depend upon the square of the detector solid angle (Knoll 00) and can be reduced by increasing the sample-to-detector distance. For coincidence summing to be a

problem, the coincident gamma rays must be of high enough intensity to be useful in the analysis and must be of high enough energy to escape the sample and its containment.

a. Uranium

Coincidence summing is present in low-enriched uranium measurements in the 120–1001 keV range; it particularly affects the 258-keV gamma ray from ^{234m}Pa. In general, measurements on high-enriched uranium are not affected because the 258-keV gamma ray is not used in the analysis. The ^{235}U isotopic result can be biased by as much as 15%, depending upon the sample-to-detector distance. The effects are pronounced for sample-to-detector distances below 5 cm and become small above about 15 cm.

FRAM version 4 incorporates a correction factor for coincidence summing. It is derived by examining the intensities of several gamma rays affected by coincidence summing in different proportions while knowing their correct branching ratios. This allows a correction to be made by comparing intensity ratios of the affected peaks to the ratios expected without coincidence summing.

b. Plutonium

Coincidence summing is not a problem with plutonium measurements because the filtering present for plutonium measurements removes the low energy coincident gamma rays.

4. Peak Area Determination

a. Background Shape

A parameter file is set up for a wide range of measurement conditions such as variable isotopic composition, sample mass, composition, container and shielding, detector resolution, as well as measurement geometry. Because measurement conditions affect the shape of the background continuum, the parameter file setup for the region must allow for a background continuum shape that will adapt itself to different conditions. Some “tricky” regions are illustrated and discussed below.

<u>Continuum at 160 keV</u> The definition of the background type for the region around 160 keV is critical as this peak is the only one available for analysis of ^{240}Pu in the 120-450 keV region. We see in Fig. VII-11 that the background has an inflection point. We customarily define a quadratic background for this region with background ROIs below 160 and above 165 keV.

<u>Continuum at 148 keV</u> The background continuum underneath the 148.6-keV peak from ^{241}Pu is usually positively sloping as is shown in Fig. VII-12. One would like to use a linear background with a smoothed step function. However, since the background is higher above 148 keV than it is below, the “step” goes the wrong way and becomes unphysical. FRAM can sense this condition and automatically recalculates the background continuum with the simpler linear form that does not incorporate a step.

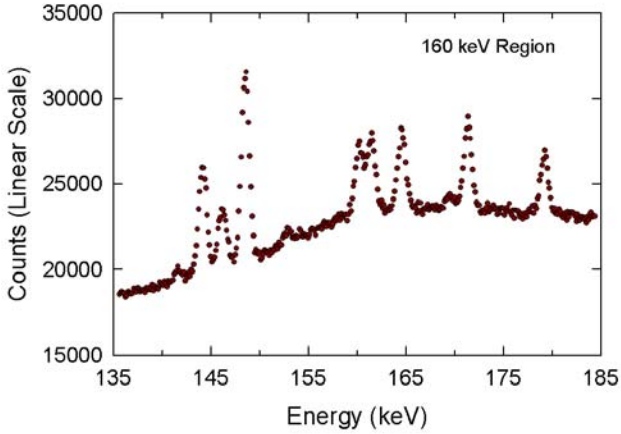

Fig. VII-11. The background in the region around 160 keV shows curvature making definition of the background continuum difficult. Poor definition can bias the ^{240}Pu peak area at 160.3 keV.

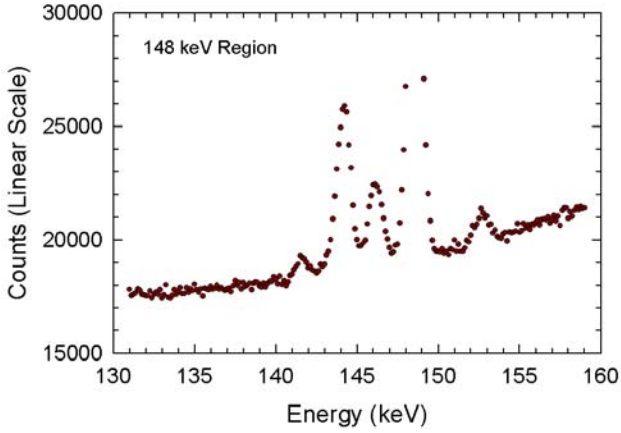

Fig. VII-12. The positive sloping background makes it difficult to calculate an accurate background continuum for the 148.6 keV from ^{241}Pu

<u>Continuum at 208 keV</u> The ^{241}Pu–^{237}U peak at 208 keV can vary over a factor of 500 in intensity relative to neighboring peaks, depending upon isotopic composition. This peak usually presents the classic case of the linear step function background type. We see in Figs VII-13, -14 that the underlying continuum can change slope above and below 208 keV. While a linear step function works well in Fig. VII-13 the continuum in Fig VII-14 is better characterized by a bilinear step having a different slope above and below the 208-keV peak. FRAM automatically switches from a bilinear step background to a linear step, if it finds the bilinear step inappropriate.

b. Interferences

FRAM can be characterized as a response function code. The peak shapes are determined in the internal calibration phase of the analysis and the peaks for analysis are predetermined by the setup of the parameter file. An unexpected peak (one not listed in the parameter file) appearing in an analyzed region, may bias the analysis of the designated peaks in the region. This bias can arise by direct interference with the peak or the interference may appear in a region used to define the background continuum thus biasing the peak area via an incorrect background subtraction. Once an interference peak is recognized, we can easily modify the parameter file to and then reanalyze the data.

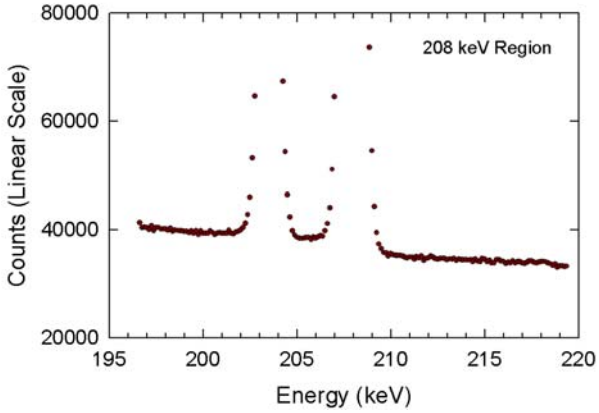

Fig. VII-13. The 208-keV region from a low burnup plutonium sample. The background continuum has the same slope above and below 208 keV.

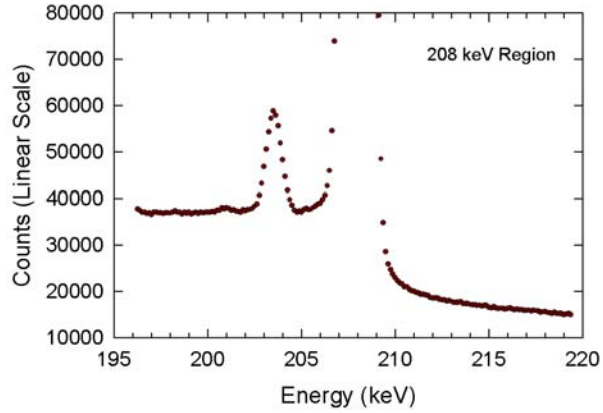

Fig. VII-14. The 208-keV region from a high burnup plutonium sample. The background continuum has different slopes above and below 208 keV.

The general-purpose plutonium parameter files delivered with version 4 of FRAM are set up to include common interferences from ^{235}U, ^{243}Am–^{239}Np, and ^{237}Np. The general-purpose parameter files are usually adequate for low concentrations but may require modification for very high concentrations. The FRAM user has another tool to discover unexpected interference peaks by displaying the analysis and background regions from the parameter file with color highlights overlaid on the spectrum. The highlighted spectrum will reveal if any unexpected interference peaks appear in a background region. Highlighting the analysis regions can show if the energy calibration matches that in the parameter file. If the highlighted peak regions do not contain the peaks, the energy calibration in the parameter file may not be appropriate for the spectrum.

E. Bias Correction

We have developed several procedures for identifying and correcting biases. In general, the procedures rely on measurement of standards, identification of the source of the bias, and correction of the bias, usually by adjustment of branching ratios.

The first step is to carefully set up the parameter file. This includes identifying the full range of measurement conditions, isotopic compositions, ^{241}Am content, interferences, and any other parameters that might affect the gamma-ray spectrum. The user then establishes the peak and background ROIs based on representative spectra. This is the most important step in making bias corrections.

1. Adjustment of Branching Ratios

If we still observe biases, even after careful setup of the parameter file, we may adjust the branching ratios to reduce or eliminate the bias. There is good justification for this approach, although it is questioned by some as inappropriate because branching ratios are imperfectly known constants of nature. Our reasoning is that we are making corrections for imperfections in the analysis in addition to correcting for uncertainties in our knowledge of the branching ratios.

One type of bias arises from peak area uncertainties caused by imperfect background subtraction. A second uncertainty comes from imperfections in the response function fitting of closely lying, overlapping peaks. A third uncertainty arises from biases in the published branching intensities. We have previously mentioned imperfections in modeling the relative

efficiency curve as a contributor to bias. Finally, the model (Gaussian plus exponential tail) used to fit the peaks is itself imperfect.

There are two principle sources of branching ratio values for plutonium, the work of Gunnink and coworkers (Gunnink 76a) and the Table of the Isotopes (Firestone 96). Any adjustment of plutonium branching ratios usually starts from these sources.

2. Observation of Peak Area Biases

We examine a FRAM analysis to look for inconsistencies in the activities calculated for gamma rays from a single isotope. We look at the consistency with consideration of the counting statistics for analyses from different samples. Any inconsistency that shows up regularly is examined in closer detail.

The bias correction for an isotope with only a single gamma ray (^{238}Pu and ^{240}Pu) can be straightforward. We examine the bias as a function of isotopic fraction. A simple branching ratio adjustment is usually indicated when the data do not show a trend with changing isotopic composition. The situation is more complex, however, if there is a trend. This could indicate unresolved or imperfect subtraction of interferences or a background continuum subtraction that does not adapt well over the full range of data.

3. Least-Squares Adjustment of Branching Ratios

A more general adjustment method utilizes high precision data from multiple measurements of samples with well-characterized isotopic compositions. A “Downhill Simplex Method” is incorporated into a special developer’s version of FRAM and used to minimize the weighted chi square of the chosen isotopic ratio(s). Multiple branching ratios are varied iteratively to find a minimum.

With this method we can obtain accuracies of a percent (relative) or less for the individual isotopic ratios. This fine-tuning usually does not make large adjustments from the published values. Indeed, if the adjustment is large (> 5 %), one should carefully examine the data to see if it is justified.

We have compared the adjusted branching ratios used in FRAM with published (Gunnink 76a, Firestone 96) values to verify the appropriateness of this approach. The FRAM values agree with the published values within the differences and uncertainties in the published values.

4. Use of Standards

All of the adjustment processes ultimately depend upon comparison of a measured value with a reference value. Thus, while gamma-ray isotopic composition measurements do not directly depend upon standards (Eq. II-1), we do rely heavily on comparison with standards for ultimate validation of the technique as well as the “fine tuning” of the analysis process. We have discussed analytical characterization issues in section VII. B. 1 and noted that they still contribute to gamma-ray isotopic analysis uncertainties for ^{238}Pu and ^{241}Am.

VIII. MAKING MEASUREMENTS FOR FRAM ANALYSIS

The FRAM analysis of a gamma ray spectrum can only be as good as the data will permit. Poor quality spectral data may limit the ability of FRAM to derive accurate results from the measurement, although the flexibility of FRAM’s analysis gives one a better chance of a good analysis than with any other analysis method. This section will present information on choosing and setting up equipment to collect high quality spectral data for FRAM analysis.

A. Choice of Detector

FRAM has been used with a wide variety of HPGe detectors, both planar and coaxial, as well as CdTe detectors. The detector procurement question will usually revolve around what size and type of HPGe detector.

First consider the mix of samples to be measured and their packaging. A coaxial detector is the appropriate choice for the user that makes a wide range of measurements on samples contained both in thin-walled and heavy-walled or shielded containers. Coaxial detectors can literally "do it all" with the exception of analyzing the 100-keV region. Specifications for a small coaxial detector often used with FRAM are shown in Table VIII-1. Planar detectors can be a good choice for samples in thin-walled containers and are required if one wishes to make measurements in the 100-keV region. Table VIII-1 also gives specifications of a planar detector successfully used with FRAM.

Many other HPGe detectors have been used with FRAM. Waste applications have used coaxial detectors of nearly 100% relative efficiency. The poorer resolution of these larger detectors may introduce some biases and require ROIs to be enlarged. We have used large semi-planar detectors (70-mm dia by 30-mm thick) very successfully for both plutonium and uranium. Measurements through thick-walled containers are usually improved if the detectors have higher efficiency than the "standard" 25%.

Table VIII-1. HPGe Detector Specifications for General Purpose FRAM Usage

Coaxial Detector	
Geometry	Coaxial, P-type germanium [1]
Efficiency	At least 25% relative efficiency at 1.33 MeV in the usual definition
1000 cps FWHM (122 keV)	≤ 750 eV at ≤ 6μs shaping time [2]
1000 cps FWHM (1.33 MeV)	≤ 1.75 keV at ≤ 6μs shaping time
30 kcps SWHM (122 keV)	≤ 880 eV at ≤ 2μs shaping time
30 kcps FWHM (1.33 MeV)	≤ 2.00 keV at ≤ 2μs shaping time
Peak Shape	[FW1/50M]/FWHM ≤ 2.50 at rates ≤ 30 kcps and time constants from 2 – 6 μs
Preamplifier/Energy Rate	Resistive feedback preamplifier with Energy Rate ≥ 50,000 MeV/s
Planar Detector	
Geometry	Planar
Crystal Size	≥ 25 mm diameter, ≥ 13 mm thick
1000 cps FWHM (122 keV)	≤ 520 eV at ≤ 6μs shaping time
50 kcps FWHM (122 keV)	≤ 580 eV at ≤ 1μs shaping time
Peak Shape	[FW1/50M]/FWHM ≤ 2.50 at rates ≤ 50 kcps and time constants from 1 – 6 μs
Preamplifier/Energy Rate	Resistive feedback preamplifier with Energy Rate ≥ 10,000 MeV/s [3]

[1] We specify P-type germanium because the resolution is usually better than that of N-type for the same detector size. N-type detectors have also been used successfully with FRAM.

[2] Shaping times are specified for analog amplifiers.

[3] The preamplifier energy rate for a planar detector is a trade off with low-rate resolution. This specification assures that the preamplifier will allow a maximum counting rate above 50 kcps for a typical plutonium spectrum. A more stringent low rate resolution specification may be achieved at the expense of the maximum preamplifier count rate.

B. Choice of Energy Range

Planar Detector With a planar detector one has the choice of 1) analyzing data above 120 keV (typically taken in 4096 channels at a gain of ~ 0.1 keV/chan to include 120–420 keV) or 2) analyzing the 100-keV region (typically taken in 4096 channels at a gain of ~0.075 keV/chan to include 0–300 keV). The 120–420 keV analysis provides more penetrability and will work through 12–15 mm of steel. The 100-keV region analysis provides better precision for plutonium in thin-walled containers at shorter counting times, compared to the higher energy analysis.

Coaxial Detector A coaxial detector is the most versatile choice if one is limited to a single detector. It can analyze data from all the samples that a planar detector can plus it can analyze data from samples contained in very substantially-shielded containers, up to and including about 25 mm of lead (Hypes 00). The amount of shielding governs the energy range used in the analysis. "Bare" samples are analyzed starting at about 120 keV. Samples shielded with about 6 mm lead or less are analyzed starting at about 200 keV. Analysis of samples with about 12 mm lead starts at about 300 keV as all gamma rays below that energy are removed by the shielding.

We typically acquire coaxial detector data in 8192 channels at a gain of 0.125 keV/chan spanning the energy range 0 – 1024 keV. This range is very convenient as it allows analysis of both uranium and plutonium spectra with the same electronic settings.

C. Collection of Pulse Height Spectra

1. Electronics

Data acquisition electronics used to collect spectral data for isotopic analysis span the range from simple analog to modern digital systems. Both types of systems have been implemented in mains-powered and battery-powered versions. The multichannel pulse height analyzers (MCA) that record the spectra have advanced over the years from large, dedicated, standalone desktop units to small, portable units consisting of a computer, an MCA board, and MCA emulator software. All MCA functions are integrated into small, portable, battery-powered systems suitable for field use. The portable MCAs also operate from mains power making them useful in both the laboratory and the field. The small size and low power requirements of portable, battery-powered analog systems usually extract a toll in system performance when compared to NIM module systems (Sampson 01).

Digital data acquisitions systems have now reached full commercial application. These systems digitize the signal directly out of the preamplifier. They offer an expanded selection of time constants and improved performance for both resolution and throughput over corresponding analog systems (Sampson 01). Digital systems, even in their portable, battery-powered form, demonstrate performance superior to the best analog systems and are recommended for any new procurement. Vo has performed extensive testing of the performance of many commercially available data acquisition systems (Vo 02).

2. Count Rate Considerations

The importance of count rate in the collection of high quality spectra cannot be overestimated. Too high a count rate may lead to degraded detector resolution, tailing from pulse pileup, and sum peaks, all of which can lead to measurement bias. Conversely, very low count rates yield spectra with too few counts and poor statistical precision. Increasing the count time to compensate for low count rate often leads to unacceptably low throughput. The count rate–resolution–throughput tradeoff is one that needs to be evaluated for every measurement system and situation. Many of the factors contributing to this question have been discussed in section VII.A.2.a. and also described by Parker (Parker 91a).

One of the first tests is the simultaneous measurement of throughput and resolution under realistic measurement conditions. The user selects a prominent peak and measures its net peak area and FWHM for a fixed count time (true or real) while varying the input count rate for a constant value of the time constant. The required peak areas and FWHM can be obtained from the MCA. The peak can be from a standard test source, ^{57}Co at 122 keV, ^{137}Cs at 661.6 keV, or from plutonium at 129.3 keV or 208.0 keV. The throughput and resolution can be plotted as shown in Fig. VII-1. The user then repeats the measurements for other time constants.

Short time constants will usually increase throughput, move the throughput maximum to a higher input rate, and make the resolution poorer. For analog systems, the resolution may worsen very rapidly at high count rates. You should operate at an input rate about 50-70% of the peak throughput rate which captures over 80% of the maximum throughput.

Sometimes the sample-to-detector distance is constrained. A large sample may produce an unacceptably high count rate with resolution that is too poor for successful analysis. These cases benefit greatly from the use of a digital spectrometer. FRAM has been successfully used with a digital spectroscopy system operating with input count rates up to 100 kcps and has made bias-free analyses for all of the conditions displayed in Fig. VII-1.

The detector and analysis region chosen can influence whether one chooses to optimize resolution or throughput. We give some general suggestions below.

<u>100 keV region, planar detector:</u> Optimization for measurements in the 100-keV region should concentrate on obtaining the best resolution at the expense of throughput. The larger intensities in this region make up for lowered throughput from increasing the time constant to 2 μs or even 3 μs from 1 μs.

<u>120-420 keV region, planar detector:</u> Optimization in this case usually concentrates on maximizing throughput by use of a 1-μs time constant and perhaps increasing the area of the detector. Resolution is secondary because we routinely use coaxial detectors with great success in this same region. Coaxial detector resolution at 122 keV is typically 1.5 times larger than that of a planar detector.

<u>120-450 keV region, coaxial detector:</u> We optimize for throughput in this region because of the lower intrinsic intensity of the gamma rays. Digital spectrometers can simultaneously improve resolution and throughput. Analog time constants can be as low as 2 μs for top quality 25-30 % relative efficiency coaxial detectors. Higher efficiency detectors usually require a longer time constant.

<u>200-800 keV region, coaxial detector:</u> This region is difficult to optimize. The intrinsic plutonium gamma-ray intensities are low which calls for larger, generally poorer resolution detectors. The peak fitting in the 637-646 keV peak region, containing five peaks including the important ^{240}Pu peak at 642.5 keV, demands the best possible resolution. Digital spectrometers improve the measurements in this region allowing FRAM to work at input rates as high as 100 kcps.

<u>120-1024 keV region, coaxial detector, U:</u> The uranium spectrum is not as complex as plutonium and does not demand as good resolution. Uranium systems can usually be optimized for throughput.

3. Pulse Pileup

a. Coincidence Summing

Coincidence summing occurs when gamma rays are emitted and detected in coincidence. It is possible for such gamma rays with energies E_1 and E_2 to be detected simultaneously in a time much shorter than the resolving time of the pulse processing electronics. The result is a new

peak at the energy of the sum of the two gamma rays. More important, for isotopic analysis, is the diminution of the individual peak areas at E_1 and E_2 .

Coincidence summing is isotope dependent and does not cancel out as random summing does. The effect is proportional to the solid angle of the detector as seen from the sample and can be reduced by increasing the sample-to-detector distance.

b. Random Summing

Random pulse pileup occurs when two pulses from independent decays are detected with a time separation shorter than the pulse-processing time of the analysis system. The result is a single distorted pulse with a pulse height unrelated to either input pulse. Such pileup can be minimized by proper pole-zero adjustment on the analog amplifier, or proper pulse-shape optimization on a digital spectroscopy system. Pileup rejection circuitry in modern amplifiers can reject the storage of pileup pulses if they can be resolved by the pileup rejecter, which is typically about 0.5 μs.

Pulse pileup can affect an isotopic measurement. The principal effect of random pulse pileup is to add misshapen peaks and structure to the spectrum. If these additional peaks fall inside a peak or background region defined in the parameter file, the analysis of that region will likely be biased. An example of random pulse pileup is shown in Fig. VIII-1. This example shows the summing of the 59.54-keV ^{241}Am peak with several peaks in the 100-keV region. The arrows show the location of the sum peaks. The sum peak that falls directly under the 160.3-keV ^{240}Pu peak is especially important. It will cause a bias in the 160.3-keV peak area and it may not be noticed if the other sum peaks are weak.

Random summing is assumed to result in equal losses throughout the entire spectrum. Thus, isotopic ratio methods should be unaffected. This assumption may not hold precisely because peak widths increase with energy, but it appears that the losses occurring from random summing do not materially affect isotopic ratio measurements. Two setup conditions also affect pulse pileup. Pileup can be reduced by operating at a shorter time constant or by operating at a lower count rate.

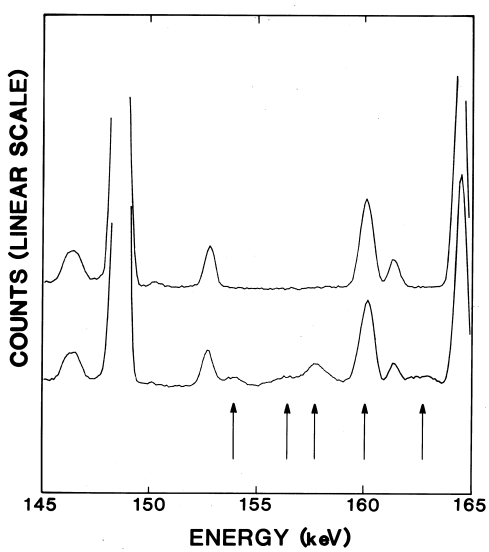

Fig. VIII-1. The effect of random pulse pileup on the 160-keV region can be dramatic. The top trace is a spectrum without pileup peaks. The bottom trace shows the effects of pileup of the 59.54 - keV ^{241}Am peak with other peaks in the 100-keV region. The arrows mark the location of the pileup peaks.

4. Filtering

Spectroscopists place absorbing materials or “filters” in front of the detector to preferentially absorb low energy radiation that is not useful for the measurement. Filters are typically chosen to have their K-absorption edge near but below the energy of the radiation to be absorbed. This maximizes the filter absorption and minimizes its effect on high-energy gamma rays. The

removal of unwanted low energy gamma rays eliminates a source of pileup summing, both random and coincidence summing.

The 59.54-keV gamma ray of ^{241}Am is almost always filtered. Its activity, 3-5 orders of magnitude greater than any other Pu gamma ray, dominates the spectrum of any Pu in a thin-walled container. If not filtered, the dead time from this gamma ray will prevent any useful information from being recorded. The unfiltered count rate from this gamma ray can often paralyze the detector and electronics.

Thin sheets of cadmium (Cd, Z=48, K shell binding energy = 26.71 keV) are most widely used to filter plutonium spectra. Tin (Sn, Z=50, K shell binding energy = 29.20 keV) is used in situations where health concerns preclude the use of cadmium. Lead (Pb, Z=82, K shell binding energy = 88.00 keV) is also used because of its wide availability.

A widely used "rule of thumb" is that the filter should be thick enough to reduce the intensity of the 59.5-keV gamma ray to the same magnitude as the intensity of the 100-keV complex of gamma and X rays. When this is met, one does not observe pileup in the 160-keV region (top trace in Fig. VIII-1).

The FRAM systems used at the Los Alamos Plutonium Facility measure the isotopic composition of plutonium over a very wide range of ^{241}Am content (< 100 ppm to > 500,000 ppm) where ppm is parts per million with respect to total plutonium. This dynamic range of nearly 10,000 makes it difficult to optimize the filter for all measurements. At Los Alamos, we use a single filter for all measurements so that the operator does not have to make filter decisions. This filter consists of about 2.0 mm of Cd backed by 0.25–0.51 mm of Cu. The copper (or like Z material) absorbs cadmium x rays. This graded filter keeps the spectrum below 80 keV as free as possible of photopeaks. It minimizes pileup summing from strong low-energy peaks. We adhere to the philosophy that any low-energy peak (below 100 keV) that is not used in the analysis is a "bad" peak. It cannot help the measurement and may hurt by contributing to sum peaks.

The "one size fits all" filter does degrade the intensity of useful photopeaks below 200 keV. The measurement precision of the ^{241}Am peak at 125.3 keV and the ^{240}Pu peak at 160.3 keV can be improved if one uses less filtering when ^{241}Am is less than 10,000 ppm. The measurement precision using the 100-keV region will be improved with filters that are less than 2.0 mm of Cd because the sum peaks do not fall into an energy region that is used in the analysis. Table VIII-2 displays the transmission of common filter components at several important gamma-ray energies.

Table VIII-2. Transmission of Common Filter Components

	Cadmium			Lead	
Energy	0.41 mm	0.81 mm	2.0 mm	0.41 mm	0.81 mm
59.5	0.127	0.016	0.000032	0.118	0.014
104.2	0.638	0.407	0.105	0.109	0.012
125.3	0.756	0.571	0.247	0.251	0.063
160.3	0.856	0.733	0.461	0.474	0.224

5. Shielding

The shielding used around the HPGe detector for analysis of plutonium isotopic composition is usually tailored to the energy range of the analysis to reduce direct photopeak interferences from other plutonium nearby. A system measuring in the 600—800 keV range requires more shielding than one used in the 100-keV region. If size and weight constraints permit, the

shielding around the side of the detector should provide an attenuation of at least 100 for the highest energy critical to the analysis.

The shielding for photopeak interferences is of primary importance, as these will directly bias the measurement. Shielding for continuum gamma rays is of secondary importance. Background gamma rays falling in the continuum will worsen precision but not the bias.

Lead (Pb) and machinable tungsten are commonly used for shields. Lead is a health hazard and is often canned in steel to alleviate that concern. Machinable tungsten is used where maximum shielding is required with minimum size; it does not require canning. Table VIII-3 shows the thickness of Pb and W shields required to provide a factor of 100 attenuation at common analysis energies.

Table VIII-3. Thickness in cm for Factor of 100 Attenuation

Energy (keV)	Pb (ρ = 11.35)	W (ρ = 15)
104	0.084	0.080
185	0.362	0.351
208	0.476	0.461
414	2.00	1.82
662	3.94	3.33
766	4.61	3.84
1001	5.97	4.83

The shield weight becomes an overriding consideration for portable systems. Because FRAM uses energies up to 1001 keV, a hand-held HPGe detector measuring isotopic composition of stacked UF_6 cylinders suffers from inadequate shielding even using the thickest practical shield (~ 12.7 mm Pb).

FRAM has been used at the Los Alamos Plutonium Facility in a mobile, mains-powered system that is easily transportable (Fig. VIII-5). This system uses about 19 mm of machinable tungsten shielding which Table VIII-3 shows provides a factor of 100 attenuation at 414 keV. Fixed FRAM systems are usually configured with at least a 5-cm-thick Pb shield around the lateral surface whether with a coaxial or planar HPGe detector. This provides a factor of 160 attenuation at 766 keV, the highest energy analyzed in a shielded-sample plutonium measurement.

Fig. VIII-5. A mobile PC/FRAM system configured on a commercial thyroid scanner cart for use at the Los Alamos Plutonium Facility. The detector shielding is 12.7 mm of machinable tungsten.

IX. DIFFICULT MEASUREMENT SITUATIONS

A. Using FRAM With Rate-Loss Correction Sources

We have successfully analyzed data taken with a rate-loss correction source attached to the detector (this correction source is used in Segmented and Tomographic Gamma Scanners performing transmission-corrected assays). The rate-loss correction source may have gamma rays that interfere directly with plutonium gamma rays used by FRAM. In addition, the gamma or x rays from the rate-loss source may randomly sum with plutonium gamma rays to produce unwanted interferences. The versatility of FRAM has allowed analysis of data from both situations (Sampson 03).

B. Simultaneous FRAM/AWCC Measurements

An AWCC user wished to perform passive coincidence measurements with the AWCC while simultaneously making an isotopic measurement with an HPGe detector. It was possible to make direct measurements using a 25% relative efficiency coaxial detector inside an *unmodified* AWCC. The sample contained 847g PuO_2 with a nominal 16% ^{240}Pu. The detector face was positioned 3.8 cm from the outer surface of the AWCC giving a gross count rate of 40 kcps. The total sample-to-detector distance was 30 cm. Each spectrum (10 of 30 min) was analyzed in the 120–450 keV and 200–800 keV regions. Table IX-1 below gives the results of the two analyses of the 10 measurements.

The measurement results are clearly more precise using the 200–800 keV analysis. Both sets of results show that spectra suitable for FRAM analysis can be obtained by collecting data through the body of the neutron counter.

Table IX-1 Results through AWCC Wall (operator ^{242}Pu) 847g PuO_2 with 16% ^{240}Pu

Analysis	Pu-238	Pu-239	Pu-240	Pu-241	Am-241
120–450 keV Analysis					
Avg: Measured/Accepted	0.9745	0.9999	1.0010	0.9842	1.0127
% RSD distribution	13.0	1.3	6.4	1.4	2.5
200–800 keV Analysis					
Avg: Measured/Accepted	1.0163	1.0049	0.9747	1.0163	0.9868
% RSD distribution	3.5	0.26	1.4	0.90	0.91

C. Measurements Through Thick Shielding

FRAM's ability to measure through very thick shielding is a well known characteristic. While we cannot document all possible measurement scenarios, we will give some examples of the extreme measurement conditions encountered for shielded samples.

1. Steel Shielding

10–12 mm of steel is the limit for reliable measurements using the 100-keV region.

a. Plutonium

Very early, it was shown that FRAM could easily analyze plutonium isotopic data from the 120–450 keV region taken through 12.5 mm of steel. Somewhat later, it was demonstrated that FRAM could analyze a plutonium spectrum taken through 25 mm of steel using the standard parameter file for the 200–800 keV region. It is clear that FRAM can measure through steel much thicker than 25 mm, but the experiments have not been performed to define a higher limit.

b. Uranium

A common problem is the measurement of low-enriched uranium in UF_6 cylinders. Cylinders containing UF_6 with enrichments in the 1 – 5 % range typically have a wall thickness of 13 mm. The wall material may be steel or a nickel alloy possessing about the same absorption properties as steel. Depleted or natural UF_6 is often found in cylinders with 16-mm-thick walls.

FRAM has no problem analyzing coaxial detector data from uranium shielded with 16 mm of steel (Sampson 01). Numerous measurements were made with a 28%-relative-efficiency coaxial detector on enrichment standards in a geometry simulating a UF_6 cylinder. Figure IX-1 displays this geometry.

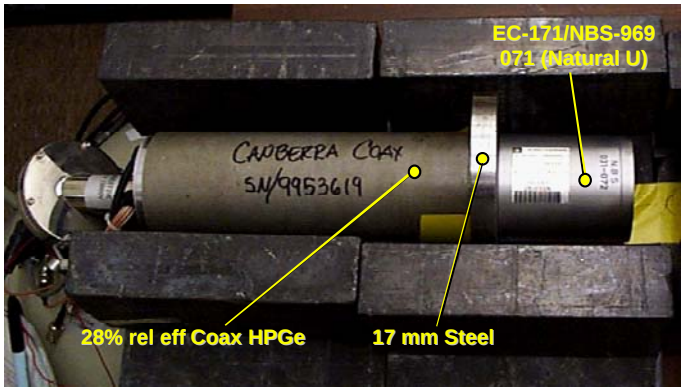

Fig. IX-1. Measurement geometry with detector, steel absorber, and sample simulating the measurement of a UF_6 cylinder.

Figure IX-2 displays, as a function of enrichment and count time, the relative standard deviation of a single measurement obtained from 15 repeat measurements. This was repeated using a semi-planar detector (70-mm diam by 30-mm thick) that yielded the same results as the coaxial detector.

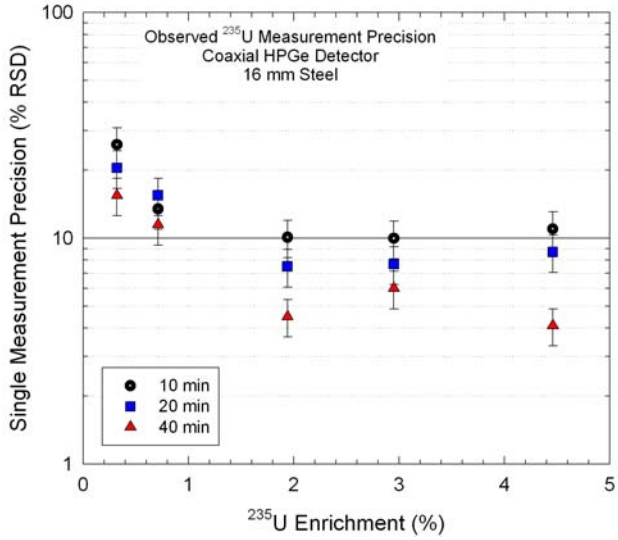

Fig. IX-2. Single measurement precision of ^{235}U calculated from 15 replicates. Five standards were measured in 8192 channels with a 28%-relative-efficiency coaxial HPGe. Measurements made in the geometry of Fig. IX-1.

FRAM has analyzed spectra acquired from type 30B UF_6 cylinders. This cylinder has 13-mm-thick steel walls. The measurements, made with a 26%-relative-efficiency coaxial detector in 8192 channels, had a precision of 6-8 % (1 RSD) for 20–30 min covering enrichments from natural to 4.7%. This is consistent with Fig. IX-2. One should consider the following when choosing between FRAM or the classical enrichment method for UF_6 cylinder assay.

The advantages of using FRAM are:

- Because FRAM does not require calibration, it is faster for a limited number of measurements than the classical enrichment method (infinite-thickness).
- The classical method requires a measurement of the cylinder wall thickness that adds time and uncertainty to the measurement and requires additional equipment.
- FRAM has no geometric reproducibility requirement. The classical enrichment method requires the geometry of the unknown be the same as for the calibration.
- FRAM can measure other materials in the facility such as scrap, waste, and oxide powder. The classical method is not able to do the other measurements without a new calibration and the assurance of a geometry that is "infinitely thick".

There are situations in which it is advantageous to use classical enrichment methods:

- The classical method has a shorter measurement time after calibration is complete.
- FRAM requires decay equilibrium (~100 days from separation) in the ^{238}U decay. The classical enrichment method does not because it measures ^{235}U directly.
- Shielding requirements are more stringent because FRAM measures up to 1 MeV. The classical enrichment method measures at 185 keV.

The discussion of gamma-ray isotopic measurements on UF_6 cylinders would not be complete without noting the capability of planar HPGe detectors. Such detectors have long been considered too small and inefficient for FRAM which measures up to 1 MeV. The IAEA asked if FRAM could analyze data from 25-mm-dia. x 16-mm-thick planar HPGe measurements of UF_6 cylinders; data that could not be analyzed with their standard technique using the 100-keV region. The data were acquired in 4096 channels at 0.25 keV/chan to match the IAEA's standard MCAs. The measurement geometry was as pictured in Fig. VIII-1 but with a planar detector in place of the coaxial detector. These measurements were very difficult for FRAM to analyze. The peaks were weak because of the small detector. Even more important was the low number of chan/keV resulting in very narrow peaks at low energy. The FWHM for the 185-keV ^{235}U peak was less than 3 channels. Measurements were made on enrichments of 0.31, 0.71, 1.94, 4.46, and 10.09 wt. % using steel thicknesses of 13 and 16 mm and count times of 15, 30, and 60 min. Each combination was measured 24 times for a total of 720 measurements.

The results (Sampson 01) from the most difficult measurement (0.31 wt. % ^{235}U for 15 min) are shown in Table IX-2. The % RSD is for a single measurement determined from the 24 replicates. The measurements in Table IX-2 demonstrate that FRAM can perform successfully in as little as 15 min, albeit with quite large uncertainties. Coaxial detector measurements are still preferred as the precision is a factor of two better than that of the planar detector (Fig. IX-1).

Table IX-2. Twenty-Four 15-min Measurements, Planar HPGe (25 mm x 16 mm)

		16-mm Steel Absorber			13-mm Steel Absorber		
Sample	Accepted wt% ^{235}U	Measured wt% ^{235}U	Meas./Accept.	% RSD	Measured wt% ^{235}U	Meas./Accept.	% RSD
EC-171-	0.3166	0.3131	0.9889	37.4	0.3556	1.1232	27.9
A1-408-1	0.7135	0.7231	1.0135	16.9	0.7100	0.9951	14.1
EC-171-	1.9420	1.9495	1.0039	18.6	1.9968	1.0282	15.7
EC-171-	4.4623	4.5950	1.0297	20.9	4.3954	0.9850	11.9
A1-324-1	10.086	10.093	1.0007	14.9	10.453	1.0364	8.0
		Average	1.0073		Average	1.0336	

2. Lead Shielding

The ability to analyze data acquired through lead shielding was one of the first "difficult applications" demonstrated for FRAM. Numerous examples of FRAM performance on lightly lead-shielded plutonium samples have already been mentioned. Hypes (Hypes 00) demonstrated that FRAM can obtain a complete Pu isotopic analysis through as much as 25 mm of lead. Figure IX-3 displays spectra for lead thickness of 0, 12, and 25 mm.

This requires some parameter file modification because low energy gamma rays "disappear" as the lead thickness increases. The 203- and 208-keV peaks of ^{239}Pu and ^{241}Pu-^{237}U are present and can be analyzed for lead thicknesses up to 6 mm. At 12 mm, we see gamma-ray peaks only above about 300 keV. This still allows analysis for ^{241}Pu using the 330- and 370-keV regions. With 25 mm of lead, the 330-keV region becomes very weak and one must measure ^{241}Pu using the 370-keV region. If the 370-keV region is not available, one cannot measure the ^{241}Pu isotopic fraction as 370.94 keV is the highest energy

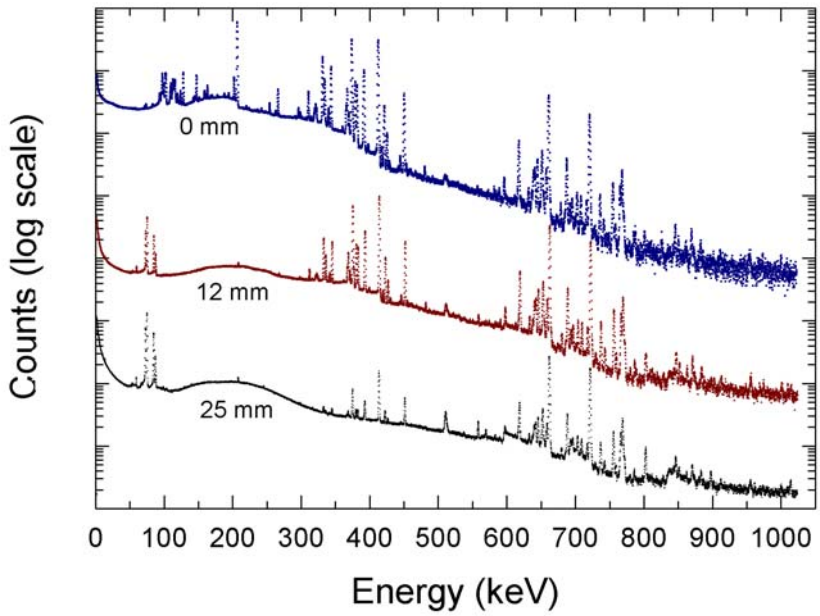

Fig. IX-3. HPGe gamma-ray spectra from a plutonium sample shielded with 0, 12, and 25 mm of lead. The peaks around 75 keV are Pb x rays from the lead shielding in front of the detector.

gamma ray emitted by ^{241}Pu or its ^{237}U daughter. It is also of interest to note the differential attenuation of the 375- and 414-keV gamma rays from ^{239}Pu. They are the most intense peaks in the 375-425 keV region in the plot below. Visually, the peaks are of about equal height with no shielding. The differential attenuation is apparent for 12 mm of lead and is approximately a factor of two for 25 mm of lead.

Note that 148.6 keV is the highest measurable gamma ray directly from ^{241}Pu. All the higher energy gamma rays come from the ^{237}U daughter. This means that ^{241}Pu-^{237}U decay equilibrium (> 45 days from chemical separation) must be present for measurement of ^{241}Pu for any samples shielded with enough lead to remove the 148-keV gamma ray (~ 1 mm of lead).

3. 9975 Shipping Container

The 9975 shipping container is difficult to measure. This container is used by DOE facilities to ship and store plutonium-bearing materials slated for disposition or long-term storage. The drum holds the nominal 13-cm-diameter DOE 3013 plutonium storage container. An interior view of a 9975 is shown in Figure IX-4.

Fig. IX-4. A view of the interior of a 9975 shipping drum showing four different layers of materials surrounding the central cavity. These layers consist of approximately 1.9 cm steel, 1.3 cm lead, and 13 cm of Cellutex.

A coaxial detector gamma-ray spectrum from approximately 4 kg of weapons plutonium in a 9975 is presented in Figure IX-5 below. It is not much different from the spectrum seen through 25 mm of lead shown in Figure IX-3. Data from samples in a 9975 are analyzed with a parameter set that uses gamma rays above 300 keV. The sawtooth structure at energies above 600 keV arises from neutron inelastic scattering from germanium in the detector.

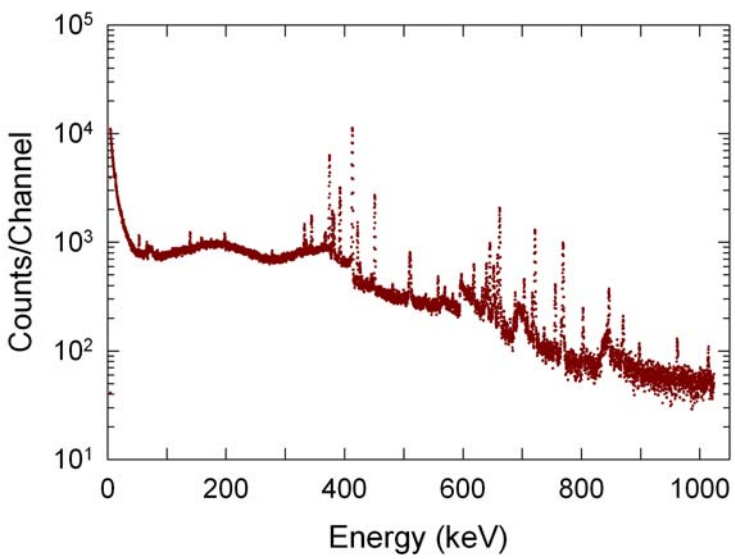

Fig. IX-5. A spectrum taken with a coaxial detector from 4 kg of weapons plutonium inside a 9975 shipping container.

D. Measurements of Am-Be Neutron Sources

FRAM has analyzed AmBe neutron sources for other heat-producing isotopes than ^{241}Am. These measurements supported calorimetry of the sources prior to disposal. It analyzed ^{239}Pu, ^{243}Am, ^{237}Np, and ^{239}Np relative to the main heat-producing isotope, ^{241}Am. Measuring neutron sources is a problem, in the long term, because of potential neutron damage to the HPGe crystal. These measurements did not result in any noticeable neutron damage and successfully demonstrated the ability of FRAM to analyze spectra containing neither plutonium nor uranium.

E. Measuring Samples with ^{237}Np

Neptunium-237 is present in all plutonium as a decay product of ^{241}Am and the ^{237}U daughter of ^{241}Pu. The level varies as a function of age, burnup (initial ^{241}Pu content), and chemical processing history. The Los Alamos archival plutonium samples used to characterize FRAM performance have ^{237}Np/Pu ratios in the range from 10^{-5} to 10^{-3}. The standard parameter files for the 120–450 keV and 200–800 keV regions delivered with FRAM quantify the ^{237}Np/Pu ratio on every measurement.

We characterize the concentration of ^{237}Np in plutonium by analysis of the gamma rays from its ^{233}Pa daughter ($T_{1/2}$ = 27.0 d). The gamma-ray activity from ^{233}Pa is in secular equilibrium with ^{237}Np after about 150 days. The decay of ^{233}Pa produces intense gamma rays at 271.5, 300.1, 311.9, 340.5, 375.4, 398.5, and 415.8 keV that can be used for the quantification of the ^{237}Np/Pu ratio and are interferences for the plutonium isotopic composition measurement.

For "normal" ^{237}Np/Pu ratios from 10^{-5} to 10^{-3}, we quantify ^{237}Np/Pu using the 312.2-keV peak. We also account for the 375.4- and 415.8-keV peaks because of their interference with prominent ^{239}Pu gamma rays. Plutonium-bearing samples containing ^{237}Np at levels above a ^{237}Np/Pu ratio of about 10^{-2} usually require additional analysis. At this level, the 312-keV line is the most intense gamma ray in the spectrum. The ^{233}Pa gamma rays contribute significantly to the dose from the sample. At Los Alamos, samples containing significant quantities of ^{237}Np are usually packaged in lead-shielded containers to reduce the dose to the sample handlers. The shielding eliminates all gamma rays below 200 keV necessitating analysis in the 200–800 keV region.

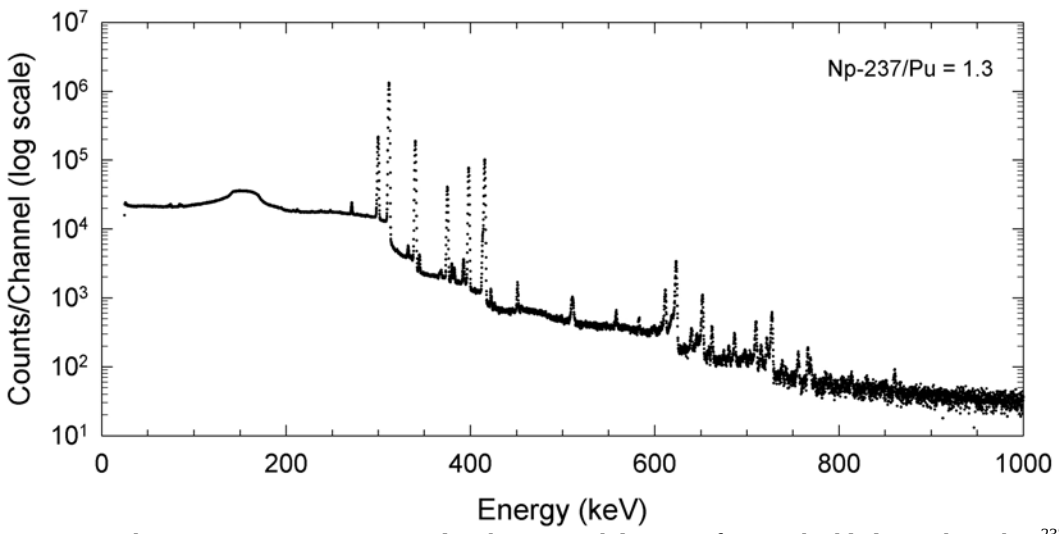

Fig. IX-6. A plutonium spectrum, measured with a coaxial detector, from a shielded sample with a ^{237}Np/Pu ratio of 1.3. This concentration is at the upper limit for neptunium analysis. The six major peaks in the 300–400 keV region are all ^{237}Np related; they overpower the plutonium peaks in the region. The three most intense peaks in the 600–650 keV region are sum peaks from ^{233}Pa gamma rays. The sum peaks also overpower the plutonium gamma rays in this region.

With a suitably modified parameter file this works up to ^{237}Np/Pu ratios of ~ 1 for samples shielded with 3 mm of lead. At a ^{237}Np/Pu ratio of about 1, the ^{233}Pa gamma rays dominate the spectrum making the plutonium analysis very difficult (see Figure IX-6). Sum peaks from the intense ^{233}Pa gamma rays dominate the region around 640 keV. FRAM can analyze spectra from samples shielded with 3 mm of lead with ^{237}Np/Pu ratios up to about 2. With extra lead filtering, we would expect to analyze spectra with ^{237}Np/Pu ratios up to about 10.

F. Measuring Samples with Very High ^{241}Am

The concentration that qualifies as "very high ^{241}Am" is ill defined, but falls in the range of ^{241}Am/Pu above 0.1. This is a convenient dividing line because most samples containing ^{241}Am solely from the decay of ^{241}Pu are below this limit. Americium-241 concentrations above 10% relative to plutonium usually arise only in residues and wastes containing ^{241}Am concentrated from purification processes. While the ^{239}Pu isotopic fraction may change by less than a factor of two over the entire range of samples encountered, the ^{241}Am/Pu ratio may change over a range of 10^6 considering all of the material streams in a plutonium processing facility. The ^{241}Am/Pu

ratio may approach 1:1 in process residues. There are several problem areas for analyzing gamma-ray spectra from samples with very high americium.

1. Americium gamma-rays dominate the spectrum. The peaks remaining from plutonium that haven't been swamped by americium ride on a large continuum from americium gamma rays. The resulting signal/background ratio is poor and the plutonium gamma-ray peaks have poor statistical precision.
2. Americium peaks normally too weak to be visible will suddenly appear in the spectrum. These "new" peaks interfere with the ROIs established for analyses of samples with "normal" americium concentrations.

The second problem can be handled by using a spectrum with very high ^{241}Am to guide the ROI selection. The first problem is more or less intractable. Items containing ^{241}Am/Pu above 0.1 are often in lead-lined containers making it necessary to analyze the 200–800 keV region, extracting ^{240}Pu at 642 keV. Figure IX-7 shows that the analysis for ^{240}Pu in this region can be difficult to impossible for samples with very high ^{241}Am because the ^{241}Am peak at 641.5 keV swamps the ^{240}Pu peak at 642.6 keV.

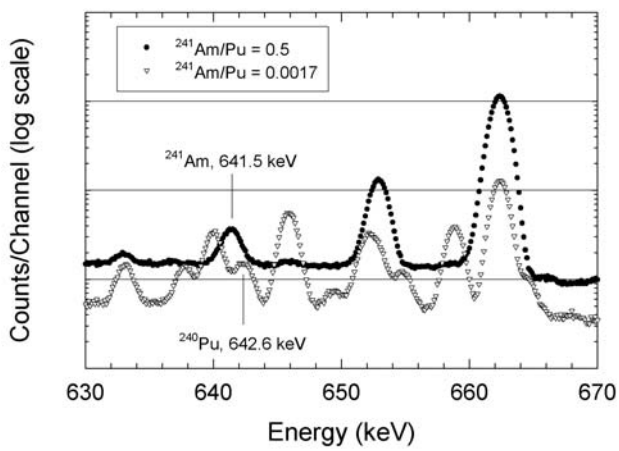

Fig. IX-7. The ^{240}Pu peak in the 600-keV region is hidden for samples with very high ^{241}Am. The FRAM analysis (200–800 keV) of the spectrum (^{241}Am/Pu = 0.5) produces a result for ^{240}Pu with a RSD of 30%. The analysis can still be used to interpret a calorimetry measurement because over 95% of the power arises from ^{241}Am. The RSD(%) for P_{eff} is < 1% for the same analysis.

G. Measuring Heat-Source Grade ^{238}Pu

FRAM has analyzed gamma-ray spectra from numerous samples of heat-source grade ^{238}Pu. The first waste shipments to WIPP from Los Alamos contained such items and all were successfully analyzed by FRAM. Such plutonium typically contains about 80% ^{238}Pu, and 2-4% ^{240}Pu with the remainder being mostly ^{239}Pu. Plutonium-241 and ^{241}Am are also present and can be analyzed. The ^{236}Pu that is originally present in parts per million (ppm) produces strong gamma-ray peaks from its thorium daughter products. We use these peaks to help define the relative efficiency curve.

We analyze the energy range from 140 keV to 860 keV from a coaxial detector operating in 8192 channels at the standard gain of 0.125 keV/chan. The analysis includes the well-known ^{238}Pu peaks at 152.7 and 766.4 keV and weaker peaks at 201.0, 742.8, and 786.3 keV. The analysis for ^{239}Pu and ^{241}Pu is straightforward using the major high-energy peaks. The usually strong 129.3-keV ^{239}Pu peak is not visible and the 203.5-keV peak is also not useful. Plutonium-240 is the most difficult isotope to analyze, as its peaks at 160.3 and 642.5 keV are undetectable. This results in very large RSD(%) values for ^{240}Pu.

X. FRAM APPLICATION WITH CADMIUM TELLURIDE (CDTE) DETECTORS

The application of an unmodified version 4 of FRAM to data taken with a 10-mm x 10-mm x 1.5-mm, Peltier-cooled, CdTe detector is another demonstration of the extreme versatility of

FRAM (Vo 02). This is the first successful application of a general-purpose isotopic analysis code to a non-cryogenic semiconductor detector. Several characteristics of CdTe spectra provide an extreme challenge for FRAM. The energy calibration is nonlinear in contrast to the highly linear calibration from HPGe. This is easily handled by the piecewise, linear calibration in FRAM. The very large tails on the photopeaks (Vo 02) are the greatest limitation to using the unmodified version 4 of FRAM.

Spectra from NaI, CdZnTe, and HPGe are overlaid with a CdTe spectrum for two different isotopic compositions in Figures X-1, -2. Note the region around 203–208 keV. The gamma-ray peaks at 203.5 keV and 208.0 keV are completely resolved for both samples. The peaks are partially resolved by CdTe for the 94% ^{239}Pu sample but the 203.5-keV peak is completely hidden by the tail of the 208-keV peak from the 64% ^{239}Pu sample. This difficult analysis situation contributes to the larger errors seen in the CdTe analysis when compared to the HPGe analysis. Nevertheless, FRAM successfully analyzes the complete isotopic distribution for samples with ^{240}Pu ranging from 3% to 26%.

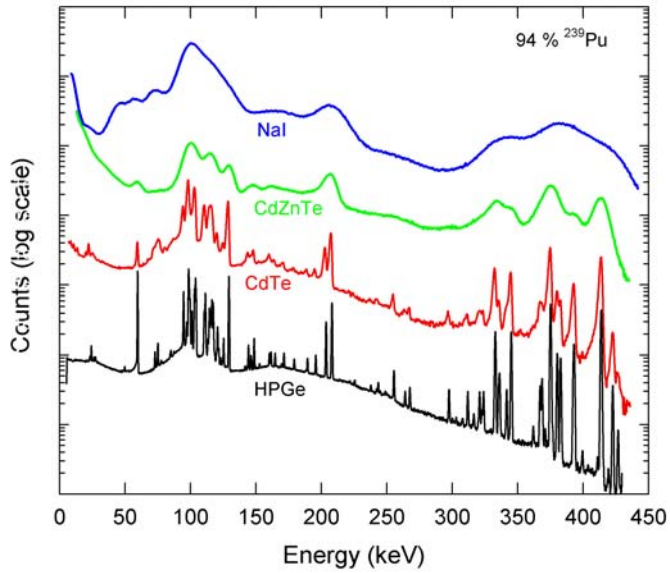

Fig. X-1. Comparison of the gamma-ray spectra from a sample containing 94% ^{239}Pu and 6% ^{240}Pu for four different detectors. Version 4 of FRAM can obtain the complete isotopic distribution from HPGe and CdTe.

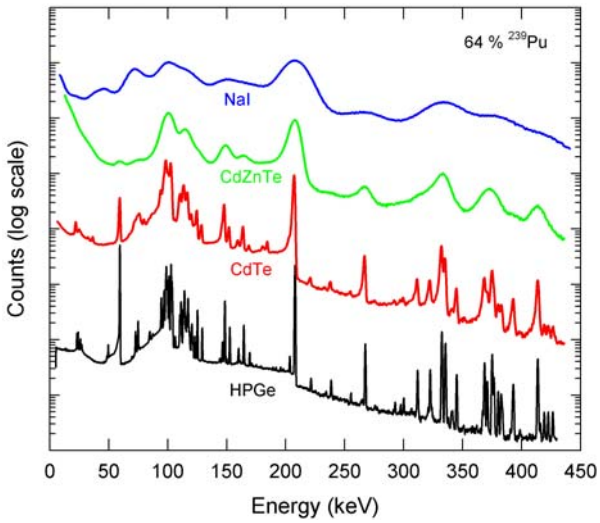

Fig. X-2. Comparison of gamma-ray spectra from a sample containing 64% ^{239}Pu and 26% ^{240}Pu for four different detectors. Version 4 of FRAM can obtain the complete isotopic distribution from HPGe and CdTe.

Table X-1 displays the average bias for measurements using CdTe on standards with ^{240}Pu in the range 3.56 - 26.39 %. The larger bias for CdTe measurements compared to HPGe arises from two sources. First, the counting statistics are poorer because of the small size of the crystal;

over a factor of 500 times smaller in volume than a 25%-relative-efficiency coaxial HPGe detector. The second source is the imperfect fit of the HPGe peak-shape model to the severely tailed CdTe peaks. There is room for significant improvement in the CdTe results by including peak-shape models that are more applicable to CdTe and applying this new analysis to the 100-keV region. Note that FRAM was successfully applied to CdTe spectra, not CdZnTe. While CdZnTe is in more common use, its resolution is too poor to allow analysis of its spectra by an unmodified version of FRAM (see Figures X-1, -2).

Table X-1. Percent Bias in FRAM Analysis of CdTe Spectra from Reference Standards

Sample	^{240}Pu mass %	Percent Bias = 100 * (Measured – Accepted)/Accepted					
		^{238}Pu	^{239}Pu	^{240}Pu	^{241}Pu	^{241}Am	P_{eff}
STDISO	3.56	-30.23	-0.33	8.98	-1.00	-3.06	0.19
PIDIE6_	5.99	-76.71	-0.06	0.97	3.00	-9.33	-2.77
STDISO	6.13	6.32	-0.67	10.24	-1.04	9.25	2.18
CBNM9	6.31	8.69	-0.45	6.67	0.68	-24.23	-1.25
STDISO	6.90	-0.53	1.41	-18.93	-2.74	-0.83	-2.65
STDISO	11.85	-6.31	0.81	-5.79	-3.13	3.25	-0.91
PIDIE6_	14.20	-17.7	-0.37	2.31	-1.32	2.26	0.03
CBNM8	14.27	-10.67	-0.14	1.06	-5.40	-4.95	-1.86
STDISO	15.52	-6.56	0.33	-1.61	-1.08	2.12	-1.07
CBNM7	18.81	-6.99	-3.75	16.38	-6.98	-6.21	-3.65
PIDIE6_	21.41	-15.82	1.99	-6.80	-4.43	-6.59	-5.68
CBNM6	26.29	-4.08	-0.37	1.50	-3.19	-3.66	-2.92
PIDIE6_	26.39	-4.44	1.16	-2.39	-1.64	-0.32	-2.01
	Avg Bias	-12.69	-0.03	0.97	-2.17	-3.25	-1.72
	Std Dev	21.73	1.39	8.86	2.59	8.02	1.96

XI. FRAM APPLICATIONS IN AUTOMATED SYSTEMS

A. ROBOCAL

FRAM is now applied in robotic systems designed to operate continuously and unattended, 24 hours/day. This places an additional burden on FRAM because may not know anything about the type of material being measured. ROBOCAL is robotic system for remote calorimetric and gamma-ray isotopic analysis of special nuclear materials operating at the Los Alamos Plutonium Facility (Hurd 89). ROBOCAL, operating since 1990, has recently been upgraded with new robotics, new computers and software, and a FRAM isotopic analysis system called the Intelligent Isotopic Unit (IIU).

1. Intelligent Isotopic Unit Autoanalysis

The IIU is designed to assay normal samples and pyrochemical residues in shielded or unshielded containers, all without operator intervention. Normally, when a range of sample types is presented to FRAM in a manual mode, the operator must choose an appropriate parameter set for each sample. The sample knowledge may be imperfect and the analysis may have to be repeated if the initial choice was bad.

In FRAM for the IIU, we have incorporated additional logic and diagnostic tests, based on the spectrum under analysis, to choose the best parameter set. The automated logic or intelligence in the modified FRAM for the IIU, automatically chooses from six different parameter sets that accommodate all combinations of unshielded, shielded, homogeneous, or heterogeneous Am/Pu, and very high ^{241}Am. The IIU acquires data using a 25-30%-efficient coaxial HPGe. The spectrum is first analyzed in the 120–450 keV region assuming it is unshielded. The data is reanalyzed, if necessary, with other parameter sets based on the results of three diagnostic tests.

- Test for Shielded Sample
  This test forms the ratio of the relative efficiency of a high-energy peak to one at low energy. The ratio is tested against an empirical limit. If it is less than the limit, the sample is not shielded, if it is greater than the limit, the sample is shielded. The test is based on the fact that absorbers attenuate low-energy peaks (decreased relative efficiency) more than high-energy ones.
- Test for Am/Pu Heterogeneity
  This test forms the ratio of Am/Pu from a low-energy peak to the ratio from a high-energy peak. If Am and Pu are homogeneous, this ratio should be unity. If Am and Pu are heterogeneous, the ratio will not be unity because of the different attenuation suffered by Am and Pu gamma rays at the same energy. The test also accounts for the uncertainties in the Am/Pu ratios. If Am/Pu heterogeneity is detected, the spectrum is reanalyzed with an Am relative-efficiency curve.
- Test for High Americium
  This test compares the measured Am/Pu fraction against a user-defined limit. A different parameter file is used for high americium because of the additional peaks that are not visible at lower concentrations. A typical user-defined limit for high Am is Am/Pu greater than 0.1.

2. Intelligent Isotopic Unit Hardware

The IIU hardware provides sample rotation and vertical translation. In addition, the detector platform varies the sample-to-detector distance to optimize count rate. The rotation and translation even out the response from heterogeneous samples. Figure XI-1 shows ROBOCAL with a sample about to be placed on the sample table.

Fig. XI-1. The ROBOCAL robot is about to place a container on the sample table of the IIU at the Los Alamos Plutonium Facility

B. ARIES NDA System

ARIES (Advanced Retirement and Integrated Extraction System) is a series of processes designed to extract plutonium metal from retired weapons components, convert it to oxide, and

package it for long-term storage, disposition, or feed for MOX fuel fabrication. The ARIES NDA system consists of three instruments and a robot, under computer control, that nondestructively quantify the plutonium mass in the product oxide containers produced by the ARIES processes. The instruments are a heat-flow calorimeter, an active-passive neutron multiplicity counter, and a FRAM isotopic analysis system. The FRAM system in ARIES uses a 25-mm dia. x 16-mm thick planar HPGe detector and collects and analyzes data in the 120–420 keV region.

The isotopic analysis system is similar in concept and execution to ROBOCAL. One major departure is that the ARIES NDA system was designed for glove-box operations. While this is no longer applicable, the original requirement is responsible for the size and configuration of the NDA system pictured in Fig. XI-2. A close-up of the FRAM detector is seen in Fig. XI-3.

Los Alamos is continuing to refine this system and plans to test other measurement regimes using different detectors and energy regions. The data in section VI indicate that other detector-energy region combinations may offer improved precision over the results in Table XI-1.

Fig. XI-2. The ARIES NDA system installed at the Los Alamos Plutonium Facility.

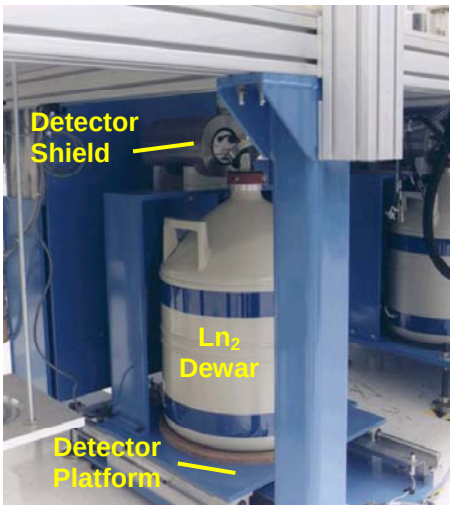

Fig. XI-3. A closeup of the FRAM isotopic analysis station.

REFERENCES

ANSI 1987 "Plutonium-Bearing Solids – Calibration Techniques for Calorimetric Assay," ANSI N15.22-1987 (American National Standards Institute, Inc., New York, 1987.

Bignan 95 G. Bignan, H. Recroix, B. Mitterrand, W. Ruhter, "Recommendations for the 242Pu Content Evaluation Using a New Algorithm," Proceedings of the Fifth International Conference, Facility Operations -- Safeguards Interface, Jackson Hole, Wyoming, September 24-29, 1995, p. 225.

Ensslin 91a N. Ensslin, Chapter 11, "The Origin of Neutron Radiation," in Passive Nondestructive Assay of Nuclear Materials, edited by Doug Reilly, Norbert Ensslin, and Hastings Smith, Jr., US Nuclear Regulatory Commission NUREG/CR-5550, March 1991.

Ensslin 98 N. Ensslin, W. C. Harker, M. S. Krick, D. G. Langner, M. M. Pickrell, J. E. Stewart, "Application Guide to Neutron Multiplicity Counting," Los Alamos National Laboratory manual LA-13422-M, November 1998.

Firestone 96 Richard B. Firestone, "Table of Isotopes, Eighth Edition," John Wiley & Sons, New York, 1996.

Fleissner 81a J. G. Fleissner, "GRPAUT: A Program for Pu Isotopic Analysis (A User's Guide)," Mound Facility report MLM-2799/ISPO-128, (1981).

Gunnink 76a R. Gunnink, J. E. Evans, and A. L. Prindle, A Reevaluation of the Gamma-Ray Energies and Absolute Branching Intensities of ^{237}U, $^{238, 239, 240, 241}$Pu, and ^{241}Am, Lawrence Livermore Laboratory report UCRL-52139, October 1976.

Gunnink 90 R. Gunnink, "MGA: A Gamma-Ray Spectrum Analysis Code for Determining Plutonium Isotopic Abundances, Volume I, Methods and Algorithms," Lawrence Livermore National Laboratory report UCRL-LR-103220, Vol. I/ISPO No. 317, Task No. A.161, (April 1990).

Hurd 89 J. R. Hurd, C. A. Bonner, C. A. Ostenak, P. F. Phelan, W. D. Powell, N. L. Scheer, D. N. Schneider, H. C. Staley, "ROBOCAL: An Automated NDA Calorimetry and Gamma Isotopic System," Los Alamos National Laboratory unlimited release LA-UR-89-3837, (1989).

Hypes 00 Philip A. Hypes, "Plutonium Source Isotopic Analysis With Up To 25 mm Pb Shielding Using the FRAM Isotopic Analysis Code," Los Alamos National Laboratory unlimited release LA-UR-00-2511 (June 2000). Proceedings of the Institute of Nuclear Material Management, 41st Annual Meeting, New Orleans, Louisiana, July 16-20, 2000.

Kelley 02 Thomas A. Kelley, Thomas E. Sampson, "Software User Manual, PC/FRAM, Version4," Los Alamos National Laboratory Unlimited Release LA-UR-02-5268.

Knoll 00 Glenn F. Knoll, "Radiation Detection and Measurement," John Wiley & Sons, New York, 2000.

Likes 91a R. Likes, Chapter 21/22, "Principles of Calorimetric Assay," in Passive Nondestructive Assay of Nuclear Materials, edited by Doug Reilly, Norbert Ensslin, and Hastings Smith, Jr., US Nuclear Regulatory Commission NUREG/CR-5550, March 1991.

Menlove 91 H. O. Menlove, Chapter 17, "Neutron Coincidence Instruments and Applications," in Passive Nondestructive Assay of Nuclear Materials, edited by Doug Reilly, Norbert Ensslin, and Hastings Smith, Jr., US Nuclear Regulatory Commission NUREG/CR-5550, March 1991.

Morel 91 J. Morel, C. Chauvenet and ESARDA Working Group on Techniques and Standards for Non-Destructive Analysis, "Intercomparison of Plutonium Isotopic Composition Measurements by X- and Gamma-Ray Spectrometry, Results from the PIDIE Exercise," DAMRI Technical Note L.P.R.I. 91/278 – MARS (1991).

Morel 00 J. Morel, C. Hill, M. Bickel, A. Alonso-Munoz, S. Napier, B. Thaurel, ESARDA NDA – WG Members, "Results From the International Evaluation Exercise for Uranium Enrichment Measurements," *Appl. Radiat. Isot.* 52 (2000), 509-522.

Parker 74 J. L. Parker and T. D. Reilly, "Plutonium Isotopic Determination by Gamma-Ray Spectroscopy," in *Nuclear Analysis Research and Development Program Status Report, January-April 1974*, G. Robert Keepin, Ed., Los Alamos Scientific Laboratory report LA-5675-PR (August 1974).

Parker 91a Jack L. Parker, Chapter 5, "General Topics in Passive Gamma-Ray Assay," in Passive Nondestructive Assay of Nuclear Materials, edited by Doug Reilly, Norbert Ensslin, and Hastings Smith, Jr., US Nuclear Regulatory Commission NUREG/CR-5550, March 1991.

Reilly 91 Passive Nondestructive Assay of Nuclear Materials, edited by Doug Reilly, Norbert Ensslin, and Hastings Smith, Jr., US Nuclear Regulatory Commission NUREG/CR-5550, March 1991, Chapters 11-17.

Sampson 86 Thomas E. Sampson, "Plutonium Isotopic Composition by Gamma-Ray Spectroscopy: A Review," Los Alamos National Laboratory report LA-10750-MS (September 1986).

Sampson 89 Thomas E. Sampson, George W. Nelson, Thomas A. Kelley, "FRAM: A Versatile Code for Analyzing the Isotopic Composition of Plutonium from Gamma-Ray Pulse Height Spectra," Los Alamos National Laboratory report LA-11720-MS (December 1989).

Sampson 91 T. E. Sampson, Chapter 8, "Plutonium Isotopic Composition by Gamma-Ray Spectroscopy," in Passive Nondestructive Assay of Nuclear Materials, edited by Doug Reilly, Norbert Ensslin, and Hastings Smith, Jr., US Nuclear Regulatory Commission NUREG/CR-5550, March 1991.

Sampson 98 Thomas E. Sampson, Teresa L. Cremers, and Walter J. Hansen, "Nondestructive Assay System for the ARIES Weapons Component Dismantlement System," American Nuclear Society Third Topical Meeting on DOE Spent Fuel and Fissile Materials Management, Charleston, SC, September 1998.

Sampson 01 Thomas E. Sampson, Philip A. Hypes, and Duc T. Vo, "FRAM Isotopic Analysis of Uranium in Thick-Walled Containers Using High Energy Gamma Rays and Planar HPGe Detectors," Los Alamos National Laboratory report LA-13832 (ISPO-463), (September 2001).

Sampson 03 Thomas E. Sampson, Thomas A. Kelley, Duc T. Vo, "Application Guide to Gamma Ray Isotopic Analysis Using the FRAM Software," Los Alamos National Laboratory report LA-14018 (xxxxx 2003)

Vo 01a D. T. Vo and T. K. Li, "Plutonium Isotopic Analysis in the 30 keV to 210 keV Range," presented at the 23rd Annual Meeting, Symposium on Safeguards and

Nuclear Material Management, Bruges, Belgium, May 8-10, 2001, Los Alamos National Laboratory Unlimited Release, LA-UR-01-2264.

Vo 02 D. T. Vo, P. A. Russo, "PC/FRAM Plutonium Isotopic Analysis of CdTe Gamma-Ray Spectra," Nucl. Instr. Meth. A 486 (2002) 813-824.

3. MEASUREMENT OF PLUTONIUM AND URANIUM ISOTOPICS WITH MGA/MGAU

Not available

4. TOMOGRAPHIC GAMMA-RAY SCANNING OF URANIUM AND PLUTONIUM

J. Steven Hansen

INTRODUCTION

Development of the Tomographic Gamma-ray Scanning (TGS) technology began in the early 1990's (Refs. 1-3) in response to an increasing demand to assay a class of materials that were difficult or impossible to assay quickly and accurately with existing NDA techniques. The problem materials exhibited arbitrary distributions of nuclear material in a matrix of extreme heterogeneity in both density and composition. Techniques which volume averaged over these heterogeneities often led to large errors and, given the difficulty of preparing representative standards, error estimates for any arbitrary samples were not reliable.

What was needed was a technique capable of viewing the sample as a composite of small volumes combined with a means of estimating the mass of the target isotopes within each small volume. Combining the principles of tomography with the power of high resolution gamma-ray spectroscopy, the TGS technique was conceptualized and within a decade the TGS technique developed into one of the most robust, versatile NDA methods used in safeguards and nuclear waste measurements across the DOE complex.

The next section describes the underlying principles of TGS at a fundamental level leaving a more detailed discussion to the TGS application guide (Ref. 4). Nevertheless, we do present here a set of idealized image reconstruction problems to provide the reader with a good conceptual feel for the general mathematical approach underlying tomographic image reconstruction. A description of the hardware modules making up a typical TGS instrument then is provided. Where appropriate we try to provide helpful design criteria and guidance for systems to be used in production applications. To assist the reader in assessing the applicability of TGS to a particular class of materials, a section on its performance then follows. The Performance Demonstration Program (PDP), sponsored by the Waste Isolation Pilot Plant (WIPP) in Carlsbad, NM, is a series of blind tests with standard waste drums designed to simulate typical materials destined to be shipped to WIPP for burial. All of the accepted NDA techniques for measurements of such materials were represented in the tests and the results provide an excellent starting point for the reader responsible for selecting the correct instruments for a particular task. Two real-life examples are given that illustrate the cost-benefit of TGS for certain classes of materials for which other NDA techniques are not well suited. The first example involves plutonium laden electro-refining salt residues at the Rocky Flats Environmental Technology Site (RFETS) in Golden, CO, and the second describes its application to a large inventory of 208-ℓ (55-gal.) drums containing uranium contaminated materials. These examples illustrate that the high throughput and low bias of the TGS technique demonstrated in the PDP can carry over to the production environment when appropriate controls are applied and systems are properly designed. The principal limitation of the TGS for the assay of uranium and plutonium arises from the propensity for high-Z materials to strongly attenuate their own gamma-rays. The extreme example of this problem is the self-attenuation of gamma rays in lumps of uranium (Z=92) and plutonium (Z=94). In materials that may contain these elements in non-microscopic sizes, a method for recognizing these conditions must exist and appropriate corrections must be applied to eliminate biases. A section is devoted to the subject of lump corrections, because of importance for the broader class of materials that are found in nuclear facilities. The TGS

technology is now quite mature and available commercially and the final section describes some designs available from commercial vendors.

MEASUREMENTS PRINCIPLES

A. General Concepts

In 1895, at the young age of 50, William Conrad Roentgen (1845-1923), working with a cathode ray tube (CRT), discovered quite by accident that some fluorescent crystals across the room gave off a green glow when the machine was on, even when the CRT was shrouded with a black cloth impenetrable by light. Such was the discovery of ionizing radiation that Roentgen named x rays. Roentgen quickly followed his discovery by becoming the world's first radiologist, exposing films with various objects, including his wife's hand (Figure 1), placed between the CRT and the film. Within a year, battle surgeons were using x rays to locate bullets in wounded soldiers and Henri Becquerel had discovered natural radioactivity. The atomic age was born.

Radiographs such as that of Mrs. Roentgen's hand have been critical tools in the fields of medical and industrial diagnostics. The radiographic technique consists of focusing a broad parallel beam of penetrating radiation upon a sample of interest and recording the effects of the unabsorbed portion of the beam upon the radiographic film. The picture or image provided by the film is really just a representation of the opacity of the sample, which varies dependant

Fig. 1 *Radiograph of Mrs. Roentgen's hand.*

upon its density, thickness, and atomic number (Z). In the case of a biological sample such as Mrs. Roentgen's hand, the calcium in the bones is of higher atomic number (Z=22) and density

than the surrounding flesh and preferentially attenuates the beam and correspondingly underexposes the film relative to the surrounding areas where bone is not present. Opacity differences as small as a few percent can be discerned under ideal conditions and high-quality images can be obtained which are an invaluable diagnostic for the medical and the industrial community. X radiography works perfectly well to image materials that do not completely attenuate the beam, that have differences in attenuation (opacity) due to internal structure that the radiographer wishes to study, and that can be oriented perpendicular to the x-ray beam. Consider the problem of producing the radiograph of Mrs. Roentgen's hand when the hand is rotated by 90° relative to the x-ray beam, i.e. thumb toward CRT and little finger toward film. The bones of the fingers would all then coalesce in the image plane and such a radiograph would be virtually useless for producing detailed images of each finger. This is the very problem that tomography was designed to solve: how to render an image of an object in three dimensions so that any arbitrary plane of interest can be displayed when the source and detector or film can not be placed at right angles to the plane of interest. The technique of tomography requires extensive manipulations of large data sets and, therefore, awaited the development of computers. As a benchmark, during the period circa 2000, some analyses could take many minutes to be completed with the speed and data handling capabilities of that time.

Consider Figure 2 which compares the radiographic method with the tomographic method using a pair of concentric metal washers as the sample. The plane of interest, xy, is parallel to the surface of the page and taking a radiograph of the washers with the orientation of beam, sample and film as depicted would be expected to produce a good image of the washers as depicted in the figure. Using tomography, one can reproduce a similar image as depicted in the figure immediately below. The method illustrated here chooses three angles of incidence relative to the two washers (horizontal, vertical and diagonal) and then moves the object (or source and detector) in small steps from one side of the large washer to the other side. In our example, for each of the three angles approximately a dozen measurements or data grabs are made in scanning from one side to the next. At each measurement point, the count rate from the radiation source is recorded by the radiation detector and varies with the inverse of the opacity of the sample along that line of incidence. The resulting count rate is often referred to as a projection or ray-sum.

Figure 3 gives a simple example defining a projection or ray-sum. In this example the sample has been divided up into 10 rows and 11 columns and the 5th row is currently being interrogated with the radiation source and the count rate is inversely proportional to the opacity as defined in the equation at the bottom of the figure. It is clear that the total opacity is simply the sum of the opacities of the different cells making up the 5th row and that the individual opacities are a product of the linear attenuation coefficient and the thickness (ΔX) of the cell.

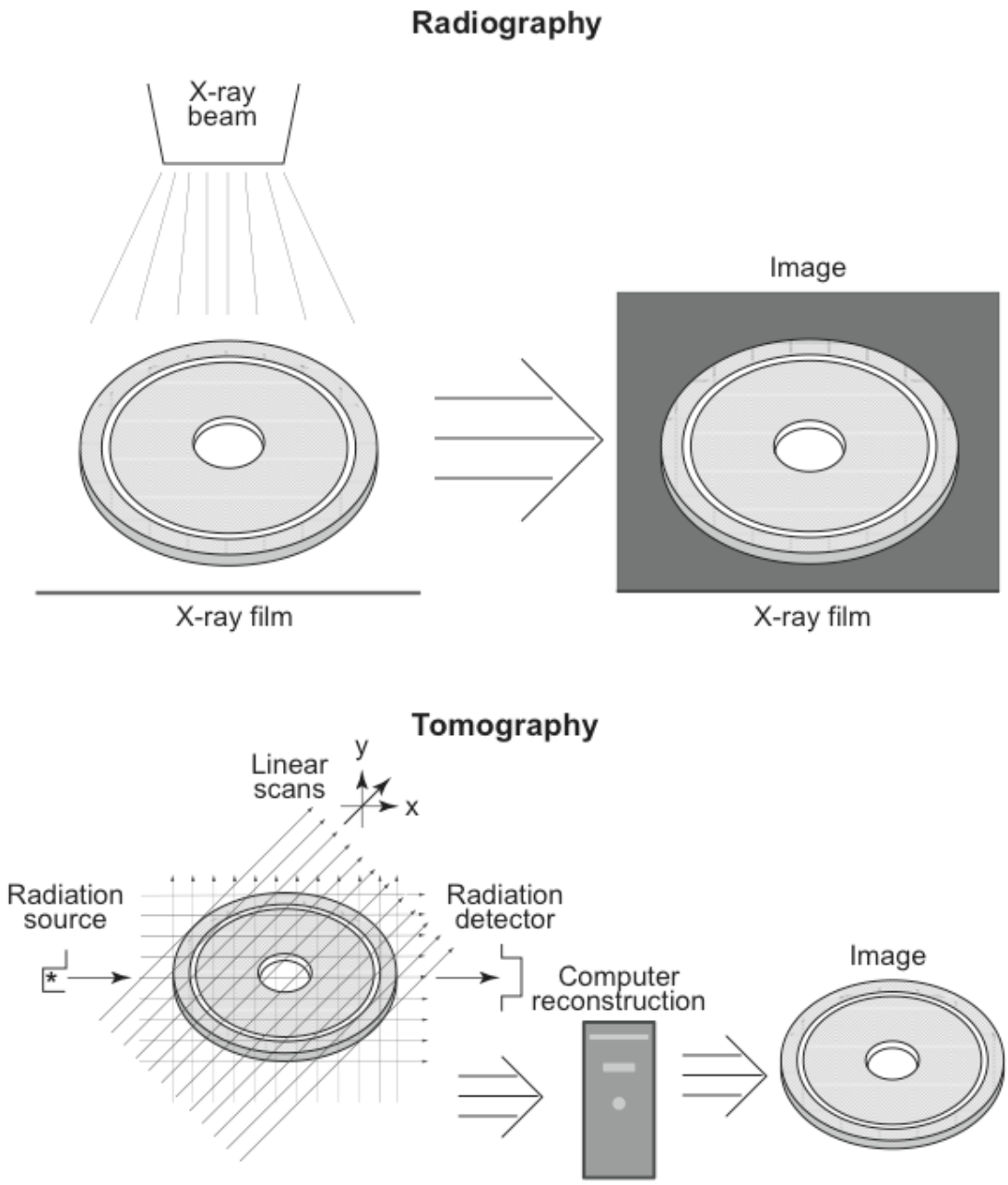

Fig. 2 *Radiography and tomography.*

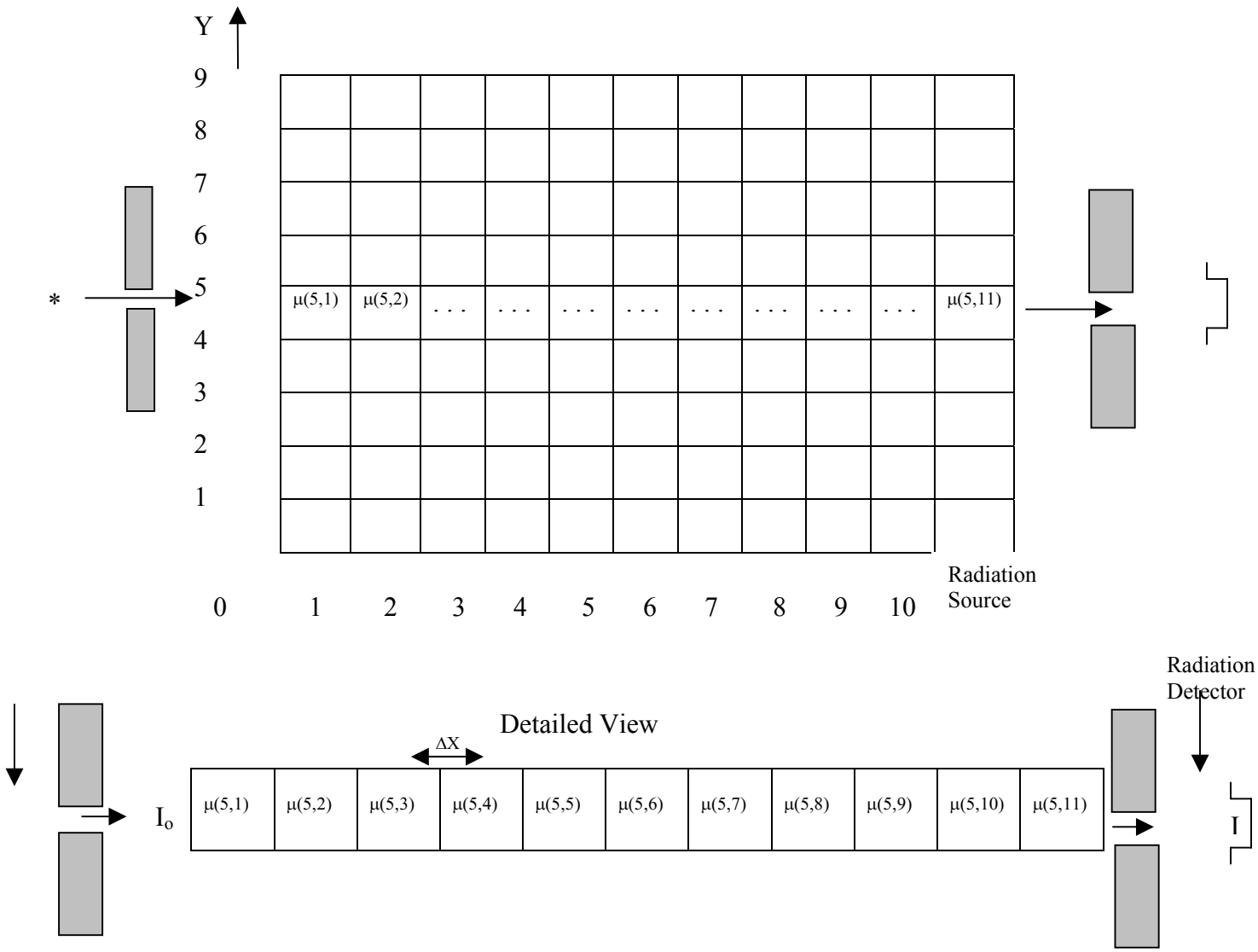

$$I = I_O\, e - \left[\mu(5,1)\Delta X_1 + \mu(5,2)\Delta X_1 \;\ldots\ldots\ldots\ldots\ldots\ldots \mu(5,11)\Delta X_{11}\right]$$
$$= I_o\, e - \left[\mu(5,1) + \mu(5,2) \ldots\ldots\ldots\ldots\ldots\ldots \mu(5,11)\right]\Delta X$$

when $\Delta X_1 = \Delta X_2 = \ldots\ldots\ldots\ldots\ldots\ldots \Delta X_n = \Delta X$

and the expression below represents the opacity of the 5th row.

$$\left[\mu(5,1) + \mu(5,2) \ldots\ldots\ldots\ldots\ldots\ldots \mu(5,11)\right]\Delta X$$

Fig. 3 *Projections or ray-sums are opacity measurements.*

B. Understanding Tomographic Image Reconstruction

Although the detailed algorithms associated with the tomographic image reconstruction from raysums can be complex, the underlying concepts can nevertheless be understood through the study of a set of simple idealized tomographic reconstructions. To this end, we use a very straightforward iterative technique to solve for the opacities of rectangular cells that geometrically define our objects and begin with the 1x1 matrix to demonstrate the rules for this technique. We then successfully apply the same rules to more complex matrices (2x2 and 3x3) and, using mathematical inference, we assume the technique will work for any matrix of arbitrary dimension.

We begin at the top of Figure 4a with the simplest case of tomography, the 1x1 matrix and the "unknown" opacity of this cell has a value of 5. As in Figure 2, we will restrict our data to horizontal, vertical and diagonal projections, whereas in real tomography other projection angles might be used to provide a larger data set. Obviously the horizontal, vertical and diagonal projections will each give a total opacity of 5. Having acquired this data we will blindly follow the rules for image reconstruction given below and compare our estimates with the actual opacity (5) of the cell. This technique we use is a common one called the Algebraic Reconstruction Technique (Ref. 5).

Rules for the Algebraic Reconstruction Technique (ART)

1. Sum and record the actual projections (P^0) for all angles.
2. Make an initial guess at the opacity (O^i) for each of the cells.
3. Calculate the projection for one of the angles for all cells using the latest estimate for the opacities. NOTE: The latest estimate in the case of the first estimate is a guess.
4. Compute each new iteration from the results of the last with the following equation where N is the number of cells in the particular projection under analysis.

$$O^{i+1} = O^i - [P^0 + (P^i - P^0)/N]$$

5. Compare final estimates of the cell opacities once all projections have been applied.

Referring to the 1x1 opacity matrix in Figure 4, our analysis begins with a guess for the initial opacity (O^i) of zero. Even with this poor guess this simple problem immediately converges to the correct result in the first iteration. This of course holds true regardless of the angle of incidence of the projection (horizontal, vertical or diagonal). In Figure 4b, within each cell, the ith opacity is given immediately above the calculated i+1 opacity with a dashed line separating the two values. In general, we have calculated estimates for the cells in the first column of each matrix. The reader may wish to verify our calculations for the remaining cells.

1 x 1 Opacity Matrix Reconstruction Example

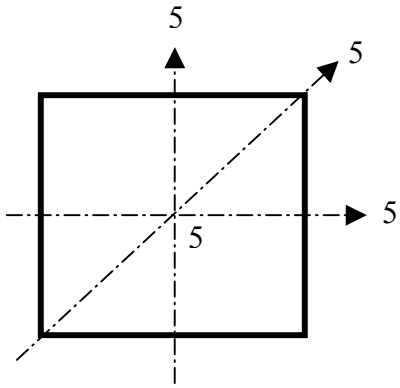

0	Guess
5	Estimate = E

For All Projections

$$E = 0 + \frac{[5-0]}{1} = 5$$

Fig. 4a

---

2 x 2 Opacity Matrix Reconstruction Example

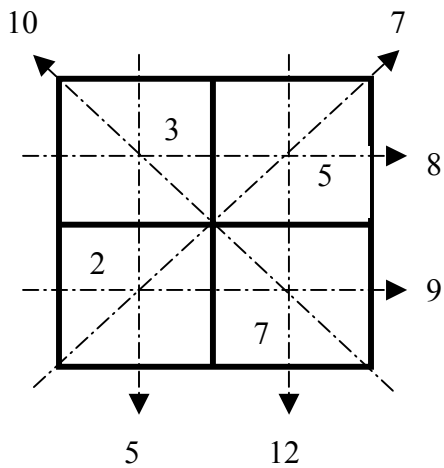

Fig. 4b

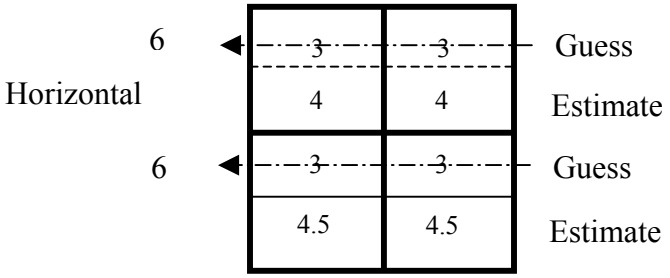

$$E = 3 + \frac{[8-6]}{2} = 4$$

$$E = 3 + \frac{[9-6]}{2} = 4.5$$

First Column Estimates

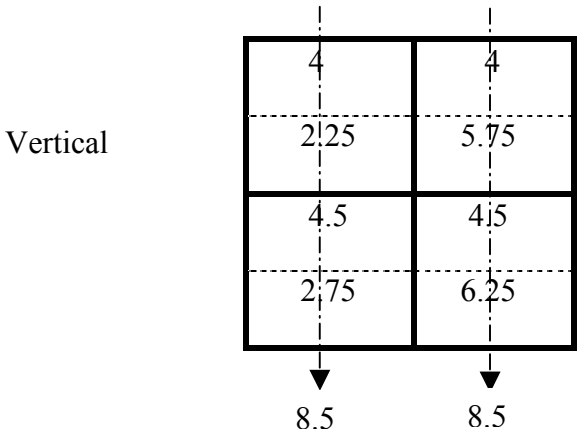

$$E = 2.25 + \frac{[10-8.5]}{2} = 3.0$$

$$E = 4.5 + \frac{[5-8.5]}{2} = 2.75$$

First Column Estimates

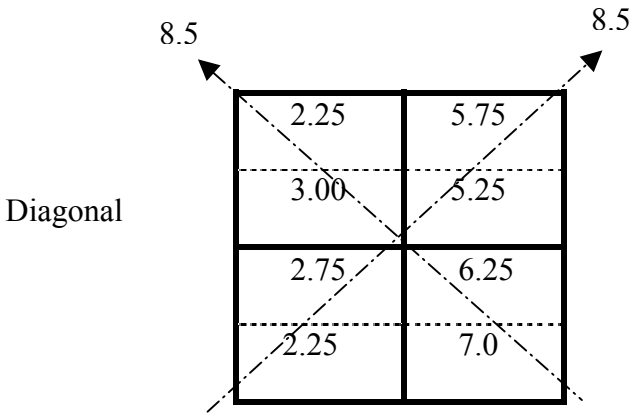

$$E = 2.25 + \frac{[10-8.5]}{2} = 3.0$$

$$E = 2.75 + \frac{[7-8.5]}{2} = 2.0$$

Actual	3	5
Estimate	3.0	5.0
Actual	2	7
Estimate	2.0	7.0

Comparison of Final Estimates with Actual Opacity.

Fig. 4b *continued.*

3 x 3 Opacity Matrix Reconstruction Example

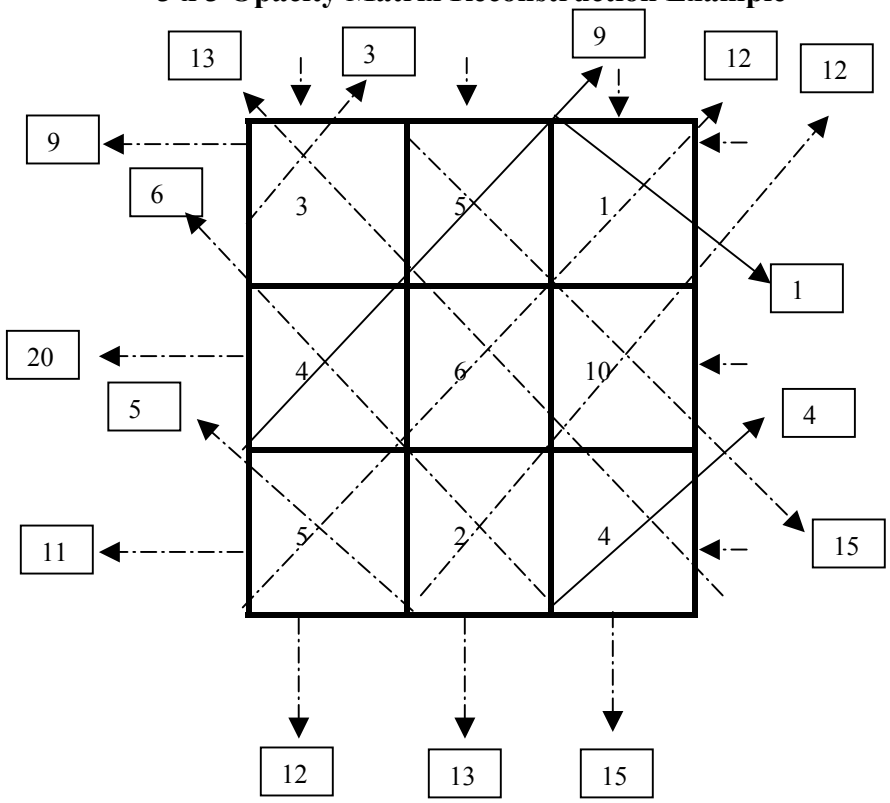

The above are the actual projections or ray-sums.

Preliminary guess and new estimates

First Column Estimate

$$E = 5 + \frac{9-15}{3} = 3$$

$$E = 5 + \frac{20-15}{3} = 6.67$$

$$E = 5 + \frac{11-15}{3} = 3.67$$

Horizontal

Guess	5	5	5
Estimate	3	3	3
Guess	5	5	5
Estimate	6.67	6.67	6.67
Guess	5	5	5
Estimate	3.67	3.67	3.67

Guess	3.0	5.0	1
Estimate	3.04	5.0	1
Guess	4.0	6.0	10.0
Estimate	4.0	6.06	10.0
Guess	5.0	2.0	4.0
Estimate	5.0	2.0	4.04

Final Estimates Compared to Actual Projections

Guess	3		1
Estimate	2.59		3.11
Guess			
Estimate			
Guess	3		4.0
Estimate	2.78		4.26

Results Without Corner Projections

Fig. 4c *The 3 x 3 image reconstruction.*

Having validated our technique for the 1x1 matrix, we now apply it to a 2x2 matrix. Note that after using the four projections for the horizontal and vertical angles of incidence, our estimates for the opacities have improved yet still are rather poor. It is generally the case in tomography that the estimates improve with the number of projections and that exact solutions are rare. Only after applying the diagonal projections to our analysis technique do we find that the technique provides a unique and correct solution, matching exactly the "unknown" opacities. In cases of matrices of larger dimension, even with simple well-defined geometries and cell opacities, unique solutions will generally not exist and final results will depend upon the number of projections and in some cases on the initial guess and the order in which the projections are taken in the analysis. The 3x3 matrix problem illustrates the problems associated with too few projections. We have eliminated the actual calculations for all but the horizontal projections. Beginning with an initial guess of 5 for all cell opacities and proceeding from the horizontal incidence to vertical to left to right diagonal and then right to left diagonal the reader can verify our results at the bottom of Figure 4c. The problem of using too few projections is made clear by comparing the results of the analysis between the two analyses: the first in which we include all of the corner projections and the second where we do not include the corner projections, Figure 4c. The results when the corner projections are not included are very poor and in the case of the upper right corner cell the estimate is in excess of three times the actual opacity.

So in conclusion, we have demonstrated that by using a simple iterative technique, three angles of incidence, and sufficient projections at each of the three angles that very good reconstructions are possible. Thus one might expect for example that by applying our technique to the problem of Figure 2, a reasonable image of the two washers could be produced. This technique was the basis for Computerized Axial Tomography (CAT) scan analysis developed during the 1970's (Refs. 6-9) that led to the Nobel Prize for Medicine in 1979. Such techniques have undergone refinements, but the underlying approach is similar to that applied to our simple problem. In the medical field, such techniques currently provide high accuracy image reproductions at the sub-millimeter level. We have discussed the reproduction of thin slices using tomography. In general, one deals with thick three-dimensional objects and thus one must look at successive slices and combine the results for each of the slices to image a three dimensional object. This will be addressed later in the context of actual TGS measurements.

C. Defining the Geometry

Figure 5 is a schematic of a generic TGS showing the general relationship of the sample, the source, and the high-resolution germanium detector. For a typical one-hour scan of a 208-ℓ drum at each of 10 to 15 axial positions, the drum would rotate at approximately three revolutions per minute while translating in a horizontal direction at approximately 30 cm/min. In Figure 6, the two coordinate systems are shown which are used to uniquely define the motion of the drum. The graph indicates the individual measurement points as a function of the angle of rotation of the drum and the distance the drum has moved from the origin. In a typical ^{239}Pu scan, the drum would start with its outer edge grazed by the collimated beam from the ^{75}Se attenuation-correction source. It would then rotate at 3 rpm while translating to a position where the ^{75}Se beam intersected the radial centerline of the drum. The direction of

translation would then reverse and the drum would return to its initial position. The round trip would take approximately 2 minutes during which time approximately 150 separate data grabs would be acquired. The mathematics relating functions defined within these two coordinate systems was published first by Johann Radon in 1917 (Ref. 10) but went undiscovered through much of the early development of the tomography technique. The idea, nevertheless, is that by means of the Radon transformation a two-dimensional function (such as the opacity as a function of position in the x,y plane) can be inferred from the projections which are defined in terms of an angle of rotation and translation of the object relative to the stationary x,y coordinate system. The drum is then moved vertically approximately 5 cm and the scan is repeated. By stacking sections or slices, one can reproduce a three-dimensional object through superposition. For those who are interested in formulations of a mathematical nature, they are referred to the original article by Radon.

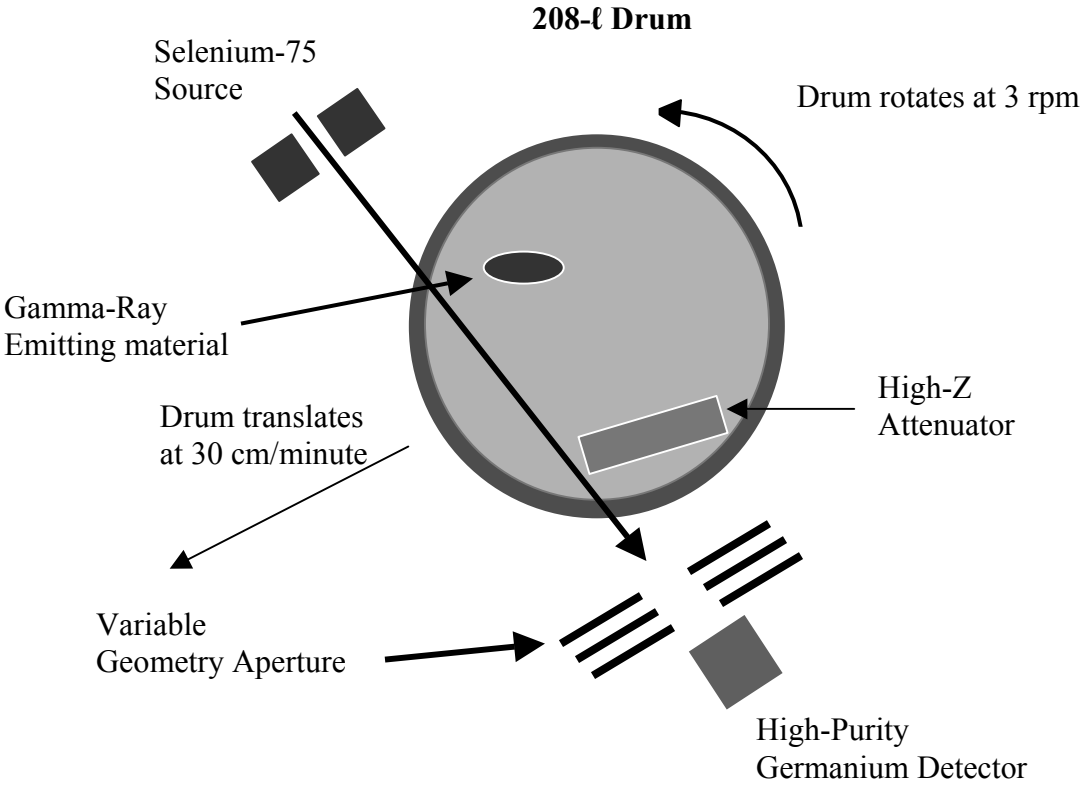

Fig. 5 *The TGS configuration in concept.*

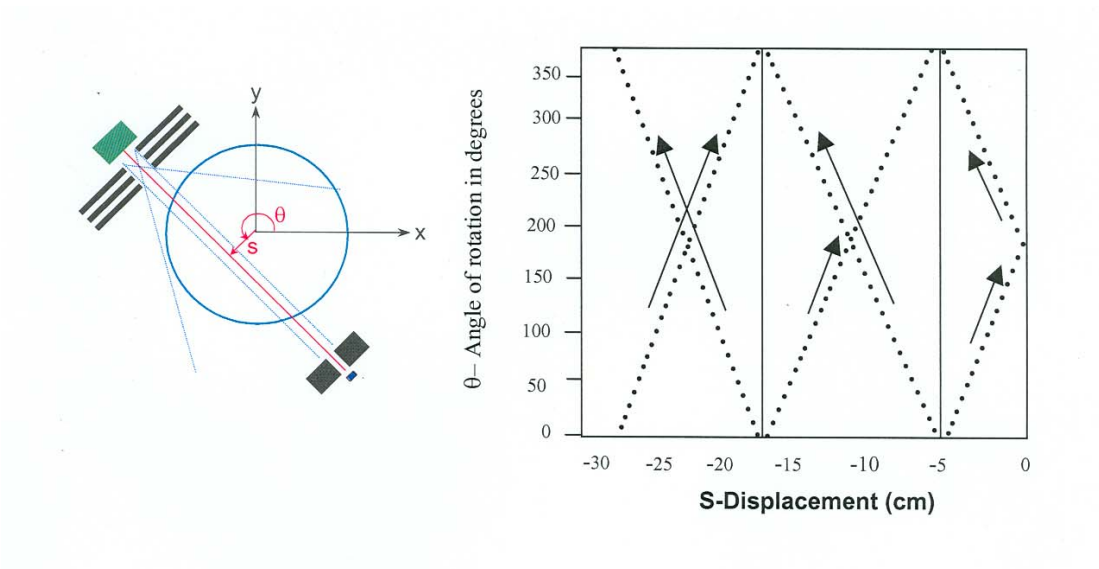

Fig. 6 *The stationary and moving coordinate systems.*

D. Attenuation and Emission Maps

The TGS method counts gamma rays emitted by plutonium or uranium in contiguous small volume elements distributed throughout the sample estimating the mass of SNM from the counting rate of certain characteristic gamma rays. The gamma rays are detected with a high-purity germanium (HPGe) detector and corrections are applied to the count rate for the attenuation by materials intervening between the small volume elements and the detector. The problem of NDA with gamma-ray tomography is one of defining a three-dimensional image of a sample (say a 208-ℓ drum) in terms of a set of three-dimensional "pixels" often termed "voxels" and assigning the appropriate mass of SNM and opacity to each voxel. In effect, the problem is reduced to conducting a gamma-ray assay for each voxel within a 208-ℓ drum. For a 208-ℓ drum divided into approximately 1500 voxels, this corresponds to breaking the problem into an assay of volumes that are roughly 5x5x5 cm^3. By suitable image reconstruction techniques, the result of a tomographic assay is to associate with each of these voxels a mass of SNM and opacity. To estimate the contribution from a particular voxel to the count rate the gamma rays from materials in the voxel are ray-traced to the detector and attenuation corrections are made by summing the opacities of the voxels through which the rays must pass. The image reconstruction of each voxel is involved since the voxels that lie between it and the detector vary as the drum rotates and translates and the germanium detector samples a large volume (many voxels) of the sample, see Figure 6. Nevertheless, by careful geometric definition of the fixed and stationary coordinate systems and the application of efficient reconstruction algorithms, high throughput, low bias, and adequate image reconstruction can be achieved. Having completed the analysis, each voxel is assigned a mass of a specific isotope and an opacity value. Combining the results for each voxel produces a map of the attenuation and another for the emission characteristics of the drum as a function of position (x,y) within the drum. Such maps are shown in Figure 7 for four drums (76 cm high x 61 cm diameter) of varying matrices and ^{235}U mass. The resolution is of the order of a voxel length, 5 cm, and the highest concentration of either matrix material or ^{235}U are indicated by

the color red. The attenuation map is to the left of the emission map for each of the four drums.

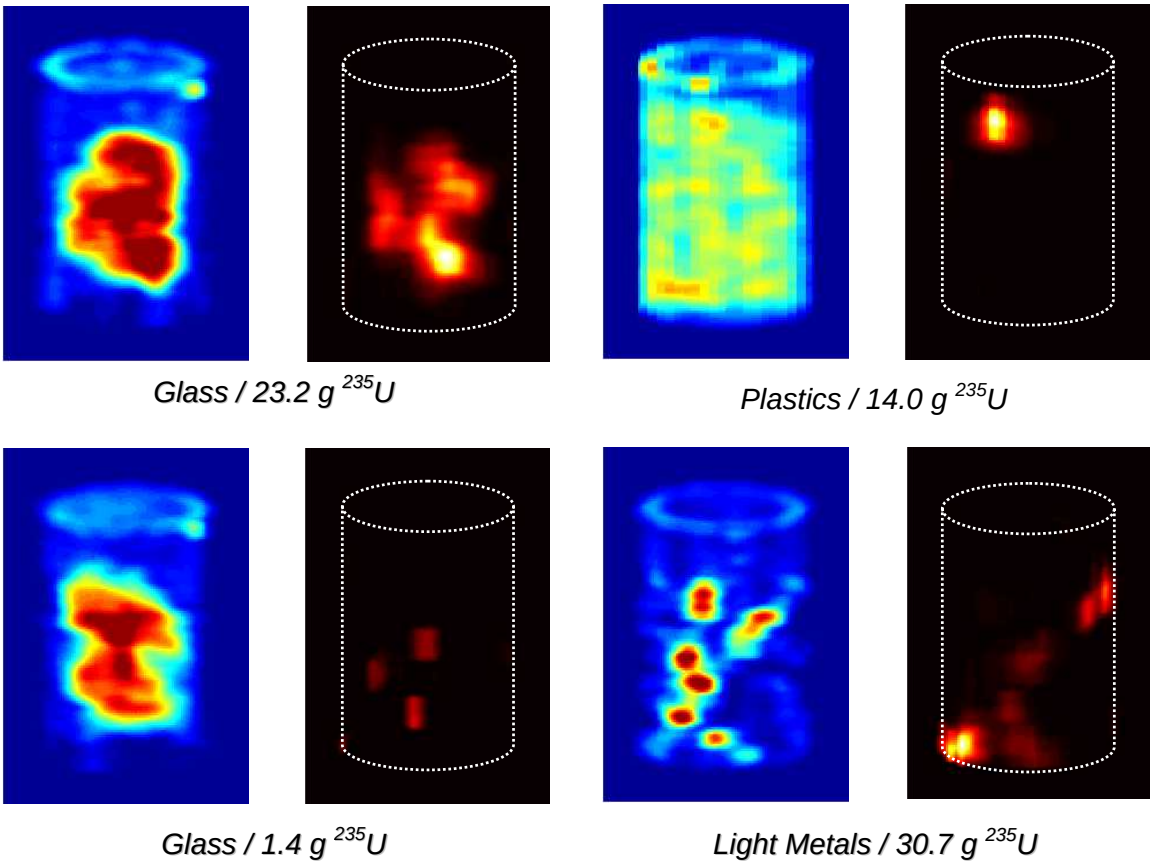

Fig. 7 *Transmission(l) and emission(r) image reconstructions.*

E. Detector Response Function

In medical tomography, high resolution imaging is essential. In the application of tomography to the assay of radiological samples, such as 208-ℓ drums of contaminated waste, throughput is the key issue and high throughput requires large apertures and large germanium detectors. As such, the view and efficiency of such detectors is great and varies for a particular point in space with the inverse of the distance from the detector and to a lesser extent to the degree the point is off the detector axis. It is important to apply these corrections to the detection efficiency and, as a general rule, a detector response curve must be generated for each aperture setting. Figure 8 is the detector response function for an x-axis distance from the detector of 92 cm and a y-axis distance varying from 0 to – 40 cm. At roughly 30 cm, the effects of the tungsten collimator eclipse the source emissions and the count rate falls to zero. Curves such as Figure 8 are normally generated by applying computer models supported by experimental measurements.

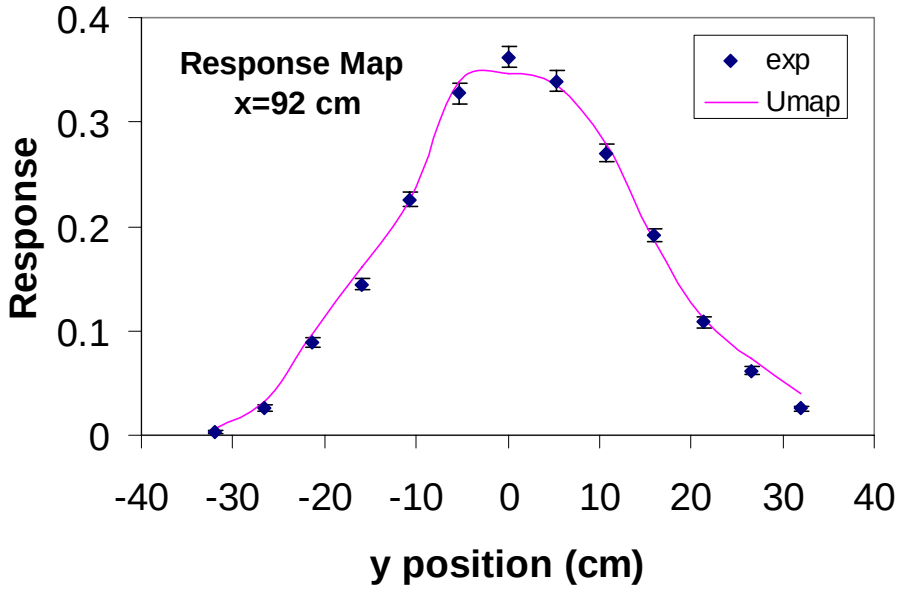

Fig. 8 *Detector response map.*

III. TGS Design Considerations

The design details of TGS systems can vary depending upon the dimensions and weight of the samples to be measured, whether the principal use is in a production environment or in a research laboratory, and to some extent upon the acceptable precision and bias. Versatility, accuracy, and throughput come at a price, but all systems require certain functions or modules to perform. In this section, we will consider the TGS as comprised of these modules and point out some of the design considerations in their selection.

Figure 9 is an engineering drawing for a TGS system fielded from 1998 – 2003 at RFETS (Transportable TGS - TTGS) and the progenitor of the commercial models available through license agreements with Los Alamos National Laboratory. The TTGS was designed for versatility, accuracy, and high throughput in a production environment. In the next section, the results from one of its major assay campaigns is described. It was designed to be very modular and it is well suited for the present discussion. The major modules are the Transmission Source Assembly, the Detector Assembly Module, the Sample Positioning System, the Data Acquisition System, and the Data Analysis Module. Each of these is discussed in turn.

A. Transmission Source assembly

The transmission source is mounted in a tungsten shield on top of a 5.5-m steel tower. A high intensity (30-200 mCi) ^{75}Se source is used to provide high throughput and penetration of dense samples (e.g. cement in 314-ℓ overpacks). Using ^{75}Se for the transmission source, gamma-ray transmission can be measured accurately at several energies (96.7, 121.1, 136.0, 264.6, 279.5, and 400.6 keV) near the important lines of ^{239}Pu and ^{235}U. By interpolating the transmission data, spatial maps of the attenuation coefficient can be accurately obtained at the gamma-ray energies of interest. The only drawback to ^{75}Se is its relatively short half-life (120 days) that

requires sources to be replaced annually. A solenoid-driven tungsten shutter (5-cm thick), when in the open position, provides a tightly collimated beam (0.3-cm diameter) of gamma rays for transmission measurements. For this system, a low-power laser/silicon diode alignment system verifies the alignment of the source and detector. Such enhancements must be considered when systems are to be placed in a rugged production environment.

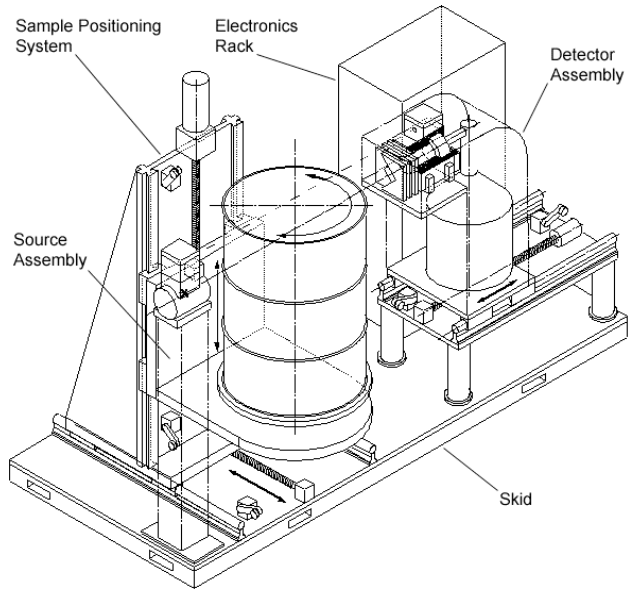

Fig. 9 *RFETS transportable TGS outline drawing.*

B. Detector Assembly

The detector assembly has a HPGe detector, a live-time source (^{109}Cd), a collimator, and shielding. The detector combines high efficiency (> 50%) with high resolution to permit gamma-ray isotopic measurements from the composite spectrum from the emission scans. The opening of the collimator is adjustable by stepping motors from 1.25 cm to 6.4 cm to accommodate a large range of sample sizes. The detector assembly is auto-positioned depending on the sample size selected by the operator. These automated provisions add cost and are not necessary for a research environment or in a production environment in which supervisory oversight can be substituted for automation. For low Pu or U mass measurements in a production environment thick tungsten shields are necessary. The detector is adequately shielded by 10 cm of tungsten.

C. Sample Positioning System

The sample positioning system has a three-axis precision stage driven by stepping motors that provided sample translation, rotation, and elevation relative to the source and detector. Note that the difference between TGS and the older segmented gamma-ray scanner (SGS) is the addition of a translation axis that allows the detector to view the sample along all possible lines that pass through it rather than just through the radial centerline as in the SGS technology. By stacking slices (axial scanning), the spatial distribution of material within the entire sample can be recovered and a three-dimensional mapping of the drum contents is possible. The RFETS system accommodates sample sizes ranging from 15 cm to 75 cm in diameter and up to

908-kg total weight. The largest samples were 303-ℓ drums and the smallest 2-ℓ cans. In a typical transmission scan of a 208-ℓ drum, the drum rotates at 3 rpm, makes 5 entire revolutions, and takes 150 data grabs of the entire spectrum for each axial layer. The total transmission scan of 16 layers takes 30 min and then the stage and drum return to the initial position, the shutter is closed, and the scan protocol is repeated with a high degree of repeatability (< 0.013 cm).

D. Data Acquisition System

High throughput and accurate, unbiased results are the hallmark of a well-designed TGS system. Current data acquisition systems, if well specified, should not be the limiting factor. General requirements might include grabbing and storing 5000 measurements per hour with individual grab times of approximately 2/3 s. Each measurement is associated with a particular projection as depicted in Figure 6. Summing these measurements provides an average spectrum suitable for post-scan isotopic abundance determinations.

E. Data Analysis System

During the emission scan, the transmission source shuttered off and net counts are recorded for regions of interest (ROI) about peaks corresponding to gamma rays emitted by the target isotope. For plutonium assays, ROIs are typically established for four well-resolved ^{239}Pu gamma rays: 129-, 203-, 345-, and 414-keV. Each of these gamma rays is used to develop an independent estimate of the distribution and mass of ^{239}Pu within the sample. When large variations are observed for the different energy estimates, the presence of self-attenuating lumps is indicated and lump correction algorithms must be applied. (See Section VI.) As the sample rotates and translates relative to the detector, the net count rate varies. The magnitude of the net count rate depends on the distance from the gamma-ray source to the detector, and the intervening attenuating material. Since the attenuation map is known for each gamma ray of interest, the net count rate can be calculated for trial distributions of the emitting material. Reconstruction of this spatial distribution of emitting material is accomplished by adjusting the trial distribution until the estimated net counts match the measurements (Refs. 6-7). The exact nature of such algorithms depends upon the approaches devised by the developers. The reader is referred to the following references which provide insight into the approaches used successfully by leading TGS designers (Refs. 12-18).

IV. Performance Evaluation in Blind Tests and Actual Facility Measurements

A major selling point of TGS has been its overall versatility and freedom from bias. In this section, we will present a small but representative set of results to help the reader evaluate the TGS approach. The first data set is from the Performance Demonstration Program (PDP) comparing TGS to a large number of competing technologies in controlled blind tests. The second and third set of results are from large production runs for classes of materials that are very difficult to assay by any technique other than TGS and validate the time and effort invested to develop the technology.

A. Performance Demonstration Program (PDP)

"The Performance Demonstration Program (PDP) for NDA consists of a series of tests to evaluate the capability for NDA of Transuranic waste (TRU) throughout the DOE complex with the major interest relating to TRU waste to be shipped for storage in the Waste Isolation Pilot Project (WIPP) in Carlsbad, NM. Each test is termed a PDP cycle. These evaluation cycles provide an objective measure of the reliability of measurements obtained from NDA systems used to characterize the radiological constituents of TRU waste."(Ref. 19)

The test results given in Figure 10 are from a series of blind tests of 208-ℓ drums of a known matrix (glass, plastic, sludge, etc) and an unknown distribution and mass of the target isotopes. Radioisotope concentrations for the set of tests were varied over a range expected in actual waste characterization activities. Measurement facilities were required to analyze the simulated waste containers using the same procedures used for normal waste characterization activities. The results are mixed and no single measurement performs better than all others for all situations. The reader is allowed to draw their own conclusions but is referred to the TGS Applications Manual (Ref. 4) that provides more details about these series of tests.

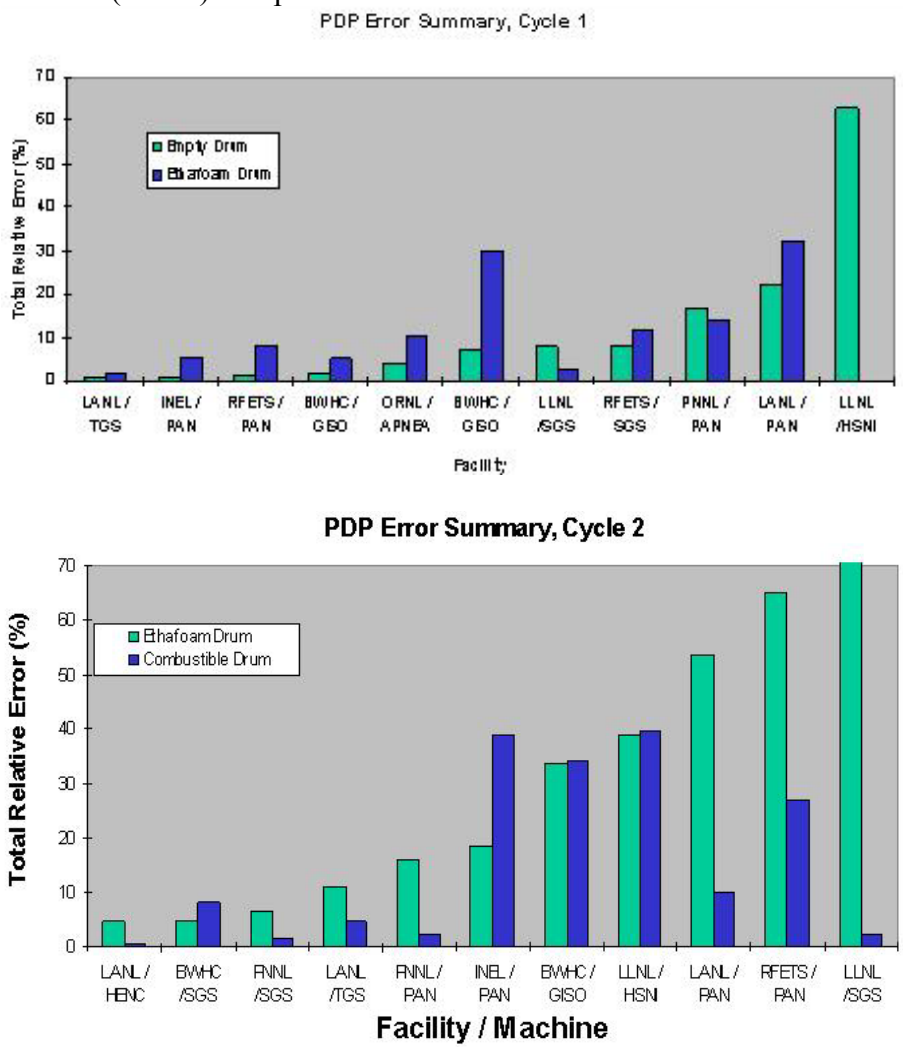

Fig. 10 *PDP results*

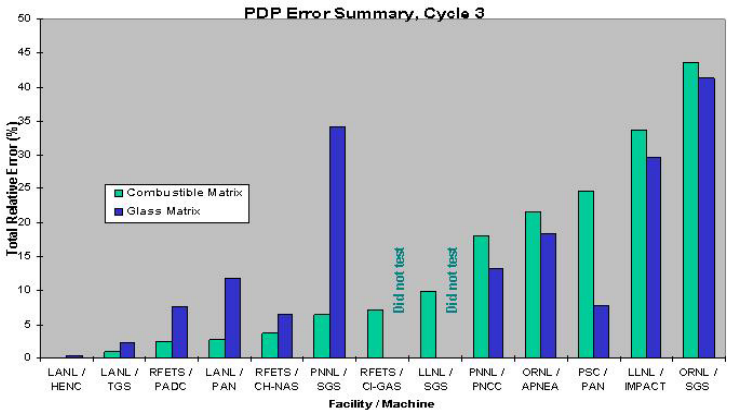

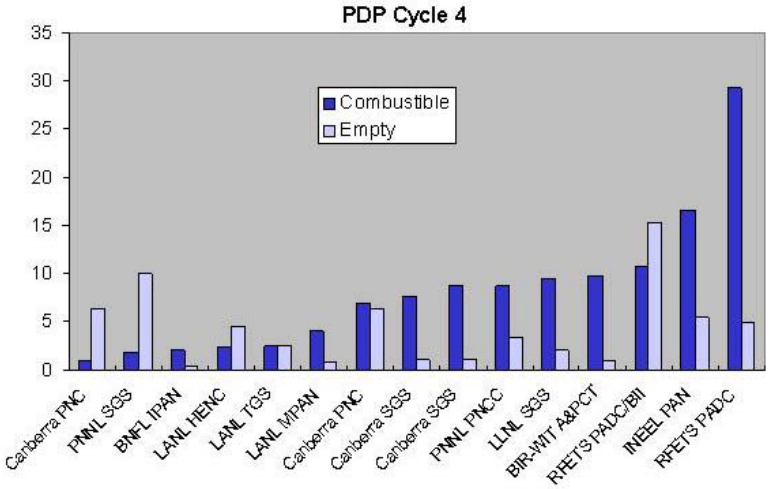

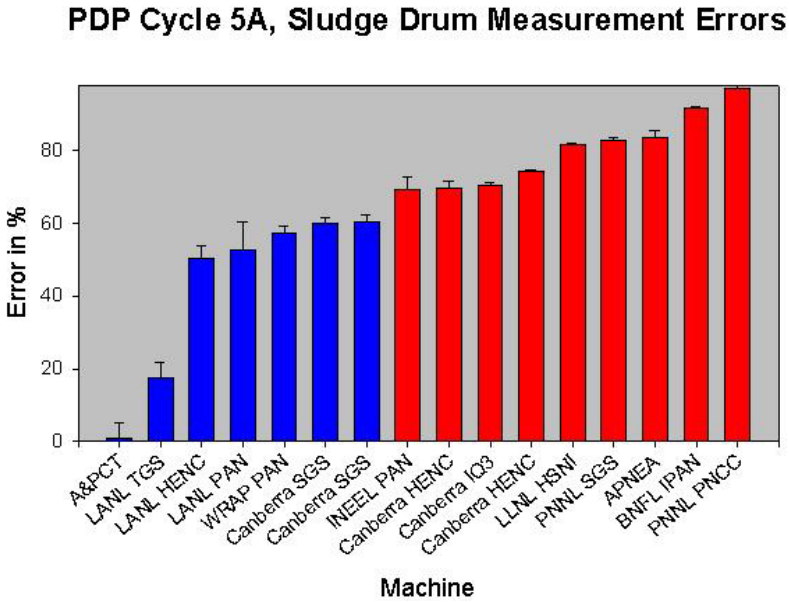

Fig. 10 *PDP results (continued).*

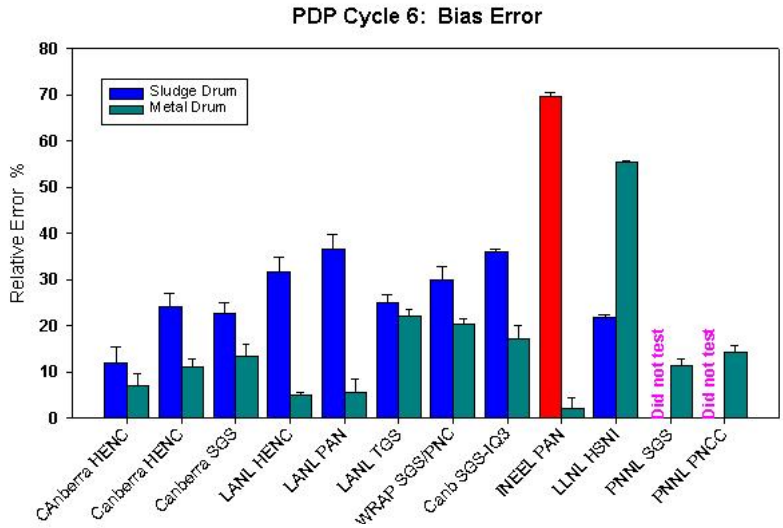

Fig. 10. PDP results (continued)

Figure 10 PDP Results Legend

Facilities: INEEL – Idaho National Engineering and Environmental Laboratory, RFETS – Rocky Flats Environmental Technology Site, SRS – Savannah River Site, WRAP – Hanford Waste Receiving and Packaging Facility, LANL – Los Alamos National Laboratory, LLNL – Lawrence Livermore National Laboratory, ORNL – Oak Ridge National Laboratory, PNNL – Pacific Northwest National Laboratory

Instrument: HENC – High Efficiency Neutron Counter (passive drum counter), SGS – Segmented Gamma Scanner, PAN – Passive Active Neutron Counter, IPAN – Imaging Passive Active Neutron Counter, TGS – Tomographic Gamma Scanner, CTEN – Combined Thermal Epithermal Neutron Counter (Active/passive counter), IQ3 – Low-level sensitivity Multi-detector gamma counter, A&PCT – Active and Passive Computed Tomography, APNEA - Active and Passive Neutron Examination and Assay System, PADC - Passive Active Drum Counter, PNCC – Passive Neutron Coincidence Counter, HSNI- High Sensitivity Neutron Instrument

B. RFETS Pyrochemical Salts

The transportable TGS was installed in Building 371 at RFETS for use in the salt repackaging program. Before the start of operations, the system demonstrated compliance with safeguards and WIPP requirements (Refs. 20-21). The system was calibrated using SGS standards. To assess the accuracy of the system, assays of electro-refining salts were compared to reference values determined by calorimetry. For each sample, the mass of ^{239}Pu was determined using TGS with lump corrections. FRAM was used to analyze the spectrum acquired by the DSPEC (commercial multichannel analyzer using direct signal processing) system during the TGS emission scan. The ^{239}Pu/Pu ratio calculated by FRAM was used with the TGS estimate of ^{239}Pu mass to determine total Pu. The results of this procedure are compared to the reference values in Table 1. The mean absolute difference between TGS and

calorimetric assay was 4.5%. The inventory difference was 2.6% (48 g out of a total of 1839 g). Based on the results of these measurements, TGS was qualified to measure electro-refining salt samples in the 25-225 gram range and began routine operation.

. Table 1. Comparison between TGS and calorimetric assay of electro-refining salts

	Calorimetric Assay	TGS/FRAM	Difference
Sample ID	Total Pu (g)	Total Pu (g)	(%)
Z10783	45.07	44.6	-1
Z10671	142.6	151	6
Z10668	186.6	184	-1
Z10626	194.0	200	3
Z10636	151.8	160	5
Z10637	171.7	196	14
Z10639	204.5	200	-2
Z10649	162.5	161	-1
Z10731	97.26	92	-5
Z10762	130.8	128	-2
Z10765	121.8	131	8
Z10781	80.63	83.2	3
Z10782	62.36	63.6	2
Z11395	87.43	92.5	6
Total	1839	1887	2.6%

Pyrochemical salts contain plutonium dissolved in NaCl as well as plutonium in the form of metal shot. These residues also contain high concentrations of ^{241}Am and other radioactive contaminants. Because the salts are highly inhomogeneous, the established SGS technique, which is based upon homogeneity within segments, could not meet the WIPP criteria for accuracy and bias. Calorimetric techniques are capable of giving reliable results, but throughput is very low requiring an average of 20 hours per package. NDA techniques based upon neutron coincidence counting were unable to provide reliable results because of the inability to establish standards for the wide range of impurities and high ^{241}Am concentrations that produced a high singles background. As such TGS was applied to the problem materials and the measurement control results are shown in Figure 11.

The low bias (0.04%) and the high throughput (10 – 20 packages per day) are very notable. The background in the radiation area was significant and demonstrated the advantage of the heavy shielding, described in Section III. Some of the packages were encased in a tin liner which strongly absorbed the emissions and increased the difficulty of the measurements. Below are provided some general guidelines that apply to the measurement of plutonium.

Performance results depend both on sample size and material density and the product of these terms that is called the areal density [g/cm^2] which is often used to express material "thickness" limitations. As a rule-of-thumb, TGS measurements of ^{239}Pu using the 414-keV gamma ray generally have better than 10% accuracy for samples with an areal density less than 90 g/cm^2 assuming the materials are relatively low atomic number.

Transportable TGS Measurement of Salts (1999-2000)

Results from 209 verification runs →

•Uncertainty per meas. = 9.4%

•Inventory Bias = (-0.04 ±0.99)%
13.461 kg (TGS)
13.467 kg (Cal/Iso)

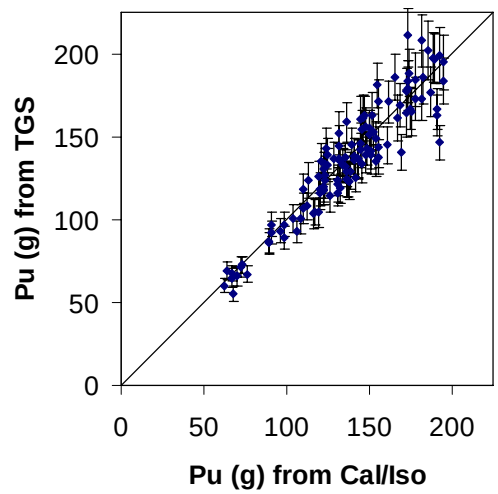

Throughput:

>5000 items / first year

10-20 items / day

Fig. 11 *Results of electro-refining salts assay at RFETS (Ref. 22). Cal/Iso is the combination of a calorimetric determination of sample power (heat) and a gamma-ray spectrometric determination of plutonium isotopic composition.*

For typical salt cans, approximately 20 cm in diameter, 10 % assays can be achieved at bulk densities of 4.5 g/cm^3. TGS is capable of accurately assaying samples that contain regions far exceeding these bulk densities so these estimates tend to be conservative. The precision that can be achieved by TGS varies from sample to sample and depends on the placement of the source, the distribution of attenuating material, collimator parameters, and the mass of SNM present in the sample. As a general rule, 0.5 g ^{239}Pu in low-density matrices with less than one-hour acquisition time is a mass limit below which measurements become unreliable (Ref. 23). For small mass samples (< 5 g) known to be homogeneous, SGS can produce the equivalent precision of TGS with shorter counting times. For example, for a 1-g sample and typical collimator settings, a 20-min SGS scan produces the same precision as a 1-h TGS scan. For samples less than 10 g ^{239}Pu, precision differences are not a significant issue and the presence of any sample heterogeneity will generally lead to more favorable TGS results.

C. Uranium Applications

1. RFETS Experience

TGS was primarily developed to assay plutonium in difficult matrices. In June 1997, TGS was deployed in Building 886 at RFETS to assay 208-ℓ drums containing waste contaminated with highly enriched uranium, HEU (Ref. 24). In this case, the materials were contaminated with solutions containing uranium and other elements including boron. The boron biased the active neutron measurements and the HEU had too little neutron output for passive

measurements. Inhomogeneities ruled out SGS and the very low heat output precluded calorimetry. The materials were primarily contaminated with uranyl-nitrate solutions and consisted of low-Z matrices of borosilicate glass, paper, plastics, cardboard, light metals, soil, and chemical waste all packaged in 208-ℓ drums. The mass of ^{235}U ranged from less than 5 g in approximately 80% of the drums to 60 g in a few cases. All of the drums with assay values less than 15 g were shipped offsite for burial. Those with greater assay values were repackaged using the TGS images to facilitate the repackaging. The lower measurement limit was approximately 0.5 g ^{235}U for the low density matrices. This work was important in providing evidence that the TGS technology applies to a wide collection of uranium items that are difficult or impossible to assay by any means.

2. Survey of Excess HEU Materials across the DOE Complex (Refs. 25-26)

Because uranium assay is not yet as widely done as plutonium assay, some general information is provided here to assist the reader in assessing the use of TGS for uranium assay. The following table indicates the amounts of uranium at various sites across the DOE complex.

Table 2. Excess HEU at DOE Sites

Facility	Excess Uranium (Tonnes)
Idaho	23.0
Pantex	17.0
Portsmouth	22.0
Oak Ridge	85.0
Savannah River	5.0
Total	174.0

Table 3. Excess HEU Material Forms at DOE Sites

Material Form	Excess Uranium (Tonnes)
Metal	87.0
Irradiated fuels/targets	29.6
Compounds	17.4
Reactor Fuel	19.1
Oxide	15.7
Other	5.2
Total	174.0

3. Relative Comparison of TGS Measurements of HEU and Pu (Ref. 27)

The safeguards community has gained considerable background in the TGS measurement of plutonium in a variety of matrices. It is not generally recognized that uranium is also well suited for TGS measurements. To facilitate the readers' appreciation for the ability of TGS to handle uranium contaminated materials, a quantitative comparison of the assay expectations is made below between HEU and plutonium for a typical assay geometry. The tables are based on the assay of 208-ℓ drums observed by a 50% efficient Ge detector. It is assumed that the

attenuating material at a thickness equivalent to half the drum diameter and at the specified Z, is sufficient to reduce the 414-keV gamma ray of ^{239}Pu by a factor of 100. This condition sets a conservative upper limit on the matrix density, corresponding to a factor of 10^4 reduction in the transmission at 414 keV, which challenges the effective dynamic range of typical Ge detectors. For convenience, the count rate at 414 keV, given this reduction, is taken to be 1 count/s. Under these same conditions, the identical matrix would reduce the 186-keV gamma ray from ^{235}U to the count rates given in Table 4a,b. It is important to note that in the absence of any attenuating matrix whatsoever, the count rate per gram would actually be greater for ^{235}U than for ^{239}Pu by a factor of approximately 2.5. This results from the higher specific activity of ^{235}U [4.34×10^4 γ/(s-g) at 185.7 keV] versus ^{239}Pu [3.42×10^4 γ/(s-g) at 413.7 keV] and the higher intrinsic detector efficiency at 186 keV than at 414 keV (approximately a factor of 2).

The conclusion that one can draw from this comparison is that for conditions conducive to ^{239}Pu assay, i.e. in matrices that produce an average attenuation of less than a factor of 100 and in matrices that consist of materials such as graphite, combustibles, oxides, fluorides, sludges and ash, the count rate per gram for uranium should be comparable to that of plutonium. It is equally important to realize that when the matrix contains elements with Z greater than 20, the low energy of the principal assay line in uranium (186 keV) strongly limits the application compared to plutonium which uses the 414-keV line which is less attenuated.

Table 4a. Excellent Candidates for TGS Assay

Isotope	Plastics, Graphite Molds Combustibles, Raschig Rings Z=6		Oxides, Fluorides Z=8,9		Light Metals Soil, Dirt, Sludge Z=13,14		Steel, Iron Z=26	
	μ[cm2/gm]	count/s	μ[cm2/gm]	count/s	μ[cm2/gm]	count/s	μ[cm2/gm]	count/s
^{239}Pu (414 keV)	0.094	1.0	0.094	1.0	0.094	1.0	0.091	1.0
^{235}U (186 keV)	0.125	0.55	0.125	0.55	0.127	0.50	0.145	0.16
Counting Ratio (Pu/U)		1.8		1.8		2.0		6.3

Table 4b. Poor Candidates for TGS Assay

	Medium Z (Tin, Cadmium, Salts) Z=50		Heavy Metals Pb, W, U, Pu Z=82	
	μ[cm2/gm]	count/s	μ[cm2/gm]	count/s
^{239}Pu	0.105	1.0	0.203	1.0
^{235}U	0.351	7×10^{-5}	1.13	2.5×10^{-9}
Counting Ratio (Pu/U)		1.4×10^4		4×10^8

Owing to this major difference in attenuation as the atomic number of the absorber increases, self-attenuation in uranium presents an especially difficult problem. The next section discusses the problems of lump detection and correction in plutonium and the success that developers have had in inventing techniques for treating the problem that eliminates bias due to self-attenuation. It has been generally recognized by experts that application of the standard plutonium lump detection and correction techniques to uranium does not lead to the same success as in plutonium. In the absence of another technique for lump detection, one must rely entirely on knowledge that the materials are free of lumps to avoid large negative biases. We suggest here an alternative approach for uranium lump detection and correction that may provide the necessary assurance that materials with uranium lumps can be easily detected and appropriate corrections applied. The study is in a very preliminary phase, but the relative simplicity of the approach shows sufficient promise to allow those who are contemplating the assay of uranium materials the opportunity to test out the preliminary assumptions.

V. Lump Correction Techniques

A. Plutonium Lump Detection and Correction Technique

An important aspect of minimizing bias in TGS measurements is to identify the presence of small lumps of plutonium and apply suitable corrections for the self-attenuation of the gamma rays from these lumps. The self-attenuation in spherical lumps is formulated in Ref. 29. Even small lumps can cause significant bias, e.g., a plutonium metal lump of only 2-mm diameter attenuates 70% of the 414-keV gamma rays emitted within it.

An approach to lump detection and correction has been developed and applied successfully for the assay of plutonium-bearing materials (Refs. 29-31). This approach involves dividing the sample into a homogeneous fraction and a "lumpy" fraction and then estimating the average plutonium lump size using the reduced count rates of lower energy ^{239}Pu peaks relative to the main 414-keV peak. A convenient means for displaying this technique is shown in Figure 12. The idea here is to estimate the mass of the plutonium in the sample using each of the high intensity lines of ^{239}Pu ignoring the effects of self-attenuation. In the presence of lumps, the low energy lines grossly underestimate the plutonium mass and by extrapolation of the mass estimates as a function of gamma-ray energy to 414 keV and beyond a corrected mass is found.

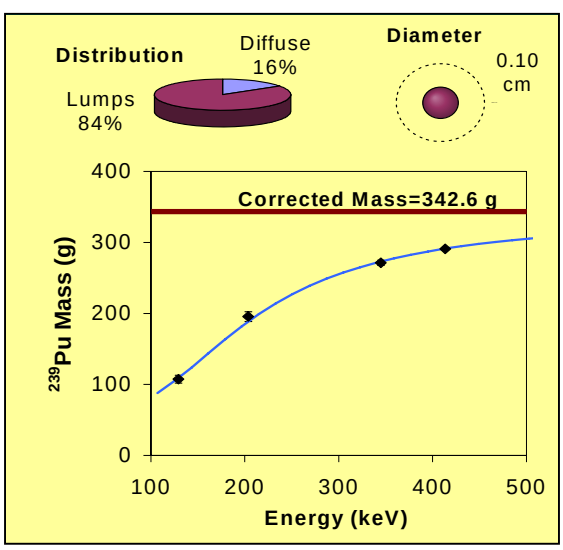

Fig. 12 *Lump Correction estimate of the mass of plutonium metal in a sample.*

B. Standard Pu Lump Correction Doesn't Work for Uranium

The success of this method for ^{239}Pu derives from the high specific activities of the lower energy gamma rays (in particular at 129 keV) and the large change in the attenuation coefficient over this energy range. Uranium poses a special problem because the only line of high intensity is relatively low in energy (186 keV) and the other lines are close in energy and have a much smaller range of attenuation coefficients. To acquire a quantitative feel for the problem, it is instructive to compare the gamma rays used for ^{239}Pu and the corresponding attenuation coefficients in the metal with the corresponding gamma rays of ^{235}U. Table 5 gives this comparison. The ratio of the attenuation coefficients at 129.3 keV and 413.7 keV is 13.8 which compares to a ratio of 1.87 for 143.8 keV and 185.7 keV of uranium. The low intensity of the 205.3-keV and 163.4-keV gamma rays of uranium (factor of 10 less than the 185.7 virtually eliminate them from being useful in a lump correction method as applied above for ^{239}Pu. Because of these large differences in sensitivity, the Pu technique described above is not feasible for uranium and a new approach has been proposed (Ref. 28) as is outlined in the following section.

Table 5. Comparing the relative intensity and attenuation coefficients of U and Pu for possible "lump detection gammas".

Plutonium			Uranium		
E (keV)	γ/(sec-gm)	μ [cm^2.gm]	E (keV)	γ/(sec-gm)	μ [cm^2.gm]
129.3	1.44×10^5	3.714	143.8	7.8×10^3	2.737
203.5	1.28×10^4	1.259	163.4	3.7×10^3	2.003
345.0	1.28×10^4	0.386	185.7	4.3×10^4	1.463
413.7	3.42×10^4	0.269	205.3	4.0×10^3	1.333

C. Proposed Technique for Uranium Lump Correction

This technique compares the self-fluorescence of the uranium K x-rays to the thorium K x-rays produced in the decay of ^{235}U as shown in Figure 13. The upper spectrum comes from a thick uranium metal disk, whereas the lower spectrum comes from two very thin uranium metal disks (~0.03 mm). The $K_{\alpha 1}$ and $K_{\alpha 2}$ x-rays from uranium are at 98.4 and 94.7 keV, respectively. They are the upper two green peaks in the spectra. The corresponding thorium x-rays are at 93.4 and 90.0 keV; they are the lower two green peaks. Note that for the thin foil, where we expect relatively little fluorescence, the ratio of the U x-ray activity to Th x-ray activity is almost one. On the other hand, the same ratio for the thick disk in the upper spectrum, where we expect more fluorescence, is much higher. The thin foil case corresponds to "no lumps" and the thick disk case corresponds to "lumps".

A quantitative comparison, given in Table 6, helps one appreciate the potential sensitivity of this proposed method to correct for "lumps" in uranium measurements.

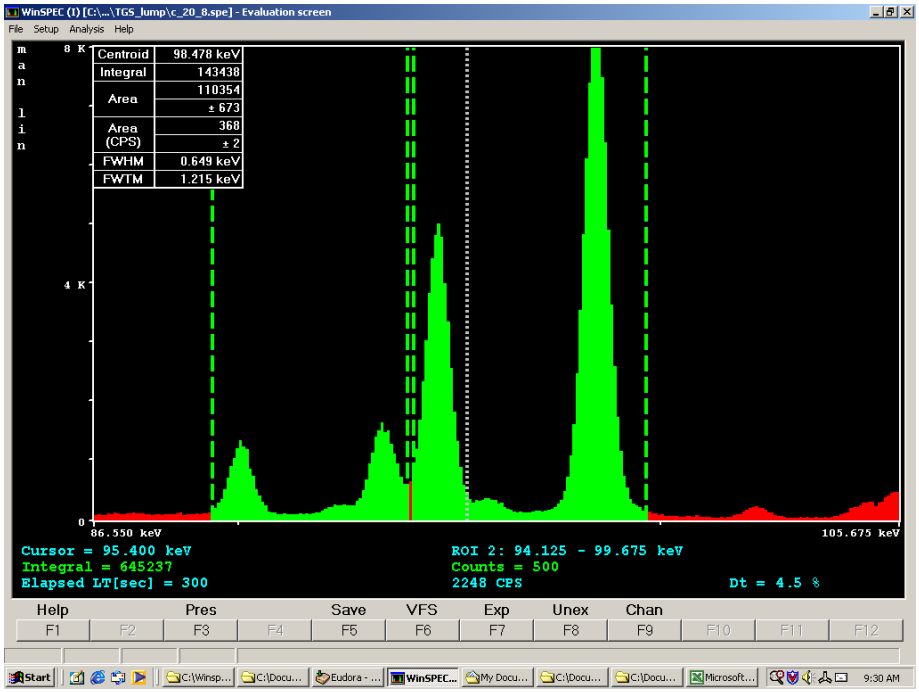

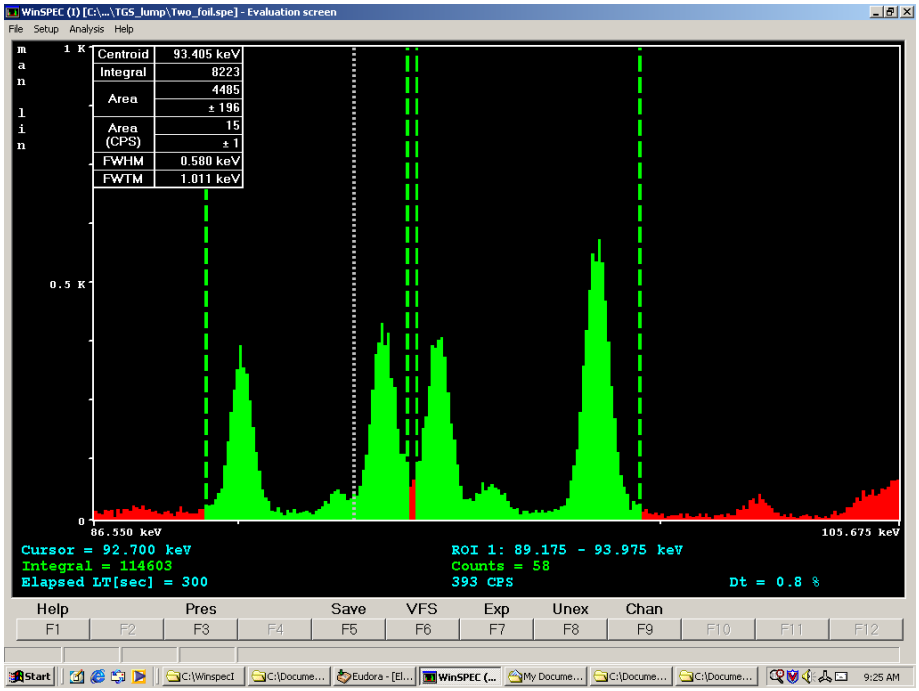

Fig. 13 *Comparison of the fluoresced uranium K x-rays with thorium K x-rays (from U decay) in a thick metal disk (upper spectrum) with those from very thin foils (lower spectrum). The lower energy ROI covers the Th Kα x-rays and the higher energy ROI covers the U Kα x-rays. Note the much higher relative intensity of the uranium x-rays from the metal disk.*

.

Table 6. Comparison of the peak areas of the fluoresced uranium x-rays in thick versus thin samples of ^{235}U

X Ray Group	Metal Disc	Two Foils
Uranium	110354	6141
Thorium	6141	4485
Ratio	18/1	1.4/1

The important fact to note in the above table is that a factor exceeding ten is observed in the ratio for thin versus thick samples, e.g. uranium solutions versus large lumps. This large factor tends to suggest excellent sensitivity to the presence of lumps and with a more careful study even a means of correcting for their presence. As the DOE complex becomes more focused on the uranium assay problem, this technique may become standardized as a means of screening uranium materials suited for TGS assay.

VI. Commercially Available Systems

With the success of the LANL developed TGS systems at RFETS, the technology was validated and license agreements negotiated with the following firms:

Antec Corporation
9076 Marshall Court
Westminster, CO 80031

BNFL Instruments
4001 Office Court Drive, No. 800
Santa Fe, NM 87505

Ametek Ortec
801 South Illinois Ave
Oak Ridge, TN 37830

Figure 14 shows two instruments that are currently available and fielded at several DOE sites.

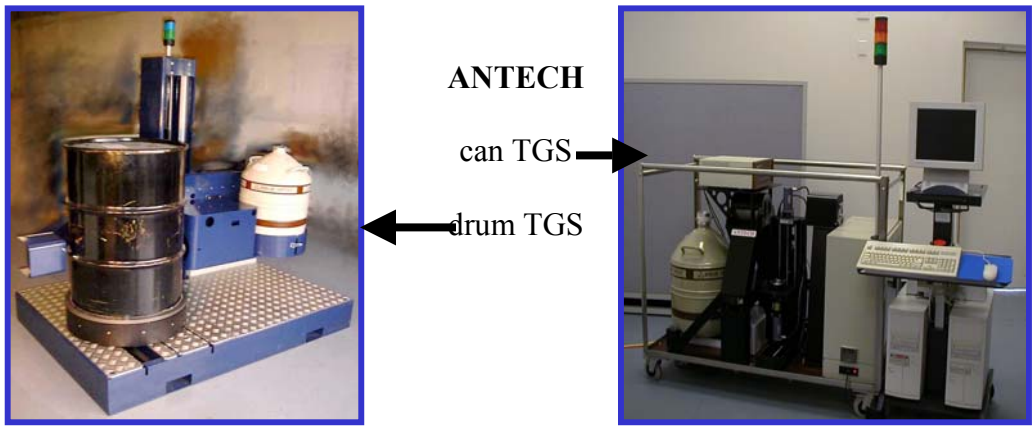

Fig. 14 *Commercially available TGS systems.*

References:

1. R. J. Estep, “Assay of Heterogeneous Radioactive Wastes by Low-Resolution Tomographic Gamma Scanning”, ANS Transactions **62**, 178 (1990)

2. S. Kawasaki, et. al. “Radioactivity Measurement of Drum Package Waste by a Computed Tomography Technique” Applied Radiation and Isotopes **41,** 983(1990)

3. R. J. Estep, and K. Sherwood, “A Prototype Tomographic Gamma Scanner for Assaying 208-liter drums” Los Alamos National Laboratory report, LA-UR-91-61 (1991).

4. J. S. Hansen et. al. “Applications Guide to Tomographic Gamma Scanning” To be published, 2004.

5. R. Gordon, “A Tutorial on Algebraic Reconstruction Techniques (ART)” IEEE Transactions **NS-21** 78 ff. (1974)

6. R. Gordon, R. Bender, and G. Herman, "Algebraic reconstruction techniques(ART) for three dimensional electron microscopy and X-ray photography," Journal of Theoretical Biology **36**,105-117, 1970.

7. G. Hounsfield, "A method of an apparatus for examination of a body by radiation such as x-ray or gamma radiation," Patent specification 1283915, The Patent Office, 1972.

8. G.N. Ramanchandran and A.V. Lakshminarayanan, "Three dimensional reconstructions from radiographs and electron micrographs: Application of convolution instead of Fourier transforms," Proceedings of the National Academy of Sciences, **68**, 2236 - 2240, 1971.

9. G. Herman and A. Naparstek, "Fast image reconstruction based on a Radon inversion formula approppriate for rapidly collected data," SIAM Journal of Applied Mathematics **33**, 511-533, 1976.

10. J. Radon, "Uber due bestimmung von funktionen durch ihre intergralwerte langsgewisser mannigfaltigkeiten (on the determination of functions from their integrals along certain manifolds," Berichte Saechsische Akademie der Wissenschaften, **29**, pp. 262 - 277, 1917.

11. L. A. Shepp and U. Vardi, “Maximum Likelihood Reconstruction for Emission Tomography” IEEE Trans. Medical Imaging, M1-1, 2 (1982)

12. R. J. Estep, “TGS-Fit: Image Reconstruction Software for Quantitative, Low Resolution Tomographic Assays” Los Alamos National Laboratory” Los Alamos National Laboratory report, LA-12497-MS (1993).

13. R. J. Estep, T. H. Prettyman and G. A. Sheppard, “Tomographic Gamma Scanning to Assay Heterogeneous Radioactive Waste” Nuc. Sci. Eng. **118** 145-152, 183-184 (1993).

14. T. H. Prettyman, R. J. Estep, and G. A. Sheppard, “Development of a tomographic instrument for tomographic nondestructive assay,” Trans. Am. Nuc. Soc. **69** 183-184 (1993). Los Alamos National Laboratory report, LA-UR-93-2580 (1993).

15. R. J. Estep, “A preliminary design Study for Improving Performance in Tomographic Assays” Los Alamos National Laboratory” Los Alamos National Laboratory report, LA-12727-MS (1994).

16. T. H. Prettyman, R. A. Cole, R. J. Estep, and G. A. Sheppard, “A maximum likelihood algorithm for gamma-ray tomographic nondestructive assay,” Nucl. Instr. Meth. **A 356,** 470-475 (1995).

17. 17.. T. H. Prettyman, “Precision estimates for tomographic nondestructive assay,” Proceedings of the 5th International Conference on Facility Operations-Safeguards Interface (American Nuclear Society, Inc., La Grange Park, Illinois 1995), ANS Order No. 700226, pp. 191-199.

18. T. H. Prettyman, L. A. Foster, and R. J. Estep, “Detection and Measurement of Gamma-Ray Self-attenuation in Plutonium Residues.” Proceedings of INMM **37**, 130-136 (1996)

19. T. H. Prettyman, “ARC_TGS User’s Manual,” Los Alamos National Laboratory Transuranic Waste Characterization/Certification Project – Records Management, TWCP-1493 (1998).

20. “Performance Demonstration Program Plan for Nondestructive Assay of Drummed Wastes for the TRU Waste Characterization Program”, Rev 0.1U. S. Dept of Energy, Carlsbad Field Office DOE/CBFO-91-1005 (Mar 22, 2001)

21. T. H. Prettyman, S. E. Betts, D. P. Taggart, R. J. Estep, N. J. Nicholas, M. C. Lucas, and R. A. Harlan, “Field experience with a mobile tomographic nondestructive assay system,” Proceedings of the 4th Nondestructive Assay and Nondestructive Examination Waste Characterization Conference, Salt Lake City, Utah (October 24-26, 1995) 109-137.

22. T. H. Prettyman, S. E. Betts, and A. C. Muscatello and D. Catlett, “Final Report on the Mobile TFS Demonstration at Rocky Flats” Los Alamos National Laboratory report, LA-UR-98-4052 (1998).

23. David J. Mercer, J. Steven Hansen, John P. Lestone, Thomas H. Prettyman, and Larry Kayler, "TGS Measurements of Pyrochemical Salts at Rocky Flats," *proceedings of the Institute of Nuclear Material Management, 42nd Annual Meeting,* Indian Wells, CA, July 15-19, 2001; Los Alamos National Laboratory report LA-UR-01-3509.

24. D. J. Mercer, T. H. Prettyman, M. E. Abhold and S. E. Betts, “Experimental Validation of Tomographic Gamma Scanning for Small Quantities of Special Nuclear Material” Los Alamos National Laboratory report, LA-UR-97-2804 (1997).

25. D. J. Mercer, S. E. Betts, T. H. Prettyman, C. D. Rael, “Tomographic Gamma Scanning of Uranium Contaminated Waste at Rocky Flats” Los Alamos National Laboratory report, LA-UR-98-2922 (1998).

26. . “A Strategic Approach to Integrating the Long-Term Management of Nuclear Materials. The Department of Energy’s Integrated Nuclear Materials Management Plan, A Report to Congress, June, 2000.

27. ”Highly Enriched Uranium, Working Group Report on ES&H Vulnerabilities Associated with the Department’s Storage of Highly Enriched Uranium., US DOE, Dec,1996.

28. J. S. Hansen, unpublished data.

29. J.-P. Francois, “On the Calculation of the Self-Absorption in Spherical Radioactive Sources.” Nucl. Instr. Methods **117**, 153-156 (1974)

30. T.H. Prettyman, J. K. Sprinkle and G. A. Sheppard, “A Weighted Least Squares Lump Correction Algorithm for Transmission Corrected Gamma Ray Non destructive Assay” Nucl. Mat. Manage. **XXII**, 682-690 (1993).

31. T.H. Prettyman, J. K. Sprinkle and G. A. Sheppard, “Performance of an Advanced Lump Correction Algorithm for Gamma Ray Assays of plutonium.” Los Alamos National Laboratory report, LA-UR-94-2477 (1994).

32. T. H. Prettyman, L. A. Foster, and R. J. Estep, "Detection and Measurement of Gamma-Ray Self-Attenuation in Plutonium Residues," Proceedings of INMM (1996) pp. 130-136.

5. NONDESTRUCTIVE ASSAY OF HOLDUP

T. Douglas Reilly

I. INTRODUCTION

The term "holdup" refers to the nuclear material deposited in the equipment, transfer lines, and ventilation systems of processing facilities. Reprocessing, fuel fabrication, conversion, and enrichment require very large facilities that can contain many pumps, ovens, centrifuges, filters, diffusers, and hundreds of kilometers of pipes and ducts. During years of operation, significant quantities of uranium and/or plutonium can build up in this equipment. Operators need to know the location and amount of holdup for reasons of accountability, criticality safety, radiation safety, waste management, and efficient plant operation. Sometimes the term holdup is also applied to in-process inventory, if this must be known for verification or accountability purposes. Holdup is difficult to measure and while it is usually a small fraction of plant throughput, it can often amount to many kilograms of nuclear material and this limits the accuracy of the nuclear material balance within the facility. A diverter could, in principle, remove one or more significant quantities (SQ) of HEU or plutonium and hide the diversion as unmeasured holdup deposits within the plant. IAEA safeguards inspectors rarely attempt to measure holdup; although they have participated with Los Alamos in a holdup measurement campaign at the Ulba Fuel Fabrication Plant in Ust-Kamenogorsk, Kazakhstan. Reference 1 presents an excellent discussion of holdup measurements.[1]

Holdup measurements must cover a range of material types as shown in Table 1 that lists some of the items measured during a holdup campaign at an HEU processing facility. Process history determines which materials may be deposited. The range of deposit thickness, presence of different material types (isotopic mixtures), and chemistry influence holdup measurements. The range of ^{235}U enrichment in some facilities includes depleted (0.3%) up to 97%, and that of ^{240}Pu at other facilities ranges from 2% to 45%. Such a range of materials is usually not found in commercial nuclear facilities. Because the equipment in large facilities is extensive, the total holdup may be large, even if deposit thicknesses are small.

Holdup measurements are usually made using gamma-ray techniques, although neutron measurements are also used. There is some experience using thermoluminescent dosimeters (TLD) to measure holdup deposits in gloveboxes or heavy equipment where it is difficult to insert gamma-ray detectors. Such dosimeters usually receive most of their dose from x-rays or low-energy gamma-rays, so the results are more susceptible to attenuation or geometry effects than those obtained with gamma-ray detectors. However, measurement performance can be comparable if the TLDs are carefully calibrated using mockups of the equipment to be measured.[2] Gamma rays have several advantages over neutrons in measuring holdup, because they are easily collimated allowing the locations and distributions of deposits to be defined. The gamma-ray peaks confirm the identities of the nuclides present. Multiple nuclides and elements can be measured independently and simultaneously by choosing the detector and peaks appropriately. Shielded gamma-ray detectors and the required electronics can be small and lightweight so that measurements can be performed in locations that are difficult to access.

Routine NDA measurements are usually conducted on well contained nuclear material items. This is not often the case for holdup measurements, especially those in plutonium processing facilities. Figure 1 shows four views of holdup measurements during the decommissioning of a

plutonium processing facility. The photographs illustrate well some of the difficulties that may arise when measuring holdup.

II. GAMMA-RAY SIGNATURES AND EQUIPMENT

Faced with a mix of material types for plutonium or uranium, the resolution provided by germanium or Peltier-cooled CdTe should be considered if there are possible biases from spectral interferences. When process knowledge is unable to specify isotopics, these high-resolution detectors may be required for preliminary surveys. When isotopic composition is sufficiently well known and interferences unlikely, even low-resolution scintillators such as sodium iodide (NaI) and bismuth germanate (BGO) can make useful holdup measurements. Table 2 lists the gamma-ray peaks commonly chosen to measure the listed nuclides.

Table 1. Example of Items Containing Holdup at Uranium Facility[3]

Process Component	HEU Content (g)
HEPA filter	< 0.2
Crop Shear	0.3 < ^{235}U < 1.2
Motor M28619	15 < ^{235}U < 61
Gear box	6 < ^{235}U < 25
Furnace B	13 < ^{235}U < 51
Spare Furnace	17 < ^{235}U < 67
Lathe	129
Freon Cart	77
Sawbench 1	0.164
cooling hut HEPA filter	17
Exhaust elbow	3.50
outgassing oven	0.105
Cooling hut	17
HEPA filter hut	6.84
Gate Valve	0.85
Pressure cookers	10.8
Exhaust Component	1.42
Riser Crusher	18

Fig. 1. Holdup measurements during Pu facility decommissioning[4]

Table 2. Common Gamma Rays for Holdup Analysis

Isotope	E_γ (keV)	Intensity (γ/g-sec)
^{238}Pu	153	5.9×10^6
^{235}U	186	4.32×10^4
^{241}Pu - ^{237}U	208	2.04×10^7
^{239}Pu	414	3.42×10^4
^{241}Am	662	4.61×10^5
^{238}U	1001	73

If scintillators like NaI or BGO are used, it should be noted that they exhibit a strong gain dependence on temperature. The effective gain of NaI may drop by one to three percent per ten-degree centigrade increase in temperature. A simple and practical stabilization technique is to regularly measure a gamma-ray source to compensate for drift. The 60-keV gamma ray from ^{241}Am ($t_{1/2}$ = 432.2 y) is commonly used as a reference peak.

Figure 2 shows the gamma-ray spectrum from low-burnup (93% ^{239}Pu) plutonium measured with four different detectors (NaI, coplanar-grid cadmium-zinc-telluride (CPG CZT), Ge, and Peltier-cooled CdTe). The detector most commonly used for holdup measurements is NaI. A NaI thickness of 1.25 cm absorbs 80% of ^{235}U gamma rays at 186 keV. A thickness of 5 cm absorbs 85% of ^{239}Pu gamma rays at 414 keV. The intermediate-resolution CZT is equal in sensitivity to the 2.5-cm-diameter NaI in spite of its limited size. Cubic CZT crystals as large as 1.5 cm on a side absorb up to 95% and 40% of gamma rays at 186 and 414 keV).

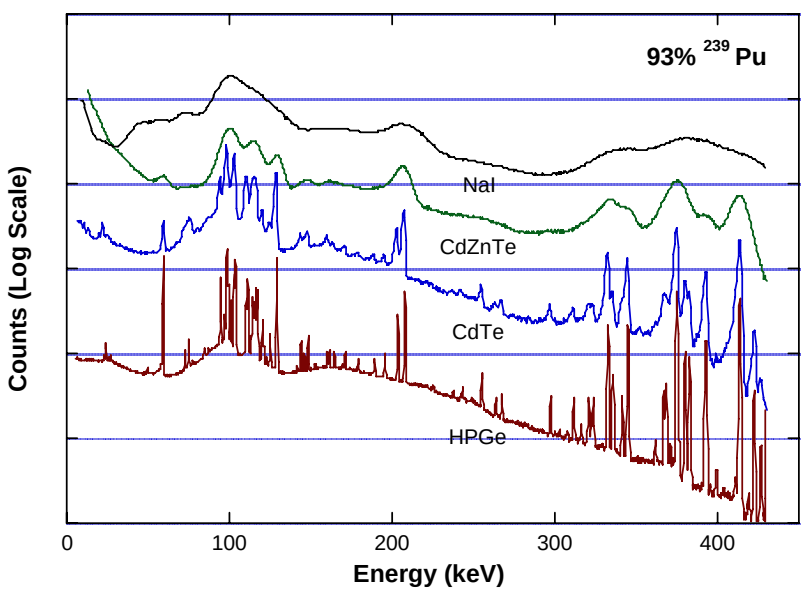

Fig. 2. Plutonium spectrum measured by NaI, CdZnTe, cooled CdTe, and high purity Ge detectors.

Interferences can add unwanted counts to the assay peak. Detectors with improved resolution and peak shape reduce bias from interference. The use of Ge detectors is generally difficult because of their weight. Recent progress with CPG CZT detectors is favorable for portable gamma-ray measurements.[5] The new solid-state detectors are also more compact, reliable, and stable than scintillators. A large CPG CZT detector can resolve interfering gamma rays from the ^{232}U decay chain that appear in recycled uranium. A gamma ray at 238 keV is produced at the end of this decay chain. It is not resolved from the 186-keV gamma in NaI, but it does not

interfere in Ge or CZT. Gamma-ray peaks from ^{241}Pu-^{237}U (332 keV), ^{241}Am (323-335 keV, 662 keV), and ^{237}Np-^{233}Pa contribute to bias in the NaI assay of ^{239}Pu at 414 keV. Many of these interferences are eliminated with CZT.

The recent availability of Peltier-cooled CdTe detectors with areas larger than 1 cm^2 (thickness is limited to 3 mm by charge transport properties) has made gamma-ray isotopic measurements for uranium and plutonium truly portable. Figure 1 illustrates the good energy resolution of CdTe. Figure 3 illustrates the compact dimensions of the CdTe detector, shown in use for portable Pu isotopics measurements in a glove box. The capability of CdTe for isotopic analysis covers 3% to 30% ^{240}Pu; it also covers ^{235}U from 0.1 to ~80%, and MOX. A 15-min. count with a CdTe detector measures the ^{240}Pu fraction to ~2% and the ^{235}U fraction to ~3%.

Fig. 3. The Peltier-cooled CdTe detector is shown measuring Pu isotopics in a glove box.

III. GENERALIZED GEOMETRY HOLDUP (GGH) ASSAY METHOD

A. Assumptions and Constraints

The Generalized Geometry Holdup (GGH) method categorizes each holdup deposit, no matter how complex, as a simple point, line, or area source.[6] This is illustrated in Figure 4 below. The GGH assay method was developed to simplify the analysis of holdup measurements performed using NaI detectors. It can, however, be used with any detector. The analysis of holdup data using GGH requires the following constraints:

1. Radiation shielding is used on the back and sides of the crystal.
2. A cylindrical collimator is installed on the front of the crystal.
3. The detector is positioned so that the deposit can be approximated as:
   a. a small point at its center, or
   b. a narrow, uniform line through its center whose length exceeds its width, or
   c. a uniform distribution that fills it (area deposit).
4. Measurements are performed at a known distance *r* between the detector and the deposit.

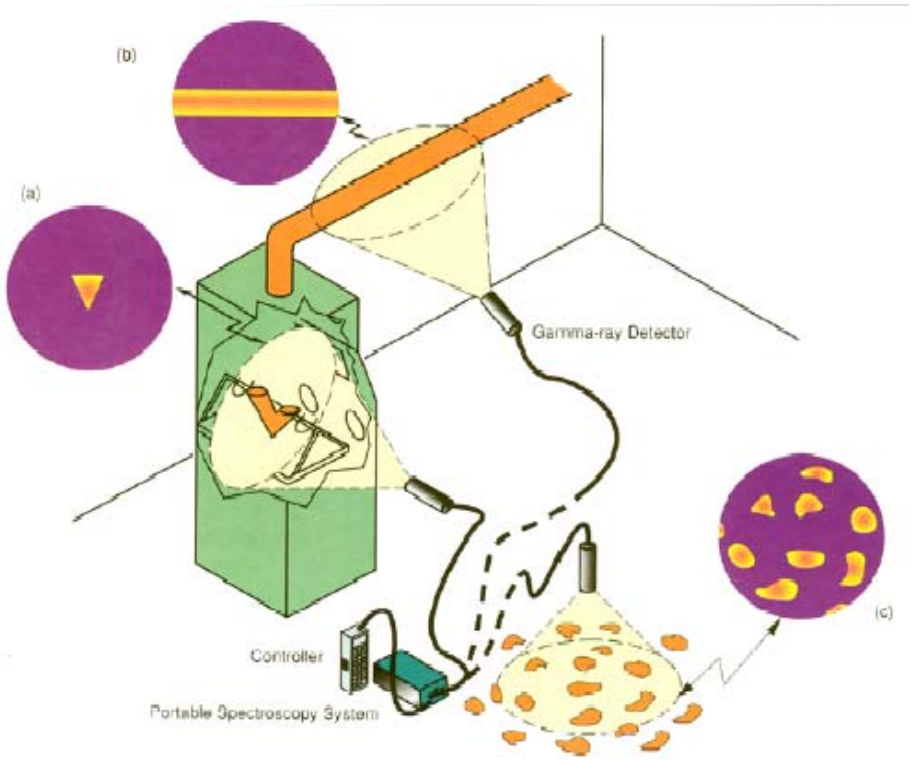

Fig. 4. Illustration of point (a), line (b), and area (c) holdup deposits.

B. Calibration

The calibration of the GGH method determines the relationship between the count rate of the measured gamma ray and the mass of the isotope of interest. Calibration for the assay of a point, line, or area deposit is accomplished with a point reference source. The response for each gamma-ray peak is measured with this source positioned on the detector axis at a known distance from the crystal. Measurements are also performed with the source displaced at fixed intervals from the crystal axis to obtain the two-dimensional radial response of the detector. These data are used to obtain the calibration for the assay of the specific isotope mass in a point, line, or area deposit. Figure 5 illustrates nine off-axis positions that can be used to determine the two-dimensional radial response of the detector. For the fixed distance, the detector response to a source at any point on the circle is the same because of rotational symmetry.

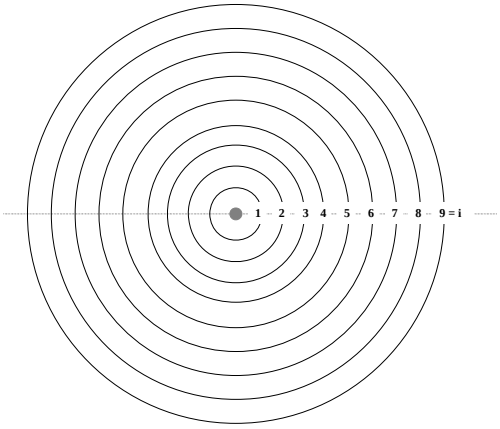

Fig. 5. Nine, equally spaced, off-axis positions of the point reference source used to measure the two-dimensional radial response of the detector.

Figure 6 shows the radial response obtained for the 414-keV gamma ray of ^{239}Pu using a 2.54-cm-diameter by 5-cm-thick NaI(Tl) detector. The length and diameter of the collimator are both 2.54 cm. The distance between the calibration source and crystal, r_0, is 40 cm. In this example, data were obtained with the point source positioned on both sides of the axis. The data in Figure 6 are used for the calibration of the assay of the specific isotope mass in a point, line, or area deposit. The point calibration uses only the axial response C_0 (s^{-1}) because the point deposit has no finite width. The point calibration constant is

$$K_P \text{ (g} \bullet \text{s} \bullet \text{cm}^{-2}) = m_0 \div (C_0 \bullet r_0^2). \quad (1)$$

The specific isotope mass measured at a distance r (C = room-background-subtracted net) is:

$$m_P \text{ (g)} = K_P \bullet C \bullet r^2. \quad (2)$$

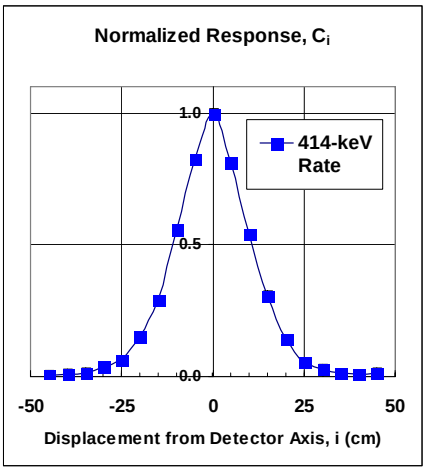

Fig. 6. The normalized count rate of the ^{239}Pu 414-keV peak vs source position. This radial response was measured at 40 cm (r_0) with a collimated NaI(Tl) detector.

For a point deposit, the specific mass is the measured mass. The random relative uncertainty, assuming only an error in C, is:

$$\sigma_R(m_P) = \sigma_R(C) \text{ ,} \quad (3)$$

where the $\sigma_R(C)$ is the random uncertainty from counting statistics.[7]

The line calibration uses both the un-normalized axial response C_0 (s^{-1}) and a geometric parameter L that is evaluated from a sum of the normalized radial responses Ci weighted by the distance between the measurement positions.[7-9] The line calibration constant is

$$K_L \text{ (g} \bullet \text{s} \bullet \text{cm}^{-2}) = m_0 \div (L \bullet C_0 \bullet r_0). \quad (4)$$

The specific isotope mass measured at a distance r from a line deposit is:

$$m_L \text{ (g/cm)} = K_L \bullet C \bullet r. \quad (5)$$

This is also called the linear density of the deposit. The random relative uncertainty in the linear density is the same as Equation 3.

The area calibration uses both the un-normalized axial response C_0 (s^{-1}) and a geometric parameter A that is evaluated from a sum of the normalized radial responses Ci weighted by the

area between the axially concentric circles that intersect the measurement positions.[7-9] The area calibration constant is:

$$K_A\ (\mathrm{g} \bullet \mathrm{s} \bullet \mathrm{cm}^{-2}) = m_0 \div (A \bullet C_0) \quad . \tag{6}$$

The specific isotope mass measured as an area deposit is:

$$m_A\ (\mathrm{g/cm}^2) = K_A \bullet C \quad . \tag{7}$$

This is also called the areal density. The random relative uncertainty in the areal density is the same as Equation 3. By adhering to the constraints above, calibration of many geometries is accomplished with a point source.

C. Performing the GGH Measurement and Assay

Because GGH count times are often very short (5–15 s), the random uncertainty can be large for individual measurements. Propagating the uncertainties of the many measurements to get the total holdup in a facility greatly reduces the random error.

The initial assay result is the specific isotope mass for a point, line or area deposit. Three additional corrections are required for equipment attenuation, finite-source dimensions, and the self-attenuation of the deposit. These corrections are described in detail in Reference 6.

D. CORRECTION FOR EQUIPMENT ATTENUATION

The specific mass of a point, line, or area deposit, m_P, m_L, or m_A is corrected for equipment attenuation effects using the formula:

$$CF_{EQ}(Z, E\gamma) = e^{\mu\rho t}, \tag{8}$$

where ρ and t are the density and thickness of the equipment. The corrected masses are

$$m_{P,EQ}\ (\mathrm{g}) = m_P \bullet CF_{EQ}(Z, E\gamma), \tag{9}$$
$$m_{L,EQ}\ (\mathrm{g/cm}) = m_L \bullet CF_{EQ}(Z, E\gamma), \text{ and} \tag{10}$$
$$m_{A,EQ}\ (\mathrm{g/cm}^2) = m_A \bullet CF_{EQ}(Z, E\gamma), \tag{11}$$

respectively. Because the correction is applied linearly, the relative uncertainties in $m_{P,EQ}$, $m_{L,EQ}$ or $m_{A,EQ}$ are unchanged from that in Equation 3.

If no correction for equipment attenuation is performed, the assay results will always be biased low. An estimate of the equipment attenuation based on the best information available gives a result that may be high or low for individual measurements, but the overall result tends to be much better than ignoring the correction altogether. In recent measurements of ^{239}Pu holdup in bulk-processing equipment in glove boxes using the 414-keV gamma ray, values of $CF_{EQ}(Z$, 414 keV) varied from a low of 1.1 (lead-lined gloves) to a high of 6.2 (steel plates on a glove-box floor).

E. CORRECTION FOR FINITE SOURCE DIMENSIONS

1. Finite Sources in Holdup Measurements

The effect of the finite dimension of a point or line deposit is substantial if the deposit width *w* is not small compared to the detector's field of view. The user may choose a measurement distance to minimize the finite-source effect, but in many situations this is not practical.

Figure 7(a) is an example of a holdup measurement where *r* is large compared to the width of the deposit in the vertical pipe. Figure 7(b) illustrates a measurement with the same detector where the diameter of the horizontal overhead duct is four times that of the pipe in Fig. 7(a).

6(a) **6(b)**

Fig. 7. (a) A collimated NaI detector is positioned to measure holdup in the pipe at the location marked by the bar-code label. In this case, the finite-source effect is small. (b) The same detector is positioned at the same distance from a horizontal duct whose diameter is four times that of the pipe in (a). In this case, the finite-source effect may be large.

The correction for the finite-source dimension of a point, line, or area deposit is applied linearly to the respective specific mass, Eqs. (9), (10), or (11), that has been corrected for equipment attenuation. The correction factor for a finite-source effect is always 1 or greater. The respective specific masses corrected for finite-source effects are

$$m_{P,FIN}\ (\mathrm{g}) = m_{P,EQ} \bullet CF_{FIN,P}\ , \tag{12}$$

$$m_{L,FIN}\ (\mathrm{g/cm}) = m_{L,EQ} \bullet CF_{FIN,L}\ , \tag{13}$$

and

$$m_{A,FIN}\ (\mathrm{g/cm^2}) = m_{A,EQ} \tag{14}$$

because

$$CF_{FIN,\mathrm{A}} = 1. \tag{15}$$

Because the finite-source correction is applied linearly, the relative uncertainty is unchanged from that given in Equation 3.

2. Concept of a Finite Source

Figures 8-9 are sketches that illustrate finite line and point deposits.

Fig. 8. The shaded region represents a finite line deposit. It is superimposed on the field of view of the detector. The circles represent the measurement positions for the calibration.

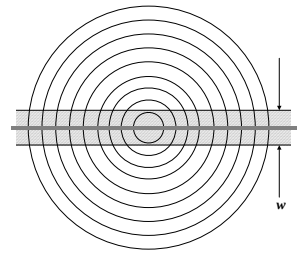

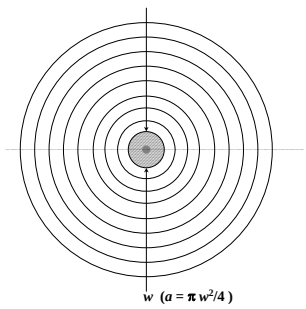

Fig. 9. The shaded area represents a finite point deposit. It is superimposed on the field of view of the detector. The finite point deposit is centered in the field of view.

3. Correcting a Measured Holdup Deposit for Finite Source Dimensions

Knowledge of w is also required for the self-attenuation corrections, as described later. It is important to perform both corrections:

- to avoid a negative bias in the measured holdup (that results from both effects), and
- to reduce the magnitude of the systematic effects associated with over-/under-estimates of the experimental width parameter w.

The six steps to apply finite-source corrections are:

1. Fit the C_i to a normalized Gaussian $G(x)$ that represents the radial response curve.

   $$C(x) = G(x) = \exp[-0.5(2.354\, x / \mathrm{FWHM})^2] , \tag{16}$$

   where "x" is the source distance from the detector axis. Figure 10 is a plot of Eq. (16).
2. Measure a holdup deposit at distance r with finite dimension w.

   $$w_0 = w \bullet (r/r_0)^{-1}. \tag{17}$$

3. Determine the normalized response, $C(w_0/2)$, at the outer edge ($x = w_0/2$) of the line or point from the plot (Figure 10) or from Eq. (16).

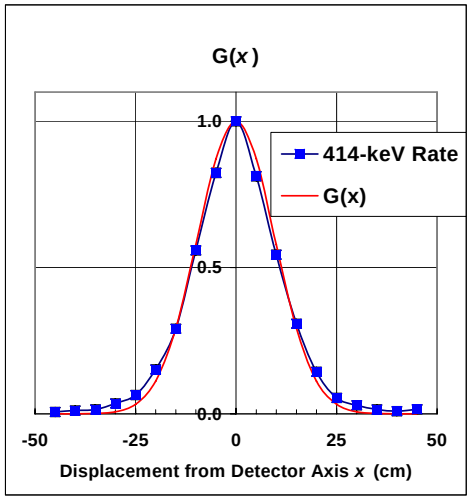

Fig. 10. The data from Fig. 6 are shown in blue. The red curve is the fit of Eq. (16) (normalized Gaussian) to these data.

4. Obtain the average of $C(w_0/2)$, the normalized response at the edge of the deposit, and 1, the normalized response at the center of the deposit, to get the effective radial response

$$C_{EFF} = [\ 1 + C(w_0/2)\ ] / 2. \tag{18}$$

5. Compute the finite-source correction factor for a line or point deposit

$$CF_{FIN,\,L} = (C_{EFF})^{-1}, \tag{19}$$

$$CF_{FIN,\,P} = (C_{EFF})^{-1}. \tag{20}$$

6. Apply the appropriate point or line finite-source correction to the equipment-attenuation corrected specific mass, Eq. (12) or (13).

In recent GGH measurements of plutonium holdup[10] in high-throughput, bulk-processing equipment inside of glove boxes, the values of $CF_{FIN,\,L}$ obtained varied from 1 (for area deposits on glove-box surfaces) to 1.25 (for line deposits of powder accumulated in troughs on the glove-box floor). The procedure described above applies to holdup deposits measured with a cylindrically collimated gamma-ray detector of any type (NaI, BGO, HPGe, CdZnTe, etc.) and any gamma-ray energy.

F. CORRECTION FOR SELF-ATTENUATION EFFECTS

1. Self-Attenuation Effects in Holdup Measurements

A characteristic of special nuclear materials is the self-absorption of gamma rays emitted by the material. The corrections are important for any gamma-ray measurement. The magnitude of the self-attenuation can be determined if the areal density of the deposit (corrected for room background, equipment attenuation, and finite-source effects) is known. Because the atomic numbers (Z) of actinides are large and the actinide density dominates the density of the deposit,

the actinide areal density is sufficient to perform the correction. The key to this correction is that the specific mass of the actinide obtained from the holdup measurement can be converted to the uncorrected areal density of the actinide. The holdup measurement of a point deposit gives the uncorrected mass of the actinide isotope. This can be converted to an uncorrected areal density by dividing by the area *a* of the point deposit, which is

$$a = \pi \bullet (w/2)^2. \tag{21}$$

2. Determining the Self-Attenuation Correction from the Measured Areal Density

The areal density of a deposit is its mass per unit area (g/cm^2). The measured specific mass of a deposit can be used to obtain the actinide areal density, $(\rho x)_{MEAS}$. The true areal density, (ρx), is obtained using this equation:

$$(\rho x)/(\rho x)_{MEAS} = \mu(\rho x)/[1-e^{-\mu(\rho x)}], \tag{22}$$

where μ is the mass attenuation coefficient (cm^2/g) of the element, compound, or mixture at the energy used for the measurement.[11] Rearranging Eq. (22) gives the true areal density (corrected for self-attenuation) as a function of the measured:

$$(\rho x) = - (\ln[1 - \mu(\rho x)_{MEAS}])/\mu . \tag{23}$$

Table 3 lists the μ values for three common forms of uranium deposits (U metal, UO_2 and U_3O_8) and two common plutonium materials.

Table 3.
Gamma-ray Mass Attenuation Coefficients

Material	E_γ (keV)	μ (cm^2/g)
U	186	1.46
UO_2	186	1.30
U_3O_8	186	1.26
Pu	414	0.270
PuO_2	414	0.250

3. Correcting a Measured Holdup Deposit for Self-Attenuation

An over- or underestimate of *w* leads to an under- or over-correction for self-attenuation. This is opposite the case of the finite-source correction. Thus, for a limited range of deposit thickness, the effects of errors in the estimates of *w* tend to compensate when both corrections are performed. Unlike the other corrections, the correction for self-attenuation, Eq. (22), is a nonlinear function of the specific mass of the deposit and it must be applied after the other corrections. For the same reason, and because the self-attenuation is determined from the areal density of the deposit, the isotope fraction must be used to convert the measured areal density of the isotope to that of the element. If more than one actinide is present, both the element and isotope fractions are multiplied for use in the conversion step.

For measurements of ^{239}Pu in bulk-processing equipment inside glove boxes using the 414-keV gamma ray, the magnitude of the correction for self-attenuation was as large as 1.11 for powder deposits on the glove-box floor.

The procedure for self-attenuation corrections is currently automated[12] in the stand-alone VisualBasic program *SelfAttn v. 1.0*. The automation is possible because of the simplicity of the approach. This software module is incorporated into the HMS3 software, which automates the plant-wide portable measurement and tracking of holdup.[13, 14]

IV. HOLDUP MEASUREMENT SYSTEM EXAMPLES

The Integrated Holdup Measurement System at the Y-12 HEU plant in Oak Ridge, Tennessee, is a good example of a comprehensive holdup measurement system.[15] The Y-12 facility identified many thousands of measurement points, each marked with a bar code label. Operators carry a small multichannel analyzer (MCA), a collimated NaI detector, and a handheld bar code reader with a data logger/controller. Thousands of locations are measured each month. Data from the data logger are downloaded into a computer running a program called HMS4. This has been used successfully for more than seven years. An extensive study was made of system performance using simulated holdup situations such as pipes, ducts, and V-blenders with known U or Pu sources. Figure 11 below shows a technician at Y-12 measuring an overhead duct.

Fig.11. GGH applied in a uranium facility to measure an overhead duct.

Figure 12 shows a similar measurement system in use at a plutonium processing facility. In this case a telescoping pole, such as used by house painters, is used to position the NaI detector near the overhead pipes and ducts. Figures 13 and 14 show other ^{235}U holdup measurements in a uranium processing facility using Ge, CZT, and NaI detectors. Figure 13 shows a very large overhead duct being measured with a portable Ge detector weighing ~10 kg with collimator. Figure 14 shows CZT and NaI detectors weighing ~1 kg each with collimators. The greater portability of the room-temperature detectors is essential for most holdup measurements.

Fig. 12. A compact NaI detector is shown during measurements of plutonium deposits in overhead ducts.

Fig. 13. A large overhead duct is measured from below with a collimated Ge detector.

Fig. 14. Measurements of ^{235}U deposits in a filter system performed with CZT and NaI.

The Rocky Flats Plant near Denver, Colorado, was closed in 1989, dismantled, cleaned, and converted into an environmental park. During its operating lifetime (~40 y), Rocky Flats accumulated large quantities of plutonium holdup in the gloveboxes, filters, calciners, pipes, and air ducts of several major processing buildings. This holdup was a significant health and criticality safety concern, and at times was a major contributor to the MUF for the facility.

During the decommissioning of the processing buildings, the holdup measurement campaigns were among the largest and most extensive ever reported. The holdup measurement teams pioneered the use of medium-resolution BGO detectors, and the use of measurements made with the detectors in contact with pipes or ducts. Although this approach is more susceptible to uncertainties in material distribution than the GGH methodology, it allows routine measurements to be made more quickly. As buildings were decommissioned and the process lines were removed and cleaned out, it was often possible to obtain comparisons between the measured holdup and cleanout values. The overall results of numerous measurements of extended equipment lines tended to be unbiased.[16]

V. NEUTRON HOLDUP MEASUREMENTS

Nuclear material processing equipment can be massive and extensive. High-throughput facilities may contain multi-kilogram deposits. The high attenuation of such equipment and deposits may challenge the capability of gamma-ray holdup measurements. In such cases, the high penetrability of neutrons may offer a more reliable option. Neutrons can be detected from pumps, furnaces, and other heavy equipment that are too dense to permit gamma rays to escape. It is difficult to shield neutron detectors from room background, but counting coincident neutrons from spontaneous fission can effectively reduce background. Large polyethylene-moderated, ^{3}He slab detectors have been used successfully to quantify in-process plutonium in glove boxes. Although the spontaneous-fission neutron yield from uranium is low for coincidence counting, the high α, n yield from fluorine enables measurements of uranium deposits using total neutrons from UF_6 and UO_2F_2 in enrichment plants.

Light weight, directional, portable neutron counters are difficult to design because of the need for a polyethylene moderator surrounding the ^{3}He tubes. However, several reasonably portable detectors have been designed and used for holdup measurements. The original portable counter was the Shielded Neutron Assay Probe (SNAP-II) fabricated in 1975 (see Figure 15). The SNAP-II had two 20-cm-long ^{3}He tubes in a 12.7-cm-diam polyethylene cylinder, wrapped in cadmium and surrounded for 240° by a 5.7-cm-thick directional shield. The intrinsic efficiency of the SNAP-II for fission neutrons was ~17% and it weighed ~10 kg. The SNAP-II was used to measure uranium holdup in operating and shut down gaseous diffusion enrichment plants and plutonium holdup in several scrap recovery facilities.

Fig. 15. Shielded Neutron Assay Probe (SNAP-II) used for U and Pu holdup measurements in heavily shielded situations.

The Portable Handheld Neutron Counter (PHNC) shown in Figure 16 is a newer counter with four ^{3}He tubes. The PHNC has no directionality, but it is more efficient and weighs less than the SNAP-II. The PHNC is designed for either singles counting of wide-area holdup sources or coincidence counting, with two PHNC slabs, of small containers of Pu materials.[17]

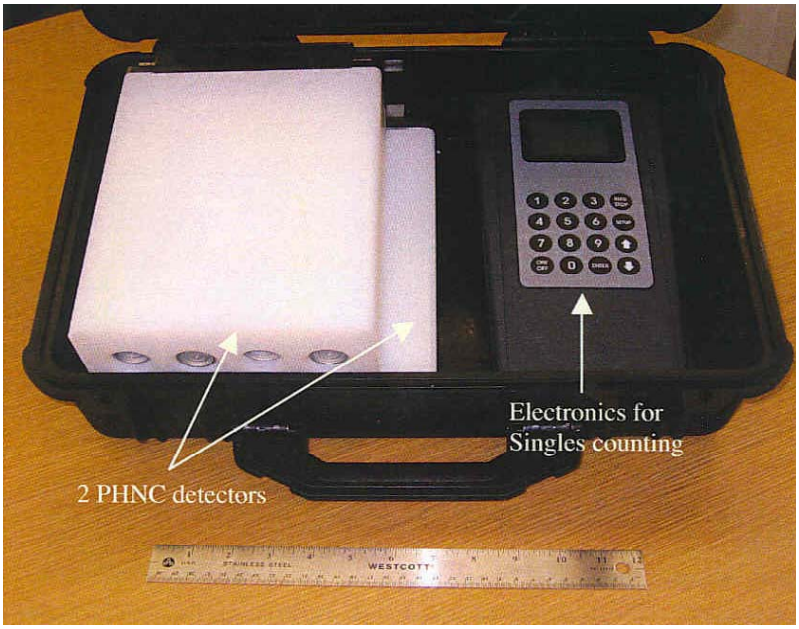

Fig. 16. Two Portable Handheld Neutron Counters (PHNC) and a related electronics package.

Large slab detectors can provide higher efficiency and better directionality if heavy shielding and collimation are added. Such detectors are too heavy for handheld operation, but they can be moved with carts or can be permanently installed to measure in-process inventory or holdup after cleanup. The slab detectors shown in Figure 17 were designed to measure holdup and in-process inventory at uranium enrichment plants.

Fig. 17. Wide-area neutron detectors used to measure holdup at uranium enrichment plants.

A new neutron holdup assay method for enrichment facilities, or in any facility with a large distributed volume of material, was recently described.[18] The Distributed Source-Term Analysis

(DSTA) technique uses Monte Carlo modeling of a centrifuge enrichment cascade hall to derive a calibration curve relating the average neutron count rate to the mass of uranium holdup. Then a portable counter, similar to the PHNC, is used to survey the average neutron count rate in the hall. This approach avoids the high attenuation problems of gamma-ray measurement, the difficulties in measuring individual pieces of equipment to obtain the total holdup, and the long measurements required to assay the entire process line.

Large slab detectors have also been used to measure plutonium holdup in rotary calciners, hydrofluorinators, and other large, highly attenuating items. Two slab detectors, each 50-cm tall by 100-cm-wide by 8-cm-thick polyethylene with ten 90-cm-long ^{3}He tubes, were placed in a rack and moved to various locations around a rotary calciner used to dry plutonium peroxide. The calciner was inside a glove box. The quantity of holdup was sufficiently high to use neutron coincidence counting, so the measurements were less sensitive to background neutrons. The detectors were calibrated with a 2-kg PuO_2 standard. After one of the measurement campaigns, the calciner was cleaned out and the recovered plutonium measured. The holdup assay agreed very well with the recovery value.[19]

Large neutron slab detectors have been used in the Plutonium Fuel Production Facility (PFPF) in Tokai-Mura, Japan, to measure holdup in glove boxes inside this automated MOX fuel fabrication facility.[20] These Glove Box Assay Systems (GBAS) were 160 cm high, 100 cm long, and 7.6 cm wide (see Figure 18). Each slab contained twenty 152-cm ^{3}He tubes. Monte Carlo calculations were used to design the detector and study its response before installation. Six slabs were originally installed in pairs on either side of a glove box. The slabs could be moved remotely to measure different locations on a glove box. A standard matrix of measurement positions was assigned for each glove box and software written to collect, analyze, and combine all the measurements. Measurement data from this system are shared by the IAEA and the facility operator. Experience at PFPF has shown a measurement uncertainty of ~5% for neutron assay and 25-30% for gamma-ray assay.

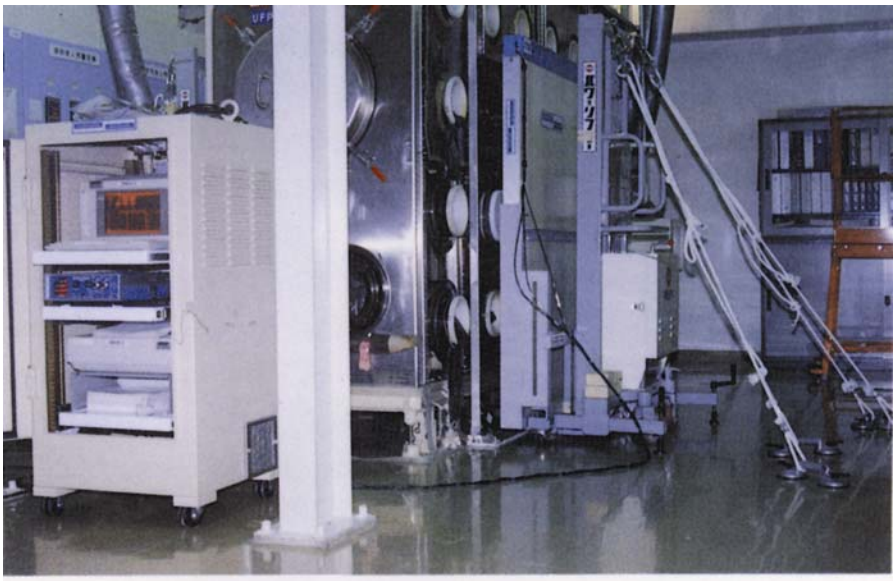

Fig. 18. Glove Box Assay System (GBAS) installed at PFPF in Tokai-mura, Japan.

VI. ACCURACY OF HOLDUP MEASUREMENTS

The precision or random error can be readily determined for all NDA measurements including holdup. Because of the many measurements performed, the overall precision is usually of the order of a few percent or less. However, the accuracy or systematic error is very difficult to determine, because it is difficult to know the true mass of nuclear material held up in the equipment of a complex facility. Often, the accuracy estimate for a holdup campaign is simply the "best guess" of the operator based on judgment and experience. Such estimates are typically in the range 25 - 50% or more, because of the many unknown factors and assumptions required to calculate the nuclear material mass. In some cases, e.g. glove boxes, known standards can be introduced and measured in addition to the holdup. In a few cases, an effort was made to clean out and recover the measured material which was then analyzed destructively and compared with the measured holdup. A complete clean out is usually difficult and costly, but this is the best way to determine holdup assay accuracy.

In the early 1980s, a holdup measurement campaign was conducted at a shut down part of the Portsmouth Gaseous Diffusion Plant in Piketon, Ohio. Gamma-ray measurements were made with a collimated NaI detector and neutron measurements were made using the slab detectors shown in Figure 17. A total of approximately 250 stages (converter, cooler, compressor, and piping) were measured during the campaign. Afterwards, three cells (12 stages each) were cleaned out and the uranium recovered. The U was also measured and recovered from an isolated converter. The results from this are summarized in Table 4. Because the gamma-ray measurements only covered the converters, they should only be compared with the neutron assay of the isolated converter. These results are typical of what one finds in such holdup studies.[21]

A six-year study was conducted on the accuracy and precision of holdup measurements using the GGH (gamma ray assay) approach to measure simulated holdup situations with well known nuclear material standards. A series of simulated holdup sources were fabricated for this study and a holdup training course; they included a pipe array, a steel pipe, an aluminum pipe, a rectangular ventilation duct, a V-Blender, and a contaminated spot on a floor. These were "salted" with U or Pu fuel rods, U metal foils, and small cans of UO_2 or PuO_2. Table 5 summarizes the results of this study which included measurements made by many people from students to holdup experts. The results shown here are "best case" vis-à-vis holdup assay accuracy.[22]

Table 4. Evaluation of PGDP Holdup Assay

Cell	**n kg U[a]**	**γ kg U[b]**	**Recovery kg U**
A	177	45	120
B	32	3	28
C	29	12	25
isolated converter	9	10	7

a. The neutron counters were not well collimated and measured an entire stage and double-counted the cooler.
b. Gamma-ray measurements covered only the converters.

Table 5. GGH Holdup Assay Evaluation

	^{235}U[a]	^{239}Pu[a]
pipe array	0.90	0.72
V-blender	1.22	1.02
Al pipe	1.03	0.97
Steel pipe	0.97	1.47
floor spot	0.96	n/a
duct	1.07	0.96

a. Number listed is the average ratio of measured U or Pu to the reference value.

The Rocky Flats Environmental Technology Site (RFETS), located near Denver, contained 802 buildings. The plant, which manufactured plutonium parts for nuclear weapons, was closed in 1989 and subjected to a 10-year cleanup campaign that ended in 2005 when RFETS was turned into a national wildlife refuge. During this period, 3.5 x 10^5 m^2 of buildings were dismantled and over 220 kg of plutonium holdup measured by a staff of 15. Holdup measurements included nearly 7 km of ductwork (~3 gPu/m), 1497 gloveboxes, and over 300 plutonium process tanks. Gamma-ray measurements were performed using HPGe and Bismuth Germanate detectors and the GGH procedures (see Figure 19). All of the measured equipment was cleaned out and the recovery values can be compared with the pre- and post-cleanout NDA holdup measurements. The cleanout data were generally within 20% of the measured holdup. Some specific building values are listed in Table 6.[23]

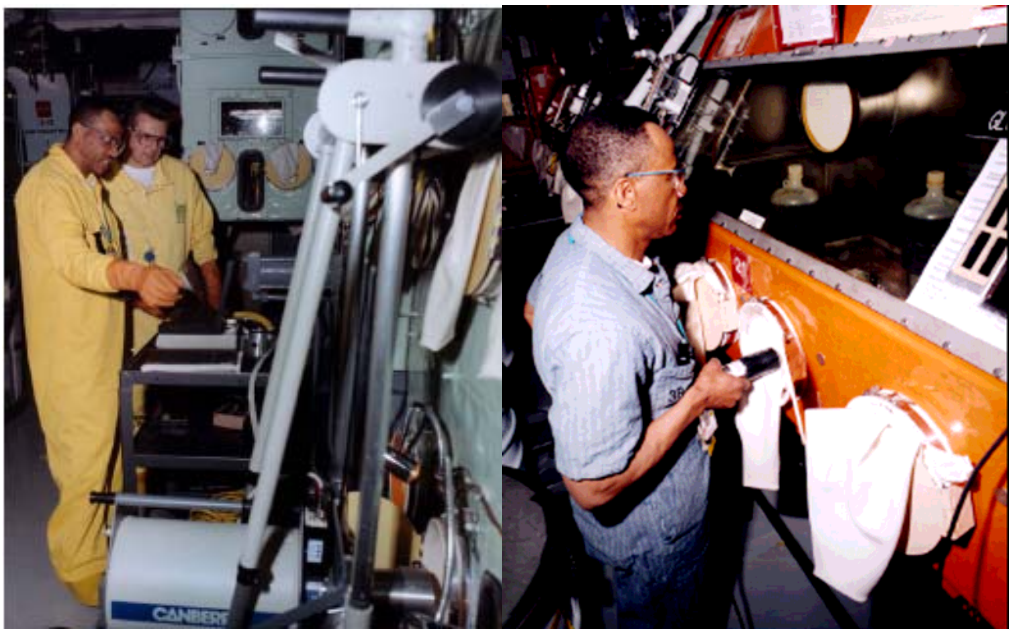

Fig. 19. Holdup measurements at RFETS: Ge on left, BGO on right.

Table 6. RFETS Holdup Data

Building	Measured/Recovered Pu
B-371 Gloveboxes	1.09
B-307 Ductwork	1.06
B-779 Total Holdup	1.13
B-A Total Holdup	1.17
B-B Total Holdup	0.97
B-C Total Holdup	1.04
B-D Total Holdup	1.03

VII. SUMMARY

A generally useful approach to the quantitative measurements of holdup invokes simple, geometric models (point, line, and area, GGH). The result is that simple calibration procedures and assay algorithms apply to most deposits. Corrections are applied for room background, equipment attenuation, the finite dimensions of point and line deposits, and the self-attenuation of gamma rays by the deposit. Knowledge of the width of a point or a line deposit is sufficient to perform the finite-source and self-attenuation corrections. The error in the finite-source correction from uncertain knowledge of the width parameter is partially cancelled by an error of the opposite sign in the self-attenuation correction. For area deposits, only the self-attenuation correction applies. It is independent of an additional parameter and is determined directly from the uncorrected holdup result.

There is a tendency for the relative finite-source effects to be larger for holdup measurements of ^{239}Pu and for the self-attenuation effects to be larger for holdup measurements of ^{235}U. This is a result of the gamma-ray assay energy. The higher energy gamma ray from ^{239}Pu penetrates the detector shield readily, causing users to measure closer to the deposits. A relative enlargement of the finite source dimension is the result of the reduction in the detector's field of view at the smaller measurement distance. The lower energy gamma ray used to measure ^{235}U is more affected by self-attenuation. However, the detector shielding is quite effective at eliminating room background, causing users to perform measurements at greater distance from the deposits. The result is a reduction in the relative finite source dimension.

A major source of bias arises from the relatively poor resolution of the portable, compact scintillator detectors that are used for holdup measurements. Effects of interfering gamma rays from complex spectra can contribute to a positive or negative bias in the holdup result obtained from measurements with scintillators. The portability of a room-temperature detector cannot be sacrificed in holdup applications. Therefore, recent progress in the manufacturing of large, room-temperature, solid-state gamma-ray detectors that perform better than scintillators is a welcome advance in technology for improved accuracy in holdup measurements.

REFERENCES

1. N. Ensslin and H. A. Smith, Jr., "Attribute and Semiquantitative Measurements," D. Reilly, N. Ensslin, H. Smith, and S. Kreiner, *Passive Nondestructive Assay of Nuclear Materials*, Chapter 20, NUREG/CR-5550, March 1991.

2. H. Preston and W. Symons, "The Determination of Residual Plutonium Masses in Gloveboxes by Remote Measurements Using Solid Thermoluminescent Dosimeters," AEA report AEEW-R1359, Winfrith, UK (1980).

3. R. A. Dewberry, S. R. Salaymeh, V. R. Casella, and F. S. Moore, HEU Measurements of Holdup and Recovered Residue in the Deactivation and Decommision Activities of the 321-M Reactor Fuel Fabrication Facility at the Savannah River Site, Savannah River National Laboratory report WSRC-MS-2004-00792.

4. P. N. Luke and E. E. Eissler, "Performance of the CdZnTe Coplanar-Grid Detectors," *IEEE Trans. Nucl. Sci.*, **43**, No. 4, pp. 207–213 (August 1995).

5. M. Talbot and M. Minette, "Closed-Down and Decommissioned Facilities Hanford PFP Experiences," INMM International Workshop of Best Practices for Material Hold-Up Monitoring, Oak Ridge, TN, October 29 – November 3, 2006 (www.inmm.org).

6. P. A. Russo, "Gamma-Ray Measurements of Holdup Plant-Wide: Application guide for Portable, Generalized Approach," Los Alamos National Laboratory report LA-14206, November 2004.

7. "Nondestructive Assay of Special Nuclear Materials Holdup," Los Alamos National Laboratory training manual LA-UR-99-2597 (August 1999 or earlier versions, beginning in February 1991).

8. P. A. Russo, H. A. Smith, J. K. Sprinkle, Jr., C. W. Bjork, G. A. Sheppard, and S. E. Smith, "Evaluation of an Integrated Holdup Measurement System Using the GGH Formalism with the M^3CA," *Proceedings of the Fifth International Conference on Facility Operation – Safeguards Interface*, LaGrange Park, IL, American Nuclear Society (1996), pp. 239-248.

9. J. K. Sprinkle, Jr., R. Cole, M. L. Collins, S.-T. Hsue, P. A. Russo, R. Siebelist, H. A. Smith, Jr., R. N. Ceo and S. E. Smith, "Low-Resolution Gamma-Ray Measurements of Process Holdup," Los Alamos National Laboratory report LA-UR-96-3482, presented at the *Third Topical Meeting on Industrial Radiation and Radioisotope Measurements and Applications*, Raleigh, North Carolina, October 1996.

10. P. Russo, M. Sumner, T. K. Li, H. Menlove, and T. Wenz, "Quantitative Verification of In-Process Inventory of High-Burnup Plutonium Using Room-Temperature Gamma-Ray

Detectors and the GGH Formalism," Los Alamos National Laboratory report LA-12953-PR, March 1997, pp. 37–48.

11. J. L. Parker, "Attenuation Correction Procedures," *Passive Nondestructive Assay of Nuclear Materials*, D. Reilly, N. Ensslin and H. Smith, Jr, and S. Kreiner, Eds., NUREG/CR-5550, LA-UR-90-732, Chapter 6, March 1991, National Technical Information Service, Springfield, VA.

12. J. B. Glick, F. X. Haas, A. G. Garrett, P. A. Russo, G. A. Sheppard, M. C. Miller, E. C. Piquette, and T. R. Wenz, "A New Approach to Performing Holdup Measurements on Glove Box Exhausts, *Nucl. Mater. Manage.* **XXI** (Proc. Issue) 64–67 (1991).

13. F. X. Haas, J. B. Glick, J. N. McKamy, A. G. Garrett, P. A. Russo, G. A. Sheppard, T. R. Wenz and M. C. Miller, "Holdup Measurements of Plutonium in Glove Box Exhausts," *Proceedings of the Fifth International Conference on Facility Operation – Safeguards Interface*, LaGrange Park, IL, American Nuclear Society (1991), pp. 237–242.

14. P. A. Russo, S. E. Smith, and J. F. Harris, "Self-Attenuation and Finite-Source Corrections for Holdup Measurements Automated by the HMS3 Software," Los Alamos National Laboratory report LA-UR-99-4442, August 1999.

15. P. A. Russo, H. A. Smith, J. K. Sprinkle, Jr., C. W. Bjork, G. A. Sheppard, and S. E. Smith, "Evaluation of an Integrated Holdup Measurement System Using the GGH Formalism with the M^3CA," *Proceedings of the Fifth International Conference on Facility Operation – Safeguards Interface*, LaGrange Park, IL, American Nuclear Society (1996), pp. 239-248.

16. F. W. Lamb, "A Frank Look at Lessons Learned During Holdup Measurements at RFETS: Part 2 - Measurements," Rocky Flats Environmental Technology Site report RFP#5560 (April 2005) to be published in the *Journal of Nuclear Material Management*.

17. H. O. Menlove, "Manual for the Portable Handheld Neutron Counter (PHNC) for Neutron Survey and the Measurement of Plutonium Samples," Los Alamos National Laboratory manual LA-14257-M, November 2005.

18. D. H. Beddingfield and H. O. Menlove, "A New Approach to Hold-Up Measurement in Uranium Enrichment Facilities," Los Alamos National Laboratory report LA-UR-00-2534, *Nucl. Mater. Manage.* **XXIX** (Proc. Issue) CD-ROM (2000).

19. D. B. Smith, "Safeguards and Security Progress Report, January-December 1985," Los Alamos National Laboratory report LA-10787-PR, March 1987, pp. 9-14.

20. M. C. Miller, H. O. Menlove, M. Seya, S. Takahashi, and R. Abedin-Zadeh, "Holdup Counter for the Plutonium Fuel Production Facility--PFPF," Los Alamos National Laboratory report LA-UR-90-2312, published in *Nucl. Mater. Manage.* **X** (Proc. Issue July 1990).

21. D. B. Smith, "Safeguards and Security Progress Report, August 1982-January 1983," Los Alamos National Laboratory report LA-9821-PR, November 1983, pp. 11-17.

22. P. A. Russo, et. al., "Evaluation of the Integrated Holdup Measurement System with the M3CA for Assay of Uranium and Plutonium Holdup," Los Alamos National Laboratory report LA-13387-MS, August 1999.

23. F. Lamb, “Facility and Process Characterization Kickoff,” Eagle Research Group presentation at INMM International Workshop of Best Practices for Material Hold-Up Monitoring, October 29 – November 3, 2006, Oak Ridge, TN, www.inmm.org.

6. PASSIVE NEUTRON MULTIPLICITY COUNTING

N. Ensslin, M. S. Krick, D. G. Langner, M. M. Pickrell, T. D. Reilly, and J. E. Stewart

6.1 INTRODUCTION

6.1.1 Purpose of the Chapter

A nondestructive assay (NDA) technique for plutonium, called passive neutron multiplicity counting, has been developed as an extension of neutron coincidence counting (Ref. 1). The new technique has led to the design and fabrication of neutron multiplicity counters, one of which is pictured in Figure 6.1. The development of new neutron counters has been accompanied by advances in data-processing electronics, analysis algorithms, and data-analysis software. Development activities have been funded primarily by the Department of Energy (DOE) Office of Security Policy, Technology Development Branch. The new technology has led to significantly better measurement accuracy for plutonium metal, oxide, scrap, and residues.

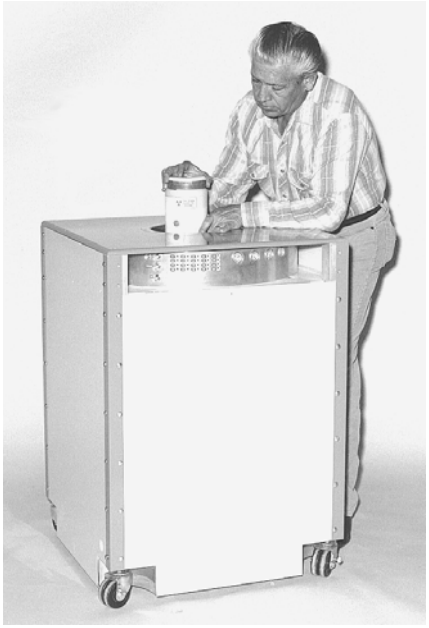

Fig. 6.1. *Photo of the Plutonium Scrap Multiplicity Counter, used for accurate assays of plutonium metal, oxide, mixed oxide, or scrap .*

This chapter describes the principles of multiplicity counter design, electronics, and mathematics. Existing counters are surveyed, and their operating requirements and procedures are defined. Current applications to different plutonium material types are described and estimates of the expected assay precision and bias are given.

6.1.2 Definition of Neutron Multiplicity Counting

Multiplicity is a word with a multiplicity of meanings! Our use of the word begins with the fact that an important NDA signature for plutonium is spontaneous fission, leading to the nearly simultaneous emission of multiple, indistinguishable neutrons. The number of neutrons emitted in spontaneous fission can vary from zero to eight. The distribution of the number of neutrons is

called the multiplicity distribution. The multiplicity distributions for spontaneous fission in ^{240}Pu and the 2-MeV-neutron-induced fission for ^{239}Pu are illustrated in Figure 6.2.

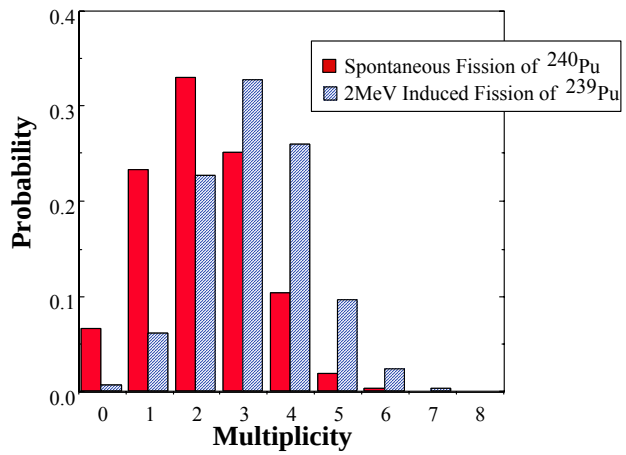

Fig. 6.2. *The spontaneous fission multiplicity distribution for ^{240}Pu and the 2-MeV-neutron-induced fission multiplicity distribution for ^{239}Pu.*

Multiplicity counting sums up separately the number of 0, 1, 2, 3, 4, 5, 6, 7, etc. neutrons within the coincidence resolving time or "gate width" of the electronics package. This measures the multiplicity distribution of neutrons that are emitted, detected, and counted within the gate width. For this reason, the word multiplicity is specifically associated with the extension of conventional coincidence counting to the collection of higher-order multiples of neutrons. However, we also associate the word multiplicity with a special neutron counter design and with the mathematics of the data analysis process.

In practice, multiplicity data analysis is usually not based directly on the observed multiplicity distribution, but on its factorial moments. The first moment is the "singles," or "totals," the second factorial moment is the "doubles" or "reals," and the third factorial moment is the "triples." Neutron multiplicity analysis works with all three of these moments, whereas conventional coincidence counting only uses the singles and doubles. Thus, when we use the word "multiplicity," we really mean that we add a third measured parameter, triple coincidences.

6.1.3 Basic Principle of Neutron Multiplicity Counting

Coincidence counting is an NDA technique that extracts quantitative information from the neutrons emitted by plutonium. Ideally, this information should determine the actual grams of ^{240}Pu-effective in the sample, where this is defined as the mass of ^{240}Pu that would give the same double coincidence response as that obtained from all the even isotopes in the sample:

$$^{240}Pu_{eff} = 2.52\,^{238}Pu + ^{240}Pu + 1.68\,^{242}Pu\,. \tag{6-1}$$

Gamma-ray spectroscopy or mass spectroscopy is then used to obtain the isotopic composition of the plutonium, which makes it possible to obtain the total Pu mass:

$$^{Total}Pu = ^{240}Pu_{eff} / (2.52\, f_{238} + f_{240} + 1.68\, f_{242})\,, \tag{6-2}$$

where f_{238}, f_{240}, and f_{242} are the fractions of the plutonium isotopes present in the sample.

In practice, the neutron flux emitted by the sample can be affected by a number of usually unknown, or incompletely known, sample or detector properties. The list of potentially unknown parameters includes the following:

1. Spontaneous fission rate–the goal of the assay,
2. Induced fission, or sample self-multiplication, and its variation across the sample,
3. The (α,n) reaction rate in the sample,
4. The energy spectrum of the (α,n) neutrons,
5. Spatial variation of the neutron multiplication,
6. Spatial variation in neutron detection efficiency,
7. Energy spectrum effects on detection efficiency,
8. Neutron capture in the sample, and
9. The neutron die-away time in the detector.

Clearly there are potentially more unknowns than conventional coincidence counting can determine. We need N measured parameters to solve for N unknown parameters. Conventional coincidence counting provides only two measured parameters, singles and doubles.

The basic principle of neutron multiplicity counting is the use of a third measured parameter, the triples, so that one can solve for three unknown sample properties, typically the fission rate (mass $^{240}Pu_{eff}$), sample self-multiplication, and the (α,n) reaction rate. The fourth and fifth unknowns are discussed in sections 6.6.5 and 6.5.8. The sixth and seventh unknown parameters, related to detection efficiency, are usually eliminated as unknowns by careful counter design and calibration. The other potential unknowns are usually less important, and are assumed to be small or constant.

Because we are solving three equations for three unknowns, the solution is exact, complete, and self-contained! This has some interesting consequences. For samples that meet the assumptions in the derivations, the assay is bias free and accurate within counting statistics. However, if a sample does not meet the assumptions, the assay may be biased. In principle, there is no need for calibration with physical plutonium standards, but it is nevertheless important to use standards for validation and bias reduction.

6.1.4 Historical Reasons for Multiplicity Counting

Historically, the benefit of passive neutron counting has been the great penetrability of neutrons. Neutrons are often the only way to rapidly assay large, dense samples. Neutrons can usually measure the entire volume of the item and they are not easily shielded, except by hydrogenous materials with or without neutron poisons such as boron. The first neutron instruments used only the total neutron count rate. However, very few plutonium materials could be accurately assayed, as implied by the long list of potential unknowns presented above.

The next development was neutron coincidence counting, which uses the spontaneous fission signature and is not affected directly by (α,n) neutrons. Coincidence counting has had wide application for international safeguards inspections. It has had a more limited application domestically because large errors can occur when measuring impure materials. The fundamental limitation of coincidence counting is that it measures only two parameters. For a typical sample, there are at least the first three unknowns listed above. Therefore, it is usually not possible to obtain accurate assays of impure samples with conventional coincidence counting. One must either assume that the (α,n) rate is known, and solve for mass and self-multiplication (Ref. 2), or assume that self-multiplication is known, and solve for mass and (α,n) rate. If the assumed information is incorrect, large errors can occur. In fact, for many impure or heterogeneous samples, neither the multiplication nor the (α,n) yield can be known beforehand.

Based on the need for better accuracy, the goal of neutron multiplicity analysis is to correctly assay in-plant materials without prior knowledge of the sample matrix. The availability of a third measured parameter makes this possible for many materials, including moist or impure plutonium oxide, oxidized metal, and some categories of scrap and waste. For the design of neutron multiplicity counters, the goal is to obtain detection efficiencies that are high and nearly independent of the sample matrix. A useful multiplicity counter should also provide relatively fast assays. At present, a practical goal for assay precision is 1% relative standard deviation (RSD) in l000 s. The limiting factor here is the poorer precision of the triples.

6.1.5 Areas of Application for Multiplicity Counting

Passive multiplicity counting has applications in a number of different areas: improved materials accountability measurements, verification measurements, confirmatory measurements, and excess weapons materials inspections. Although the historical motivation for developing the technique was improved accountability measurements of impure plutonium, new applications have arisen in the areas of verification and confirmation because the technique does not require prior knowledge of the sample, or prior calibration with standards. For similar reasons, multiplicity counting is coming into use for IAEA inspections of excess weapons materials, where the goal is to verify materials with limited production records.

Multiplicity counting can be used for all plutonium samples, but the additional information is beneficial primarily on impure samples. For some material categories multiplicity may not be helpful because of the limited precision of the triple coincidences. These materials include small Pu samples, some Pu-bearing waste, or process residues that are so impure that the high (α,n) reaction rate ruins the precision of the triples. For pure Pu metal or oxide, the additional multiplicity information is not needed, and conventional coincidence counting provides better precision and sufficient accuracy. However, if there are any doubts about the Pu purity, the multiplicity and conventional results can be compared, and the more accurate result can be used. Additional information on multiplicity applications and expected performance is provided in Section 6.7.

6.1.6 Advantages and Disadvantages of Multiplicity Counting

The advantages of multiplicity counting are summarized in the following list:

1. The measurement accuracy for impure Pu is much greater than for conventional coincidence counting.
2. Information on sample self-multiplication and (α,n) reaction rate is obtained.
3. Calibration for many material types does not require representative standards.
4. Typical measurement time, 1000–2000 s, is short compared to other techniques.
5. If a high-efficiency multiplicity counter is used for conventional coincidence counting, one can use very short counting times, and obtain somewhat better accuracy.

The disadvantages of multiplicity counting are as follows:

1. Multiplicity counters are more costly than conventional coincidence counters.
2. Multiplicity counters requires somewhat more floor space and height than conventional counters of the same cavity size.
3. The measurement time for good precision on triples, typically 1000–2000 s, is longer than the 100–300 s counting time used for most conventional coincidence assays.
4. For plutonium samples that do not meet the analysis assumptions, some assay biases still remain. These biases must be removed using correction factors, special calibration procedures, physical standards, or calorimetry on outliers.

6.2 MULTIPLICITY COUNTER DESIGN PRINCIPLES

6.2.1 Multiplicity Counter Design Goals

The development of multiplicity counting has led to the development of a new generation of thermal neutron multiplicity counters. Like coincidence counters, multiplicity counters are thermal neutron well counters that use ^{3}He tubes embedded in polyethylene. However, their design represents an advance in the state-of-the-art. The overall goal of the design process is to minimize the effects of detector-dependent variables, such as those summarized in Section 6.1.3. In terms of these variables, the goals for multiplicity counter design include the following:

1. Maximize the detection efficiency to increase the triple coincidence count rate, which is proportional to the third power of the efficiency, typically 40% - 60%.
2. Minimize deadtime losses by substantially increasing the number of preamp/discriminator circuits used to read out the ^{3}He tubes, as described in Section 6.4.3. Multiplicity counters utilize 20 or more circuits, as compared to 6 in conventional counters. The triples rate is much more sensitive to electronic deadtime than the doubles and singles rates.
3. Minimize the detector die-away time to decrease accidental coincidences and thereby improve the "signal-to-noise" ratio for triples.
4. Minimize the effects of sample placement, or variable plutonium distribution, by making the radial and axial efficiency profile of the sample cavity as flat as possible.
5. Minimize the influence of the emitted neutron energy spectrum on the efficiency.

6.2.2 Monte Carlo Design Calculations

In the design of multiplicity counters, Monte Carlo (MCNP) and Figure of Merit codes are used to supplement what has been learned from past designs of conventional coincidence counters. The codes can be used to study design choices such as tube placement; number, size, and gas pressure of tubes; tube bank layout; placement of different neutron moderator or reflector materials; the use of cadmium liners; etc. After the design and fabrication of the counter is completed, the counter's actual efficiency, die-away time, efficiency profiles, and counting precision are compared with the calculations. The results so far have been in excellent agreement, validating this approach. A recent version of the Monte Carlo code, MCNPX, can directly simulate the singles, doubles, and triples count rates from a known neutron source (Ref. 3). Monte Carlo design calculations are typically performed to a 1-sigma precision of 0.5% to 1.0%. Figure 6.3 is a schematic used in the Monte Carlo design of the Plutonium Scrap Multiplicity Counter pictured in Figure 6.1.

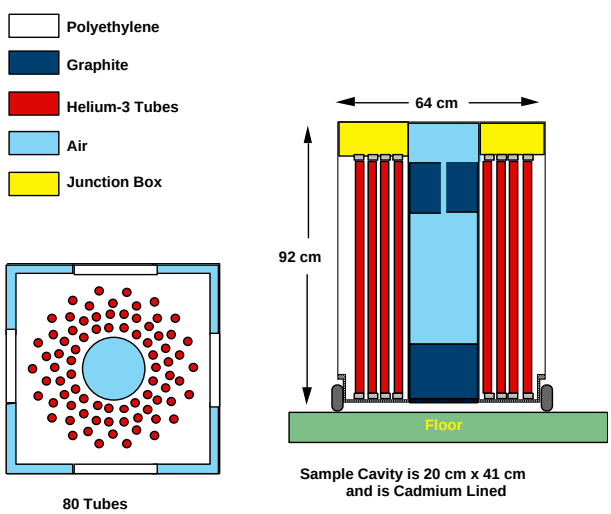

Fig. 6.3. *Monte Carlo Design schematic for the Plutonium Scrap Multiplicity Counter (Ref. 2).*

The MCNP code can be used to calculate the expected detection efficiency as a function of neutron energy to test the "flatness" of the multiplicity counter design. Multiplicity counters achieve their flat response largely through the use of multiple rings of ^{3}He tubes placed at different depths in the polyethylene moderator. Figure 6.4 plots the relative count rate for the four rings in the Pyrochemical Multiplicity Counter as a function of neutron energy. The Pyrochemical Multiplicity Counter has 4 rings of ^{3}He tubes and is specifically designed to measure samples with variable (α, n) yields and neutron energies. Each ring responds differently, but the sum of all four is nearly constant.

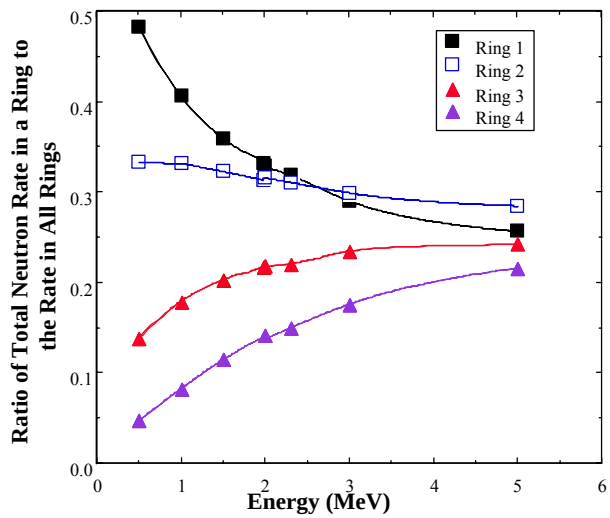

Fig. 6.4. *Relative count rates for the four rings in the Pyrochemical Multiplicity Counter as a function of neutron energy. Ring 1 is the inner ring.*

6.2.3 Figure of Merit Calculations

Because MCNP provides an estimate for the efficiency and die-away time, a Figure of Merit code can be used to determine the optimum design needed to achieve the desired measurement precision. One Figure of Merit code developed for multiplicity counting analysis (Ref. 4) determines assay variance from the neutron multiplicity distribution. This distribution is predicted from the detector design parameters obtained from MCNP. The expected values of the sample mass, self-multiplication, and (α,n) reaction rate, and the count time, electronic gate width, and pre-delay are entered into the code which then predicts the expected single, double, and triple count rates, and determines the assay variance.

Once the sample mass and size range have been defined, these calculations can be used to define the target efficiency and die-away time needed to obtain a given assay precision in a given time. Figure 6.5 illustrates the expected assay precision vs. ^{240}Pu mass for plutonium oxide samples in a 50% efficient counter, for a 1000-s count time. From this, one can determine whether 50% efficiency is sufficient. For impure samples, the assay precision deteriorates rapidly with increasing (α, n) rates. The Figure of Merit calculation is a fast way to estimate the efficiency, die-away time, and count time needed to provide a given assay precision.

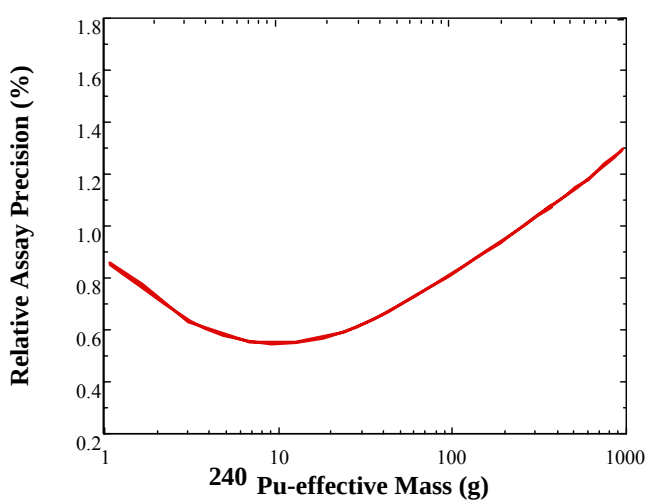

Fig. 6.5. *Figure of Merit calculation of expected assay precision (RSD) vs. ^{240}Pu mass for PuO^2 in a 50% efficient multiplicity counter for 1000-s counts.*

6.3 SOME EXISTING MULTIPLICITY COUNTERS

6.3.1 Basic Differences between Multiplicity and Conventional Coincidence Counters

Multiplicity counters are similar in construction to coincidence counters. Both are thermal neutron detectors that utilize polyethylene-moderated ^{3}He proportional counters. Both employ Amptek preamp/discriminators and shift-register-based electronics, although for multiplicity counting the electronics must collect the multiplicity distribution (see Section 6.4.3).

Multiplicity counters are designed to maximize efficiency and minimize die-away time, as described in the previous section. They have much lower deadtimes, and their detection efficiencies are less dependent on energy. Conventional coincidence counters can be used for multiplicity analysis, but their lower efficiencies and longer die-away times lead to very long counting times. Table 6.1 lists some of the multiplicity counters that are currently in use in DOE facilities and provides a summary of their most important features (Ref. 1).

6.3.2 In-Plant (Pyrochemical) Multiplicity Counter

Based on experience gained with earlier developmental counters, the In-Plant or Pyrochemical Multiplicity Counter was designed specifically for in-plant use to optimize the parameters important for multiplicity assay. The counter has two halves, so that it could be installed around a glovebox well. Figure 6.6 is the design schematic used in the Monte Carlo calculations to determine the optimum tube spacing, 1.59 cm, and the best choice of end plug materials. The result is a very high performance counter with a single-exponential die-away curve. The individual ring responses are illustrated in Figure 6.4.

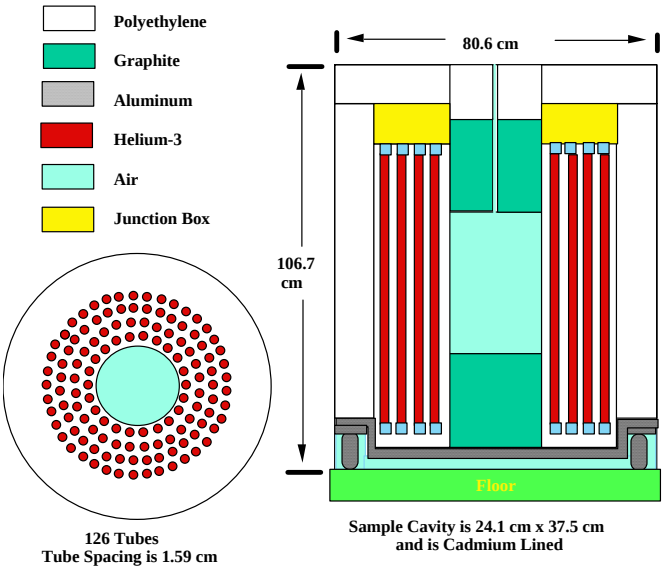

Fig. 6.6. *Design schematic for the In-Plant (Pyrochemical) Multiplicity Counter (Refs. 6 and 7).*

The In-Plant Counter was used in the Los Alamos Plutonium Facility to assay Pu metal, oxide, and high (α,n) electro-refining salts. The counter was also used at the Livermore Nuclear Materials Facility to assay low and high burnup Pu metal and oxide.

Table 6.1. Survey of Some Multiplicity Counters in DOE Facilities (Ref. 1)

Multiplicity Counter Name	Location	Application	No. of tube rings	No. of ^{3}He tubes	No. of Amptek preamps	Derandom-izer	Multi-plicity deadtime (ns)	Neutron Det. Eff.(%)	Die-Away Time (μs)	Cavity Size
Five-Ring Multiplicity Counter	Los Alamos	Technology Development	5	130	34	Yes	36	53	49	16.5 cm D x 25.4 cm H
Three-Ring Multiplicity Counter	Los Alamos	Technology Development	3	60	12	Yes	83	45	63	20 cm D x 30 cm H
Pyrochemical Multiplicity Counter	Los Alamos	In-plant metals, oxides	4	126	36	No	90	57	47	24 cm D x 38 cm H
Plutonium Scrap Multiplicity Counter	Hanford, Japan	Pu Inventory Verification	3 ½	80	19	No	121	55	47	20 cm D x 41 cm H
ARIES Neutron Counter	Los Alamos	Pu metals and residues	3 ½	80	20	Yes	60	55	47	20 cm D x 41 cm H
FB-Line Multiplicity Counter	Savannah River	Metal, oxide inventory	4	113	24	Yes	50	58	50	20 cm D x 41 cm H
30-Gallon Multiplicity Counters	Rocky Flats, Livermore	Inventory Verification	3	126	54	Yes	25	42	55	30-Gallon Drum
High-Efficiency Neutron Counter	Los Alamos	Waste assay	2	113	16	No	171	32	50	55-Gallon Drum
Epithermal Neutron Multiplicity Ctr.	Los Alamos	Pu inventory Verification	4	121 10atm	27	Yes	37	65	22	20 cm D x 43 cm H
KAMS Neutron Multiplicity Counter	Savannah River	Receipts Verification	3	198 10atm	54	Yes	19	52	37.3	55-gallon Drum
Super HENC Multiplicity Counter	Rocky Flats,	Standard Waste Box Assay		260 10atm	32	Yes		40.3		Standard Waste Box

6.3.3 Plutonium Scrap Multiplicity Counter

The Plutonium Scrap Multiplicity Counter (PSMC) is a relatively compact, high efficiency counter for the measurement of impure Pu and mixed oxide scrap. The PSMC is pictured in Figure 6.1 and a design schematic is given in Figure 6.3. Relative to the In-Plant counter, the PSMC uses many fewer ^{3}He tubes for nearly the same efficiency. This was achieved by reducing the number of ^{3}He tubes in each ring in proportion to the decrease in the neutron flux density in the moderator. Thus the outer ring of ^{3}He tubes is only about half filled, and in Table 6.1 the PSMC is described as having 3½ rings of tubes. The axial efficiency profile is constant to within ±2% over the height of the cavity, making it easier to place most scrap containers within the flat portion of the efficiency profile.

The first PSMCs were used for inventory verification campaigns in Japan and at Hanford, and additional counters are now commercially available. An in-line, active/passive, multiplicity counter very similar in design to the PSMC was developed for permanent installation in the Los Alamos Plutonium Facility (Ref. 5). This counter, called the ARIES Neutron Counter, has a split body so that it can be installed around a glove-box well.

6.3.4 FB-Line Multiplicity Counter

The FB-Line Neutron Multiplicity Counter (FBLNMC) is designed to measure impure plutonium at the Westinghouse Savannah River Site FB-Line Facility. The FBLNMC can be applied to impure samples that range in Pu mass from a few tens of grams to several kilograms; coincidence counting or multiplicity counting can be used. Monte Carlo calculations helped design the high-efficiency (57%) detector, which has 113 ^{3}He tubes. The axial efficiency profile varies by less than ±2% over the height of the cavity, and the radial efficiency variation over 16 cm is only 1.5% at the midplane of the sample cavity. The energy response profile is identical to that of the Pyrochemical Multiplicity Counter. A derandomizer circuit (see Section 6.4.4) reduces the deadtime by more than a factor of 2, to 50 ns. The individual ring outputs can be read by auxiliary scalars to diagnose sample anomalies. The ratio of rates in the inner and outer rings can also provide a sensitive indication of the mean energy of the neutrons from a sample and is strongly influenced by the sample matrix or (α,n) neutrons.

6.3.5 30-Gallon Multiplicity Counters

The 30-Gallon (109-liter) Multiplicity Counters are an important extrapolation of design concepts to a larger sample volume. The number of ^{3}He tube rings is reduced to three to save cost, and aluminum corner reflectors help maintain a good spatial response. To facilitate loading heavy drums or ATR400 storage containers, a hexagonal design is used, with the two front sides forming the doors. The mechanical arrangement of the counter and doors is shown in Figure 6.7. The counter has an efficiency of 42% and a die-away time of 55 μs, which is sufficient for assay of bulk plutonium in the kilogram range. Fifty-four Amptek preamp/discriminators and a derandomizer circuit are used to obtain an extremely low deadtime of 25 ns. One 30-Gallon Counter was used at Rocky Flats for IAEA inspections of excess weapons materials (Refs. 6 and 7). Another counter is installed at the Livermore Nuclear Materials Facility, where it is used for inventory verification.

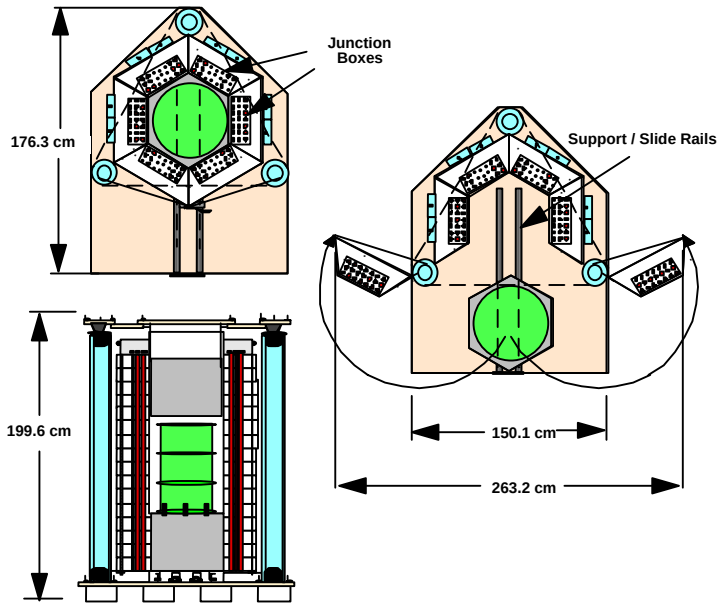

Fig. 6.7. *Mechanical schematic for the 30-Gallon Multiplicity Counter.*

6.3.6 High-Efficiency Neutron Counter (HENC)

The High-Efficiency Neutron Counter (HENC) is a waste-drum counter developed jointly by Canberra Industries and Los Alamos National Laboratory. This counter was designed to be a high efficiency, low detectability, passive neutron coincidence counter with multiplicity and segmented Add-a-Source matrix correction capability. The design was optimized on the basis of a detectability limit figure of merit, resulting in a limit of 0.5 mg $^{240}Pu_{eff}$ by singles counting and 1.7 mg by doubles counting at sea level. An automated drum handling system opens the assay chamber door, loads drums from the conveyor system, and rotates the drums while they are being assayed. Figure 6.8 is a top view of the HENC.

Fig. 6.8 *High-Efficiency Neutron Counter (HENC).*

6.3.7 Epithermal Neutron Multiplicity Counters

The thermal neutron multiplicity counters described above utilize 4-atm ^{3}He tubes. A new design concept, the Epithermal Neutron Multiplicity Counter (ENMC), uses 121 10-atm tubes in closely packed rings with less polyethylene moderator (Ref. 8). This enables the ENMC to detect both thermal and epithermal neutrons, resulting in an efficiency of 65% and a die-away time of only 22 μs. For bulk samples of plutonium, ENMC assay times are 5 to 40 times shorter than prior thermal neutron multiplicity counters. The largest relative gains are for the most impure items with high (α, n) rates, where such gains reduce counting times from hours to 20 or 30 minutes. Additional information on ENMC design and performance are given in Chapter 8.

An Inventory Sample Counter (INVS) was designed to fit inside the ENMC sample chamber for assay of small inventory samples. The INVS insert has 21 ^{3}He tubes in 3 tight rings. The combined ENMC/INVS has an efficiency of 80% and a die-away time of 19 μs. A new drum-sized multiplicity counter has been designed and fabricated for receipts verification at the Savannah River K-Area Material Storage Facility which utilizes 198 10-atm ^{3}He tubes to achieve an efficiency of 52%.

6.3.8 SuperHENC Multiplicity Counter

The largest neutron multiplicity counter built to date also uses epithermal neutron design concepts. The SuperHENC (Super High Efficiency Neutron Counter) has a cavity large enough to accommodate 1900-ℓ Standard Waste Boxes and also provides Add-a-Source matrix corrections using a ^{252}Cf source that is shuffled in and out of the assay cavity. SuperHENC uses 260 10-atm ^{3}He tubes to achieve an efficiency of 40.3 %. This counter is mounted in a 14.6 m x 2.6 m x 4.1 m high trailer, Figure 6.9. It was fabricated and used to measure transuranic waste containers before shipping to the Waste Isolation Pilot Plant (WIPP) in Carlsbad, New Mexico (Ref. 9).

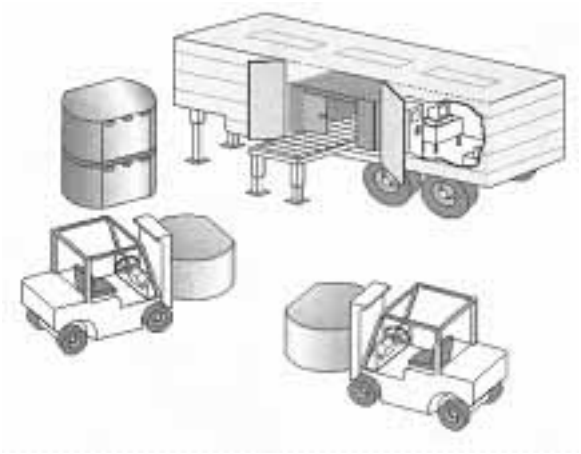

Fig. 6.9. *SuperHENC Multiplicity Counter* .

6.4 MULTIPLICITY ELECTRONICS

6.4.1 Thermal Neutron Detection Electronics

The electronics for thermal neutron multiplicity counters are similar to those used for conventional coincidence counters. They are based on the detection of neutrons with ^{3}He

proportional counters embedded in a polyethylene moderator (Refs. 1 and 10). Modern thermal coincidence and multiplicity detectors both utilize Amptek circuits to amplify the ^{3}He output pulses from the ^{3}He tubes and convert the pulses above a discriminator threshold to digital pulses. Multiplicity counters usually have 80-130 ^{3}He tubes, and many more Amptek circuits to provide very short electronic deadtimes.

Amptek A-111 hybrid circuits have a charge-sensitive preamplifier, an amplifier with a bipolar output, a discriminator set to provide 50-ns output pulses, and a pulse-shaping circuit. They provide sufficient gain and signal-to-noise ratio if the ^{3}He tubes are operated at 1680 V. The Amptek time constant is set to about 150 ns which is the minimum recovery time before they can provide another output pulse. Each Amptek is mounted on a small circuit board that also provides an output pulse to drive a light-emitting diode that flashes when a neutron is detected. Figure 6.10 illustrates one channel processing the input signals from three ^{3}He tubes.

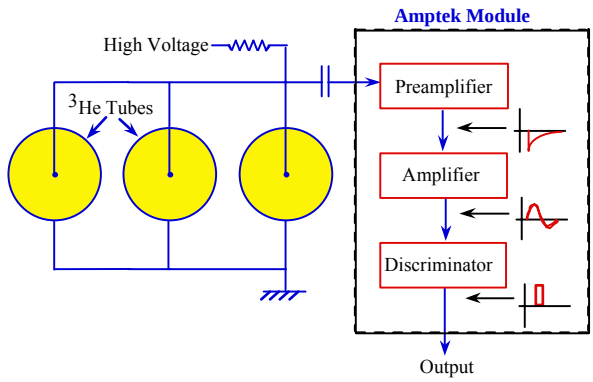

Fig. 6.10. *Electronic layout with one Amptek channel processing the input signals from three ^{3}He tubes (Ref. 1).*

The multiplicity counter contains one or more "junction boxes," where ^{3}He tubes are mounted to provide good grounding. The junction boxes are split into two horizontal layers, with the bottom one providing high-voltage (HV) distribution lines and isolation capacitors. The top layer holds the Amptek boards, the wires that provide the boards with +5V DC, and the 50-ns discriminator output lines. Also, all of the LED outputs are brought to a single display panel on the side of the junction box. This provides the operator with a quick visual diagnostic to ensure that all Amptek channels are operating. The junction box has an O-ring seal and is equipped with several desiccant holders. This helps prevent breakdown in the HV distribution network, which can cause electronic noise bursts that are detected as spurious coincidences.

Individual Amptek modules are connected via an OR circuit to provide a single input to the shift register circuit used to collect correlated events (Section 6.4.5). The use of many Ampteks greatly reduces the deadtime, because it's unlikely that neutrons detected at about the same time produce pulses that are processed by the same module. However, the OR-gate does have a small deadtime due to accidental overlaps of the 50-ns input pulses (Ref. 1).

6.4.2 Derandomizer Circuit

The OR circuit described above can be replaced with a "derandomizer" circuit that eliminates this source of deadtime. This is a useful addition to coincidence counters operating at high count rates or to multiplicity counters, because the triples counts are very sensitive to deadtime. The derandomizing buffer holds pulses from the Amptek modules and releases them synchronously with the derandomizer clock (typically 10-16 MHz) such that no pulses overlap. The word "derandomizer" refers to the fact that the input events are now synchronized.

One derandomizing circuit is implemented in a field-programmable gate array (FPGA) installed in the junction box. The derandomizer has 32 input channels that can hold up to three

events from each of 32 Amptek circuits. There are seven outputs: four of eight channels each, two of 16 channels each, and one of all 32 summed channels. The outputs are clocked at a 10-MHz synchronous rate and produce a 50-ns pulse for each input event. With a derandomizer, a conventional shift register can operate at count rates approaching 2 MHz with virtually no synchronizer counting losses. A multiplicity counter can have a triples deadtime correction of about 50% at a count rate of 500 to 900 kcps, but the correction depends on the type of neutron source as well as the count rate.

There is a second derandomizer. If a shift register coincidence circuit is operating with a 4 MHz clock, then each stage of the shift register corresponds to 250 ns. If two input pulses arrive within 250 ns, then one of them can be lost because one stage can only hold one pulse. To prevent this loss, a derandomizer is placed at the input to store pulses until there is space available in the shift register. The use of two derandomizers arose historically. The one at the shift register input is the original one. The Amptek derandomizer was added later to further reduce the deadtime.

6.4.3 The Neutron Pulse Stream and Coincidence Gates

The thermal neutron detector input electronics described above provide a stream of pulses, each representing one detected neutron, to the input of the shift register circuit. The pulse stream contains a combination of spontaneous fission, induced fission, (α,n) neutrons, and external background events. One way to visualize this pulse stream is the histogram shown in Figure 6.11. This is the distribution in time of additional detected neutrons that follow after each detected starting neutron. The data for the plot of count vs. time are obtained from a large number of starting neutrons. The neutrons detected after the starting neutron are counted in time bins according to their detection times relative to the starting neutron time (t=0). The starting neutrons can be correlated or uncorrelated to other neutrons. If only random, uncorrelated events are detected, the distribution is on the average constant in time. If correlated events from fission are also present, then the correlated neutrons produce an exponential distribution in time, where the time constant is the detector die-away time. The time distribution is given by

$$N(t) = A + \mathrm{R}e^{-\left(\frac{t}{\tau}\right)} , \qquad (6\text{-}1)$$

where N(t) is the neutron population at time t, A is the accidental or random count rate, R is the real or correlated count rate, and τ is the mean neutron lifetime in the counter (die-away time). In Figure 6.11 the dark red bars represent fission neutrons correlated to the initial pulse (R in Eq. 6-1). The striped bars are from fissions that are not correlated to the starting neutron, because it was a random neutron or from a different fission. The white bars are (α,n) or background neutrons. Note that the accidental coincidences contain both the white and stripped bars. Figure 6.11 also shows two coincidence counting intervals (or gates), the R+A (Reals plus Accidentals) and A (Accidentals only). These are described in Section 6.4.5 below.

6.4.4 Predelay Circuit

Because of deadtime and pulse pileup in the ^{3}He tubes, Ampteks, OR gates, or other electronic components, the actual time distribution of Fig. 6.11 does not continue as a rising exponential all the way to t=0. So that this loss of events at short times does not bias the measurements, a short shift register called the “predelay” is located between t=0 and the R+A gate. This circuit delays the start of the coincidence counting interval until a short time interval (the predelay) has passed. The length of the predelay is based on the speed of the amplifier, the storage capacity of any derandomizer, and the expected count rate. If the amplifier baseline is not fully restored in a time less that the predelay, the effect extends into the R+A gate and a bias results. The Amptek A-111 amplifier requires a predelay of only 3 μs for a bias of less than

0.01% at a count rate of 500 kHz. At very high count rates, as the derandomizer stretches pulse strings out in time, it may create strings longer than the predelay and a bias.

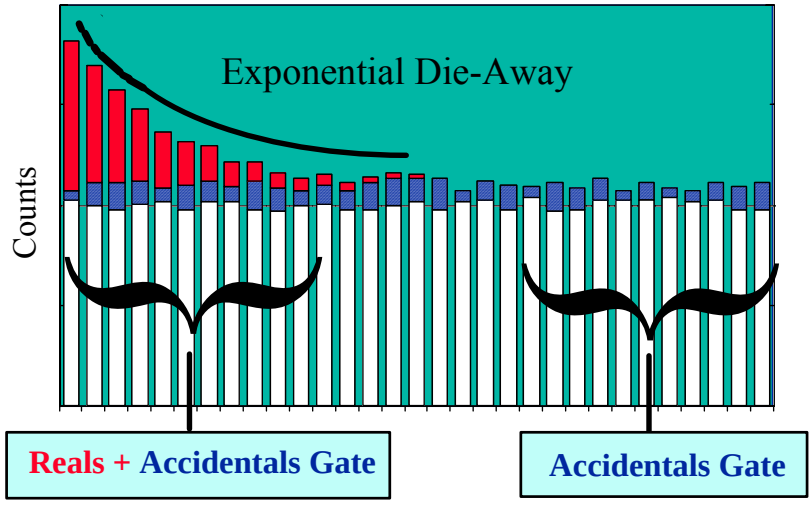

Fig. 6.11. *Histogram of detected neutrons in a pulse stream. A measured distribution with exponential die-away is above the histogram, and the (Reals + Accidentals) and (Accidentals) coincidence gates are below the histogram.*

6.4.5 Multiplicity Shift Register Basics

To extract the fission rate and multiplicity information from the neutron pulse stream in Figure 6.11, we need to extract the correlated neutrons from the background of uncorrelated ones. The multiplicity shift register circuit achieves this in an elegant fashion by separating the incoming pulse stream into correlated and uncorrelated events. Originally, this was done by storing all incoming pulses for a given interval, the gate-width G, in an integrated circuit called a shift register. The circuit has a series of clock-driven flip-flops linked in stages. For example, a 128-stage shift register driven by a 4-MHz clock (0.25 μs/stage) defines a gate of 32 μs. Incoming pulses shift through the register one stage at a time and the whole process takes 32 μs. The shift register collects all possible neutron pairs in an inherently deadtime-free manner.

Operation of a shift register can be visualized by referring to Figure 6.11. This figure shows a prompt gate of width G that opens after the predelay and that collects real and accidental coincidences. After a delay much longer than the detector die-away time (up to 4096 μs), another gate is opened that collects only accidental events. Additional shift registers provide this long delay and second gate. Within counting statistics, the number of accidental events collected in the A scaler is the same as in the R+A scaler. Thus the difference between the counts collected in the R+A gate and those collected in the A gate is the desired real coincidence signal R. Additional details on the operation of the shift register are given in Refs. 1 and 11. In modern coincidence and multiplicity electronics, memory circuits are used to simulate the shift registers.

There is more information in a neutron pulse stream than single and double neutron events. In multiplicity counting, we look at the distribution of 0's, 1's, 2's, 3's, etc. to deduce the multiplicity distribution. Special electronics is required to measure the neutron multiplicity distributions in the R+A and A coincidence gates. These electronics record the number of times each multiplicity occurs in the gates. For example, if seven neutron pulses are in the R+A gate when another neutron arrives, then "1" is added to the R+A counter that tallies sevens. Figure 6.12 is a simplified circuit diagram of the multiplicity shift register electronics.

Separate multiplicity distributions are measured for the R+A and A gates. Table 6.2 shows typical R+A and A distributions obtained from a 60-g plutonium oxide sample measured in a multiplicity counter with roughly 56% efficiency. Each distribution contains the number of times each multiplicity occurred in the corresponding gate. As an example from this table, seven neutron pulses were found 183 times in the R+A coincidence gate, and 42 times in the A coincidence gate.

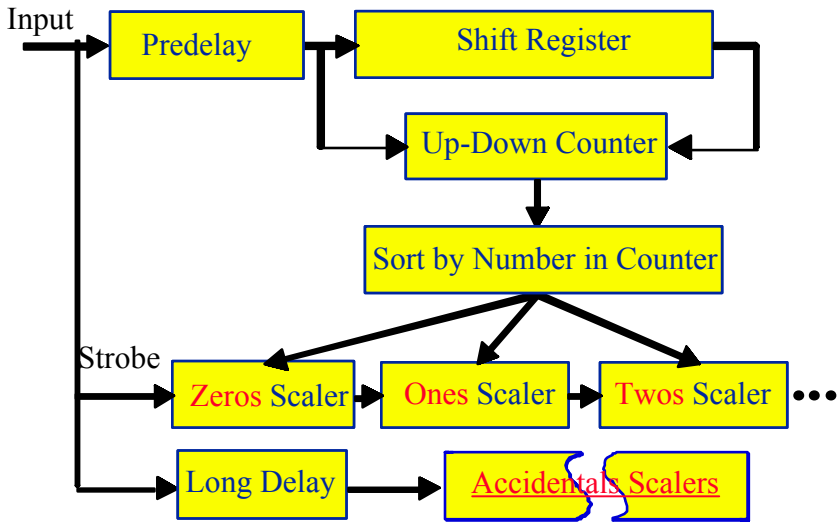

Fig. 6.12. *Multiplicity shift-register block diagram.*

The sum of all multiplicities in the A distribution (37,153,097) is the total number of triggers, because the singles scaler is situated at the output of the A scaler. The sum of all the multiplicities in the R+A distribution (37,153,123) is not always exactly equal to the total number of triggers because the R+A gate interval is shifted by 4096 μs from that of the A gate. (For a purely random pulse stream, the two distributions are the same within statistical errors.) For a correlated pulse stream, the R+A distribution has more high-multiplicity events, and the A distribution has more low-multiplicity events.

Table 6.2. Multiplicity Distribution for a 60-g Plutonium Oxide Sample.

Multiplicity	Counts in (R+A Gate) f(i) distribution	Counts in (A Gate) b(i) distribution
0	26804360	29731130
1	8187530	6222207
2	1772831	1016603
3	325270	157224
4	53449	22387
5	8231	3093
6	1237	402
7	183	42
8	30	8
9	2	1
10	0	0

The two distributions in Table 6.2 can be analyzed to obtain the number of single, double and triple neutron pulses. Note that the number of 1's, 2's, and 3's in Table 6.2 is not what we call the singles, doubles, and triples counts! Instead, the singles is the sum of all the triggers. The doubles is the sum of all the triggers times the mean of the R+A distribution minus the mean of the A distribution, which is the same as a conventional shift register output. The triples is a more complex unfolding of the R+A and A distributions (Equations 6-5 and 6-6 in Section 6.5.5).

In other words, we are using the complete multiplicity distributions to compute their first, second, and third factorial moments which we can relate to singles, doubles, and triples. The reason that we have to measure very high multiplicities, 8's, 9's, 10's, etc., is that the average number of events inside the gate of the shift register is the singles count rate times the gate width. For example, if the singles rate is 100,000 cps and the gate width is 64 μs, the average number of events in either the R+A or the A gate sampled at random times is 6.4. So even for a purely random neutron source, we will record two R+A and A multiplicity distributions that range from 0's to 15's or 20's, with their peak around 6 or 7.

6.4.6 Deployed Multiplicity Shift Registers

The first stand-alone multiplicity shift register is the MSR4, built as a doublewide nuclear instrumentation module (NIM). The singles counting register is 32 bits deep, and the R+A and A registers are 44 bits deep. There are 256 multiplicity registers for the R+A gate and 256 for the A gate, so multiplicities from 0 to 255 can be accumulated. There is no front panel display, and the unit must be controlled through a serial interface with a computer. Several commercial versions of this are now available. Some versions are designed to be more portable, and others utilize time correlation analyzers to collect all of the time intervals between incoming pulses as they arrive.

A recent development is the Advanced Multiplicity Shift Register (AMSR), which decouples sampling of the R+A and A gates. The A gate is sampled at the clock speed, much faster than the sampling of the R+A gate. This improves the precision of the A rate, thereby reducing count times for all coincidence and multiplicity measurements. The count times are reduced by roughly a factor of 2 for a given precision.

6.5 MULTIPLICITY MATHEMATICS

6.5.1 Assumptions in the Equations

This section provides equations for ^{240}Pu mass and other sample parameters in terms of the neutron time distributions measured by multiplicity counters. The equations are based on fundamental assumptions about the fission process and the process of neutron emission and detection which set limits on their accuracy and range of applicability. To the extent that the theoretical model matches the plutonium samples, the measured singles, doubles, and triples rates provide an exact solution for the $^{240}Pu_{eff}$ mass, its multiplication M, and its (α,n) rate. To the extent that the model is not a perfect match, we can expect to encounter some biases or limitations in the multiplicity technique. In this regard, the following assumptions are important to remember:

(1) It is assumed that all induced fission neutrons are emitted simultaneously with the original spontaneous fission or (α,n) reaction (the superfission concept) (Ref. 12).
(2) It is assumed that the detector efficiency and the probability of fission are uniform over the sample volume. This assumption is called the "point model" because it is equivalent to assuming that all neutrons are emitted at one point. The weighted point model described in Section 6.5.9 provides some improvements to this assumption.
(3) It is assumed that (α,n) neutrons and spontaneous fission neutrons have the same energy spectrum, so that the detection efficiency, the fission probability, and the induced-fission multiplicity are the same for both neutron sources. This assumption is not valid for many (α,n) sources.
(4) It is assumed that the neutron die-away time in the sample/detector combination is well approximated by a single exponential time constant.

6.5.2 The Spontaneous Fission Process

The starting point for the multiplicity equations is the spontaneous fission process in plutonium which provides the assay signature for multiplicity and conventional coincidence counting. The primary source of spontaneous fission neutrons in plutonium is usually the isotope ^{240}Pu, although the other even isotopes also contribute to the yield. The effective ^{240}Pu mass is that mass of ^{240}Pu that would give the same double coincidence response as that obtained from all the even isotopes in the actual sample:

$$^{240}Pu_{eff} = 2.52\,^{238}Pu + ^{240}Pu + 1.68\,^{242}Pu \quad . \tag{6-2}$$

The coefficients 2.52 and 1.68 are the ratios of the spontaneous fission decay rates and second factorial moments of the multiplicity distributions. The available nuclear data on these coefficients has an RSD of about 2 to 3% (Ref. 13). The emitted multiplicity distribution from ^{240}Pu is shown in Figure 6.2, and the spontaneous fission neutron yields of plutonium and related nuclides are tabulated in Ref. 1.

For ^{240}Pu, the average number of neutrons emitted per spontaneous fission, or the mean multiplicity ν_1, is about 2.154. From the ^{240}Pu spontaneous fission yield of about 1020n/s-g, and the mean multiplicity of 2.154, we can deduce that ^{240}Pu has a spontaneous-fission rate F of about 473.5 fissions/s-g. The spontaneous-fission neutron energy spectrum follows a Maxwellian distribution and has an average energy of about 1.96 MeV. The second factorial moment ν_2 is about 3.789, and the third factorial moment ν_3 is about 5.211. (Published values will vary depending on the nuclear data selected for the computation.)

6.5.3 Description of (α,n) Reactions

Many heavy nuclei, including the odd and even isotopes of plutonium, decay by alpha particle emission as well as by spontaneous fission. Indeed, alpha decay is much more common than spontaneous fission, even for a heavy nuclide such as ^{252}Cf. The alpha-decay half-lives and yields for these nuclei are tabulated in Ref. 1.

The alpha particles emitted by plutonium have an average energy of about 5.2 MeV, and those emitted by uranium are about 4.7 MeV. Alpha particles of this energy have a very short range and do not escape from even the thinnest sample cans. However, they can have a tremendous effect on the neutron count rate. This is because they lead to (α,n) reactions in low-Z matrix materials, including oxygen, water, fluorine, etc. We define the ratio of (α,n) neutrons to spontaneous fission neutrons by the parameter α. For pure plutonium metal samples, α=0. For oxides and other elements, (α,n) reaction yields are tabulated in Ref. 1 and in other publications. From these yields, we can compute α for samples of pure plutonium oxide (with ^{241}Am in-growth) from the following equation:

$$\alpha = \frac{13400 f_{238} + 38.1 f_{239} + 141 f_{240} + 1.3 f_{241} + 2.0 f_{242} + 2690 f_{Am241}}{1020(2.54 f_{238} + f_{240} + 1.69 f_{242})} \quad . \tag{6-3}$$

The thick target (α,n) yields for other common elements, and the average energy of the neutrons that are emitted, are also tabulated in Ref. 1. From these tables we can see which low-Z elements are most likely to significantly increase the neutron emission rate of the sample.

Of course, the goal of neutron multiplicity counting is to provide an accurate assay independent of the sample (α,n) yield and to provide a value for α without other available information. However, samples with α>0 may have a neutron energy spectrum different from the spontaneous fission neutron energy spectrum. Fortunately, for the most common element present, oxygen, the average energy of the (α,n) neutrons is 2.03 MeV, very close to the average of the spontaneous fission neutrons, 1.96 MeV.

6.5.4 Definition of Sample Multiplication

Neutrons from either spontaneous fission or (α,n) reactions can induce fissions in a sample. When a neutron induces a fission, a multiplication event has occurred. Neutron-induced fission is the most common multiplication event, but other reactions such as (n,2n) are possible. Some neutrons may be captured without causing the release of any neutrons, as in (n,γ) or (n,p) reactions. Or, neutrons may leak out of the sample without undergoing any interactions.

We define ν_i to be the average number of neutrons created by induced fission, and p as the probability that a neutron will induce a fission. A neutron can induce a fission with probability *p* and disappear with probability (1-*p*). The total multiplication M_T is the total number of neutrons after multiplication, ignoring capture, divided by the number of neutrons that were started. If 100 neutrons are started in the sample and an additional 59 are created by multiplication events, M_T is 1.59.

We also define a quantity called the net leakage multiplication M_L. This reflects the fact that not all the neutrons from induced fissions will escape the sample, instead some will be captured. M_L is always less than or nearly equal to M_T, depending on the value of *p*. The following approximate relationship is for the net leakage multiplication:

$$M = \frac{1-p}{1-p\nu_i} \tag{6-4}$$

We have dropped the subscript L, and from now on we will use M for the leakage multiplication. This is the appropriate quantity for multiplicity counting because it is the measure of the neutrons that escape the sample and are available for detection.

For actual samples, ν_i, *p*, and M will depend on the neutron energy spectrum, the sample composition, and the sample density. There is no direct means of determining M for an unknown sample. It may be calculated by Monte Carlo codes, estimated from the observed doubles to singles ratio when α is known, or calculated from the observed triples to doubles ratio using the multiplicity equations. Because the ratio of triples to doubles is a strong measure of multiplication, this ratio is the primary determinant of M in the multiplicity equations.

Not only does neutron reflection or leakage affect sample multiplication, but sample multiplication itself affects the response of the counter. As M increases, the die-away time of the counter increases because the neutrons that induce fissions create a new source of neutrons. When the die-away time changes, the fraction of coincidence events accepted by the electronics also changes. However, if the detector well is lined with cadmium, thermal neutrons cannot return to the sample, and the increase in die-away time is small and usually negligible.

6.5.5 Measured Singles, Doubles, and Triples Count Rates

The singles, doubles, and triples count rates are obtained from the multiplicity shift register described above. The multiplicity shift register measures the foreground multiplicity distribution *f(i)* in the R+A gate and the background distribution b(i) in the A gate, as given in Table 6.2. The software computes the factorial moments f_1, f_2, b_1, and b_2 of these distributions, as described in Ref. 1. The singles rate S is the total number of trigger events that arrive at the shift register per unit time. In terms of the factorial moments, the doubles rate D and the triples rate T are given by:

$$D = S(f_1 - b_1) \tag{6-5}$$

$$T = S(f_2 - b_2 - 2b_1(f_1 - b_1))/2 \tag{6-6}$$

Figure 6.13 is a histogram of the multiplicity distributions in the R+A and A gates from a 3.8-kg plutonium metal sample (Ref. 1). The high singles rate from this sample yields multiplicities as high as 20. At these high rates, the R+A and A distributions do not look very different to the eye, so the use of factorial moments and equations 6-5 and 6-6 is essential to unfold the correct doubles and triples count rates. These rates must also be carefully corrected for background count rates and electronic deadtimes.

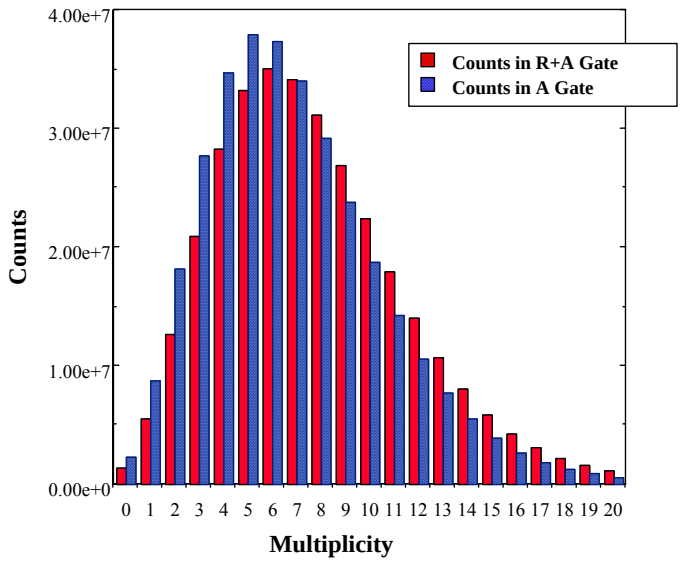

Fig. 6.13. *Multiplicity distribution for a 3.8-kg plutonium metal sample measured in a 56% efficient multiplicity counter.*

6.5.6 Analytical Definition of Singles, Doubles, and Triples Count Rates

We also need analytical expressions for singles, doubles, and triples count rates in terms of the multiplicity distribution emitted by the sample, detected by the multiplicity counter, and counted by the multiplicity shift register. These equations were derived by Böhnel (Ref. 12) and Cifarelli and Hage (Ref. 14) based on the point model and other assumptions described earlier, and are described in more detail in Reference 1.

$$S = F\varepsilon M \nu_{s1}(1+\alpha) \tag{6-7}$$

$$D = \frac{F\varepsilon^2 f_d M^2}{2}\left[\nu_{s2} + \left(\frac{M-1}{\nu_{i1}-1}\right)\nu_{s1}(1+\alpha)\nu_{i2}\right] \tag{6-8}$$

$$T = \frac{F\varepsilon^3 f_t M^3}{6}\left\{\nu_{s3} + \left(\frac{M-1}{\nu_{i1}-1}\right)\left[3\nu_{s2}\nu_{i2} + \nu_{s1}(1+\alpha)\nu_{i3}\right] + 3\left(\frac{M-1}{\nu_{i1}-1}\right)^2 \nu_{s1}(1+\alpha)\nu_{i2}^{\,2}\right\} \quad . \tag{6-9}$$

where F = spontaneous fission rate,
ε = neutron detection efficiency,
M = neutron leakage multiplication,
α = (α,n) to spontaneous fission neutron ratio,
f_d = doubles gate fraction,
f_t = triples gate fraction,
ν_{s1}, ν_{s2}, ν_{s3} = factorial moments of the spontaneous fission neutron distribution,

ν_{i1}, ν_{i2}, ν_{i3} = factorial moments of the induced fission neutron distribution.

The doubles gate fraction f_d is the fraction of the detected doubles that are actually counted inside the gate width G of the multiplicity shift register. For a neutron detector with a die-away time characterized by a single exponential with time constant τ, f_d is given by

$$f_d = e^{-P/\tau}(1 - e^{-G/\tau}) . \tag{6-10}$$

where τ = detector die-away time,
G = shift register gate width, and
P = shift register pre-delay.

The triples gate fraction is then given by $f_t = f_d^{\,2}$ but is usually determined experimentally because the die-away curve for a real detector is not exactly a single exponential.

6.5.7 Final Solution for Sample Mass, Multiplication, α

Eqs. 6-7 through 6-9 relate singles, doubles, and triples rates to the unknown sample parameters, and Eqs. 6-5 and 6-6 calculate the doubles and triples rates from the multiplicity shift register; these are the relationships needed for multiplicity analysis. For measurements of large mass items in small containers, the detection efficiency ε is usually assumed to be a known parameter obtained from careful measurement of a californium reference source. Then Eqs. 6-7 through 6-9 can be solved for the $^{240}Pu_{eff}$ mass m_{240}, α, and M. The solution for M is obtained first by solving the following equation:

$$a + bM + cM^2 + M^3 = 0 , \tag{6-11}$$

where the coefficients are functions of S, D, and T:

$$a = \frac{-6T\nu_{s2}(\nu_{i1} - 1)}{\varepsilon^2 f_t S(\nu_{s2}\nu_{i3} - \nu_{s3}\nu_{i2})} , \tag{6-12}$$

$$b = \frac{2D\left[\nu_{s3}(\nu_{i1} - 1) - 3\nu_{s2}\nu_{i2}\right]}{\varepsilon f_d S(\nu_{s2}\nu_{i3} - \nu_{s3}\nu_{i2})} , \tag{6-13}$$

$$c = \frac{6D\nu_{s2}\nu_{i2}}{\varepsilon f_d S(\nu_{s2}\nu_{i3} - \nu_{s3}\nu_{i2})} - 1 , \tag{6-14}$$

Once M is determined, the sample fission rate, F, is given by

$$F = \frac{\left[\dfrac{2D}{\varepsilon f_d} - \dfrac{M(M-1)\nu_{i2}S}{\nu_{i1} - 1}\right]}{\varepsilon M^2 \nu_{s2}} . \tag{6-15}$$

The second term in the numerator of Eq. 6-15 represents the effect of sample self-interrogation due to induced fission, which must be subtracted from the emitted doubles to obtain the spontaneous fission rate. Once F is obtained, the sample's ^{240}Pu effective mass m_{240} is given by

$$m_{240} = \frac{F}{(473.5\, fissions/s - g)}. \tag{6-16}$$

Also, the sample's α value is given by

$$\alpha = \frac{S}{F\varepsilon\nu_{s1}M} - 1. \tag{6-17}$$

If the item's isotopic composition is known, the total Pu mass can be calculated from

$$Pu = m_{240} / (2.52\, f_{238} + f_{240} + 1.68\, f_{242}). \tag{6-18}$$

where f_{238}, f_{240}, and f_{242} are usually obtained by mass or gamma-ray spectroscopy.

For measurements of low Pu mass items in large containers, such as waste drums, the detection efficiency ε may vary from item to item. In this situation, it may be a good approximation to assume that sample self-multiplication, M, equals 1. Then M can be considered a known parameter, and one can solve Eqs. 6-7 to 6-9 for m_{240}, α, and ε. The equations for this case are given in Ref. 1.

6.5.8 Weighted Point Model Equations

The point model assumptions of constant neutron energy and uniform multiplication can cause significant biases in measurements of impure Pu metal and large, dense Pu oxides. For example, multiplication inside such items is not uniform, but is actually much larger in the center and falls off towards the surface. To correct for these biases, weighted point model equations (Ref. 6) have been developed to add variable-multiplication weighting factors to the expressions in Eqs. 6-8 and 6-9. The weighting factors are obtained from Monte Carlo simulations using the MCNPX code (Ref. 2) which supports the simulation of spontaneous fission sources and can tally the source and detected neutron multiplicity distributions.

The weighting factors are introduced for both the spontaneous fission and (α,n) contributions to the doubles and triples rates to account for multiplication variations. The MCNPX code is used to model items with widely varying geometries, densities, and impurities to obtain simulated singles, doubles, and triples count rates. The weighting factors are then selected to correct for the biases observed in the simulated assays. For unknown samples, the weighted point model equations are used to compute M, α, and m_{240}, but require solving a fifth-order equation for multiplication. Use of the weighted point model equations to correct for multiplication bias is described in Section 6.6.4 below.

6.6 MULTIPLICITY CALIBRATION AND MEASUREMENT CONTROL

6.6.1 Multiplicity Data Analysis Software

Multiplicity analysis software is required for computer control of the electronics, data analysis, calibration and measurement control, and all routine sample measurements. Current software includes the LANL International Neutron Coincidence Counting (INCC) and DEMING Least-Square Fitting codes (Ref. 16) and the Canberra Industries NDA 2000 codes. This software includes background and deadtime corrections, quality control tests, and statistical error analysis. They also can collect and analyze data for passive coincidence counting, active

coincidence counting, and active multiplicity counting. The calibration and measurement control procedures described in this section are based on the INCC code.

6.6.2 Detector Characterization Measurements

A series of detector characterization measurements are required to define the parameters used for data collection, calibration, and measurement control. The room background count rates should be measured. Typical singles, doubles, and triples count rates are 100 to 1000 cps, 1 - 2 cps, and 0.1 - 0.2 cps. Then a well characterized ^{252}Cf reference source should be measured. This provides a normalization measurement to be used for daily measurement control and calibration. The reference source can also be used to determine the detection efficiency, ε. The ^{252}Cf reference source is also used to determine the detector die-away time, τ, by making measurements at different gate widths. The coincidence gate width G is typically set to a value similar to the die-away time.

Lastly, multiplicity analysis requires that careful deadtime corrections be applied to the singles, doubles, and especially to the triples count rates. The singles and doubles rates can be corrected for deadtime according to the following equations:

$$S_0 = S_m e^{\delta S_m/4} \tag{6-19}$$

$$D_0 = D_m e^{\delta S_m} \tag{6-20}$$

where $\delta = A + BS_m$, A and B are the deadtime coefficients, the subscript "m" means measured, and "0" refers to the quantity corrected for deadtime. The coefficients A and B depend on the multiplicity counter, particularly on the number of Amptek circuits. One way to determine A and B is to very carefully and reproducibly measure californium sources of different strengths and adjust A and B to obtain the same doubles/singles ratio for all sources.

The complex equations used for correcting the triples rate are built into the INCC code (Refs. 1 and 16) and use a constant parameter Δ called the multiplicity deadtime. The parameter Δ can be determined by measuring a weak and a strong ^{252}Cf source. The ratio of triples to doubles should be independent of the ^{252}Cf source strength after deadtime corrections, so the deadtime can be determined by adjusting Δ to give the same triples/doubles ratio. For multiplicity counters, typical values of the doubles deadtime coefficient are 0.1 to 0.6 μs, and typical values for the multiplicity deadtime coefficient are 25 to 170 ns. Examples of multiplicity deadtime coefficients are included in Table 6-1.

6.6.3 Multiplicity Calibration Procedure

Because multiplicity counters are used to assay a wide range of impure Pu items, representative physical standards are usually not available. It is possible to calibrate the counter directly by solving the singles, doubles, and triples equations for M, α, and m_{240} using three measured detector parameters: ε, f_d, and f_t. To the extent that the plutonium items satisfy the assumptions of the point model, this provides an accurate assay. However, whenever possible, traceable physical standards should be used to validate this procedure or to remove remaining biases caused by errors in the point model assumptions.

The initial determination of the detection efficiency using a ^{252}Cf reference source can be biased because of small uncertainties in the neutron yield of the source and slight differences in energy between ^{252}Cf and Pu fission neutrons. The efficiency should be corrected with Monte Carlo calculations. The magnitude of the adjustment will depend on the detector, but will typically be in the range of 1 to 2%. If Monte Carlo calculations show a significant difference in neutron detection efficiency between a point source and the actual plutonium items, the efficiency can be adjusted accordingly.

The doubles and triples gate fractions are calculated from the singles, doubles, and triples rates measured with the ^{252}Cf reference source using the following equations:

$$f_d = \frac{2\nu_{s1} D}{\varepsilon \nu_{s2} S} \ , \tag{6-21}$$

$$f_t = \frac{3 f_d \nu_{s2} T}{\varepsilon \nu_{s3} D} \ . \tag{6-22}$$

In these equations ν_{S1}, ν_{S2}, and ν_{S3} are the factorial moments of the ^{252}Cf source distribution from Ref. 1 or elsewhere. Typical values are ν_{s1} = 3.757, ν_{s2} = 11.948, ν_{s3} = 31.636. If one or more physical standards are available, the calibration can usually be improved by adjusting f_t to obtain the best assays for the standards. This corrects for uncertainties in the nuclear data parameters of ^{252}Cf and plutonium and for differences between the actual items assayed and the point-model assumptions. The adjustment to f_t may be on the order of 10%.

If M or α for the physical standards is known, it may also be helpful to vary ε and obtain the best agreement with the known M, α, and mass values. This approach can only be helpful if M or α is well known. Otherwise, it will introduce a bias into the assays that will increase as M or α increases. In general, if there is no independent information on M or α for the standards, changes to ε are not advisable unless based on Monte Carlo calculations. An exception to this is where a number of well-known samples are available with characteristics very similar to the unknowns. In this case, all three detector parameters can be varied to provide the best assays.

After calibration, it is also helpful to verify the applicability of the multiplicity counting technique by measuring some items to which the technique is going to be applied. The measurements should be verified relative to calorimetry or some other traceable process. If new material categories need to be measured that may not be appropriate for multiplicity counting, some fraction of the measurements should undergo some verification process.

6.6.4 Multiplication Bias Correction

If large Pu metal or dense oxide items are to be measured, a variable bias correction is needed to correct multiplicity assays for the nonuniform probability of fission inside large multiplying items (Ref. 17). This correction is best added during the calibration procedure, but it can also be applied afterwards. The multiplicity software analysis code includes this correction in the form:

$$CF = 1 + a(M-1) + b(M-1)^2 \tag{6-23}$$

where M is the measured sample multiplication, and CF is a multiplicative factor that increases the calculated value of m_{240} in Equation 6-16. An empirical set of coefficients appropriate for metal items in different multiplicity counters is a = 0.0794 and b = 0.1386 (Ref. 17). These empirical coefficients were derived from known plutonium items and are not necessarily applicable to all Pu metal items and all counters. The correction factor approaches 1 as M approaches 1, so it can be left on even if the counter is only used to assay non-metallic items.

The weighted point model equations discussed in Section 6.5.8 provide a more robust bias correction within the framework of the multiplicity analysis equations. Fig. 6.14 compares the performance of the weighted point model on 232 metal samples measured in the Savannah River FB-Line multiplicity counter to the performance on 66 simulated metal cylinders, ranging in shape from pancakes to rods, that were used to determine the doubles and triples weighting factors (Ref. 15). The Savannah River bias correction coefficients are a = 0.1460 and b = 0.1485. Because the Savannah River and MCNPX curves in Fig. 6.14 are similar, these coefficients may be less dependent on Pu geometry, impurities, or counter cavity size.

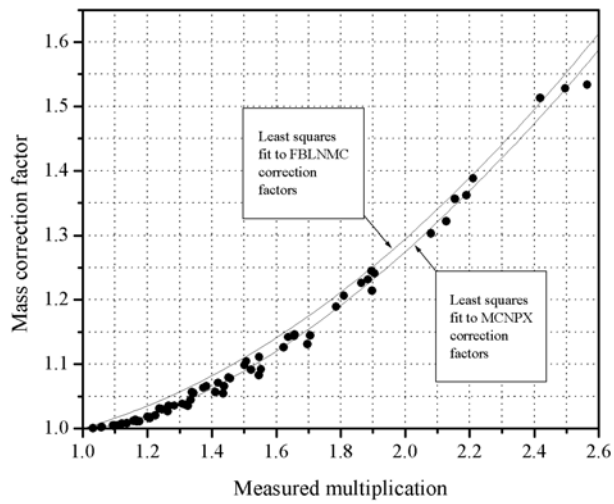

Fig. 6.14 $^{240}Pu_{eff}$ mass correction factor vs. measured multiplication for two sets of Pu metal samples. The measured set consists of 232 Pu metal items (upper curve). The computational set has 66 Pu metal cylinders used to determine the doubles and triples weighting factors set (lower curve).

Measurements of impure Pu metal show that the coefficients still vary with high levels of impurities and that the weighted point model can have an alpha-dependent bias for items with α values of 0.5 or more. Nevertheless, an added benefit of the weighted point model equations for impure Pu metals is that the actual α value is determined much more accurately. The standard point model overestimates α for large metal samples, often causing a Pu metal item to appear to be impure when it is actually pure (Ref. 15).

6.6.5 Ring Ratio Diagnostic

Monte Carlo calculations and laboratory measurement campaigns have shown that the ratio of the singles in the inner and outer rings is a good indicator for neutron energy spectrum shifts that may bias the assay. For example, Figure 6.4 plots the relative responses of the four ^{3}He tube rings in the Pyrochemical Multiplicity Counter as a function of energy. Low energy neutrons are preferentially detected in the inner ring, and high energy neutrons in the outer rings. The neutron energy spectrum affects the overall efficiency, the probability of induced fission, and the induced fission multiplicity distribution. These effects are usually not large, but can cause energy-dependent biases in Pu measurements of items with large amounts of (α,n) emitting impurities or neutron moderators.

Most multiplicity counter electronics packages provide separate measurements of the inner and outer singles count rates and can thereby provide an estimate of the average energy of the (α,n) neutrons. A correction procedure based on ring ratios has been developed for the standard point model, but not yet for the weighted point model. Even if the correction is not used, the ring ratio provides a useful diagnostic that can warn of high levels of impurities or moderators that may bias the assay.

6.6.6 Measurement Control Procedures

Measurement control is used by nuclear facilities to verify proper operation of their multiplicity counters. Quality control tests usually include a checksum test on the shift register electronics, the accidentals/singles test, an outlier test, a measurement control chi-squared limit, a declared-minus-assay limit, and a high voltage test limit (Ref. 16). For all measurements, the total count time should be split up into a series of smaller runs, such as 10 runs of 100 s for a total count time of 1000 s. This allows the outlier test to reject runs with unusually large double or triple coincidence bursts due to cosmic rays or other interferences.

Background runs should be done daily when the instrument is in use, or more frequently if there is reason to believe that the room background is changing significantly. Normalization runs should be done daily using a ^{252}Cf reference source or standard to ensure that the counter is operating correctly. Occasional measurements of a known item or representative standard is a good practice to verify system operation. Other recommended measurement control or assay procedures are described in Ref. 1.

6.7 PASSIVE MULTIPLICITY APPLICATIONS AND PERFORMANCE

6.7.1 Expected Assay Precision

Multiplicity counter precision is determined primarily by the statistical uncertainty in the singles, doubles, and triples counts and the reproducibility of sample placement. The dominant uncertainty is usually in the triples and is determined primarily by detector efficiency, die-away time, count time, count rate, neutron multiplication, and the (α,n) rate. The propagated uncertainty in the Pu mass is usually estimated by the analysis software in one of two ways: from the statistical scatter between the multiple runs that make up a single assay, or from theoretical methods that have been benchmarked against measurements of the observed scatter (Refs. 4 and 16). In either case, the quoted error is not a Total Measurement Uncertainty (TMU), but consists only of counting statistics and calibration uncertainties.

Figure 6.15 provides rough estimates of the predicted assay repeatability due to counting statistics for Pu metal (α=0), oxide (α=1), scrap (α=5), and residues (α=20) for a high-efficiency multiplicity counter (Ref. 4). The α values of such materials vary, but the values selected here are representative. Note that the repeatability due to counting statistics is always better for conventional coincidence counting than for multiplicity analysis.

6.7.2 Typical Assay Bias

Assay bias for multiplicity counting is very low for samples that meet the mathematical assumptions of the point model. However, in practice, container and matrix factors may yield noticeable biases. Table 6-3 provides a summary of typical performance for multiplicity assay of nuclear materials commonly found in DOE facilities and can be used to estimate performance for other similar applications. The observed repeatability and bias estimates include the uncertainties from neutron counting, gamma-ray isotopic analysis of the ^{240}Pu effective fraction, and reference values based on calorimetry/isotopics or destructive analysis.

One important question for safeguards personnel is when to use multiplicity counting versus conventional coincidence counting. Factors to be considered in selecting either conventional or multiplicity counting vary with material type. They include Pu mass, (α,n) reactions, available detector efficiency, self-multiplication, neutron energy effects, spatial distribution of fissile material, other matrix effects, available counting time/required precision, and container size and shape. For impure samples with unknown multiplication and α, the accuracy for multiplicity counting is usually much better. However, if the conventional coincidence and multiplicity results are the same within counting statistics, then it may be better to use the more precise conventional results. Other considerations for several major material types are given in the following sections.

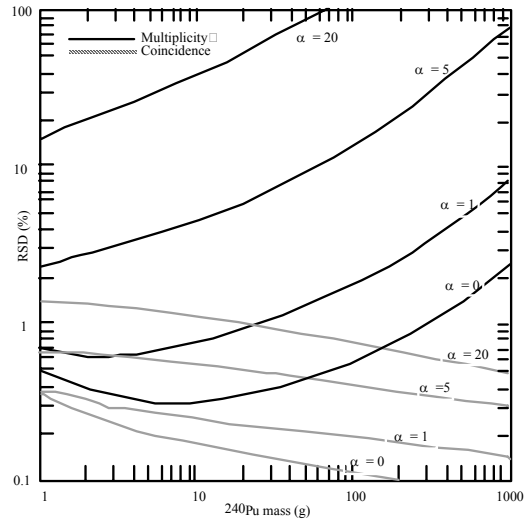

Fig. 6.15. *Estimated precision for multiplicity and conventional coincidence assay using a multiplicity counter with a detector efficiency of 50%, a gate width is 64 μs, a die-away time is 50 μs, and a predelay of 3 μs. The background is 100 cps, and the counting time is 1000 s.*

6.7.3 Plutonium Metal

Pure plutonium metal has $\alpha = 0$, so conventional coincidence counting (known-α) will give assays with better precision. In reality most metal items contain some impurities, and their surface is usually oxidized. Actual α values range from 0.1 to about 1.0, which would produce unacceptable biases in conventional coincidence counting.

Plutonium metal buttons are dense, compact samples for which the theoretical point model does not correctly describe multiplication. The variable-multiplication correction described in Section 6.5.8 is usually needed to obtain good assay results, as illustrated in Figire 6.14 above. The weighted point model equations have also provided good results at Savannah River (Ref. 15). All of the metal measurements summarized in Table 6.3 have used a multiplication bias correction, except for those taken recently at Livermore with cans placed in the center of the 30-Gallon Multiplicity Counter. The Livermore metal data can be fit with small multiplication bias coefficients, or fit equally well without any correction.

6.7.4 Plutonium Oxide

Pure plutonium oxide yields neutrons from spontaneous fission and from (α,n) reactions on oxygen. Depending on burnup, α is in the range 0.4 - 0.8. If some impurities are present, it is conservative to estimate that $\alpha = 1$. Multiplicity information is not needed if the oxide is so pure that α can be calculated and the known-α approach can determine the mass and the multiplication from the singles and doubles rates. Most oxides in DOE facilities are impure, with α values between 1 and 4; for these multiplicity counting is significantly more accurate than coincidence counting because of induced fissions caused by (α,n) neutrons and changes in multiplication caused by density variations.

Table 6-3. Typical Multiplicity Counter Performance on Various Nuclear Materials.

Nuclear Material Category	No. Items/ Meas.	Pu Mass (g)	(α,n)/sf Rate α	Count Time (sec)	RSD (%)	Bias (%)
Pu metal	13	200-4000	0 - 1.3	1800	4.6%	1.3%
	14	1500-5000	0	1800	2.7%	-0.1%
	283	5 – 2300	-0.2 - 1.7	1000	2.8%	0.4%
	32	2000	0		0.5%	-0.8%
	6	1100-2100	0 – 0.6		2.2%	2.0%
Calex Std.	8	398	1	1800	1.3%	0.3%
	150	398	1	1000	1.4%	0.8%
Pu oxide	45	500-5000	1	1800	2.2%	0.0%
Impure Pu oxide	12	20 – 875	0.7 - 4.3	1000	2-3%	0.8%
	261	4 – 1800	0.2 - 3.2	1800	2.3%	0.3%
	7	20 - 800	0.6 – 0.8	5000	0.7%	0.5%
Pu scrap	16	80 - 1175	1 – 6	3600	5.7%	-1.6%
	24	2000	1 – 6	1800	5.8%	-1.0%
	17	300 - 1400	2 – 30	1000	11.4%	-2.1%
Pu residues	10	40 - 300	13 - 29	3000	4.8%	0.9%
	8	160 - 340	7 – 34	3600	18.8%	-9.2%
	17	0 – 10	-1 – 82	1000	24%	-2.3%
	21	10 - 40	-4 – 29	1000	22%	1.8%
	16	40 - 400	0.4 – 13	1000	17%	-1.4%
Pu waste	est.	1	5	1000	10%	2 – 5%
U/Pu oxide	8	200-800g	1 – 2	1000	1 - 2%	1-3%
Pu inventory verification	106	1000-4000	1 – 6	1800	4.2%	0.6%
	67	300-1000	1 – 10	1200	8%	0.0%
	90	1 - 4000	1 – 6	6-12 h	10%	-0.5%
	150		0.8 – 4.5	1000	5%	0.2%

Figure 6.16 compares coincidence and multiplicity assays of 8 pure oxide samples and 7 impure oxide samples. The coincidence results include the known-α correction. The pure oxide samples have an average assay/reference ratio of 1.004 ± 1.4% by coincidence counting, and 1.006 ± 0.66% by multiplicity counting. The impure oxide samples are 1.039 ± 8.2% by coincidence counting, and 1.005 ± 0.68% by multiplicity counting.

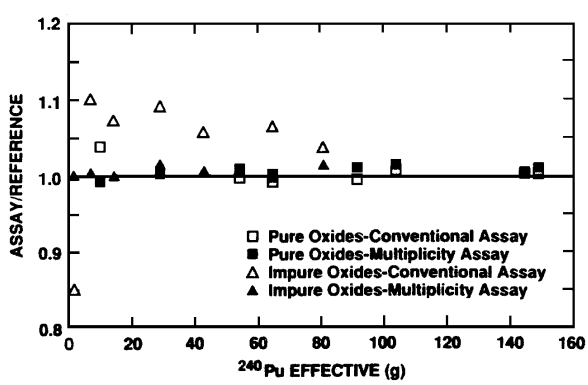

Fig. 6.16. *Comparison of conventional coincidence and multiplicity assays of pure and impure plutonium oxide samples.*

6.7.5 Plutonium Scrap

Scrap is plutonium-bearing material left over from processing activities that can be recycled. It can include relatively pure metal or oxide, or materials with large quantities of matrix elements like fluorine and beryllium. For multiplicity counting, we define scrap as items with α in the range of 1 to 6. The best assay technique for scrap depends on the nature of the item. An impure metal item is best assayed with multiplicity counting, but an item with very low multiplication and a very high (α,n) rate, like waste, is best assayed with coincidence counting. The selection of multiplicity or coincidence depends on whether the lower bias with multiplicity assay, which can correct for induced fissions, outweighs the loss of precision. Conventional coincidence counting usually provides an upper mass limit because it undercorrects for multiplication.

If the scrap contains moderating materials, or if it emits enough (α,n) neutrons with energies much different from fission neutrons, then the detection efficiency can vary from item to item. The ratio of count rates in the inner and outer rings is sensitive to neutron energy, and very impure scrap items display dramatic changes in their ring responses. Figure 6.17 illustrates the measured ratio of Ring 1 to Ring 4 as a function of mean energy in the In-Plant Multiplicity Counter. The ring ratio can be a valuable tool in identifying items that contain gross impurities and in distinguishing metal from oxide.

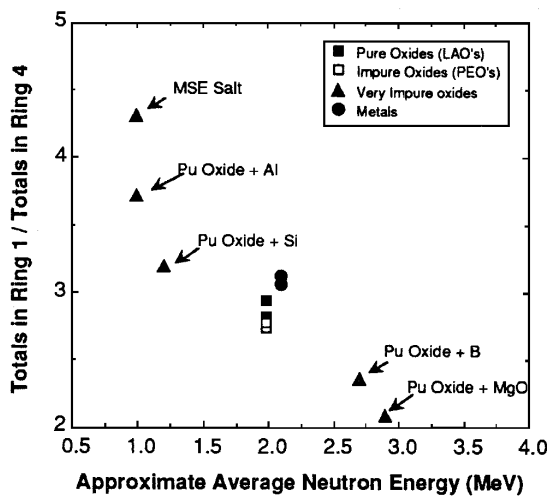

Fig. 6.17. *The measured ratio of Ring 1 to Ring 4 as a function of mean neutron energy for various samples in the In-Plant Multiplicity Counter.*

6.7.6 Plutonium Residues

Residues are plutonium-bearing materials retained during production operations. They can include ash, combustibles, inorganics, salts from pyrochemical processes, and wet items. Residues are often packaged in large cans, have significant quantities of SNM, and are very heterogeneous and difficult to measure. Because many residues contain large quantities of elements like fluorine and beryllium, they may exhibit α values of 10 to 30 or more. Multiplicity counting is the only feasible passive neutron option, but extremely long count times may be needed to get good triples precision. For samples with unknown (α,n) rates, multiplicity analysis is far less biased than conventional coincidence counting.

A recent example is the measurement of Pu-bearing salts at the Livermore Nuclear Materials Facility with a 30-Gallon Multiplicity Counter. The results are given in Table 6.3 for 3 mass ranges, depending on the success of the chemical separation process that yielded the salts. All multiplicity measurements were referenced to much slower but very accurate

calorimetry/isotopics measurements. Even at high α, the multiplicity results appear unbiased, but with a larger RSD.

For measurements of high-α Pu scrap and residue items, the Epithermal Neutron Multiplicity Counter (ENMC) is a good approach for obtaining much shorter counting times. At Hanford, the ENMC reduced assay times by factors of 8 to 40 relative to a thermal neutron multiplicity counter.

6.7.7 Plutonium Waste

Multiplicity counting can improve the assay of Pu waste in 208-liter drums or Standard Waste Boxes (~1900-liter) even though they contain only a few grams of plutonium. The additional information can flag the presence of shielding materials, detect highly multiplying items, or correct for (α,n)-induced fissions or detector efficiency variations. The expected assay precision for multiplicity analysis of waste drums has been estimated using a Figure of Merit code and is included in Table 6-3. Multiplicity assay will have poor precision relative to conventional coincidence counting, but may be more accurate because the bias from (α,n) induced fissions is corrected. (Note that when we use multiplicity analysis to solve for detector efficiency rather than sample multiplication, the RSD increases by a factor of 3 to 4 over the entire mass range and is 5% to 15% at best.) For screening at the TRU-waste detectability limit, multiplicity counting usually does not have sufficient precision.

6.7.8 Mixed Uranium/Plutonium Oxide

Mixed oxides do not meet the assumptions used in the multiplicity mathematics, and must be assayed with caution. The induced fission multiplicity distributions, fission cross sections, and capture cross sections in uranium are different from those in plutonium. If the calibration constants appropriate for plutonium are used to assay plutonium oxides that have a large uranium concentration relative to their plutonium content, the assay results tend to bias low (Ref. 17). If the coefficients are adjusted to fit a particular MOX material with a fixed U/Pu ratio, then the multiplicity performance can be good. Assay of high-burnup MOX items containing a few hundred grams of Pu with the Plutonium Scrap Multiplicity Counter in Japan gives 1% to 2% assay precision.

6.7.9 Plutonium Inventory Verification

Multiplicity counting can be used successfully for inventory verification. The technique provides a better verification than is possible with coincidence counting because it requires less initial inventory information. This section provides some general guidelines on inventory verification measurements, with past results as examples.

For inventory verification, it is helpful to segregate items into categories such as calibration and measurement control standards, Pu metal, low-α Pu (impure oxides and scrap), and high-α plutonium (residues with $\alpha > 6$). These categories can be defined by the observed sample multiplication, mass, α, or measurement precision. For low-α Pu, count times of 1000 to 1800 s are usually sufficient to eliminate counting statistics as a significant contribution to the overall precision. For high-α Pu, multiplicity counting may not be the preferred option because of the long count times required. The overall precision of multiplicity counting for total Pu mass has a lower limit of about 2% RSD once the error on $^{240}Pu_{eff}$ determined by gamma-ray spectroscopy is folded in. At some facilities, the use of stream-average isotopics may provide better results and eliminate the time required for gamma-ray isotopics.

For example, Figure 6.18 compares known-α coincidence assay and multiplicity assay for IAEA Physical Inventory Verification measurements at Rocky Flats using a 30-Gallon Multiplicity Counter (Refs. 15 and 16). Multiplicity improved the average agreement between declared and assay by nearly a factor of two over the best conventional approach. Multiplicity

verified 61% of the samples to within ±3%, and 100% to within ±18%. Overall, 1σ agreement between multiplicity and site declarations was 4.2 % for all items.

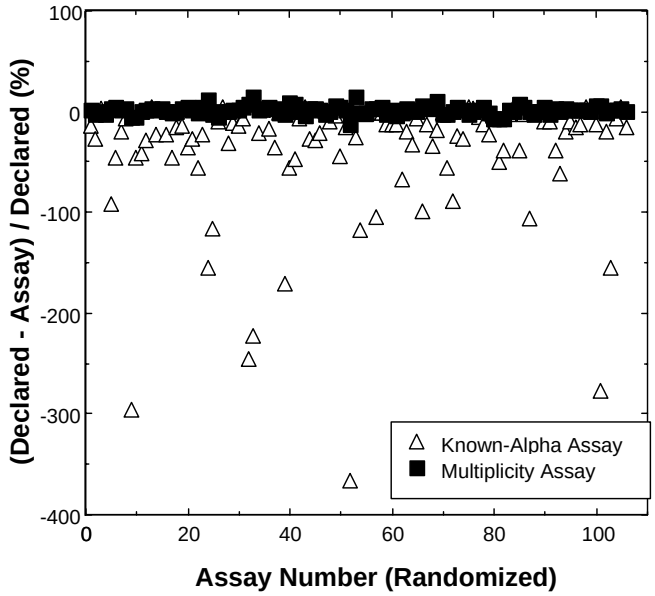

Fig. 6.18. *Comparison of known-α conventional coincidence assay and multiplicity assay for some measurements using a 30-Gallon Neutron Multiplicity Counter.*

For metal items, the data analysis should include a multiplication bias correction. Inventory verification may also require the assay of storage containers with more than one sample can. Although this does not satisfy the assumptions in the point model, experience does not indicate any observable biases in the multiplicity assay due to this effect. For example, the Physical Inventory Verification exercises at Rocky Flats (Refs. 15 and 16) required measurements of 10-gal. drums, with each drum containing two Pu oxide cans. There was no significant bias in the assay results due to the presence of two cans stacked one above the other.

A novel and difficult application of multiplicity counting to bulk inventory verification at Savannah River was reported in. The inventory consisted of cans of Pu or U/Pu stacked in varying configurations in sealed 18-, 36-, 110-, or 208-liter drums in metal, oxide, scrap, scrub alloy, or other forms. A californium shuffler with multiplicity electronics was used for active assay of uranium and passive assay of plutonium. The shuffler's relatively low efficiency of 18% required long count times, and Pu multiplicity assays were only possible for items with α values up to 6. A potential liability of multiplicity counting was that the sample cans were stacked two or more to a drum. Again, no additional biases were observed in the multiplicity assays that could be attributed to this effect. For this inventory, 73 of the 90 drums containing plutonium were verified to within 25%, and the average bias was only -0.5%.

Multiplicity measurements of bulk Pu items in shielded 9975 shipping containers have been carried out as part of Initial Physical Inventory Verification measurements at the Savannah River KAMS Facility (Ref. 20). The measurements were made with the drum-sized KAMS multiplicity counter, which is designed to correct for the presence of a thick layer of shielding material in each drum. The average assay over reference value for the entire measurement campaign was 1.002.

Experience suggests that a small fraction of the inventory has multiplicity assays well outside the reasonable expected limit of error because of unknown matrix effects that do not meet the point model assumptions. These outliers require calorimetry and/or gamma-ray isotopics to

resolve. However, multiplicity counting can substantially reduce the number of items that require these techniques and thereby allow an increase in measurement throughput.

REFERENCES

1. N. Ensslin, W. Harker, M. Krick, D. Langner, M. Pickrell, and J. Stewart, "Application Guide to Neutron Multiplicity Counting," Los Alamos National Laboratory report LA-13422-M, November 1998.

2. N. Ensslin, "A Simple Self-Multiplication Correction for In-Plant Use," Proc. 7th ESARDA Symposium on Safeguards and Nuclear Material Management, Liege, Belgium May 1985.

3. J. S. Hendricks *et.al*., "Monte Carlo Neutron-Photon Extended Code," Los Alamos National Laboratory report LA-UR-04-0570 (2004).

4. N. Ensslin, M. S. Krick, and N. Dytlewski, "Assay Variance as a Figure-of-Merit for Neutron Multiplicity Counting," Nuclear Instruments and Methods, A290 (1990) 197-207.

5. T. E. Sampson, T. L. Cremers, J. C. Martz, and W. R. Dvorzak, "An NDA System for Automated, In-Line Weapons Component Dismantlement," Proc. 34th Annual INMM Meeting, Scottsdale, Ariz., July 18-21, 1993.

6. D. G. Langner, J. B. Franco, J. G. Fleissner, V. Fotin, J. Xiao, and R. Lemaire, "The Performance of the 30-Gallon Drum Neutron Multiplicity Counter at the Rocky Flats Environmental Technology Site," Los Alamos National Laboratory report LA-UR-96-2569, Proc. 37th Annual INMM Meeting, Naples, FL, July 28-31, 1996.

7. D. G. Langner, J. B. Franco, R. K. Larsen, V. Fotin, R. Lemaire, P. Pham, J. Xiao, T. Moriarty, and B. Heaysman, "Assay of Impure Plutonium Oxide with the Large Neutron Multiplicity Counter for IAEA Verification of Excess Weapons Material at the Rocky Flats Environmental Technology Site," Los Alamos National Laboratory report LA-UR-97-2650, Proc. 38th Annual INMM Meeting, Phoenix, AZ, July 20-24, 1997.

8. J. E. Stewart, H. O. Menlove, D. R. Mayo, W. H Geist, and N. Ensslin, "Epithermal Neutron Multiplicity Counter (ENMC): Current Developments and Applications," Proc. 41st Annual INMM Meeting, New Orleans, LA, July 2000.

9. J. B. Franco, H. O. Menlove, C. D. Rael, N. Stoner, and M. Clapham, "SuperHENC: Final Performance and Certification Summary," Los Alamos National Laboratory report LA-UR-01-6459, December 2001.

10. T. W. Crane and M. P. Baker, Chapter 13, "Neutron Detectors," in Passive Nondestructive Assay of Nuclear Materials, edited by T. D. Reilly, N. Ensslin, and H. A. Smith, US Nuclear Regulatory Commission NUREG/CR-5550, March 1991.

11. N. Ensslin, Chapter 16, "Principles of Neutron Coincidence Counting," in Passive Nondestructive Assay of Nuclear Materials, edited by T. D. Reilly, N. Ensslin, and H. A. Smith, US Nuclear Regulatory Commission NUREG/CR-5550, March 1991.

12. K. Boehnel, "The Effect of Multiplication on the Quantitative Determination of Spontaneously Fissioning Isotopes by Neutron Correlation Analysis," Nuclear Science and Engineering 90, 75-82 (1985).

13. P. M. J. Chard and S. Croft, "A Database of ^{240}Pu-effective and ^{235}U-effective Coefficients for Various Fertile and Fissile Isotopes," 19th Annual ESARDA Symposium, Montpellier, France, May 13-15, 1997.

14. D. M. Cifarelli and W. Hage, "Models for a Three Parameter Analysis of Neutron Signal Correlation Measurements for Fissile Material Assay," Nucl. Instr. Meth. A251, 550 (1986).

15. M. S. Krick, W. H. Geist, and D. R. Mayo, "A Weighted Point Model for the Thermal Neutron Multiplicity Assay of High Mass Plutonium Samples," Los Alamos National Laboratory report LA-14157 (2005).

16. M. S. Krick, W. C. Harker, P. M. Rinard, T. R. Wenz, W. Lewis, P. Pham, and P. De Ridder, "The IAEA Neutron Coincidence Counting (INCC) and the DEMING Least-Square Fitting Programs," Los Alamos National Laboratory report LA-UR-98-2378, Proc. 39th Annual INMM Meeting, July 26-30, 1998, Naples, Florida.

17. D. G. Langner, M. S. Krick, J. E. Stewart, and N. Ensslin, "The State-of-the-Art of Thermal Neutron Multiplicity Counting," LA-UR-97-2734, Proc. 38th Annual INMM Meeting, Phoenix, AZ, July 20-24, 1997.

18. J. E. Stewart, M. S. Krick, R. J. Lemaire, J. Xiao, V. Fotin, L. McRae, D. Scott, and G. Westsik, "Assay of Scrap Plutonium Oxide by Thermal Neutron Multiplicity Counting for IAEA Verification of Excess Materials from Nuclear Weapons Production," Los Alamos National Laboratory report LA-UR-96-2515, Proc. 37th Annual INMM Meeting, Naples, FL, July 28-31, 1996.

19. J. E. Stewart, M. S. Krick, D. G. Langner, and T. R. Wenz, "Neutron Multiplicity Assay of Impure Materials Using Four Different Neutron Counters," Los Alamos National Laboratory report LA-UR-98-2597, Proc. 39th Annual INMM Meeting, July 26-30, 1998, Naples, Florida.

20. W. H. Geist, M. R. Mahmoud, and O. S. Seo, "IAEA Multiplicity Measurements at the KAMS Facility," Los Alamos National Laboratory report LA-UR-03-4727, Proc. 44th Annual INMM Meeting, Phoenix, AZ, July 13-17, 2003.

7. ACTIVE NEUTRON MULTIPLICITY COUNTING

N. Ensslin, W. H. Geist, M. S. Krick, and M. M. Pickrell

7.1 INTRODUCTION

7.1.1 Definition of Active Neutron Multiplicity Counting

A nondestructive assay technique for bulk, highly-enriched uranium (HEU), called active neutron multiplicity counting, has been developed as an extension of passive neutron multiplicity counting. Development of this technique began about fifteen years ago (Ref. 1, 2, and 3), but there is still only limited literature and field experience. The purpose of this chapter is to document what is known to date and to give the reader a feel for the expected measurement performance of this technique.

As described in Chapter 6, passive multiplicity analysis usually uses neutron singles, doubles, and triples count rates to solve for plutonium mass, multiplication, and alpha. Active multiplicity analysis was developed to provide a similar capability for uranium. The doubles and triples count rates are used to solve for the sample multiplication and the induced fission rate. An Active Well Coincidence Counter (AWCC) or similar instrument is used to induce fissions in the ^{235}U, so the singles rate is not used because it is dominated by the large background from the AmLi interrogation sources. However, active multiplicity counting is more complex than passive multiplicity counting because there is an additional new parameter: the interaction of the AmLi source neutrons with the assay sample which is called the “coupling.” The ^{235}U mass depends on both the induced fission rate and the "coupling," and this parameter must also be determined, as described in Section 7.2.4.

This chapter will describe the equations used for active multiplicity, how measurements are made, and what measurement performance can be expected. The rest of this introductory section will describe the historical reasons for the development of this technique, its advantages and disadvantages, and its areas of application.

7.1.2 Historical Reasons for Active Multiplicity Counting

Active neutron coincidence counting using an AWCC equipped with AmLi interrogation sources is a standard technique for assay of ^{235}U, as described in Chapter 17 of Ref. 4. Calibration curves are normally obtained by counting uranium standards and plotting the double coincidence rate vs. ^{235}U mass. Because of neutron multiplication and absorption in the uranium, the calibration curves are nonlinear and are sensitive to the geometry and ^{235}U density of the item. The calibration curve approach works extremely well for many situations, and often yields nearly linear calibrations because of cancellation between multiplication and absorption effects.

To obtain accurate results with the calibration curve approach, the calibration standards must be representative of the assay items. Some of the important sample characteristics are the enrichment, density, geometry, and material composition. However, appropriate calibration curves are not always available, either because suitable standards are not available, or because the important characteristics of the items to be assayed are not well known. For example, uranium metal and uranium oxide items cannot be assayed with the same calibration curve, so representative physical standards of both material types are needed. For large mass HEU metal items, variations in the geometry of the items, or how they are stacked in the can, will change the

self-multiplication dramatically and cause large biases in the assay result. In general, the measurement bias will increase as the characteristics of the calibration standards and assay items diverge.

The goal of active neutron multiplicity counting is to use both the double and triple coincidence rates to provide a new measured parameter that solves for sample self-multiplication and thereby removes most of the bias caused by irregular sample geometry and density. This technique is much less sensitive to differences between the standards and the unknowns, and has a number of potential areas of application.

7.1.3. Areas of Application for Active Multiplicity Counting

Active neutron multiplicity counting has potential applications in shipper/receiver confirmation, inventory verification, or accountability measurements of uranium in difficult material forms. DOE facilities contain many metric tons of uranium in varied materials forms, including mixed oxides and metals, weapons components in shielded storage drums, high-density scrap/waste, remote-handled waste, and non-self-protecting irradiated fuels. The capability for direct accountability, inventory verification, or shipper/receiver verification of the ^{235}U is often not available because of the difficult measurement geometries involved. The use of active multiplicity counting can reduce inventory differences, expedite materials consolidation, and help reduce security and storage costs.

Some specific material forms for which active multiplicity counting may help provide less biased measurements, or provide ancillary information on sample self-multiplication or uranium enrichment, are listed below (Ref. 5). The technique could often be most useful if larger volume counters, or especially faster neutron counters (as described in Chapter 8) were available.

1. Measurement of kilogram quantities of HEU in metal, irregular metal scrap, or very impure oxide form. Uniform metal pieces of constant geometry are best assayed with conventional coincidence counting because of the better precision of the doubles rate.
2. Verification of uranium weapons components or weapons assemblies.
3. Assay of 5A UF_6 cylinders containing 10 to 20 kg of HEU. Measuring the self-multiplication may make it possible to correct for variations in the UF_6 shape that occur during freezing.
4. Accountability or verification of the HEU mass in U/Pu metal scrap, U/Pu oxide, high-density U/Pu waste, or HEU metal contaminated with Pu.
5. Measurement of alternative nuclear materials such as U-233 oxide, Np metal, or Np oxide. This may require development of additional NDA techniques such as combined neutron/gamma-ray/calorimetry or new active/passive neutron-based approaches.
6. Shipper/receiver verification or inventory verification of HEU stored in shipping containers. These are often shielded for personnel dose reduction, making the measurements very difficult. This may require development of new capabilities utilizing neutron generator-based NDA with associated particle imaging.
7. Accountability, verification, or outlier resolution of high-density HEU scrap/waste, low-density HEU scrap/waste, and remote-handled waste for safeguards termination. Better active/passive techniques that provide matrix and geometry-independent results may be required.
8. Accountability or verification measurements of un-irradiated, non-self-protecting U/Pu fuel assemblies, HEU fuel rods, and U-233 fuel assemblies.

7.1.4. Advantages and Disadvantages of Active Multiplicity Counting

The advantage of active multiplicity counting is the ability to provide a more accurate measurement for many of the HEU material forms described above. This is because information on sample self-multiplication is obtained without prior knowledge. As a result, calibration for some material types will require far fewer representative standards, at the cost of reduced accuracy. Fabrication costs for physical standards will be reduced, and assay biases associated with poorly defined items that lack representative calibration standards will be lessened. The measurement time, typically 1000s or more, is still relatively short compared to calorimetry or sampling and analytical chemistry.

The disadvantages of active multiplicity counting include the longer measurement times required to provide good precision on the triple coincidences (at least 1000s compared to the 100 to 300s counting times used for most conventional active coincidence assays). This can be reduced by the use of an active multiplicity counter, but this instrument costs more than a conventional AWCC. Also, the determination of the sample mass is not straightforward, requiring determination of a new parameter, the coupling, as described later.

7.2 ACTIVE MULTIPLICITY EQUATIONS

7.2.1 Overview

The analysis equations for active multiplicity counting are derived from those for passive multiplicity counting, as given in Chapter 6, and are similar in form. They are again based on the measured neutron singles, doubles, and triples count rates. The most important difference is the use of an active well counter equipped with AmLi sources to induce fissions in the ^{235}U. Thus, the fission rate to be solved for is not a passive rate, but an induced one. Also, the measured singles are dominated by the AmLi sources, and are usually not useful for assay. For the same reason, the parameter "alpha," a measure of (α, n) -induced neutrons, is not relevant. The equations are no longer self-contained, but now require additional information to determine the coupling between the AmLi source neutrons and the assay sample.

The active multiplicity analysis equations are also based on the assumptions described in Chapter 6 for passive multiplicity analysis. If actual measurement geometries and samples do not meet all of these assumptions, we can expect to encounter some biases or limitations. Specifically, the "point model" assumption that the neutron detector efficiency and the probability of fission are uniform over the sample volume is not always valid. The neutron counters used for active multiplicity analysis, like the AWCC, were not designed to provide a completely flat efficiency profile across the sample volume. More importantly, the assumption of constant fission probability across the sample volume is not valid for bulk HEU, and a multiplication bias correction has not yet been developed for active multiplicity analysis. The relationships for coupling as a function of multiplication that are described below tend to compensate for these effects, but not completely.

7.2.2 Singles, Doubles, and Triples Count Rates

The neutron multiplicity electronics and software yield the first three reduced factorial moments of the measured neutron multiplicity distribution, which are the singles, doubles, and triples counts, respectively. Theoretically, the singles, doubles, and triples count rates (S, D, T) are given by

$$S = S_0 + B + S_s + FM\varepsilon_f \nu_{s1} \tag{7-1}$$

$$D = \frac{F\varepsilon_f{}^2 f_d \nu_{s2}}{2} \bullet C_d \tag{7-2}$$

$$T = \frac{F\varepsilon_f{}^3 f_t \nu_{s3}}{6} \bullet C_t \ , \tag{7-3}$$

where S_o = singles count rate from the AmLi sources without a sample present,
B = background singles rate,
S_s = change to S_o due to scattering and absorption of AmLi neutrons by the sample,
F = induced fission rate in sample,
M = neutron multiplication
ε_f = efficiency for detecting induced fission neutrons,
ν_{s1}, ν_{s2}, ν_{s3} = first, second, and third reduced factorial moments for AmLi-induced fissions in ^{235}U. (Note that these symbols have a different definition for active versus passive multiplicity counting.)
C_d = a correction factor for self-multiplication of doubles,
C_t = a correction factor for self-multiplication of triples,
f_d = doubles gate fraction, and
f_t = triples gate fraction.

For a neutron detector with a die-away time characterized by a single exponential with a time constant τ, the doubles gate fraction f_d is given by

$$f_d = e^{-P/\tau}(1 - e^{-G/\tau}) \, . \tag{7-4}$$

where τ = detector die-away time,
G = shift register gate width,
P = shift register pre-delay.

The triples gate fraction is given approximately by

$$f_t = f_d{}^2 \tag{7-5}$$

but is usually determined experimentally. Note that ε_f is the efficiency for detecting induced fission neutrons. There is also a different (lower) efficiency ε_a for detecting AmLi source neutrons that pass through the shielded endcaps and still get detected.

In principle, the induced singles count rate could be used to determine the ^{235}U mass. In practice, the singles are dependent on AmLi neutron source scattering, neutron absorption, and background fluctuations. For large ^{235}U masses of well-defined geometry, useful assays have been obtained by singles counting if varying background is not a problem. But in general the active multiplicity approach described below, based on doubles and triples count rates, is much more accurate.

7.2.3 Calculation of Sample Self-Multiplication

Expressions for the correction factors C_d for doubles self-multiplication and C_t for triples self-multiplication can be derived from the passive multiplicity equations. In terms of the self-multiplication M, the expressions are as follows (Refs. 1 and 3):

$$C_d = M^2\left[1+\frac{(M-1)\nu_{s1}\nu_{i2}}{\nu_{s2}(\nu_{i1}-1)}\right] \tag{7-6}$$

$$C_t = M^3\left[1+\frac{(M-1)(3\nu_{s2}\nu_{i2}+\nu_{s1}\nu_{i3})}{\nu_{s3}(\nu_{i1}-1)}+\frac{(M-1)^2 3\nu_{s1}\nu_{i2}^{\ 2}}{\nu_{s3}(\nu_{i1}-1)^2}\right] \tag{7-7}$$

where ν_{i1}, ν_{i2}, ν_{i3} = first, second, and third reduced factorial moments for subsequent generations of fission neutron-induced fissions in ^{235}U.

Using Eqs. 7-6 and 7-7 for the self-multiplication correction factors and Eqs. 7-2 and 7-3 for D and T, it is possible to solve for sample self-multiplication without knowing the fission rate F, which cancels out in the ratio T/D. The self-multiplication M can be obtained by solving the following cubic equation (Ref. 1):

$$\begin{aligned}
&M^3 + M^2\left[\frac{3\nu_{s2}(\nu_{i1}-1)\nu_{i2}+\nu_{s1}(\nu_{i1}-1)\nu_{i3}-6\nu_{s1}\nu_{i2}^{\ 2}}{3\nu_{s1}\nu_{12}^{\ 2}}\right] \\
&+M\left[\frac{\nu_{s3}(\nu_{i1}-1)^2+3\nu_{s1}\nu_{i2}^{\ 2}-3\nu_{s2}(\nu_{i1}-1)\nu_{i2}-\nu_{s1}(\nu_{i1}-1)\nu_{i3}-(3T/D\varepsilon_f)(f_d/f_t)\nu_{s1}(\nu_{i1}-1)\nu_{i2}}{3\nu_{s1}\nu_{12}^{\ 2}}\right] \\
&+\frac{3T}{D\varepsilon_f}\frac{f_d}{f_t}\left[\frac{\nu_{s1}(\nu_{i1}-1)\nu_{i2}-\nu_{s2}(\nu_{i1}-1)^2}{3\nu_{s1}\nu_{12}^{\ 2}}\right]=0.
\end{aligned} \tag{7-8}$$

The triples/doubles ratio provides a good measure of the neutron multiplication, as documented in Ref. 6. A value for the multiplication is needed to perform active multiplicity assays and is useful by itself to help authenticate uranium samples.

7.2.4 Definition of Sample Coupling

Equations 7-1 through 7-3 are similar to those used in passive multiplicity counting. However, for active multiplicity counting, F is the rate at which neutrons from the AmLi interrogation

sources induce first generation fissions in ^{235}U, rather than the ^{240}Pu-effective spontaneous fission rate. Therefore, active multiplicity analysis requires a new parameter called the "coupling" which describes the induced fission rate, F, in terms of the AmLi source strength, Y, and the mass *m* of ^{235}U in the assay sample:

$$F = CmY \tag{7-9}$$

where C = coupling,
F = induced fission rate in sample from the AmLi neutrons,
Y = total output of both AmLi sources (neutrons/s), and
m = mass of ^{235}U in grams.

The coupling depends on the item's geometry, ^{235}U density, chemical and isotopic composition, and location in the assay chamber. In broader terms, it depends on the solid angle between the sample and the AmLi sources, the neutron multiplication in the sample, and other neutron moderation, scattering, and absorption effects. For these reasons, the coupling will not be linear with sample mass.

If we substitute Eq. 7-9 into Eqs. 7-2 and 7-3 for the doubles and triples count rates, the product *Cm* appears together in both equations. Thus we cannot solve for the sample mass *m* without using some additional information to obtain an equation for the coupling. During the development of active multiplicity counting, several different expressions for the coupling have been derived.

The original uranium metal measurements at Savannah River Site and Y-12 (Ref. 2) used a coupling equation of the form

$$CY = a + \frac{b}{m^{1/3}}\ , \tag{7-10}$$

where *a* and *b* are calibration constants. This equation was selected so that the fission rate F in Eq. 7-9 would have the form $am + bm^{2/3}$. One term is proportional to sample mass, as expected for high-energy interrogation neutrons, and one term is proportional to the sample's surface area, as expected for low-energy interrogation neutrons.

Later work revealed an empirical relationship between the coupling and the multiplication (Ref. 3 and 6). This was an important discovery because the multiplication can be obtained from the triples/doubles ratio independent of sample mass or coupling, as described in the previous section. Monte Carlo calculations for a series of metal and oxide standards (Ref. 7) showed that the coupling was inversely related to the multiplication because of the increasing penetration of the AmLi source neutrons at lower ^{235}U densities. The coupling was also found to be nearly independent of ^{235}U mass and density. A good fit to the data was obtained with the following equation:

$$C = a - \frac{b(M-1)}{1 + c(M-1)}\ , \tag{7-11}$$

where *a*, *b*, and *c* are calibration coefficients. This relationship between the coupling and the multiplication is illustrated in Figure 7.1 (Ref. 6).

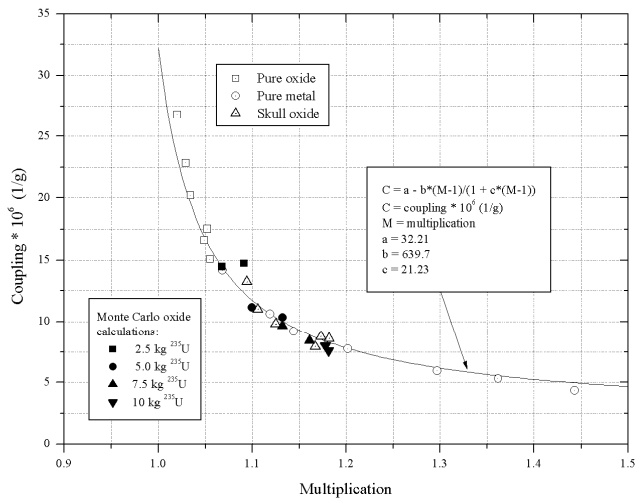

Fig. 7.1 Coupling as a function of multiplication for three categories of uranium samples (Ref. 6).

With the coefficients shown in Figure 7.1, Eq. 7-11 was applied to a series of very impure "skull oxide" items measured at Y-12 (Ref. 6). Because these items had known masses, fill heights, enrichments, and diameter, and were relatively uniform, it was possible to calculate their multiplication by Monte Carlo. The calculated values compared very well with those obtained using the triples/double ratios. The coupling and the multiplication correction factor tend to compensate each other, so that the product is insensitive to ^{235}U mass over a relatively large range. This provides a quantitative explanation for why an almost linear calibration curve of double coincidences versus ^{235}U mass works well for AWCC measurements of many metal and oxide items. For active multiplicity analysis, the use of calibration curves of coupling versus multiplication looks promising for the assay of uranium samples whose detailed characteristics are not known, such as irregular pieces of metal and impure oxide.

A mathematical relationship for the coupling as a function of the solid angle between the sample and the AmLi sources and the sample multiplication has also been developed (Refs. 8 and 9). This relationship can be written as

$$C = k\varphi(\Omega)\varphi(M), \tag{7-12}$$

where $\phi(\Omega)$ represents the dependence of the coupling on the source-sample geometry, $\phi(M)$ represents the dependence of the coupling on the flux depression within the sample, and k is a scaling factor determined from calibration standards. To obtain an expression for $\phi(M)$, this approach derives the "loss-to-fission ratio" of first fission generation neutrons that are leaking out of the sample as

$$\frac{P(loss)}{P(fission)} = \frac{\nu_{i1}M}{M-1} - 1\,. \tag{7-13}$$

If leakage is the main loss mechanism, then this ratio is the probability of a fission neutron leaking from the sample divided by the probability that it will induce further fission. And if fission is the main absorption mechanism, then the flux depression of the AmLi interrogation

neutrons is just the ratio of the probability that they will pass through the sample to the probability that they will be absorbed in fission. If a similar functional form is assumed to apply to AmLi neutrons entering the sample, the coupling can be written as

$$C = k\varphi(\Omega)\left(\frac{\nu_{i1}M}{M-1} - 1\right). \tag{7-14}$$

Once the coupling is determined from calibration curves of coupling versus multiplication using physical standards and/or Monte Carlo calculations, the product of the scaling constant k and $\phi(\Omega)$ is calculated by dividing the coupling by the $\phi(M)$ term. The approach works well for disks placed on top of each other in different configurations, as described in Section 7.5.4.

Monte Carlo calculations have also been used to study the coupling for uranium geometries and matrices for which standards are not available (Ref. 10). The calculations used the MCNPX code, which is capable of modeling the induced fission coincidence rate in uranium from an AmLi interrogation source (Ref. 11). The MCNPX results were benchmarked to measurements made with an AWCC, and then the code was used to model one set of metal items and two sets of oxide items in a cylindrical geometry. For cases where sample diameter was constrained, so that solid angle effects were minimized, the relationship between coupling and multiplication is nearly collapsed to a single curve, as shown in Figure 7.2.

The relationship shown in Figure 7.2 is almost independent of item characteristics, with significant divergence only at multiplications below 1.05. The fit shown through the data was determined with a complex combination of linear and exponential functional forms, and is a specific empirical fit to the detector and sample geometries selected for the study. The authors recommend that this approach be used by each facility undertaking active multiplicity measurements until such time as a more generic approach becomes available. Each facility should re-calculate the curve of coupling versus multiplication with their active well counter and their available physical standards, and supplement with MCNP calculations if necessary, in order to obtain the curve needed to analyze their data.

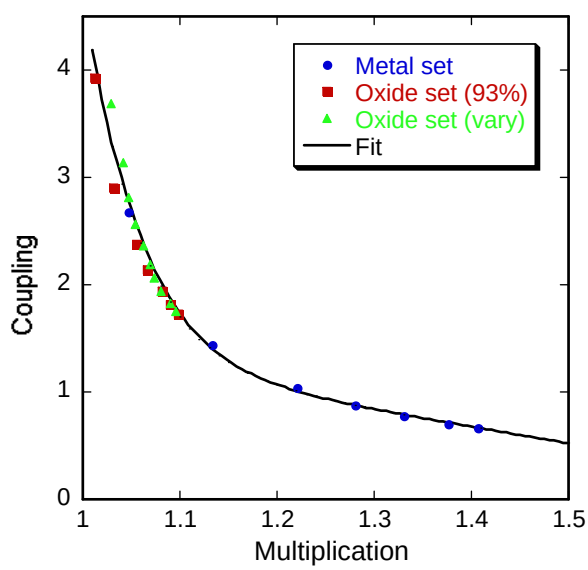

Fig. 7.2. The Monte Carlo modeled relationship between the multiplication and the coupling for three material types: uranium metal, uranium oxide of constant enrichment, and uranium oxide of variable enrichment. The black line is an empirical fit to all the data points (Ref. 10).

7.2.5 Determination of Uranium Mass

Once the sample multiplication M is obtained from the ratio of T/D using Eq. 7-8, the rate *F* of AmLi-induced fissions in the sample is obtained from the doubles count rate (Eq. 7-2), corrected for self-multiplication using Eq. 7-6. A relationship for coupling as a function of M and/or *m* must be selected, using one of the approaches described in the preceding section. The ^{235}U mass *m* is then given by

$$m = \frac{F}{CY} . \tag{7-15}$$

If the uranium enrichment is known, the total uranium mass is the result *m* divided by the enrichment. An alternative analysis method is explained in Ref. 12.

7.3 ACTIVE MULTIPLICITY MEASUREMENT PROCEDURES

7.3.1 Measurement Hardware

Most active multiplicity measurements to date have been carried out with conventional AWCCs that contain AmLi sources to induce fission events in the uranium. The AWCC measurement cavity is typically configured to have a detection efficiency of about 27% to 30% and a neutron die-away of about 52 µs. The only hardware change is the use of a multiplicity shift register to collect neutron single, double, and triple coincidence events. The AmLi sources do not produce a very high count rate, so a variety of existing multiplicity shift registers (including those without derandomizer circuits) or list mode modules can be used for this application. However, the AmLi neutron sources do produce a large number of accidental coincidence events that limit the assay precision, as described in more detail in Section 7.4.

The Epithermal Neutron Multiplicity Counter (ENMC) has also been used for active multiplicity measurements by designing and constructing a new set of active end plugs (Ref. 13). Several different design ideas were studied, including varying the end plug material, recessing the interrogation neutron sources, and shielding the interrogation sources with reflector materials. The optimum solution was to construct the endplugs from polyethylene without the interrogation sources recessed or shielded. Because the ENMC uses higher pressure ^{3}He tubes than the AWCC, the MCNP-calculated efficiency for the active mode was near 55%, with a die-away time around 19 µs. This large reduction in the die-away time relative to the AWCC reduces the number of accidental coincidences from the AmLi interrogation neutron source. Running the ENMC in active mode will reduce the assay time for uranium samples by a factor of approximately ten over the standard AWCC.

In the future, neutron counters designed specifically for active multiplicity counting may become available. There are several design goals for reducing the accidental coincidence background from the AmLi sources. The first goal is to design a counter that minimizes the interrogation neutron detection efficiency and maximizes the induced fission neutron detection efficiency. This will result in less random interrogation neutrons accidentally falling within the

coincidence gate. The second goal is to build a counter with as small a die-away time as possible. This will allow for a reduction in the coincidence gate width that reduces the accidental coincidence rate proportionally. Both goals may be realized by the development of a liquid scintillator-based neutron counter (Refs. 14 and 15). This counter could have a good efficiency of about 25% and a die-away time and coincidence gates as short as 30 ns. This would yield another order of magnitude reduction in assay time for HEU, and allow much smaller samples (about 100g or more) of HEU to be measured by active multiplicity counting. The current status of liquid scintillator counters is described in Chapter 8.

7.3.2 Measurement Software

Active multiplicity analysis requires the use of a software package to acquire and analyze data from the multiplicity shift register. Measurement control options, quality control tests, and calibration and least-squares fitting options are also needed in the software. These tasks can be accomplished with the INCC and Deming codes (Ref. 16), or several commercial software packages that utilize the same analysis algorithms. These codes include data collection and analysis algorithms for passive coincidence counting by several different algorithms, passive multiplicity counting, active coincidence counting, active minus passive coincidence counting, and active multiplicity counting. At this time the active multiplicity option in the INCC code only determines the neutron multiplication from the triples/doubles ratio, but does not determine the uranium mass. The calculation of sample coupling and ^{235}U mass requires the use of a separate spreadsheet. Complete active multiplicity analysis will be added to the INCC code in the near future.

7.3.3 Detector Characterization

Detector characterization measurements and software setup procedures for active multiplicity counting are similar to those described in Chapter 6 and in Ref. 17 for passive multiplicity counting. These measurements will determine the background singles, doubles, and triples count rates, the detector efficiency and die-away time, and the multiplicity shift register gate width and gate fractions. Because of the low count rates encountered in active multiplicity analysis, the coincidence and multiplicity deadtime coefficients can be set to the detector manufacturer's recommended values without further measurements. An exception might be if the detector is to be used for active/passive measurements of U/Pu, which will require very careful determination of the deadtime corrections.

Because active measurements are involved, it is important to fix and document the position and orientation of the AmLi sources in their holders and the position of all cadmium liners and metal reflectors in the assay chamber. Most importantly, the position of the uranium item must be carefully controlled and documented. For example, the shape and magnitude of the coupling curve will depend on whether the items are always placed on a fixed stand, independent of their fill height, or whether they are positioned at different heights to keep the uranium itself in the center of the assay chamber.

7.3.4 Measurement Control and Calibration

Measurement- and quality-control procedures for active multiplicity counting are again similar to those described in Chapter 6 and in Ref. 17 for passive multiplicity counting. These will

usually include a checksum test on the shift register electronics, the accidentals/singles test, an outlier test which rejects runs that lie outside a limit, a measurement control chi-squared limit, a declared-minus-assay quality check limit, and a high voltage test limit. For all measurements, the count time should be split up into a minimum of 10 runs, with an individual length of 10 to 100s. This makes it easier to diagnose electronic noise or instrument drift problems, and makes it possible to use quality control outlier tests. The outlier tests can reject runs with unusually large double or triple coincidence bursts due to cosmic rays. Background runs should be done daily when the instrument is in use, or more frequently, if there is reason to believe that the room background is changing significantly. Also, normalization runs should be done daily with a neutron source or physical standard to ensure that the counter is operating correctly.

The calibration process for active multiplicity counting consists of several distinct steps.

1. First one must determine the fission neutron detection efficiency ε_f, the doubles gate fraction f_d , and the triples gate fraction f_t as part of the process of detector characterization. These values are used by the software code to calculate the correct multiplication M for each item using the doubles and triples count rates (Eq. 7-8). Representative physical standards of known multiplication should be used to validate this calculation if possible.
2. A relationship for coupling as a function of multiplication M and/or sample mass *m* must be selected. The best approach to date (Ref. 10) is to develop a new curve of coupling as a function of M with each facility's actual neutron counter and the physical standards or working reference materials available at that site. If necessary, the coupling curve can be supplemented with Monte Carlo modeling of the containers to be measured. However, one cannot model the singles, doubles, and triples count rates accurately because of uncertainties in the AmLi source spectra, the neutron source strength Y, the amount of source shielding in the detector, the exact detector geometry, etc. So the modeling study can provide the relative shape of the curve, but one or more representative physical standards will be needed to provide absolute values.
3. In principle, the multiplication correction and the coupling curve contain enough information to provide calibrated assays using Eq. 7-15. This approach should be validated against representative physical standards or working reference materials if at all possible.
4. The active multiplicity calibration procedure does not need to be repeated unless there is a significant change to the physical configuration of the unknown items to be measured or to the detector, new electronics are installed, or measurement control limits cannot be maintained.

7.3.5 Item Measurement Procedure

Active multiplicity measurements should be made with the uranium content of the item centered in the assay chamber. For example, a 15% difference in response was reported in Ref. 2 by misplacing cans of HEU metal by about 5cm vertically. The item should also be centered radially in the counting chamber to minimize position effects caused by efficiency variations. This counting geometry should be maintained for all standards and assay items.

The count time should be sufficient to provide the desired measurement precision. One percent RSD on the triple coincidence counts is desirable, which typically requires 1000 seconds or more of counting time, as described in Section 7.4.

Item measurement data should be corrected for the small double and triple coincidence background from the AmLi neutron interrogation sources by the multiplicity counter's data acquisition and analysis software. This background is due to electronic pulse pileup and/or source impurities. It may also be necessary to correct for the double and triple coincidence backgrounds from cosmic-ray induced spallation neutrons. This correction is proportional to the total mass of uranium present in the chamber, and can be large at high uranium masses because uranium is a very high-Z material with a good cross section for producing spallation neutrons. It is also good to correct the measurements for spontaneous fission in ^{238}U.

The final solution for the desired ^{235}U mass *m* then requires the following steps:

1. The active multiplicity option in the software code can determine the neutron multiplication from the triples/doubles ratio using Eq. 7-8.
2. Using a separate spreadsheet, the sample coupling is obtained from the previously determined curve of coupling as a function of multiplication M. This curve should incorporate the AmLi neutron source strength Y.
3. The rate F of AmLi-induced fissions in the sample is obtained from the doubles count rate (Eq. 7-2), corrected for self-multiplication using Eq. 7-6.
4. The ^{235}U mass *m* is obtained from Eq. 7-15. If the relationship for coupling involves the uranium mass *m* as well as the multiplication M, then the solution for *m* can be obtained by iteration or by developing a new analytical equation that solves for *m* in closed form. (The small corrections for cosmic-ray induced spallation and ^{238}U spontaneous fission may also require iteration.)
5. The total uranium mass is the result *m* divided by the enrichment.
6. The measurement precision in the triples/doubles ratio and the resultant multiplication M is provided by the software analysis package, but the final uncertainty in the ^{235}U mass is not currently available. The dominant source of counting uncertainty is usually the triples, so this can be estimated and propagated in the final spreadsheet analysis. This would provide a value for the final measurement precision, but not a Total Measurement Uncertainty (TMU) that includes all possible sources of error. Additional information on measurement uncertainties is given in the next section.

7.4 ACTIVE MULTIPLICITY COUNTING PRECISION

7.4.1 Calculation of Expected Counting Precision

As mentioned earlier, active multiplicity counting involves relatively low count rates compared to passive multiplicity counting. Most of the singles events are just due to the AmLi sources, and there are not many doubles and triples from induced fissions. Indeed, the AmLi neutrons are the major source of accidental double and triple coincidences that limit assay precision. This leads to an important question: are enough real triple coincidences detected to make active multiplicity analysis a useful analysis technique for realistic uranium items and practical counting times?

To answer this question, calculations of the expected measurement precision due to counting statistics were carried out with an active version of the Figure of Merit code used for the design of passive multiplicity counters (Refs. 1, 18, 19). The code predicts the expected single, double, and triple count rates and their estimated precision by calculating the factorial moments of the expected neutron multiplicity distribution. The multiplicity distribution does not need to be measured, but is predicted from pre-selected sample and detector design parameters. The code

also computes the triples/doubles ratio and its uncertainty in order to obtain an estimate of the multiplication and its uncertainty. For active multiplicity counting, the Figure of Merit code requires an estimate for coupling. The empirical relationship between coupling and self-multiplication from Figure 7 in Ref. 6 was used. The code was benchmarked by comparison with measurements of bulk uranium metal and oxide samples.

Calculations of the expected measurement precision were done for three detector options: a thermal neutron counter like the AWCC, the Epithermal Neutron Multiplicity Counter (ENMC), and a future liquid scintillator-based fast neutron counter (Ref. 19). The properties of the three detector options are summarized in Table 7-1. All three options assumed a cylindrical sample cavity of about 20 cm in diameter and 25cm high, plus 2.5 cm of lead shielding between the cavity and the neutron detectors for the scintillator-based option. The selection of upper and lower end plug material (polyethylene, graphite, or nickel) affects fission neutron detection efficiency, AmLi neutron detection efficiency, and die-away time. The selection shown in Table 7-1 is intended to optimize active assay precision while still retaining a relatively penetrating AmLi neutron interrogation spectrum in the sample cavity.

Table 7-1. Detector parameters used for performance calculations (Ref. 19).

Active Detector System Name	No. of Neutron Det.	AmLi Source Strength (n/s)	End Plug Material	Fission Neutron Detection Efficiency	AmLi Neutron Detection Efficiency	Die-Away Time (micros)	Coinc. Pre-Delay (micros)	Coinc. Gate Width (micros)
Active We	42	20000	poly	26.7%	6.94%	52	3	64
Epitherma	121	40000	poly	55.0%	16.00%	19	3	28
Liquid Sci	24	1000000	nickel	25.0%	0.60%	0.030	0.005	0.050

7.4.2 Results for Thermal Neutron Counting

Assay precision for a thermal neutron counter was calculated using a standard AWCC configuration with 42 ^{3}He tubes (4-atm) to detect thermal neutrons (Ref. 19). The AWCC was assumed to be in the fast mode, with polyethylene end caps and a cadmium-lined sample cavity. Although the AWCC usually employs two AmLi neutron sources that each emit about 50,000 n/s, the calculations assumed a total yield of 20,000 n/s. This is because Figure-of-Merit calculations for active multiplicity show a minimum in the precision curve with an optimum source yield in range of 20,000 to 50,000 n/s (Ref. 1).

Figure 7.3 illustrates the calculated relative standard deviation (RSD) for active multiplicity assay for the AWCC, the ENMC, and the liquid scintillator, assuming 1000-s counting times (Ref. 19). Counting precision for the AWCC does not achieve 1% unless the item contains 4 kg or more of ^{235}U. By comparison, the curves for conventional coincidence counting can achieve 1% at 2 kg of ^{235}U. The counting precision is always better for conventional coincidence counting than for multiplicity analysis, but in this example it is not much better. But we can conclude that 1% active multiplicity measurements cannot be achieved with an AWCC in 1000-s count times except for large metal items.

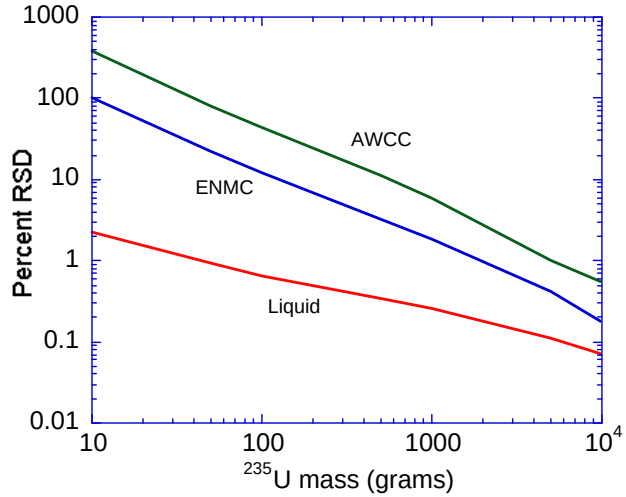

Fig. 7-3. Estimated RSD for the active multiplicity assay as a function of ^{235}U mass (g) in uranium metal for the three detector options summarized in Table 7.1 with 1000-s counting times (Ref. 19).

Benchmark measurements showed that the calculated precision curves were usually within 15 to 25% of the actual observed uncertainties. In-plant measurements at Savannah River and Y-12 confirmed a useful active multiplicity assay precision of 1 to 2% RSD in 1000s counting time for 4 kg or more of ^{235}U metal using a conventional AWCC (Ref. 2).

7.4.3 Results for Epithermal Neutron Counting

The new ENMC (Ref.13) contains more ^{3}He tubes, at 10-atm pressure, and less moderator material than the AWCC, allowing it to detect epithermal neutrons before thermalization. For active multiplicity counting with the ENMC, the predicted counting precision is illustrated in Figure 7.3 (Ref. 19). All calculations again used the parameters summarized in Table 7-1. For the ENMC, the basic cavity design and geometry are similar to the AWCC, and the coupling values should be similar. Over the mass range from 10 to 10,000 g ^{235}U, the ENMC is predicted to have roughly 2 to 4 times lower RSD than the conventional AWCC, which would imply 4 to 16 times shorter counting times for active multiplicity analysis. Stated differently, the ENMC should be able to do active multiplicity analysis of 1 kg or larger samples in 1000 s to within 1% RSD, whereas the AWCC needs 4 kg or larger samples to obtain the same precision.

These predicted count time factors for the ENMC relative to the AWCC were benchmarked by measuring a series of ^{235}U oxide standards, each with about 1 kg of uranium but with different enrichments (Ref. 13). Each standard was counted to a 1% doubles precision in both counters. The counters were configured in a similar manner with the same cavity height and interrogation sources. Shown in Table 7-2 are the count times and the count time ratio (AWCC/ENMC) for each standard. This factor ranges from 5.1 to 10.7 for the doubles count rate over the measured mass range. The triples count rate will have even better ratios.

Table 7-2. Count time factors required to reach a fixed 1% precision for each standard (Ref. 13).

^{235}U Mass (g)	AWCC count time(s)	ENMC count time(s)	Count time factor
116.8	52800	8220	6.4 ± 1.1

128.4	47400	6540	7.3 ± 1.4
170.5	33840	3150	10.7 ± 1.7
265.0	11250	1980	5.7 ± 1.1
372.1	12180	1480	8.2 ± 1.3
515.4	5910	830	7.1 ± 1.1
658.8	3690	720	5.1 ± 0.9
904.0	3500	355	9.9 ± 2.0

7.4.4 Results for a Future Fast Neutron Counter

If faster active neutron assay systems could be developed to increase facility throughput on uranium inventory verification measurements, this would provide large benefits in measurement time and operating cost. For example, wherever the RSD for a measurement is reduced by a factor of 3, the count time required to obtain that RSD is reduced by a factor of 9.

The third detector option in Table 7-1 is a proposed array of very fast NE213 or BC501 liquid scintillators assembled into a fast neutron coincidence counter (Refs. 14 and 15). This option can provide good total neutron detection efficiency if enough liquid scintillator cells are used. Each cell requires pulse shape discrimination electronics to separate neutron recoil events in the scintillator from the Compton-scattered gamma rays. Because fast fission neutrons are detected very quickly in the scintillators, the "die-away time" is really just the time-of-flight of the neutrons from the sample into the detector cells, roughly 30 ns or less for a typical can-sized counting chamber. The coincidence resolving time can then also be extremely short, leading to very low accidental coincidence counting rates. Also, the ability to discriminate against the lower energy AmLi neutrons makes it feasible to use very large interrogation sources and increase the induced fission rate.

For active multiplicity counting, the performance of a liquid-scintillator-based fast neutron counter in Figure 7.3 is predicted to be good enough for 1% or better assay precision over nearly the entire ^{235}U mass range (Ref. 19). If this can be realized in practice, then a liquid scintillator-based counter could provide active multiplicity results for almost all DOE facility inventory materials within 1000-s counting times or less.

7.5 ACTIVE MULTIPLICITY MEASUREMENT PERFORMANCE

7.5.1 Factors that Affect Measurement Performance

This section summarizes the information available to date on active multiplicity measurement performance in DOE facility or laboratory campaigns. As described in the previous section, the limited precision of the triple coincidences in a reasonable counting time provides a limit on the attainable performance. However, other factors may bias the measurement, and their effect may exceed that of counting statistics.

Active multiplicity assays can be biased by a number of usually unknown, or incompletely known, sample or detector properties. These can include spatial variations in neutron self-multiplication or detection efficiency resulting from matrix effects such as neutron moderation, absorption, scattering, or capture. The item's size, shape, and density can affect the coupling parameter, and its radial and axial placement in the well counter can also affect coupling and neutron detection efficiency. If the calibration procedure provides a relationship for coupling as a function of multiplication that is based on some representative physical standards, then many of

the potential sources of assay bias are already folded into this relationship. Other samples with larger variations in matrix effects may still lead to measurements biases. But in most cases the ability to measure sample multiplication and the use of a representative coupling curve makes active multiplicity assays more bias-free than conventional coincidence assays, as described in this section.

7.5.2 Uranium Metal Field Measurements

In-plant active multiplicity measurements of bulk, highly-enriched uranium metal have been carried out at the Savannah River Fuel Tube Fabrication Facility and the Y-12 Uranium Processing Facility (Ref. 2). The measurements were made with standard AWCCs outfitted with multiplicity shift registers. The sample cans contained HEU metal chunks, plates, and cylinders, which typically filled the cans to within several centimeters of the top. The mass of ^{235}U varied from about 0.4 to 17 kg.

Figure 7.4 illustrates one set of Y-12 data on a series of HEU metal cans (and one can of impure oxide) with the observed doubles response plotted as a function of ^{235}U mass. The data show the non-linear effect of the coupling between the AmLi sources and the sample, which causes the response curve to bend down, and the effects of sample self-multiplication, which causes a very high and variable response at a ^{235}U mass of 16 kg. One 16 kg ^{235}U sample was measured three times: as received, with the can tamped down so that the metal pieces would have a closer packing and higher self-multiplication, and with the pieces loosened. This yielded the cluster of the three highest data points on the graph. Also note that the oxide data point does not lie on the same response curve as the metal samples. The scatter in the conventional AWCC assay of these samples, which is based on the observed double coincidence rate, is 25% (RSD).

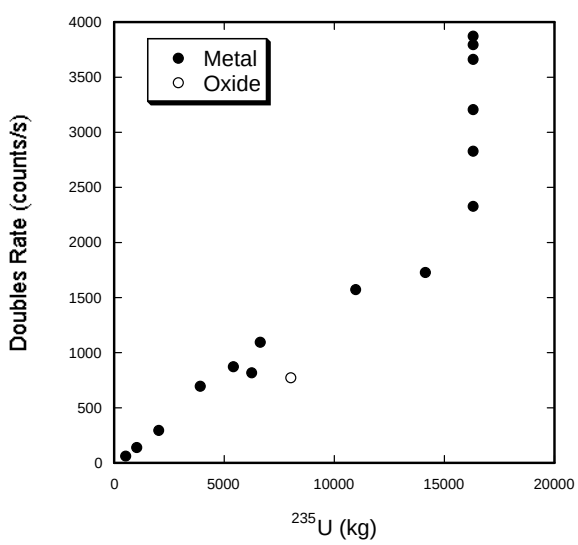

Fig. 7.4. Y-12 data on HEU metal and oxide samples measured in an AWCC. The observed doubles are plotted as a function of ^{235}U mass (Ref.2).

The active multiplicity results are plotted in Figure 7.5, which illustrates the multiplication-corrected double coincidence rate as a function of ^{235}U mass. The corrected rates provide a smooth fit through all of the metal data and the one oxide sample. The non-linear shape of the curve is attributed to the non-linear dependence of the coupling. The active multiplicity assay is consistent with the tag values to within 2% (RSD). This is remarkable agreement, considering the wide variety of samples and the initial, uncorrected scatter of 25% (RSD) (Ref. 2).

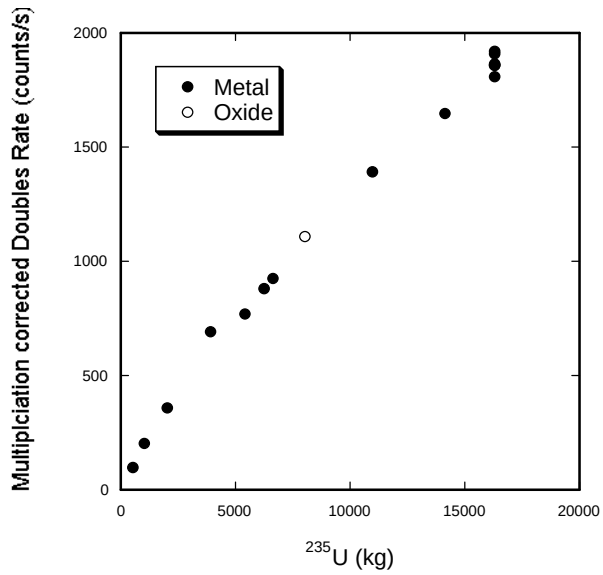

Fig. 7.5. Y-12 data on HEU metal and oxide samples measured in an AWCC. The triples-to-doubles ratio is used to correct the doubles response, and the self-multiplication-corrected doubles are plotted as a function of ^{235}U mass (Ref.2).

7.5.3 Uranium Oxide Field Measurements

Seven skull oxide (very impure U_3O_8) samples were measured at the Y-12 Uranium Processing Facility (Ref. 6). These contained 55% to 84% uranium by weight and also contained erbium, a strong thermal neutron absorber. The measurements were performed in a standard AWCC, but with an erbium liner to reduce the sensitivity of the measurements to that impurity. For the 7 skull oxide containers, the conventional calibration curve fit is 9.1% RSD with a doubles precision of about 1%. The active multiplicity analysis used Eq. 7-11 for the coupling (Figure 7.1) and yields a 4.4% RSD. The standard deviation from counting statistics is about 2%, so the dominant error is from the coupling estimate in Eq. 7-11.

These oxide measurements show a correlation between sample density and the observed triples-to-doubles ratio that is good enough to provide a quantitative correction factor rather than just a diagnostic flag. After the self-multiplication correction is applied, a smooth non-linear response curve is obtained, suggesting that the effects of sample geometry on coupling may be tolerable.

7.5.4 Laboratory Measurements of Uranium Metal Standards

A laboratory measurement campaign with HEU metal disks to evaluate active multiplicity analysis in a controlled setting is reported in Ref.9. An AWCC was used to measure the disks in several different configurations to allow a comparison of conventional calibration curve analysis and active multiplicity analysis. Three measurements were taken with a different number of disks (different mass) in compact geometry for use as calibration points. The rest of the measurements were performed with the pucks arranged in 15 different configurations using aluminum metal spacers, as illustrated in Figure 7.6. The count times ranged from 5 to 10 minutes which generally resulted in a precision in the triples count rate of better than 3%.

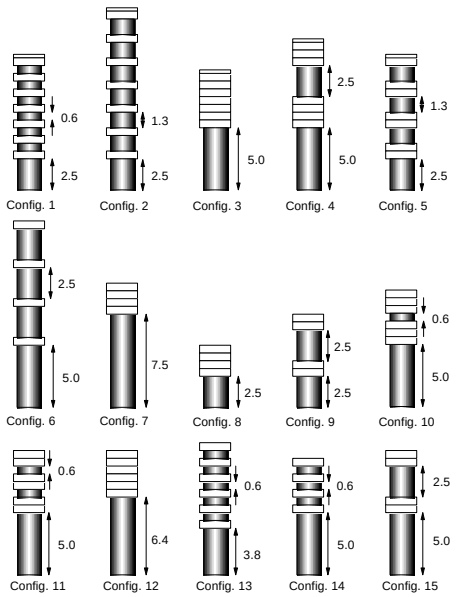

Figure 7.6. The 15 different configurations of uranium disks. The disks are represented by rectangles, and the aluminum spacers are shown as cylinders, with their heights given in cm. Each uranium disk has a mass of approximately 528 grams except for one which has about half the mass. The configurations labeled 3, 7, and 12 were used for calibration.

A conventional calibration curve of doubles count rate as a function of ^{235}U mass was determined from the three calibration configurations using a polynomial expression (Ref. 9). Using that calibration curve, the assays for the remaining 12 configurations are biased low by 6.5% with a scatter of 4.4% (RSD).

For active multiplicity analysis, the three calibration data points were used to solve for the scaling constant in the coupling relationship in Eq. 7-14, using the multiplication values obtained from the triples/doubles ratios. The solid angle factor $\phi(\Omega)$ was assumed to be constant and the actual scaling factor derived from the three calibration standards was the product $k\phi(\Omega)$. This scaling factor was constant to within 1%, suggesting that this approach works well for disks placed on top of each other in different configurations in the center of the assay chamber with no strong radial variations. The ^{235}U masses for the other configurations were then calculated from Eq. 7-15. The results are biased low by only 0.3%, with a scatter of 2.9% (RSD).

The active multiplicity results are in better agreement with the known mass than the calibration curve results, as summarized in Figure 7.7. This improvement is the result of using both the doubles and triples count rate to solve for the multiplication, which is dependent on the uranium material configuration. The current work used the same material form for both the determination of the scaling factor and the assay measurements. Experimental work to determine the sensitivity of the scaling factor to other materials forms is needed.

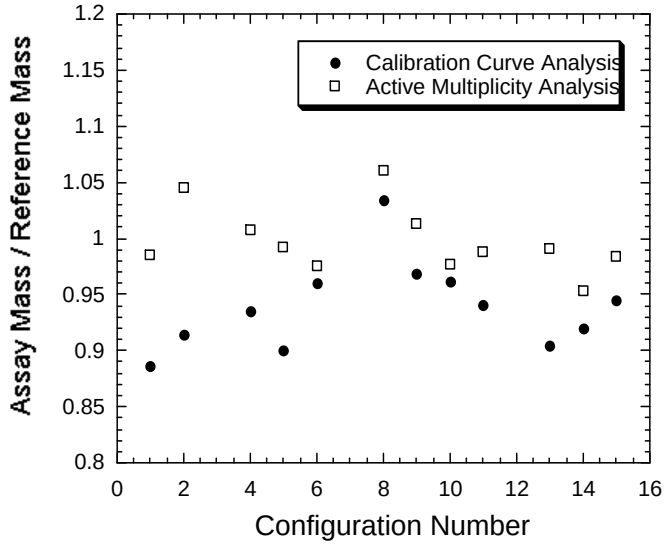

Figure 7.7. Comparison between the calibration curve analysis results (solid circles) and the active multiplicity analysis results (open squares) for the different HEU metal disk configurations. An unbiased result will have an Assay Mass / Reference Mass value of unity (Ref. 9).

7.5.5 Uranium Metal and Oxide Modeling Results

A Monte Carlo study undertaken to better understand the relationship between the multiplication and the coupling as the geometry of the sample varies is reported in Ref. 10. The modeling allows a wide range of material characteristics to be explored. In this case, uranium metal and oxide items in the range of 1 to 3 kg were modeled in a variety of different cylindrical geometries. To benchmark the Monte Carlo calculations, a uranium metal sample was measured in an AWCC. This step is essential because of uncertainties in the AmLi neutron source strength, the AmLi energy spectrum, the exact position of the AmLi sources within their containers, and other spatial variations that affect the doubles and triples gate fractions. These uncertainties limit the absolute agreement between the Monte Carlo calculations and measurements to about 10%, but the calculations can provide good relative comparisons.

The Monte Carlo study modeled a set of metal items, a set of oxide items with a constant enrichment of 93%, and a set of oxide items with constant mass but variable enrichment. The results were analyzed with both the conventional calibration curve and active multiplicity techniques. Calibration curves for the conventional analysis were obtained by fitting the modeled doubles rate versus mass for the three material types. Ten uranium masses (metal or oxide) were chosen randomly, the neutron count rates were modeled, and the results were analyzed with the three conventional calibration curves and an active multiplicity analysis based on a single curve of coupling versus multiplication (Fig. 7.2).

The results of the analysis are shown in Table 7-3. The active multiplicity analysis technique results have a bias 2% with a scatter of 5% (RSD). This technique did much better than all 3 of the conventional calibration curves. For two items, the active multiplicity assays were more than 5% different from the true value. These items were oxide samples with a low multiplication (less than 1.05). The relationship between the multiplication and the coupling at small values of multiplication changes very rapidly with multiplication, and is not as well defined. Any small errors in the multiplication can lead to large errors in the coupling and the mass.

7.5.6 Modeling of Inhomogeneous Uranium Items

A modeling study of inhomogeneous items is reported in Ref. 10. There were situations where facilities needed to measure oxide mixed with metal pieces, or cans of metal chunks. To simulate this, the modeling study distributed 10, 20, or 50 metal spheres throughout a can of uranium oxide. The sphere radius was randomly chosen and varied up to a maximum of either 0.5 or 1 cm. For each combination of the number of spheres and maximum radius, five randomly generated samples were modeled.

Table 7-3. Ratio of the assay mass divided by the true mass used in the Monte Carlo m for 10 randomly generated samples. Shown are the mass ratios for the 3 conventional calibration curves (the metal, constant enrichment, and variable enrichment material typ and the active multiplicity analysis technique.

Item mass (g) and type	Metal Calibration Curve	Oxide Calibration Curve (93%)	Oxide Calibration Curve (variable)	Active Multiplicity Analysis
580 (oxide)	1.59	1.17	1.02	1.05
342 (metal)	1.04	0.70	0.53	1.03
1184 (oxide)	1.34	1.08	1.02	1.00
1366 (metal)	1.00	0.78	0.72	1.00
308 (oxide)	1.68	1.16	0.94	1.07
149 (metal)	1.06	0.68	0.41	0.98
88 (oxide)	1.55	0.98	0.54	1.10
126 (oxide)	1.59	1.04	0.68	0.99
2346 (metal)	1.00	0.89	0.89	0.99
483 (oxide)	1.48	1.05	0.89	0.94
Average	1.33	0.95	0.77	1.02
RSD	0.28	0.18	0.22	0.05

Table 7-4 summarizes the results of the 5 Monte Carlo calculations for each of the different sphere characteristics (Ref. 10). For these inhomogeneous items, the oxide calibration curve modeled with the constant enriched material and the active multiplicity results generally did best. The metal calibration curve leads to large biases for materials that are still relatively dilute. The Monte Carlo study showed how the calibration curve results become biased when the standards do not represent the assay items. The study also showed that the active multiplicity analysis has the potential to overcome some of the limitations of the calibration curve analysis.

Table 7-4. Ratio of the assay mass divided by the true mass used in the Monte Carlo model for inhomogeneous U oxide items with embedded metal spheres.

No. of spheres	Max sphere radius (cm)	^{235}U mass(g)	M	Metal	Oxide (93%)	Oxide (variable)	Active multiplicity
0		1227	1.07	1.25	1.00	0.94	0.96
10	0.5	1248	1.07	1.24	0.99	0.94	0.96
10	1.0	1423	1.09	1.19	0.97	0.93	1.00

20	0.5	1262	1.07	1.24	0.99	0.93	0.96
20	1.0	1505	1.09	1.17	0.96	0.92	1.01
50	0.5	1337	1.08	1.22	0.98	0.93	0.98
50	1	2144	1.14	1.07	0.94	0.95	1.09
Average				1.20	0.98	0.93	0.99
RSD				0.06	0.02	0.01	0.05

7.5.7 Expectations for Other HEU Materials

The measurement results reported in this section show that active multiplicity counting provides a more robust assay than conventional coincidence counting because it provides additional information, the sample self-multiplication. For material types where it is possible to construct a curve of coupling as a function of multiplication and/or mass, active multiplicity analysis can provide useful shipper/receiver or inventory verification measurements without a large number of representative standards, like passive multiplicity counting. For example, active multiplicity will give relatively unbiased results between uranium metal and oxide, even if the counting precision is reduced. Like passive multiplicity counting, it may be appropriate to calculate each item's mass by both conventional and multiplicity analysis, and compare the results. The conventional analysis will have better precision, but if the two approaches differ by much more that the expected scatter, then the active multiplicity results should be less biased.

Future work on active multiplicity counting will include the study of additional geometries and material types and the development of better relationships between coupling, multiplication, and mass. Equally important, the future use of epithermal or fast neutron counters will allow the technique to be extended to the wide variety of low or medium mass uranium scrap that is present in DOE facilities. As new high efficiency, large volume passive neutron counters go into service, it will be possible to add active end plugs that enable verification of excess weapons materials stored in drums. And, future fast multiplicity counters with very low accidental coincidence backgrounds may be able to do both passive and active multiplicity measurements of mixed HEU/Pu oxides in cans, or inventory verification of mixed HEU/Pu items in large drums.

REFERENCES

1. N. Ensslin, M. S. Krick, D. G. Langner, and M. C. Miller, “Active Neutron Multiplicity Counting of Bulk Uranium,” Los Alamos National Laboratory report LA-UR-91-2470, Proc. 32nd Annual INMM Meeting, New Orleans, LA, July 28-31, 1991.

2. N. Ensslin, M. S. Krick, W. C. Harker, M. C. Miller, R. D. McElroy, P. A. McClay, W. L. Belew, R. N. Ceo, L. L. Collins, and P. K. May, “Analysis of Initial In-Plant Active Neutron Multiplicity Measurements,” Los Alamos National Laboratory report LA-UR-93-2631, Proc. 34th Annual INMM Meeting, Scottsdale, AZ, July 18-21, 1993.

3. M. S. Krick, N. Ensslin, D. G. Langner, M. C. Miller, R. N. Ceo, P. K. May, and L. L. Collins, Jr., “Active Neutron Multiplicity Analysis and Monte Carlo Calculations,” LA-UR-94-2440, Proc. INMM Annual Meeting, Naples, FL, July 17-20, 1994.

4. T. D. Reilly, N. Ensslin, H. A. Smith, and S. Kreiner, Passive Nondestructive Assay of Nuclear Materials," US Nuclear Regulatory Commission NUREG/CR-5550, March 1991.

5. N. Ensslin, M. K. Smith, C. R. Rudy, and P. A. Russo, LANL; C. A. Pickett, ORNL; W. Brosey, Y-12, and J. Swanson, LLNL, "The SO-20 MC&A Modernization Plan Measurement Needs Summary," Los Alamos National Laboratory report LA-UR-04-4189, Proc. INMM Annual Meeting, Orlando, FL, July 2004.

6. M. S. Krick, N. Ensslin, R. N. Ceo, and P. K. May, "Analysis of Active Neutron Multiplicity Data for Y-12 Skull Oxide Samples," Los Alamos National Laboratory report LA-UR-96-343, Proc. 37th Annual INMM Meeting, Naples, FL, July 28-31, 1996.

7. J. F. Briesmeister, Ed. , "MCNP - A General Purpose Monte Carlo Code for Neutron and Photon Transport," Los Alamos National Laboratory report LA-12625-M, Ver. 4A (November 1993).

8. C. A. Beard, N. Ensslin, and W. H. Geist, "Relationship Between Source-Sample Coupling and Multiplication for Active Multiplicity Assay," Nuclear Engineering Teaching Laboratory, University of Texas at Austin, unpublished technical report PRC 159, R9000 (1998-2000).

9. W. H. Geist, N. Ensslin, L. A. Carrillo, and C. A. Beard, "Advanced Analysis Techniques for Uranium Assay," Los Alamos National Laboratory report LA-UR-01-3331, Proc. 42th Annual INMM Meeting, Indian Wells, CA, July 15-19, 2001.

10. W. H. Geist and K. Frame, "Modeling Active Neutron Coincidence Counters with MCNPX," Los Alamos National Laboratory report LA-UR-04-4355, Proc. 45th Annual INMM Meeting, Orlando, FL, July 18-22, 2004.

11. J. S. Hendricks *et.al*., "Monte Carlo Neutron-Photon Extended Code," Los Alamos National Laboratory report LA-UR-04-0570 (2004).

12. M. M. Pickrell, "An Alternative Method for Analyzing Active Neutron Multiplicity Data," unpublished technical note, August 2004.

13. W. H. Geist, J. E. Stewart, H. O. Menlove, N. Ensslin, and C. Shonrock, "Development of an Active Epithermal Neutron Multiplicity Counter (ENMC), Los Alamos National Laboratory report LA-UR-00-2721, Proc. 41st Annual INMM Meeting, New Orleans, LA, July 16-20, 2000.

14. K. C. Frame, W. H. Geist, J. P. Lestone, A. P. Belian, and K. D. Ianakiev, "Characterizing the Detector Response and Testing the Performance of a new Liquid Scintillator Counter for Neutron Multiplicity Measurements of Enriched Uranium," Los Alamos National Laboratory report LA-UR-03-4899, presented at the 44th Annual INMM Meeting, Phoenix, AZ, July 13-17, 2003.

15. K. C. Frame, W. A. Clay, W. H. Geist, J. P. Lestone, A. P. Belian, and K. D. Ianakiev, "Neutron and Gamma Pulse Shape Discrimination in a Liquid Scintillator Counter for

Neutron Multiplicity Measurements of Enriched Uranium," Los Alamos National Laboratory report LA-UR-04-4868, Proc.45th Annual INMM Meeting, Orlando, FL, July 18-22, 2004.

16. M. S. Krick, W. C. Harker, P. M. Rinard, T. R. Wenz, W. Lewis, P. Pham, and P. DeRidder, "The IAEA Neutron Coincidence Counting (INCC) and the DEMING Least-Squares Fitting Programs," Los Alamos National Laboratory report LA-UR-98-2378, Proc. 39th Annual INMM Meeting, Naples, FL, July 26-30, 1998.

17. N. Ensslin, W. C. Harker, M. S. Krick, D. G. Langner, M. M. Pickrell, and J. E. Stewart, "Application Guide to Neutron Multiplicity Counting," LA-13422-M, September 1998.

18. N. Ensslin, M. S. Krick, D. G. Langner, D. W. Miller, and M. C. Miller, "Measurement of the Assay Precision of the Active Neutron Multiplicity Technique," Los Alamos National Laboratory report LA-UR-2359, Proc. 33rd Annual INMM Meeting, Orlando, FL, July 19-22, 1992.

19. N. Ensslin, W. H. Geist, M. S. Krick, D. R. Mayo, and J. E. Stewart, "Performance Calculations for Fast Active Neutron Assay," Los Alamos National Laboratory report LA-UR-99-4058, Proc. 40th Annual INMM Meeting, July 25-29, 1999, Phoenix, AZ.

8. FAST AND EPITHERMAL NEUTRON MULTIPLICITY COUNTERS

Mark M. Pickrell, Kevin Veal, and Norbert Ensslin

I. Introduction and Problem Statement

This chapter will discuss the designs and motivation for the most modern of neutron multiplicity counters. These are the Epithermal Neutron Counters and the Fiber-Based Fast Neutron Counters. Both systems are addressing the same measurement issue: items that are difficult to measure by neutrons because the coincidence and multiplicity accidentals rate is too high. The high accidentals rate causes a large uncertainty in the counting statistics, which degrades the measurement precision. Traditionally, these measurement problems have been so severe that, in some cases, neutron assay by multiplicity or coincidence counting became impractical.

The first section of this chapter will be a review and inventory of the types of measurement cases that have suffered from this problem. We will review and discuss the range of neutron measurement cases that have been difficult or impractical to address with neutron multiplicity counting. These will be disparate in their apparent measurement difficulty, but will have a common thread: they will all have a high accidentals rate.

The following section will discuss the underlying physics of these neutron measurements. First, we will consider the common aspect of all the measurement cases and show that all have a high accidentals rate. Second, we will show that the high accidentals rate does indeed vitiate the measurement precision. Third, we will discuss the counter parameters that can mitigate the problem of high accidentals. Again, this section will be quantitative: we will show the relative improvement as a function of detector efficiency and die-away time, which leads immediately to the basic design parameters of an improved neutron detector.

The last section will discuss detectors that were designed specifically to address these counter parameters, namely a high efficiency and a low die-away time. We will discuss a survey of these instruments and describe the physics and engineering trade-offs that lead to particular designs. Two general types of detector will be discussed: the epithermal neutron multiplicity counter (ENMC) and the fiber-optic-based neutron detector. The ENMC is based on and is an extension of existing neutron counters. It is predicated on traditional neutron counting technology, but extends that technology based on the need for mitigating the specific problems of high accidentals measurements. The fiber-optics systems are a radically different type of neutron detector. The essential benefit is that it extends the potential capability of neutron detectors significantly beyond what conventional designs might be capable of. However, this improvement has a cost of degraded performance in other parameters and also it is less robust because it is a newer technology. These new approaches may indicate the future of neutron detector development, though.

The underlying logic of this chapter follows a direct progression: 1) address and inventory the spectrum of neutron assays that are difficult-to-measure, 2) show that these measurement challenges have a common basis, namely the high accidentals rate, 3) show that the accidentals rate can be improved by improving certain detector parameters, namely the efficiency and die-away time, and 4) discuss the new detectors that achieve improvement in efficiency and die away time.

II. Measurement Problems Addressed by Epithermal Neutron Counting

The ENMC and the new generation of neutron counters (HLNCC10, ENMC/INVS, SuperHENC, Collar, KAMS NMC, etc.) designed with closely-packed high-pressure ^{3}He tubes make it possible to effectively address a number of measurement problems for the first time. These measurement problems cannot be solved in a timely, cost-effective manner with the older generation of thermal neutron counters. The problem categories include passive multiplicity measurements of impure plutonium items with moderately-high alpha values, active/passive measurements of HEU/Pu, and active multiplicity assay of many forms of HEU.

A. Impure Plutonium

The combination of the new ENMC and the Advanced Multiplicity Shift Register (which reduces count times by an additional factor of 2) enables passive multiplicity measurements of impure plutonium metals and oxides ranging in mass from milligram to kilogram quantities. The ENMC may also enable passive assays of U-238 in quantities greater than 1 kg. For multiplicity measurements of impure Pu, the increase in α with increasing impurities hurts the counting precision on triple coincidences, eventually making the required counting time too long. The ENMC's higher efficiency and shorter die-away time leads to dramatic reductions in counting time. At an α value of 1, the ENMC is about 10 times faster than a thermal neutron multiplicity counter for the same 1% precision. At an α value near 8 (very impure Pu), the ENMC is about 20 times faster for the same 1% precision. But the practical limit of the ENMC is around α values of 10 to 12, where the counting time for 1% precision begins to exceed one hour. It should also be noted that the ENMC counter design has a relatively flat detection efficiency profile as a function of neutron energy, providing an essentially bias-free assay for α values from 0.1 to 0.3 (impure metal) to 7 to 12 (very impure oxide).

B. HEU Materials

The DOE Complex contains many metric tons of excess HEU materials including mixed HEU/Pu, U weapons components in shielded storage drums, high-density HEU scrap/waste, remote-handled waste, and non-self-protecting irradiated fuels. DOE/NNSA nuclear facilities often need the capability to do fast, timely accountability, shipper/receiver verification, vault inventory verification, or waste characterization measurements of SNM materials. Identified validated needs include the following material categories: HEU metal, HEU metal and oxide pieces, pure HEU oxide, impure HEU oxide, high-density HEU scrap/waste, low-density HEU scrap/waste, remote-handled waste, and U-233 oxide. Shipper/receiver or inventory verification measurements of some of these materials need to be done in shipping containers. These are often shielded for personnel dose reduction, making the measurements very difficult. Large volume epithermal neutron multiplicity counters outfitted with active interrogation sources may provide a practical approach to these measurement problems.

C. Mixed HEU/Pu

The ENMC will provide new capabilities for accountability or verification of the U mass in mixed HEU/Pu materials, including metal scrap in irregular shapes, U/Pu oxide, high-density

U/Pu waste, or un-irradiated, non-self-protecting U/Pu fuel assemblies. The measurement of mixed HEU/Pu items requires that the neutron counter be used for both an active and a passive measurement. The passive measurement is usually made by multiplicity counting to determine the ^{240}Pu content with minimal bias. The active measurement is made by doubles coincidence counting to determine the ^{235}U content with sufficient precision. Because the active measurement also induces fissions in ^{239}Pu, this contribution needs to be subtracted from the total observed doubles rate to obtain a difference doubles rate that is related to the ^{235}U content.

Calculations of the expected precision for the HEU portion of mixed HEU/Pu measurements made with the ENMC outfitted with active end caps were carried out. The Figure of Merit calculations assumed 1000s counting times for 93% enriched HEU and Pu with 10% ^{240}Pu. For a mixture of 1500g HEU and 500g Pu, the ENMC measurement had a total statistical uncertainty on the difference doubles rate of 2%, whereas the AWCC was 4%. For a mixture of 500g HEU and 1500g Pu, the ENMC measurement had a total statistical uncertainty on the difference doubles rate of 3%, whereas the AWCC was 26%. This example shows that the ENMC can provide much better measurement capability for mixed HEU/Pu, especially if the Pu component is large.

D. Additional Applications for Fast Neutron Counters

A future generation of fast neutron counters based on liquid scintillators or other technology may provide another order of magnitude improvement in performance over the ENMC. The expected counting precision for such counters is described in Chapter 7, Section 7.4.4. The most important potential benefit is the capability to do active multiplicity counting with 1% or better assay precision over nearly the entire ^{235}U mass range. Thus, liquid-scintillator-based neutron counters could provide active multiplicity results for almost all DOE facility inventory materials with reasonable counting times. Potential applications would also include fast scintillator detector arrays for active/passive measurements of some forms of domestic research reactor fuel, foreign research reactor receipts fuel, and remote-handled transuranic waste. These materials often do not have high enough radiation doses to be self-protecting, and, therefore, require safeguards measurements.

III. The Physics of High Accidentals Multiplicity Counting

There is a common physics feature to all of the “difficult” problems discussed in section II. All of these measurements have a high neutron accidentals rate. The accidentals rate applies to either doubles (coincidence) counting or triples (multiplicity) counting. In both cases, it refers to those cases where by sheer probability; multiple (either two, three, or more) neutrons are detected and counted within the time window of the multiplicity shift-register gate. These counts appear as correlated, but are indeed merely chance coincidence. The multiplicity formalism separates out the chance coincidences (accidentals) from the true coincidences (called reals), using a statistical model. In the mathematics of neutron multiplicity counting, described in chapter 6, the accidentals counts are called the background distribution. The notation is either $b(i)$ or $Q(i)$, depending on the reference. For conventional shift-register-based neutron coincidence counting, the accidentals are counted in the Accidentals or “A” gate.

In this chapter, we will use two approaches to illustrate the effects of the accidentals on the multiplicity precision. The first method will be to use a numerical calculation of the neutron

multiplicity rates (for singles, doubles, and triples) and their associated variances, as well as the resultant multiplicity assay precision which considers the combined variances of all of the measured quantities and the inversion of the point model equations. This numerical calculation follows the theoretical formalism developed by Ensslin, et.al. The second approach will be analytical with an approximate calculation for the expected variance of the doubles counts. The mathematics for the triples variance is more complicated, and does little to elucidate the underlying physics. For that, we will rely on the Ensslin Figure of Merit (FOM) numerical calculations. However, for the doubles, the analytical result does illustrate the basic dependence of variance on the accidentals.

It is the effect of accidentals that substantially changes the variance behavior for neutron multiplicity counting compared to, say, counting individual neutrons or counting any individual, uncorrelated particle or event. From classical probability, if a measurement is made of any system that satisfies the conditions for a Poisson process, then relative error of the count (percent error) scales as $1/\sqrt{n}$, where n is the number of counts. Therefore, if singles, doubles, and triples counts in multiplicity all obeyed Poisson statistics, we would expect the relative standard deviation to scale the same way for all of them. However, that is not the case. The singles do indeed follow this relationship, nearly, but the behavior of the doubles and triples are quite different.

Figure 1 below illustrates some of these points. Using the Ensslin FOM code we calculate the variance for the singles, doubles, triples, and multiplicity assay. In order to vary the accidentals rate strongly, we varied the assay mass over a large range, from 0.01 grams to 100,000 grams. The parameter alpha (alpha is the ratio of alpha-n neutrons to fission neutrons) is fixed at zero. The sample leakage multiplication is fixed at unity. The detector efficiency is 35%, the die away time is 50 μsec, the predelay is 3 μsec, and the gate width is 50 μsec, and all of these are fixed.

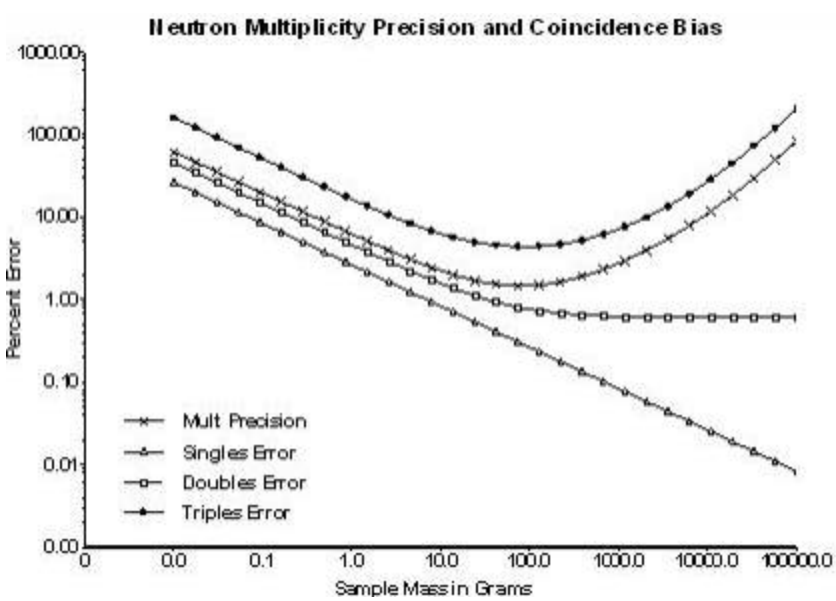

Fig. 1. Measurement variance versus sample mass for different multiplicity orders.

The results of Figure 1 demonstrate the effects on variance from the accidentals. The singles relative standard deviation does indeed scale as $1/\sqrt{n}$, as is expected, (note the graph is a log-log plot). However, the behavior of the doubles and triples relative standard deviation (RSD) is quite different. At low masses the doubles RSD scales as $1/\sqrt{n}$, but at modest mass values the scaling stops and the doubles RSD remains nearly constant. By contrast, the triples RSD scales as $1/\sqrt{n}$ for low masses, but above about 100 grams, for this particular case, the triples RSD actually increases at a rate that is nearly proportional to the count rate. The total multiplicity assay RSD depends on the variances of singles, doubles, and triples, and it also increases after about the 100 gram level.

This general behavior can also be addressed analytically, using the point model equations. We repeat the point model equations derived earlier.

$$S = Fm_{240}\varepsilon M \nu_{s1}(1+\alpha) \tag{1}$$

$$D = \frac{Fm_{240}\varepsilon^2 f_d M^2}{2}\left[\nu_{s2} + \left(\frac{M-1}{\nu_{i1}-1}\right)\nu_{s1}(1+\alpha)\nu_{i2}\right] \tag{2}$$

$$T = \frac{Fm_{240}\varepsilon^3 f_t M^3}{6}\left\{\nu_{s3} + \left(\frac{M-1}{\nu_{i1}-1}\right)\left[3\nu_{s2}\nu_{i2} + \nu_{s1}(1+\alpha)\nu_{i3}\right] + 3\left(\frac{M-1}{\nu_{i1}-1}\right)^2 \nu_{s1}(1+\alpha)\nu_{i2}^{\ 2}\right\} \tag{3}$$

where,

F = spontaneous fission rate, 473 fission/s-g ^{240}Pu, so that m_{240} = effective ^{240}Pu mass,
ε = neutron detection efficiency,
M = neutron leakage multiplication,
α = (α,n) to spontaneous fission neutron ratio,
f_d = doubles gate fraction,
f_t = triples gate fraction,
ν_{s1}, ν_{s2}, ν_{s3} = first, second, and third reduced moments of the spontaneous fission neutron distribution,
ν_{i1}, ν_{i2}, ν_{i3} = first, second, and third reduced moments of the induced fission neutron distribution.

Consider first the case of the singles, which are simply the total number of neutrons detected. There are no accidentals to subtract from the totals, because there are no coincidences, accidentals or otherwise. Using the point model equation for the singles, we note that the singles variance scales approximately as: $1/\sqrt{n}$, because there are no accidentals to change this scaling.

Next consider the variance for the doubles, which are also classical coincidences. These equations are best understood in two limiting cases: the case where the plutonium mass (m_{240}) is low and the other case where it is high. "Low" and "high" will be defined in the equations. For the case of coincidence counting (doubles only), an excellent measure of the variance is:

$$\sigma = \sqrt{(R+A)+A}\ . \tag{4}$$

where *(R+A)* is the total count in the "reals plus accidentals" gate (the signal triggered gate) and A is the total count in the "accidentals" gate (the random triggered gate). In a multiplicity shift register these values are calculated as the factorial moment summations over the foreground, $f(i)$, distribution and the background, $b(i)$, distribution. The value for *R* is simple the doubles rate from the multiplicity equations above times the count time:

$$R = D \cdot t \quad . \tag{5}$$

The accidentals rate can be calculated from the totals rate. The total accidentals value is the accidentals rate times the count time:

$$A = GtS^2 \quad . \tag{6}$$

where *G* is the shift register gate width and *S* is the singles rate from the multiplicity equations above. Note that the singles rate and the doubles rate are proportional to the plutonium mass, but the accidentals rate is proportional to the mass squared:

$$\begin{aligned} S &\propto m_{240} \\ A &\propto m_{240}^2 \\ D &\propto m_{240} \end{aligned} \tag{7}$$

Combining these equations and solving for the Relative Standard Deviation we obtain:

$$\sigma_{rel} = \frac{\sqrt{Dt + 2GtS^2}}{Dt} \quad . \tag{8}$$

Now, consider the two limiting cases. In the case of low mass, the second term in the numerator, $2GtS^2$, which depends on the square of the mass, becomes arbitrarily smaller than the first term, which is linear with the mass. Therefore, at sufficiently low mass, the second term is negligible, and the equation for the RSD simplifies to:

$$\sigma_{rel} \propto 1 \Big/ \sqrt{t\varepsilon m_{240}} \tag{9}$$

which scales as $1/\sqrt{n}$, just as the FOM calculations show in Figure 1, for masses less than 100 grams of plutonium. The variance is limited by the statistical precision of the reals counting. The triples behave in the same fashion.

By contrast, consider the case of large mass, namely m_{240} is sufficiently large that the second term in the numerator is much larger than the first term: $2GtS^2 >> Dt$. Then, the equation for the RSD scales as:

$$\sigma_{rel} \propto \frac{\sqrt{\tau}}{\varepsilon\sqrt{t}} \quad . \tag{10}$$

In this case, the total variance is dominated by the accidentals, and the scaling of the variance with efficiency, die-away time, and plutonium mass is quite different than for the low mass case. We have also assumed that the system is optimized so that the gate fraction is proportional to the die-away time, τ. Indeed, there is no change in variance with mass! The usual benefit of improved statistics is lost. Note also that the RSD improves with short die-away time and large detection efficiency. A similar (but more complicated) calculation can be done for the triples measurement, which shows that the triples RSD actually increases with mass, just as the FOM calculation illustrated in Figure 1.

The clear result is that in the case of a high accidentals rate, the variance induced by the accidentals can be the dominant contribution to the measurement variance. In the limit of large masses, therefore large accidentals, the variance contribution from the Poisson statistics of the reals rate is negligible compared to the variance contribution of the accidentals. Other measurement problems that also have a high accidentals rate will be affected in the same way.

Another example of a high-accidentals-rate measurement problem is active neutron multiplicity counting. Active neutron counting uses a neutron source to interrogate a fissile sample that has a low spontaneous fission rate. Enriched uranium is a common example. The significance of active multiplicity counting is that the interrogating source provides a high level of totals neutrons (but no real coincidence or triples counts). Because the accidentals rate (for doubles) scales as $\dot{A} = G\,\dot{T}^2$, where G is the shift register gate width and $\dot{T}$ is the totals rate, the accidentals rate is very high as well. Figure 2 illustrates this point. For a nominal set of active measurement conditions: ^{235}U range from 100 to 10,000 grams, doubles rate of 10 counts per gram, interrogation neutron rate of 10^6, and the same detector parameters as before. Figure 2 illustrates that the high accidentals rate caused by the interrogating source has substantially increased the doubles and triples precision. By contrast, the singles variance is not affected as much. These RSD values are much higher than for the passive multiplicity case, where no interrogating source is used.

Another example is the case of materials with a high alpha. The affect of alpha is similar to

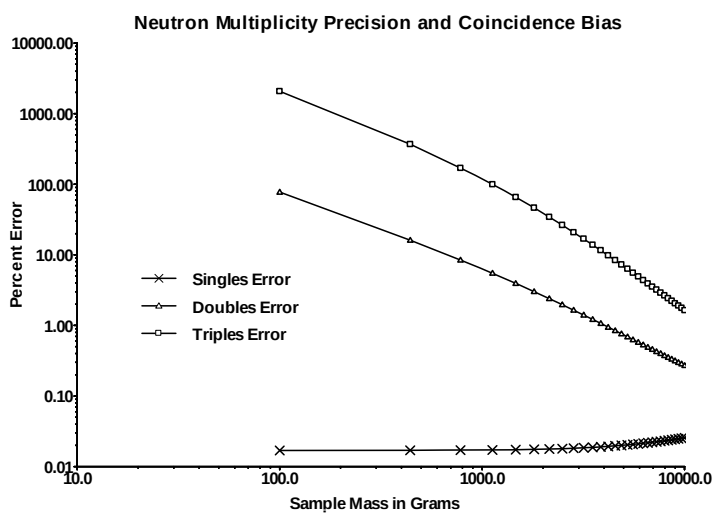

Fig. 2. Multiplicity error components versus sample mass.

that of an interrogating source. The alpha-n neutrons appear as singles, but they increase the totals rate, which increases the accidentals rate. We consider a nominal case that is similar to the calculation plotted in Figure 1, (the detector parameters are identical). We hold the mass fixed at

1000 grams and vary the alpha from 0.1 (essentially zero) to 5. The results are plotted in Figure 3. Note that the RSD for the doubles and triples increases, because the totals rate increases and therefore the accidentals rate increases. However, the RDS for the singles decreases, because the totals rate increases and this improves the statistical precision.

In all of these cases, the neutron measurement problem is made challenging by a high accidentals rate for the doubles and triples counts. In these instances, the variance contribution of the accidentals dominates the variance of the measurement. Knowing that the accidentals have such a profound impact, we can consider design changes in the neutron detectors that can reduce the variance contribution from accidentals. The evaluation proceeds from the equations derived above which approximates the doubles variance in the limit of high accidentals, (we do not need to consider the case of low accidentals for this part of the discussion).

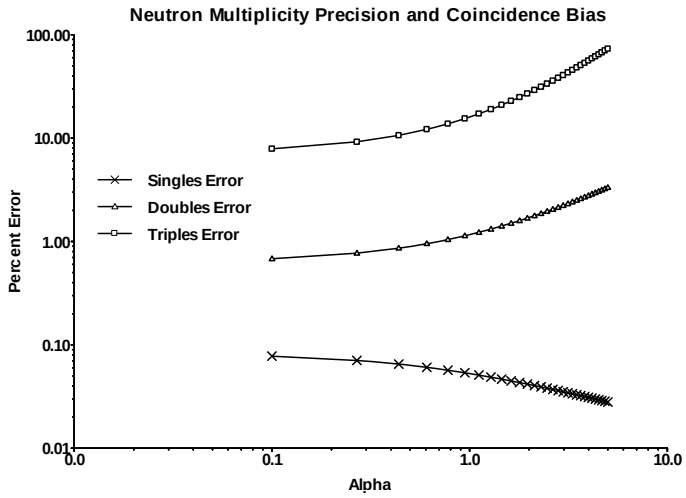

Fig. 3. Multiplicity precision versus alpha (α)

An increase in efficiency improves the precision of the multiplicity and coincidence measurements, which we demonstrate with a figure of merit calculation. In Figure 4, we plot the case that efficiency is increased. The other detector parameters are the same as for Figure 1,

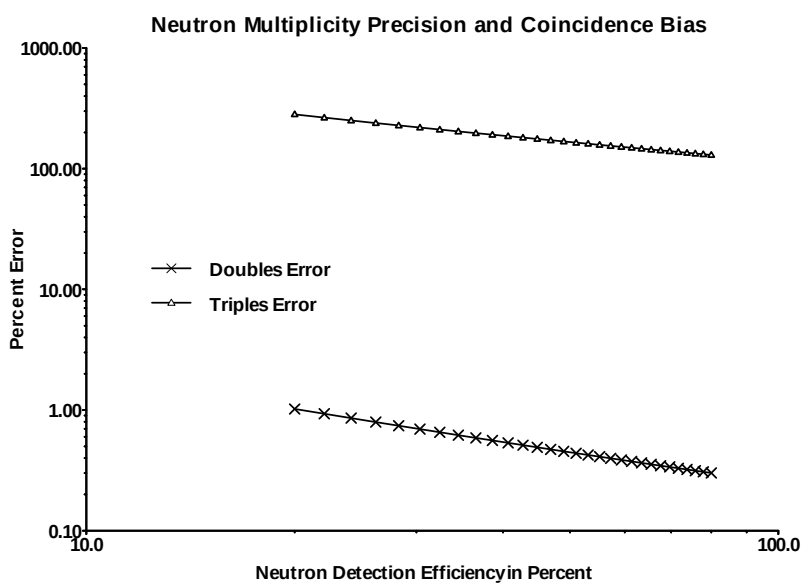

Fig. 4. Figure of Merit calculation: varying efficiency.

however, the mass value is chosen to be 100,000 grams, which (from Figure 1) is well into the regime of accidentals-dominated variance for the doubles and triples. In this calculation, the efficiency varies from 20% to 80%. Figure 4 shows, consistent with equations 9 and 10, that the efficiency improves the variance for multiplicity counting in both the low mass (limited by real coincidence counting statistics) and the high mass (limited by the accidentals rate) cases.

For completeness, we also note that the variance for the opposite case, when the mass is low is also improved as efficiency is increased. Die away time has little effect, though. The significance is that a counter with high efficiency and low die away time will improve the variance over the entire spectrum of measurement cases: from the limiting case where accidentals are the dominant contribution to variance at the high end, to the limiting case where counting statistics of the real coincidences at the low end. These effects can also be seen from the FOM calculations. Figure 5 is identical to Figure 4 except that the mass value is 1 gram instead of 100,000 grams of plutonium. Again, the efficiency is varied from 20% to 80%.

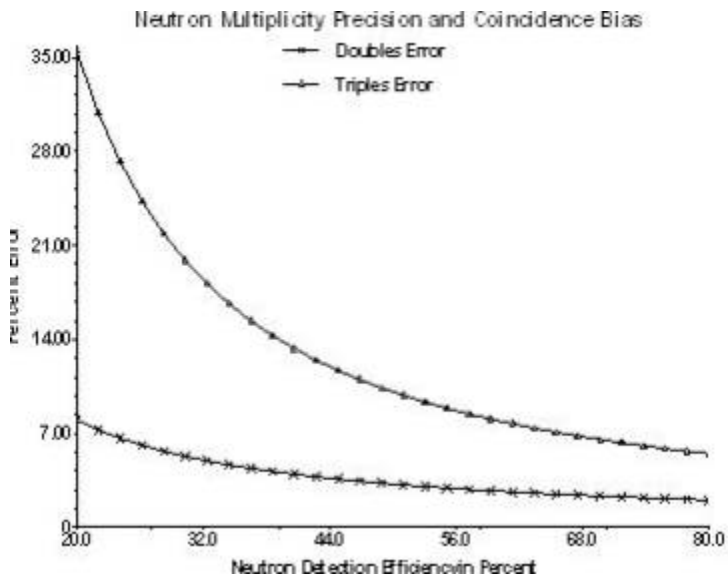

Fig. 5. Figure of Merit calculation: varying efficiency

Finally, we calculate, using the FOM code, the improvement in detector performance (i.e. reduction in variance) when the die-away time is decreased. Figure 6 plots the same case as Figures 4 and 5, except that the efficiency is held constant at 35%, the mass is 100,000 grams, the gate width is reduced to 35 μsec, and the die away time is varied from 20 μsec to 60 μsec. For the case of doubles and triples, the variance is improved when the die-away time is reduced and the efficiency is increased. Although we did not develop the analytical expressions for triples, the effect is more pronounced.

These effects can be understood from the basic physics. The correlated gate in a shift register, which is the signal triggered gate, measures both the reals and the accidentals. In order to measure the correlated neutron moments (the real doubles and triples), the accidentals rate must be subtracted off. The accidentals are measured by opening up a second gate, the random-triggered gate for a second measurement. The random triggered gate measures only uncorrelated neutrons. Because these two numbers are subtracted, their variances must add. Therefore, the total variance includes contributions from both the reals and the accidentals. When the die-away time is reduced, the gate width is reduced proportionately. As the gate width is reduced, the

amount of accidentals that are counted is reduced, and the contribution to the variance is correspondingly reduced.

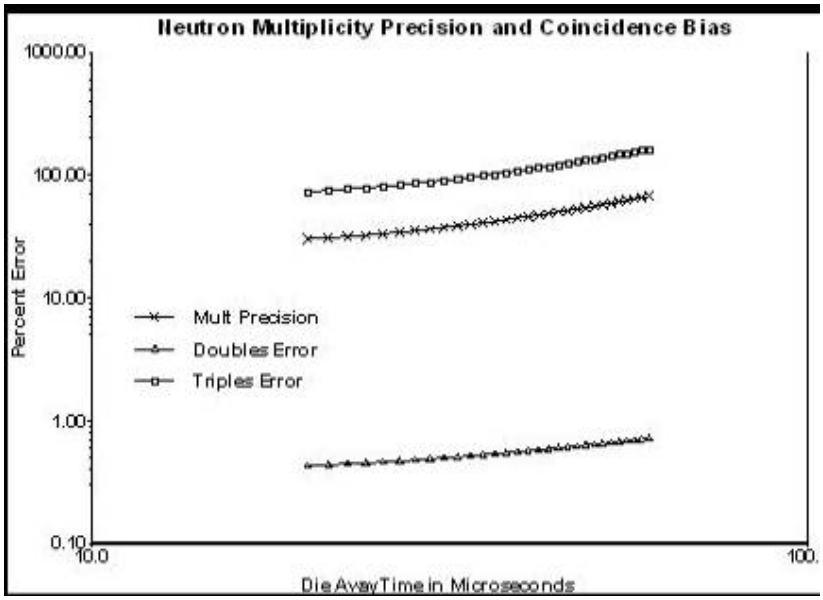

Fig. 6. Figure of Merit Calculation: Vary Die Away Time

The conclusions from this discussion are that high accidentals, caused by high mass, high alpha, or active interrogation significantly degrade the precision of multiplicity measurements. However, a neutron detector that has a high efficiency and a low die away time can significantly mitigate this problem.

IV. Fast and Epithermal Neutron Multiplicity Counters

In this section we will discuss the designs of modern neutron counters, which were specifically developed to address the class of measurement problems described above, and which are characterized by a high accidentals rate. There are two systems we will consider: the Epithermal Neutron Multiplicity Counter (ENMC) and the Fiber-Optic-Based Fast neutron counter. The ENMC is an existing design, which has been built and field tested. In experimental and numerical tests, the instrument has proven to be considerably more precise (all other measurement parameters being equal) than previous state-of-the-art instruments. By contrast, the fiber optic fast neutron detector is an experimental device that is intended to extend the basic measurement parameters beyond what is practical for ^{3}He-based neutron detectors. In particular, this fast neutron system has a neutron die-away time of 3.8 μsec, compared to a nominal 22 μsec for an ENMC and a 47 μsec die-away for a Plutonium Scrap Multiplicity Counter (PSMC). Both systems will be discussed in this section.

A. Epithermal Neutron Multiplicity Counter

The design of the ENMC follows largely from the existing technological base of thermal neutron counters, namely, it is a well-type counter that uses polyethylene to moderate neutrons and ^{3}He tubes to detect the neutrons. The pulse amplification, discrimination, and pulse counting electronics are identical to conventional neutron well counters. The ENMC differs from more

conventional counters in that it has a much higher efficiency and a lower die away time. Table 1, below, summarizes the operation parameters of the ENMC compared to an AWCC and a PSMC. The ENMC has an efficiency of 65%, which is significantly larger than the PSMC, which has an efficiency of 53%. It also has a much shorter die away time compared to the PSMC, 22 μsecs compared to 47 μsecs.

Table 1: Design Parameters for an ENMC and PSMC

Parameter	AWCC	PSMC	ENMC
He-3 Tubes	4 atm	4 atm	10 atm
Efficiency	33%	53%	65%
Die-Away Time	51 μs	47 μs	22 μs
High Voltage	1680 V	1680 V	1720 V
Pre-Delay	3 μs	3 μs	1.5 μs
Gate	64 μs	64 μs	24 μs
Deadtime	225 ns	120 ns	37 ns

There are three essential design features of the ENMC that enabled the improvement in die-away time and efficiency. These are:

1. The ENMC uses 10 atm ^{3}He detection tubes rather than the more typical 4 atm tubes. The higher pressure ^{3}He captures more of the thermalized and epithermal neutrons. Higher pressure ^{3}He detectors have also been used to upgrade existing neutron counters, and have improved detection efficiency and reduced die-away time.
2. The ENMC uses less polyethylene moderator than conventional designs. With less moderator, the neutrons may not become fully thermalized (hence the name).
3. The ENMC uses multiple rings of detectors embedded in polyethylene. Other modern neutron well counters have also used this design, but for the ENMC it is particularly important.

The significance of the ENMC design features is understood best in the context of how a neutron counter actually detects neutrons. The general process has three basic steps:

1. The neutron impinges on the polyethylene moderator and is thermalized (principally by the hydrogen). The thermalization occurs because the high energy neutron collides with (typically) a hydrogen atom and loses much of its energy. After (generally) several collisions, the neutron energy is about the same as the thermal energy of the moderator (room temperature).
2. After the neutron is thermalized, it typically undergoes several more collisions with the moderator material and moves (essentially by diffusion)

through the detector until it is lost by one of several processes. Ideally, a conventional neutron detector would work best if the neutron became thermalized immediately adjacent to a ^{3}He detector so that it could be instantly captured. However, more commonly the neutron becomes fully moderated in the polyethylene some distance from a detector tube and must transport (by a random walk process of several collisions) to the ^{3}He tube.

3. The neutron is lost. There are three basic loss processes:
   a) The neutron is captured and detected by the ^{3}He gas in one of the detector tubes.
   b) The neutron transports outside of the detector and is lost.
   c) The neutron is absorbed by the hydrogen in the polyethylene.

The goal of the detector design is to optimize these processes so that the efficiency is as large as possible and the die-away time is as short as possible. Efficiency is increased when the fraction of neutrons lost by ^{3}He capture is large compared to the competing lost processes (e.g. hydrogen absorption). Die away time is made shorter by reducing the time between thermalization and capture. The ENMC achieves these objectives by using high pressure ^{3}He tubes and a minimum of polyethylene moderator. The detector tubes are closely spaced in the

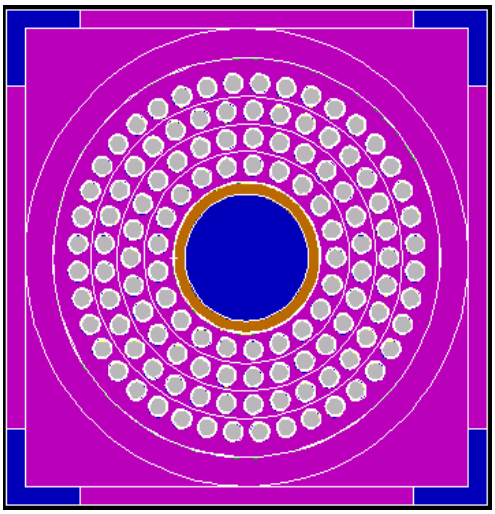

Fig. 7. MCNP plot of cross section of ENMC detector.

polyethylene moderator. When a neutron impinges on the detector, there is just barely enough polyethylene to moderate it (because of the close spacing of the ^{3}He tubes). Once the neutron is moderated or partially moderated, it will be in close proximity to a detector tube. Therefore, the neutron will not remain in the moderator material for a long period of time and the die-away time is kept short. Because the detector tube pressure is high, the neutrons have a high probability of being captured, so the efficiency is high. The multiple rings of detectors ensures that most of the neutrons are captured, even though the moderator density is low. Figure 7 plots the cross sectional view of the ENMC detector and Figure 8 shows a cut-away side view.

The ENMC was designed using the MCNP neutron transport code. The detector geometry and spacing was optimized for best efficiency and die-away time. The optimal design point differs from other MCNP-optimized designs because the detector tubes had 10 atm of ^{3}He rather than the conventional 4 atm. That, and the 4-layer design shepherded the design optimization toward the minimal polyethylene design.

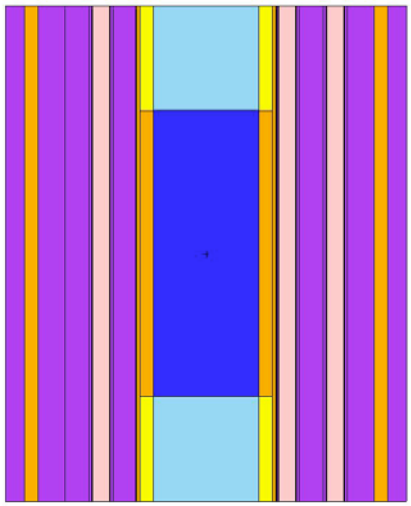

Fig. 8. MCNP plot of ENMC detector. Side cut-away view.

Figure 9 below shows the relative trade off between improved efficiency and die-away, calculated using the MCNP code. As the moderator is increased, the efficiency does improve until it plateaus. However, as the moderator is increased, the die-away time also increases. The ENMC design was optimized to achieve the best combination of die-away time and efficiency possible. The figure of merit was the reduction of the variance due to the accidentals, as also described in equations 9 and 10.

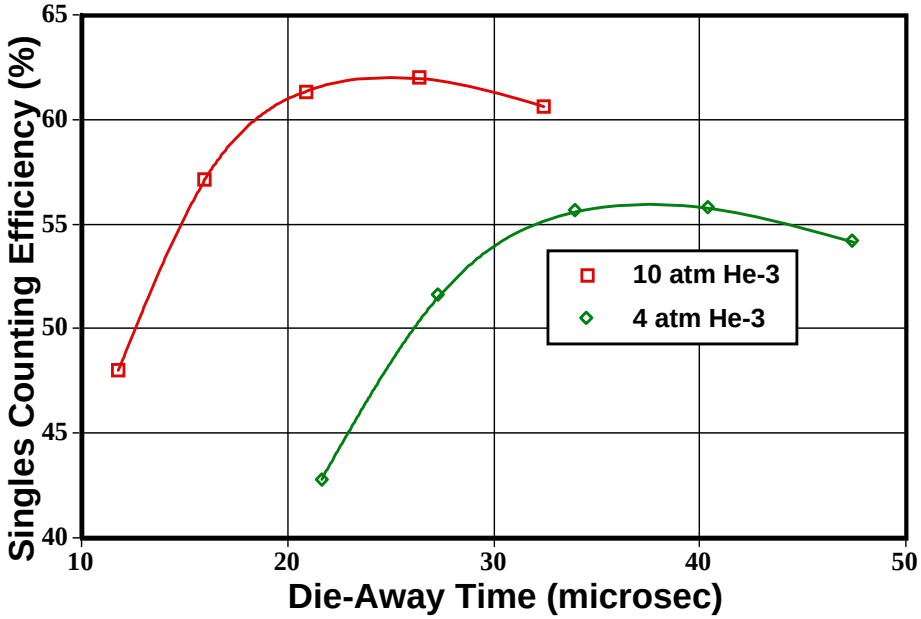

The mechanical design of the ENMC detector groups the 127 detector channels into 4 axial rings and 27 electrical channels. Each channel has an AMPTEC preamplifier-amplifier-discriminator attached. A de-randomizing buffer is also included in the intrinsic counter electronics. The output of the counter is connected to any standard neutron multiplicity shift register. A picture of the ENMC counter is shown in Figure 10.

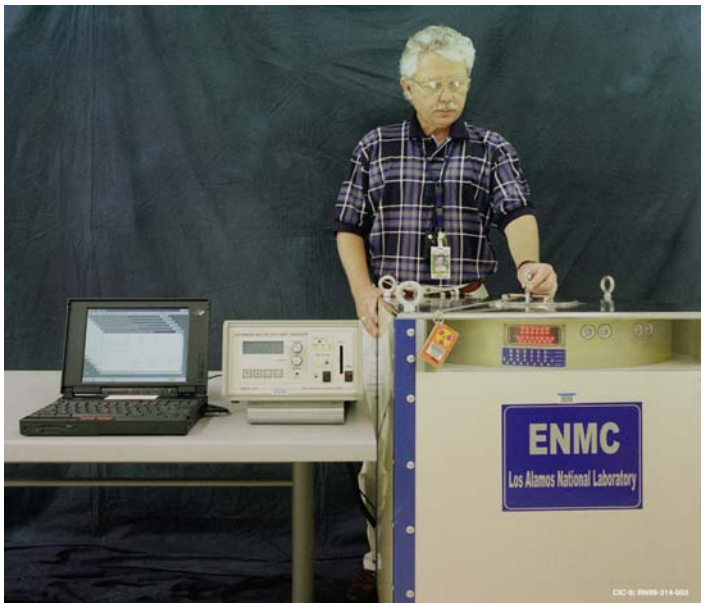

Fig. 10. Picture of ENMC detector.

A variation of the ENMC includes a counter insert, called the Inventory Sample Counter (INVS). Inserting the INVS counter adds an additional 21 detector tubes in two rings to the counter system. The addition of the INVS increases the over all efficiency to 80%, and the die-away time remains 22 μsec. The MCNP design for the modified ENMC is shown in Figure 11.

The ENMC (with and without the INVS insert) has been extensively tested. The experimental results confirm that figure-of-merit analysis described above. For a given sample type and count time, the ENMC provides assays with better precision than earlier neutron counter designs. We compare measurements taken with the ENMC to the Plutonium Scrap Multiplicity Counter (PSMC), which had been the state-of-the-art instrument. Table 2 below lists the relevant performance characteristics of the ENMC and the PSMC.

Table 2: Operational Parameters for an ENMC and a PSMC Counter

Detector	Efficiency (%)	Pre-delay (μs)	Gate Width (μs)	Doubles Gate Fraction	Triples Gate Fraction	Die-Away Time (μs)
PSMC	53	3	64	.651	.441	47
ENMC	65	1.5	24	..621	.404	21.8
ENMC/INVS	80	1.5	24	.605	.399	18.8

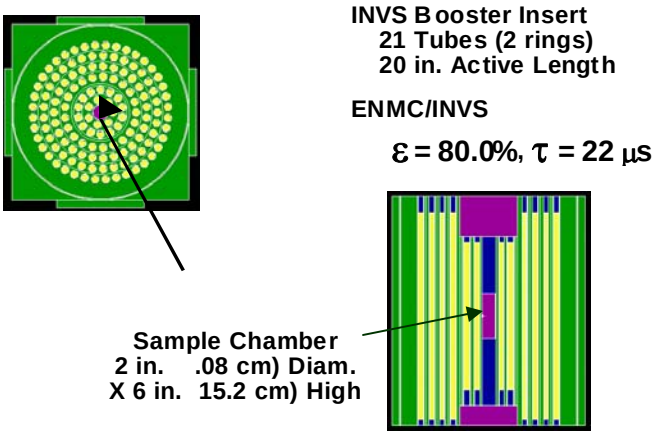

Fig. 11. MCNP plots of ENMC detector with INVS module inserted.

Table 3: Count time comparisons between different counters

Detector	Working Reference Material				
	LANL STD-ISO3,6,9,12	LANL STD-11	LANL STDSRP12-1	Hanford PFP 41-86-03-240	LANL LAO261C10
PSMC	7.3	170	34	1,352	27
ENMC	1.6	36	5.6	64	2.7
Ratio PSMC / ENMC	4.6	4.7	6.1	21	10

The ENMC can be compared to previous multiplicity counters either by comparing the assay time required to achieve a particular precision, or by comparing the measured precision for a fixed count time. These two methods are physically equivalent but illustrate the improved performance in different ways. Table 3 below compares count times (in minutes) and the count time ratios between the ENMC and the PSMC for various different reference standards. The standards were chosen to test the limits in precision induced by a high accidentals rate: both high mass and high alpha are represented. The samples were counted for a time sufficient to achieve a 1% RSD precision. This comparison clearly shows that for all other parameters equal, the ENMC achieves significantly better multiplicity precision than the PSMC detector (or conversely, a shorter count time for the same precision).

Multiple measurements of reference standards were also made to evaluate the accuracy of the ENMC. These included a broad range of materials, plutonium masses, alphas and multiplication. The masses varied from 0.691 grams of plutonium to 1,500 grams of plutonium, a range of alpha from 0.1 to 12, and a multiplication of 1 to 1.2. The results are plotted in Figure 12 against the known values for these reference standards. The results of Figure 12 show that the ENMC has achieve a high level of operational accuracy, over a broad range of test cases. In all cases a full multiplicity assay was performed.

B. Fast Neutron Counters

The ENMC has proven to be a significant advancement in the capability of neutron multiplicity counters. Research is being conducted to extend the capabilities even further. The intent of this research is to advance the improvement by reducing die away time and increasing detection efficiency, beyond that of the ENMC. Again, the design approach has been motivated by the die away time and efficiency scaling discussed earlier. Although these new methods are not yet operational, this discussion provides a snap shot into the current directions and state of neutron multiplicity counter research.

Experiments to develop very fast neutron counters approach the problem of neutron detection from an entirely different technological perspective, which do not build on the general designs of existing, conventional neutron detectors. The “fiber” Neutron Capture Counter for Residues (NCCR) is a prototype neutron multiplicity counter with a very short die-away time. The neutron sensor uses a ZnS:Ag scintillator loaded with ^{6}Li (as fluoride), which captures thermal and epithermal neutrons. The energetic alpha particle and triton released in the capture reaction produce light in the scintillator. The light is transported by 1-mm-diameter wavelength-shifting optical fibers to the photomultiplier tubes at opposite ends of the ^{6}Li-scintillator/fiber assembly.

Figure 13 illustrates the alternating layers of ^{6}Li-scintillator and fiber ribbon that make up these neutron detector elements, consisting of 22 layers each of fiber and ^{6}Li-scintillator.

Fig. 13. The sketch shows two layers of the 22-layer sensor elements of the NCCR.

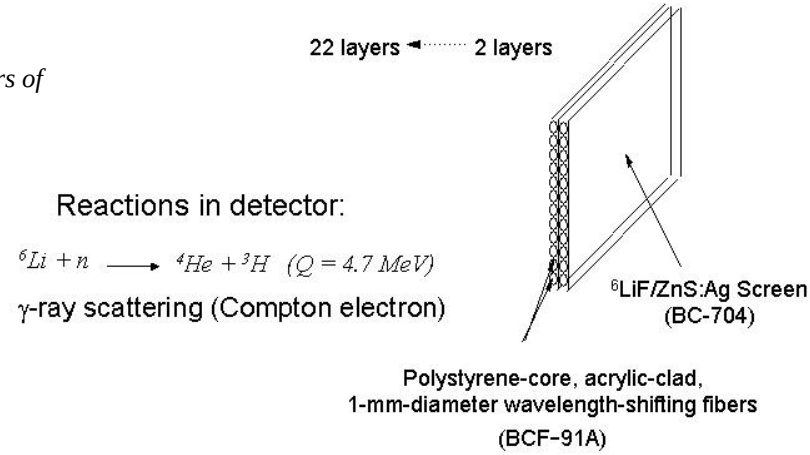

The moderator consists of the plastic fiber and hydrogenous binder in the LiF-ZnS mixture. These are intimately combined with the ^{6}Li capture material. The relatively high density of capture nuclides contributes to epithermal capture, which results in a shorter neutron die-away time. The intimate mix of moderator and capture media also contributes. Thus, the NCCR has a neutron die-away time of 4 μs.

Figure 14 is a photograph of three of 12 detector elements of the NCCR. These make up one side of the four-sided neutron well counter.

Fig. 14. Three of 12 NCCR detector elements are assembled to form one side of the four-sided neutron well counter. PMTs are coupled optically at the ends of each element. Signals from opposite ends of each element are combined into a single preamplifier. Note meter stick in foreground.

V. References

1. K. Boehnel, "The Effect of Multiplication on the Quantitative Determination of Spontaneously Fissioning Isotopes by Neutron Correlation Analysis," Nuclear Science and Engineering 90, 75-82 (1985).
2. J. F. Briesmeister, Ed. , "MCNP - A General Purpose Monte Carlo Code for Neutron and Photon Transport," Los Alamos National Laboratory report LA-12625-M, Ver. 4A (November 1993).
3. D. M. Cifarelli and W. Hage, "Models for a Three Parameter Analysis of Neutron Signal Correlation Measurements for Fissile Material Assay," Nucl. Instr. Meth. A251, 550 (1986).
4. N. Dytlewski, M. S. Krick, and N. Ensslin, "Measurement Variances in Thermal Neutron Coincidence Counting," Nucl. Instr. Meth. A327, 469-479 (1993).
5. N. Ensslin, M. S. Krick, and N. Dytlewski, “Assay Variance as a Figure-of-Merit for Neutron Multiplicity Counting,” Nuclear Instruments and Methods, A290 (1990) 197-207.
6. N. Ensslin, Chapter 11, "Neutron Origins," in Passive Nondestructive Assay of Nuclear Materials," edited by T. D. Reilly, N. Ensslin, and H. A. Smith, US Nuclear Regulatory Commission NUREG/CR-5550, March 1991.
7. N. Ensslin, Chapter 16, "Principles of Neutron Coincidence Counting," in Passive Nondestructive Assay of Nuclear Materials," edited by T. D. Reilly, N. Ensslin, and H. A. Smith, US Nuclear Regulatory Commission NUREG/CR-5550, March 1991.
8. N. Ensslin, M. S. Krick, D. G. Langner, and M. C. Miller, “Active Neutron Multiplicity Counting of Bulk Uranium,” Los Alamos National Laboratory report LA-UR-91-2470, Proc. 32nd Annual INMM Meeting, New Orleans, LA, July 28-31, 1991.
9. N. Ensslin, M. S. Krick, D. G. Langner, and M. C. Miller, "Active Neutron Multiplicity Counting of Bulk Uranium," Nucl. Mater. Manage. XX (Proc. Issue), 433-437 (1992).
10. N. Ensslin, M. S. Krick, D. G. Langner, D. W. Miller, and M. C. Miller, “Measurement of the Assay Precision of the Active Neutron Multiplicity Technique," Los Alamos National Laboratory report LA-UR-2359, Proc. 33rd Annual INMM Meeting, Orlando, FL, July 19-22, 1992.
11. N. Ensslin, M. S. Krick, W. C. Harker, M. C. Miller, R. D. McElroy, P. A. McClay, W. L. Belew, R. N. Ceo, L. L. Collins, and P. K. May, “Analysis of Initial In-Plant Active Neutron Multiplicity Measurements,” Los Alamos National Laboratory report LA-UR-93-2631, Proc. 34th Annual INMM Meeting, Scottsdale, AZ, July 18-21, 1993.
12. N. Ensslin, W. C. Harker, M. S. Krick, D. G. Langner, M. M. Pickrell, and J. E. Stewart, "Application Guide to Neutron Multiplicity Counting," LA-13422-M, September 1998.
13. N. Ensslin, W. H. Geist, M. S. Krick, D. R. Mayo, and J. E. Stewart, "Performance Calculations for Fast Active Neutron Assay," Los Alamos National Laboratory report LA-UR-99-4058, Proc. 40th Annual INMM Meeting, July 25-29, 1999, Phoenix, Arizona.
14. K. C. Frame, W. H. Geist, J. P. Lestone, A. P. Belian, and K. D. Ianakiev, "Characterizing the Detector Response and Testing the Performance of a new Liquid Scintillator Counter for Neutron Multiplicity Measurements of Enriched Uranium," Los Alamos National Laboratory report LA-UR-03-4899, presented at the 44th Annual INMM Meeting, Phoenix, AZ, July 13-17, 2003.
15. K. C. Frame, W. A. Clay, W. H. Geist, J. P. Lestone, A. P. Belian, and K. D. Ianakiev, "Neutron and Gamma Pulse Shape Discrimination in a Liquid Scintillator Counter for Neutron Multiplicity Measurements of Enriched Uranium," Los Alamos National Laboratory

report LA-UR-04-4868, presented at the 45th Annual INMM Meeting, Orlando, FL, July 18-22, 2004.
16. W. H. Geist, N. Ensslin, L. A. Carrillo, M. S. Krick, D. R. Mayo, and P. A. Russo, "Initial Results of Fast Active Neutron Coincidence Measurements," Los Alamos National Laboratory report LA-UR-99-3476, Proc. 40th Annual INMM Meeting, July 25-29, 1999, Phoenix, Arizona.
17. W. H. Geist, N. Ensslin, L. A. Carrillo, and C. A. Beard, "Advanced Analysis Techniques for Uranium Assay," Los Alamos National Laboratory report LA-UR-01-3331, Proc. 42th Annual INMM Meeting, Indian Wells, CA, July 15-19, 2001.
18. W. H. Geist, L. A. Carrillo, N. Ensslin, K. Ianakiev, D. R. Mayo, and M. C. Miller, "Evaluation of a Fast Neutron Coincidence Counter for the Measurement of Uranium Samples," Nuclear Instruments and Methods in Physics, A 470 (2001) 590-599..
19. W.H. Geist and K. Frame, "Modeling Active Neutron Coincidence Counters with MCNPX," Los Alamos National Laboratory report LA-UR-04-4355, …….
20. W. Hage and D. M. Cifarreli, "Correlation Analysis with Neutron Count Distributions in Randomly or Signal Triggered Time Intervals for Assay of Special Nuclear Materials," Nuclear Instruments and Methods A236, 165 (1985).
21. W. C. Harker and M. S. Krick, "Software Users Manual Windows NCC," Version 1.24, Los Alamos National Laboratory report, Copyright 1997 by the Regents of the University of California, September 1996.
22. M. S. Krick and W. C. Harker, "Multiplicity Neutron Coincidence Counting User's Manual," Los Alamos National Laboratory report LA-UR-93-1394 (April 1993).
23. M. S. Krick, N. Ensslin, D. G. Langner, M. C. Miller, R. N. Ceo, P. K. May, and L. L. Collins, Jr., “Active Neutron Multiplicity Analysis and Monte Carlo Calculations,” LA-UR-94-2440, INMM Meeting Proc., July 1994.
24. M. S. Krick, N. Ensslin, R. N. Ceo, and P. K. May, "Analysis of Active Neutron Multiplicity Data for Y-12 Skull Oxide Samples," Los Alamos National Laboratory report LA-UR-96-343, Proc. 37th Annual INMM Meeting, Naples, FL, July 28-31, 1996.
25. M. S. Krick, "Thermal Neutron Multiplicity Counting of Samples with Very Low Fission Rates," LA-UR-97-2649, Proc. INMM Annual Meeting, July 1997.
26. D. G. Langner, M. R. Sweet, S. D. Salazar, and K. E. Kroncke, " FB-Line Neutron Multiplicity Counter Operation Manual," Los Alamos National Laboratory report LA-...., October 1997.
27. M. C. Miller, R. C. Byrd, N. Ensslin, W. C. Feldman, M. S. Krick, T. H. Prettyman, and P. A. Russo, "Conceptual Design of a Fast Neutron Coincidence Counter for Verification of Special Nuclear Materials," LA-UR-96-1171, Third Topical Meeting on Industrial Radiation and Radioisotope Measurements and Applications, Raleigh, N. C. 27605, October 6-9, 1996.
28. M. C. Miller, R. C. Byrd, N. Ensslin, M. S. Krick, D. Mayo, D. J. Mercer, T. H. Prettyman, and P. A. Russo, "A Fast Neutron Detection System for Verification of Special Nuclear Material," LA-UR-97-2806, Proc. INMM Annual Meeting, July 1997.
29. M. C. Miller, R. C. Byrd, N. Ensslin, W. C. Feldman, M. S. Krick, T. H. Prettyman, and P. A. Russo, "Design of a Fast Neutron Coincidence Counter," J. Applied Radiation Isotopes, Vol. 48, pp. 1549-1555, 1977.
30. M. C. Miller, R. S. Biddle, S. C. Bourret, R. C. Byrd, N. Ensslin, W. C. Feldman, J. J. Kuropatwinski, J. L. Longmire, M. S. Krick, D. R. Mayo, P. A. Russo, and M. R. Sweet,

"Neutron Detection and Applications Using a BC454/BGO Array," LA-UR-98-1813, Presented at the 1998 Symposium on Radiation Measurements and Applications, Ann Arbor, Michigan, May 11-14, 1998, and published in Nuclear Instruments and Methods in Physics Research A422 (1999) 89-94.

31. M. M. Pickrell, "An Alternative Method for Analyzing Active Neutron Multiplicity Data," unpublished technical note, August 2004.
32. H. A. Smith and N. Ensslin, Chapter 23, "NDA Applications Guide," in Passive Nondestructive Assay of Nuclear Materials," edited by T. D. Reilly, N. Ensslin, and H. A. Smith, US Nuclear Regulatory Commission NUREG/CR-5550, March 1991.
33. J. E. Stewart, et. al., “A Versatile Passive/Active Neutron Coincidence Counter for In-Plant Measurements of Plutonium and Uranium,” in Proceedings of the 13th ESARDA Symposium on Safeguards and Nuclear Material Management, Avignon, France, 14-16 May 1991 (pp. 317-323).
34. J. R. Wachter, E. L. Adams, and N. Ensslin, “Prototype Fast Neutron Counter for the Assay of Impure Plutonium,” INMM/ANS Conference on the Safeguards / Facility Process Interface, San Diego, Nov. 1987
35. M. S. Zucker and N. Holden, "Energy Dependence of the Neutron Multiplicity P_ν in Fast Neutron Induced Fission of $^{235,238}U$ and ^{239}Pu," IAEA Conference on Nuclear Safeguards Technology, Vienna, November 1986, Vol.2

9. SHUFFLERS
Phillip M. Rinard

I. INTRODUCTION

A. Purpose of this Chapter

Shufflers were first conceived in 1969 as a method to assay uranium nondestructively. About 20 shufflers have been built in the US, and several others have been built in France and the United Kingdom. The purpose of this chapter is to introduce the technology, design, and operation of shufflers to readers who have little or no familiarity with this type of nondestructive assay system. A shuffler has a movable ^{252}Cf source that induces fission in fissile nuclei (^{235}U, ^{239}Pu) and is then moved away from the sample being assayed while a neutron counter measures delayed neutrons from fission. Shufflers are most often used to measure ^{235}U. The virtue of the shuffler technique is that the delayed neutron signal is proportional to the ^{252}Cf strength, yet the background is very low, because the source is shielded when delayed neutrons are counted.

For readers who want more technical detail than what is presented here, several published reports are cited as references. The Shuffler Application Guide, Ref. 1, is recommended as the first document to read, because it is the most comprehensive single reference to shuffler physics, design, calibration, and operation. The guide also includes an extensive bibliography of shuffler research at Los Alamos. Refs. 2–4 are also recommended. The first two discuss the detailed theory behind shufflers, with applications used as illustrations. The third report is concerned with the shuffler design most widely used to assay 200-liter drums (or smaller items) and discusses applications and results for assays of uranium and plutonium in a wide range of matrices.

B. The Motivation for Shufflers

1. History of Shufflers

In the 1960s, the Los Alamos safeguards group, under the direction of G. R. Keepin, began assaying fissile materials using delayed neutrons released after irradiation by neutrons from D-T reactions in a Van de Graaff accelerator. Measurements of delayed neutron parameters by Keepin and others formed a strong basis for applying delayed neutrons to uranium measurements.[5] When ^{252}Cf became available in the latter half of that decade, the advantages of using an intense isotopic source were quickly noted: reliable and predictable neutron emission rate, simple maintenance, and neutron energies too low to stimulate (n,2n) and (n,p) reactions. The main disadvantage was also clear: ^{252}Cf must be shielded at all times because it cannot be turned off. A D-T accelerator is likely to be less expensive than a ^{252}Cf source, but considering operating costs there is no significant monetary difference between the accelerator and isotopic sources.

Among the ^{252}Cf-based instruments proposed in 1969 was one in which a small capsule containing ^{252}Cf was “shuffled” pneumatically between storage and irradiation positions.[6] Fissions were induced in the fissile material and delayed neutrons counted after the ^{252}Cf source was returned to a shield. Figure 1 shows the “shuffling” process.

2. The Shuffler's Role Among Other NDA Instruments

Gamma-ray instruments perform excellent assays of uranium and plutonium samples of limited size. Gamma rays are more readily attenuated than neutrons, so even with good attenuation corrections there is a point where the attenuation is too large and assays are no longer possible. Before this point, plutonium samples emit enough neutrons from spontaneous fissions to make passive neutron counting feasible. Total neutron, coincidence neutron, and neutron multiplicity counters have evolved to provide accurate assays of plutonium. The shuffler technique does not compete with passive counters because spontaneous fission neutrons become a hindering background for a shuffler instead of a signal on which an assay is based; several exceptions will be noted later.

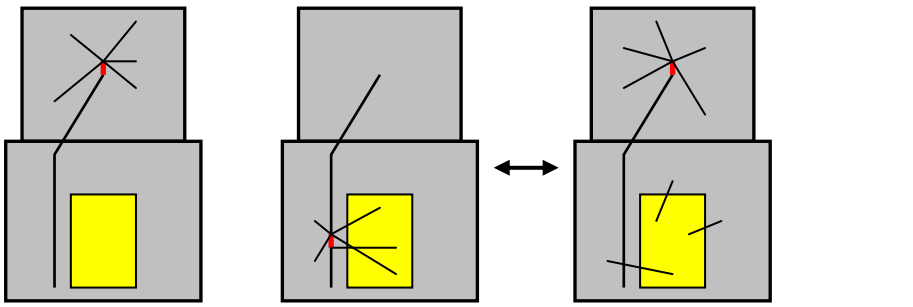

Fig. 1. The ^{252}Cf source alternates between the upper storage block and the lower assay chamber containing the object to be assayed (yellow). It is stored for the background count (a) and again after the irradiation (b) to count delayed neutrons (c). Steps (b) and (c) are repeated many times until the desired precision is reached. This "shuffling" of the source between two positions gives rise to the name of the instrument. For this illustration the source should be scanned along the side of the object during the irradiation (b) while the object rotates. Detector tubes surround the object to record the delayed neutrons (c).

However, uranium's passive neutron emission is far weaker than plutonium's and passive counters only work for large masses (> 1 kg) of ^{238}U. Active well coincidence counters (AWCC) were developed for uranium assay and their use overlaps some shuffler applications. An AWCC has AmLi sources above and below a can-sized container of uranium. Neutrons from the AmLi induce fissions and the fission neutrons are distinguished from the AmLi neutrons through their time correlations in time. The detected AmLi neutrons generate a high background that limits the precision (and sensitivity) of the AWCC.

An obvious niche for shufflers is in high-precision assays of bulk uranium where gamma-ray instruments cannot be used. Bulky items can be assayed with neutrons where gamma rays are strongly attenuated. The precision is better than an AWCC because the shuffler background during the count is very low. Since this initial application, the use of shufflers has expanded to other circumstances. For instance, a shuffler for bulk uranium can be a passive counter for bulk plutonium by keeping the ^{252}Cf source inside its shield while a passive count is taken. The shuffler's assay chamber can be designed to meet the criteria for passive counters, and one instrument then serves two roles.

3. Applications of Los Alamos Shufflers

This overview begins with an application for which shufflers are uniquely qualified: assaying large masses of dense uranium metal and oxide. Two variants of a shuffler for 200-liter drums

Fig. 2. The Uranium Scrap Shuffler had a hoist to raise and lower the heavy cans of scrap. A computer in an air-conditioned electronics rack was used to control the instrument and analyze the data.

are described, with applications to both large uranium masses and small waste quantities. Shufflers for unusual applications are also described. In these cases, high gamma-ray background rates or interference by neutrons from plutonium or curium make a shuffler necessary. Extensive details on all of these shufflers can be found in the bibliography.

a. Savannah River Uranium Scrap Shuffler

A shuffler (Figure 2) was built for the Savannah River Site (SRS) in 1978 to assay the mass of ^{235}U in cans of scrap metal from the billet extrusion process of making production fuel assemblies. This involved kilograms of uranium metal with enrichments from 50% to 80%. The spectrum-tailoring feature was retained to avoid interference from fissions in ^{238}U. Gamma rays could not be applied to these materials and the AWCC had just been developed. The only practical instrument was the shuffler, and its precision gave it an advantage over an AWCC.

b. Savannah River Billet Shuffler

The Billet Shuffler (Figure 3), installed at SRS in 1992, complemented the Uranium Scrap Shuffler. The Billet Shuffler determined the ^{235}U contents in billets prior to extrusion into fuel tubes. It was important to know the ^{235}U mass accurately to properly fuel the production reactors.

Fig. 3. Ed Adams opens the door to the assay chamber of the Billet Shuffler. The large cylinder in the foreground stores the ^{252}Cf source. Two simulated billets are on the cart to the right.

This shuffler had a precision of 0.25% (1σ) and an accuracy of 0.5% (1σ), even though the assay time (including background) was only 10 minutes. Such performance was possible because of the large ^{235}U loading (1.7 kg) and the billet's hollow core. A relatively small ^{252}Cf source (30 to 60 μg) was shuffled in and out of the center of the billet, making unusually efficient use of the irradiating neutrons. The excellent accuracy was made possible by the creation and careful characterization of calibration billets.

After the shutdown of the production reactors, the Billet Shuffler was used to measure uranium ingots prior to their shipment to Oak Ridge National Laboratory (ORNL). It assayed thousands of uranium ingots that previously would have become billets. The Billet Shuffler was then moved to a reactor building to help with decommissioning.

c. The "Standard" 200-liter-Drum Shuffler and Its Predecessors

There has an evolutionary progress in shufflers designed for 200-liter drums. In the late 1970s, a prototype shuffler for drums was created at Los Alamos by taking a passive neutron counter and adding a ^{252}Cf storage block and electronics. It was used to gain experience with 200-liter drum assays. Years later it was moved to Los Alamos's Chemistry and Metallurgy Research (CMR) Building to fill a temporary need and then was scraped. A unique feature of the shuffler was the shielding material in the walls of the assay chamber: water.

This shuffler was redesigned for Savannah River in 1984 to measure the uranium masses from fractions of a gram to hundreds of grams in a waste drum. Flux monitors were included to correct for matrix effects. These were two low-efficiency ^{3}He tubes that counted while the ^{252}Cf source irradiated a drum. One of the tubes was wrapped in cadmium so that moderators in a drum would affect the ratio of counts from these tubes. As a drum rotated on a turntable, the ^{252}Cf source scanned vertically to produce a distribution of delayed neutron precursors proportional to the distribution of uranium.

The shuffler was partially redesigned for the Portsmouth Gaseous Diffusion Plant to take advantage of improvements in electronics and ^{252}Cf motion control. Two of these shufflers (Figure 4) were delivered to Portsmouth in 1989 and 1991. Los Alamos commercialized this shuffler with Canberra Industries, which has since built two models for Los Alamos (Figure 5),

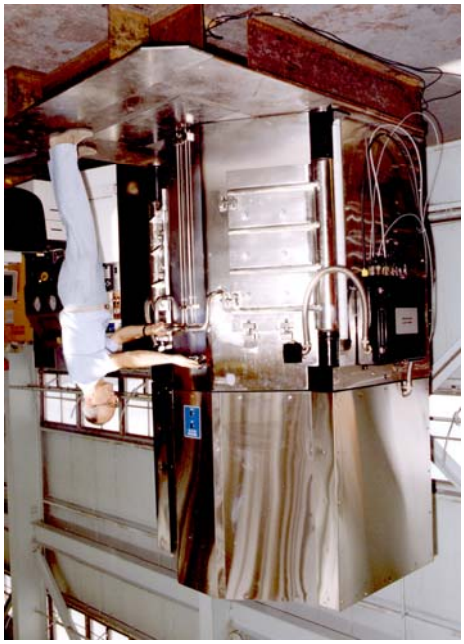

Fig. 4. Phil Rinard opens the doors of the Portsmouth Shuffler. Before shipping to Portsmouth, it was assembled and tested at Los Alamos on a riser. After installation, it sat flush with the floor. This design was commercialized through Canberra Industries.

Fig. 5. Sandra Hildner opens the doors of the shuffler for 200-liter drums at the Los Alamos Plutonium Facility to reveal a 200-liter drum. This shuffler is used to measure pyrochemical salt residues. These salts have very high ^{241}Am levels that produce large α,n rates that defeat passive coincidence methods. The shuffler can override this neutron background and achieve good measurement results.

one for Lawrence Livermore National Laboratory, and one for the Y-12 Plant at Oak Ridge. The applications of these shufflers have reached well beyond waste quantities to miscellaneous inventory items (grams to many kilograms of ^{235}U, ^{233}U, and ^{237}Np). The design in Figure 4 is now the “standard” 200-liter-drum shuffler.

d. The "Pass-Through" 200-liter-Drum and Boxed-Waste Shufflers

Savannah River requested two shufflers for 200-liter waste drums and boxed waste that could reside on materials accountability boundaries and decide, from an assay, whether a drum or box was allowed outside the boundary. A container inside the boundary entered the input door of the shuffler and was measured. If the uranium mass was below a preset limit, the output door opened and the container was now outside the boundary. Otherwise, the input door reopened and the container was kept within the boundary. This automated process avoided the costs of having to repeatedly open a boundary and use guards to check people in and out.

Fig. 6. The output side of the shuffler has a longer conveyer section to allow containers to be stored while new containers are assayed. Shown here are 200-liter drums, a HEPA filter, and a cardboard box

One of these shufflers had a conveyor system (Figure 6) that ran through the shuffler and moved the containers automatically. This shuffler was installed in 1993, not far from the Scrap and Billet shufflers. After the production reactors were shut down and fuel tube production ceased, it was adopted by Argonne National Laboratory at the Idaho National Engineering and Environmental Laboratory (INEEL).

e. Spent Naval Fuel Shuffler

The Spent Naval Fuel Shuffler (Figure 7) is one of the largest shufflers ever built. This shuffler, also known as the Fluorinel and Storage (FAST) Facility Shuffler, measured the uranium content in a spent-fuel assembly prior to reprocessing. Intense, fission-product gamma rays made it impossible to measure uranium gamma rays. In commercial reactor, low-enriched spent fuel, the buildup of ^{244}Cm creates an intense passive neutron rate that prevents a shuffler from detecting the much weaker delayed neutron signal from uranium (and also prevents passive counting for plutonium). But in highly enriched naval fuel, the ^{244}Cm buildup is much smaller, so this shuffler could assay for uranium directly. It required a 1- to 3-mg ^{252}Cf source, which is larger than usual for shufflers but not unusual in industrial applications of ^{252}Cf. The shuffler was built for the Idaho Chemical Processing Plant (ICPP), now known as the Idaho National Laboratory (INL).

Because the spent fuel had to remain within a hot cell, the shuffle body had also to stay there. Nevertheless, a large neutron shield was necessary to hold the ^{252}Cf source when it wasn't irradiating a fuel assembly and to protect workers who might enter the shuffler's general area. The ^{3}He tubes were shielded from fission-product gamma rays by 10 cm of lead. An assembly was moved vertically at a steady rate through the shuffler. The ^{252}Cf source performed its series of shuffles on the various segments of the fuel. In effect, the source scanned the fuel length, but the fuel did the vertical scanning. The shuffler became part of the reprocessing operations and

Fig. 7. George Eccleston and Tom Van Lyssel assemble the Spent Naval Fuel Shuffler for testing. A container is suspended above a small tube where assays are done on waste material inside the container. A larger tube to the left is for the fuel assemblies. A motor in the center ran an automated hoist. The motor at the bottom of the photograph is the stepping motor for the ^{252}Cf source.

proved to be very accurate. A second, smaller tube passing through the shuffler's body was provided to assay canisters of waste using the same ^{252}Cf source, but this capability was never applied.

f. Dounreay Reprocessing Solid-Waste Shuffler

The breeder reactor fuel reprocessing plant at Dounreay, Scotland, generates leached hulls and centrifuge bowls that may contain residual amounts of plutonium. Passive neutron counting is impossible in this case because ^{244}Cm, a prolific neutron emitter, is often present. Fission products and attenuation ruled out gamma-ray methods. The British installed a D-T generator to induce fissions in plutonium, but it proved a maintenance problem for a continuously operating plant. Los Alamos installed a shuffler at Dounreay in 1987 and it has been an integral part of the plant process ever since (Figure 8).

The shuffler takes a passive count. If no neutrons are found, there is no plutonium. If the passive count is positive, it may be caused by plutonium, curium, or both. An active assay is performed for the plutonium mass. A 3-mg ^{252}Cf source, when new, is used to override the worst ^{244}Cm case. Baskets of hulls or bowl parts are scanned past the irradiation position and the delayed neutron counts indicate the total plutonium mass. The shuffler's computer controls the hoist to ensure that the basket's position is properly synchronized with the ^{252}Cf source.

The computer, the electronics, and the stepping motors were upgraded in 1995.

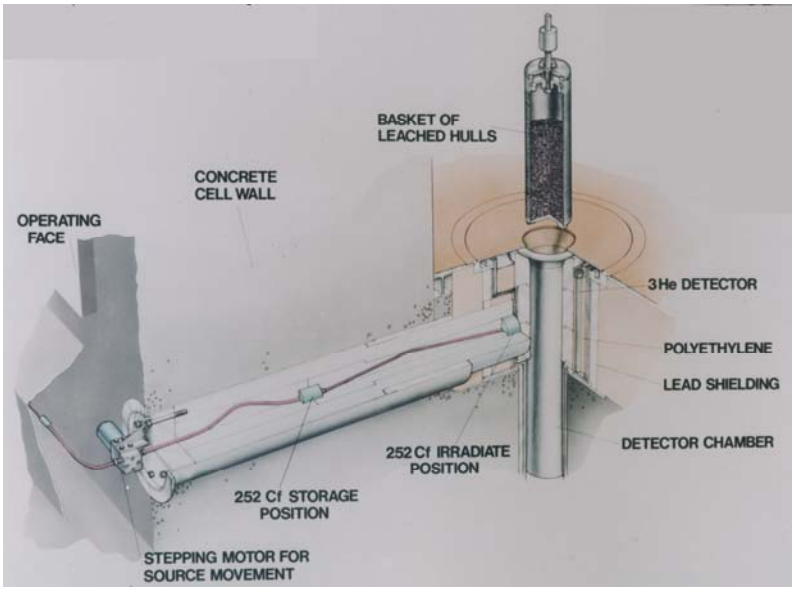

Fig. 8. The components of the Dounreay shuffler. A cylinder of polyethylene extends through the hot cell wall and the ^{252}Cf source is stored in the center of the wall. A basket of waste is lowered into the assay chamber while measurements are taken. The electromechanical components are in the corridor on the left edge of this drawing.

4. Applications of Shufflers in Europe

The nature and applications of shufflers in Europe are similar to those in the US. Initially, ^{252}Cf sources were moved pneumatically in shufflers in the UK and France, as was suggested in the first Los Alamos paper on the shuffler concept. It is a rapid way to move the source and uses technology familiar to reactor workers. However, scanning a large object during irradiation cannot be done and variations in the time used to move the source are large. Los Alamos shufflers use a stepping motor to move a strong, flexible, steel cable to which the source is attached. This technique is fast, reliable, and accurate. The source also can be easily moved at a slow speed to scan a large object (200-liter drum) during irradiation. The stepping motor and cable technique was adopted many years ago in both France and the UK. The French have even combined a more powerful motor with a large drum for winding the cable, resulting in even shorter times and longer distances to move the source.

Shufflers have been developed at Harwell in England for 200-liter drums, bags of waste, and mixed fissile materials. Liquid samples, dissolver tank residues, bags of waste, and 800-liter drums of leached hulls have been measured at the Cadarache Nuclear Center in France.

C. Shuffler Basics

The ideal measurement condition has a strong signal in the presence of a weak background. Uranium's passive neutron signals are weak and the passive gamma-ray signals are easily attenuated to the point where they cannot be detected. The AWCC generates a strong signal by inducing fissions and counting fission neutrons. However, the AmLi sources in the AWCC also produce a high background that limits the application of the AWCC to a ^{235}U mass greater than 10 g. Increasing the AmLi source strength beyond 10^5 n/s is counterproductive because the background rate also increases and the precision is harmed rather than helped. Furthermore, the size of the object measured by an AWCC is limited to a diameter and height of about 25 cm; the non-uniformity of the irradiating neutron flux becomes prohibitive beyond these dimensions.

The shuffler can generate the same or stronger signal as the AWCC, but with a much smaller background, even though it counts delayed neutrons that are less than 1% as numerous as prompt neutrons. The delayed neutron production rate is boosted by using a strong source (e.g., 10^{10} n/s) and the background rate is kept low by shielding the ^{252}Cf source during delayed neutron counting. The assay chamber can be relatively large (200-liter drum) without sacrificing uniformity of irradiation because the small ^{252}Cf capsule can be easily scanned and the drum rotated during the irradiation. For a detailed theoretical treatment of shufflers, see Refs. 1 and 2.

1. Delayed Neutrons

$$P(t) = \sum_{j=1}^{6} P_j(t) = \sum_{j=1}^{6} \beta_j \bar{\nu} e^{-\lambda_j t} \ . \qquad (1)$$

$P_j(t)$ is the population of the *jth* group of precursors, $\bar{\nu}$ is the average number of neutrons per fission, and β_j is the fraction of the fission neutrons that are delayed, so $\beta_j \bar{\nu}$ is the average of delayed neutrons produced per fission by group *j*. The decay constant for group *j* is λ_j. The parameters of the six groups vary among the uranium and plutonium isotopes (also thorium and neptunium) but are well known from measurements. These parameters are necessary to calculate required ^{252}Cf masses or expected count rates.

To gain a sense of their values, examine Table I for the parameters of ^{235}U and ^{239}Pu. The group half-lives are shown instead of the decay constants for quicker understanding of the behavior of delayed neutrons. (Uncertainties can be found in Ref. 2.) If one assay follows another, there should be a pause to allow the previous precursors to decay; 4 minutes is generally sufficient because the longest-lived precursors are not the most productive. The time decays of the precursors of these two important isotopes are shown in Figure 9; the amplitudes are per fission and reflect the different values of $\beta_j \bar{\nu}$. The two values of $\bar{\nu}$ in Table I are approximate because $\bar{\nu}$ actually has a slight dependence on the energy of the captured neutron.

TABLE I
DELAYED NEUTRON PARAMETERS FOR ^{235}U AND ^{239}Pu

	^{235}U. $\bar{\nu}$ = 2.43*		^{239}Pu. $\bar{\nu}$ = 2.88*	
Group j	$T_{1/2}$ (s)	$\beta_j \bar{\nu}$	$T_{1/2}$ (s)	$\beta_j \bar{\nu}$
1	55.72	0.00052	54.28	0.00021
2	22.72	0.00346	23.04	0.00182
3	6.22	0.00310	5.60	0.00129
4	2.30	0.00624	2.13	0.00199
5	0.610	0.00182	0.618	0.00052
6	0.230	0.00066	0.257	0.00027
sum	-------	0.01580	-------	0.00610

* These values are for thermal neutron fission. Actual values generally are slightly larger.

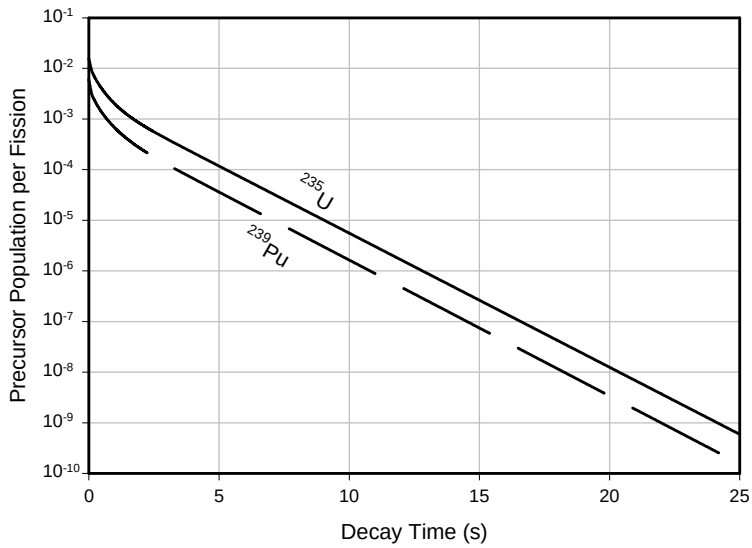

Fig. 9. After a fission, the average number of delayed neutron precursors present is shown as a function of time after the fission. The curve for an isotope is accurately expressed as a sum of six curves (one for each precursor group). Each group has an exponential decay but their sum isn't exponential until the short-lived precursors have decayed for about 5 s.

2. The Shuffler Principle

The principle behind a shuffler assay is illustrated in Figure 1. The general shape of the standard 200-liter-drum shuffler is used in this illustration. If an assay must be done in a specified time, optimum times of the various stages can be calculated to optimize the precision of the resulting count rate. For example, in the standard 200-liter-drum shuffler, the typical assay time is somewhat arbitrarily set at 1000 s. The background count uses the first 270 s of this time and the background is about 20-30 cps. Generally, 34 shuffles are performed, during each of which the irradiation is about 11.6-s long and the count time is about 7 s. The rest of the 1000 s (about 98 s) is spent moving the source and handling the intermediate data. The precision changes slowly as these times are modified, so the times are not critical. It is important that the times of all the steps are closely replicated during each of the shuffles; this is easily done by the computer and stepping motor to within a millisecond or so.

The user can easily modify any of these parameters to best match the current circumstances. If the assay time is doubled to 2000 s, the background time and shuffle number should also be doubled. The irradiation and count times for a given shuffle should not be changed because they are based on the nuclear parameters in Table I and the background rate. Should the background rate be much higher than 30 cps, the irradiation and count times should be reconsidered, as described in Ref. 2.

During a 7-s count most, but not all, of the delayed neutrons will be released (Figure 9). A small number will "carry over" into the next count time. Better use of the assay time is made by "sacrificing" some of the delayed neutrons and re-irradiating to replenish the precursor population. See Ref. 2 for more details.

3. Pertinent Properties of ^{252}Cf

The important property of ^{252}Cf for shuffler applications is its very high yield of spontaneous fission neutrons: 2.34×10^{12} n/s•g. This is 10^5 times greater than the yield of ^{244}Cm and 2×10^9 times greater than the yield of ^{240}Pu. It has the intensity of a small accelerator without the electronics and irregular variations in yield, plus a lower neutron energy. However, it cannot be turned off and it disappears with a half-life of 2.645 y.

For those who deal in curies, one gram of ^{252}Cf corresponds to 536.1 Ci. So 1 mCi of ^{252}Cf corresponds to a yield of 4.635×10^6 n/s, and 1 μCi gives 4635 n/s.

The half-life is short enough that a source must be oversized initially to have a useful lifespan. For a source to have a useful life of at least three years, it must be at least twice as large as necessary. Practical lifetimes are closer to 10 years, either because initial sizes are four times the minimum required, the precision is preserved by increasing the assay time, only materials with masses larger than the design minimum are measured, or some degradation of precision is acceptable.

Shufflers do not care that spontaneous fission neutrons are time correlated. The energy spectrum of spontaneous fission neutrons is very important. The usual expression for the spectrum is the Watt equation (Figure 10):

$$N(E) = e^{-E/a} \sinh(\sqrt{bE}), \qquad (2)$$

where E is the neutron energy in MeV and, for ^{252}Cf, a = 1.025 MeV and b = 2.926 MeV^{-1}. The average neutron energy is 2.3 MeV, but the most probable energy is 0.90 keV. The median energy is 3.27 MeV. This spectrum is used in the Monte Carlo calculations discussed later.

^{252}Cf is produced in the high-flux reactor at Oak Ridge. Table II presents the basic nuclear data used by the Radiochemical Engineering Development Center at Oak Ridge, where Cf is generated and sources are produced. John Bigelow and Joe Knauer kindly provided this information. For four of these six nuclides ($^{250, 251, 252, 254}$Cf) it is easy to calculate the emission rates given in Table II. The expression is:

$$\text{Emission rate} = \bar{\nu}\,(\text{SF Branching Fraction})\,[(\ln 2)/T_{1/2}]\,[6.02214 \times 10^{23} / (\text{At. Wt.})]. \qquad (3)$$

To get the emission rate in (n/g•s), the half-life must be in seconds. The spontaneous fission branching fraction is normally 1 minus the α-decay branching fraction. "At. Wt." is the atomic weight of the isotope.

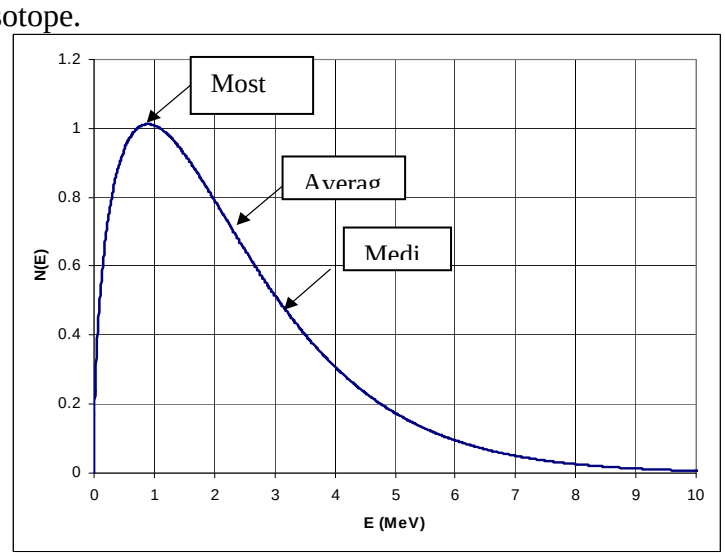

Fig. 10. The energy spectrum of ^{252}Cf neutrons (Watt equation). The average, most probable, and median energy are marked.

TABLE II
BASIC NUCLEAR DATA FOR Cf NUCLIDES

Nuclide	Half-Life ($T_{1/2}$)	α-Decay Branching Fraction	Spontaneous Fission (SF) Branching Fraction	$\bar{\nu}$ for SF	(α,n) Rate from Oxygen per Gram of ^{x}Cf	Total Neutron Emission Rate (n/g•s)
^{249}Cf	351 y	≈ 1.0	5.2×10^{-9}	3.4	≈ 3700	6.34×10^{3}
^{250}Cf	13.20 y	0.99921	0.00079	3.53	negligible	1.117×10^{10}
^{251}Cf	898 y	≈ 1.0	9.0×10^{-6}	3.7	negligible	1.955×10^{6}
^{252}Cf	2.645 y	0.96904	0.03096	3.768	negligible	2.314×10^{12}
^{253}Cf	17.81 d	0.0031	unknown	unknown	negligible	8.406×10^{4}
^{254}Cf	61.9 d	0.00299	0.99701	3.93	negligible	1.204×10^{15}

Fortunately, the worst uncertainties have no practical significance for shufflers because only two nuclides have important emission rates in a source: ^{250}Cf and ^{252}Cf. The production protocol is optimized for ^{252}Cf with its modest half-life, so the long-lived nuclides are not as abundant and the short-lived nuclides are gone before the source reaches a user. Figure 11 shows the relative neutron emission rates from ^{250}Cf and ^{252}Cf for three decades after creation. The initial relative

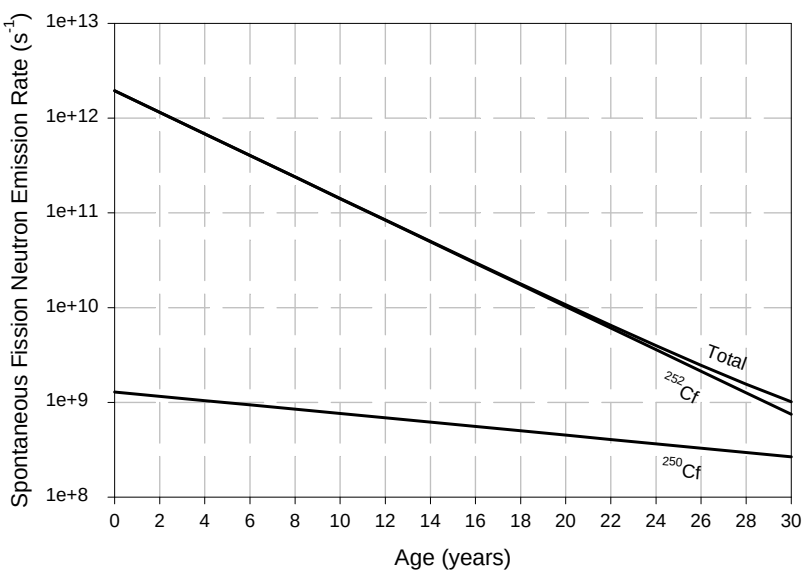

Fig. 11. Neutron emission rates as a function of time from one gram of Cf with the mixture of nuclides in Table III. The lowest curve is the rate from ^{250}Cf; the middle curve is the rate from ^{252}Cf; the upper curve is the sum of these two. The curves for ^{252}Cf and the sum are indistinguishable until an age of about 20 years.

abundances used are shown in Table III. The ^{250}Cf fraction of the neutron emission rate is shown in Figure 12.

TABLE III
INITIAL RELATIVE ABUNDANCES OF Cf NUCLIDES
This is a realistic example, but abundances vary among batches.

Nuclide	Relative Abundance (Fractional)
^{249}Cf	0.009424
^{250}Cf	0.115183
^{251}Cf	0.032461
^{252}Cf	0.837696
^{253}Cf	0.005236
^{254}Cf	0.000000

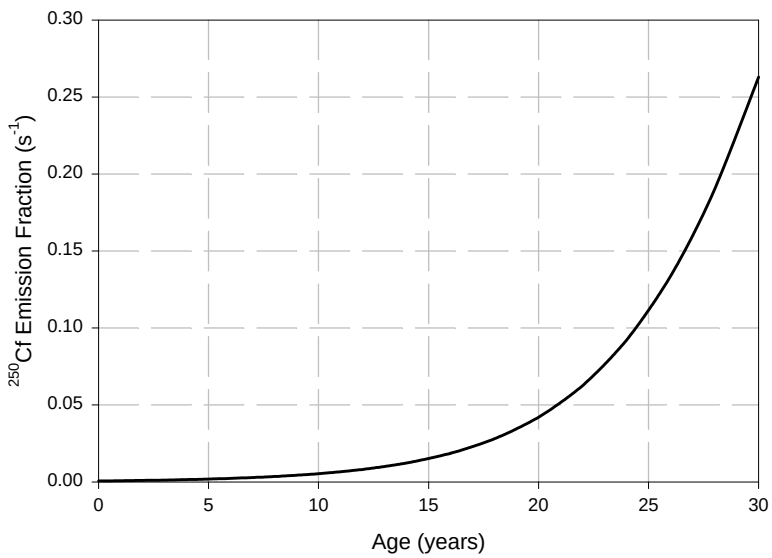

Fig. 12. The ^{250}Cf contribution to the total neutron emission rate from the Cf described in Table III increases with time because ^{252}Cf decays more quickly. It takes 13 years for ^{250}Cf to contribute 1%, but only an additional 8 years (21 years total) to reach 5%. The fraction grows to 25% in another 9 years (30 years total).

In practice, it is possible to ignore californium isotopes other than ^{252}Cf in shufflers because a source is not used for 20 years. An old shuffler source has other uses and its mixture of isotopes should be understood to avoid inaccurate results.

The neutron dose rate from 1 μg of ^{252}Cf at one meter without any shielding is 2.34 mrem/hr. The gamma rays contribute another 0.140 mrem/hr. The total dose rate is therefore 2.48 mrem/hr/μg at one meter with no shielding. The standard 200-liter-drum shuffler uses a 550-μg source when new, so the dose rate at one meter in air for such a source is 1.24 rem/hr. When loading a new source into a shuffler, the source is unshielded for about 15 s and nobody is closer than 2 meters. Under those conditions, the nearest person receives about 1.4 mrem. Doses measured during the loading process have been about 10 mrem, which includes the dose received from working around the shipping cask to prepare for the brief loading operation. The short time needed to insert a new source is the key to producing such a small dose to the handler and practice with a dummy source helps keep the time short.

An advantage of using ^{252}Cf for shufflers is the tiny mass and volume needed for a source with a large yield (e.g. 10^{10} n/s). All of the standard capsules overwhelm the size of the actual source; the capsules are made almost entirely of solid steel. The californium may be

electrodeposited on a small wire, which is cut in pieces to produce various neutron yields. Los Alamos uses standard, certified packages used for decades by Oak Ridge and Savannah River. The californium is double encapsulated in steel. The inner capsule has a small cavity for the wire, a diameter of about 0.5 cm, and a length of about 2.5 cm. This capsule goes inside an outer capsule, which has a diameter of about 0.75 cm and a length of about 3.7 cm. Both capsules are welded and have passed extensive durability tests under conditions much worse than in a shuffler.

One end of the outer capsule has a threaded nub. A steel coupler screws onto this nub and also onto a flexible steel cable with a wire wound around the outside, which serves as a coarse thread. All threads and set screws are cemented with LokTite to ensure that they will not come undone. The many sources attached in this manner have never accidentally detached from the cable, despite the immense number of shuffles of the sources.[7]

4. Factors That Complicate Assays

While it is easy to place an object in a shuffler and record the delayed neutron count rate a few minutes later, converting the count rate to an accurate mass of ^{235}U (or other fissile isotope) requires careful preparation. Calibration is important and not always simple.

When measuring ^{235}U, there is always some ^{238}U present. The probability of ^{238}U fissioning is essentially zero unless the energy of the absorbed neutron is more than 1 MeV. The ^{252}Cf energy spectrum of Fig. 10 makes it clear that, unless modified, there will be fissions in ^{238}U. Actually, some ^{238}U fissions occur regardless of the energy spectrum of the irradiating source because fission neutrons from ^{235}U have an energy spectrum not too different from ^{252}Cf. Some relief comes from the lower probability that a high-energy neutron will induce a fission in ^{238}U, but this is less than a factor of two. With high-enriched uranium there is more relief from the small quantity of ^{238}U (10% or less). On the other hand, the average number of delayed neutrons from a fission of ^{238}U is 2.6 times that of ^{235}U. The ^{238}U complication can be nearly eliminated with "spectrum tailoring," reducing the energies of the ^{252}Cf neutrons below 1 MeV before they reach the uranium. This is done by placing additional steel between the ^{252}Cf source and the measured sample.

While fissions in ^{238}U require high-energy neutrons, fissions in ^{235}U are more likely as the neutron energy decreases. The various matrices that might be put into the standard 200-liter-drum shuffler have a wide range of effects[4] that have been dealt with in various ways. Within such a large volume as a 200-liter drum, the same mass of ^{235}U can produce different count rates depending on its distribution throughout a moderating matrix, so a method of determining the distribution and correcting for it has been developed and implemented.[8]

II. Shuffler Performance

The performance of any NDA instrument is expressed by a set of parameters such as:

- Precision or Reproducibility. These words are synonyms, but only "precision" will be used. If a measurement is repeated many times, the precision is the standard deviation of the results. It may be expressed in the same units as the measurement, or as percent of the average of the measurements. In the latter case, it is called a relative precision. The standard deviation is often expressed in units of the σ of normal (Gaussian) distributions, where $\pm 1\sigma$ gives the range of values in which 68.3% of the measured values should fall. The item measured may be left untouched during this process or removed and replaced

between measurements to include handling effects. The time span of the measurements may be short (less than a day) or long (many days or years) to exhibit stability over time.

- Accuracy. This is a comparison of the measurement result and the best estimate of the true value. The difference is usually expressed as a percent of the true value; a smaller percent means better accuracy. Sometimes "bias" is used in this same sense. Sources of inaccuracy are sorted into systematic and random. The most notorious random causes are inherently beyond full control. Examples are the randomness in radioactive decay and backgrounds from cosmic rays. Cosmic rays can be mitigated with shielding and other techniques, but because it is impractical to work in deep mines, the cosmic-ray problem is almost always present. Systematic inaccuracies are caused by incomplete knowledge of the instrument, its calibration standards, or the materials being measured. Whatever errors exist in the calibration standards are passed along to the assay results.
- Sensitivity or Minimum Detectable Mass. These two terms are synonyms here, but whichever is used requires some supplementary information before it has meaning. The usual way to express sensitivity, the smallest mass that can be said to be measured with a stated certainty, is to relate the signal and noise "strengths" and define when the signal is just distinguishable from fluctuations in the noise. In shufflers, the signal is the delayed neutrons, while the noise is the background neutrons. A common practice is to define the sensitivity as the mass of fissile material that generates a delayed neutron count rate that is 3 times the 1σ error (random and systematic) of the background rate.
- Assay Time and Throughput. These are related, but not identical, concepts. The assay time is the time it takes to perform a complete measurement. Throughput is how many measurements can be completed in a given time. Throughput includes the time needed to change samples and enter information into the computer. The assay time may be 1000 s (16.67 min.) but the throughput might be three items an hour. Assay time directly affects precision and sensitivity, and it affects accuracy through precision.

With terminology defined, each performance characteristic will be examined for shufflers.

A. Precision

Precision is a shuffler strength. An intense ^{252}Cf source can be used to generate a large count rate of delayed neutrons and yet the background is low because the source is shielded while delayed neutrons are counted. The precision also depends on the mass and type of fissile isotope present. The probabilities of fissioning ^{235}U or ^{239}Pu are quite similar over a wide range of neutron energies, but ^{235}U produces about 2.6 times as many delayed neutrons per fission while spontaneous Pu fissions raise the background rate, affecting the precision. Everything else being equal, the precision with ^{235}U is better than with ^{239}Pu. This is also true when ^{235}U is compared with ^{233}U, ^{238}U, and ^{237}Np, just to name a few more isotopes.

The shuffler hardware affects the precision. Most of the hardware is fixed. However, the assay chamber is usually lined with cadmium to keep very low energy neutrons out of the chamber; this liner may be removed in just a few minutes. With everything else held the same, the precision can be greatly improved by not using a cadmium liner. The low-energy neutrons emerging from the moderating walls have high probabilities of inducing fissions and the count rate is greatly boosted. This can be effective in some circumstances, but it is generally a poor assay technique. The goal of an assay is not to get the best precision, but to get the best possible accuracy. If low-energy neutrons are allowed to dominate the fissions, the correlation between

count rate and mass becomes more complex as the mass. The self-shielding effect is accentuated and accuracy suffers. Table IV lists ways to improve precision, with cautionary notes.

B. Accuracy

Accuracy requires precision, but precision does not ensure accuracy. If the delayed neutron count rate is poorly known, the best calibration curve in the world cannot produce an accurate result. But a count rate with fantastic precision is meaningless without an accurate calibration curve. Accuracy is a relative term and depends on the use to be made of the result. A verification measurement checks a declared value, but is not as good as the declared value and does not replace it; it does not demand great accuracy. Accountability measurements should have the best possible accuracy and may replace declared values. For waste quantities, a poor accuracy may be tolerable because a large error in a small mass is still a small mass; a 100% error in 1 g is only 1 g. However, improving the accuracy becomes important when the measured mass plus some multiple of its uncertainty bumps into a regulatory limit. In this case, the waste may have to be placed in a category where handling and storage is more expensive.

TABLE IV - Improving Precision

To improve precision…	But be aware that…
Use a larger ^{252}Cf source.	More shielding is required and the size and weight of the shuffler grow exponentially.
Shorten the irradiation distance between the ^{252}Cf source and the fissile material.	If this produces a large inequality in the neutron flux for different places, the accuracy can suffer as the distribution of fissile material changes.
Use metal reflector behind ^{252}Cf to send more neutrons toward the fissile material.	This will never hurt the precision, but there may not be space for the 5-10 cm of iron (or other dense metal).
Surround the ^{252}Cf with metal to "tailor" the neutron energy spectrum toward lower energies.	Unwanted fissions in fertile isotopes (like ^{238}U) may be reduced, but self-shielding effects will be greater and the source will have to be somewhat stronger.
Use thermal and epithermal neutrons.	Self-shielding is a much larger problem even though count rates may increase.
Measure larger fissile masses.	The choice of masses is usually beyond the user's control. Self-shielding and multiplication effects grow, sometimes balancing each other nicely, but usually not.
Use longer assay times.	Throughput will decrease.
Use low background rates.	Poorly designed shielding may increase cosmic-ray interactions and hence the background rate. A larger storage block for the ^{252}Cf source reduces the background rate, but is the reduction commensurate with the increase in cost and improvement in performance?
Use more detector tubes or tubes with better sensitivity.	The procurement and fabrication costs increase.

The following shufflers made for Savannah River were specified to have exceptional accuracies because kilograms of uranium were involved: the Scrap Shuffler (0.3% for chips; 1.5% for floor sweepings), the Product Oxide shufflers (0.36%), and the Billet Shuffler (0.5%). On the other hand, the Liquid Raffinate Shuffler was specified by the Westinghouse Idaho Nuclear Co. to have an accuracy of 10% because it was more important to complete an assay in 100 s with a concentration of only 0.034 g/l (0.07 g-^{235}U in the 2-liter assay chamber).

Because a shuffler's precision is usually very good, accuracy is primarily set by the quality of the calibration. For the excellent accuracies of the three Savannah River shufflers mentioned above, the calibrations were extensive. Standards were carefully prepared and sampled for chemical analysis. For the Billet Shuffler, the billets were fabricated to small tolerances, so variations among billets were small except for the ^{235}U enrichment. The metal pieces for the Scrap Shuffler had irregular geometries, but this was not a major point. The Product Oxide shufflers had to work with oxides whose densities could vary, but with careful handling the variation was slight. With the development of very accurate calculational techniques (see Reference 3), the ability to calculate calibrations is possible and has been applied by Livermore and Los Alamos.

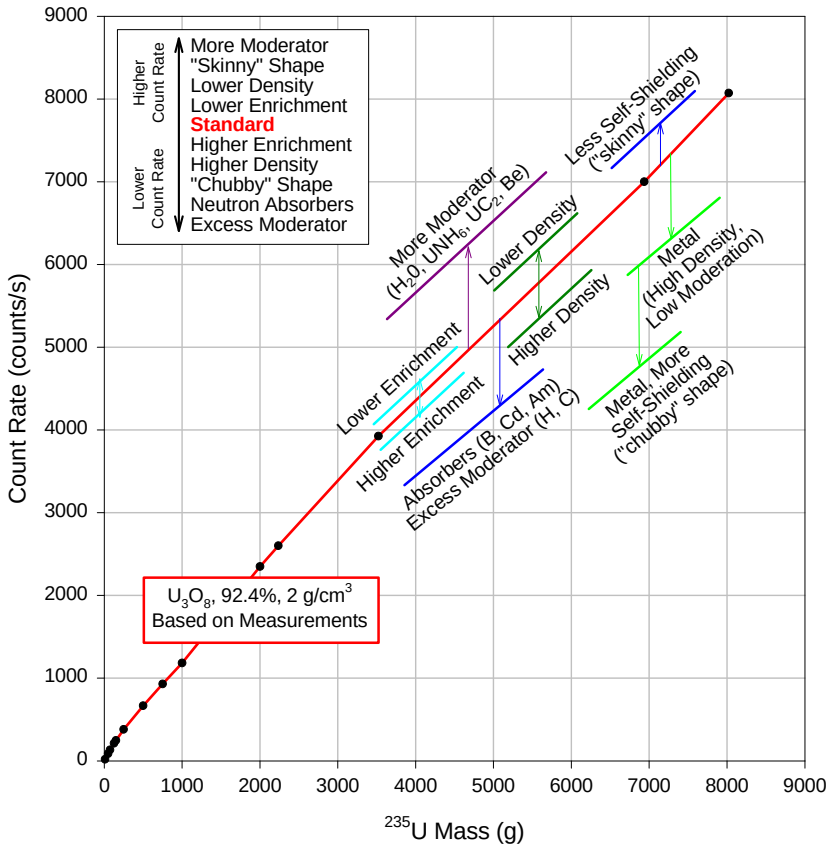

Fig. 13. When the material being measured has characteristics different from the calibration standards, the accuracy can be adversely affected. In this example, the calibration shown by the red line is for U_3O_8 with 92.4% ^{235}U and 4 g/cm^3. Potential changes are shown and the qualitative effect of each is indicated (exaggerated for clarity).

Standards based on powders (e.g. U_3O_8) require special attention because powder density changes with handling or even while sitting on a shelf. The powder density can be changed by as

much as 20% by shaking or tapping a can.[9] This changes the self-shielding of the material and, therefore, the count rate. A handling procedure should be established and adhered to strictly to make sure the calibration curve is appropriate for each measurement.

Figure 13 shows qualitatively how material variations can affect the accuracy of the calibration curve. Figures 14 and 15 are examples of measured and calculated effects of changes in chemical and physical form.

There are several ways to extend a calibration and minimize the number of standards. Calculational techniques are particularly useful in this context. If all the details of the model are correctly described, the accuracy of the result is as good as measured values. Extension of

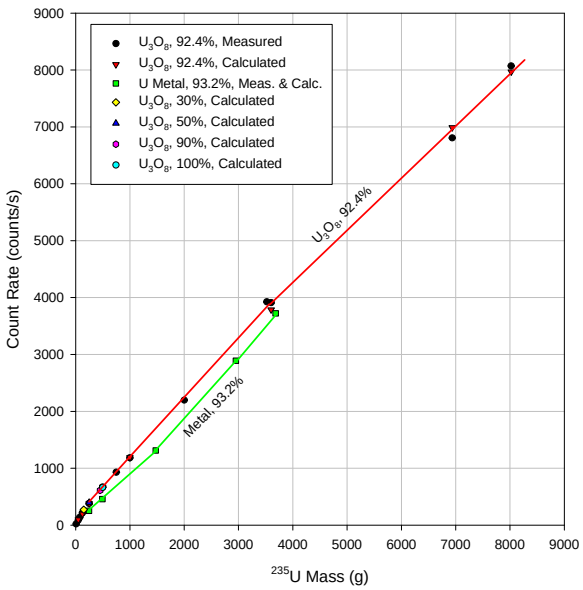

Fig. 14. The curve in red is the measured calibration for dry U_3O_8, 92.4% enriched. The effect of deviations from this have been calculated and are shown for comparison. Using metal disks (6-cm diameter) greatly reduces the count rate for the same mass of ^{235}U because of self-shielding from the higher density (19 instead of 4 g/cm^3). Enrichment effects are better seen in Fig. 15

traditional standards is also possible. For example, a 200-liter drum of waste paper has a large amount of hydrogen that affects the count rate. A calibration done with one amount of paper has an accuracy problem for another drum with a paper density that differs by, say, 20%. You could have another calibration curve to handle this drum, but how would you know which calibration to use? The use of flux monitors and polyethylene sleeves and the measurement of fissile material distribution to address this problem are discussed later. Table V lists some ways to improve accuracy.

TABLE V - Improving Accuracy

To improve accuracy…	But be aware that…
Improve the precision.	See potential problems given in Table IV.
Use calibration standards that match what you wish to measure and are known to at least the accuracy needed for the assays.	These can be expensive and may even be virtually impossible to build.
Control packaging and the matrix materials to match your standards.	This may be out of your control, despite your best attempts.
Handle containers of powders (e.g., U_3O_8) in a consistent manner to avoid changing the densities.	Some trial and error with handling techniques may be necessary to discover what works. Changes in density during storage may occur. Training users will be needed.
Scan larger objects with the ^{252}Cf source during the irradiations to create a distribution of precursors matching the distribution of fissile material.	Some trial and error with scanning techniques may be necessary to find the best one.
Use flux monitors to measure changes in hydrogen (moderator) density.	A measurement program with different moderator densities is needed to calibrate the flux monitor rates.
Use count rates in individual detector banks to find the distribution of fissile material within a moderating matrix.	A measurement campaign is needed to correlate the count rates with the different possible distributions.

C. Sensitivity or Minimum Detectable Mass

What is the smallest fissile mass that can be measured with a high probability (e.g. 95%) such that the signal is not a statistical fluctuation of the noise? That is one way to define sensitivity or, more descriptively, the minimum detectable mass. A shuffler cannot distinguish a delayed neutron from neutrons caused by cosmic-ray interactions or from the stored ^{252}Cf source.

The starting point for calculating the sensitivity is to express it in mathematical terms as the ratio of the delayed neutron counts, D, to the total uncertainty in the background counts, σ_B. This ratio is usually set to 3, to express the requirement that the signal be larger than the fluctuations in the noise. If $D/\sigma_B = 3$, it is sometimes said that the signal is 3σ above background. When the minimum detectable mass, m_s, is present, the delayed neutron counts have the special value of D_s. The two are related through the calibration function, after converting the counts into a rate over a count time T_D.

$$\frac{D_s}{T_D} = f(m_s) \tag{4}$$

The uncertainty in a shuffler's delayed neutron count has a simple expression.[2]

$$\sigma_D = \sqrt{D + B\frac{T_D}{T_B} + B\left(\frac{T_D}{T_B}\right)^2} \ , \tag{5}$$

where

D = delayed neutron counts (not rate),
B = background counts (not rate),
$T_{D,B}$ = count time for delayed neutrons and background

As for all instruments, the sensitivity is limited by the background rate. Shuffler background rates are generally 10-40 cps, depending on the design and working environment. The definition of sensitivity is expressed with D_s/σ_B set usually to 3. The minimum necessary number of delayed neutron counts, D_s, follows from taking the ratio of Eqs. (4) and (5).

$$\frac{D_s}{\sigma_B} = \frac{T_D f(m_s)}{\sqrt{T_D f(m_s) + B\frac{T_D}{T_B} + B\left(\frac{T_D}{T_B}\right)^2}} . \qquad (6)$$

The minimum detectable mass m_s is found by solving this equation. If the calibration is a straight line through the origin (as for waste), this is easy to do algebraically.[3] For the most complex calibrations Eq. (6) can be solved by numerical methods (such as the Newton-Raphson method).

D. Choosing the Assay Time

In any NDA instrument, the assay time is usually a compromise that best meets conflicting specifications. The comparison in Table VI shows more advantages of using long assay times, but in practice rather short assay times (10 to 16 min.) are generally used because throughput is the main driver.

TABLE VI - Assay Times

Advantages of Long Assay Times	Advantages of Short Assay Times
Better precision.	Better throughput.
Better sensitivity.	Better immunity to changing conditions (e.g., background)
Can use smaller ^{252}Cf for a given precision, reducing cost and size.	
Can use smaller detection efficiencies for a given precision, reducing cost.	

Equation (6) is a good way to estimate the assay time needed to reach a measurement goal. The background and delayed neutron count rate must be known as well as possible. The latter depends on the ^{252}Cf mass, so there are many linked factors. As a rule of thumb, about a quarter of the assay time is spent on a background count. If the background rate is much different than the 10-40 cps mentioned earlier, a new study should be made of the fraction of total time spent on background counting. It is possible to do one long background count and use it for all assays of the day (or more), if it is clear that the background rate will not change. This would be the

most efficient use of all the time available, but it is rarely done because it is not certain that the background rate is constant. The background rate was *not* measured with each assay for the Liquid Raffinate Shuffler because the assay time had to be a short as possible (100 s) to ensure catching a high ^{235}U concentration as quickly as possible. A background count was taken periodically and used for many succeeding assays.

Los Alamos shufflers have always used an assay time set before the assay begins, expressed through the background time and the various parameters defining the shuffles. An alternative is to terminate the assay when a desired relative precision has been reached, up to some maximum number of shuffles. The average count rate then should be adjusted for the difference in the number of shuffles just used and the number used during calibration. This is another source of inaccuracy that is easily avoided by using a fixed assay time.

III. CREATING A SHUFFLER

A. Basic components

1. Hardware

A shuffler design centers on the assay chamber, which must be large enough to hold the biggest container, but no bigger than necessary. A snug fit between the assay chamber and the objects to be assayed is ideal, but even a small can may be quite adequately assayed in the 200-liter-drum shuffler despite the unequal sizes. Most containers should be rotated to make the irradiation more uniform throughout their volumes.

The ^{252}Cf source needs a storage block to reduce the dose rate from the source to the level specified by the user. In Los Alamos shufflers, the ^{252}Cf source is moved with a stepping motor that drives a cable attached to the source; positioning is quick and accurate. An alternative used in older European shufflers is to drive the source pneumatically. This is fast, but it can place the source at only two positions and cannot be used for scanning. Pneumatic methods have been dropped in favor of stepping motors.

The assay chamber is surrounded by neutron detectors, which are ^{3}He tubes with 2.5 cm diameters and pressures of 4 atm. For higher detection efficiency, the gas pressure can be as much as 10 atm. The tubes are electronically grouped and one signal cable receives the signals from several detectors, usually by connecting a set of detectors to one amplifier. The standard 200-liter-drum shuffler has six banks of detectors surrounding the side of the assay chamber, plus a bank above and a bank below the chamber. The amplifiers are now commercially available and built around the AmpTek 111 amplifier.

Flux monitors are also ^{3}He tubes, but are made less efficient to keep their interactions at a high but acceptable rate while the ^{252}Cf source is nearby. This inefficiency is accomplished by reducing the gas pressure, reducing the diameter, reducing the length, or some combination of these.

Figure 16 shows the electronic connections among the various shuffler components, with the coincidence counter as an optional feature. For a more detailed description of shuffler electronics, see the Application Guide.[1]

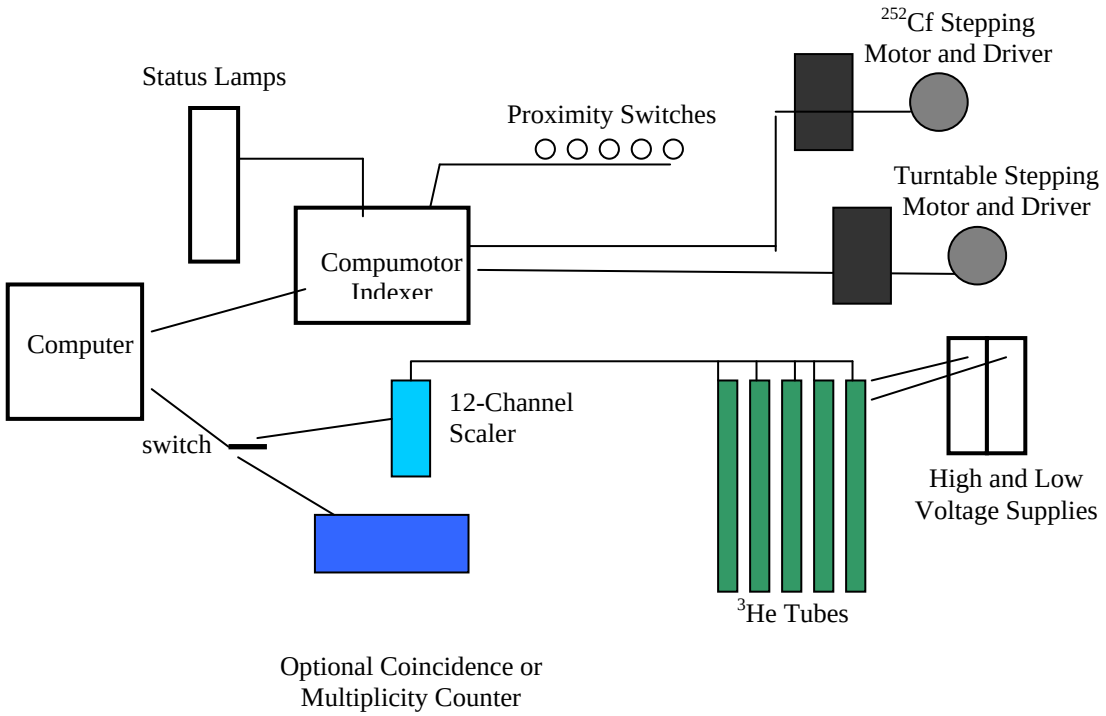

Fig. 16. The electrical connections among shuffler components. A serial data line from the computer normally goes to a 12-channel scaler, but for passive counting it is switched to a coincidence or multiplicity counter.

Shuffler computers have followed the evolution of computers themselves. Various DEC models and the FORTRAN language were used in the 1970s and into the 1980s. Then DOS-based machines and C were used from the late 1980s to the mid-1990s. Currently, the computers use a Windows variant and Visual C++. The basic operations and the results are independent of the platform chosen. The mathematical algorithms in the data analysis have been virtually unchanged throughout.

2. Software

The shuffler computer can run two entirely separate codes: the shuffler code and the INCC code for performing passive assays. Shuffler software is only covered briefly; the Application Guide[1] should be consulted for a more detailed description. Software controls the hardware and analyzes the neutron counts. Users can control software to the extent of setting important parameters and initiating measurement sequences, but the basic actions during a measurement are performed automatically by the computer. The shuffler software has several standard features, including:

- Perform assays, calibration measurements, precision measurements, bias checks, and standard checks.
- Perform safety checks to confirm that all proximity switches and lamps are working properly.
- Review archived results.
- Assign “general” parameters that are common to all measurements.
  - Nuclear constants: half-lives and delayed neutron yields for the six groups of precursor nuclei; the half-life of ^{252}Cf; and the reference date for the ^{252}Cf source.
  - Bias and precision check parameters.

- Assign “item-specific” parameters, one set for each container size and material type to be measured. Each type of item has a unique name given in the general parameters.
- Assay parameters: distances, speeds, accelerations, and pauses used for irradiation; length of the background count; and whether or not to rotate the turntable, and to use the flux monitors.
- Calibration parameters: Each item type has its own calibration parameters with variances and covariances. The standard expression provided is a third-order polynomial, but each item type can have more than one set of parameters for different ^{235}U enrichments.
- Diagnostics: This is a set of “primitive” actions that can be performed to check specific shuffler components (e.g. move source, store source, test door switch, test rotator, etc.)

Regardless of the operating system and programming language, shufflers do fundamentally the same things in the same way. Most importantly, the data analysis code has been stable for more than a decade and the assay results are independent of the computer used.

3. Safety features

The most novel hazards associated with shufflers arise from the ^{252}Cf sources. The masses of these sources have ranged from 1 to 3000 μg, according to the measurement problem. A microgram is a small source, but if unshielded, the dose rate at one meter is 2.5 mrem/hr. The standard 200-liter-drum shuffler may have as much as 550 μg of ^{252}Cf that delivers 1100 mrem/hr at one meter if unshielded. Clearly, the shuffler must be designed to keep the source shielded at all times. A complete list of safety features is found in the Ref. 1.

- If the assay chamber door is not closed and securely latched, the Indexer cannot move the ^{252}Cf source from its store position.
- The amount of shielding needed is specific to the facility. Maximum dose rates on the surface of a shuffler are generally specified by the facility and have been lowered from the early days. The older limits were 5 mrem/hr in contact; more recently, 0.5 mrem/hr has been the standard.
- One way to reduce dose rates without increasing costs is to use a barrier that increases the distance from the shuffler’s surface to people. This may be a few inches or a few feet. For example, if the dose rate on the surface of a storage block 61 cm thick is 0.6 mrem/hr, a barrier of only 5 cm beyond the shuffler’s surface will have a dose of 0.5 mrem/hr on its surface.
- There is never any good reason to “hug” a shuffler during measurements.

B. Physics Design

The physics design defines parameters that will ensure the shuffler meets the performance specifications. It is a paper and computer study that is done before any design drawings are made. The gross features of the design are defined by the physics calculations. Actual shuffler design is treated only briefly here.

1. User Specifications

Ref. 1 provides an extensive list of questions that must be answered by the facility procuring the shuffler.

2. Minimum Delayed Neutron Count Rate

The next step is to calculate the minimum delayed neutron count rate that will meet the performance specifications. The set of specifications can be summarized by a sentence such as "Measure a 500-g sphere of 94% enriched U metal with 1% relative precision in 1000 s." The material has been specified along with the precision and assay time. In this section, only the relative precision and assay time are needed. The material description will be used in the next section.

If there are no background counts, the relative precision of a delayed neutron count D is $1/\sqrt{D}$. For 1% relative precision, D is 10,000 counts. The full 1000 s could be devoted to this count, so the minimum count rate needed is a leisurely 10 counts/s. The ^{252}Cf source needed for this case would be relatively small and will be calculated in a later section.

But having no background counts is not realistic. Cosmic-ray interactions can be reduced by shielding, and the neutrons leaking into the assay chamber from the ^{252}Cf source can be reduced by even more shielding. How much are you willing to pay in cost and space for a reduced background rate? No shuffler has ever taken any special measures to reduce cosmic-ray-induced neutrons, and typical background rates from cosmic rays are 15 cps to nearly zero. Leakage from the ^{252}Cf storage block may add another 15 cps or less. Background rates of 30 cps are not unusual, but they have also been lower. The minimum count rate needed is D_s/T_c, as given in Eq. (4). The relative precision is the ratio of the count uncertainty with the count, as given in Eq. (6).

For the example given above and a background rate of 30 cps, the relative precision is 1% after a 270-s background count and a 240-s delayed neutron count when D is 17,688 counts. This typical background rate has forced us to count about 77% more delayed neutrons to reach the same relative precision. This count (and the corresponding 73.7 cps) is not unusual, and is in fact routine for the shuffler to produce, but the right ^{252}Cf mass must be chosen.

3. The Minimum ^{252}Cf Mass, Detection Efficiency, and Assay Chamber Shape

The remaining shuffler design depends on the mass of the ^{252}Cf that is needed to generate the minimum count rate needed to meet the specifications. What is the smallest mass that provides the desired relative precision in the time allowed? The detection efficiency is also directly involved at this point and the shape of the assay chamber has a role in determining it. But neither of these can be known accurately without a detailed design. An iterative process can be applied. With some experience, only a single pass through the process may be needed.

Pick a plausible detection efficiency for the first iteration. Something close to 20% is common for shufflers with a single layer of comfortably spaced ^{3}He tubes in polyethylene, but as much as 60%, could be achieved with multiple layers of tubes. The energy spectrum for delayed neutrons should be used, not the spectrum for ^{252}Cf or other prompt neutrons.

Pick an approximate size and shape for the assay chamber. If the final shape will snugly fit around the container, a looser fit will lead to a larger answer for the minimum ^{252}Cf mass. If the object does not have axial symmetry, several orientations should be used in calculations to get an average.

Next, calculate the probability that a single neutron from the ^{252}Cf source will induce a fission in the specified material, using the provisional assay chamber. It is difficult to do this accurately without a Monte Carlo simulation because the probability of inducing a fission is a function of neutron energy. The Los Alamos Monte Carlo code MCNP has been successfully used to calculate the fission probabilities for shufflers at Los Alamos and in Europe. A proven code uses continuous analog techniques to track neutron interactions within the shuffler materials, so changes in energy of the neutrons are correctly taken into account.

Assume that a model of the shuffler and a 500-g sphere of uranium have been made and the calculated fission probability is 7.89×10^{-4} fission per ^{252}Cf neutron. This includes fissions caused by fission neutrons as well as ^{252}Cf neutrons. The average number of neutrons released from a fission is known for all the fissile materials of interest to safeguards (for ^{235}U this is about 2.43). The average ^{252}Cf neutron produces 1.92×10^{-3} fission neutrons, but only a small fraction of these neutrons are delayed. In the case of ^{235}U, that fraction is about 1.6%, so the average ^{252}Cf neutron produces 3.07×10^{-5} delayed neutrons. The detection efficiency can be calculated with MCNP for a specified array of ^{3}He tubes. For our example, assume the result is 24%.

Some delayed neutrons are released while the ^{252}Cf irradiation is still in progress. These cannot be distinguished from ^{252}Cf neutrons and do not contribute to the count. The fraction of neutrons that can be counted while the ^{252}Cf source is stored depends on the irradiation scheme. A 20% fraction is a representative value and will be assumed here. This fraction can be calculated from a set of times for the different stages of a shuffle and the number of shuffles.[2]

The average ^{252}Cf neutron has the following probability of leading to a delayed neutron (dn) count:

$$(3.07 \times 10^{-5}\ \text{dn}/^{252}\text{Cf n})(0.24\ \text{reaction/dn})(0.20\text{count/reaction}) = 1.47 \times 10^{-6}\ \text{count/Cf n}.$$

If the ^{252}Cf emits one neutron per second, it will take almost a million seconds (12 days) to get one count. We need 73.7 cps, as calculated in the preceding section. One microgram of ^{252}Cf emits 2.34×10^{6} neutrons/s. So the minimum mass of ^{252}Cf needed to get 1% relative precision in 1000 s can be calculated as follows:

$$(m_{Cf})(2.34 \times 10^{6}\ \text{n/s})(1.47 \times 10^{-6}\ \text{count/Cf n}) = 73.7\ \text{counts/s},$$
$$m_{Cf} = 21.4\ \mu\text{g}.$$

4. The Initial ^{252}Cf Mass

If you fabricate a shuffler and put in the minimum ^{252}Cf mass, it will meet the specifications today, but not next year. In 147 days the neutron yield from the californium will be 90% of the original yield. In 2.65 years the yield is cut in half. The initial ^{252}Cf mass must allow for the time span during which the specifications are to be met. If our uranium sphere example specifies a useful life of 6 years, then the mass after 6 years of decay will be 21.4 μg and the initial mass at time zero is 103 μg.

5. ^{252}Cf Shielding

Once a mass of ^{252}Cf is chosen, the overall dimensions of the new shuffler can be calculated. The storage block has one set of dimensions and the assay chamber has another. The assay

chamber must be large enough to hold the objects to be measured and have wall thickness to shield personnel from the ^{252}Cf radiations.

One microgram of ^{252}Cf produces a dose rate of 2.45 mrem/hr at one meter, if unshielded. Our 150-μg example would produce 368 mrem/hr at one meter, a rate that must be reduced to the facility's acceptable value with shielding. Assume that the facility wants no more than 0.5 mrem/hr in contact with the shuffler. Two decisions must be made: What material or materials will constitute the shields, and what are their thicknesses? The answers are different for the storage block and the assay chamber.[10]

a. Storage Block

For the 150 μg of ^{252}Cf example, what is the overall size of the shield that will give only 0.5 mrem/hr on contact? Our measured shielding data shows that we will have 0.5 mrem/hr on the surface of a 1.2-m-wide shield if the ^{252}Cf mass is 43 μg. In other words, 150 μg behind 61 cm of shielding will have a contact dose rate of 1.7 mrem/hr, not 0.5 mrem/hr. It is not clear how much larger the shield would have to be to meet the specifications because our data stops at a thickness of 66 cm. and the neutron dose rate has begun to flatten out with thickness.

b. Assay Chamber Walls

A storage block that has a width of 1.2 m means that the source positioned in the block's center is surrounded by 0.6 m of shielding. The simplest approach to the thickness of the walls of the assay chamber might seem to be to use 0.6 m. of the same shielding. But the detector tubes need to be in embedded in polyethylene that doesn't contain boron, and this polyethylene should extend behind the tubes for several inches. Furthermore, the storage block's small core of heavy metal is rarely used in the assay chamber, with the rare exception of taking shielding credit for the metals used in spectrum tailoring.

The inner geometry of the assay chamber is fixed independently of the shielding. Figure 17 shows a cross section of the standard 200-liter-drum shuffler that uses as much as 550 μg of ^{252}Cf. The assay chamber is hexagonal to approximate the circular shape of the drum. The guide tube for the ^{252}Cf source runs along a block of iron. It acts as a reflector to send 25% more neutrons toward the drum and does no important spectrum tailoring.

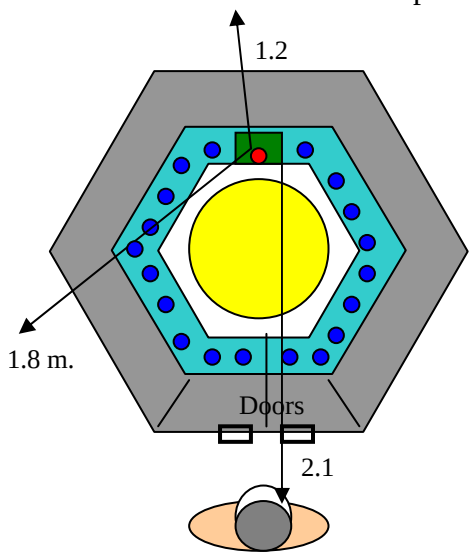

Fig. 17. A horizontal cross section of the standard shuffler for 200-liter drums is shown with an operator positioned in front of the doors. A drum is surrounded by detector tubes embedded in polyethylene, which is wrapped with an outer layer of borated polyethylene and 1.2 cm. of lead to form the shielding. Distances to the ^{252}Cf source and the amounts of shielding in the different directions are shown.

Detector tubes are embedded in polyethylene and surround the drum; there are more above and below the drum. The shielding beyond the detector region is composed of alternating layers of polyethylene and borated polyethylene, however, it is only about 36 cm thick.

6. Assay Chamber

The design of the assay chamber gets to the heart of a shuffler. The rest of the instrument supports the action within the assay chamber. The assay chamber generally has the first four components in the following list and may have any of the others.

- An empty chamber to receive the object to be measured.
- One or more doors that provide access to the chamber.
- Neutron detector tubes and amplifiers surrounding the chamber.
- A guide tube for the ^{252}Cf source and its flexible cable.
- An optional thin layer of cadmium around the inside wall of the chamber.
- An optional metallic reflector behind the source to send more ^{252}Cf neutrons toward the object.
- An optional spectrum tailoring set of materials.
- An optional turntable to rotate the object during the measurement.

7. Detector Tube Arrays

Detector tubes are usually embedded in banks of rectangular or semicircular pieces of polyethylene. A cross section of a rectangular bank is shown in Figure 18. Holes are drilled into the polyethylene at the tube position. A semicircular bank would have the same parameters.

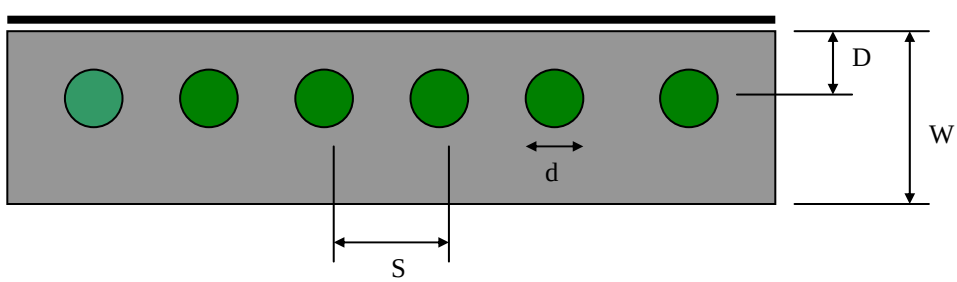

Fig. 18. A detector bank consists of ^{3}He tubes embedded in polyethylene. The heavy line at the top is an optional layer of cadmium and stainless steel lining the assay chamber. The assay chamber is located above the cadmium and steel liner. The important geometric parameters are indicated.

The width, *W*, of the bank is often 10 cm. because it works well and is a standard size for polyethylene. The tube diameter, *d*, is typically 2.5 cm, so the holes for the tubes are drilled slightly larger (e.g., 2.7 cm). The depth, *D*, between the tubes' centers and the side of the bank facing the fissile material affects the detection efficiency as a function of neutron energy, and the spacing, *S*, between tubes affects the detection efficiency for a given depth. For delayed neutrons, the depth, *D*, is smaller than the depth used in passive neutron counters for spontaneous fission neutrons. A general-purpose depth for shufflers is 3.8 cm. A spacing, *S*, less than 5 cm is counterproductive because a tube absorbs low-energy neutrons from its immediate vicinity and the tubes compete for these neutrons when they are too close together. They can be spaced as far

apart as desired if the detection efficiency needed is still met. Monte Carlo calculations are useful in designing the array of tubes needed to meet the shuffler's specifications

8. ^{252}Cf Motion Requirements

Delayed neutrons are produced during the irradiation, but cannot be counted against the background from the ^{252}Cf source. During the irradiation, their emission rate grows because many precursors have lifetimes longer than the irradiation time. When the irradiation ends, the emission rate of delayed neutrons begins to diminish rapidly. After an 11-s irradiation of ^{235}U, most of the delayed neutrons are released in the next 20 s. Obviously, you will count a larger fraction of these delayed neutrons if the ^{252}Cf source is removed quickly. This defines the most important feature of whatever is to move the source within the shuffler. It is less crucial to move the source into the irradiation position quickly, but a rapid motion here makes the mathematical expressions of a shuffler actions more accurate.

How quickly should the source move from the assay chamber back to the storage block? Some early Los Alamos shufflers used stepping motors tuned to run as fast as possible, and these sources moved about 1.5 m in about 0.33 s. But the tuning process was time-consuming and unique for a given set of equipment, and aging effects would require periodic retuning. It was decided to give up 10% of the delayed neutrons and use a slower, but very reliable, stepping (or servo) motor system from Compumotor that needs no maintenance. A move of 1.5 m is now generally done in about 0.75 s. To make up for the 10% drop in counts, the mass of the ^{252}Cf source can be increased by 10% or the assay time can be increased by about 10%. This sacrifice is well worth the elimination of the maintenance problems.

IV. CALIBRATION PROCEDURES

The shuffler measures a count rate of delayed neutrons and we must know how to convert that to fissile mass (^{235}U, ^{239}Pu, etc.). We can tell the shuffler's computer how to do the mathematics for us, but we have to figure it out ourselves first.

The best way to determine the calibration is to measure physical standards in the shuffler that accurately represent the items to be measured. The standards ideally match the items to be measured in all relevant respects (materials, size, shape, density, mass, isotopics, packaging, moisture content, and matrices). Standards usually have to be certified, meaning that the procedure used to fabricate the standards is accepted by regulatory agencies and a paper trail follows the standard to show how the procedure was followed. Sometimes such ideal standards exist, sometimes they can be made, but many times they do not exist and never will be made because of variations among the items.

A. Matrix Issues

The matrix is all the material in the item except the fissile material you want to measure. If you want to measure ^{235}U, then the oxygen in U_3O_8 is part of the matrix. Even the ^{238}U and other uranium isotopes are matrix material. The moisture and any other contaminants mixed with the U_3O_8 are matrix materials, as is even the container that holds the U_3O_8. If the can is inside a drum with fiberboard spacers, add the spacers to the matrix.

Some matrix materials are benign, but others affect the measured count rate in important ways. Anything with hydrogen can be important because neutrons lose much of their energy

when they scatter off hydrogen (think of the collision of two billiard balls). As hydrogen-bearing matrix is added near the fissile material, the count rate first goes up because the lower-energy neutrons induce more fissions. However, as more hydrogen is added, the count rate can go down as neutron captures in hydrogen compete with fissions. The impact varies with the position of the fissile material with respect to the hydrogenous matrix, making the count rate vary with position.[4]

A matrix of iron is much more benign because neutrons scatter without losing much energy (think of a ping-pong ball bouncing off a bowling ball). With 211 kg of iron in a 200-liter drum, the count rate was reduced by 4.5% compared with an empty drum,[4] a small but non-negligible fraction.

Techniques have been developed to mitigate the effect of hydrogen in 200-liter drums where the effects can be large simply because there is more room for matrix material than in small cans. The original technique used flux monitors built into the assay chamber. These were low-efficiency ^{3}He tubes whose outputs were counted during the irradiation. They counted a small fraction of the neutrons that came directly from the ^{252}Cf source, a larger fraction of neutrons that scattered off the moderating walls, and another large fraction of neutrons that entered the drum and returned with reduced energies. It is these last neutrons that we really want to count; the others are unavoidable background. One of the flux monitors was wrapped in cadmium to absorb low-energy neutrons, making it rather insensitive to the matrix in a drum. The other monitor rate changed significantly with the amount of hydrogen. The ratio of the flux monitors is independent of the ^{252}Cf source strength and can be used to correct for hydrogen.[4]

A hardware solution is to envelop the drum with about 1.9 cm of polyethylene. A sleeve made from a septic tank liner fits around a 200-liter drum very nicely; adding a top and bottom completes the envelopment. The result is a huge reduction in an otherwise large variation in count rate with the position of the fissile material. This happens because the first one or two collisions happen in the external polyethylene, reducing the range of energies of the neutrons entering the drum. The matrix effect is greatly reduced by the sleeve.[4] The calibration no longer has to deal with count rates changing with position.

However, a polyethylene sleeve increases the self-shielding problem because the neutron energies are lower. If the drum contains waste with small particle sizes, this is not an important issue. But if large pieces are present, the assay will be biased low by self-shielding.

If the positions of the uranium in a drum can be determined, a correction factor can be applied to each piece of uranium. This technique, developed for the standard 200-liter drum, does not require any extensive modification to the hardware. A stepping motor must be used for the turntable instead of an analog motor, but this is easy. The Compumotor Indexer Model 4000 can drive four motors, so even this module needs no change. The software needs extensive modification because the data collection and analysis is quite different from the conventional assay.

Six detector banks around the sides of a 200-liter drum, plus banks above and below the drum, are used to give a low-resolution (≈10 cm) “picture” of the distribution of fissile material within the drum. The drum does not rotate during a set of shuffles. The count in a bank depends on the relative positions of the ^{252}Cf source and the fissile material to that bank. To get enough information to locate the material, the drum is rotated 60° and another set of shuffles is done. This is continued for a full revolution of the drum. The mathematical algorithm is then applied to calculate the amount of fissile material in each of the 39 cells of equal volume within the drum. This algorithm uses calibration data from measurements on a standard placed sequentially in

each of the 39 (or so) cells. It is not necessary that the matrix be homogenous, as is usual with the conventional shuffler measurement, only that it is known and the calibration drum accurately reflects the distribution. The count time is approximately doubled with this technique, but this only means going from 15 min to 30 min.

For many matrices, there is no need to make a matrix correction. Cans of high-fired oxide have a rather benign and constant matrix (oxygen, steel walls) and what minor effects arise are automatically included in the calibration. Uranium carbide has an important matrix component, but it, too, is present in fixed relations with the uranium and can be included in the calibration as long as the geometric form is fixed. Each measurement should be analyzed for matrix effects and the most appropriate way to handle matrix problems.

B. Calculated Calibrations

What about materials that do not have calibration standards? The creation of new, certified standards is expensive and time consuming—a set of six U_3O_8 standards with 0.5 to 4.0 kg of uranium from the National Institute of Standards and Technology cost $100,000 in 1999. If the items of interest are unique, it makes little sense to create a standard and double the inventory. However, the calibration with U_3O_8 standards cannot be applied reasonably to U metal, UC_2, ^{233}U, ^{239}Pu, etc., because there will be large biases (Figure 13).

Can one calculate shuffler count rates and bypass the lack of physical standards? The topic is controversial, but it can be demonstrated to be very accurate. What is needed is not just an approximate calculation, but results that are as accurate as measured calibration data. This requires great attention to detail and as much benchmarking as possible. The close agreement between calculated and measured results is demonstrated in Figures 14 and 15. At the time of this writing, a methodology for accepting calculated calibrations for shufflers has been established at LANL.

A computational procedure for the standard 200-liter-drum shuffler has been developed[3] and can be readily applied to any other shuffler. For this large assay chamber, the ^{252}Cf source usually scans even a small can of oxide; scanning is not always necessary, but it is usually done. This means that the neutron flux entering the fissile material varies with time, greatly complicating the calculation. The situation would be much simpler if the source were stationary, so if the 200-liter-drum shuffler with a scanning source can be accurately described, the process will work for other shufflers.

Here are the steps in the procedure to calculate absolute shuffler count (MCNP stands for Monte Carlo Neutron and Photon code):

- Create an accurate MCNP model of the shuffler, including the fissile material and container.
- For each fissile mass, use MCNP to calculate the fission probabilities at representative positions of the ^{252}Cf source. For a 75-cm scan distance, a calculation at every 5 cm is adequate.
- Perform a separate MCNP calculation for the detection efficiency of delayed neutrons.
- Use the fission probabilities to calculate the six-group precursor populations at the end of the first irradiation. These are the numerical solutions of six differential equations.
- Calculate the count of delayed neutrons after the prescribed number of shuffles.
- Get the count rate by dividing the count by the sum of the individual count times.

- Use the set of masses and count rates to form the calibration curve.

This plan works and results in a reliable, accurate calibration curve. Ref. 3 provides details of the procedure and a comparison with measurements on uranium metal and oxides. A recently added delayed neutron patch in MCNPX simplifies the above process but both techniques work. Figure 14 shows measured and calculated rates for U_3O_8 calibration standards; there is no significant difference between the sets of calculated and the measured count rates. Similarly accurate calculations have been done for metals of uranium, plutonium, and their combination.

C. Enrichment Issues

The shuffler is used to measure the mass of ^{235}U, but ^{238}U is inevitably also present, and because it fissions, it adds to the delayed neutron count rate. If the enrichment is constant, the calibration curve automatically includes the effect and gives accurate ^{235}U masses (this is the case in Figure 14 with 92.4% enrichment).

If the enrichment is variable, two techniques have been applied to avoid biased results. The first is spectrum tailoring, which involves surrounding the ^{252}Cf source with a selection of metals to reduce the neutron energies below 1 MeV. This avoids fissioning the ^{238}U except by high-energy neutrons from fissions of ^{235}U; this effect is generally negligible. The Savannah River Uranium Scrap shuffler used spectrum tailoring successfully to avoid the enrichment problem.

Spectrum tailoring is not always practical. The flux of neutrons into the fissile material is reduced by the spectrum-tailoring materials, but a larger mass of ^{252}Cf can almost always be used to compensate. If the source scans a 200-liter drum, the spectrum-tailoring metal would have to extend over the full distance (75 cm), increasing the weight and cost accordingly. If a 550-μg source is normally used, the tailored source might need a mass of 1000 μg or more. The size of the shuffler would grow at least another 30 cm in all dimensions because of the additional shielding required.

The second technique is software based. If standards exist with different enrichments, the shuffler software can interpolate among calibration curves for different enrichments. The best approach to the enrichment issue at a particular facility needs to be decided early in the physics design phase by considering the measurement specifications, facility installation requirements, and the practicalities of shuffler designs.

V. DATA ANALYSIS

The assay chamber is the heart of the hardware and the data analysis is the heart of the software. Everything about a measurement comes together in the data analysis.

A. Raw Count Rates

Background counts are taken at the start of a measurement and delayed-neutron counts are taken after each irradiation. These are the “raw” counts that are converted into “raw” count rates using the measured times.

1. Background Counts

Before a background count is taken, the software ensures that the ^{252}Cf source is in the store position. Leakage of ^{252}Cf neutrons into the assay chamber increases rapidly as the source approaches the assay chamber, so it is important to put the source in a standard position where it contributes only a few counts a second. About a fourth of the assay time is spent on the background count. If the background is dramatically higher or lower than usual, the background count time should be changed to optimize the precision of the assay result.

2. Flux Monitor Counts

Flux monitors produce counts during the irradiations even if they are not used in the data analysis.

3. Post-irradiation Counts

These counts are from both background and delayed neutrons. None of these counts are corrected for dead-time losses because the rates are always low (e.g. under 10,000 cps).

B. Background Subtraction

The delayed neutron count rate is extracted from the post-irradiation count rate by subtracting the background count rate. The background rate for the inefficient flux monitors is always negligible compared to their very high count rates.

C. ^{252}Cf Decay Correction

The ^{252}Cf decays continuously and if this is not taken into account, measurements on the same item would be smaller each day. This is easily avoided by adjusting the delayed neutron count rate for the decay after some convenient reference date. The best value we have for the decay constant is 7.172×10^{-4} d^{-1}. A year after the reference date, the delayed neutron count rate is multiplied by 1.2995 to adjust for decay; after 5 years, the multiplier is 3.7062. The half-life of ^{252}Cf is known well enough to make this correction accurate for the useful life of the source.

No adjustment is included for ^{250}Cf neutrons because sources are not used more than 10 years and the number of ^{250}Cf neutrons is negligible compared with neutrons from ^{252}Cf, even after 20 years of decay (Figure 11).

D. Flux Monitor Matrix Correction

If hydrogenous matrices are involved in assays, the flux monitors might be used to correct for different amounts of hydrogen. The ratio of the flux monitor counts is a measure of hydrogen content, but the exact relationship depends on the nature of your materials and the shuffler design. A series of measurements on standard containers must be done to reveal the relationship and then built into the shuffler software.

Flux monitors are not needed if the matrices are not hydrogenous, if calibrations have been done for amounts of hydrogen that will be encountered, or if the position-correction style of assay is used.

E. Calibration Curve

The object of an assay is finally achieved when the corrected count rate *r* is used to calculate a mass of the fissile material *m* using a calibration curve. The only curve commonly used is a third-order polynomial with *r* expressed as a function *m* (as preferred by statisticians):

$$r = a_0 + a_1 m + a_2 m^2 + a_3 m^3.$$

Waste materials are likely to have only a_0 and a_1 nonzero. Measurements of oxides and metals up to 8 kg have been very well described by this polynomial. The four coefficients are determined from measurements on physical standards or from carefully calculated absolute count rates. They have a set of variances and covariances that can be specified and used to help calculate the uncertainty in a mass.

Figure 14 shows a calibration for U_3O_8 standards up to 8 kg. Self-shielding is evident for the first 750 g and then the curve becomes linear. The standards with masses of 3600 g or less are certified accurate; the higher masses are less certain.

The statistical uncertainties in the various counts are calculated and combined with the calibration variances and covariances to generate a total uncertainty (1σ) in the measured mass. In practice, the variances and covariances usually dominate the uncertainty[11], so careful and extensive measurements of calibration standards can have beneficial effects on the quality of future measurements.

F. Measurement Control

DOE regulations require a measurement control plan for an assay instrument. Periodic measurements on standards must be performed to check that the instrument is working properly. Each facility determines an appropriate plan, so only the basics are discussed here.

The standards chosen for measurement control checks might be calibration standards, but need not be. If oxide powders are chosen, the density of a powder is likely to change with handling and even without handling (thanks to gravity's relentless effort). Take measurements after shaking the can to loosen the powder and after tapping the can on a table top to settle the powder; the results may vary by 7% or more simply from a change of density that affects self-shielding. Using a powder for measurement control (or calibration) should include a handling procedure to ensure about the same density for all measurements. With this understood, powders have been used very successfully for measurement control purposes.

REFERENCES

1. P. M. Rinard, "Application Guide to Shufflers," Los Alamos National Laboratory report LA-13819-MS, September 2001.

2. P. M. Rinard, "Shuffler Instruments for the Nondestructive Assay of Fissile Materials," Los Alamos National Laboratory report LA-12105, May 1991.

3. P. M. Rinard, "Calculating Shuffler Count Rates," Los Alamos National Laboratory report LA-13815-MS, June 2001.

4. P. M. Rinard, E. L. Adams, H. O. Menlove, and J. K. Sprinkle, Jr., "The Nondestructive Assay of 200-liter Drums Containing Uranium and Transuranic Waste Using Passive-Active Shufflers," Los Alamos National Laboratory report LA-12446-MS, November 1992.

5. G. R. Keepin, *Physics of Nuclear Kinetics* (Addison-Wesley Publishing Co., Inc., Reading, Massachusetts, 1965), Chapter 4.

6. G. R. Keepin and R. B. Walton, "Nuclear Safeguards Applications of ^{252}Cf," in *Californium-252: Proceedings of a Symposium* (U. S. Atomic Energy Commission, Division of Technical Information, 1969).

7. F. H. Cverna, G. W. Eccleston, E. P. Elkins, and T. Van Lyssel, "Test Results for the FAST Facility Delayed Neutron Interrogator Source Transfer System," Los Alamos National Laboratory report LA-8684-MS, January 1981.

8. P. M. Rinard, "Implementing a Technique to Improve the Accuracy of Shuffler Assays of Waste Drums," Institute of Nuclear Materials Management, 37th Annual Meeting, Naples, Florida, July 1996, pp. 1282–1288.

9. P. M. Rinard, "Measuring the Fill Height of Sealed Cans with a Compound Pendulum," Los Alamos National Laboratory report LA-12964-MS, June 1995.

10. P. M. Rinard, C. Passard, and G. Bignan, "Comparison of Shuffler Data Analysis Techniques," Los Alamos National Laboratory report LA-12468-MS, December 1992.

11. H. E. Hootman, "Estimation of ^{252}Cf Shielding Requirements," Savannah River Laboratory report DP-1232, April 1970.

10. PRINCIPLES AND APPLICATIONS OF CALORIMETRIC ASSAY

D. S. Bracken, and C. R. Rudy

I. Introduction

Calorimetry is the quantitative measurement of heat. Applications of calorimetry include measurements of the specific heats of elements and compounds, phase-change enthalpies, and the rate of heat generation from radionuclides. The most successful radiometric calorimeter designs fit the general category of heat-flow calorimeters. Calorimetry is used as a nondestructive assay (NDA) technique for determining the power output of heat-producing nuclear materials. The heat is generated by the decay of radioactive isotopes within the item. Because the heat-measurement result is completely independent of material and matrix type, it can be used on any material form or item matrix. Heat-flow calorimeters have been used to measure thermal powers from 0.5 mW (0.2 g low-burnup plutonium equivalent) to 1,000 W for items ranging in size from less than 2.54 cm to 60 cm in diameter and up to 100 cm in length.

Calorimetric assay is the determination of the mass of radioactive material through the combined measurement of its thermal power by calorimetry and its isotopic composition by gamma-ray spectroscopy or mass spectroscopy. Calorimetric assay has been routinely used at U.S. and European facilities for plutonium process measurements and nuclear material accountability for the last 40 years [EI54, GU64, GU70, ANN15.22, AS1458, MA82, IAEA87]. Calorimetric assay is routinely used as a reliable NDA technique for the quantification of plutonium and tritium content. Calorimetric assay of tritium and plutonium-bearing items routinely obtains the highest precision and accuracy of all NDA techniques. Plutonium items usually contain varying amounts of ^{241}Am, which can be accounted for during the assay.

Uniqueness of Calorimetry NDA

Advantages

Calorimetric assay offers several distinct advantages over other NDA techniques and chemical analysis as follows:

- The calorimeter heat measurement is completely independent of material and matrix type; self attenuation cannot occur.
- No physical standards are required.
- The thermal power measurement is traceable to the U.S. or other National Measurement Systems through electrical standards used to directly calibrate the calorimeters or to calibrate secondary ^{238}Pu heat standards.
- Calorimetric assay can been used to prepare secondary standards for neutron and gamma-ray assay systems [IAEA87, AS1207, HY99, LE00].
- The heat from the entire item is measured, and the response of a well-designed calorimeter is independent of the source location inside the measurement chamber.
- P_{eff} remains the same (with correction for nuclear decay) as long as the isotopic composition is not changed; therefore, the same P_{eff} is applicable to a batch of material regardless of form.
- Calorimetry is very precise and nearly bias free. Biases can be quantitatively determined during instrument calibration.
- Only nuclear criticality safety considerations and the volume of the measurement chamber limit the quantity of material that can be measured in a calorimeter.
- Calorimetric assay is the most accurate method, NDA or otherwise, for the measurement of tritium and ^{241}Am.

- Calorimetry is the only practical measurement technique available for many physical forms of tritium compounds.

Limitations

Calorimetric assay is largely independent of the distribution of the nuclear materials in the matrix, but the accuracy can be degraded for materials with inhomogeneous isotopic composition because of uncertainty in determining the effective specific power. Calorimetry measurement times are typically longer than other NDA techniques. The packaging cannot change the heat output of the material but it is usually the determining factor for measurement time. Typical assay times are between one and eight hours. The calorimeter cannot distinguish between heat produced by radioactive decay and heat produced by other sources (e.g., phase changes and chemical reactions).

Heat from chemical reactions is generally not an issue because most items measured with calorimetric assay are hermetically sealed dry items. In addition, any large time dependence on the heat output would be an indication of heat from a chemical reaction.

Thermal Power Production from Radionuclides

The principal decay modes, specific heats, half-lives, and the associated uncertainties are listed in Table 1 for all plutonium isotopes, ^{241}Am, and tritium. Included in Table 1 are the specific power and half lives for uranium isotopes. The majority of the heat measured by calorimetry is due to spontaneous alpha-particle emission, except for ^{241}Pu and tritium, which predominately decay through beta decay. Each radionuclide has a disintegration energy associated with its particular decay scheme; for example, ^{240}Pu decays to ^{236}U with the emission of an alpha particle and the release of 5.15 MeV. The total reaction energy for alpha decay is the sum of the alpha-particle kinetic energy and the recoil energy of the daughter nucleus. The alpha particle and daughter nucleus have very short ranges in matter. Thus, virtually all of the energy released by alpha decay will remain within the item as heat. If the daughter product is not in the ground state after decay, an additional small amount of energy is released in the form of gamma-ray and internal conversion electron energy. The electron and low-energy gamma-ray energy is absorbed in the item. The rate of energy emission is equal to the product of the total decay energy and the activity. This product for a single radionuclide is called specific power, P, and is used to convert the power measurement into a mass of material. For multi-isotopic items, the analytical factor used to convert the heat measurement to mass of material is effective specific power, P_{eff}. The determination of P and P_{eff} will be discussed in later sections.

The determination of energy losses in matter is more complicated for beta emitters than with alpha emitters. With beta decay, the total reaction energy is in the form of a beta particle, neutrino, and the excitation and recoil energy of the daughter. The energy loss due to bremsstrahlung radiation, emitted as a result of deceleration of the beta particle, is negligible for ^{241}Pu and tritium; therefore, nearly all of the kinetic energy of the beta particle is absorbed by the item as heat. The neutrino is not absorbed in the item, therefore its energy is lost. The thermal power measured by a calorimeter from beta-decaying radionuclides is the product of the activity and the average beta-particle energy, which is on average one third of the maximum disintegration energy.

All of the uranium and plutonium isotopes listed in Table 1 have very small spontaneous fission branching rations. When fission does occur, the fission daughter products will deposit all of their kinetic energy within the item. After fission, the daughter products can initially be in an excited energy state; this small amount of energy is released in the form of gamma rays and internal conversion electrons. The low-energy electromagnetic emissions will be highly attenuated in the item, container, and walls of the calorimeter depositing their energy with a resultant rise in the temperature of the calorimeter measurement well. The higher energy gamma-ray emissions can escape the calorimeter with minimal attenuation; thus, their energy is not measured. Another product of fission is neutrons. Because neutrons are very penetrating, a portion of the neutrons will escape the calorimeter without depositing their kinetic energy. The resultant total heat and heat loss because of fission is extremely small (<<1%) compared to the total heat release of the items measured. Quantitative details can be found in reference [BR02].

Table 1. Nuclear Parameters of Commonly Assayed Nuclides

Isotope	Dominant Decay Mode[1]	Specific Power (mW/g)	% Std. Dev.	$T^{1/2}$ (y)	% Std. Dev.	References
^{238}Pu	α	567.57	0.05	87.74	0.05	WA77,ST78
^{239}Pu	α	1.9288	0.02	24119	0.11	ST78,SE78,GU78
^{240}Pu	α	7.0824	0.03	6564	0.17	RU84,LU84,BE84,ST84,JA78,ST84
^{241}Pu	β	3.412	0.06	14.348	0.15	MA80,GA80,DE81,JO82,OE68
^{242}Pu	α	0.1159	0.22	376300	0.24	OS76
^{241}Am	α	114.2	0.37	433.6	0.32	JO82,OE67
Tritium	β	324	0.14	12.3232	0.017	RU77
^{233}U	α	2.81E-1	-	1.591E5	-	Calculation
^{234}U	α	1.80E-1	-	2.44E5	-	Calculation
^{235}U	α	6.00E-5	-	7.038E8	-	Calculation
^{236}U	α	1.75E-3	-	2.342E7	-	Calculation
^{238}U	α	8.51E-6	-	4.468E9	-	Calculation

[1]For all of the nuclides listed, the dominant decay mode has a branching ratio >99.99%.

A source of heat loss to consider is the loss of neutrons following (α, n) reactions. The lost neutron energy can be shown to be negligible, even for high-efficiency radioisotope neutron generators. For example, the neutron yield for ^{9}Be(α, n) per 10^{6} ^{241}Am alpha particles is 70. Assuming that all the neutrons escape capture and using the fact that the average neutron energy is comparable to the Q-value of the original alpha decay, the fraction of lost heat would be 0.007%.

II. Heat-Flow Calorimeter Operation, Calibration, and Calculations

All calorimeters have four elements in common: (1) sample chamber, (2) well defined thermal resistance, (3) temperature sensor, and (4) an environment; these components are presented in a simple schematic in Figure 1. The interrelationship of these four components and the hardware that is used for each determine the type of calorimeter.

Radioactive material with a long half-life continuously produces heat at nearly a constant rate. There is some change due to decay and in growth of daughter products, but the time scale for a measurable change is generally weeks to months. Therefore, the most appropriate calorimeter design for radioactive material is an isothermally jacketed heat-flow calorimeter. The design of the calorimeter is determined by the size and heat output of the items to be measured and the required accuracy.

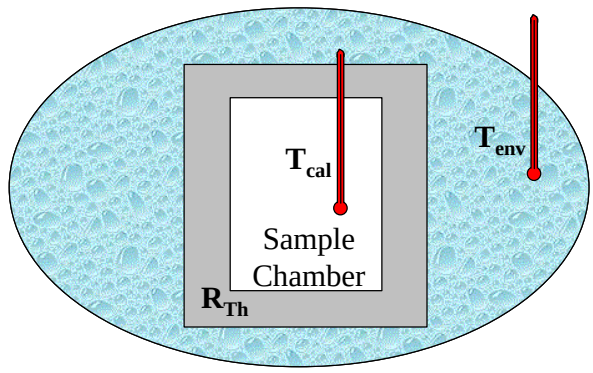

Figure 1. Schematic of the minimum components necessary to perform a heat measurement.

Heat-Flow Calorimeters

A heat-flow calorimeter consists of a sample chamber insulated from a constant temperature environment by thermal resistance and a means to measure the temperature difference across the thermal gradient produced by the thermal resistance and thus the heat generated by an item in the sample chamber. When an item is placed in the calorimeter, the temperature gradient across the thermal resistance is disturbed, and the gradient changes with time until it converges to a constant value and equilibrium is achieved. The heat produced in the sample chamber raises its temperature and causes heat to flow across the thermal resistance into the environment according to

$$\frac{dQ}{dt} = \frac{(T_{cal} - T_{env})}{R_{Th}} = \frac{\Delta T}{R_{Th}} \quad , \qquad (1)$$

where Q is the heat energy, R_{Th} is the thermal resistance, T_{cal} is the internal calorimeter temperature, and T_{env} is the external environment temperature. At equilibrium, dQ/dt is constant and ΔT, usually measured in volts, is proportional to the power of the item. The magnitude of the shift in the measured voltage (passive mode) or supplied power (servo mode) is used to determine the thermal power of the item in the calorimeter.

The curve describing the approach of the temperature difference to equilibrium is a function of several exponentials with different time constants. The time constants are related to the specific heats and thermal conductivities of the item matrix material, packaging, and, in some instances, the calorimeter. An example of a typical calorimeter approach to equilibrium is presented in Figure 2. Equilibrium may be detected by visual inspection of the measurement data vs time or through statistical tests [SM03, BU01] performed on a set of the latest data points in the time series. Statistical prediction algorithms [PE88,FE79, MA87, WE97, SM00, SM01] may be used earlier during transient temperature conditions to predict equilibrium and reduce measurement time. These typically consist of exponential functions that are used to fit the measurement data. The fitted parameters are then used to predict the final equilibrium power. The temperature of the item to be measured may be adjusted using preconditioning baths to shorten the time required to reach equilibrium.

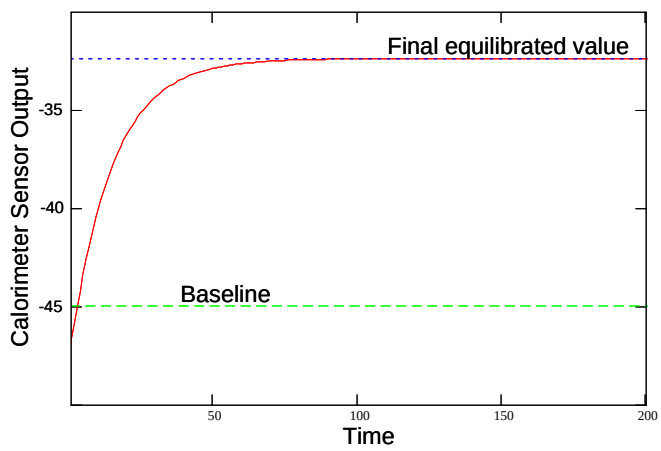

Figure 2. Typical calorimeter sensor output after item insertion.

The type and placement of the temperature sensors, the heat-flow path, and the type of heatsink are what differentiates between types of heat-flow calorimeters used for measuring radionuclides. The heat flow is directed to areas where the sensors are located by the use of conductive and insulating material or controlling temperatures.

The simplicity of a calorimeter measurement would allow a user to manually collect the necessary data to determine the item power by visually taking the sensor readings from the display of a digital multimeter. The results could be calculated by hand following the procedures described later in this Section. In practice it is much better to have a data-acquisition system display results and measurement diagnostics in real time. The data-acquisition system should also calculate results and store data. These software features ultimately increase facility productivity by automatically doing tasks that the operator would need to do manually. The calorimeter data acquisition, control, and analysis software package should be user-friendly, stable, and reliable. Software should store individual meter readings, provide graphical real-time display, reliably detect equilibrium, and provide a means of predicting equilibrium values. Ideally, the software should also be able to control multiple calorimeters with one computer, be easily configurable, and provide assay results in watts [SM00, SM01, BI00].

Calorimetric Assay Overview

The first step in a calorimeter measurement is to determine the zero power sensor output of the calorimeter. This measurement is designated a baseline, BP_0, for passive calorimeters and basepower, W_0, for servo-controlled calorimeters. Heat-flow calorimeters are typically operated in one of two modes, passive or servo controlled. Servo-controlled mode is also known as power-replacement mode or active mode. These two modes of operation will be discussed in detail latter. The baseline/basepower measurement does not need to be done before every item measurement if the calorimeter is stable with time. The frequency of baseline/basepower measurements is normally determined by facility quality-control statisticians and is based on the observed sensor drift of the calorimeter. All baseline/basepower measurements are performed with no heat-producing material in the measurement chamber of the calorimeter. In some instances, the void space of the measurement well is filled with a low heat capacity thermal conductor to decrease measurement time. The operation of many radiometric calorimeters requires the item to be placed in a "calorimeter can" before being placed in the measurement well of the calorimeter. The "calorimeter can" is an inner liner with a high tolerance fit that prevents accidental contamination of the inside of the calorimeter and can reduce measurement time, if the item is loaded properly into the "calorimeter can," because of good thermal contact with the calorimeter.

The calorimeter must be fully closed before any measurement is initiated. This may include the insertion of insulating plugs into the calorimeter or the movement of the body of the calorimeter into a closed position. No items, such as wires, should transverse the measurement well of the calorimeter to the outside room. A significant source of calorimeter noise is room temperature fluctuations influencing the sensors [SA04].

After the baseline/basepower measurement is completed, the calorimeter is opened and the item to be measured is placed in roughly the volumetric center of the calorimeter measurement well. The void space in the calorimeter or "calorimeter can" should be filled with a conductive material to prevent the possible loss of measurement precision, increasing bias, and/or increased measurement time. An item assay is initiated with the operating software. When thermal equilibrium has been established or predicted, the software should automatically terminate the calorimeter measurement. An additional baseline/basepower run may be taken after the item measurement if indicated by facility baseline/basepower requirements.

Calibration of a calorimeter is necessary to determine the power of an unknown item from the observed calorimeter output. Two types of heat standards are commonly used to calibrate calorimeters. The most reliable type of heat standard used in U.S. facilities is a radioactive source of known power whose calibration is traceable to the National Institute of Standards and Technology (NIST). These standards are normally made from ^{238}Pu oxide that is well characterized both chemically and physically. Plutonium-238 heat standards are used for calibrations more frequently than electrical-resistance heaters. Electrical heat standards contain an electrical circuit consisting of standard resistors and standard voltage cells. Such standards are traceable to the NIST or other national measurement systems. The resistor is used in place of a radioactive source, and the power dissipated in an electrical heater is measured using calibrated meters and calibrated resistors. The specifics of the calorimeter calibration depend on whether the calorimeter is operated in the servo or passive mode. During all calibration measurements, the calorimeter should be operated in the same manner used to make assay measurements.

The magnitude of heat-distribution error and convection noise should be quantified during initial calibration if the calorimeter will be operated under nonideal conditions.

Mass Calculation

The thermal power emitted by a test item is directly related to the quantity of radioactive material in it, and the total power generated by ionizing radiation absorbed in the item is measured by the calorimeter. The mass (m) of radionuclides present is calculated from the measured thermal power of an item (W) using the relationship

$$m = \frac{W}{P_{eff}} \quad , \qquad (2)$$

where P_{eff} is the effective specific power calculated from the isotopic composition of the item. For all multinuclide items, the P_{eff} is not a constant and needs to be corrected for the decay and growth of the constituent radionuclides. See reference [RE91A] for details on decay correction of plutonium-bearing items. For monoisotopic items, the specific power, P, of the radioisotope is used in place of P_{eff}. The details of determining P_{eff} and P are discussed in the following two sections.

Specific Power

The specific power, P, is the rate of energy emission by ionizing radiation per unit mass of a single radionuclide. Nuclear decay parameters can be used to calculate the specific power, in watts per gram, of a single radionuclide according to the equation

$$P = \frac{2119.3}{T_{1/2} * A} * Q \quad , \qquad (3)$$

where Q is the total disintegration energy (MeV) for alpha-particle emitters, or the average energy (MeV) of beta-particle emitters, $T_{1/2}$ is the half-life (years), and A is the gram atomic weight of the radionuclide. The specific power, P, can also be determined empirically, based on a total heat, W, measurement in watts of a single isotope, i, of known mass, m, of material in grams by rearrangement of Equation 2 to

$$P_i = \frac{W}{m} . \qquad (4)$$

The specific powers of a number of radionuclides are listed in Table 1. The values for the plutonium and americium isotopes were taken from reference [ANSI 15.22]. The uranium specific powers were calculated using Equation 3. Examination of Equation 4 shows that the specific power can be determined from direct measurement of an isotopically pure sample. The specific powers of ^{239}Pu, ^{240}Pu, ^{241}Pu, and ^{242}Pu were determined empirically on nearly pure isotopic samples. The ^{239}Pu and ^{240}Pu values were based on collaborative experiments [ST78, SE78, GU78, RU84, LU84, BE84, ST84, JA78, ST84A] while ^{241}Pu and ^{242}Pu specific powers were determined by individual experimenters [MA80, GA80, DE81, JO82, OE68, OS7620-25]. Equation 2 was used to calculate the specific power of ^{238}Pu and ^{241}Am [WA77, ST78, JO82, OE67].

The specific powers listed in Table 1 span a large range of values from a high value of over half a watt per gram of ^{238}Pu to a low value of less than 10 nW per gram of ^{238}U. The magnitude of P is inversely proportional to the half-life of the radionuclides regardless of the element. No isotopic determination is needed to determine total radioactive material mass for items containing a single isotope.

Effective Specific Power

Most items other than tritium do not contain a single radioactive isotope but rather multiple isotopes and/or multiple radioactive elements. An effective specific power, P_{eff}, in units of power per unit mass must be obtained for these items. The effective specific power of the material in the item is calculated by

$$P_{eff} = \sum_i R_i * P_i \quad , \tag{5}$$

where i includes all heat-producing radionuclides present, R_i is the abundance of the i-th radionuclide in the item, typically expressed as a mass fraction, and P_i is the specific power of the i-th radionuclide in the item in watts/gram.

Two methods exist for determining P_{eff}, a computational method and an empirical method. The computational method uses Equation 5 for determining P_{eff} and is appropriate when isotopic composition measurements can be made. The relative abundances of the radionuclides can be determined destructively using mass spectroscopy [ANN104, ANN572, AS697] or nondestructively using gamma-ray spectroscopy [RE91B, AS1030]. When measuring items in sealed containers, high-resolution gamma-ray spectroscopy using intrinsic germanium detectors is the only option for determining P_{eff}. The uncertainties on P_{eff} using gamma-ray measurements for plutonium-bearing items are generally less than 0.5%. If mass spectroscopy is used to determine P_{eff} of plutonium-bearing items, the ^{238}Pu contents should be determined using alpha spectrometry [AS697A] and ^{241}Am contents should be determined radiochemically. The effective specific power uncertainty is normally 0.1%, for isotopically homogeneous items. The computational method using gamma-ray spectroscopy for isotopic analysis is the dominant technique used in conjunction with calorimetry.

The empirical method of determining the effective specific power involves a calorimeter measurement to determine the total power produced by the sample and a chemical analysis to determine the total amount of nuclear material in the sample. Substituting these values into Equation 2 P_{eff} can be determined. The empirical method is potentially more accurate and precise than the computational method. The method can only realistically be implemented cost effectively on discrete batches of process materials or when it is difficult to determine the relative isotopic abundances of an item or batch of material. As with using mass spectroscopy in the computational method, the empirical method is a destructive technique that generates waste and requires long assay times to complete the analysis. These time and waste issues have increased the exclusive use of NDA techniques for the quantitative determination of special nuclear material (SNM) mass.

Passive Mode

In the passive mode, the most basic mode of heat-flow calorimeter operation, the only generated heat comes from the item being measured, and if a Wheatstone bridge sensor is used,

the small resistance heating of the sensors is due to the current required to excite the bridge inside the thermel.

The calibration of a passive mode calorimeter consists of determining the calorimeter sensitivity, *S*, the conversion factor between the differential voltage or resistance output of the sensor system and the thermal power of the item being measured. Whether radioactive heat standards or electrical calibration heaters are used, a series of calibration points within and bracketing the expected operating range should be measured. The number of points will depend on the magnitude of the calorimeter differential sensitivity and the calibration accuracy required. A minimum of three different standard powers should be used. The form of the calibration curve varies according to the calorimeter design but is usually well represented by a quadratic function.

A baseline measurement of the zero power calorimeter output is made. The equilibrium value of the calorimeter output is recorded as the baseline, $BP_{0(1)}$. A heat standard is then placed in the center of the calorimeter can. A measurement is started, and the equilibrium sensor output is recorded as BP_{std}. A baseline measurement is made after removing the heat source from the calorimeter can and recorded as $BP_{0(2)}$. Whether using radioactive or electrical heat standards, the calorimeter can must be removed from the calorimeter and opened between each measurement, baseline or standard. This removal is necessary even when using electrical standards to simulate as closely as possible real calorimeter operating conditions.

The average baseline, $BP_{0(av)}$ is calculated using

$$BP_{0(av)} = \frac{BP_{0(1)} + BP_{0(2)}}{2}. \tag{6}$$

Using the known power output of the heat standard, W_{std}, the calorimeter sensor value, BP_{std}, and the calculated average baseline, $BP_{0(av)}$, the sensitivity of the calorimeter can be calculated using

$$S = \frac{BP_{std} - BP_{0(av)}}{W_{std}}. \tag{7}$$

The sensitivity, *S*, is not usually a constant but varies slightly with the wattage of the standard, W_{std}, over the measurement range of the calorimeter. The change in sensitivity with power is described by

$$S = S_0 + k * W_{std} \quad , \tag{8}$$

where S_0 is the mathematically determined sensitivity for zero power and *k* is the slope of the varying sensitivity. For most calorimeters, the magnitude of *k* is less than 1% of the zero power sensitivity over the operating power range. The sensitivity usually decreases with increasing power, which is qualitatively consistent with increased thermal conductivity of the material forming the primary thermal resistance. For example, the conductivity of dry air, a common thermal-gap material, increases at the rate of 0.3% per C°. The intrinsic high-order nonlinearity of thermopile sensors can lead to differential sensitivities that are negative or positive but still relatively small compared to the base sensitivity.

Three replicate measurements (minimum) are made at each power level, with each standard measurement bracketed by a baseline measurement as previously detailed. This detailed sensitivity determination at different power levels is typically done once after a calorimeter is fabricated. By combining Equations 7 and 8 and rearranging for net sensor output, BP_{std}-$BP_{0(av)}$, the equation to relate sensor output to watts is

$$\left(BP_{std} - BP_{0(av)}\right) = S_0 * W_{std} + k * W_{std}^2. \tag{9}$$

The fit parameters S_0 and k are determined by a least-squares fit to a plot of net sensor output as a function of standard watts. Because calorimeter noise is a function of the power of the item being measured, increasing variability with increasing power, the residuals of the least-squares fit will not be normally distributed. However, the parameter estimates are not affected by this abnormal distribution.

Actual calibration data used to determine the fit parameters in Equation 9 are presented in Figure 3. The data presented in Figure 3 were obtained using a twin-bridge water-bath calorimeter. Three to five heat standards measurements were made at each power. The linearity of the calorimeter response to power is typical of water-bath calorimeters.

A plot of the first derivative of calorimeter calibration data is normally designated a differential sensitivity plot. The data are presented as a differential plot in the bottom of Figure 3. It is easier to visually quantify the differential sensitivity of the calorimeter and the relative precision of the measurements at the different powers on a differential sensitivity plot than it would be from the top plot in Figure 3. It is apparent in the bottom plot in Figure 3 that multiple measurements were made using the three lowest-power heat standards; this observation is not possible in the top plot. The precision of this calorimeter is good enough so that the multiple measurements, three each, at the largest two powers are not resolved on this scale.

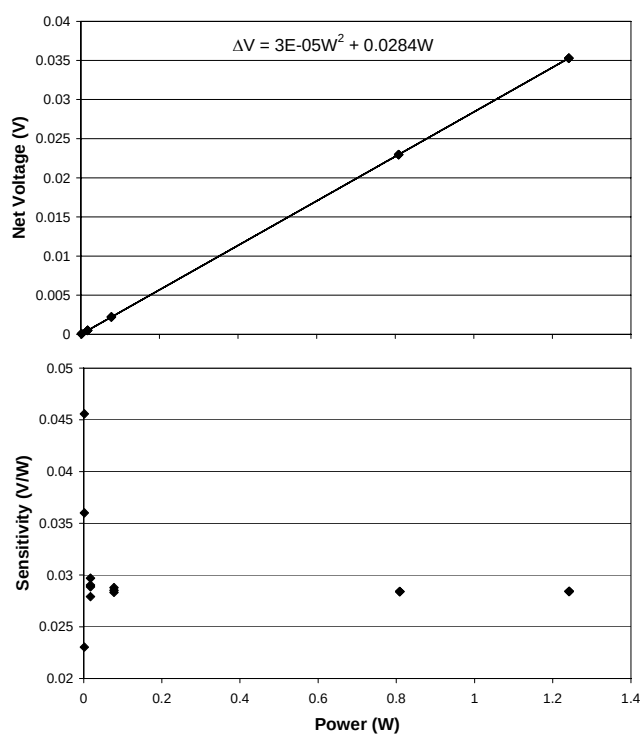

Figure 3. Top. Calibration data for a twin-bridge water-bath calorimeter. Bottom. Differential sensitivity of data presented in top plot.

The passive-mode thermal power is determined by solving Equation 9 for an unknown power, W_i. The solution to the quadratic equation when S_0>0, [MA82A] is, for k<0:

$$W_i = \frac{-S_0}{2*k} - \left[\left(\frac{-S_0}{2*k}\right)^2 - \left(\frac{BP_0 - BP_i}{k}\right)\right]^{1/2}, \tag{10}$$

and if k>0, then W_i is

$$W_i = \frac{-S_0}{2*k} + \left[\left(\frac{-S_0}{2*k}\right)^2 - \left(\frac{BP_0 - BP_i}{k}\right)\right]^{1/2}. \tag{11}$$

Equations 10 and 11 are specialized rearrangements of the more familiar form of the quadratic equation:

$$x = \frac{-b \pm \sqrt{b^2 - 4*a*c}}{2*a}. \tag{12}$$

This solution is necessary due to the rounding errors that occur using equation 12 when the product of *a* and *c* is much smaller than *b* squared.

Servo Mode

In servo mode, the inside of the calorimeter is maintained at a constant temperature through the internal heater and a servo-controlled feedback signal. A schematic flow diagram for calorimeter digital servo-control is presented in Figure 4. The digital voltage meter (DVM) measures the signal from the Wheatstone bridge. The voltage reading is sent to the computer and compared to a control point voltage. The magnitude and sign of the difference between the reading and control point determine the adjustment made to the heater via the programmer and power supply. The temperature of the calorimeter measurement chamber is held several degrees above the temperature of the constant-temperature heatsink. The constant-temperature differential is proportional to the sensor signal (voltage or resistance).

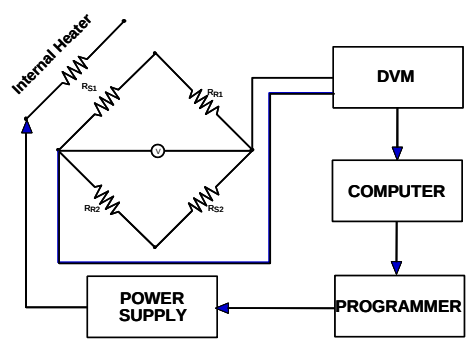

Figure 4. Schematic diagram of calorimeter digital servo control.

Calibration of a servo-mode calorimeter consists of setting the sensor output setpoint voltage corresponding to a specific base power and determining the stability of the heater power.
A single sensitivity point, S, must be determined by making a single measurement of a heat standard. Any power within the operating range of the calorimeter is satisfactory. The bridge potential average, $BP_{0(av)}$, is determined as it was for the passive mode. The bridge potential setpoint (BP_{sp}) is calculated using

$$BP_{sp} = BP_{0(av)} + S * W \quad . \tag{13}$$

The heater power is servo controlled to maintain a constant sensor output equal to BP_{sp}. The actual supplied heater power (W_0) used to maintain BP_{sp} may be slightly different from the target value, W, because of the uncertainty in S used to calculate the setpoint. Measuring a standard power that is as close as possible to the value of W will minimize the difference between W and W_0. The item power is the difference between the measured basepower, W_0, with no item in the calorimeter and the measured heater power, W_H, at equilibrium with the item present. Therefore, carefully matching W and W_0 will not increase the performance of the calorimeter in any way; it will only minimize the difference between the requested basepower and the actual basepower.

The base power, W, of a calorimeter operated in servo mode should be set 10%–20% higher than the highest-power item expected to be measured. If the basepower is set less than the power of the item to be measured, the calorimeter will not be operating in servo control at equilibrium, and a power determination cannot be made. For some calorimeter designs a servo-controlled calorimeter can be used in passive mode if it has been calibrated as described above.

The basepower, W_0, is determined the same way as a baseline is determined in passive mode. The calorimeter can is filled with a conductive material and no heat-generating items. The heater power measurement at equilibrium is the basepower, W_0, corresponding to BP_{sp}. Replicate measurements should be made of the basepower to determine the standard deviation of the value. The calorimeter is opened and closed between repeat measurements of basepower.

When a heat-generating item is inserted into the measurement chamber, the external power applied by the closed-loop controller is decreased to precisely maintain the same signal differential. The controller power drops over time until the calorimeter and item come back to the original internal temperature of the calorimeter. The power of the item being measured is the difference between the two control power readings at equilibrium.

The calculation of item power, W_i, in servo mode is

$$W_i = W_0 - W_H \quad , \tag{14}$$

where W_0 is the basepower with no item in the calorimeter and W_H is the power supplied to the calorimeter with the item in the calorimeter. The measurement time for the servo mode of operation can be shorter than for the passive mode because the calorimeter components are at the equilibrium temperature and the servo-controlled internal heater can supply heat to actively bring the item to equilibrium.

Assay Error Determination

Mixed Radionuclides Example: Plutonium and ^{241}Am Mass

The mass, M, of plutonium in an item is the total power, W, divided by the effective specific power, P_{eff}, of the item. The measurement of these two quantities is independent so the relative uncertainty for the plutonium mass, M, can be written as

$$\frac{\sigma_M}{M} = \left[\frac{\sigma_W^2}{W^2} + \frac{\sigma_{P_{eff}}^2}{P_{eff}^2} \right]^{1/2} . \tag{15}$$

The uncertainty in the power measurement, σ_W, can be obtained from replicate power measurements of heat standards or from historical data. It should include both precision and bias components. The uncertainty in P_{eff}, σ_{Peff}, comes from the uncertainty in the isotopic fractions, R_i, and isotopic specific powers, P_i. The uncertainties in the isotopic fractions are determined from uncertainties in the various techniques that might be used for the isotopic analysis, such as mass spectroscopy, alpha counting, or gamma-ray spectroscopy. There are sufficient gamma rays in plutonium to provide independent measured isotopic ratios of the major contributors to the item thermal power: ^{238}Pu, ^{240}Pu, and ^{241}Pu with respect to ^{239}Pu, and ^{241}Am with respect to total plutonium that allow R_i to be calculated. The mass fraction of ^{242}Pu, usually a minor contributor to the thermal power, is determined by isotopic correlation using the other plutonium isotopic data. The correlation technique is necessary because of the absence of gamma rays from ^{242}Pu. The uncertainties in the isotopic specific powers, P_i, as determined by different experiments, were previously given in Table 1. The test method for determining isotopic composition by gamma-ray spectroscopy is described in "C1030 Standard Test Method for Determination of Plutonium Isotopic Composition by Gamma-Ray Spectrometry" [AS1030]. Several commercially available gamma-ray analysis codes not only provide the isotopic composition but also the uncertainties of the isotopic fractions and the specific power of the item being measured. Error propagation of the isotopic fractions is discussed in Reference [SA83].

The uncertainty of the ^{241}Am mass mixed with plutonium is

$$\frac{\sigma_M}{M} = \left\{ \left(\frac{\sigma_W}{W} \right)^2 + \left(\frac{K}{P_{eff}} \right)^2 \left[\left(\frac{\sigma_K}{K} \right)^2 + \left(\frac{\sigma_{R_{Am}}}{R_{Am}} \right)^2 \right] + \left(\frac{R_{Am}\sigma_{P_{Am}}}{P_{eff}} \right)^2 \right\}^{1/2} , \tag{16}$$

where

$$K = P_{eff} - P_{Am} R_{Am} , \tag{17}$$

where P_{Am} is the specific power of ^{241}Am, R_{Am} is the mass ratio of ^{241}Am to plutonium, W is the thermal power, and σ_x are the respective uncertainties [AS1458].

Single Radionuclide Example Tritium Mass

The uncertainty of the effective specific power, P_{eff}, of tritium is the same as the isotopic specific power uncertainty; 0.00045 Watt [RU77]. Dividing by the specific power of tritium, 0.3240 W/g, results in

$$\frac{\sigma_{P_{eff}}}{P_{eff}} = 0.0014 . \tag{18}$$

So for tritium, the relative uncertainty of the tritium mass is

$$\frac{\sigma_{tritium}}{M_{tritium}} = \left[\left(\frac{\sigma_W}{W} \right)^2 + (0.0014)^2 \right]^{1/2} . \tag{19}$$

For any item containing a single radionuclide, the contribution to the uncertainty caused by the isotopic composition determination is dependent only on the specific power uncertainty for that isotope and the uncertainty on W.

Details of measurement control can be found in [BR02, ANN15.54, AS1009, ANN15.20].

III. Measurement Performance

Calorimetric assay is considered the "gold standard" of NDA measurements for items containing more than 0.5 kg of plutonium of any form in a container less than 25.5 cm in diameter. Because calorimetry can measure entire items with very high precision and low bias, the results are often comparable to destructive analysis measurements. Calorimetry is frequently used as a standard measurement to determine uncertainties and/or biases in other NDA techniques such as neutron counters [AS1207] and tomographic gamma scanner systems [HY99, LE00].

The accuracy and reliability of calorimetric assay are primarily dependent on the thermal power generated by the item and on the methods used to determine P_{eff}. The total measurement uncertainty on P_{eff} determined for pure homogeneous items using gamma-ray spectroscopy is comparable to the power measurement uncertainty [SA99]. Major factors that can affect the precision of P_{eff} determined by gamma-ray isotopic assay can be found in [AS1030]. Major factors that can affect the bias of P_{eff} determined by mass spectrometric methods can be found in [AS697]. For materials containing reasonable concentrations of plutonium (>100 g Pu/liter), the precision and bias of calorimetric assay are comparable to good chemical assay techniques [WE95]. In this case, the largest source of calorimetry error is due to the uncertainty of the specific powers, P_i, of the individual radionuclides. For single radionuclide items, the uncertainties will be due only to the power measurement and the specific power of the radionuclide. The precision of a calorimeter measurement is dependent on the sensitivity of the calorimeter, baseline stability, and item power.

For impure or heterogeneous items, calorimetric assay can have lower uncertainties than destructive analysis techniques [WE95A] because of destructive analysis sampling error. The power measurement integrates all of the heat produced by the item regardless of inhomogeneity, and for heterogeneous items, the determination of P_{eff} by gamma-ray spectroscopy is a more representative average of the entire item than destructive analysis. In this case, in which the isotopic composition of the plutonium is determined by gamma-ray spectroscopy, the final uncertainty in the gram value determined by calorimetric assay is dominated by the uncertainty of the mass fractions, R_i, in P_{eff}. Quantitative examples of the measurement precision and bias obtainable using calorimetric assay are presented in the following subsection.

Calorimetric Assay Precision and Bias Data

Calorimetry Exchange

The DOE Calorimetry Exchange (CALEX) Program distributed identical PuO_2 items containing 400 g of plutonium with 5.86% ^{240}Pu by weight. The program tabulates the results from the facility's measurements, yearly. Each facility collects data in a manner suitable for its own operations. The plutonium content and isotopic composition reference values of the mother lot of PuO_2 material used for these standards were measured by coulometry and mass spectrometry/alpha counting by four analytical laboratories. The power of the CALEX standard during the time periods of measurements described below was about 1 W.

Calorimeter biases for 23 calorimeters at five Department of Energy (DOE) facilities are presented in Figure 5. The dashed vertical lines separate the data submitted by each laboratory. These data were collected for the CALEX program over a 15-month period starting in October 1993. All measurements have a bias of less than ±0.8%. The average bias is 1.0004 with a standard deviation of the average of ±0.0002. The error expected on a single measurement would be 0.3% one relative standard deviation (1RSD).

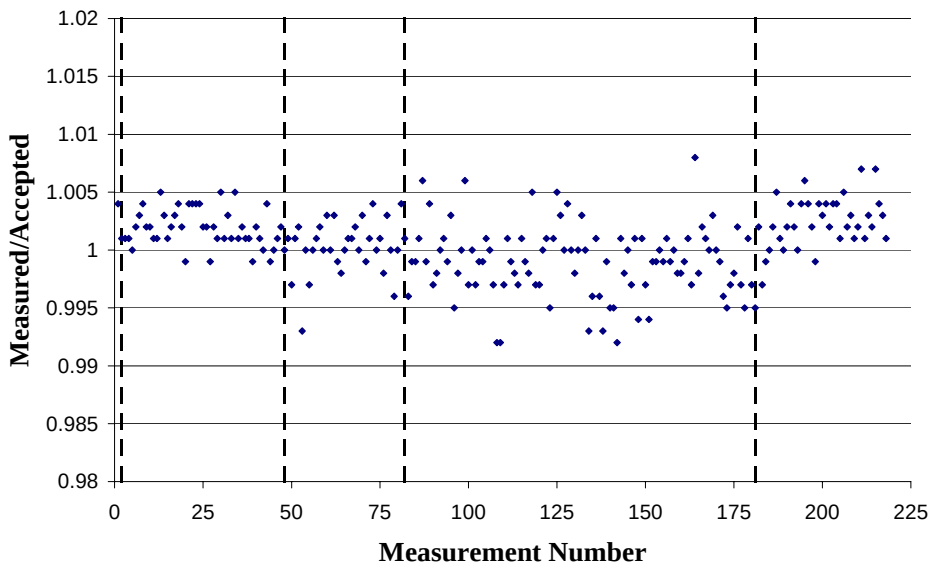

Figure 5. Calorimeter measurement biases for heat measurements of the CALEX standards. Measurements were taken over a 15-month period by five DOE laboratories using 23 different calorimeters.

The results of multiple calorimetric assay measurements by three facilities on the CALEX standards are shown in Table 2 [SP99]. The calorimetry and gamma-ray measurements used to determine plutonium mass variabilities and biases reported in Table 2 were taken over a one-year period. The within-facility variability and the bias of the calorimetric assay were calculated from results reported by each facility decayed to a common date. Each facility used different gamma-ray analysis codes for the isotopic measurements. For some, the reported values are the averages of measurements of the standard item with different calorimeters.

Table 2. Calorimetry/Gamma-Ray Assay Measurement of CALEX Standards[1]				
Facility	Within-Facility Variability, g	Within-Facility Variability, % RSD	Bias, g	Bias, % RSD
A[2]	1.5	0.38	0.03	0.01
B[2]	1.5	0.38	-0.40	-0.10
C[3]	1.4	0.36	0.04	0.01

[1]All masses are in grams of plutonium decayed to a common date.
[2]Measurements made using multiple water-bath twin-bridge calorimeters.
[3]Measurements made using "air-bath" calorimeter.

CALEX data taken at five different DOE facilities are presented in Table 3. The data were collected over an eight-year period from 1990 to 1998. Not all facilities reported results each year. Therefore, the averages contained data from a maximum of eight years and a minimum of five years. Presented in Table 3 are the average percent measurement bias and percent relative standard deviation (RSD) from repeated measurements for P_{eff} and item power. The percent bias and percent RSD are comparable for power and P_{eff} measurements on this item.

Table 3. CALEX Precision and Bias Data for P_{eff} and Power				
Facility	Power		P_{eff}	
	% Bias[1]	% RSD[2]	% Bias[1]	% RSD[2]
A	0.11	0.61	-0.23	0.10
B	0.08	0.22	0.07	0.26
C	-0.01	0.17	0.13	0.21
D	-0.08	0.30	0.02	0.20
E	0.17	0.21	-0.18	0.48

[1]% Measurement Bias = 100*[Measured – Accepted)/Accepted].
[2]% Relative Standard Deviation is based on repeated measurement of the same item.

Heat Standards

Data collected from a measurement control program can be used to calculate the precision and bias of the power measurement. A summary of the precision and bias of the power measurement obtained from replicate measurements of ^{238}Pu heat standards in production facilities over a 0.5—1.0 year period is shown in Table 4. Generally, the greater the thermal power of an item in a calorimeter, the better the relative precision. Extensive calorimetric assay precision and bias data can be found in references [BI00A, SP99, LO90, FL86, WE95A, WE95, LI87]; all of these references are summarized in [BR02].

Table 4. Calorimeter Power Measurement Precision and Bias					
Heat standard Power, Watts	Calorimeter diameter, m	Calorimeter Type, operation mode	Number of Meas.	Precision, % RSD	Bias, %
98.0	0.06	rod, servo	29	0.065	0.02
3.5	0.15	rod, servo	55	0.09	0.00
4.0	0.25	twin, passive[1]	22	0.05	0.03
4.9	0.30	twin, passive[1]	34	0.06	0.05
0.0786	0.04	Solid state, passive[2]	10	0.23	0.001

[1]Pooled results from two calorimeters.
[2]Measurements made in laboratory.

Tritium

Calorimetry was used to measure the quantity of tritium gas in containers. Because tritium was the only radioactive isotope, no isotopic measurements were required for the assays. After the calorimeter measurement, the gas was quantitatively transferred to tanks with calibrated volumes, and the quantity of tritium was determined using calibrated pressure and temperature transducers and mass spectrometric analyses. A comparison of measurement results between calorimetry and pressure/temperature measurements in a calibrated volume combined with mass spectrometric analysis (PVT/MS) was made for 50 containers [LI87]. The tritium content of the containers ranged from 15 to 16 g. The relative mean bias for the calorimetric assay compared to PVT/MS was -0.12%. One RSD of the mean was 0.05%. A twin-bridge water-bath calorimeter was used for the calorimeter measurements.

Automated Plutonium Assay System (APAS)

The precision observed from repetitive calorimeter measurements of six items containing 26 to 258 grams of Pu (17% ^{240}Pu) in PuO_2-UO_2 (26% Pu) was calculated; the results are shown in Table 5 [BI00A]. These 1,872 measurements were made over a 56-day period using a robotic loader with 24-hour-a-day operation. The calorimeter was a water-bath over-under twin bridge. A common P_{eff} factor for all six items was determined using the plutonium isotopic composition and ^{241}Am content that was determined by mass spectrometry and alpha counting. The calorimeter can size was 6.4 cm in diameter × 16.5 cm high. The calorimeter measurement time was fixed at 1 hour. The calorimeter was run in the servo mode, and the items were preconditioned to reduce the measurement time. The high-precision results listed in Table 5 are direct evidence that automated loading and unloading of items into the calorimeter can improve measurement precision. The APAS was the first implementation of a robotics-operated calorimetry assay system and showed that continuous, fast calorimeter measurements could be performed over long periods of time with high accuracy. The results also confirm the relationship between calorimeter precision and item power.

Table 5. Automated Plutonium Assay System Measurement Results[1]						
ID	Mass[1,2], g by Chem	Mass[2], g by Cal[3]/MS/α[4]	Precision[5], g	Precision, % RSD	Bias, g	Bias, %
4	257.70	257.54	0.14	0.06	-0.16	-0.06
5	206.09	206.06	0.13	0.06	-0.03	-0.02
6	206.18	206.12	0.14	0.07	-0.06	-0.03
7	128.81	128.94	0.12	0.09	0.13	0.10
8	77.28	77.35	0.12	0.15	0.07	0.09
9	25.79	25.99	0.11	0.42	0.20	0.78

[1]Mass of plutonium determined by coulometry using reference material NBS 949E. Plutonium percentage of mixed oxide, 0.25759, based on triplicate measurements of six samples.
[2]Plutonium masses reported here decayed to a common date.
[3]Final results based on 117 replicate calorimeter measurements per item.
[4]Isotopic composition determined by 12 replicate measurements by mass spectrometry (^{239}Pu, ^{240}Pu, ^{241}Pu, ^{242}Pu) and six replicate alpha-counting (^{238}Pu, ^{241}Am) measurements. Average Pu isotopic and ^{241}Am results were used to calculate P_{eff}.
[5]Precision because of calorimetry power replicate measurements.

Possible Sources of Bias because of Calorimeter Design

The following sections will describe possible sources of bias during calorimetry measurements. For most calorimeter designs, these effects are negligible but their magnitude should be quantified for all calorimeters. If a measurable effect is observed, the bias should be corrected by creating a bias correction curve across the range of the parameter being characterized.

Weight Effects

A shift in the calorimeter signal proportional to the mass of the item in the sample chamber is known as the “weight effect.” The shift is caused by stressing the temperature-sensing element of the calorimeter and is typically linear with mass. To evaluate this effect, a series of paired baseline measurements is made. First, the baseline is measured with the sample chamber empty. Second, the baseline is measured with the sample chamber loaded with non-heat-producing material of approximately the same mass as the heaviest items to be assayed. If an effect is observed, further tests should be performed at other masses to verify the linearity of the effect. Bias corrections can be made for weight effects by weighing the item to be measured and making the correction to the calorimeter output. If a weight effect is observed, the bias correction factor should be confirmed periodically as a part of the measurement control program.

Well-designed modern calorimeters should not show a weight effect. Weight effect can be identified with a single measurement of significant mass after the calorimeter has been fabricated. If a weight effect is not observed for a calorimeter, it does not need to be reevaluated.

Heat Distribution Error (HDE)

Heat distribution error (HDE) is a variation in the calorimeter response because of the location of the heat source within the measurement chamber. For example, the same heat source may

produce a larger calorimeter output in the bottom of the sample chamber than in the top. The HDE could lead to a bias if the source location is unknown. HDE is quantified by measuring the same heat source placed at different vertical positions within the calorimeter measurement well. Multiple measurements are necessary to determine if the calorimeter output for the various positions is statistically different or the same. The power of the heat source should be the same or greater than the highest expected power of the items to be measured. The magnitude of an HDE will increase with increasing power. If an HDE is measured, the uncertainty associated with HDE must be included in the final uncertainty of the power determination. An HDE can be minimized or removed by fabricating thick-walled calorimeter cans if a reduction in sample chamber size can be accommodated. Another possible solution is placing additional insulation at the top and/or bottom of the measurement chamber. The magnitude, polarity (loss or gain), and position of the HDE dictates which solution is best suited for a particular HDE. Well-designed calorimeters should not show an HDE.

Heater-Lead Error

Heater-lead error is potentially present for any calorimeter designed with built-in heaters or using insertable heaters. Even though the heater may be removable, the electrical leads should always be part of the calorimeter even during sample runs, because the heat loss or gain through the electrical leads is present when the heater is in use [BI97, BR02A]. If they are not present during item measurements, the thermal resistance of the calorimeter is changed and the electrical calibration is no longer valid. The magnitude and outcome of the effect is dependent on the design of the calorimeter (i.e., twin or gradient) and heater (insertable or fixed), the powers being measured, and what the heaters are used for (i.e., calibration, servo mode, or calorimeter response check).

For electrical calibration purposes, a four-terminal heater should be employed with two current-carrying leads and two leads for making potential measurements. The same size, type, and length of wire should be used for these leads so that the lead errors can be measured and compensated for. The use of identical wire is also necessary for heater-lead heat generation and leakage compensation in twin calorimeters. The heater circuit used in twin calorimeters is shown in Figure 6. In the configuration shown in Figure 6, passing the same current through two leads on each side of the twin calorimeter compensates for the heat generated in the leads of the calibration heater. The heater leads are usually not brought directly out of the calorimeter. The leads usually exit the calorimeter along a path that maximizes the heater-lead contact with the controlled environment. This configuration is usually accomplished by winding around the circumference of the calorimeter, as physically close to the reference temperature as possible. The heater leads should be of low-electrical resistance compared to the heater to reduce heater-lead resistive heating. The use of low-resistance copper leads minimizes electrical resistance but also constitutes a heat-leakage path out of the calorimeter, potentially leading to an electrical calibration that is biased low.

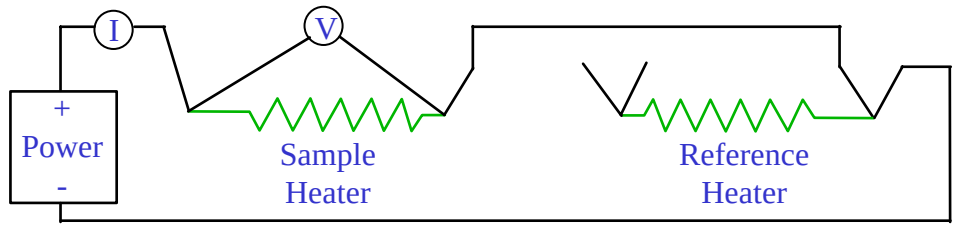

Figure 6. Twin calorimeter heater-circuit diagram.

Estimation of calorimeter heater-lead heat in gradient calorimeters is accomplished by passing a series of different currents through one current lead and out the corresponding potential lead in series. The calorimeter output at each current is compared to the calorimeter zero. The correction for the heater-lead errors should be calculated from

$$\frac{V_i - V_0}{S_i} = a\left(I_i^2 R_h\right) \quad , \tag{20}$$

where V_i is the calorimeter sensor signal with measured current, I_i, in the leads, V_0 is the sensor signal with no current in leads, S_i is the sensitivity, a is a proportionality constant relating the heat in leads to that from the heater resistance, and R_h is the heater resistance.

When the internal or insertable heater is used for calibration, the high-impedance digital voltmeters used for voltage and current measurements must be calibrated against certified electrical reference standards. If current is measured indirectly through a voltage drop across a calibrated resistor, the resistor must be a certified standard resistor. A stable high-precision power supply must be used to supply power to the heater. The calibrated voltmeter(s) and, if used, resistor must be recertified with a frequency consistent with facility-defined metrology practices.

If electrical heaters are used for calibration, a check of heater bias should be made against a certified heat standard. This check is most important for high powers, greater than a few watts, and very small powers, less than 200 mW. The cross measurement should be done if any portion of the heater circuit is changed or if a new calibration is made.

Possible Assay Interferences

- Interferences for calorimetry are those processes that would add or subtract thermal power from the power of the radionuclides being assayed.
- Interferences can be phase changes or endothermic or exothermic chemical reactions, such as oxidation.
- Radioactive decay energy can drive endothermic reactions in aqueous solutions.
- Undetected heat-generating radionuclides would add additional thermal power to the measurement.
- The accuracy of the method can be degraded for materials with inhomogeneous isotopic composition because of the increased uncertainty in the isotopic ratios.
- Room-temperature variation may affect the stability of the reference temperature and increase measurement uncertainty.

- Noise in the electronics AC supply power generated by machinery may increase the measurement uncertainty.
- Energy can be lost due to high-energy gamma rays with large branching ratios.

Parameters Affecting Assay Time

Calorimetry measurement times are typically longer than other NDA techniques. The packaging conditions and matrix of the item cannot change the heat output of the material, but they are usually the determining factor for measurement time. Time series data collected with a twin-bridge water-bath calorimeter operated in passive mode are presented in Figure 7 [SM01A]. The series of lines represent different matrix conditions. The effect of matrix on measurement time is apparent in Figure 7. It can also be seen that the matrix has no effect on the magnitude of the final answer (i.e., the bridge potential at equilibrium). For each measurement presented in Figure 7, the calorimeter can, including the matrix and source, was pre-equilibrated to the same temperature before insertion into the calorimeter. Pre-equilibration was done to minimize the time response due to starting temperature variability, therefore maximizing the time sensitivity to matrix. The different matrices containing the same 1.25 W heat standard reached equilibrium in a time range of 3 to 14 hours. The matrices in order of increasing time to equilibrium were 1/2 full salt, full foil, full salt, 1/2 full copper, and full copper.

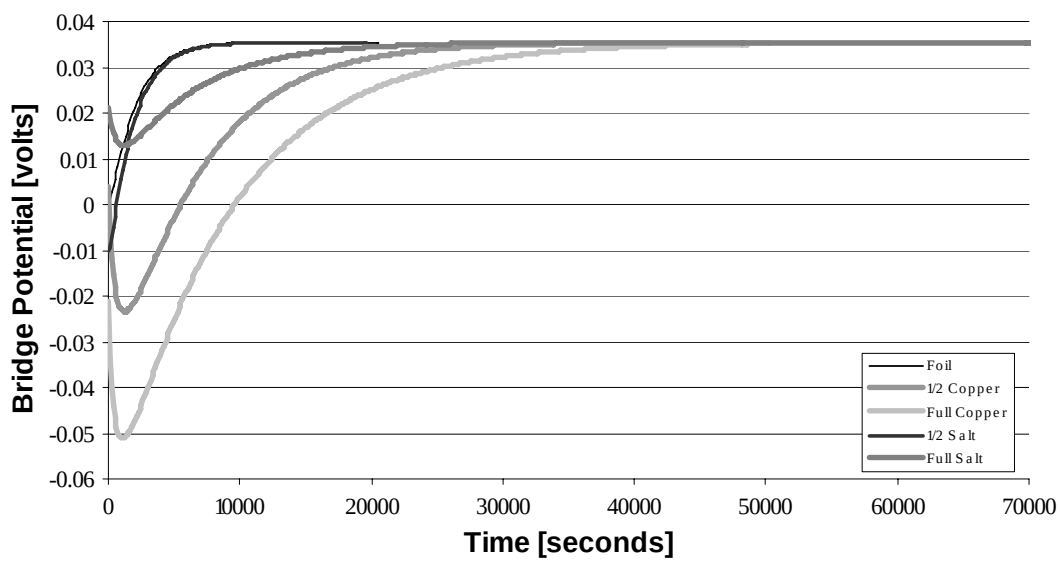

Figure 7. Graphical presentation of calorimetry matrix independence. The lines decrease in shade and increase in width with increasing time to equilibrium for clarity.

Typical assay times are between one and eight hours. Small, well-packaged thermally conductive samples can be assayed in less than one hour, but large nonconductive items, such as salts, and poorly packaged items (i.e., multiple layers of air gaps and thermal insulators) can take as long as 24 hours. Pre-equilibrating the sample temperature to match the final internal calorimeter temperature can reduce the measurement time of any sample. Pre-equilibration is usually used with a calorimeter operating in servo-control mode. An inherent benefit of the Department of Energy (DOE)/(OSS)-developed heat-flow calorimeters is that equilibrium prediction can also be used to reduce measurement times by 40% or more, depending on measurement conditions. The thermal diffusivity of the matrix of the item and its packaging will determine the thermal time constant for heat transfer from the item and hence the measurement time. Increases in measurement time are expected for items with large masses and small power, items that make poor thermal contact with their containers, items that contain a large amount of insulating material or dead air spaces, and items with multiple layers of containment.

The measurement time for the servo mode of operation can be shorter than for the passive mode because the calorimeter components are such that the equilibrium temperature and the servo-controlled internal heater can supply heat actively to drive the item to equilibrium.

The time necessary for a calorimeter to reach thermal equilibrium during the assay of an item is dependent on a number of factors: initial temperature of item relative to final equilibrium temperature of the item/calorimeter (sample preconditioning can reduce measurement time by reducing this difference), type of heat-flow calorimeter used (passive or active), calorimeter size and thermal properties (thermal conductivity and total heat capacity) of the fabrication materials, thermal properties of the item and item packaging (usually more important than calorimeter properties), size and weight of the item and the calorimeter, use of an equilibrium prediction algorithm, and required assay accuracy.

Measurement time data are presented in Table 6 and show the effects of matrix type on measurement time. The columns labeled “Eq. Time” list the times in hours it took the calorimeter to reach equilibrium. All of the items were pre-equilibrated to 24.0°C before insertion into the calorimeter. The initial internal calorimeter temperature was 25.0°C. Pre-equilibration was done so the matrix effects could be seen more easily. The calorimeter can had a volume of about three liters. The can was filled with the matrix type listed in Table 6. Measurements were made under two-power conditions: zero power and 0.8 watts of power. The size and weight of the heat standard were negligible compared to the volume of the calorimeter can, with the exception of air as the matrix. Times-to-equilibrium tracked well for both power conditions.

IV. Types of Heat-Flow Calorimeters

A variety of heat-flow calorimeter designs has been used to measure nuclear material. Four major designs that have been used for accountability measurements are (1) water-bath calorimeters, (2) solid-state calorimeters, (3) isothermal “air bath” calorimeters, and (4) fuel rod calorimeters. The air-bath and fuel-rod calorimeters described below have been operated exclusively in the servo mode, and the water-bath calorimeters have been operated in the passive or servo mode. Solid-state and water-bath calorimeters can be operated in passive or servo mode if internal heaters are built into the design.

Table 6. Item Measurement Time Dependence on Matrix Material.				
	No heat source		0.8 watt source	
Matrix Type	Mass (kg)	Eq. Time (h)	Mass (kg)	Eq. Time (h)
Air	0.668	4.8	0.766	5.0
Poly beads	1.722	25.0	1.723	18.7
Al foil (1)	0.094	6.8	0.094	5.0
Al foil (2)	0.286	6.0	0.287	5.8
Copper shot	15.820	25.3	15.824	21.5
Salt	3.102	15.0	3.358	15.0
Al bars/foil	3.636	17.0	3.636	15.0
Sand	4.580	15.0	4.580	13.8
Steel shot	13.782	27.0	13.782	30.0
Lead shot	20.738	12.5	20.739	12.5
Poly beads	1.728	20.0	-	-
Sand	4.670	16.5	-	-

Calorimeters are used to measure material in sealed storage containers (off-line) and to measure material in process (in-line). Calorimeters have been fabricated for use during material processing by mounting the calorimeter under gloveboxes. Off-line calorimeters are essential for routine facility accountability measurements, evaluation of shipper/receiver differences, and measurement of difficult material categories with unknown and/or heterogeneous matrices. Transportable calorimeters have also been built that can be moved from area to area within a facility or between facilities. Different calorimeter designs will be described in the following sub-sections.

Water-Bath Calorimeter

Heat-flow calorimeter designs developed under the OSS Technology Development Program are the most extensively used calorimeter designs throughout the DOE complex. These high-precision calorimeters are based on nickel-wire temperature sensors connected in a Wheatstone bridge configuration. A precision temperature-controlled water bath is commonly used to provide a constant reference temperature and infinite heatsink. Over two hundred heat-flow calorimeters have been built for use throughout the DOE complex and the world over the last 50 years. Currently a total of about 50 Wheatstone bridge calorimeters are being used for accountability measurements of plutonium and tritium at Los Alamos National Laboratory (LANL), Lawrence Livermore National Laboratory (LLNL), Rocky Flats, Hanford, Savannah River, and other sites.

The elements common to all current Wheatstone bridge calorimeters are labeled in Figure 8. The components are described starting from the innermost elements in Figure 8. The measurement chamber (sample and reference) is occupied by a removable calorimeter can that holds the item being assayed and provides good thermal contact with the chamber wall while preventing any potential contamination of the inside of the calorimeter. If an internal heater is specified in the calorimeter design, the circumferences of both measurement chambers are wound with manganin wire, which is used as the internal calorimeter heater. Two lengths of nickel wire are wound concentrically about the internal heater windings and serve as two sensor arms of the Wheatstone bridge. The thermal resistance between the sample sensor windings and the water bath are identical to the thermal resistance between the reference sensor windings and the water bath. This thermal resistance matching is done to maximize cancellation of water-bath temperature fluctuations in the Wheatstone bridge. The sensitivity of the calorimeter is directly proportional to the thermal resistance of the thermal gap. The thermal gap material usually consists of up to 0.3 cm of air or up to 1.0 cm of epoxy, for either type of calorimeter. The wider the thermal gap, the larger the internal temperature rise of the sample chamber for a given thermal power. The insulating material at the top and bottom of the measurement cells is used to force all of the heat radially through the sensing element.

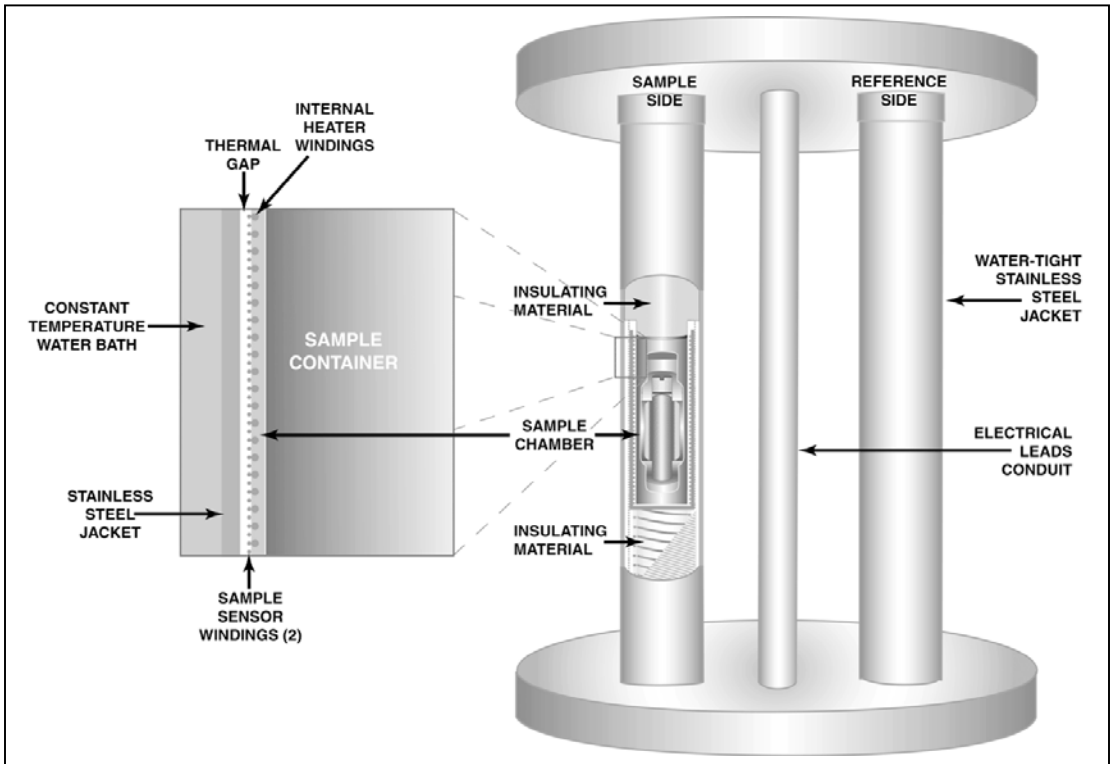

Figure 8. Schematic of a twin-bridge heat-flow calorimeter with basic components labeled.

The outermost surface of the calorimeter is a stainless-steel jacket. The stainless-steel jacket is used to keep the inside of the calorimeter dry when submerged in the water bath. A water bath with stirrer or circulating pump is used to maintain a constant reference temperature and serves as a heatsink. The water-bath reference temperature is maintained using feedback servo control. These units may use refrigeration compressors, resistance heaters, thermoelectric cooling units, evaporative cooling, or any combination of the above-listed for temperature control. The thermally stable reference bath is controlled to better than ±0.001 C°, which is critical to high-precision, low-power measurements.

Twin- and gradient-bridge are the two broad classes of water-bath calorimeters commonly in use. For both types of calorimeters, the Wheatstone bridge circuit shown in Figure 9 is used to measure heat flow. The reference and sample arms of the bridge are wound with high-purity nickel wire. The change in resistance with temperature is linear with a sensitivity of about +0.6% per C°. The temperature rise in the sample side caused by the presence of radioactive material causes the resistance of the sample arms of the Wheatstone bridge to increase while the resistances of the reference arms remain constant. This resistance change causes an imbalance in the bridge and the voltage across the bridge (the bridge potential) changes in proportion to the size of the temperature change. The reference sensor wire arms and sample sensor wire arms of the Wheatstone Bridge are each helically wound interleaved (bifilar winding) and concentrically around a cylindrical chamber. The differentiation between twin- and gradient-bridge is made based on where the arms of the Wheatstone bridge are placed relative to each other. In the twin-bridge configuration, two windings are on one measurement chamber and two windings are on an identical measurement chamber as in Figure 8. A schematic of a gradient-bridge calorimeter is presented in Figure 10. In this case, the two windings are wound concentrically about the inner pair of windings with a thermal gap between the two pairs. Twin-bridge calorimeters have also been built with the reference thermel located under and coaxial to the sample thermel (“over-under” design) to save space. This configuration is also presented in Figure 10.

Twin-bridge calorimeters are usually placed in a large (550–1,000 liters) water bath to provide a stable reference temperature. These water baths are mixed using a propeller on a shaft rotated by a motor. Multiple calorimeters have been fitted into one water bath. For heat-flow calorimeters using a water-bath reference temperature, the identical windings on the reference chamber are used as a fixed reference resistance for two arms of a Wheatstone bridge while the sample sensor windings around the sample chamber change resistance as a result of heat flow from the sample. Small reference-bath temperature fluctuations are further corrected for by the twin-bridge design. Because both the reference and sample windings have identical thermal heat paths to the reference bath, any resistance changes in the windings caused by temperature fluctuations are canceled in the twin-bridge configuration.

Gradient-bridge calorimeters usually have circulating water through an outer jacket of the calorimeter connected to a separate temperature conditioning system through connecting hoses. Smaller volumes of water, less than 76 liters, are required for this type of water-bath system. The smaller water volumes and connecting hoses increase the reference temperature noise caused by ambient room-temperature fluctuations. Also, with the gradient design, cancellation of reference temperature fluctuations are not maximized because of the time lag between when the reference arms of the bridge change resistance from temperature change and the time the sample windings change resistance because of the same temperature change of the water bath. Although the gradient calorimeter is more sensitive to bath temperature fluctuations, for higher-power measurements, these fluctuations do not add significantly to the measurement uncertainty.

A block diagram of the instrumentation and communication typically used to operate a Wheatstone bridge calorimeter is presented in Figure 11. All of the electronics used are standard, commercially produced items. A 7.5-digit digital multimeter is used to read out bridge potential, and 6.5-digit multimeters are used to read out bath temperature, bridge current, and room temperature. A General Purpose Interface Bus (GPIB) bus is used as the communication link between the electronics and the computer.

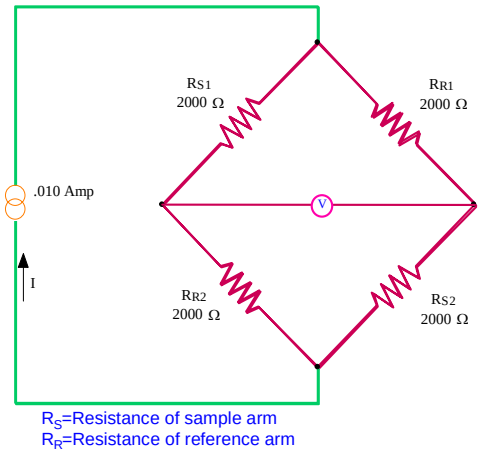

Figure 9. Example schematic of a balanced Wheatstone bridge circuit.

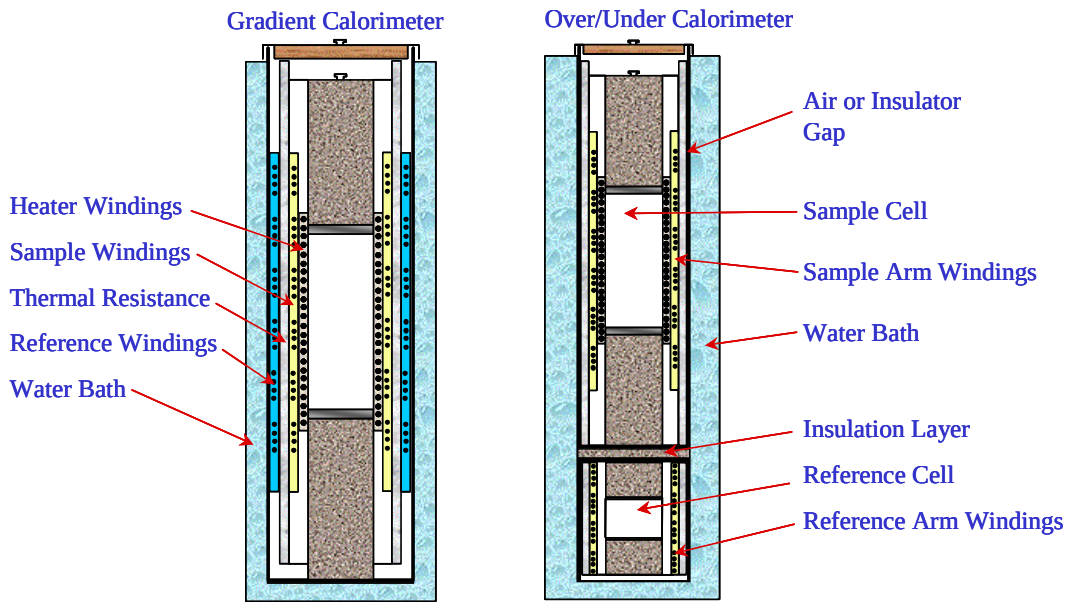

Figure 10. Schematic diagram of gradient and over-under Wheatstone bridge calorimeter.

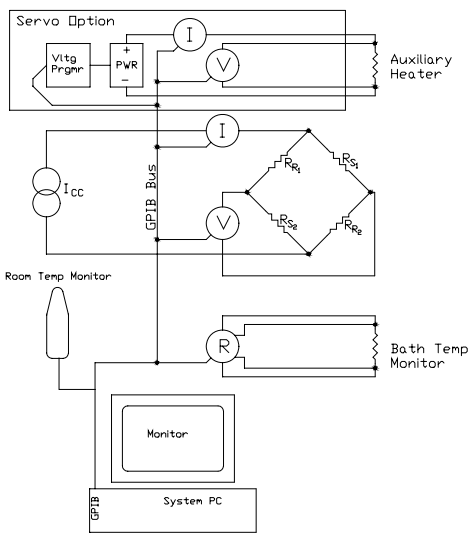

Figure 11. Typical Wheatstone bridge calorimeter electrical and communication configuration.

The advantages of twin-bridge calorimeters compared to gradient-bridge are best cancellation of thermal effects, lowest standard deviation of bridge potential, lowest detection limits, best precision and accuracy, and long-term stability.

The advantages of gradient-bridge calorimeters compared to twin-bridge are having the smallest footprint, using the fewest materials in construction, more suited to closed bath system, and making the smallest transportable calorimeter.

Solid-State Calorimeter

Solid-state calorimeters use thermopile components as heat-flow sensors [BR00, BR98, BR97]. A thermopile consists of numerous thermocouple pairs electrically connected in series. Thermocouples are formed by electrically joining one set of ends of two dissimilar conductors or semiconductors. A temperature difference between two thermocouple junctions causes the development of an electromotive force, known as the relative Seebeck effect that is proportional to the temperature difference. The greater the temperature difference, the larger the voltage measured from the sensor. The thermopile hot junctions are placed facing the sample chamber, but the cold junctions are held at the reference temperature.

A picture of a small-sample, solid-state calorimeter is presented in Figure 12. This calorimeter uses thermopile heat-flow sensors. It was designed and fabricated at Los Alamos National Laboratory and it is called the Solid-State Calorimeter System. It was fabricated from commercially available components and is capable of making high-precision measurements comparable to those made using much larger heat standards calorimeters. The data-collection electronics for the solid-state calorimeter system are commercially purchased digital voltmeters. Another benefit of using high-sensitivity thermopile sensors in calorimetric NDA systems is that the calorimeters are more robust, with excellent portability and baseline stability.

Figure 12. Picture of a high-precision solid-state calorimeter in a water bath. The IBM laptop in the foreground is used for data acquisition.

A matched pair of thermopile heat-flow sensors is used as a replacement for the more commonly used Wheatstone bridge sensors. The sensors are used in a twin configuration where one cylinder is used as a reference chamber for the cylinder that contains the heat-producing item. The electrical difference between the sample thermopile output and the reference thermopile output is measured using a nanovoltmeter.
The availability of commercially produced high-sensitivity thermopile sensors has made them a viable alternative to the high-purity nickel wire used in a Wheatstone bridge sensor. With the passive thermopile sensor there is no self-heating of the calorimeter as there is with the constant current applied to a Wheatstone bridge. Without self-heating, more accurate measurement of low-power items can be made. A water bath is used as a constant temperature heatsink, and when drained, the system is portable. After moving, the calorimeter is ready to make measurements within 24 hours.

With a source power of ~10 mW, equivalent to 4 grams of low-burnup plutonium, the relative standard deviation of six measurements using the solid-state calorimeter system was 0.11%. The extremely low noise of the heat-flow sensor has a standard deviation of 0.1 to 0.2 μV, allowing for high-precision measurements of items with powers in the submilliwatt range. The sensor response to heat is linear.

The advantages of thermopile heat-flow sensors compared to Wheatstone bridge sensors include the following: lower cost, wide commercial availability, scalability to any size or shape, passive signal, insensitivity to mechanical strains, intrinsically low noise, stable baseline (zero power output), increased portability, increased robustness, and no sensor self-heating.

The extremely stable baseline value makes it possible to reduce the frequency of or eliminate baseline measurements.

Figure 13. Photograph of the LVC with the calorimeter in up position after the 208-l drum has been loaded. The circular insulation below the drum is the LVC pedestal.

Large Volume Calorimeter (LVC)

The large-volume calorimeter (LVC) [BR04] is capable of measuring the power output from a standard 60-cm-diameter 208-l drum. With special positioning considerations, cylindrical items of up to 66 cm in diameter and up to 100 cm long can be measured in the LVC. The LVC uses thermopile heat-flow sensors that were developed for the solid-state calorimeter. The footprint of the calorimeter is 104 cm wide by 157 cm deep and 196 cm high in the closed position. The space for a standard electronics rack is also necessary.

The 208-l drums are lifted and placed onto the LVC pedestal using a drum handler. The pedestal is exposed by lifting the entire LVC shell and sensors. A photograph of the calorimeter in the open position is presented in Figure 13. The pedestal is a circular insulating plug of extruded polystyrene that prevents item heat leakage out the bottom of the calorimeter. The calorimeter consists of three concentric cylinders closed on the top and open on the bottom for the insertion of the 208-l drums and pedestal.

The LVC uses two conductive temperature zones heated by silicone rubber encapsulated wire surface heaters to provide a constant reference temperature to the cold side of the thermopile heat-flow sensors. Temperature control is achieved through servo controlled feedback loops for each heater. The temperature feedback signal is obtained from each heater through four-wire resistance readout of a thermistor. The LVC does not use any water or other significant neutron moderating or reflecting materials for temperature control. The LVC does not have the ability to actively cool.

In order to maintain a relatively small overall size, the LVC does not use any compensating chamber to reduce thermal noise in the reference temperature. Drift of the reference temperature is the largest source of noise in the system.

Isothermal "Air-Bath" Calorimeter

Isothermal air-bath calorimeters consist of three concentric cylinders separated by a heat-transfer medium. Each of the cylinders is equipped with temperature sensors. Nickel sensor wire and/or chains of thermistors may be used. The outermost cylinder is surrounded by a controlled temperature air bath rather than a water bath. The temperature sensors are measured using conventional Wheatstone bridge circuitry or by direct resistance measurement using a high-resolution multimeter. Power to control the temperature of each of the cylinders is supplied by power amplifiers. Heater coils are wound around each cylinder for this purpose.

The isothermal calorimeter operates so that each of the three concentric cylinders is at a successively lower temperature as one moves from the inner cylinder (measurement chamber) to the outer cylinder. This difference in temperature results in a temperature gradient and heat flow from the inner cylinder to the outer cylinder. The calorimeter operates in servo mode. The system controller works to maintain a constant total thermal power in the measurement chamber.

The total thermal power present in the measurement chamber is the power from the internal heaters and the power from the item being measured. Isolation from the thermal environment is achieved by circulating air through an exterior chamber either by forced air cooling using room temperature air or by a closed-loop air circuit employing a thermoelectric cooling unit to provide a sufficiently low heatsink temperature [AS1458].

Rod Calorimeter

The thermal unit of the rod calorimeter is made up of a sample chamber, item insertion/removal plug, thermal shielding, and a highly controlled heat-removal path. The calorimeter is operated in the servo mode. The heat removal path is through a highly conductive (typically copper) solid rod across which a constant temperature differential is maintained. The upper end of the rod, located at the base of the measurement chamber, is held at a constant temperature by supplying heat to the base (or side) of the measurement chamber. The lower end is held to a lower temperature, which creates a constant temperature differential. The thermal power supplied to the base of the measurement chamber is measured.

The thermal shield is made up of several components. The purpose of the thermal shield is to create a zero heat-transfer envelope around the measurement chamber with the exception of a highly controlled heat-removal path through the copper rod. Multiple constant-temperature thermal shields may be used. Depending on the ambient temperature variations, one or two shields may be incorporated. For lower power measurements, the outermost constant temperature shield is typically a controlled temperature enclosure. Temperature measurements are made using high-precision resistance measurements of a thermistor. The plug used to insulate the item being measured is a component of the zero heat-transfer envelope and mitigates thermal effects resulting from gaseous pressure differentials in the measurement chamber.

The thermal unit uses from 4–12 closed-loop control systems for control of the thermal shielding and heat removal. Control requires temperature measurement, computer control algorithms with digital-to-analog (D/A) conversion, and power supplies for driving the heaters and coolers of the thermal unit. The computer D/A outputs are connected to power supplies for driving the heaters/coolers. The power supplies are high grade, low noise, and configured in an operational amplifier mode. System stability analysis is automated and based on power variations and temperature indicators [AS1458].

V. Calorimetric Assay Applications

Table 7. Measurement Methods for LANL Pu Inventory Mass % for Each Material Form[1]

Material form	Calorimetry + gamma spec	Analytical chemistry	Neutron counter + gamma spec	Segmented gamma scanner
Metal	71%	29%	0.3%	0%
Compounds pure	64%	35%	0.9%	0.3%
Compounds impure	72%	23%	2.6%	2.6%

[1]From LANL Material Accounting and Safeguards System (MASS) database April 1999.

At present, calorimetric assay is the most precise and accurate NDA technique for the assay of many physical forms of plutonium and tritium. Calorimetry has been applied to a wide variety of plutonium-bearing solids, including metals, alloys, oxides, fluorides, mixed plutonium-uranium oxides, mixed oxide fuel pins, waste, and scrap (e.g., ash, ash heels, salts, crucibles, and graphite scarfings) [RO81, RE91]. An example of the importance of calorimetric assay of plutonium-bearing items at LANL is presented in Table 7.

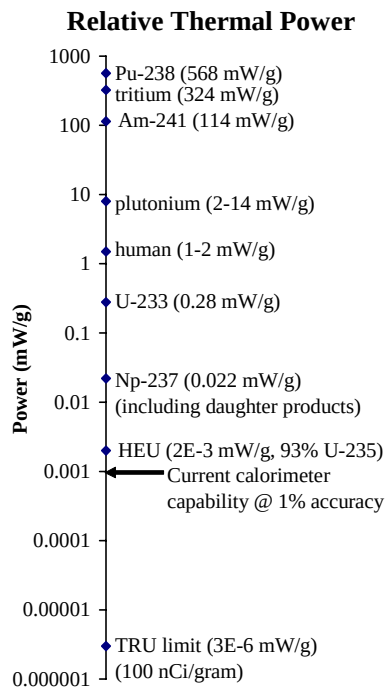

Figure 14. Relative thermal power of actinides.

Calorimetric assay has applications in a number of different areas: shipper/receiver measurements, accountability measurements, calibration of NDA standards, process control measurements, outlier resolution, and product acceptance measurements.

Of the items listed above, calibration of NDA standards and outlier resolution can only be done nondestructively using calorimetry.

Calorimetric assay can be applied to a number of different radionuclides: Plutonium, HEU, ^{233}U, ^{237}Np, ^{242,244,245}Cm, ^{250,252}Cf, ^{241,242m,243}Am, tritium, and fission products. It can be accurately used for any of the above items that fit in the instrument measurement well and are free from any chemical reactions. Figure 14 presents the range of specific powers for some of the radionuclides listed above. Items in the previous list will be discussed in the following subsections.

Plutonium

Calorimetric assay is most frequently used to measure plutonium-bearing items with varying amounts of ^{241}Am. The total amount of ^{241}Am is dependent on the time since separation and the fraction of plutonium that was originally ^{241}Pu. High-resolution gamma-ray spectroscopy measurements are usually made to determine the plutonium isotopic and ^{241}Am mass fractions; therefore, the effective specific power for plutonium-bearing items, using Equation 5. Sample calculations of typical effective specific powers for high- and low-burnup plutonium are shown in Table 8. The fraction of thermal power from each plutonium nuclide is also listed in Table 8. It should be noted that because of the inclusion of ^{241}Am, the sum of the relative fractions is greater than one by the amount of ^{241}Am contained in the sample. The mass fraction of ^{241}Am is in terms of grams per gram of plutonium. The final gram quantity of the item is determined by dividing the power by the effective specific power as shown in Equation 2.

Table 8: Plutonium Effective Specific Power Calculations.				
Radionuclide	Ri	Pi (mW/g)	Ri*Pi (mW/g)	Power (%)
High Burnup				
Pu-238	0.0120	567.57	6.8108	58.15
Pu-239	0.6253	1.9288	1.2061	10.32
Pu-240	0.2541	7.0824	1.7996	15.40
Pu-241	0.0668	3.412	0.2279	1.95
Pu-242	0.0419	0.1159	0.0049	0.04
Am-241	0.0145	114.4	1.6588	14.13
Sum	1.0146		11.6818	100.00
Low Burnup				
Pu-238	0.0001	567.57	0.0327	1.47
Pu-239	0.9636	1.9288	1.8586	83.43
Pu-240	0.0356	7.0824	0.2522	11.32
Pu-241	0.0006	3.412	0.0019	0.08
Pu-242	0.0002	0.1159	0.0000	0.00
Am-241	0.0007	114.4	0.0822	3.69
Sum	1.0007		2.2277	100.00

^{238}Pu Heat Standards Calibration and Traceability

According to ISO Guide 30 [ISO30], a reference material is an item of one or more whose property values are sufficiently homogeneous, stable, and well-established to be used for the calibration of an apparatus, the assessment of a measurement method, or for assigning values to materials. Traceability is an unbroken chain or pathway of measurement comparisons to the nationally accepted reference base. In the case of heat standards, the power measurement is traceable to NIST electrical, resistance, and voltage standards and measured with certified voltage meters. The goal should be to ensure that the standards and the materials to be measured are consistent in all important characteristics that may affect the NDA measurements. Included in ISO Guide 30 are the criteria necessary for an entity to make certified reference material (CRM). A CRM is accompanied by a certificate stating that one or more of the values are certified by a procedure that establishes traceability and uncertainty at a stated level of confidence. For heat standards with a long pedigree, the power is usually certified to 0.05%–0.1%, 95% confidence limit. The power output of ^{238}Pu heat standards used in the United States and certified by the Safeguards Science and Technology group at LANL are CRMs according to the International Standards Organization (ISO) Guide 30.

^{238}Pu oxide heat standards are the heat standard of choice across DOE facilities. Many of the ^{238}Pu heat standards used in the United States have been calibrated and in use for over 25 years. The calibration certification period is usually five years. Periodic recalibration by a heat standards calorimeter is necessary because of uncertainty in the isotopic composition, thus increasing the uncertainty in future decayed power outputs and regulations requiring recalibraton. Details of heat standards recertification can be found in reference [BR02].

Plutonium-238 heat standards have a nominal isotopic composition of 80% ^{238}Pu, 17% ^{239}Pu, and minor amounts of ^{241}Pu and ^{240}Pu. To minimize radiation dose, the oxygen used to make the oxide is usually enriched in ^{16}O to reduce the neutron dose from ^{17}O(α, n) reactions.

Tritium

Calorimetry can be used to measure the quantity of tritium in containers. In most cases tritium is the only radioactive isotope present; therefore, no isotopic measurements are required for the assays. A confirmatory gamma-ray assay may be necessary to confirm the lack of additional radionuclides for items with uncertain histories. High-precision and low-bias assays can be made on items containing more than approximately 0.01 g of tritium.

Highly Enriched Uranium (HEU)

Uranium with a natural abundance of 0.7% ^{235}U generates too little thermal power to be accurately quantified by calorimetric assay. The major component of natural uranium, ^{238}U, has too long a half-life, 4.5×10^9 years, to generate sufficient thermal power. As the 7.0×10^8 y ^{235}U mass fraction increases during enrichment, the specific power of uranium increases. Although the specific power of ^{235}U is higher than ^{238}U, the major contributor to the increase of effective specific power is the ^{234}U that is enriched along with the ^{235}U. The specific power for ^{234}U is nearly 0.2 mW/g more than three orders of magnitude larger than for ^{235}U; this is due to its relatively short half-life of 2.45×10^5 y. For an enrichment of 93% ^{235}U, the ^{234}U mass fraction is about 1%. With a mass fraction of 1%, the ^{234}U component supplies about 96% of the total thermal power from the uranium, 1.85 mW/kg. This is a power density that can be measured to an accuracy of about 1% by some calorimeters.

Table 9. Calorimetric assay of HEU results.

Material	Fraction U-235 (Wt %)	U Mass (chem.) g	U Mass (cal assay) g
U oxide	91.3	990	960 +/- 52
U oxide	66.0	990	860 +/- 31
U oxide	52.1	989	975 +/- 53
U metal	93.17	3954	4069 +/- 70

The other necessary measurement for NDA HEU calorimetric assay is determination of the uranium isotopic composition by gamma-ray spectroscopy. This requires the measurement of the relative gamma-ray peak ratios of ^{234}U, ^{235}U, and ^{238}U. An additional isotope, ^{236}U, is difficult to measure because of the lack of a suitable gamma ray; however, the ^{236}U mass fraction is typically less than 1%; therefore, not accounting for this isotope will lead to a small bias. The 121-keV gamma-ray from ^{234}U decay is critical to relate the mass fraction of ^{234}U to that of ^{235}U. The closest intense ^{235}U line above the K absorption edge of uranium is at 144 keV. Calorimetric assay measurement results on HEU metal and oxide are shown in Table 9. These measurements were made with a 12.5 cm diameter twin-bridge, water-bath calorimeter on well-characterized material [RU97].

The precision for the 1-kg items ranged from 12 to 18 % RSD, while the thermal power for the 4 kg item, 7.8 mW, was measured with a precision of about 1% RSD. The low specific power of HEU limits calorimetric assay to matrices with high uranium content, such as metal, oxides, U alloys, and high-grade scrap.

^{233}U

Another isotope of uranium, ^{233}U, is produced in a reactor by irradiation of ^{232}Th source material. An NDA technique to quantify ^{233}U is in development [RU03]. The half-life of ^{233}U, 1.59×10^5 y, is short enough so that measurable power is produced. Another power-generating isotope, ^{232}U, is produced along with the ^{233}U. Most of the gamma rays from ^{233}U materials are due to the coproduced ^{232}U. The decay schemes of ^{233}U and ^{232}U are shown in Figure 15. The short-lived 69.8 years ^{232}U decays to 1.9 years ^{228}Th that then serves as the parent of a series of subsequent decays terminating in ^{208}Pb. Some of the ^{232}U progeny are intense gamma-ray emitters, particularly ^{208}Tl that emits a series of high-energy gamma rays, the highest energy transition yielding a 2.6 MeV line. The gamma-ray flux rate is high enough so that ^{233}U must be handled behind radiation shielding. The decay rate, and the associated gamma dose rate, of the ^{232}U progeny is within 1% of the ^{232}U parent after 14 years. For ^{233}U materials of this age and older, one can then equate the progeny decay rates with the ^{232}U parent. The relatively short half-life of ^{232}U and the subsequent alpha decays contribute a significant fraction of the total heat from a ^{233}U item. For a $^{232}U/^{233}U$ mass fraction of 50 ppm, the decay heat from the ^{232}U component equals the heat from the ^{233}U component.

In parallel with the ^{232}U decay chain, a series of decays result from the ^{233}U decay chain. Uranium-233 decays into 7,340 years ^{229}Th that also serves as the parent of a series of nuclides, some of which generate high-energy gamma rays. The long-lived ^{229}Th produced by ^{233}U decay grows in at the rate of 4.4 ppm/y. The decay chain of ^{229}Th is also shown in Figure 15. Among the ^{229}Th progeny, the isotopes ^{213}Bi and ^{209}Tl have high enough gamma-ray branching ratios so that their gamma rays can be observed for aged ^{233}U. The activities of these species reach effective secular equilibrium with the ^{229}Th activity after several months. The decay of these ^{233}U progeny contributes a small fraction of the total heat.

From Figure 14 one sees that the specific power of ^{233}U is about an order of magnitude less than plutonium. This indicates that ^{233}U can be measured with precisions somewhat less than Pu for similar masses of materials. The powers, however, are within the range of applicability for most calorimeters. Another consideration for calorimetric assay of this material is that a fraction of the decay energy is in the form of high-energy gamma rays that will escape the measurement chamber. The 2.6-MeV gamma ray from ^{208}Tl represents about 2.5 % of the decay energy from ^{232}U decay. This effect can be reduced by the use of shielding material in the calorimeter chamber. Only the decay energy and mass fractions of ^{233}U and ^{232}U and their progeny are used in the calculation of P_{eff}. However, ^{234}U may also be produced in mass fractions up to several percent; exclusion of this nuclide from the calculation of P_{eff} can lead to biases.

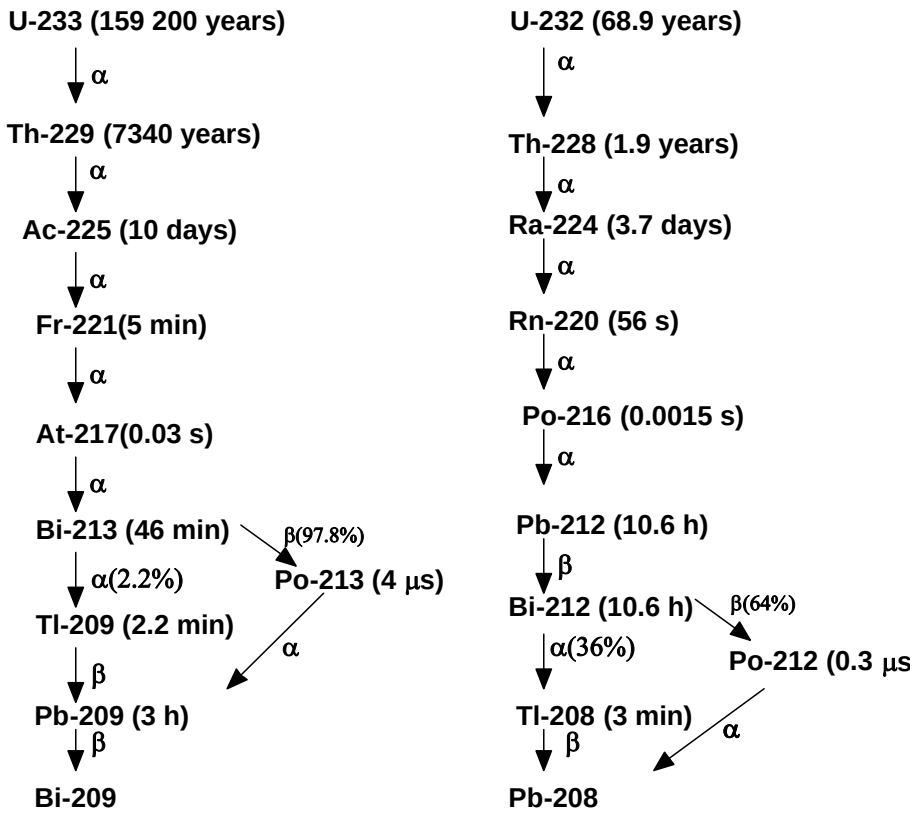

Figure 15. Radioactive decay of ^{232}U and ^{233}U progeny.

A more difficult part of ^{233}U calorimetric assay is the determination of the mass ratio ^{232}U/^{233}U because of the intense gamma flux from ^{232}U progeny, particularly ^{208}Tl. The most intense high-energy gamma ray of ^{233}U, 317 keV, has a specific activity similar to the ^{239}Pu 414 keV line. The ^{232}U progeny gamma flux generates a high Compton background in the germanium detector that requires a long count time to observe and obtain good counting statistics for the 317-keV peak. A spectrum of ^{233}U in this energy region measured by a germanium detector is shown in Figure 16. The spectrum required a measurement time of 48 hours and was measured through the port of a hot cell.

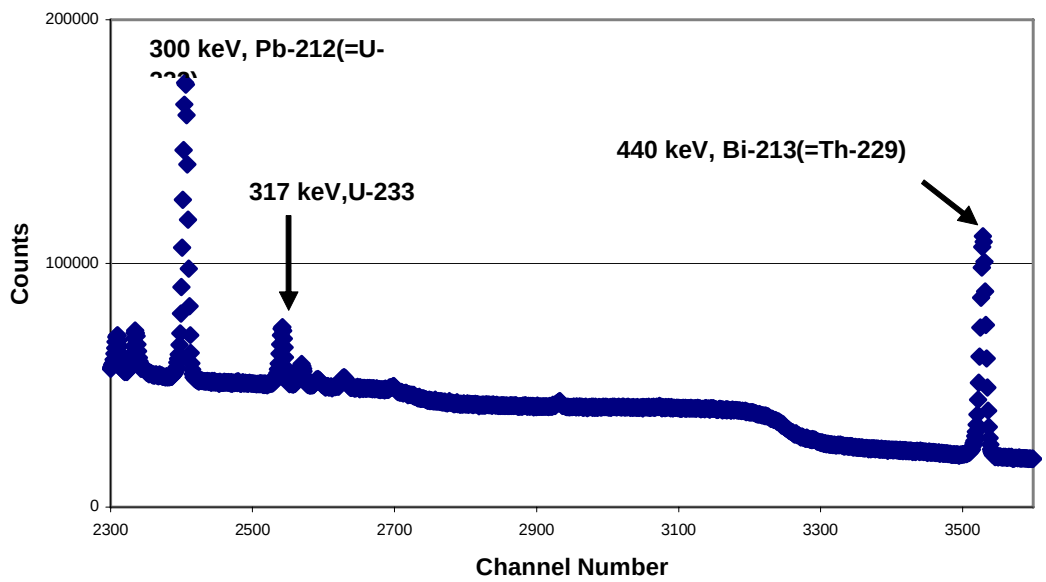

Figure 16. Important gamma rays for ^{233}U calorimetric assay.

Calorimetry and gamma-ray measurements were performed on 17 ^{233}U items with masses ranging from 41 grams to 343 grams. Gamma-ray measurements yielded ^{232}U/^{233}U ratios ranging from 4.3 to 27.9 ppm. The age of the ^{233}U, i.e., the time since chemical separation of ^{233}U from its progeny, was estimated from the ratio of ^{229}Th/^{233}U obtained from the ^{213}Bi to ^{233}U gamma ray ratio using the relationship

$$\frac{N_{Th-229}}{N_{U-233}} = \frac{\lambda_{U-233}}{\lambda_{Th-229}\lambda_{U-233}}\left(1 - e^{-(\lambda_{Th-229}-\lambda_{U-233})*t}\right) \quad , \qquad (21)$$

where N_{Th-229}/N_{U-233} is the atom ratio, λ_{Th-229}, λ_{U-233} are decay constants; and t is the time after separation. The total mass of the ^{233}U as determined by calorimetric assay was 2.17 kg as compared to the book value of 2.22 kg.

If the age of a ^{233}U item is known and the ratio of ^{229}Th/^{232}U can be determined by gamma rays of their respective progeny, then the ratio ^{232}U/^{233}U can be determined by

$$\frac{N_{U-232}}{N_{U-233}} = \left(\frac{N_{U-233}}{N_{Th-229}}\right)\left(\frac{N_{Th-229}}{N_{U-233}}\right) \quad , \qquad (22)$$

where N_i/N_j are the respective atom ratios. Using the result from this equation, P_{eff} for the ^{233}U material can be calculated. The advantage of using this more indirect way of determining the ^{232}U/^{233}U ratio is that one can use the high energy ^{212}Bi and ^{209}Tl gamma rays in the region 1.5–1.6 MeV, where the Compton background is lower then in the 0.3-MeV region, and the gamma rays are high enough in energy to penetrate significant thicknesses of shielding and intense enough to permit shorter counting times. Good agreement was observed between the direct determination of ^{232}U/^{233}U ratios that required 48-h counting times and the indirect known age technique that required 0.5-h counting times with the material in a lead-shielded drum. The high-energy ^{209}Tl 1567-keV gamma ray could be used directly with other gamma techniques

such as segmented gamma scanning to determine the ^{233}U content in heavily shielded items. Figure 17 presents a high-energy gamma ray spectrum of an aged ^{233}U item.

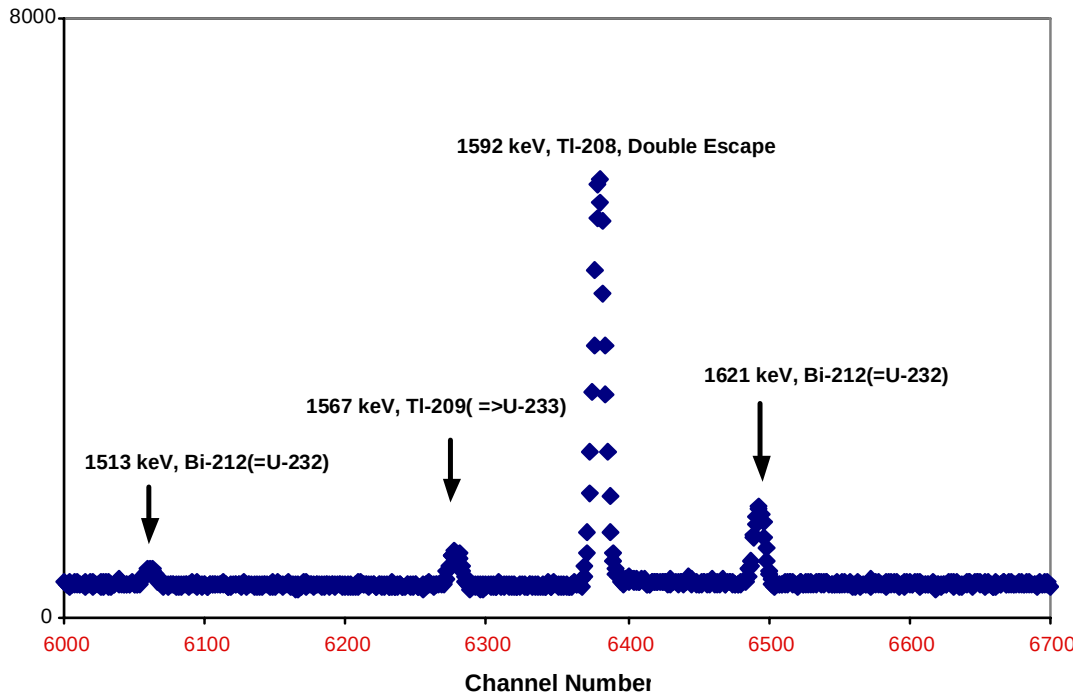

Figure 17. High-energy gamma rays for ^{233}U calorimetric assay using the 1567-keV ^{209}Tl

VI. Calorimetry Applied in Unconventional Ways

The calorimeter power measurement can be combined with other nondestructive assay information to determine previously untenable NDA measurement needs. Some of the potential applications of combining calorimetry with neutron and gamma-ray assay will be discussed in the following subsections. Calorimetry can also be applied independently to determine specific activities, total thermal power, and the specific activity of transuranic materials. Using calorimetry to determine transuranic-specific activity is discussed in the last subsection.

Combined Calorimetry/Neutron/Gamma-Ray Assay

Isotopic analysis is required for application of the calorimetric assay technique to items containing multiple types of power-generating isotopes. For most types of special nuclear material there is sufficient gamma-ray information to determine the relative abundance of these isotopes. Some nuclides, however, emit gamma rays with intensities too low to be detected. One example is ^{242}Pu. For most forms of plutonium, the mass fraction of ^{242}Pu is low and its mass fraction also can be estimated through the use of isotopic correlations, where the measured ratios of other plutonium isotopes are used to estimate the ^{242}Pu mass fraction. But in some cases the ^{242}Pu mass fraction is high, and/or there are less-accurate isotopic correlation relationships for the material type being assayed, such as for high-burnup plutonium or any previously processed plutonium. It has been found that by combining neutron counting and gamma-ray spectroscopy

with calorimetry, one can experimentally determine the ^{242}Pu mass fraction. The methodology is described below.

The measured ratio of spontaneous fission neutron emission rate to thermal power is defined by k in the following equation.

$$k = \frac{\sum_i n_i g_i}{\sum_i p_i g_i} \quad , \tag{23}$$

where n_i is the neutron emission rate of isotope i, n/s/g, caused by spontaneous fission, g_i is the mass of isotope in grams, and p_i is the isotopic specific power, W/g. The constants n_i and p_i are isotopic nuclear properties listed in reference [RE91]. The sum includes all the plutonium isotopes and ^{241}Am. The numerator of the equation is the item total neutron spontaneous fission rate that can be determined by neutron-coincidence or neutron-multiplicity counting or even singles counting techniques if there are no (α, n) or multiplication contributions. The denominator is the item power from a calorimeter measurement. We rearrange this equation so that the terms involving ^{242}Pu are on the right-hand side and divide the equation by the masses of all Pu isotopes except ^{242}Pu

$$\frac{\sum_{i'} (kp_{i'} - n_{i'}) g_{i'} + (kp_{Am} - n_{Am}) * g_{Am}}{\sum_{i'} g_{i'}} = \frac{n_{242} - kp_{242}}{g_{total} - g_{242}} \quad , \tag{24}$$

where the primes represent ^{238}Pu, ^{239}Pu, ^{240}Pu, and ^{241}Pu, and g_{total} is the total mass of plutonium in the item. The following ratios are determined by gamma-ray spectroscopy of the plutonium isotopes and ^{241}Am with measurable gamma-ray intensities.

$$R_{i'} = \frac{g_{i'}}{\sum_{i'} g_{i'}}, R_{Am'} = \frac{g_{Am-241}}{\sum_{i'} g_{i'}} \quad . \tag{25}$$

With the above definitions of R_i, the previous equation can be rearranged to yield,

$$R_{242} = \frac{1}{1 + (n_{242} - kp_{242}) \Big/ \sum_j (kp_j - n_j) * R_j} \quad , \tag{26}$$

where the summation is over the measured plutonium isotopes and ^{241}Am. All of the terms on the right hand side of the equation are physical constants and are the results of calorimetry, neutron counting, and gamma-ray measurements.

The mass fractions of the other components would be corrected by the following equation

$$R_i = R_{i'} (1 - R_{242}) \quad . \tag{27}$$

Once the mass fractions have been determined, then P_{eff} can be calculated and the calorimetry or neutron measurement result can be used to determine the plutonium mass.

Some results of using this technique on plutonium enriched in ^{242}Pu are shown in Table 10. The final masses in Table 10 were calculated using P_{eff} determined from the *cal*/*n*/α methodology. A similar approach has been investigated by Abousahl et al [AB03] with calorimeter, neutron, and gamma-ray measurements performed on medium-burnup PWR fuel pellets (6.5% ^{242}Pu). They found that better agreement with mass spectrometry results was

obtained with this technique than with isotopic correlations. The reported average relative difference between mass spectrometry and gamma-ray spectroscopy results for ^{242}Pu ranged from 0.45 +/- 1.59 % (RSD) to 4.14 +/- 2.59% depending on the gamma-ray peaks and versions of the gamma-ray code (MGA) used for the isotopic determination. Accurate ^{242}Pu mass fractions are important for plutonium assay using neutron coincidence count rates [AB03].

Table 10. Combined calorimetry/neutron/gamma-ray results on enriched plutonium.

ID	Type	% ^{242}Pu (book)	% ^{242}Pu (cal/n/γ)	Pu, g (book)	Pu, g (cal/n/γ)
G17	Metal	88.8	90.6	363	358
G17A	Metal	88.8	90.9	391	372
G20A	Metal	88.8	90.9	53	55

The same methodology described above could be applied to uranium enriched in ^{236}U. Gamma rays from ^{236}U have a low emission rate so that it is difficult to assay. Gamma-ray information is available for the other uranium isotopes ^{234}U, ^{235}U, and ^{238}U so that partial mass fractions can be determined. This information in combination with passive neutron and calorimetry measurements could be used to determine the ^{236}U mass fraction. Other combinations of radionuclides could be measured with calorimetry and neutron counting such as ^{244}Cm and plutonium or enriched uranium mixed with low levels of plutonium.

Uranium Enrichment by Combined Calorimetry/Neutron Counting

Recent developments have been made in NDA to determine uranium enrichment without gamma-ray measurements by combining calorimetry and neutron counting [RU99, RU99A]. This new technique could be useful for large items and/or items heavily shielded with high atomic number material.

The thermal power and spontaneous fission neutron emission rate of uranium have different behaviors with increasing ^{235}U enrichment. The specific power of uranium increases with increasing ^{235}U mass fraction, primarily because of the simultaneous enrichment of ^{234}U. The neutron emission rate shows the opposite behavior with increasing enrichment. The major contributor to uranium neutron emission is ^{238}U, which has a neutron emission rate 45 times that of ^{235}U. As the ^{238}U mass fraction decreases with increasing ^{235}U mass fraction, the uranium neutron emission rate decreases. The ratio of uranium thermal power to neutron emission rate thus increases with ^{235}U enrichment. Figure 18 shows the calculated ratio of power to neutron emission rate for various ^{235}U enrichments. The power to neutron emission rate increases about four orders of magnitude from depleted uranium to a ^{235}U enrichment of 97% by mass. As a result, the ratio of a calorimeter measurement result to a measured spontaneous fission neutron counting result could be used to predict the enrichment of uranium. The advantage of this technique is that the enrichment of shielded uranium could be determined even though the usual ^{235}U gamma rays would be attenuated to an unusable level. The neutrons are more penetrating radiation, and the thermal flux cannot be shielded as effectively. The low specific power and low neutron emission rate would limit the applicability of this technique to multi-kilogram quantities of uranium.

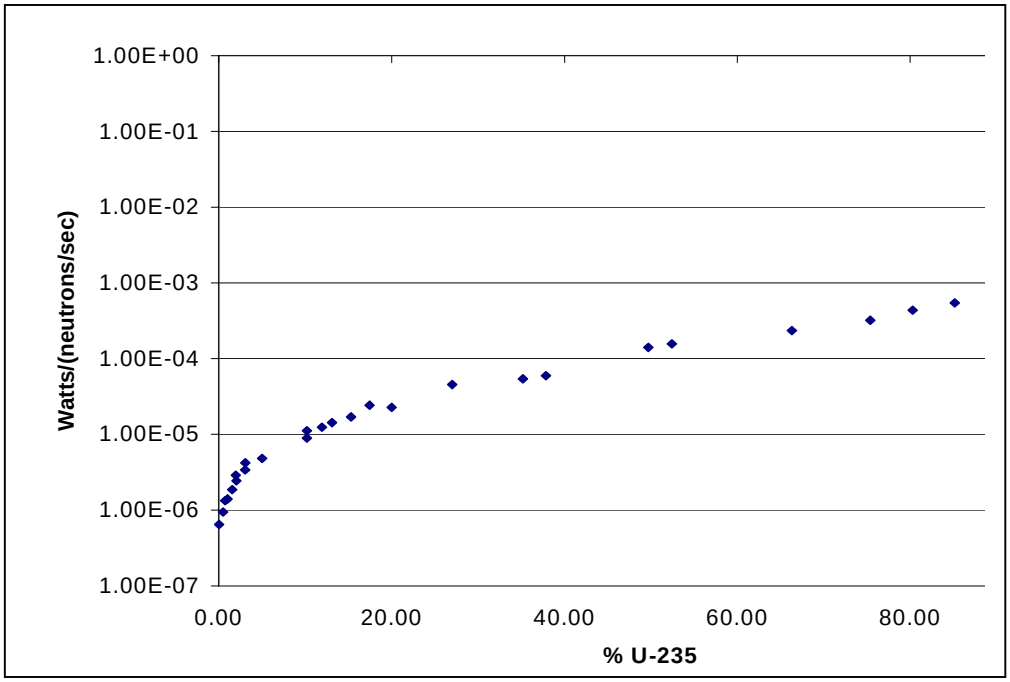

Figure 18. Uranium specific power (W)/neutron emission rate (n/s) dependence on ^{235}U enrichment.

Calorimetric Specific Activity Determination

The total alpha activity of transuranic (TRU) materials can be determined by using calorimetry independently [RU00A, RU00]. This allows all of the benefits of the calorimeter heat measurement to be applied to the activity measurement of TRU waste. The most important benefit is the integrating nature of the measurement. All of the TRU waste activity will be measured by the calorimeter because the heat produced from decay cannot be created or destroyed, shielded or attenuated.

A calorimeter is similar in principle to an event-counting nuclear instrument operated in the rate-meter mode. The calorimeter is measuring the average decay rate of the radioactive material inside the measurement chamber. The efficiency of the calorimeter is nearly 100%; therefore, all of the detectable energy is captured. The thermal power (joules/s) measured by the calorimeter can be directly converted into the total decay rate (dis/s) of the material if the average decay energy of the nuclear species in the calorimeter can be calculated.

Nearly all of the radioactive decays of uranium and transuranic elements are alpha decays. One of the plutonium isotopes, ^{241}Pu, decays primarily by beta decay, but this represents typically less than 2% of the total power emitted by alpha decay from other associated plutonium isotopes. Americium-241 is always associated with plutonium; therefore, its power contribution should be included. The Q values for alpha decay are the energy released by plutonium isotopes and ^{241}Am and these range from 5.0 MeV for ^{242}Pu to 5.6 MeV for ^{241}Am. The decay energy rate (MeV/s) can be transformed into thermal power (joules/s). The result is independent of the half-lives of the plutonium and ^{241}Am isotopes. For ^{242}Pu the corresponding power-to-decay factor is 29.5 mW/Ci and ^{241}Am 33.4 mW/Ci. In Figure 19 a plot of these conversion factors is given for plutonium with different isotopic compositions. The overall range of this conversion factor is

less than 7%. A direct calorimeter thermal power measurement could be used to measure the total alpha activity of a sample within a few percent. The procedure would be to perform the calorimeter measurement and divide the result by the appropriate factor in Figure 19. For example, for plutonium with 6% ^{240}Pu the factor would be close to 31.2 mW/Ci. The result will be independent of the matrix and the isotopic or elemental inhomogeneity of the sample.

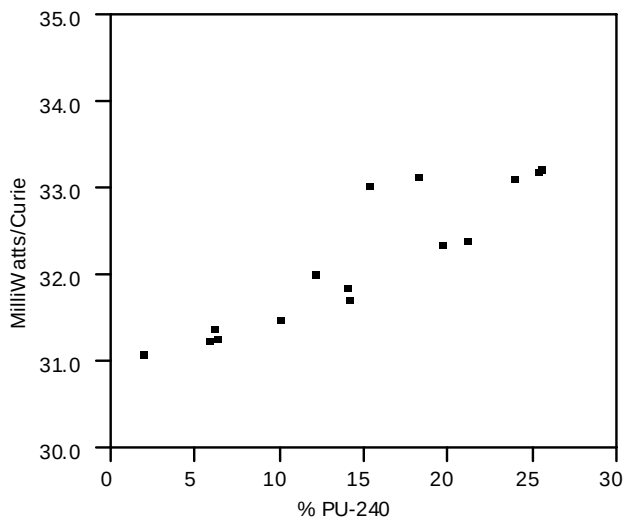

Figure 19. Thermal power/alpha activity ratios for various plutonium burnups.

VII. References

[AB03] S. Abousahl, P. van Belle, H. Ottmar, "Measurement of the Pu content and Isotopic Abundances by Combined Calorimetry, Neutron Coincidence Counting and Gamma Spectrometry," Proc. 25th Annual ESARDA Symp., May 13–15, 2003 Stockholm, Sweden.

[ANN104] Methods for Chemical, Mass Spectrometric, and Spectrochemical Analysis of Nuclear-Grade Plutonium Dioxide Powders and Pellets, ANSI N104-1973 (American National Standards Institute, Inc., New York, 1973).

[ANN572] Methods for Chemical, Mass Spectrometric, Spectrochemical, Nuclear, and Radiochemical Analysis of Nuclear-Grade Plutonium Metal, ANSI N572-1974 (American National Standards Institute, Inc., New York, 1974).

[ANN15.20] American National Standard Guide to Calibrating Nondestructive Assay Systems, ANSI N15.20.

[ANN15.22] American National Standard for Nuclear Materials—Plutonium-Bearing Solids Calibration Techniques for Calorimetric Assay, ANSI N15.22-1987.

[ANN15.54] American National Standard for Instrumentation – Radiometric Calorimeters—Measurement Control Program, ANSI N15.54.

[AS697] Standard Test Method for Chemical, Mass Spectrometric, and Spectrochemical Analysis of Nuclear-Grade Plutonium Dioxide Powders and Pellets, ASTM Standard C 697, Sections 139–147.

[AS697A] Standard Test Method for Chemical, Mass Spectrometric, and Spectrochemical Analysis of Nuclear-Grade Plutonium Dioxide Powders and Pellets, ASTM Standard C 1458-00, Sections 121-128.

[AS698] Standard Test Method for Chemical, Mass Spectrometric, and Spectrochemical Analysis of Nuclear-Grade Mixed Oxides ((U, Pu)O_2), ASTM Standard C 698.

[AS1009] Standard Guide for Establishing a Quality Assurance Program for Analytical Chemistry Laboratories Within the Nuclear Industry, ASTM Standard C 1009.

[AS1030] Standard Test Method for Determination of Plutonium Isotopic Composition by Gamma-Ray Spectrometry, ASTM Standard C 1030.

[AS1207] Standard Test Method for Nondestructive Assay of Plutonium in Scrap and Waste by Passive Neutron Coincidence Counting, ASTM Standard C 1207.

[AS1458] Standard Test Method for Nondestructive Assay of Plutonium, Tritium, and 241Am by Calorimetric Assay, ASTM Standard C 1458.

[BE84] R. J. Beckman, S. F. Marsh, R. M. Abernathy, and J. E. Rein, "Plutonium-240 Half-Life Determined by Isotope-Dilution Mass Spectrometric Measurement of the Grown-in Uranium-236," *International Journal of Applied Radiation and Isotopes*, **35**, 163–169 (1984).

[BI97] R. Biddle, J. R. Wetzel, and R. Cech, "Design and Performance of Low-Wattage Electrical Heater Probe," Proceedings of the 38th Annual Meeting of the Institute of Nuclear Materials Management, Phoenix, AZ, July (1997).

[BI00] R. S. Biddle and C. M. Schneider, "MultiCal—Software System for Calorimeter Control," Proceedings of the Institute of Nuclear Materials Management 41st Annual Meeting, New Orleans, LA, July 17–20, 2000.

[BI00A] J. Briden, M. F. Duff, R. L. Fultz, W. E. Kesling, J. R. Wetzel, A. R. Campbell, C. Fellers, J. F. Lemming, and C. R. Rudy, "Automated Plutonium Assay System (APAS) Redux," Proceedings of the Institute of Nuclear Material Management 41st Annual Meeting, New Orleans, LA, July 16–20, 2000.

[BR97] D. S. Bracken, R. Biddle and R. Cech, "Design and Performance of a Vacuum-Bottle Solid-State Calorimeter," Proceedings of the 38th Annual Meeting of the Institute of Nuclear Materials Management, Phoenix, AZ, July (1997).

[BR98] D. S. Bracken, R. Biddle, and C. Rudy, "Performance Evaluation of a Commercially Available Heat Flow Calorimeter and Applicability Assessment for Safeguarding Special Nuclear Materials," Proceedings of the 39th Annual Meeting of the Institute of Nuclear Materials Management, Naples, FL, July (1998).

[BR00] D. S. Bracken and P. Hypes, "Solid-State Calorimeter," Proceedings of the 41st Annual Meeting of the Institute of Nuclear Materials Management, New Orleans, LA, July (2000).

[BR02] D. S. Bracken, R. S. Biddle, L. A. Carrillo, P. A. Hypes, C. R. Rudy, C. M. Schneider, M. K. Smith, "Application Guide to Safeguards Calorimetry," LA-13867-M, January (2002).

[BR02A] D. S. Bracken, J. E. Schauer, and M. R. Newell, "Measured Biases Between Calorimeter Electrical Calibration System and PU-238 Heat Standards," Proceedings of the 43rd Annual Meeting of the Institute of Nuclear Materials Management, Orlando, Florida, June (2002).

[BR04] D. S. Bracken, "Performance Testing of a Large Volume Calorimeter," Proceedings of the 45th Annual Meeting of the Institute of Nuclear Materials Management, Orlando, Florida, July (2004)

[BU01] T. Burr, M. Smith, J. R. Gattiker, and D. S. Bracken, "Detecting and Characterizing Equilibrium in Calorimetry," Proceedings of the Annual Meeting of the American Statistical Association, August (2001)

[DE81] P. DeBievre, "Isotope Dilution Mass Spectrometry: Some Present Limitations and Possibilities to Overcome These," Minutes of SALE program participants meeting, July (1981) 188–207.

[EI54] J. F. Eichelberger, K. C. Jordan, S. R. Orr, and J. R. Parks, "Calorimetric Determination of the Half-Life of Polonium-210," *Physical Review* **96**, 719 (1954).

[FE79] C. L. Fellers and P. W. Seabaugh, "Real-Time Prediction of Calorimeter Equilibrium," *Nuclear Instruments and Methods* **163**, 499 (1979).

[FL86] J. G. Fleissner and M. W. Hume, Comparison of Destructive and Nondestructive Assay of Heterogeneous Salt Residues, RFP-3876, 1986.

[GA80] E. L. Garner, L. A. Machlan, "Mass Spectrometric Measurements to Determine the Half-Life of ^{241}Pu," NBS Special Publication 582, *National Bureau of Standards*, 1980, June, pp. 34–40.

[GU64] S. R. Gunn, Radiometric Calorimetry: A Review, *Nuclear Instruments and Methods* **29**, 1 (1964).

[GU70] S. R. Gunn, Radiometric Calorimetry: A Review (1970 supplement) *Nuclear Instruments and Methods* **85**, 285 (1970).

[GU78] S. R. Gunn, A calorimetric determination of the specific power of plutonium-239, *International Journal of Applied Radiation and Isotopes* **29**, 497–499 (1978).

[HY99] P. Hyman, V. Gupta, and D. Sullivan, Nuclear Materials Safeguards Matrix-Specific Qualification & Continuous Bias Correction Programs, Minutes of the Measurement Evaluation Program Meeting, New Brunswick Laboratory, Argonne, IL, May 26–27, 1999.

[IAEA87] "In-Field Calibration of Neutron Correlation Counter via Calorimetry and High Count Rate Gamma-Ray Isotopic Abundance Measurements," IAEA-SM-293/126, *Nuclear Safeguards Technology 1986* **2**, 239–249 (1987).

[ISO30] Guide to Terms and Definitions Used in Connection with Reference Materials, International Organization for Standardization, ISO Guide 30 (1992).

[JA78] A. H. Jaffey, H. Diamond, W. C. Bentley, D. G. Graczyk, and K. F. Flynn, Half-Life of ^{240}Pu, *Physical Review C*, **18**, 969–974 (1978).

[JO82] K. C. Jordan, unpublished results, Monsanto Research Corporation, Mound Laboratory, Miamisburg, Ohio (1982).

[LE00] J. P. Lestone, T. H. Prettyman, and J. D. Chavez, "Performance of the Skid-Mounted Tomographic Gamma Scanner for Assays of Plutonium Residues at RFETS," Proceedings of the Institute of Nuclear Material Management 41st Annual Meeting, New Orleans, LA, July 16–20, 2000.

[LI87] C. N. Lindsay, R. E. Sprague, and J. A. Brandenburg, A Measurement Control Study for Tritium Gas, MLM-2441, (1987).

[LO90] V. L. Longmire, T. L. Cremers, W. A. Sedlacek, S. M. Long, A. M. Scarborough, and J. R. Hurd, "Isotopic Ratios and Effective Power Determined by Gamma-Ray

Spectroscopy vs. Mass Spectroscopy for Molten Salt Extraction Residues," *Nuclear Materials Management*, Vol. XXXI Proceedings Issue, 1990.

[LU84] L. L. Lucas, and J. R. Noyce, The Half-Life of Plutonium-240, *International Journal of Applied Radiation and Isotopes* **35**, 173–176 (1984).

[MA78] A. Macdonald and D. J. Savage, Plutonium Accountancy in Reprocessing Plants by Ceric Oxidation, Ferrous Reduction and Dichromate Titration, *Nuclear Safeguards Technology* 1978, IAEA, Vienna, Austria, 1979, Vol. I, PP. 651–663.

[MA80] S. F. Marsh et al, "Plutonium-241 Half-Life Determined by Mass Spectrometric Measurements of ^{241}Pu: ^{242}Pu Ratios, *International Journal of Applied Radiation and Isotopes* **31**, 629–631 (1980).

[MA82] "The Use of Calorimetry for Plutonium Assay," J. A. Mason, UKAEA Report SRDP-R100, 1982

[MA82A] *Numerical Analysis: A Practical Approach*, Melvin J. Maron, Macmillan Publishing Co., Inc., New York, 1982, pp. 22.

[MA87] R. L. Mayer, Application of Prediction of Equilibrium to Servo-controlled Calorimetry Measurements, Proceedings of the Institute of Nuclear Materials Management 28th Annual Meeting, Newport Beach, CA, July 12–15, 1987.

[OE67] F. L. Oetting and S. R. Gunn, A Calorimetric Determination of the Specific Power and Half-Life of ^{241}Am, **29**, 2,659–2,664 (1967).

[OE68] F. L. Oetting, "Average Beta Energy of Plutonium-241 by Calorimetry, *Physical Review* **168**, No. 4, 1,398–1,401 (1968).

[OS76] D. W. Osborne and H. E. Flotnow, Half-Life of ^{242}Pu from Precise Low Temperature Heat Capacity Measurements, *Physical Review C* **14, No. 3**, 1,174–1,178 (1976).

[PE88] R. B. Perry and S. Fiarman, "Recent Developments in Fast Calorimetry," Proceedings of the Institute of Nuclear Materials Management 29th Annual Meeting, Las Vegas, NM, June 26–29, 1988.

[RE91] "Passive Non-Destructive Assay of Nuclear Materials," Doug Reilly, Norbert Ensslin, and Hastings Smith, Jr., Eds., NUREG/CR-5550, 1991, pp 641–660.

[RE91A] "Passive Non-Destructive Assay of Nuclear Materials," Doug Reilly, Norbert Ensslin, and Hastings Smith, Jr., Eds., NUREG/CR-5550, 1991, pp. 620–623.

[RE91B] "Passive Non-Destructive Assay of Nuclear Materials," Doug Reilly, Norbert Ensslin, and Hastings Smith, Jr., Eds., NUREG/CR-5550, 1991, pp. 221–271.

[RO81] "Handbook of Nuclear Safeguards Measurements," D. R. Rogers, Eds., NUREG/CR-2078, 1981, pp. 533–550.

[RU77] C. R. Rudy and K. C. Jordan, "Tritium Half-Life," Mound Facility Report MLM-2458, December 1977.

[RU84] C. R. Rudy, K. C. Jordan, and R. Tsugawa, Calorimetric Determination of the Half-Life of Plutonium-240, *International Journal of Applied Radiation and Isotopes* **35**, 177–180 (1984).

[RU97] C. Rudy, D. S. Bracken, P. Staples, L. Carrillo, R. Cech, M. Craft, J. McDaniel, and D. Fultz, "Transportable Calorimeter Measurements of Highly Enriched Uranium," Proceedings of the 38th Annual Meeting of the Institute of Nuclear Materials Management, Phoenix, AZ, July (1997).

[RU99] C. R. Rudy, "Determination of Average U-235 Enrichment and Mass of Uranium Metal without Gamma-Ray Spectroscopy," Proceedings of the 40th Annual Meeting of the Institute of Nuclear Materials Management, Phoenix, AZ, July (1999).

[RU99A] C. R. Rudy, Correlative Assay of Uranium with Calorimetry, Neutron Counting, and Mass Spectrometry Data, *Nuclear Instruments and Methods in Physics Research A* **437**, 501 (1999).

[RU00] C. Rudy, D. Bracken, M. Smith, and M. Schanfein, "Calorimetry of TRU Waste Materials," Presentation/Paper at 7th Nondestructive Assay Waste Characterization Conference, Salt Lake City, Utah, May 23-25, 2000, LA-UR-00-1741.

[RU00A] C. Rudy, D. Bracken, M. Smith, and M. Schanfein, "Calorimetry of TRU Waste Materials," Presentation/Paper at Spectrum 2000 International Conference, Chattanooga, TN, September 24–28, 2000, LA-UR-00-3761.

[RU02] C. Rudy, L. A. Foster, P. A. Hypes, L. A. Carrillo, "Combined Neutron/Calorimetry/Gamma-Ray Assay of SNM," Proceedings of the Institute of Nuclear Material Management 43rd Annual Meeting, June 23–27, 2002, Orlando, Florida.

[RU03] C. R. Rudy, P. A. Hypes, and J. R. Fitzpatrick, "Passive Nondestructive Assay of U-233," Proceedings of the Institute of Nuclear Material Management 44th Annual Meeting, July 13–17, 2003, Phoenix, Arizona.

[SA64] A. Savitzky and M. J. E. Golny, *Anal. Chem.* **36**, 1627 (1964).

[SA83] T. E. Sampson and R. Gunnink, The propagation of errors in the measurement of plutonium isotopic composition by gamma-ray spectroscopy, *Journal of the Institute of Nuclear Materials Management*, **XII, No 2.**, 39–48 (1983).

[SA99] T. S. Sampson, "Gamma-Ray Isotopic Analysis Development at Los Alamos," Los Alamos National Laboratory document, LA-13667-MS, November 1999.

[SA04] P. A. Santi, D. S. Bracken, and M. K. Smith, "Mitigation of Calorimeter Noise," Proceedings of the Institute of Nuclear Materials Management 45th annual Meeting, Orlando, FL, July 18–22, 2004, LA-UR-04-4358.

[SE78] P. W. Seabaugh and K. C. Jordan, "Calorimetric Determination of the Half-Life of Plutonium-239," *International Journal of Applied Radiation and Isotopes*, **29**, 489–496 (1978).

[SM00] M. K. Smith and D. S. Bracken, "The Development of a Multi-Exponential Prediction Algorithm for Calorimetry," Proceedings of the Institute of Nuclear Materials Management 41st Annual Meeting, New Orleans, Louisiana, July 17–20, 2000.

[SM01] M. K. Smith and D. S. Bracken, Calorimeter Prediction Based on Multiple Exponentials, *Nuclear Instruments and Methods A*, Accepted for publication, 2001.

[SM01A] Morag K. Smith, Phillip A. Hypes and David S. Bracken, "Thermal Response Based Item Identification," Proceedings of the Institute of Nuclear Materials Management 42nd Annual Meeting, Indian Wells, CA, July 15–19, 2001.

[SM03] MultiCal Version 4.0, Morag Smith, Thomas Kelley, and David Bracken, Proceedings of the 44th Annual INMM Meeting, Phoenix, Arizona, June (2003).

[SP99] "Calorimetry Exchange Program, Quarterly/Annual Data Report, Calendar Year 1998," prepared by M. Irene Spaletto and David T. Baran, NBL-353, May 1999.

[ST78] W. W. Strohm, The Measurement of the Half-Life of Plutonium-239 by the U. S. Half-Life Evaluation Committee, *International Journal of Applied Radiation and Isotopes*, **29**, 481–483 (1978).

[ST84] F. J. Steinkruger, G. M. Matlack, R. T. Beckman, The Half-Life of ^{240}Pu Determined by Specific-Activity Measurements, *International Journal of Applied Radiation and Isotopes*, **35**, 171–172 (1984).

[ST84A] W. W. Strohm, The Measurement of the Half-Life of Plutonium-240 by the U. S. Half-Life Evaluation Committee, *International Journal of Applied Radiation and Isotopes*, **35**, 155–157 (1984).

[WA77] A. H. Wapstra and K. Bos, The 1977 Atomic Mass Evaluation, *Atomic Data and Nuclear Data Tables*, **19, No. 3**, (1977).

[WE95] T. L. Welsh, L. P. McRae, C. H. Delegard, A. M. Liebetrau, W. C. Johnson, W. Theis, R. J. Lemaire, and J. Xiao, "Comparison of NDA and DA Measurement Techniques for Excess Plutonium Powders at the Hanford Site: Statistical Design and Heterogeneity Testing," Proceedings of the 36th Annual Meeting of the Institute of Nuclear Materials Management, New Orleans, Louisiana, July (1995) Vol. XXIV.

[WE95A] T. L. Welsh, L. P. McRae, C. H. Delegard, W. C. Johnson, W. Theis, R. J. Lemaire, W. Theis, M. S. Krick, J. E. Stewart, and J. Xiao, "Comparison of NDA and DA Measurements Techniques for Excess Pu Powders at the Hanford Site: Operator and IAEA Experience," Proceedings of the 36th Annual Meeting of the Institute of Nuclear Materials Management, New Orleans, Louisiana, July (1995) Vol. XXIV.

[WE97] J. R. Wetzel, T. E. Sampson, and T. L. Cremers, "Calorimeter in the Aries Recovery System," Proceedings of the Institute of Nuclear Materials Management 38th Annual Meeting, Phoenix, Arizona, July 20–24, 1997.

11. USEFUL NUCLEAR DATA FOR NDA

T. Douglas Reilly

Useful Nuclear Date – Index

1. Principal NDA Gamma-Ray Signatures
2. Major Gamma-Rays from Common Calibration Sources
3. Major K x rays of uranium and plutonium
4. Gamma Rays of ^{238}Pu
5. Gamma Rays of ^{239}Pu
6. Gamma Rays of ^{240}Pu
7. Gamma Rays of ^{241}Pu
8. Gamma Rays of ^{237}U
9. Gamma Rays of ^{241}Am
10. Kα x-ray energies, intensities and intrinsic line widths
11. Mass attenuation coefficients for various elements
12. Spontaneous Fission Neutron Yields
13. (α,n) Neutron Yields
14. Thick-Target Yields from (α,n) Reactions
15. Nuclear Data Table and Figures in PANDA

1. Principal NDA Gamma-Ray Signatures

Isotope	Energy keV	Activity γ/g-s	Mean Free Path High-Z, ρ	Low-Z, ρ
^{234}U	120.9	9.35×10^{4}	0.23	69
^{235}U	143.8	8.40×10^{3}	0.36	73
	185.7	4.32×10^{4}	0.69	80
^{238}U	766.4	2.57×10^{1}	10.0	139
	1001.0	7.34×10^{1}	13.3	159
^{238}Pu	152.7	5.90×10^{6}	0.40	75
	766.4	1.387×10^{5}	9.5	139
^{239}Pu	129.3	1.436×10^{5}	0.27	71
	413.7	3.416×10^{4}	3.7	106
^{240}Pu	45.2	3.80×10^{6}	0.07	25
	160.3	3.37×10^{4}	0.45	76
	642.5	1.044×10^{3}	7.4	127
^{241}Pu	148.6	7.15×10^{6}	0.37	74
	208.0	2.041×10^{7}	0.86	83
^{241}Am	59.5	4.54×10^{10}	0.14	38
	125.3	5.16×10^{6}	0.26	70

2. Major Gamma-Rays from Common Calibration Sources

Isotope	Half-Life	Energy (keV)	Remarks
^{241}Am	433 y	59.54	Many much weaker others
^{137}Cs	29.9 y	661.64	Mono-energetic source
^{133}Ba	10.9 y	81.0, 276.40, 302.85, 356.00, 383.85	Other weaker lines
^{60}Co	5.3 y	1173.23, 1332.51	
^{22}Na	2.8 y	511.01	Annihilation radiation
		1274.51	
^{55}Fe	2.7 y	5.9, 6.5	Mn K x rays for low energy cal
^{109}Cd	1.2 y	88.04	Mono-energetic source
^{54}Mn	312 d	834.8	Mono-energetic source
^{65}Zn	244 d	511.01	Annihilation radiation
		1115.5	
^{57}Co	271 d	122.06, 136.47	
^{75}Se	120 d	121.12, 136.00, 264.65, 279.53, 400.65	

3. Major K x rays of uranium and plutonium

X Ray	Levels (Final-Initial)	Energy (keV) Uranium	Energy (keV) Plutonium	Intensity Uranium	Intensity Plutonium
$K_{\alpha 2}$	$K - L_2$	94.67	99.55	61.9	62.5
$K_{\alpha 1}$	$K - L_3$	98.44	103.76	100	100
$K_{\beta 1}$	$K - M_3$	111.30	117.26	22.0	22.2
$K_{\beta 2}$	$K - N_{2\text{-}5}$	114.5	120.6	12.3	12.5
$K_{\beta 3}$	$K - M_2$	110.41	116.27	11.6	11.7

4. Gamma Rays of ^{238}Pu

	Energy	Intensity	Error	Energy	Intensity	Error
	43.447	3.93×10^{-4}	0.3	200.98	9.56x10-6	0.5
U $K_{\alpha 2}$	94.658	1.05x10-6	1.4	705.6	5.03x10-10	40.0
U $K_{\alpha 1}$	98.442	1.69x10-6	1.0	708.4	5.00x10-9	10.0
	99.846	7.24x10-5	0.2	742.82	5.17x10-8	1.0
$K_{\beta 3}$	110.421	2.00x10-7		766.41	2.19x10-7	0.6
$K_{\beta 1}$	111.300	3.90x10-7		786.3	3.28x10-8	1.0
$K_{\beta 4}$	114.333			805.4	1.29x10-9	15.0
$K_{\beta 2}$	114.561	1.58x10-7		808.2	8.00x10-9	3.0
$K_{\beta x}$	115.400			851.7	1.29x10-8	2.0
	152.680	9.56x10-6	0.5			

R. Gunnink, J. E. Evans, and A. L. Prindle, “A Reevaluation of the Gamma-Ray Energies and Absolute Branching Intensities of ^{237}U, $^{238, 239, 240, 241}$Pu, and ^{241}Am,” Lawrence Livermore Laboratory report UCRL-52139, October 1976.

5. Gamma Rays of ^{239}Pu

	Energy	Intensity	Error
	30.040	2.17x10-6	3.0
	38.664	1.05x10-4	1.0
	40.410	1.62x10-6	10.0
	42.060	1.65x10-6	3.0
	46.210	7.37x10-6	10.0
	46.690	5.80x10-7	6.0
	51.629	2.70x10-4	0.2
	54.040	2.00x10-6	1.4
	56.838	1.13x10-5	1.0
	65.741	4.53x10-7	4.0
	67.670	1.61x10-6	2.0
	68.720	5.10x10-6	1.0
	77.607	3.90x10-6	0.7
	78.420	1.52x10-6	1.4
	89.590		
U $K_{\alpha 2}$	94.660	4.22x10-5	0.3
	96.130	2.23x10-7	20.0
	98.441	6.76x10-5	0.3
U $K_{\alpha 1}$	98.780	1.22x10-5	3.0
	103.020	2.17x10-6	1.6
	110.421	7.95x10-6	0.8
	111.300	1.55x10-5	0.6
	111.890	3.07x10-7	10.0
$K_{\beta 2}$	114.333	6.28x10-6	2
$K_{\beta 4}$	114.561		
$K_{\beta x}$	115.380	6.49x10-6	1.5
	116.260	5.97x10-6	1.5
	119.708	3.00x10-7	2

Energy	Intensity	Error
123.62	1.97x10-7	6.0
124.51	6.13x10-7	3.0
125.21	7.11x10-7	2.0
129.294	6.26x10-5	0.2
141.657	3.20x10-7	2.0
143.35	1.73x10-7	4.0
144.211	2.83x10-6	0.6
146.077	1.190x10-5	0.6
158.1	1.00x10-8	10.0
160.16	6.20x10-8	20.0
161.45	1.20x10-6	0.4
167.81	2.93x10-8	25.0
171.344	1.105x10-6	0.8
173.7	3.05x10-8	25.0
179.19	6.58x10-7	1.0
184.55	2.12x10-8	30.0
188.23	1.09x10-7	10.0
189.32	8.30x10-7	2.0
193	8.87x10-8	10.0
195.66	1.064x10-6	0.5
196.87	3.70x10-8	12.0
203.537	5.60x10-6	0.2
225.37	1.56x10-7	4.0
227		
237.38	1.44x10-7	4.0
242.08	7.31x10-8	7.0
243.38	2.53x10-7	2.0
244.92	5.10x10-8	10.0
248.95	7.24x10-8	10.0
255.38	8.05x10-7	2.0
263.93	2.61x10-7	3.0

R. Gunnink, J. E. Evans, and A. L. Prindle, “A Reevaluation of the Gamma-Ray Energies and Absolute Branching Intensities of ^{237}U, $^{238, 239, 240, 241}$Pu, and ^{241}Am,” Lawrence Livermore Laboratory report UCRL-52139, October 1976.

5. Gamma Rays of ^{239}Pu

Energy	Intensity	Error	Energy	Intensity	Error
265.7	1.58x10-8	25	428.4	1.00x10-8	10
281.2	2.15x10-8	15	430.08	4.30x10-8	3
285.3	1.91x10-8	20	445.72	8.70x10-8	2
297.49	5.02x10-7	2	446.82	8.45x10-9	15
402.87	5.13x10-8	8	451.474	1.89x10-6	0.3
307.85	5.47x10-8	7	457.61	1.49x10-8	1
311.74	2.58x10-7	2	461.25	2.27x10-8	1
316.41	1.36x10-7	3	463.9	2.78x10-9	10
319.68	4.80x10-8	10	473.9	5.36x10-10	50
320.88	5.36x10-7	1	481.54	4.60x10-8	0.6
323.81	5.42x10-7	1	487.06	2.65x10-9	8
332.838	5.060x10-6	0.2	493.08	8.68x10-9	3
336.107	1.134x10-6	0.3	497	4.61x10-10	50
341.51	6.62x10-7	0.4	526.4	5.72x10-10	30
345.014	5.592x10-6	0.2	538.8	3.05x10-9	6
350.8	1.75x10-8	20	550.5	4.22x10-9	6
354	7.31x10-9	40	557.3	3.82x10-10	50
361.89	1.22x10-7	5	579.4	8.58x10-10	20
367.05	8.65x10-7	0.3	582.89	6.15x10-9	3
368.55	9.03x10-7	0.3	586.3	1.53x10-9	10
375.042	1.570x10-5	0.1	596	3.90x10-10	50
380.166	3.051x10-6	0.2	597.99	1.67x10-8	3
382.751	2.587x10-6	0.2	599.6	1.99x10-9	12
392.53	5.527x10-6	0.2	606.9	1.20x10-9	10
393.14			608.9	1.16x10-9	10
399.51	6.10x10-8	4	612.83	9.46x10-9	5
406.9	6.35x10-9	40	617.1	1.34x10-8	5
411.15	6.8x10-8	50	618.28	2.04x10-8	3
413.712	1.489x10-5	0.1	619.21	1.21x10-8	6
422.586	1.193x10-6	0.4	624.78	4.57x10-9	4
426.68	2.328x10-7	1.5	633.15	2.53x10-8	1.2

R. Gunnink, J. E. Evans, and A. L. Prindle, “A Reevaluation of the Gamma-Ray Energies and Absolute Branching Intensities of ^{237}U, $^{238, 239, 240, 241}$Pu, and ^{241}Am,” Lawrence Livermore Laboratory report UCRL-52139, October 1976.

5. Gamma Rays of ^{239}Pu

Energy	Intensity	Error	Energy	Intensity	Error
640.075	8.20x10-8	0.6	786.9	8.61x10-10	10
645.969	1.489x10-7	0.4	788.5	3.52x10-10	20
649.321	7.12x10-9	7	792.9	2.00x10-10	20
650.529	2.70x10-9	15	796.9	1.49x10-10	20
652.074	6.55x10-8	0.6	803.2	6.37x10-10	7
654.88	2.25x10-8	1.2	805.9	2.76x10-10	15
658.929	9.69x10-8	0.7	808.4	1.21x10-9	5
664.587	1.657x10-8	1.6	813.7	4.51x10-10	10
668.2	3.93x10-10	30	816	2.41x10-10	15
670.8	8.60x10-11	50	821.3	5.52x10-10	10
674.05	5.15x10-9	3	826.8	1.80x10-10	30
685.97	8.73x10-9	3	828.9	1.33x10-9	6
688.1	1.11x10-9	10	832.5	2.96x10-10	12
690.81	5.57x10-9	5	837.3	1.91x10-10	20
693.2	5.00x10-10	30	840.4	4.81x10-10	10
697.8	7.35x10-10	20	844	1.34x10-9	5
699.6	7.91x10-10	20	879.2	3.61x10-10	10
701.1	5.12x10-9	3	891	7.93x10-10	10
703.73	3.95x10-8	0.4	895.4	7.49x10-11	30
712.96	5.16x10-10	12	898.1	1.75x10-10	20
714.71	7.85x10-10	10	905.5	7.51x10-11	30
717.72	2.74x10-8	0.4	911.7	1.37x10-10	25
720.3	4.85x10-10	10	918.7	8.44x10-11	35
727.9	1.24x10-9	5	931.9	1.27x10-10	35
736.5	3.00x10-10	30	940.3	4.96x10-10	10
742.7	3.75x10-10	30	955.6	3.09x10-10	10
747.4	8.07x10-10	20	957.6	3.20x10-10	10
756.4	3.47x10-8	0.4	979.7	2.76x10-10	15
763.7	3.24x10-10	50	982.7	1.08x10-10	25
766.6	2.75x10-9	5	986.9	2.09x10-10	20
777.1	2.78x10-10	25	992.7	2.66x10-10	15
779.61	1.36x10-9	6	1005.7	1.78x10-10	15
			1009.4	1.40x10-10	20

R. Gunnink, J. E. Evans, and A. L. Prindle, “A Reevaluation of the Gamma-Ray Energies and Absolute Branching Intensities of ^{237}U, $^{238, 239, 240, 241}$Pu, and ^{241}Am,” Lawrence Livermore Laboratory report UCRL-52139, October 1976.

6. Gamma Rays of ^{240}Pu

	Energy	Intensity	Error		Energy	Intensity	Error
	45.232	4.53x10-4	0.2	$K_{\beta 4}$	114.333	9.32x10-8	
U $K_{\alpha 2}$	94.658	6.36x10-7	5	$K_{\beta 2}$	114.561		
U $K_{\alpha 1}$	98.422	1.02x10-6	5	$K_{\beta x}$	115.4		
	104.224	6.98x10-5	0.4		160.28	4.02x10-6	0.7
$K_{\beta 3}$	110.421	1.18x10-7			642.48	1.245x10-7	1
$K_{\beta 1}$	111.3	2.30x10-7			687.7	3.55x10-8	1.5

R. Gunnink, J. E. Evans, and A. L. Prindle, “A Reevaluation of the Gamma-Ray Energies and Absolute Branching Intensities of ^{237}U, $^{238, 239, 240, 241}$Pu, and ^{241}Am,” Lawrence Livermore Laboratory report UCRL-52139, October 1976.

7. Gamma Rays of ^{241}Pu

	Energy	Intensity	Error		Energy	Intensity	Error
	44.2	4.18x10-8		$K_{\beta 3}$	110.421	5.90x10-7	1.5
	44.86	8.36x10-9		$K_{\beta 1}$	111.3	1.09x10-6	1
	56.32	2.50x10-8		$K_{\beta 5}$	111.89	3.31x10-8	
	56.76	9.75x10-9		$K_{\beta 2}$	114.34	1.60x10-7	
	71.6	2.86x10-8	10	$K_{\beta 4}$	114.56	3.64x10-7	
	77.1	2.22x10-8	3	$K_{\beta x}$	115.4	1.34x10-7	
U $K_{\alpha 2}$	94.658	3.03x10-6	0.5		121.2	6.85x10-9	
U $K_{\alpha 1}$	98.442	4.85x10-6	0.5		148.567	1.87x10-6	0.3
	103.68	5.90x10-7	0.6		159.955	6.74x10-8	

8. Gamma Rays of ^{237}U

	Energy	Intensity	Error		Energy	Intensity	Error
	26.34	2.43x10-2	0.5	$K_{\beta x}$	118.43	8.23x10-3	
	33.19	1.30x10-3	1.6		164.58	1.84x10-2	0.5
	43.43	2.40x10-4	7		208.000	2.17x10-1	0.2
	51.005	3.40x10-3	2		221.73	2.12x10-4	2
	59.536	3.45x10-1	0.2		234.24	2.05x10-4	2
	64.832	1.30x10-2	0.5		267.54	7.40x10-3	0.5
$K_{\alpha 2}$	97.071	1.58x10-1	0.4		332.354	1.21x10-2	0.3
$K_{\alpha 1}$	101.066	2.52x10-1	0.3		335.405	9.70x10-4	1
$K_{\beta 3}$	113.3	3.04x10-2	0.5		337.75	8.90x10-5	5
$K_{\beta 1}$	114.23	5.85x10-2	0.3		340.45	1.65x10-5	20
$K_{\beta 5}$	114.95	3.35x10-3	10		368.605	4.29x10-4	2
$K_{\beta 2}$	117.34	7.90x10-3			370.934	1.103x10-3	1.4
$K_{\beta 4}$	117.58	1.56x10-2					

R. Gunnink, J. E. Evans, and A. L. Prindle, “A Reevaluation of the Gamma-Ray Energies and Absolute Branching Intensities of ^{237}U, $^{238, 239, 240, 241}$Pu, and ^{241}Am,” Lawrence Livermore Laboratory report UCRL-52139, October 1976.

9. Gamma Rays of ^{241}Am

Energy	Intensity	Error	Energy	Intensity	Error
26.344	2.45x10-2	0.1	203.87	2.90x10-8	6
32.183	1.74x10-4	1	208.000	7.91x10-6	0.5
33.197	1.26x10-3	0.3	221.73	4.24x10-7	1
59.536	0.359		233.87	4.64x10-8	6
97.072	1.18x10-5	2	234.33	6.57x10-9	40
98.951	2.03x10-4	0.5	246.7	2.42x10-8	10
101.066	1.90x10-5	1.4	260.9	1.21x10-8	15
102.966	1.95x10-4	0.5	264.85	9.04x10-8	4
			267.54	2.63x10-7	2
113.300	2.37x10-6		271.58	6.37x10-9	30
			275.68	6.57x10-8	5
114.23	4.72x10-6		291.21	3.08x10-8	10
			292.78	1.42x10-7	3
114.95			304.23	1.01x10-8	20
117.34	2.30x10-6		322.503	1.518x10-6	0.6
			332.354	1.490x10-6	0.3
117.58			335.405	4.960x10-6	0.3
118.43			337.72	4.29x10-8	5
			350.56	1.19x10-8	20
122.994	1.00x10-5	0.8	358.36	1.20x10-8	20
125.292	4.09x10-5	0.5	368.605	2.17x10-6	0.3
139.530	5.34x10-8	20.0	370.934	5.23x10-7	0.8
146.557	4.61x10-6	1	376.595	1.383x10-6	0.7
150.11	7.40x10-7	2	383.74	2.82x10-7	1.5
169.06	1.4x10-8	30	390.54	5.90x10-8	4
164.580	6.67x10-7	3.0	406.37	1.45x10-8	15
165.93	2.32x10-7	4	419.24	2.87x10-7	2
169.557	1.73x10-6	1	426.39	2.46x10-7	2
175.09	1.82x10-7	5	429.84	1.15x10-8	20
190.4	2.19x10-8		442.75	3.52x10-8	7
191.9	2.16x10-7	4	452.21	2.40x10-8	10

R. Gunnink, J. E. Evans, and A. L. Prindle, “A Reevaluation of the Gamma-Ray Energies and Absolute Branching Intensities of ^{237}U, $^{238, 239, 240, 241}$Pu, and ^{241}Am,” Lawrence Livermore Laboratory report UCRL-52139, October 1976.

Gamma Rays of ^{241}Am

Energy	Intensity	Error	Energy	Intensity	Error
454.62	9.70x10-8	3	737.29	9.00x10-8	3
459.59	3.63x10-8	7	755.91	7.60x10-8	3
467.98	2.88x10-8	7	759.46	1.67x10-8	5
486.3	1.00x10-8	30	763.4	1.96x10-9	30
512	1.15x10-8	20	766.92	5.00x10-8	3
514.2	2.58x10-8	10	770.58	4.74x10-8	4
522	9.46x10-9	30	772.13	2.66x10-8	5
574	1.25x10-8	15	777.2	6.10x10-10	50
582.6	2.32x10-9	50	780.5	2.50x10-9	20
586.52	1.31x10-8	15	788.8	3.88x10-9	15
590.28	2.86x10-8	7	801.9	1.36x10-8	10
587.42	7.41x10-8	4	811.8	6.05x10-9	12
619.001	5.94x10-7	1	819.3	4.00x10-9	15
627.2	5.64x10-9	30	822.6	2.18x10-9	25
633.01	1.26x10-8	15	828.5	2.43x10-9	25
641.42	7.10x10-8	4	851.5	3.77x10-9	15
652.96	3.77x10-7	2	854.7	2.00x10-9	20
662.421	3.64x10-6	0.3	859.2	816x10-10	30
669.9	3.80x10-9	30	862.6	5.34x10-9	10
675.8	6.40x10-9	20	887.5	2.22x10-9	20
680.06	3.13x10-8	5	898.4	7.22x10-10	40
688.77	3.25x10-7	1.5	902.5	3.00x10-9	15
693.49	3.68x10-8	4	912.4	2.50x10-9	20
696.44	5.34x10-8	3	922.2	1.91x10-9	20
709.41	6.41x10-8	2	928.8	5.52x10-10	50
721.991	1.96x10-6	0.4	945.7	5.60x10-10	50
729.52	1.33x10-8	10	955.7	5.78x10-9	10
731.5	4.70x10-9	30			

R. Gunnink, J. E. Evans, and A. L. Prindle, “A Reevaluation of the Gamma-Ray Energies and Absolute Branching Intensities of ^{237}U, $^{238, 239, 240, 241}$Pu, and ^{241}Am,” Lawrence Livermore Laboratory report UCRL-52139, October 1976.

10. Kα x-ray energies, intensities and intrinsic line widths

	Energy	Intensity ratio	Width eV		Energy	Intensity ratio	Width eV
U $K_{\alpha 1}$	94.661	0.625	104	Np $K_{\alpha 2}$	101.066		
U $K_{\alpha 2}$	98.441			Pu $K_{\alpha 1}$	99.531	0.63	112
Np $K_{\alpha 1}$	97.071	0.628	108	Pu $K_{\alpha 2}$	103.748		

11. Mass attenuation coefficients for various elements

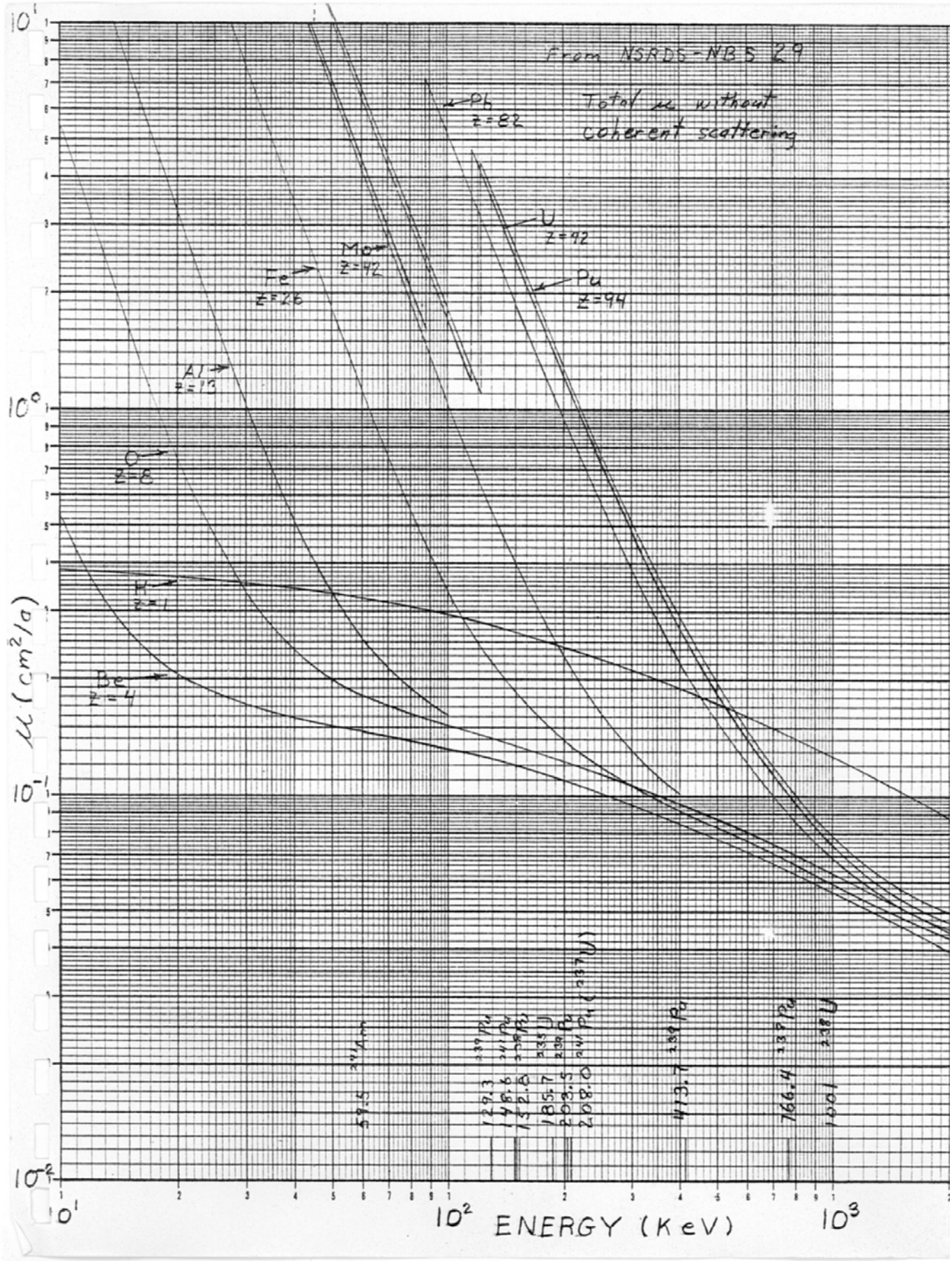

12. Spontaneous Fission Neutron Yields

Isotope A	Protons Z	Neutrons N	Half-Life	Fission Yield (n/s-g)	Spontaneous Multiplicity	Thermal Multiplicity
^{232}Th	90	142	1.41×10^{10} y	$>6 \times 10^{-8}$	2.14	1.9
^{232}U	92	140	71.7 y	1.3	1.71	3.13
^{233}U	92	141	1.59×10^{5} y	8.6×10^{-4}	1.76	2.4
^{234}U	92	142	2.45×10^{5} y	5.02×10^{-3}	1.81	2.4
^{235}U	92	143	7.04×10^{8} y	2.99×10^{-4}	1.86	2.41
^{236}U	92	144	2.34×10^{7} y	5.49×10^{-3}	1.91	2.2
^{238}U	92	146	4.47×10^{9} y	1.36×10^{-2}	2.01	2.3
^{237}Np	93	144	2.14 x 106 y	1.14×10^{-4}	2.05	2.70
^{238}Pu	94	144	87.74 y	2.59×10^{3}	2.21	2.9
^{239}Pu	94	145	2.41×10^{4} y	2.18×10^{-2}	2.16	2.88
^{240}Pu	94	146	6.56×10^{3} y	1.02×10^{3}	2.16	2.8
^{241}Pu	94	147	14.35 y	5×10^{-2}	2.25	2.8
^{242}Pu	94	148	3.76×10^{5} y	1.72×10^{3}	2.15	2.81
^{241}Am	95	146	433.6 y	1.18	3.22	3.09
^{242}Cm	96	146	163 d	2.10×10^{7}	2.54	3.44
^{244}Cm	96	148	18.1 y	1.08×10^{7}	2.72	3.46
^{249}Bk	97	152	320 d	1.0×10^{5}	3.40	3.7
^{252}Cf	98	154	2.646 y	2.34×10^{12}	3.757	4.06

13. (α,n) Neutron Yields

Isotope A	Total Half-Life	Yield (α/s-g)	Mean Energy (MeV)	(α,n) Yield in Oxide (n/s-g)	(α,n) Yield in UF_6/PuF_4
^{232}Th	1.41×10^{10} y	4.1×10^{3}	4.00	2.2×10^{-5}	
^{232}U	71.7 y	8.0×10^{11}	5.30	1.49×10^{4}	2.6×10^{6}
^{233}U	1.59×10^{5} y	3.5×10^{8}	4.82	4.8	7.0×10^{2}
^{234}U	2.45×10^{5} y	2.3×10^{8}	4.76	3.0	5.8×10^{2}
^{235}U	7.04×10^{8} y	7.9×10^{4}	4.40	7.1×10^{-4}	0.08
^{236}U	2.34×10^{7} y	2.3×10^{6}	4.48	2.4×10^{-2}	2.9
^{238}U	4.47×10^{9} y	1.2×10^{4}	4.19	8.3×10^{-5}	0.028
^{237}Np	2.14 x 106 y	2.6×10^{7}	4.77	3.4 x 10-1	
^{238}Pu	87.74 y	6.4×10^{11}	5.49	1.34×10^{4}	2.2×10^{6}
^{239}Pu	2.41×10^{4} y	2.3×10^{9}	5.15	3.81×10^{1}	5.6×10^{3}
^{240}Pu	6.56×10^{3} y	8.4×10^{9}	5.15	1.41×10^{2}	2.1×10^{4}
^{241}Pu	14.35 y	9.4×10^{7}	4.89	1.3	1.7×10^{2}
^{242}Pu	3.76×10^{5} y	1.4×10^{8}	4.90	2.0	2.7×10^{2}
^{241}Am	433.6 y	1.3×10^{11}	5.48	2.69×10^{3}	
^{242}Cm	163 d	1.2×10^{14}	6.10	3.76×10^{6}	
^{244}Cm	18.1 y	3.0×10^{12}	5.80	7.73×10^{4}	
^{249}Bk	320 d	8.8×10^{8}	5.40	1.8×10^{1}	
^{252}Cf	2.464 y	1.9×10^{13}	6.11	6.0×10^{5}	

14. Thick-Target Yields from (α,n) Reactions

Element	Yield per 10^6 α @ 4.7 MeV (^{234}U)	Yield per 10^6 α @ 5.2 MeV (Pu)	Mean n Energy (MeV) for 5.2 MeV α
Li	0.16 ± 0.04	1.13 ± 0.25	0.3
Be	44 ± 4	65 ± 5	4.2
B	12.4 ± 0.6	17.5 ± 0.4	2.9
C	0.051 ± 0.002	0.078 ± 0.004	4.4
O	0.040 ± 0.001	0.059 ± 0.002	1.9
F	3.1 ± 0.3	5.9 ± 0.6	1.2
Na	0.5 ± 0.5	1.1 + 0.5	
Mg	0.42 ± 0.03	0.89 ± 0.02	2.7
Al	0.13 ± 0.01	0.41 ± 0.01	1.0
Si	0.028 ± 0.002	0.076 ± 0.003	1.2
Cl	0.01 ± 0.01	0.07 ± 0.04	

15. Nuclear Data Tables and Figures in PANDA

Title	Table/Figure	Page
HPGe gamma-ray spectrum of HEU	Fig. 1.7	12
HPGe gamma-ray spectrum of DU	Fig. 1.9	14
HPGe gamma-ray spectrum of Pu	Fig. 1.10	15
HPGe gamma-ray spectrum of spent MTR fuel	Fig. 1.13	20
HPGe gamma-ray spectrum of spent PWR fuel	Fig. 1.14	21
Linear attenuation coefficient of NaI (graph)	Fig. 2.3	29
Compton Edge energy	Fig. 2.9	37
Mass attenuation coefficient of various elements (graph)	Fig. 2.12	39
HPGe gamma-ray spectrum of low-burnup Pu	Fig. 5.1	97
HPGe gamma-ray spectrum of natural uranium	Fig. 5.2	98
Expression for net full-energy peak area	Table 5-5	128-9
Mass attenuation coefficient of various element (graph)	Fig. 6.1	162
Attenuation correction factors for slab, cylinder, and sphere	Fig. 6.3	168
Gamma rays from uranium nuclides	Table 7-1	197
^{241}Am contribution to ^{237}U gamma-ray peaks	Fig. 8.2	224
Useful plutonium gamma rays in various energy regions	Table 8-2	228
Separated Pu gamma-ray spectrum in 40-keV region	Fig. 8.5	229
Peak energies and intensities in 40-keV region	Table 8-3	230
Peak energies and intensities in 100-keV region	Table 8-4	231
Gamma-ray spectrum in 100-keV region	Fig. 8.6	232
Peak energies and intensities in 125-keV region	Table 8-5	233
Gamma-ray spectrum in 125-keV region	Fig. 8.7	234
Peak energies and intensities in 148-keV region	Table 8-6	235
Gamma-ray spectrum in 148-keV region	Fig. 8.8	236
Peak energies and intensities in 160-keV region	Table 8-7	236
Gamma-ray spectrum in 160-keV region	Fig. 8.9	237
Peak energies and intensities in 208-keV region	Table 8-9	239
Gamma-ray spectrum in 208-keV region	Fig. 8.10	239
Peak energies and intensities in 332-keV region	Table 8-10	240
Gamma-ray spectrum in 332-keV region	Fig. 8.11	241
Gamma-ray spectrum in 375-keV region	Fig. 8.12	242
Peak energies and intensities in 375-keV region	Table 8-12	243
Gamma-ray spectrum in 640-keV region	Fig. 8.13	244
Peak energies and intensities in 640-keV region	Table 8-13	245
Measured prompt fission multiplicity distributions	Table 11-2	342
Characteristics of ^{252}Cf	Table 11-7	351
Total neutron cross section of ^{239}Pu	Fig. 12.3	362
Low-energy total neutron cross section of cadmium	Fig. 12.5	363
Fission cross section for important U and Pu nuclides	Fig. 12.6	364
Neutron cross section of common materials	Table 12-3	368-9
Fuel and core parameters for PWR, BWR, and FBR	Table 18-1	530
Mass distribution of thermal fission products of ^{235}U and ^{239}Pu	Fig. 18.2	533
Nuclides measurable by gamma rays in irradiated fuel	Table 18-3	535
Fission-product gamma ray activity variation with cooling time	Fig. 18.6	540
Typical magnitudes of holdup in facility equipment	Table 20-3	598

Specific power values for plutonium nuclides	Table 21-1	621
Guide to NDA techniques	Table 223-1	670-7
Standard deviation of the standard deviation (repeated assay)	Table A-2	681
Biological effects of whole body radiation	Table B-3	687
Minimum critical masses for fully-reflected, bare spheres	Table C-1	690